Physical Principles of Plastic Deformation

P. Polukhin, S. Gorelik and V. Vorontsov

Mir Publishers
Moscow

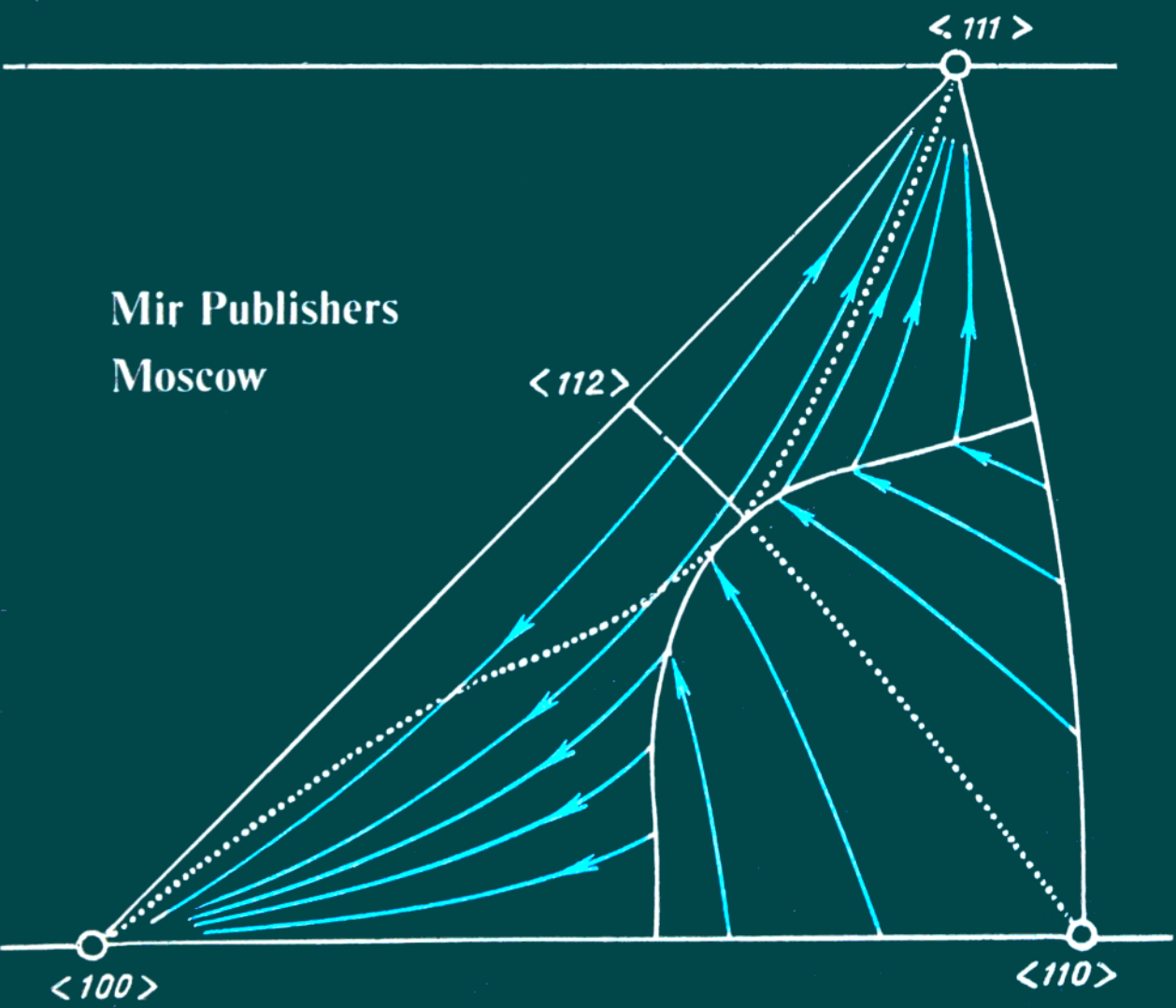

The book covers a wide circle of problems related to the behaviour and properties of metals and alloys, single and polycrystals in plastic deformation. The phenomena of strain-hardening, softening, recrystallization, texture formation (in particular, of deformation and recrystallization textures) are discussed from the standpoint of the theory of dislocations and the theory of structural imperfections in real crystals.
The book is intended for students specializing in plastic working of metals and may be of use for students, post-graduates, engineers and research workers engaged in the physics of metals, physical metallurgy, and heat treatment of metals and alloys.

Physical Principles of Plastic Deformation

П. И. Полухин, С. С. Горелик, В. К. Воронцов

Физические основы пластической деформации

Издательство «Металлургия»
Москва

P. Polukhin, S. Gorelik and V. Vorontsov

Physical Principles of Plastic Deformation

Translated from the Russian
by
V. Afanasyev

Mir Publishers
Moscow

First published 1983
Revised from the 1982 Russian edition

The Russian Alphabet and Transliteration

А а	a	К к	k	Х х	kh
Б б	b	Л л	l	Ц ц	ts
В в	v	М м	m	Ч ч	ch
Г г	g	Н н	n	Ш ш	sh
Д д	d	О о	o	Щ щ	shch
Е е	e	П п	p	ъ	”
Ё ё	e	Р р	r	ы	y
Ж ж	zh	С с	s	ь	’
З з	z	Т т	t	Э э	e
И и	i	У у	u	Ю ю	yu
Й й	y	Ф ф	f	Я я	ya

На английском языке

© Издательство «Металлургия», 1982
© English translation, Mir Publishers, 1983

Contents

Preface 9

1 Interatomic Forces. Metallic Crystals and Their Elastic Properties 11

1. Bond Forces in Crystals. Crystalline Structure of Metals 11
2. Elastic Deformation of Crystals 24

Recommended Literature 29

2 Elementary Theory of Structural Imperfections in Crystals 30

1. Structural Imperfections in Real Crystals 30
2. Elastic Properties of Dislocations 40
3. Dislocations in Typical Crystal Structures 59
4. Movement and Intersection of Dislocations. Interactions Between Dislocations and Point Defects 72
5. Surface and Volume Defects 80
6. Methods for Detection and Examination of Dislocations 90
7. Initiation of Dislocations 100

Recommended Literature 102

3 Plastic Deformation of Single Crystals 103

1. Deformation by Slip 103
2. Deformation by Twinning 122
3. The Shear Mechanisms of Plastic Deformation Associated with Intercrystalline Reorientation 135
4. The Mechanisms of Diffusion Plasticity 140
5. Deformation of F.C.C. Crystals 145
6. Deformation of B.C.C. Crystals 158
7. Deformation in Hexagonal Metal Crystals 159
8. The Theories of Work Hardening 166

Recommended Literature 179

4 Plastic Deformation of Polycrystals 180

1. Mechanisms of Grain-boundary Plastic Deformation . . . 180
2. Effect of Grain Boundaries on Deformation Process and the Pattern of τ-γ Curve 190
3. Locality of Deformation in Polycrystals 193
4. The Pattern of Deformation and the σ-ε Curves for Some Polycrystalline Metals 195
5. Calculation of Stress-strain Curves for Polycrystals from the Data on Single Crystals 201
6. Effect of Grain Size on Plasticity and Flow Stress of Polycrystals 202
7. The Role of Twinning in Plastic Deformation of Polycrystals 207
8. The Structure and Properties of Plastically Deformed Polycrystals 209

Recommended Literature 218

5 Deformation Textures 219

1. General Concepts. Classification of Textures 219
2. Methods of Texture Analysis. Pole Figures 223
3. General Principles of the Influence of Stressed-strained State on the Type of Deformation Texture 230
4. Effect of Deformation, Crystallochemical Nature of Materials and Alloying on the Type of Deformation Texture 235
5. Anisotropy of Principal Properties in Textured Materials 243

Recommended Literature 249

6 Characteristics and Driving Forces of Softening Processes (Recovery, Polygonization and Recrystallization) in Deformed Metals and Alloys 250

1. The Mechanisms and Temperature Levels of Recovery and Polygonization 251
2. The Mechanism and Temperature Level of Recrystallization 259
3. Driving Forces of Recrystallization at Various Stages 270

Recommended Literature 274

7 Recrystallization in Heating After Cold Deformation (Static Recrystallization) 275

1. Effect of the Conditions of Deformation and Heating on the Mechanism of Recrystallization and Type of Microstructure 275
2. Effect of Atomic Structure of Alloy, Solute Impurities and Disperse Phases of Recrystallization 283
3. First-order Recrystallization Diagrams 291

Recommended Literature 298

8 Recrystallization During Hot Deformation (Dynamic Recrystallization) 299

1. Effect of Conditions of Hot Deformation and Cooling on Recrystallization Mechanism 299
2. Effect of Chemical and Phase Compositions 314
3. Recrystallization Diagrams in Hot Deformation 315

Recommended Literature 319

9 Recrystallization with Non-uniform Deformation and Inhomogeneous Phase Composition 320

1. Principal Types of Structural Inhomogeneity 320
2. Structural Inhomogeneities Caused by Deformation . . . 324
3. Structural Inhomogeneities Caused by Inhomogeneities in Phase Composition 331

Recommended Literature 334

10 Recrystallization Textures 335

1. The Principal Theories of Formation of Recrystallization Textures 337
2. The Principal Types of Texture Changes in Recrystallization 339

Recommended Literature 347

11 Fracture 348

1. The Phenomenological Theory of Brittle Fracture . . . 349
2. Dislocation Mechanisms of Fracture 352
3. The Ductile-brittle Transition 355
4. Ductile Fracture 357
5. Effect of Various Factors on Ductile Fracture 358
6. Effect of Hydrostatic Pressure on Fracture 361
7. Criteria of Ductile Fracture 369

Recommended Literature 371

12 Resistance of Metals to Plastic Deformation 372

1. General Characteristic of σ_s-θ-$\bar{\varepsilon}$-$\dot{\bar{\varepsilon}}$ Diagrams 375
2. Effect of Type of Crystal Lattice, Chemical Composition and Structure of Metal on Strain Resistance . . . 383
3. Mechanisms of Plastic Deformation in Various Ranges of ε, $\dot{\varepsilon}$ and θ Parameters 395
4. Effect of Surrounding Medium and Size Factor on Strain Resistance 395
5. Effect of Loading History on Strain Resistance 397

Recommended Literature 402

13 Ductility and Deformability of Metals and Alloys 403

1. Effect of Chemical and Phase Composition on Ductility of Metals and Alloys 407
2. Effect of Structure and Structural and Chemical Inhomogeneity on Ductility of Metals and Alloys 413
3. Effect of Temperature and Rate of Deformation on Ductility 421
4. Effect of the Type of Stressed State on Ductility 427
5. Effect of Surrounding Medium and Size Factor on Ductility of Metals and Alloys 431

Recommended Literature 437

14 Thermomechanical Treatment 438

1. The Essence and Types of Thermomechanical Treatment 438
2. Structural Changes in HTHT. The Role of Process Factors 443
3. Examples of Application of HTHT 450

Recommended Literature 452

15 Superplasticity and Its Applications in Plastic Working of Metals 453

1. Principal Characteristics of Plastic Deformation under Conditions of Superplasticity 454
2. Effect of the Conditions of Deformation, Microstructure and Composition of Metal on Superplasticity and Principal Parameters of the Process 459
3. The Atomic Mechanism of Superplasticity 464
4. Practical Application of Superplasticity in Plastic Working of Metals 469

Recommended Literature 476

Index 477

Preface

The theoretical and technological principles of modern plastic working of metals are based on a complex body of knowledge including divisions of physics and mechanics of solids, physics of real crystals, physical metallurgy, physical chemistry, theory of deformation friction, etc.

The problems of the physics of plasticity and strength constitute one of the fundamental branches of physical metallurgy and solid-state physics. The laws of plastic deformation, which is one of the most popular methods of metal working, are of substantial practical importance. Plastic deformation is used as a process of metal working for changing the shape of metal articles and the structure and properties of the metal. These tasks are often solved in parallel. Under real conditions, plastic deformation often appears as a spontaneous process resulting in relaxation of stresses formed by a gradient of temperatures or friction forces, a difference in the coefficients of thermal expansion or unit volumes of phases, etc.

The requirements to the quality of materials and products and to the stability of their properties are becoming increasingly more rigorous. The list of materials which can be worked by plastic deformation is ever increasing and includes materials of more complicated composition. New methods of plastic working are being introduced, such as high-speed deformation, thermomechanical treatment, superplastic deformation, etc.

In view of this, specialists in plastic deformation, and in the first place technologists in plastic working of metals require a deep knowledge of the atomic mechanisms of deformation and of the nature of factors which can affect these mechanisms.

The proposed textbook is an extended course of lectures on the physical principles of plastic deformation, which has been delivered for several years at the Moscow Institute of Steels and Alloys. The Authors have also used the experience gained at the polytechnical institutes in Leningrad, Gorky and Sverdlovsk, the Moscow State University, and some other Soviet higher educational institutions.

The book has been written on the basis of modern concepts of

the dislocation theory of metals. It analyses the structural imperfections in crystals, the mechanisms of plastic deformation, specifics of plastic deformation of single and polycrystals, variations in the structure and properties caused by deformation and heating, dynamic recrystallization, etc., the process properties of metals and alloys, such as the strain resistance (flow stress) and ductility which is an especially important characteristic, since plastic working is only possible when the ductility of a metal has not been exhausted.

Owing to the combined efforts of experimenters and theoretical scientists, among which it is worth to name W. T. Read (USA), A. H. Cottrell (Great Britain), J. Friedel (France), A. Seeger (FRG), Ya. I. Frenkel, G. V. Kurdyumov, I. A. Oding, V. I. Trefilov (USSR), the science of imperfections (defects) of crystal structure has become the theoretical basis on which modern concepts of the nature of strength, plasticity and fracture are being developed.

The modern theory of dislocations explains qualitatively the variations of strength and plasticity of various materials under various conditions and in some cases makes it possible to estimate quantitatively the mechanical and process properties of metals and alloys.

The Authors would like to express their acknowledgement to Ch. V. Kopetsky, Corresponding Member of the USSR Academy of Sciences, and to the teachers of the chair of plastic working of metals, headed by Prof. A. K. Grigoryev, D. Sc., at the Leningrad Polytechnical Institute, for their critical analysis of the manuscript and valuable comments which have improved the book appreciably.

1 Interatomic Forces. Metallic Crystals and Their Elastic Properties

1. Bond Forces in Crystals. Crystalline Structure of Metals

The distances between atoms (molecules) in gases are quite large and exceed many times the size of atoms (molecules) proper. In condensed states, i.e. in liquids and solids, each atom is in close vicinity of its neighbours. A particular arrangement of atoms in condensed state is determined by the nature and magnitude of interatomic forces, pressure and temperature.

The interaction between atoms can lead to the formation of an aggregate only when the process reduces the energy of the system. When atoms move closer together to form crystalline aggregates, their electrons occupy lower energy levels than those typical of an isolated atom. In that case, the system has the lowest energy.

Interatomic Forces and Types of Bond in Crystal Lattice

The equilibrium distance between nearest atoms in a crystal $r = r_0$ (Fig. 1), which corresponds to the minimum of energy of the system, U_0, is determined by the equality of competing attraction and repulsion forces between valence electrons and ions.

The lowest potential energy U_0 is called the *bond energy*. It is equal to the work that is needed to move neighbouring atoms to infinity.

Atomic bonds are differentiated mainly by the type of attraction forces (*2* in Fig. 1), since the energy of repulsion (*1* in Fig. 1) is as a rule associated with deformation of electron shells of atoms and is substantial only at distances not exceeding the atomic diameter.

Atomic interaction can be characterized by three parameters:

1. Radius of action r' at which attraction forces are negligible ($P < 0.1P_{max}$). The forces are termed long-range if $r' \gg r_0$ and short-range at $r' \approx r_0$.

2. The nature of distribution of electron density and valence electrons in space. If this distribution possesses spherical symmetry, i.e. is isotropic, P is a function of distance only, $P = f(r)$, and the

bonds are non-oriented. Each atom (ion) tends to be surrounded by as high as possible number of neighbour atoms; this is the case of *ionic and metallic bonds.*

If the electron density of valence electrons is anisotropic, P is a function of r, φ, and θ, i.e. $P = f(r, \varphi, \theta)$ (in spherical coordinates) and the bonds are oriented. The number of nearest atoms to a given one (the coordination number) is equal to the number of directions in which the electron density is at a maximum. This is the case of *covalent bond.*

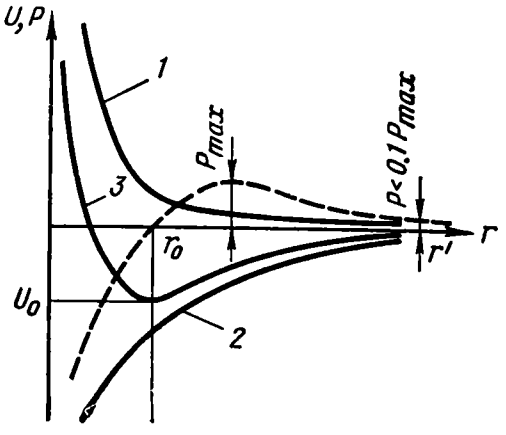

Fig. 1. Curves of potential energy (U): (*1*) due to repulsive forces only, (*2*) due to attractive forces only and (*3*) total energy; the force of interaction P between a pair of atoms versus the distance r between them is shown by a dashed line

3. The bond energy: it is strong if $U_0 > 1$ eV and weak if $U_0 < 1$ eV.

Ionic, or heteropolar, bond. This is the simplest type of interatomic bond. Elements with a small number of electrons on the outer shells (cations) give up these electrons while atoms with an almost filled outer shell (anions) take up electrons easily. A crystal then consists of positive and negative ions, rather than of neutral atoms. The reduction of energy on attachment of an electron to an atom of anion is higher than the increase of energy on detachment of an electron from an atom of cation. The energy of an aggregate composed of positive and negative ions reduces even more owing to the fact that each ion of one sign has ions of opposite sign as its nearest neighbours. This occurs due to the *electrostatic (Coulomb) attraction of oppositely charged ions.* The particular arrangement of opposite-sign ions and accordingly the particular type of crystal lattice are determined by the ratio of atomic radii of cation and anion. This is associated with the fact that the lattice of ionic crystals is stable only when the cores of ions of one sign are in direct contact with the cores of opposite-sign ions (Fig. 2).

The *coordination numbers* Z of crystals with some particular ratios of ionic radii of cation and anion, R_c/R_a, are as follows:

R_c/R_a	0.73-1.37	0.41-0.73	0.22-0.41	0.15-0.22
Z	8	6	4	3

The typical structures for the coordination number of 6(NaCl), 8(CsCl), and 4(CaF_2) are shown in Fig. 2.

Repulsion forces increase extremely quickly at small distances between ions, so that the energy of ionic crystals can be written in

the following form:

$$U = -(Ae^2/r) + B/r^{10} \quad (1)$$

where A and B are constants; e is the charge of electron; and r is the distance between ions.

The first term in expression (1) is the variation in the energy due to attraction forces (see curve *2* in Fig. 1) and the second one, due to repulsion forces (curve *1* in that figure). The energy of interaction due to repulsion forces only contains the tenth power of r and thus can be neglected in rough calculations. Usually $A = 1$. Substituting e and $a = 3 \times 10^{-8}$ cm, we find that $U_0 = 4.8$ eV at $r = a$. Therefore, this is a *long-range bond* [$U \approx -(e^2/r)$ and $U \neq 0$ at any r].

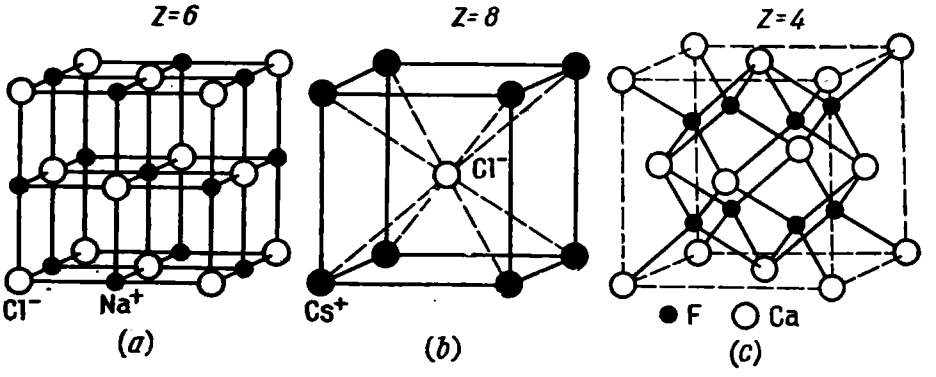

Fig. 2. Crystal structures of some ionic compounds
(*a*) NaCl; (*b*) CsCl; (*c*) CaF_2

Ionic-bond crystals, to name NaCl, CsCl, CaF_2 as typical examples (see Fig. 2), are characterized by a high melting point, high values of strength and hardness, and a low coefficient of thermal expansion.

Ionic crystals, with only few exceptions, such as AgCl, AgBr, AgI or TlI, are usually brittle and non-plastic.

Covalent, or homopolar, bond. In this case, the energy of atoms decreases on the formation of an aggregate owing to combination of valence electrons into electron pairs. The number of nearest neighbours for each atom (Z is the coordination number) is determined by the number of valence electrons by the rule $8 - N$, where N is the number of valence electrons in an atom and 8 is the number of wave functions which can be formed for valent s- and p-states.

Such a pair of electrons, with one electron belonging to one atom and the other, to a neighbouring atom of an opposite spin, bonds these two atoms together. Bonds of this type can appear between atoms whose outer electron shells are filled at least 50 per cent. By the formation of valence electron pairs, the outer electron shells of these atoms turn out to be filled up to eight electrons in each.

Covalent bonding can form molecules or crystals. For instance, two atoms of chlorine each of which has seven electrons on the outer

3*p* level, possess a pair of common electrons and form a molecule. An atom of germanium, with four electrons on the outer shell, has one electron common with each of four neighbouring atoms and thus possesses eight collective electrons. An electron can pass from the shell of one atom to that of another, without detaching fully from each of them. Each atom surrounded by four neighbours is the centre of a tetrahedron. Thus, a tridimensional cubic structure of the type of diamond is formed (Fig. 3).

Covalent bonds are *oriented*, with the angles between them being dependent on the number and type of electrons participating in bonding. For instance, the elements of subgroup IVB (C, Si, Ge) have spherical electron shells of *s*-orbitals, while the electron shells of the three *p*-orbitals are extended in three mutually perpendicular directions. The hybridized *sp*-orbitals formed in the crystal lattice of these elements have an identical shape and are directed towards the corners of a regular tetrahedron. The elements of subgroup VB have only three unpaired electrons: each atom is connected by covalent bonds with only three nearest neighbours (Fig. 3*b*), which forms a two-layer pack with covalent bonds in them. Packs are combined into a complex tridimensional structure which is typical of As, Sb and Bi. Packs are bonded together by weak van der Waals bonds. The resulting structure has highly anisotropic physical properties. This is why the elements of subgroups VB and VIB have an elevated brittleness and cannot be plastic-worked easily.

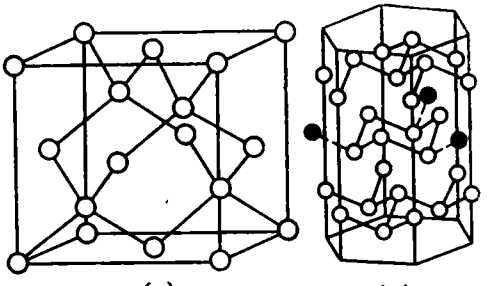

Fig. 3. Crystal structures of elements formed by the rule $(8 - N)$ (*a*) diamond (element of subgroup IVB); (*b*) antimony (element of subgroup VB)

A characteristic feature of covalent-bond crystals, associated with the oriented nature of bonds, is that they have a low efficiency of space filling, i.e. the ratio of volume occupied by atoms in the unit cell to the volume of the cell proper. For instance, the efficiency of space filling of the lattices of diamond, germanium and silicon (the most typical covalent-bond substances) is only 0.34. In other words, their atoms occupy roughly only one-third of the lattice volume. The result is that the volume of interstices in such lattices is rather high. The radius of a sphere inscribed into an interstice is close to that of the atom ($0.85\ R_{at}$).

Because of the oriented bonds, covalent-bond crystals have a low plasticity (high Peierls-Nabarro locks).

Molecular bond is caused by van der Waals forces which appear due to the polarizing effect produced by the field of electrons moving around the nucleus of a given atom on the motion of electrons around the nucleus of a neighbouring atom. Owing to fluctuation (random

motion) of electrons of one of the moving neutral atoms, the centres of gravity of the negative and positive charges are separated and give rise to a dipole moment on one of the atoms, which in turn produces a respective dipole moment on the other. The result is that the energy of the system (aggregate) becomes lower. Attraction forces of electrostatic nature are compensated by repulsion forces which prevent mutual penetration of electron shells one into another.

Van der Waals forces are *weak* (weaker than electrostatic forces), *short-range*, and *central*. Typical examples of molecular-bond substances are crystals of noble gases. Since the bond forces are weak, these crystals can exist only at very low temperatures. Van der Waals forces are typical of some anisotropic crystals formed from elements of groups V-VII by the rule $(8 - N)$ (see Fig. 3*b*). In these crystals, van der Waals forces are operative between atomic layers (rows, molecules), while covalent bonds connect atoms in a layer (row or molecule).

Metallic bond can appear between atoms whose valence electrons are only weakly bonded with the nucleus. As has been demonstrated experimentally, the electron density of valence electrons in metals is uniformly distributed over the volume of crystals. On this basis, the structure of such crystals can be represented as an ion core immersed into a gas of collective valence electrons. Repulsion forces acting between ions are compensated for by the interaction of the electrons of such a 'gas' with ions.

Assuming that bonds in metals are non-oriented, it should be expected that all metals must have crystal lattices with the closest packing of atoms. Actually, however, less compact structures (b.c.c.) in metals are no less common than the closest packed (f.c.c. and c.p.h.) lattices. This can be explained by an increase of the energy of the electron gas of valence electrons with an increase of compactness, by superposition of covalent bonds on the metallic bonds, etc.

The total energy of a system is the sum of the energy of repulsion of ions (electrons) and the energy of attraction of ions and electrons. In a crystal bonded by metallic bond forces, the components of energy are as follows:

$$U = -Ae^2/r + B/r^2 \qquad (2)$$

where the first term is the potential energy of free electrons and the second is their kinetic energy. Their sum gives the resulting curve of energy distribution (see Fig. 1) where $U_0 = U_{sub}$ is the work to be performed to transform a metal crystal into gas of positively charged ions, i.e. the sum of the heat of sublimation and the ionization potential of free atoms is U_0.

Mixed bond. All the four types of bond described above are not strictly isolated and do not exclude one another. The type of bond can depend on temperature and pressure. For instance, germanium at room temperature is a semiconductor and typical covalent-bond

material. At high temperatures and very high pressures it acquires metallic properties (electric conductivity). A mixed, covalent-metallic bond can appear in cases when an atom has two incomplete outer shells. For instance, Ni and Fe each have an incomplete $3d$-shell.

Table 1. Bond Energy of Some Typical Crystals (after B. Chalmers, V. I. Vladimirov)

Type of bond	Crystal	Energy, eV/atom	Type of bond	Crystal	Energy, eV/atom
Ionic	NaCl	8	Metallic	Cu	3.51
	LiF	10		Fe	4.13
Covalent	Diamond (C)	7.4		Co	4.4
				Ni	3.7
	SiC	12		Al	3.2
Molecular	Ar	0.1	Mixed covalent-metallic	W	8.74
Metallic	Na	1.13			

This property is possessed by transition metals and elements of subgroup IVB of the Periodic Table. The metallic bond is formed here by outer-shell electrons. Electrons of an incomplete shell can produce covalent bonds, which increases the bond energy and makes it dependent on orientation angles and reduces the radius of action, with all the consequences characteristic of covalent bond (Table 1).

Principal Types of Crystal Structure of Pure Metals

The most common types of crystal lattice in metals are face-centred cubic (f.c.c), close-packed hexagonal (c.p.h.) and body-centred cubic (b.c.c.). The first two of them have the closest possible packing of atoms (closest packing). Any lattice has crystallographic planes of the closest packing (Fig. 4); f.c.c. and c.p.h. lattices differ from each other in the nature of stacking of closest-packed layers.

Let the positions of atoms (spheres) lying in a plane coincident with the plane of drawing be denoted by A (see Fig. 4). Bright and dark triangles (B and C respectively) represent the centres of pits between atoms (spheres) of layer A into which atoms of the next closest-packed layer can be laid. If they are laid into positions B, the pits in this second layer, into which atoms of a third layer can be laid, will occupy positions A and C, and so on.

If closest-packed layers are stacked in a sequence $ABCABC...$, there forms a face-centred cubic (f.c.c.) lattice. A sequence $ABABA$ (or $ACACA...$ or $BCBCB...$) gives a hexagonal close-packed lattice. The efficiency of space filling of these lattices is the same and equal to 0.7405.

Face-centred cubic (f.c.c.) lattice. In an f.c.c. lattice, the closest-packed layers lie in {111} planes, with ⟨110⟩ directions being the

closest-packed directions in which neighbouring atoms are in direct contact with one another (Figs. 5 and 6).

Atoms in an f.c.c. lattice (Fig. 5*a*) are arranged at corners of a unit cell with side a and in the centres of its faces. Each atom is surrounded by 12 nearest neighbours. The distance between the centres of neighbouring atoms is $a/\sqrt{2} = 0.707a$ (Fig. 5*b*). An important characteristic of crystal lattices is the size and number of interatomic volumes, or interstices. The largest interstices (bright circles) are in the centre of the cube and in the mid of its edges (Figs. 5*c* and 6*b*). In an f.c.c. lattice, each of such voids is surrounded by six atoms arranged at corners of a regular octahedron (see Fig. 5*c*) and is called an *octahedral void*, or *octahedral interstice*. Smaller voids are inside the tetrahedron and called *tetrahedral* (Fig. 5*d*). In an f.c.c. crystal, there are two tetrahedral voids of radius $\rho = 0.225r$ and one octahedral void of radius $\rho = 0.41r$ per each atom.

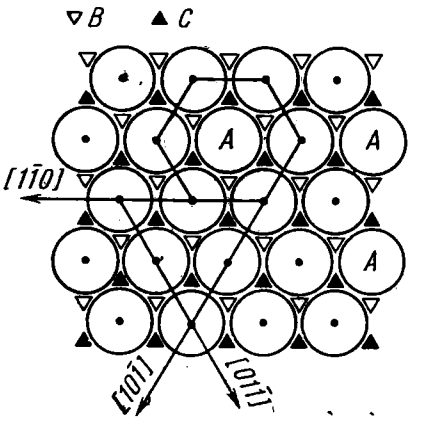

Fig. 4. Closest packing of atoms (spheres) in a layer. Atoms (spheres) are assumed to touch one another

For interstitial impurity atoms, it is energetically favourable to occupy exactly octa- and tetrahedral voids, rather than any other interstices. The f.c.c. lattice is typical of a number of metals including Cu, Ag, Au, Al, Th, Pb, Mn (γ), Fe (γ), Co (β), Ni, Ir, Pt, etc.

Close-packed hexagonal (c.p.h.) lattice. This lattice is obtained by stacking close-packed planes on one another in a sequence *ABABAB* (Fig. 7). In this lattice, {0001} planes are closest-packed (and called *basal planes*) and $\langle 11\bar{2}0 \rangle$ directions are closest-packed ones (see Fig. 7). The axial ratio in a unit hexagonal cell is $c/a = 1.633$. In most hexagonal-lattice metals, however, this ratio is noticeably lower than that for the perfect crystal, so that the so-called prismatic planes of the type $\{10\bar{1}0\}$, rather than basal planes, are closest packed, and the packing density of pyramidal $\{10\bar{1}1\}$ planes is also higher. Thus, as the c/a ratio diminishes, slip in prismatic planes and even in pyramidal planes begins to play ever greater part in plastic deformation, in addition to the slip in basal planes (for more detail see Ch. 3).

In an ideal c.p.h. lattice, voids similar to those in the f.c.c. lattice occupy the centres of regular octahedrons and tetrahedrons (bright circles in Fig. 7*b* and *c*). The diameters of rigid spheres which can be inserted into these voids are equal to $0.41r$ for octahedral voids and $0.255r$ for tetrahedral ones. As in the f.c.c. lattice, there are two tetrahedral voids and one octahedral void per each atom.

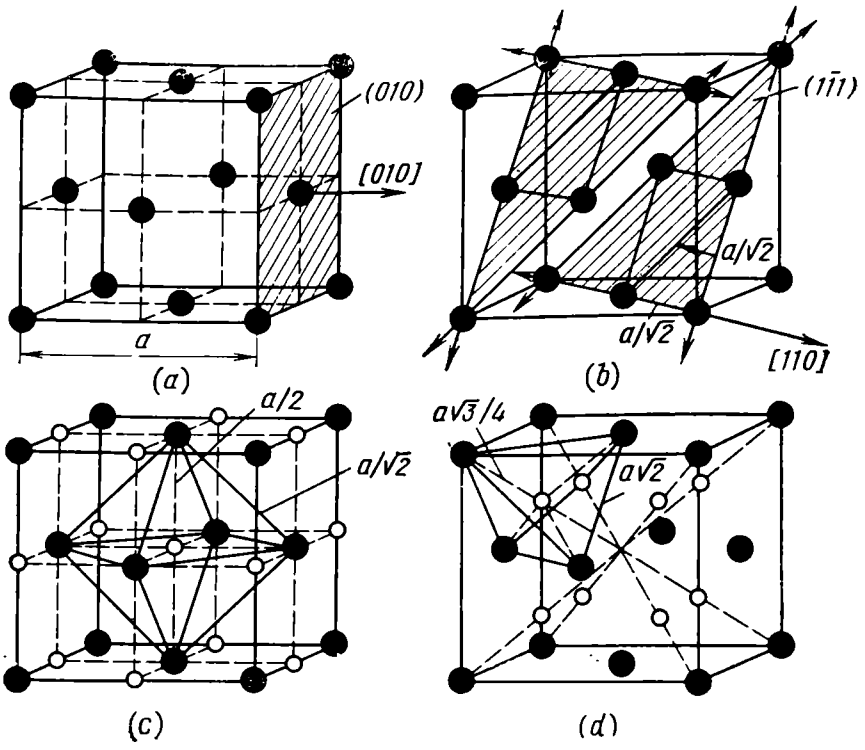

Fig. 5. Face-centred cubic (f.c.c.) lattice
(*a*) unit cell; (*b*) closest-packed planes; (c) octahedral voids (bright circles); (*d*) tetrahedral voids (bright circles)

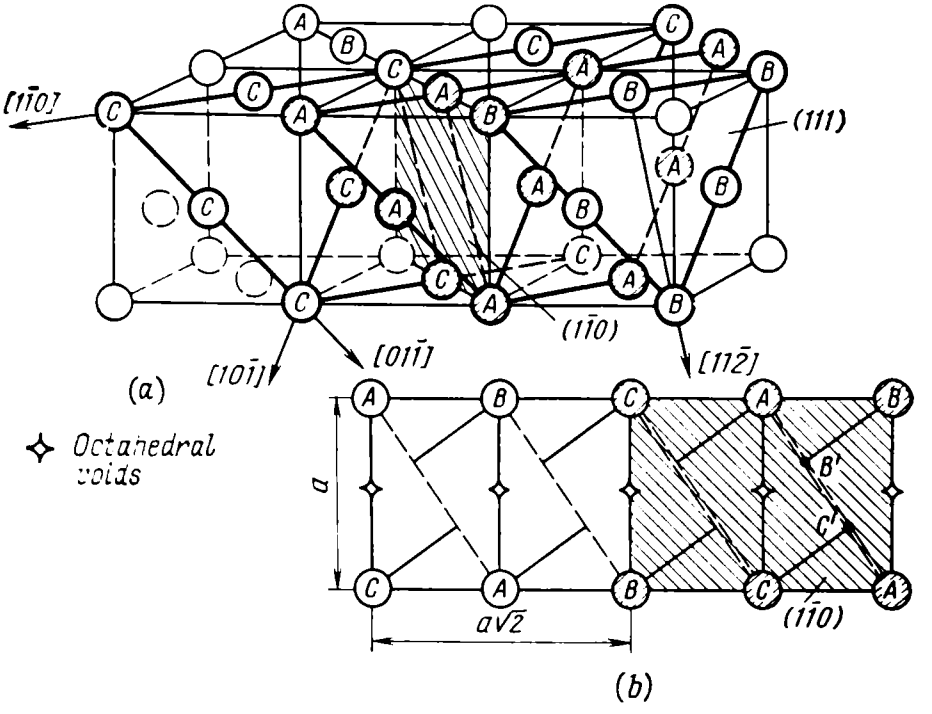

Fig. 6. Principal directions and closest-packed (111) planes in an f.c.c. crystal (*a*) and their projections onto the (1$\bar{1}$0) plane (*b*)

Thus, the f.c.c. and c.p.h. lattices differ from each other only in the stacking sequence of close-packed layers. In the energy aspect, the difference between these two structures is insignificant, so that the stacking sequence of layers can be disturbed easily during the growth or plastic deformation of a crystal, leading to the formation of what is called stacking faults.

Body-centred cubic (b.c.c.) lattice is typical of Li, Na, K, Rb, Cs, Ca (at $t > 464$°C), Ba, Ti (β), Zr (β), Hf (β), V, Nb, Ta, Cr,

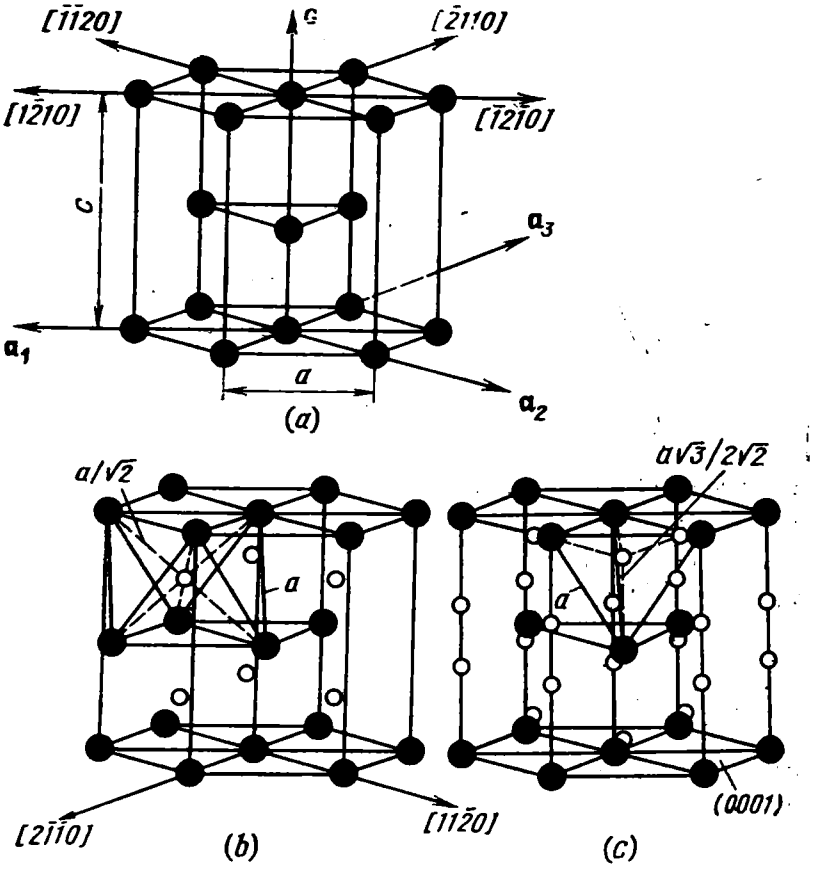

Fig. 7. Close-packed hexagonal (c.p.h.) lattice
(a) elementary cell with the periods a and c; (b) octahedral voids; (c) tetrahedral voids. The principal planes and directions are indicated

Mo, W, Mn (δ), Fe (α and δ) and some other metals. The efficiency of space filling of the b.c.c. lattice is 0.68, i.e. it is looser packed than c.p.h. or f.c.c. Atoms in the b.c.c. lattice are arranged in the corners and in the centre of a unit cell (Fig. 8*a*). Any atom in the b.c.c. lattice has eight nearest neighbours at a distance of $0.5\sqrt{3}a = 0.866a$ from it. The coordination number of this lattice is equal to eight. The b.c.c. lattice has no close-packed planes, but a close-packed ⟨111⟩ direction in which neighbouring atoms touch one another (see Fig. 8*a*).

The closest-packed planes are {110} and also {112} (see Figs. 61 and 82*b*) which include a ⟨111⟩ direction.

Octahedral voids (Fig. 8*b*) are surrounded by six atoms occupying sites at vertices of an irregular octahedron. They are arranged in the mid of edges and faces of the cube of a unit cell. There are four

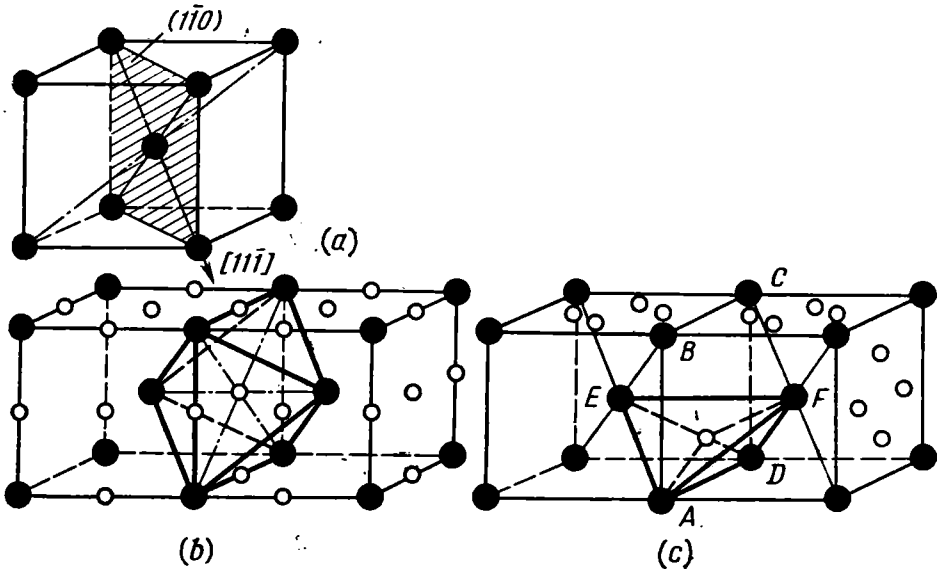

Fig. 8. Body-centred cubic (b.c.c.) lattice

(*a*) elementary cell with the direction [11$\bar{1}$] and plane (1$\bar{1}$0) of closest packing; (*b*) octahedral voids on visible faces of the lattice (O) and a tetrahedron constructed for an octahedral void in the face centre; (*c*) ditto, for a tetrahedral void. The positions of the four tetrahedral voids in the face *ABCD* can be seen by rotating the separated tetrahedron around the edge *EF* until the edge *AD* coincides successively with *AB*, *BC* and *CD*

tetrahedral voids on each face (Fig. 8*c*) each of them being surrounded by four atoms at vertices of a regular tetrahedron.

Assuming that the b.c.c. structure is constructed of rigid spheres, the radius of a sphere which can be placed into a tetrahedral and an octahedral void is respectively $0.291r$ and $0.154r$, i.e. the greatest size of a sphere that can be inscribed into a b.c.c. lattice is smaller than in closer-packed c.p.h. and f.c.c. lattices. This fact is obviously responsible for a lower solubility of interstitial impurities in b.c.c. lattices. The higher looseness of the b.c.c. lattice can be explained by the fact that it has three octahedral and six tetrahedral voids per each atom.

The Stress-strain Relationship in an Ideal Crystal

Expressions (1) and (2) which describe the bonding forces in the crystal lattice are particular cases of Ioffe's general equation:

$$U = -A/r^m + B/r^n \qquad (3)$$

where A and B are constants; m and n are the exponents of the energy due to only attractive or respectively repulsive forces (see Fig. 1), with $n > m$ always.

The minimum of the potential energy of a pair of atoms, i.e. the bond energy $U = U_0$, is obtained at $r = r_0$ (see Fig. 1), when $dU/dr = 0$ and $Am/r_0^{m+1} = Bn/r_0^{n+1}$.

Noting this relationship in the equation of bonding forces (3), we obtain an expression similar to that proposed by A. H. Cottrell:

$$\frac{dU}{dr} = P = \frac{Am}{r_0^{m+1}} \left[\left(\frac{r_0}{r} \right)^{m+1} - \left(\frac{r_0}{r} \right)^{n+1} \right] \tag{4}$$

Equations (3) and (4) are written for a pair of interacting atoms, whereas we have to account for the interaction of all atoms in a crystal. The conclusions obtained are applicable to the interaction of all N ith and jth atoms which form pairs in a crystal:

$$U = \frac{1}{2} \sum_{i,\, j=1}^{N} U(\mathbf{r}_i - \mathbf{r}_j) \tag{5}$$

where $U(\mathbf{r}_i - \mathbf{r}_j)$ is the energy of interaction of a pair of atoms with coordinates $\mathbf{r}_i$ and $\mathbf{r}_j$.

It follows from expression (4) that if a crystal is subjected to mechanical action (tension, compression, or shear), the original interatomic spacing r_0 may change to $r = r_0 \pm \Delta r$. In uniaxial tension, the external stress σ applied cannot exceed σ_{max} which corresponds to the maximal bonding forces in the crystal lattice, P_{max}, in Fig. 1. The greatest elastic displacement of atoms will then be described by the relationship:

$$\frac{dP}{dr} = 0 \text{ or } r_{max} = r_0 \sqrt[n-m]{\frac{n+1}{m+1}} \tag{6}$$

For 'soft' (i.e. compressible) atoms, $m = 1$, $n = 3$ and $r_{max} = 1.41$ or $\Delta r_{max} = 0.41 r_0$. When repulsion is associated with overlapping of electron shells, which is typical of metals and ionic crystals, atoms are less compressible and n may increase up to 11. With $n = 11$ and $m = 1$, $\Delta r_{max} = 0.2 r_0$. For a case with $n = 11$ and $m = 6$ (van der Waals forces) substitution of m and n into (6) gives $\Delta r_{max} = 0.115 r_0$. Thus, depending on the type of bond in a crystal lattice, the stress σ can be found from (4):

$$\sigma = \frac{A_1 m}{r_0^{m+1}} \left[\frac{1}{(1+\varepsilon)^{m+1}} - \frac{1}{(1+\varepsilon)^{n+1}} \right] \tag{7}$$

where A_1 is a constant proportional to A and $\varepsilon = \Delta r / r_0$ is a characteristic of strain in Lagrangian notation.

The stress σ can attain the highest value σ_{max} (corresponding to P_{max} in Fig. 1) at appreciable elastic deformations of the crystal (Table 2) and high elastic displacements of atoms.

Table 2. Stress-strain Relationships for Crystals with Various Values of m and n

Equation relating σ and ε	ε_{max}, %	Deviation, %, from Hooke's law on deformation, %		
		10	1	0.1
$n=3, \quad m=1$				
$\sigma=E(\varepsilon+3.5\ \varepsilon^2+8\ \varepsilon^3+15\ \varepsilon^4+\ldots)$	41	44.5	3.58	0.35
$n=11, \quad m=7$				
$\sigma=E(\varepsilon+7.5\ \varepsilon^2+36\ \varepsilon^3+130\ \varepsilon^4+\ldots)$	20	124	7.87	0.75
$n=11, \quad m=6$				
$\sigma=E(\varepsilon+11.5\ \varepsilon^2+61.6\ \varepsilon^3+247.8\ \varepsilon^4+\ldots)$	11	201	12.1	1.21

As is well known, real crystals cannot withstand such a high elastic deformation and show a noticeable plastic (residual) deformation already at $\varepsilon = 0.05$-0.2 per cent. Slight displacements or deformations can produce a residual deformation only in cases when the energy level of a real crystal is raised substantially by certain factors, say, by internal stresses. This suggests that structural imperfections should exist in a crystal lattice.

Expanding the term in brackets in (7) into a binomial series, we obtain:

$$\sigma = \frac{A_1 m (m-n)}{r_0^{m+1}} \left[\varepsilon + \frac{(m+1)(m+2)-(n+1)(n+2)}{(m-n)\,2!} \varepsilon^2 + \frac{(m+1)(m+2)(m+3)-(n+1)(n+2)(n+3)}{(m-n)\,3!} \varepsilon^3 + \ldots \right] \tag{8}$$

Denoting the constant for a given metal, $[A_1 m (m-n)]/r_0^{m+1}$, as the modulus of elasticity E, we find that the stress-strain relationship for ideal crystals is non-linear (see Table 2) and that the deviation from Hooke's law $\sigma = E\varepsilon$ [the first term in equation (8)] is insignificant only on slight deformations.

A similar conclusion has been drawn by Jensch who has represented the non-linear relationship between stress and strain in the form:

$$\varepsilon = \sigma/E + k(\sigma/E)^2 + k^2(\sigma/E)^3 + \ldots \tag{9}$$

Equation (9) can be obtained from (7). In particular, taking in (7) $m = 1$, $n = 3$ and neglecting ε^2, ε^3, ε^4 as being small compared with ε, we have:

$$\sigma = \frac{2A_1\varepsilon}{r_0^2(1+4\varepsilon)} \quad \text{or} \quad \varepsilon = \frac{\sigma}{E}\left(1-4\frac{\sigma}{E}\right)^{-1}$$

where $E = 2A_1/r_0^2$, i.e. by analogy with what has been taken earlier.

Expanding $(1-4\sigma/E)^{-1}$ into a binomial series, we obtain Jensch's formula in the form:

$$\varepsilon = \frac{\sigma}{E} + 4\left(\frac{\sigma}{E}\right)^2 + 4^2\left(\frac{\sigma}{E}\right)^3 + \cdots \tag{10}$$

whence it is seen that the coefficients k in formula (9) contain the exponents m and n which characterize variations in the energy of attractive and repulsive forces. It follows from (9) and (10) that Hooke's law is applicable only at $\sigma \ll E$, i.e. on slight deformations. Dislocation-free crystals, or whiskers, possessing a perfect crystal lattice can be deformed elastically up to 3-4 per cent; on heavier deformations they exhibit deviations from Hooke's law (Fig. 9). In further discussion, Hooke's law will be used only for slight displacements of atoms.

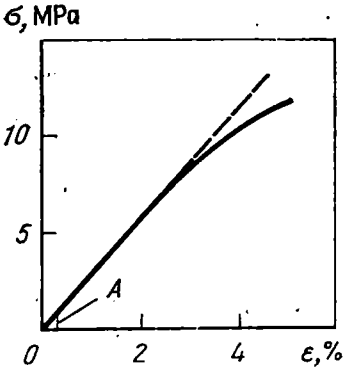

Fig. 9. The σ-ε curve for Fe whiskers 1μm in diameter. A is the stress at which plastic flow begins

As follows from the analysis of bonding forces in a crystal lattice, deformation in crystals has a peculiar feature that their behaviour in tension and compression is not identical, since (see Fig. 1) P_{max} can be attained in tension $(+\Delta r)$ but cannot in compression $(-\Delta r)$.

The theoretical strength of a crystal. By substituting the extremum condition (6) for $P = P_{max}$ (see Fig. 1) in expression (4) and replacing A by A_1, we obtain the following theoretical maximum stress (the theoretical strength) of a crystal:

$$\sigma_{max} = \frac{A_1 m (n-m)}{r_0^{m+1}} \left(\frac{n+1}{m+1}\right)^{\frac{m+1}{m-n}} \frac{1}{n+1}$$

or, noting that $E = [A_1 m (n-m)]/r_0^{m+1} = 2G(1+\nu)$, where ν is Poisson's ratio and G is the shear modulus, for $\nu = 0.3$, we have:

$$\sigma_{max} = 2.6G\left(\frac{n+1}{m+1}\right)^{\frac{m+1}{m-n}} (n+1)^{-1} \tag{11}$$

Substitution of m and n for various types of bond gives the following values of the theoretical strength: $\sigma_{max} = 0.325\,G$ for $m = 1$ and $n = 3$; $\sigma_{max} = 0.105G$ for $m = 1$ and $n = 11$, and $\sigma_{max} = 0.15G$ for $m = 6$ and $n = 11$.

These calculated values of theoretical strength of a crystal turn out to be substantially greater (by a factor of 10^2 to 10^3) than the actual strength.

Ya. I. Frenkel has used an elegant and simple classical method for estimating the theoretical shear resistance. It is assumed in his

method that a layer of atoms is sheared by x relative to another layer under the action of a stress applied (Fig. 10). Due to the symmetry of the lattice, we have $\sigma = 0$ at $x = ka/2$, where $k = 0, 1, 2, \ldots$; $\sigma > 0$, i.e. the lattice offers resistance to the stress applied at $0 < x < a/2$; and $\sigma < 0$ at $a/2 < x < a$. The simplest function which satisfies these conditions is of the form $\sigma = c' \sin 2\pi x/a$. The constant c' can be found at small displacements x: $\sigma = c'(2\pi x/a)$. From Hooke's law, $\sigma = Gx/a$, and therefore, $c' = G/2\pi$ and the highest shear stress of the crystal lattice is $\sigma_{max} = G/2\pi = 0.16G$, i.e., as in calculations by formula (11), the theoretical shear resistance is a few orders of magnitude greater than the values typical of real crystals.

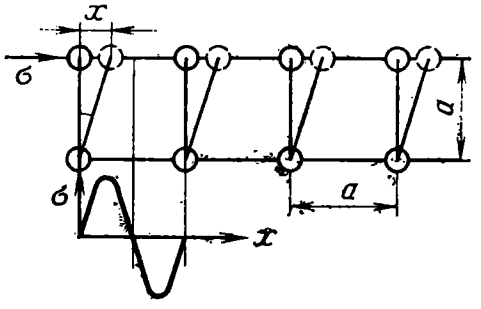

Fig. 10. A diagram to calculate the theoretical shear resistance

The substantial difference between the theoretical and actual strength of metals suggested that one has to regard a real crystal containing imperfections (defects, see Ch. 2) rather than an ideal crystal with a regular arrangement of atoms. In 1934 G. I. Taylor, E. Orowan and M. Polanyi have introduced, independently of one another, the concept of shear (slip) of a portion of crystal relative to another portion by way of dislocation movement. This concept has revolutionized the physics of strength and plasticity. The theory of dislocations developed most intensively in post-war years and at present is an inseparable part of solid state physics and of physical principles of strength and plasticity.

2. Elastic Deformation of Crystals

With a uniaxial stressed state and slight deformations, $\sigma = E\varepsilon = c\varepsilon$ and $\varepsilon = s\sigma$, where s is the constant of elastic yieldability and c is the constant of elastic stiffness, or simply yieldability, or stiffness.

In the general case, a crystal may be in a complex stressed state, with all the components of the stress tensor σ_{ij} ($i, j = 1, 2, 3$) being present. A component of the strain tensor, say ε_{11}, will then depend on each of the σ_{ij} components, i.e.

$$\varepsilon_{11} = s_{11ij}\sigma_{ij} = s_{1111}\sigma_{11} + s_{1112}\sigma_{12} + s_{1113}\sigma_{13} + s_{1121}\sigma_{21} + s_{1122}\sigma_{22} + s_{1123}\sigma_{23} + s_{1131}\sigma_{31} + s_{1132}\sigma_{32} + s_{1133}\sigma_{33} \quad (12)$$

Similar expressions are valid for other components ε_{kl} ($k, l = 1, 2, 3$), so that

$$\varepsilon_{kl} = s_{klij}\sigma_{ij} \quad (13)$$

where s_{klij} is the 4-rank tensor of elastic yieldabilities of the crystal (i.e. 81 constants).

In particular, it follows from (13) that if a single stress, say, a normall stress σ_{11} is applied to a crystal having no axes of symmetry, this will cause distortion of the crystal angles in addition to normal deformations ε_{11}, ε_{22}, ε_{33}, i.e. the components ε_{12}, ε_{23} and ε_{31} will appear.

Solving equation (13) as a set of equations for σ_{ij}, we find

$$\sigma_{ij} = c_{ijkl}\varepsilon_{kl} \tag{14}$$

which is another evidence that a single stress can cause the appearance of all deformations ε_{kl} in a crystal.

Since the tensors σ_{ij} and ε_{kl} are symmetrical ($\sigma_{ij} = \sigma_{ji}$; $\varepsilon_{kl} = \varepsilon_{lk}$), we get:

$$\left.\begin{aligned} &\varepsilon_{kl} = s_{klij}\sigma_{ij} = s_{klji}\sigma_{ji} \text{ and } s_{klij} = s_{klji} \\ &\varepsilon_{lk} = \varepsilon_{kl} = s_{lkij}\sigma_{ij} = s_{klij}\sigma_{ij} \text{ and } s_{lkij} = s_{klij} \end{aligned}\right\} \tag{15}$$

It follows from formulae (15) that in the total number of 81 constants, only 36 remain non-identical. Since $\varepsilon_{lk} = \varepsilon_{kl}$, system (12) contains six lines, but as follows from (15), $s_{1112} = s_{1121}$, $s_{1113} = s_{1131}$, $s_{1123} = s_{1132}$, etc. similarly for each line, i.e. only six coefficients of the total of nine s_{klij} coefficients remain in each line of the type of (12). Thus, there are six equations of the type of (12) with six non-identical yieldability coefficients s_{klij} in each, i.e. a total of 36. Similar considerations hold also true for c_{klij}: there are $6 \times 6 = 36$ coefficients of stiffness in the whole. Since the number of independent components of the stress and strain tensor is also six, it is reasonable to perform further calculations in matrix form where $\sigma_{ij} = \sigma_m$, $\varepsilon_{kl} = \varepsilon_n$ and m and n may take up values from 1 to 6:

$$\begin{vmatrix} \sigma_{11} & \sigma_{12} & \sigma_{13} \\ \sigma_{21} & \sigma_{22} & \sigma_{23} \\ \sigma_{31} & \sigma_{32} & \sigma_{33} \end{vmatrix} \rightarrow \begin{vmatrix} \sigma_1 & \sigma_6 & \sigma_5 \\ \sigma_6 & \sigma_2 & \sigma_4 \\ \sigma_5 & \sigma_4 & \sigma_3 \end{vmatrix};$$

$$\begin{vmatrix} \varepsilon_{11} & \varepsilon_{12} & \varepsilon_{13} \\ \varepsilon_{21} & \varepsilon_{22} & \varepsilon_{23} \\ \varepsilon_{31} & \varepsilon_{32} & \varepsilon_{33} \end{vmatrix} \rightarrow \begin{vmatrix} \varepsilon_1 & \frac{1}{2}\varepsilon_6 & \frac{1}{2}\varepsilon_5 \\ \frac{1}{2}\varepsilon_6 & \varepsilon_2 & \frac{1}{2}\varepsilon_4 \\ \frac{1}{2}\varepsilon_5 & \frac{1}{2}\varepsilon_4 & \varepsilon_3 \end{vmatrix} \tag{16}$$

On replacement of tensor indices by matrix ones:

tensor indices . . .	11	22	33	23,32	31,13	12,21
matrix indices . . .	1	2	3	4	5	6

additional multipliers 2 and 4 are introduced:

$s_{ijkl} = s_{mn}$ when both m and n are equal to 1, 2 or 3

$2s_{ijkl} = s_{mn}$ when either m or n is equal to 4, 5 or 6

$4s_{ijkl} = s_{mn}$ when both m and n are equal to 4, 5 or 6

The validity of these rules can be proved easily by comparing, for instance, the notations for $\varepsilon_{11} = s_{11ij}\sigma_{ij}$ and $\varepsilon_1 = s_{1m}\sigma_m$ or for $\varepsilon_{23} = s_{23ij}\sigma_{ij}$ and $\varepsilon_4 = s_{4m}\sigma_m$*. We then have:

$$\varepsilon_n = s_{nm}\sigma_m; \quad \sigma_m = c_{mn}\varepsilon_n \tag{17}$$

The matrix of constants s_{mn} and c_{mn} is composed of six lines and six columns.

As is known from the theory of elasticity, an increment of strain work is

$$dA = \sigma_{ij}d\varepsilon_{ij} = \sigma_m d\varepsilon_m \tag{18}$$

If the deformation process is isothermal and reversible, $dA = dw$, where dw is the increment of free energy. Using (17) and (18), we get:

$$dw = c_{mn}\varepsilon_n d\varepsilon_m \tag{19}$$

Since dw is the total differential, $\partial w/\partial\varepsilon_m = \sigma_m = c_{mn}\varepsilon_n$. Differentiation of the two extreme portions with respect to ε_n gives: $\partial\,(\partial w/\partial\varepsilon_m)/\partial\varepsilon_n = c_{mn}$. Since the left-hand portion is symmetrical with respect to m and n and since w is a function of state only, we conclude that the order of differentiation is inessential, i.e. energy consideration lays on additional limitations: $c_{mn} = c_{nm}$; $s_{mn} = s_{nm}$. Therefore, the matrices of elastic constants are symmetrical, i.e. only 21 unlike constants remain from the total number of 36. In view of symmetry of the crystal, the number of independent constants decreases.

The s_{mn} matrices for typical metallic structures of the cubic system (f.c.c. and b.c.c.), hexagonal system and for an isotropic medium are respectively of the form:

$$\begin{vmatrix} s_{11} & s_{12} & s_{12} & 0 & 0 & 0 \\ \cdot & s_{11} & s_{12} & 0 & 0 & 0 \\ \cdot & \cdot & s_{11} & 0 & 0 & 0 \\ \cdot & \cdot & \cdot & s_{44} & 0 & 0 \\ \cdot & \cdot & \cdot & \cdot & s_{44} & 0 \\ \cdot & \cdot & \cdot & \cdot & \cdot & s_{44} \end{vmatrix}; \quad \begin{vmatrix} s_{11} & s_{12} & s_{13} & 0 & 0 & 0 \\ \cdot & s_{11} & s_{13} & 0 & 0 & 0 \\ \cdot & \cdot & s_{33} & 0 & 0 & 0 \\ \cdot & \cdot & \cdot & s_{44} & 0 & 0 \\ \cdot & \cdot & \cdot & \cdot & s_{44} & 0 \\ \cdot & \cdot & \cdot & \cdot & \cdot & a \end{vmatrix};$$

$$\begin{vmatrix} s_{11} & s_{12} & s_{12} & 0 & 0 & 0 \\ \cdot & s_{11} & s_{12} & 0 & 0 & 0 \\ \cdot & \cdot & s_{11} & 0 & 0 & 0 \\ \cdot & \cdot & \cdot & a & 0 & 0 \\ \cdot & \cdot & \cdot & \cdot & a & 0 \\ \cdot & \cdot & \cdot & \cdot & \cdot & a \end{vmatrix} \tag{20}$$

where $a = 2\,(s_{11} - s_{12})$.

* The reader is invited to make the proof.

Thus, we have three constants (s_{11}, s_{12}, s_{44}) for f.c.c. and b.c.c. crystals, five constants (s_{11}, s_{12}, s_{13}, s_{33}, s_{44}) for c.p.h. crystals, and two (s_{11} and s_{12}) for an isotropic medium. The stress-strain relationship for an isotropic medium can be written in the form of (17) or in a conventional form of Hooke's generalized law:

$$\varepsilon_1 = s_{11}\sigma_1 + s_{12}\sigma_2 + s_{13}\sigma_3$$
$$\varepsilon_1 = [\sigma_1 - \nu(\sigma_2 + \sigma_3)]/E$$
$$\varepsilon_4 = 2(s_{11} - s_{12})\sigma_4; \quad \varepsilon_4 = \sigma_4/G$$

It follows from the foregoing that

$$s_{11} = 1/E; \; s_{12} = -\nu/E; \quad 2(s_{11} - s_{12}) = 1/G \qquad (21)$$

where G is the shear modulus and ν is Poisson's ratio.

Since elastic constants are numerous [see (20)], the elastic properties of a crystal cannot be described completely by a single surface. If a rod is cut out from a crystal parallel to an arbitrary axis ox_1' and a load applied to it, it is possible to measure the modulus E' in that direction. From (21) we have: $E' = 1/s_{11}'$; s' is related to s_{mn} through the direction cosines l_1, l_2, l_3 of the angles between the axes of the specimen and the crystallographic directions. In particular, we have for cubic crystals

$$s_{11}' = s_{11} - 2(s_{11} - s_{12} - 0.5s_{44})(l_1^2l_2^2 + l_2^2l_3^2 + l_3^2l_1^2) \qquad (22)$$

and for hexagonal crystals

$$s_{11}' = (1 - l_3^2)s_{11} + l_3^4 s_{33} + l_3^2(1 - l_3^2)(2s_{13} + s_{44}) \qquad (23)$$

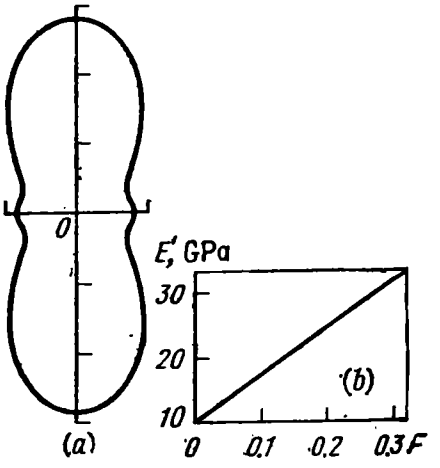

Fig. 11. Central section of the characteristic surface for s_{11}' in zinc (*a*) and variation of $E'(F)$ in a lead single crystal (*b*)

The surface (23) demonstrates that the elastic constant is anisotropic and depends on direction (Fig. 11*a*).

The elastic yieldability s_{11}' of cubic (f.c.c. and b.c.c.) crystals is a function of direction or the orientation factor $F = l_1^2l_2^2 + l_2^2l_3^2 + l_3^2l_1^2$. F is equal to zero in the direction of [100] axes of the cube where $s_{11}' = s_{11}$ and is at a maximum in [111] direction where $F = 1/3$. The magnitude of $E' = 1/s_{11}'$ of lead (f.c.c. lattice) may change by a factor of more than 3 depending on F (Fig. 11*b*).

For cubic crystals, the measure of their anisotropy is the ratio $c_{44}/0.5(c_{11} - c_{12})$ (Table 3). The constant c_{44} is the measure of shear resistance in the cube plane along a [100] direction, while the term $0.5(c_{11} - c_{12})$ determines the shear resistance in a plane (110) along [110].

Table 3. Stiffness, GPa, of Selected Metals

Metal	Lattice	Elastic constants of stiffness			
		c_{11}	c_{12}	c_{44}	$\frac{2c_{44}}{c_{11}-c_{12}}$
		Cubic lattices			
Al	f.c.c.	108.2	62.3	28.5	1.2
Cu	f.c.c.	108.4	121.4	75.4	3.2
Fe	b.c.c.	287	141	116	2.4
Pb	f.c.c.	46.6	39.2	14.4	4.0
Mo	b.c.c.	460	176	110	0.8
Ni	f.c.c.	246.5	147.3	124.7	2.5
W	b.c.c.	501.0	198	151.4	1.0
		Hexagonal close-packed lattice			
Cd	$c/a=1.886$	121.0	48.1	18.5	44.2 *—51.3 **
Mg	$c/a=1.623$	59.7	26.2	16.4	21.7 *—61.7 **
Zn	$c/a=1.856$	161	34.2	38.3	50.1 *—61.0 **

* c_{13}. ** c_{33}.

As may be seen, most metals possess a noticeable elastic anisotropy.

The elastic characteristics of a polycrystal consisting of a large number of single crystals with different elastic moduli and different orientations are however calculated as averaged properties of a single crystal. A good agreement between the averaged (calculated) elastic constants and their experimental values may be indicative of an insignificant effect of grain boundaries on the elastic characteristics of a metal. On passage to plastic deformations, however, one has to account for the effect of grain boundaries (see Chs. 4, 12, and 13).

The data of Table 3 show that the anisotropy of elastic properties depends on the type of crystal lattice, lattice parameter, and the nature of bonding forces, since $E = Am\,(n - m)/r_0^{m+1}$ increases with a decrease of atomic spacing.

The speed of propagation of an elastic (sonic) wave $v = \sqrt{E\rho}$ (ρ = density) is quite high in metals: v=1 300-5 100 m/s, and therefore, the rate of elastic deformation may be substantially higher than the practically feasible rates of load application. This is why elastic deformation occurs instantaneously and has no effect on the elastic constants of the metal.

At higher temperatures, the distance between atoms increases, thus increasing the energy of the system and weakening the bonding forces; for that reason, the elastic modulus decreases roughly by 2-4 per cent per every 100°C.

The isotropy in a polycrystalline material can be disturbed if strain hardening (cold plastic deformation) leads to the formation of a preferable orientation, or texture. Variations of elastic constants

upon recrystallization annealing are observed in cases when the annealing process has resulted in the appearance of recrystallization textures of a type different from the original deformation texture.

Alloying can change the crystal lattice parameter and the interatomic forces. Since the lattice parameter of a solvent depends almost linearly on the concentration of an alloying (solute) element, the relationship between the concentration of an alloying element and the elastic modulus is close to linear.

Alloying can either increase or decrease the modulus of elasticity, depending on the effect it produces on bonding forces in the crystal lattice.

RECOMMENDED LITERATURE

1. Bernstein M. L., Zaimovsky V. A., *The Structure and Mechanical Properties of Metals.* Moscow, Metallurgiya, 1970 (in Russian).
2. Chalmers B., *Physical Metallurgy.* New York, John Wiley, 1959.
3. Cottrell A. H., *Dislocations and Plastic Flow in Crystals.* Oxford, Clarendon Press, 1953.
4. McLean D., *Mechanical Properties of Metals and Alloys.* New York-London, John Wiley, 1962.
5. Nye J. F., *Physical Properties of Crystals.* Oxford, Clarendon Press, 1964.
6. *Physical Metallurgy.* Ed. by R. W. Cahn. Amsterdam, North-Holland Publishing Co., 1965.
7. Vladimirov V. I., *Physical Theory of Plasticity and Strength.* Part 1. Crystal Lattice Defects. Leningrad, Leningrad Polytechnical Institute, 1973 (in Russian).

2 Elementary Theory of Structural Imperfections in Crystals

Real crystalline bodies (especially polycrystalline) always have some or other structural imperfections which produce an enormous effect on the structure-sensitive properties of these bodies. Of special importance is their effect on plasticity and strength of crystalline materials.

The science on the atomic structure of these imperfections, their energy, interactions, mobility, and their influence on the properties of materials is one of the most important divisions of modern solid state physics.

In view of the numerous types of imperfections and of various modes of their interaction with one another and with impurities, quantitative mathematical description of their behaviour is linked with certain difficulties.

1. Structural Imperfections in Real Crystals

Geometrically, structural imperfections (defects) in crystals can be divided into four groups: (1) point defects; (2) linear defects; (3) surface (or plane) defects; and (4) volume defects.

Point defects are those whose dimensions in all three directions are commensurable with those of atoms. They include *vacancies* (Schottky defects); interstitial atoms, i.e. atoms occupying interstices; *interstitial* and *substitutional impurity atoms* whose size differs from that of base atoms forming the lattice; and combinations of these defects.

Atoms occupying sites of a crystal lattice oscillate at a frequency of approximately 10^{13} s^{-1}. Owing to this oscillative motion, which takes place at any temperature, atoms can interact with one another and exchange their kinetic energy. The average kinetic energy of thermal oscillations of atoms is equal to (3/2) kT. At room temperature, (3/2) $kT \approx 0.03$ eV, which is much lower than the energy required to form point defects (1-4 eV). Owing to fluctuations of kinetic energy (deviations from its mean value), however, atoms

can overcome potential barriers. The probability of this act increases with increasing temperature by an exponential law. If in this process an atom moves from its site in the crystal lattice into an interstice, there form a vacancy and an interstitial atom (*Frenkel defect*).

If an atom moves from its normal position in the site of the crystal lattice onto the surface of the crystal, there appears a vacancy (*Schottky defect*).

Interstitial atoms and vacancies in a crystal are centres of local elastic dilatation or compression of the lattice (Fig. 12). The stresses

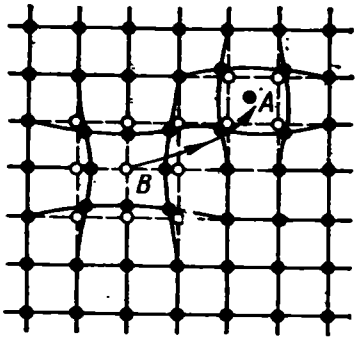

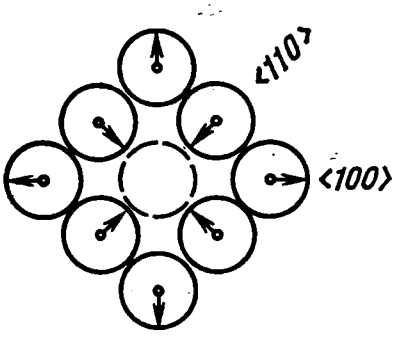

Fig. 12. (*left*) An interstitial atom (*A*) and a vacancy (*B*) form a Frenkel defect in a simple crystal lattice

Fig. 13. Directions of displacements of atoms around a vacancy in {100} plane of an f.c.c. lattice

and strains around such a centre diminish inversely proportional to the third power of the distance from that centre. Noticeable displacements of atoms occur at distances of one or two atomic diameters.

In many real crystals, the field of atomic displacements produced by a vacancy is anisotropic. For instance, the nearest neighbours of a vacancy in an f.c.c. crystal (Fig. 13) are displaced by 0.84% of the atomic spacing towards the vacancy, whereas the second layer is displaced by +0.25% away from that vacancy and the third layer is displaced by —0.03%.

An interstitial atom increases the spacing between the surrounding atoms in the matrix by 20 per cent, which leads to a more substantial increase in stress and strain than on the formation of a vacancy. For that reason the energy to form a vacancy in a crystal is lower than that required for the formation of an interstitial atom. In the f.c.c. lattice of copper, the energy for the formation of a vacancy is $E_v = 1$ eV, against $E_i = (2.5\text{-}3.5)$ eV for the formation of an interstitial atom. Point defects always require energy for their formation, and therefore, increase the enthalpy of the system ($\Delta H > 0$), but, if present in certain concentrations, which are higher at higher temperatures of the body, they are stable thermo-

dynamically and thus unavoidable. An explanation to this is that the presence of point defects increases both the enthalpy and the entropy of the system. Up to a definite concentration n_{eq}, the entropy term $T\Delta S$ turns out to be higher in magnitude than ΔH. As a result, the total variation of the free energy $\Delta F = \Delta H - T\Delta S$ in the presence of point defects at a concentration $n \leqslant n_{eq}$ turns out to be less than without them. Such point defects are stable thermodynamically. It is clear that the equilibrium concentration of point defects is higher at a higher temperature and at a lower creation energy:

$$(n : N) = \exp(-E : kT)$$

where n is the highest number of stable point defects; N is the total number of atoms; E is the activation energy of the formation of a point defect; and k is Boltzmann's constant.

Calculations for copper have given the following equilibrium concentrations of vacancies:

T, K	300	700	1 100	1 350
$(n : N)$	10^{-19}	10^{-8}	10^{-5}	10^{-4}

The energy for the formation of interstitial atoms is substantially higher than that of vacancies and, as has been demonstrated by calculations, the concentration of interstitial atoms in copper at 1 000°C is quite low, only 10^{-39}, i.e. many orders of magnitude lower than the concentration of vacancies.

In view of the high distortions of the crystal lattice around an interstitial atom, the *activation energy of its migration*, E_m, is lower than that for migration of a vacancy. In copper, the activation energy of migration is 1 ± 0.5 eV for vacancies and 0.16 ± 0.10 eV for interstitials, i.e. interstitial atoms are more mobile than vacancies. Since the concentration of vacancies is much more higher than that of dislocated atoms, the vacancy mechanism plays the predominant part in the processes of self-diffusion, i.e. redistribution of atoms of the base substance. An atom near a vacancy has an elevated energy and can occupy its site. The time of 'existence' of a vacancy in a site of the crystal lattice depends on temperature. For cadmium, this time is roughly equal to one day at room temperature and only 4×10^{-4} s near the melting point, i.e. the frequency of diffusion jumps of vacancies is 0.25×10^4 s^{-1}.

The rate of migration of atoms of the base substance (self-diffusion) by the vacancy mechanism is substantially lower than the rate of migration of vacancies, since the probability for an atom to exist near a vacancy is not high and decreases with decreasing concentration of vacancies.

The rate of migration of substitutional impurity atoms (heterodiffusion) is higher than that of atoms of the base substance owing

to the additional energy of elastic distortion of the lattice in the local volume around an impurity atom.

Interstitial impurities can migrate more intensively, since no substantial deformation of the lattice is needed for an interstitial impurity atom to migrate from one interstice to another. A b.c.c. lattice has a lower efficiency of space filling than c.p.h. and f.c.c. lattices and octahedral and tetrahedral voids in it differ only slightly from each other in the size of spheres which can be inscribed in them. Diffusion of interstitial impurities in this lattice occurs more quickly than in an f.c.c. lattice where an octahedral void is separated from a tetrahedral one by a close packing of atoms. Both in b.c.c. and f.c.c. lattices, however, diffusion of atoms through vacancies takes place much more slowly than through interstices.

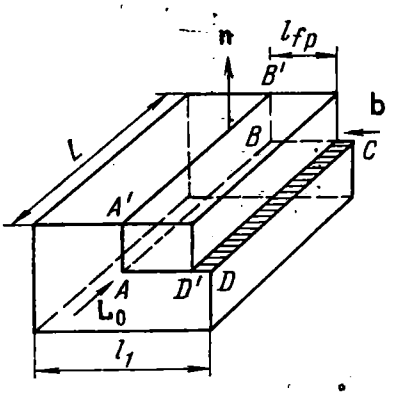

Fig. 14. An edge dislocation AB formed by incomplete shear. The shear vector is marked by an arrow

The concentration of Schottky and Frenkel defects can be influenced by irradiation and plastic deformation, as well as by temperature. As a first approximation, the concentration of vacancies increases proportional to deformation and can be determined from the relationship $n/N = (10^{-5}\text{-}10^{-6})\,\varepsilon$, where ε is the relative deformation, per cent. Such vacancies are called strain-induced. The highest concentration of strain-induced vacancies is obtained on sign-alternating loading. With a combined effect of a high temperature and heavy deformation, the concentration of vacancies can reach $(5\text{-}10) \times 10^{-4}$ which corresponds to a concentration of 2.5-5 per cent of displaced atoms. In this case, vacancies can probably have an effect on the process and mechanism of plastic deformation, though the effect of strain-induced vacancies on the strength and plasticity of metals is usually not high. Point defects produced by plastic deformation or irradiation are thermodynamically unstable.

Linear imperfections (defects) of the crystal lattice have the size of an atomic order in two dimensions and an appreciable extent in a third dimension. This group of defects includes dislocations which can be of the edge, screw or mixed type.

Dislocations can multiply easily at heavy deformations and their density can rise up to 10^{12} cm^{-2}. Dislocations possess a high mobility and are capable of oriented movement under the action of external stresses applied and for that reason are the principal contributors to plastic deformation in crystalline bodies.

An edge dislocation can be formed by shear of one portion of a crystal relative to another portion through one atomic spacing, but only through a fraction of the crystal length $l = AD$, rather

than through its whole length l_1 (Fig. 14). By this process, an additional plane $AA'B'B$ (extra-plane) forms in the top portion of the crystal. *The boundary AB of the extra-plane inside the crystal is properly a dislocation.* Its length L is usually 10^{-7}-10^{-5} nm. Since the slip plane $ABCD$ has not propagated through the whole length l_1 of the crystal and shear has taken place only in a portion of the crystal up to the boundary AB, it may be said that a *dislocation is the boundary of incomplete shear* and that its free-path length is $l_{fp} = AD$. An extra-plane acts as a wedge, i.e. produces a strong distortion of the crystal lattice (Fig. 15), especially in the vicinity

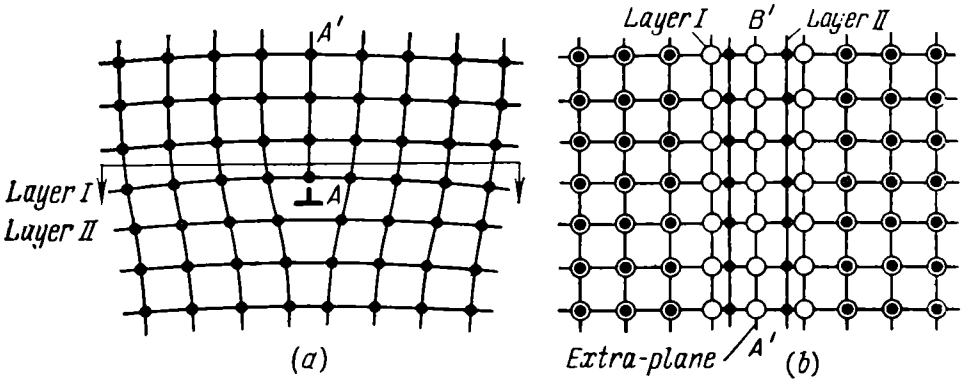

Fig. 15. An edge dislocation in a cubic lattice
(*a*) side view; (*b*) top view (bright dots are atoms of layer I and black ones, atoms of layer II)

of the atoms whose sites are located on the dislocation line AB. The layer I near the dislocation is compressed and layer II is tensioned, i.e. the interatomic spacings above the edge $A'B'$ of the extra-plane are smaller and those below that edge are higher, than in an undistorted lattice. An edge of an extra-plane is denoted by symbol $\perp$ (see Fig. 15*a*) if the extra-plane is above it and the dislocation is respectively called *positive*. If the extra-plane is located in the bottom portion of a crystal, the dislocation is termed *negative* and denoted $\top$. The difference between positive and negative edge dislocations is purely conditional, but the sign of dislocations is important when analysing interactions of dislocations.

The highest distortion of the crystal lattice is observed in the core of a dislocation of a diameter of roughly two interatomic spacings, with the centre in the dislocation proper (see Fig. 15). The distortion of the crystal lattice and the shear associated with a dislocation can be measured by the *Burgers vector*, which characterizes the energy of a dislocation and the forces acting on it. The Burgers vector is a section required to close a special-kind loop called the *Burgers circuit*. This is constructed by passing counter-clockwise from atom to atom around a portion of the crystal lattice containing a dislocation (Fig. 16*b*). A similar path is constructed for a portion of the crystal incorporating no dislocation (Fig. 16*a*). The number

of atoms is counted in both circuits. The Burgers vector **b** is the vector that should be introduced into the loop in the perfect crystal so as to close the path and match atom *1* in the example considered with atom *14*.

The Burgers vector can be resolved into basal vectors of the lattice: $\mathbf{b} = l\mathbf{i} + m\mathbf{j} + n\mathbf{k}$, where **i**, **j**, **k** are basal vectors of the crystal lattice which coincide with the crystallographic directions of the

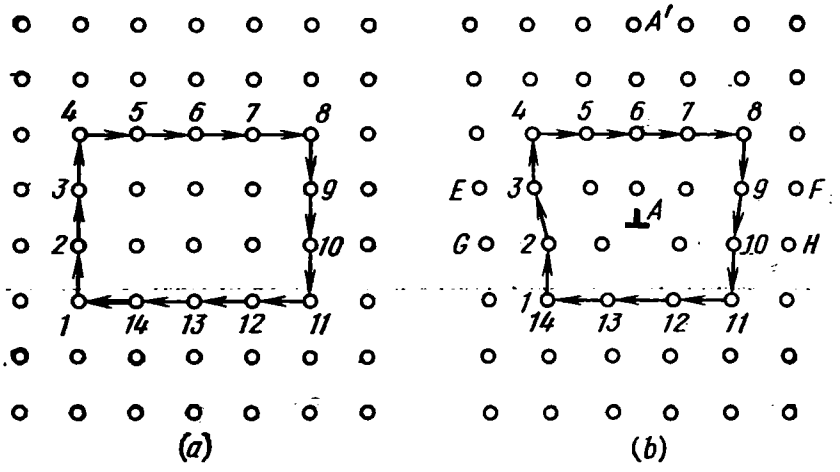

Fig. 16. Construction of the Burgers circuit and the Burgers vector b for an edge dislocation
(a) a portion of crystal free of dislocations; (b) a portion containing a dislocation

edges of a unit cell in that lattice. If l, m, $n = 0, 1, 2, \ldots$, the respective dislocations are called *perfect*. Otherwise, i.e. if l, m, and n are not integers, dislocations are *partial*.

Unit dislocations are such whose Burgers vector is equal in magnitude to one atomic spacing (translation vector); unit dislocations are always perfect.

In partial dislocations, the Burgers vector is smaller than the translation vector of the lattice.

Multiple, or *superdislocations* are those whose Burgers vector is greater than the lattice vector.

The Burgers vector is described by its magnitude b:

$$b = |\mathbf{b}| = \sqrt{b_x^2 + b_y^2 + b_z^2} \quad (\mathbf{b}_x = l\mathbf{i};\ \mathbf{b}_y = m\mathbf{j};\ \mathbf{b}_z = n\mathbf{k})$$

which is often called *power*, and by its direction $\mathbf{b} = ra\,[lmn]$, where $[lmn]$ are symbols of the crystallographic direction of vector **b**; a is the lattice period; and r is the greatest common divisor (Table 4).

Figure 17 illustrates a simple cubic lattice with the Burgers vectors $\mathbf{b}_1, \mathbf{b}_2, \ldots, \mathbf{b}_6$ whose magnitude is $b = ra\sqrt{l^2 + m^2 + n^2}$; the symbolic notation of directions **b** and determination of the magnitude (power) b are given in Table 4.

Table 4. Determination of Magnitude of Burgers Vectors $\mathbf{b}_1$, $\mathbf{b}_2$, ..., $\mathbf{b}_6$ (see Fig. 17) and Notation of Their Crystallographic Directions

Burgers vector	Vector components			Notation of direction	Vector magnitude
	$b_x = li$	$b_y = mj$	$b_z = nk$		
$\mathbf{b}_1$	0	a	0	$[0a0] = a\,[010]$	$a\sqrt{0+1^2+0} = a$
$\mathbf{b}_2$	a	a	0	$[aa0] = a\,[110]$	$a\sqrt{1^2+1^2+0} = a\sqrt{2}$
$\mathbf{b}_3$	a	a	$-a$	$a\,[11\bar{1}]$	$a\sqrt{3}$
$\mathbf{b}_4$	0	$a/2$	$-a/2$	$a/2\,[01\bar{1}]$	$a/\sqrt{2}$
$\mathbf{b}_5$	$-a/2$	$-a/2$	a	$a/2\,[\bar{1}\bar{1}2]$	$a\sqrt{3/2}$
$\mathbf{b}_6$	$a/4$	$a/4$	$-a/2$	$a/4\,[11\bar{2}]$	$a\sqrt{3/8}$

As may be seen from these examples (see Fig. 17 and Table 4), the Burgers vector $\mathbf{b}_1$ describes a perfect dislocation, the vectors $\mathbf{b}_4$ and $\mathbf{b}_6$ are smaller than the lattice parameter and describe partial dislocations, and the vectors $\mathbf{b}_2$, $\mathbf{b}_3$ and $\mathbf{b}_5$ are multiple and refer to superdislocations.

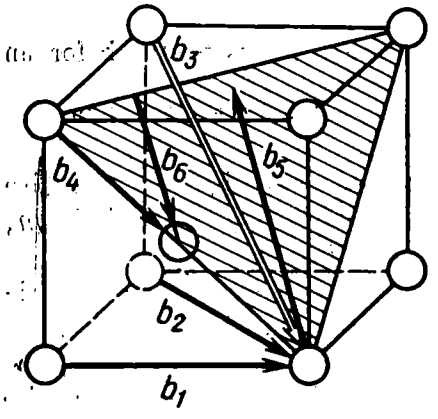

Fig. 17. Burgers vectors in a simple cubic lattice

If the Burgers vector **b** lies in the plane of movement of a dislocation *ABCD* with the normal **n**, i.e. $\mathbf{nb} = 0$ ($\mathbf{b} \perp \mathbf{n}$), the displacement is termed as *simple shear*, or *slip*, and the movement of the dislocation is called *conservative*, since it does not change the density in the slip plane *ABCD* with the normal **n** (see Fig. 14).

If the Burgers vector **b** does not lie in the plane of dislocation movement, i.e. if $\mathbf{nb} \neq 0$, this movement is *non-conservative* and the moving dislocation leaves behind either vacancies or interstitial atoms, depending on the sign of the component **b** which is parallel to vector **n**. In cases when the density in the slip plane is not changed, the movement of a dislocation must involve mass transfer to that plane or away from it by diffusion of individual atoms which is especially intensive at elevated temperatures.

If the Burgers vector **b** is parallel to vector $\mathbf{L}_0$ ($\mathbf{bL}_0 = 0$) (see Fig. 14), $\mathbf{nL}_0 = 0$ and $\mathbf{nb} = 0$. The last equality relates to a conservative movement of a dislocation whose Burgers vector is parallel to the dislocation line. This is what is called a *screw dislocation* (Fig. 18). The Burgers circuit and Burgers vector of a screw dislocation are constructed as for an edge dislocation. First, the origin

of the path is chosen, say, point a_1 (Fig. 18*a*). A portion of the crystal incorporating a screw dislocation is then passed around starting from that point: $a_1b = 9a$ (a is the atomic spacing); $bc = 6a$; $cd = 9a$; $de = 1a$; $ea_1 = 6a$. The path is closed and the initial and the final atoms coincide. In the path around a perfect portion of

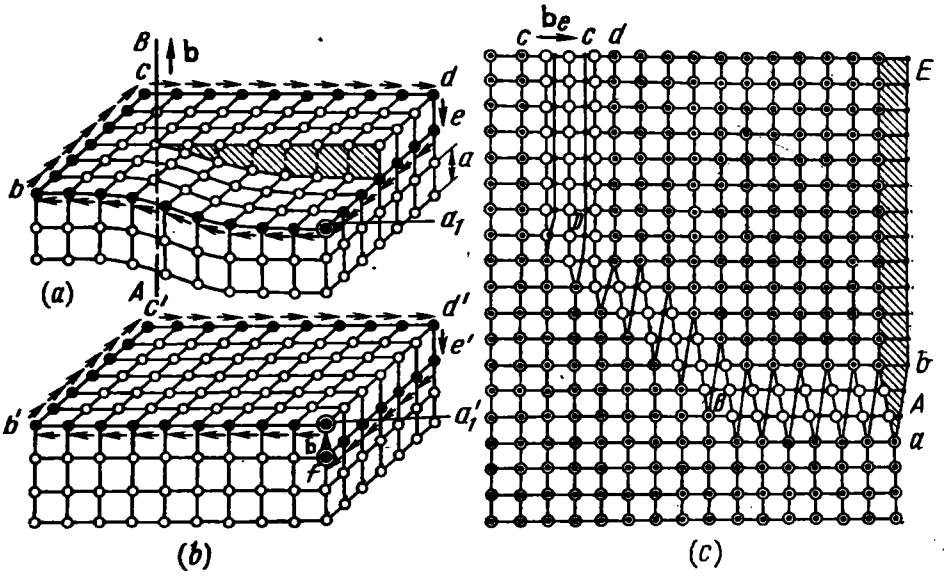

Fig. 18. The Burgers circuit
(*a*) around a screw dislocation; (*b*) an equivalent circuit in a perfect crystal: *AB*—dislocation line; **b**—the Burgers vector; (*c*) top views of a screw (*AB*), edge (*CD*) and mixed (*DB*) dislocation

the crystal (Fig. 18*b*), atom to atom paths are the same: $a_1'b' = a_1b = 9a$; $b'c' = bc = 6a$; $c'd' = cd = 9a$; $d'e' = de = 1a$; $e'f = ea_1 = 6a$, but the last atom, f, does not coincide with the first, a_1', by the magnitude of the Burgers vector **b** which closes the Burgers circuit in the perfect crystal.

With an edge dislocation *CD* (Fig. 18*c*, see also Fig. 15) with the Burgers vector $\mathbf{b}_e$, there is a zone *cd* where the crystal lattice is distorted by a magnitude less than $\mathbf{b}_e$. Similarly, for a screw dislocation *AB* (see Fig. 18*c*) with the Burgers vector $\mathbf{b}_s$, there is a zone *ab* where the crystal lattice is distorted by a magnitude less than $\mathbf{b}_s$. As may be seen from the figure, the remaining portion of the crystal retains the perfect structure of the lattice. These considerations for edge and screw dislocations with the Burgers vectors $\mathbf{b}_e$ and $\mathbf{b}_s$ also hold true for a mixed dislocation *DB* with the Burgers vector $\mathbf{b}_m = \mathbf{b}_e + \mathbf{b}_s$, where there is a distortion near *DB* (displacement of atomic layers) by a magnitude less than $\mathbf{b}_m$.

For a screw dislocation, any cylindrical surface for which $\mathbf{L}_0$ is the generatrix (Fig. 19*a*) can serve as a slip surface. The transition of a moving screw dislocation from one slip plane onto another is called *cross slip* (see Fig. 19*a*).

It should be noted that the vector $\mathbf{L}_0$ of an edge dislocation may lie arbitrarily in a plane perpendicular to **b** (Fig. 19*b*) and the half-plane will have a 'broken' edge in that case. Slip can then occur along any surface for which **b** is the generatrix. This process is described as *pencil slip* (see Fig. 19*b*).

It may be concluded from the foregoing that:

1. The Burgers vector characterizes dislocations only; it is normal to the line of an edge dislocation and parallel to the line of a screw

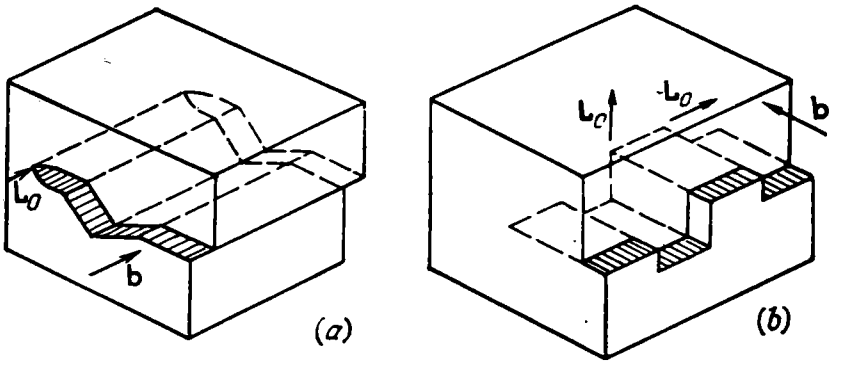

Fig. 19. Dislocation slip schematically
(*a*) cross slip of a screw dislocation; (*b*) pencil slip of an edge dislocation

dislocation. The angle between the dislocation line and the Burgers vector along a mixed dislocation may be different.

2. The Burgers vector of defects of non-dislocation type (point defects) is equal to zero, since the Burgers circuit around any point defect is closed.

3. The Burgers vector is the same along the whole dislocation line and is an invariant of a dislocation. The invariance of the Burgers vector has the following consequence: a dislocation cannot be interrupted within the crystal—it must either form a closed loop or emerge onto the free surface or else combine with other dislocation lines.

A dislocation line can branch (Fig. 20*a*); the closure failure of its Burgers circuit, i.e. the magnitude of the Burgers vector $\mathbf{b}_1$ proper will then be constant not only on movement along the dislocation line, but also on the transition through node N. In the direct vicinity of node N and further along the whole length L_{02} and L_{03}, the Burgers circuit remains unclosed by the same value $\mathbf{b}_1$, i.e. $\mathbf{b}_1 = \mathbf{b}_2 + \mathbf{b}_3$. Thus, if the dislocation lines are seen from the node N and the circuit is passed in the same direction (say, counter-clockwise), we have that $\sum_i \mathbf{b}_i = 0$.

In f.c.c. crystals, a {111} plane can contain three unit Burgers vectors of a length $0.5a$ ⟨110⟩: $0.5a\,[10\bar{1}]$; $0.5a\,[0\bar{1}1]$; and $0.5a\,[\bar{1}10]$, where a is the constant of the cubic lattice. These vectors correspond to movement from a corner of the cube to the centre of its face (i.e.

are equal to the unit vector of the lattice) and thus ensure the possibility for the formation of symmetrical triple joints (Fig. 20*b*) which combine with the formation of hexagonal dislocation networks in plane {111} (Fig. 20*c*).

Dislocations of all the types mentioned are usually present in real crystals. The dislocation structure is even more complicated in close-packed crystal lattices in the presence of partial dislocations. The total length L_Σ of all dislocation lines in a volume V

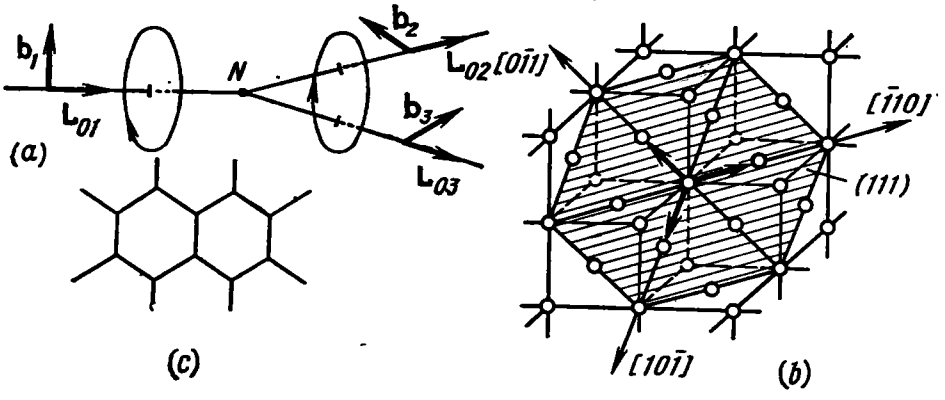

Fig. 20. Dislocation nodes
(*a*) branching of a dislocation line with the Burgers vector $\mathbf{b}_1$; (*b*) a symmetrical triple joint in (111) plane of an f.c.c. lattice; (*c*) hexagonal dislocation network in (111) plane

is called the *dislocation density* $N_d = L_\Sigma/V$, cm^{-2}. In annealed metal, $N_d \approx 10^6$ $cm^{-2} = 10^6$ cm/cm^3, i.e. each square centimetre of the surface is intersected by a million of dislocations of the total length of 10 km. In deformed (work-hardened) metal, $N_d = 10^9$-10^{13} cm^{-2}, i.e. the total length of dislocations may reach a hundred thousand kilometres.

Thus, the dislocation density and the associated distortion of the crystal lattice are quite high, especially if we note that, unlike point defects, dislocations produce long-range distortions. The dislocation densities N_d, cm^{-2}, for some materials in various states are as follows:

Annealed single crystal	10^5-10^6
Cold-deformed steel	10^{11}-10^{12}
Silver upon deformation $\varepsilon = 11\%$	2.2×10^{10}
Ditto, 21%	5.2×10^{10}
Ditto, 32%	6.8×10^{10}

Let us imagine that a side of cubic centimetre of a metal with dislocations is increased 10^3 times, i.e. to a size of 10 m. On such a magnification, the dislocation structure of the metal can be represented as spider's web of a thickness of 1 μm which fills the whole volume of the cube, with the average distance between dislocation lines of an order of 0.1 mm. No object at the other side of the cube can naturally be seen through such a thick web.

2. Elastic Properties of Dislocations

All defects cause distortion of the crystal lattice and therefore are sources of internal stresses. In the core of a dislocation (of radius $r < 2a$) where the short-range order of atom arrangement has been disturbed, elastic displacements of atoms are so appreciable that the linear theory of elasticity is inapplicable, whereas the use of the theory of finite deformations involves substantial difficulties. The linear theory of elasticity gives satisfactory results for distances from the centre of a dislocation axis $r \geqslant 2a$. Therefore, the distorted region formed by a dislocation can be imagined as a combination of two regions: in the first, distortions of the short-order arrangement of atoms are observed in the dislocation core; in the second, elastic distortions of the crystal lattice are small, with correspondingly small fields of elastic displacements and stresses in the region $r \geqslant 2a$. The contributions of these components to various physical effects are different. For instance, the structure of the core of a dislocation determines its mobility, short-range interaction with impurities, etc. The linear theory of elasticity can evaluate this situation only qualitatively. Since the stresses on a dislocation diminish slowly with increasing distance from its core, the region in which the linear theory of elasticity can be applied successfully turns out to be quite large and, by analysing the elastic properties of dislocations, we can obtain a reliable picture of the stress field around a dislocation: its energy, the force on the dislocation; the forces of interaction between dislocations; the tension. It is also possible to solve problems associated with multiplication of dislocations, their interaction with other defects in the crystal lattice, etc.

The stress field on a dislocation. In 1907, V. Volterra has developed a theory of internal stresses in elastic bodies which form by cutting off a portion of a body and connecting the edges of the cut together; in this problem, the integral of the displacement gradient over a closed contour has a finite increment b. A similar picture can be imagined to appear on the formation of an edge or screw dislocation. Thus, some general problems in the theory of elasticity have been solved long before the appearance of the theory of dislocations and their application has turned out to be effective for studying the stress fields on dislocations.

The *stress field around a screw dislocation* can be determined easily by using Volterra's model consisting of a hollow cylinder with the inner radius r_0 which represents the radius of a dislocation core, and the outer radius r_1 which is commensurable with the size of grains and equal to half the distance between screw dislocations (Fig. 21). A screw dislocation is formed by shifting the shaded section plane (Fig. 21*a*) along the generatrix by the magnitude of the Burgers vector **b**, with subsequent locking of the shifted portions; as a result, stresses appear in the cylinder and should be determined.

We will assume in further discussion that the cylinder is of an infinite length and the problem reduces to an elastic problem of plane deformation. Helicoidal twisting of the cylinder is prevented by applying an additional torque to its ends. We assume the problem to be isotropic. With these assumptions, the displacements in the cylinder are as follows:

$$u_r = u_\theta = 0; \quad u_1 = u_2 = 0;$$

$$u_3 = b\theta/2\pi = [b \arctan (x_2/x_1)]/2\pi$$

The respective deformations $\varepsilon_{ij} = 0.5\,(\partial u_i/\partial x_j + \partial u_j/\partial x_i)$ can be found by differentiation of u_3, x_1 and x_2. In that case there are

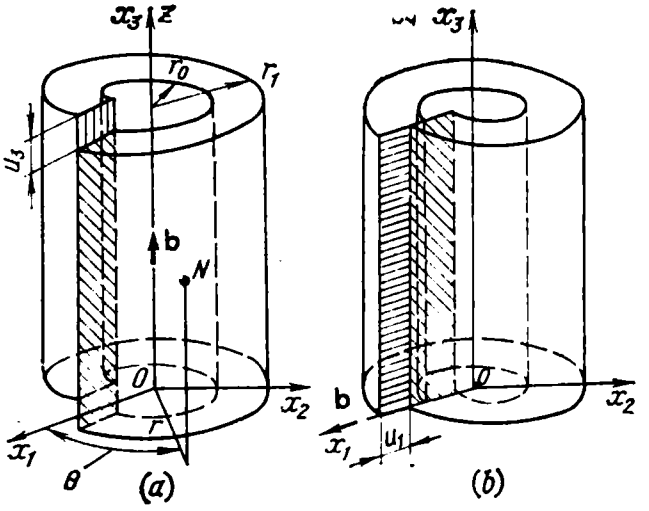

Fig. 21. Volterra's model of (*a*) screw dislocation and (*b*) edge dislocation, oriented along the Ox_3 (Oz) axis

no normal deformations, while shear strains and stresses are operative in the plane x_1Ox_2. Since $\sigma_{13} = 2G\varepsilon_{13}$ and $\sigma_{23} = 2G\varepsilon_{23}$, we have:

$$\sigma_{13} = -\frac{Gb}{2\pi}\frac{x_2}{x_1^2+x_2^2}, \quad \sigma_{23} = \frac{Gb}{2\pi}\frac{x_1}{x_1^2+x_2^2} \tag{24}$$

$$\sigma_{12} = \sigma_{11} = \sigma_{22} = \sigma_{33} = 0$$

or in polar coordinates (see Fig. 21*a*):

$$\sigma_{z\theta} = \frac{Gb}{2\pi r}; \quad \sigma_{rz} = \sigma_{r\theta} = \sigma_{rr} = \sigma_{\theta\theta} = \sigma_{zz} = 0 \tag{25}$$

The *stress field around an edge dislocation* is found by a more intricate method. Use is made of a model of edge dislocation (Fig. 21*b*), assuming the deformation is plane [$\sigma_{23} = \sigma_{31} = 0$; $\sigma_{33} = \nu\,(\sigma_{11} + \sigma_{22})$, where ν is Poisson's ratio] and the medium

is isotropic. The stresses

$$\sigma_{11} = \partial^2\Phi/\partial x_2^2; \quad \sigma_{22} = \partial^2\Phi/\partial x_1^2; \quad \sigma_{12} = -\partial^2\Phi/\partial x_1\,\partial x_2 \tag{26}$$

are determined by solving the biharmonic equation $\nabla^4\Phi = 0$ with respect to the stress function Φ (Airy's function). The general expression of Airy's function is determined by satisfying the principal

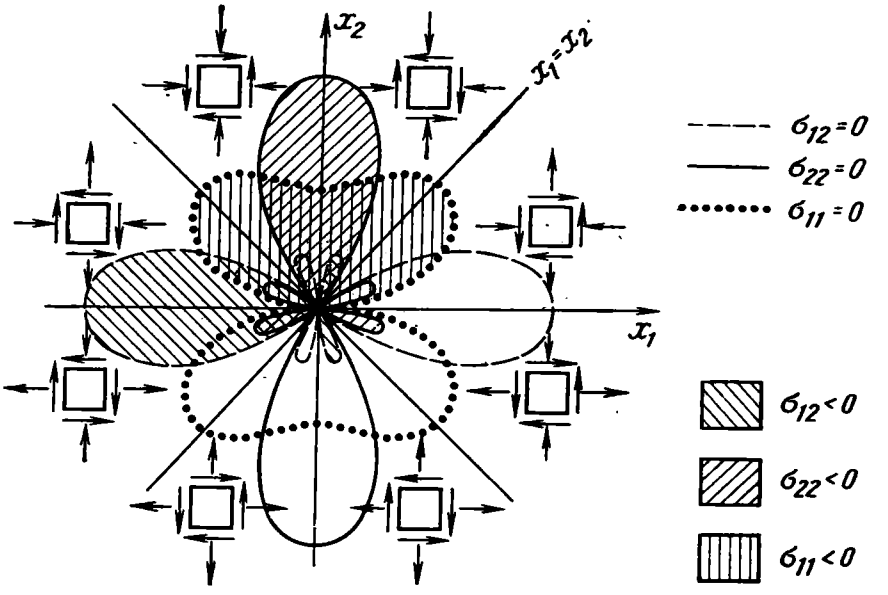

Fig. 22. Lines of equal stress $\sigma_{ij} = 0$ ($i, j = 1, 2$) around an edge dislocation with the centre at the intersection of the axes x_1 and x_2. The positive Burgers vector **b** is directed along the x_1 axis. Stressed-state diagrams are given for each of the eight sectors

singularities of the stress field of an edge dislocation and of boundary conditions according to which the resulting stress on the outer surface is zero. The stress function is then as follows:

$$\Phi = \frac{Gbx_2}{2\pi(1-\nu)} \ln \sqrt{x_1^2 + x_2^2}$$

Differentiation of Φ gives the components of the stress field around an edge dislocation in Cartesian coordinates:

$$\sigma_{22} = D\frac{x_2(x_1^2 - x_2^2)}{\rho^2}; \quad \sigma_{11} = -D\frac{x_2(x_2^2 + 3x_1^2)}{\rho^2};$$

$$\sigma_{12} = D\frac{x_1(x_1^2 - x_2^2)}{\rho^2} \tag{27}$$

where $\rho = x_1^2 + x_2^2$; $D = Gb/2\pi(1 - \nu)$.

In polar coordinates

$$\sigma_{rr} = \sigma_{\theta\theta} = -(D \sin\theta)/r; \quad \sigma_{r\theta} = -(D\cos\theta)/r \tag{28}$$

As follows from equation (27), the normal stress σ_{11} is compressive above the slip plane ($x_2 > 0$) and tensile below that plane ($x_2 < 0$) (Fig. 22); shear stresses have the highest magnitude at $x_2 = 0$ (in

the slip plane); vertical stresses σ_{22} are compressive above a positive dislocation and tensile, below it.

Analysis of formulae (25), (27) and (28) suggests the following conclusions:

1. The field of a screw dislocation is characterized by that there are no elongations, but only shear (pure torsion); the field is axisymmetrical, i.e. does not depend on the angle θ.

2. The field of an edge dislocation is unsymmetrical and characterized by shears and elongations.

3. Stresses around dislocations of both types vary proportional to $1/r$, i.e. much more slowly than stresses due to a point defect which vary proportional to $1/r^3$. *The stress field on dislocations is a long-range field.*

4. As follows from formulae (25) and (28), stresses in the vicinity of a dislocation core approach the theoretical strength of the crystal, $Gb/2\pi$, at $r = b$. In the range $r = (1.5\text{-}2)b$ where the linear theory of elasticity still gives satisfactory results, the elastic deformation is equal to 8-10 per cent and the stresses are quite high and may reach 50 per cent of the theoretical strength of the crystal.

5. Stresses depend linearly on the shear modulus G and the magnitude of the Burgers vector $\mathbf{b}$, i.e. on the magnitude (power) of a dislocation. For the same power of dislocation $|\mathbf{b}|$, the stresses of an edge dislocation field are higher than those of a screw dislocation field.

The energy of dislocations. Dislocations increase the energy of a crystal by introducing lattice distortions. The energy of a screw dislocation can be determined under the assumption that the crystal behaves as an elastic isotropic body, i.e. obeys Hooke's law. Then, according to the linear theory, the unit (per unit volume) potential energy is $e = 0.5\sigma\varepsilon = 0.5\sigma^2/G$. Noting Hooke's law, we obtain for a screw dislocation:

$$e_s = (0.5\sigma_{z\theta}^2/G) = Gb^2/8\pi^2r^2 \tag{29}$$

The total energy of a dislocation is obtained by integration of expression (29) over volume V:

$$E_s = \int_V e_s \, dV = \int_0^L dz \int_0^{2\pi} d\theta \int_{r_0}^{r_1} \frac{Gb^2 r \, dr}{8\pi^2 r^2} = \frac{Gb^2 L}{4\pi} \ln \frac{r_1}{r_0} \tag{30}$$

As may be seen, expression (30) has been integrated within definite limits of r, $r_1 \geqslant r \geqslant r_0$, which has a certain physical sense. Indeed, $\ln (r_1/r_0)$ tends to infinity as $r_0 \to 0$ and $r_1 \to \infty$, which, on the one hand, is physically unrealizable; on the other hand, the magnitude of r_0 is limited by the dislocation core where Hooke's law is inapplicable, while r_1 is limited by the size of the crystal (crystallite) or by deviation from the law of stress distribution (25),

since the interaction of unlike dislocations can lower stresses at high values of r.

Assuming that formula (29) is applicable for $r_0 > 1.5b \approx 5 \times \times 10^{-8}$ cm, where the deformation $\varepsilon < 0.1$ and the linear theory of elasticity is still fairly true, and taking $r_{1\max} \approx 1$ cm (the highest grain size) and $r_{1\min} = 10^{-5}$ cm for a dislocation density $N_d = = 10^{10}$ cm^{-2} ($r_{1\min} = 1/\sqrt{N_d}$), we obtain:

$$\ln \frac{r_{1\max}}{r_0} = \ln \frac{1}{5 \times 10^{-8}} \approx 17$$

$$\ln \frac{r_{1\min}}{r_0} = \ln \frac{10^{-5}}{5 \times 10^{-8}} \approx 5.3 \qquad (31)$$

i.e. the magnitude of $\ln r_1/r_0$ may vary by a factor of three. Using the mean geometric value of $\ln r_1/r_0 = 0.5 \ln r_{1\min} r_{1\max}/r_0^2 \approx 9$, we get

$$E_s \approx Gb^2L/2 \qquad (32)$$

Accounting for the contribution of the energy of dislocation core to formula (30), we obtain a modified expression:

$$E_s = \frac{Gb^2L}{4\pi} \ln \left(\frac{r_1}{r_0} + [Z_d \right) \qquad (33)$$

where $Z_d = 1$ to 3. Thus, as follows from the calculations, the energy of the dislocation core is substantially lower than the energy in the region $r_1 \geqslant r \geqslant r_0$ of long-range action of elastic stresses. Similarly, we can write for an edge dislocation:

$$E_e = \frac{Gb^2L}{4\pi(1-\nu)} \left[\ln \frac{r_1}{r_0} - 1 \right] \qquad (34)$$

In this case, too, formula (32) can be applied for various estimations.

Thus, we can draw the following conclusions.

1. The energy of a dislocation is proportional to the shear modulus and *second power of the Burgers vector*. This conclusion is true for any type of dislocation.

2. The energies of a screw and an edge dislocation are of the same order of magnitude [see formulae (33) and (34)] but, for the same dislocation power, the energy of an edge dislocation is slightly higher than that of a screw dislocation.

3. The energy of a dislocation having a length of one atomic plane (i.e. $L = b$) is rather high. At $G = 3 \times 10^6$ N/cm^2 and $b = = 3 \times 10^{-8}$ cm, it is

$$E_{L=b} = Gb^2L/2 = Gb^3/2 \approx 3 \text{ eV}$$

Since the dislocation length $L \gg b$, its energy $E_d \gg 10$ eV (for $L = 10^{-7}$ nm, $E_d \approx 9 \times 10^2$ eV). It is much higher than the energy of thermal oscillations $E_t = kT$ (k = Boltzmann constant) and at temperatures 300-2 000 K, $E_t = (2.5\text{-}17.5) \times 10^{-2}$ eV $\ll E_d$. Since

thermodynamic equilibrium requires a corresponding concentration of defects $n_d = N \exp(-E/kT)$ (where E is the energy of nucleation of defects and N is the number of probable sites of their nucleation), thermal motion can initiate defects with an energy of only 2-3 eV. The elastic energy for the formation of a dislocation, E_d, is however much higher than 2-3 eV, and therefore, dislocations can never be thermally stable defects and their number is independent of temperature. In this respect, dislocations differ essentially from point defects whose equilibrium concentration increases with temperature proportional to $\exp(-E/kT)$. Thus, neither energy fluctuations nor an increase of temperature can form a new dislocation. Since the number of dislocations is independent of temperature, their concentration at thermodynamic equilibrium must be equal to zero. Due to the presence of low Peierls-Nabarro locks* in metals, however, even slight thermal stresses formed on crystallization or cooling after annealing are often sufficient to cause plastic deformation and the appearance of dislocations, especially when external mechanical actions are operative. For that reason, metals always have a certain original dislocation density due to prior actions and no annealing procedure can reduce the dislocation density to zero. At present, only covalent-bond crystals (germanium, silicon, etc.) can be prepared dislocation-free, since their bonds are characterized by high Peierls-Nabarro locks.

4. The contribution of the dislocation core to the energy of a dislocation is roughly 10 per cent, i.e. the main contribution to the dislocation energy is due to long-range stress fields.

Forces on a dislocation. The energy of a dislocation is proportional to its length. On an increase of the length of a dislocation, its elastic energy also increases. Since any system tends to minimize its energy, a dislocation line behaves as an elastic filament, i.e. it always tends to straighten in order to reduce its length. By analogy with the surface tension in liquids**, the energy of a unit length of dislocation

$$E_{L=1} = 0.5Gb^2 = f \tag{35}$$

is the *force of linear tension of a dislocation* directed along the dislocation line.

When a dislocation moves in an elastic stress field, it performs work. Noting this circumstance, one can operate with the concept of a certain force f acting on the unit length of a dislocation as on an independent physical object which actually is neither a body nor a particle, but a special configuration in the regular arrangement of atoms. Under the action of external forces (see Fig. 14), a dislocation

* On Peierls-Nabarro stresses and locks see formula (49).

** As is known, the coefficient of surface tension of liquids can be regarded either as a force acting on the unit length of an imaginary section through the liquid surface or as an excess energy of a unit surface area.

moves through a path l_1 equal to the length of the crystal, emerges on the free left-hand side of the crystal and forms a jog of width b. The work a_1 performed by the force f on the unit length of dislocation will then be $a_1 = fl_1$ and the work on the total length L, $A_1 = fl_1L$. Thus, the work A_1 has been determined by considering a gradual displacement of the dislocation on its path l_1, which has resulted in a shear through b along the whole length l_1 under the action of external forces. Considering the transition from the original to the final state and assuming that external forces produce uniformly distributed shear stresses τ in the slip plane, it can be said

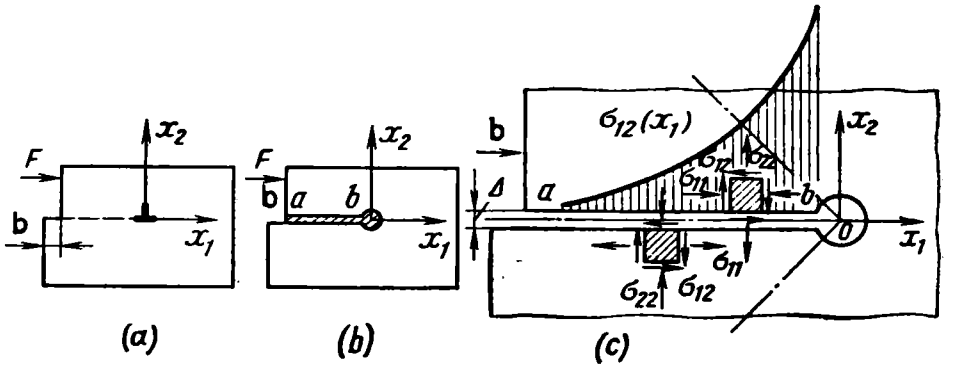

Fig. 23. Two equivalent diagrams of the formation of dislocations
(a) under the action of an external force F; (b) and (c) by the formation of a notch which is then displaced by **b**; in (b) and (c), $\sigma_{22} = 0$ at $x_2 = 0$. With the thickness Δ of the cut, $\sigma_{22} \neq 0$. These stresses do not however perform work on the path of displacement, since $\sigma_{22} \perp \mathbf{b}$ (c)

that the force $\tau l_1 L$ has performed the work $A_2 = \tau l_1 L b$ on path b. Since work depends only on the initial and the final state, $A_1 = A_2$ and

$$fl_1L = \tau l_1 L b \quad \text{or} \quad f = \tau b \tag{36}$$

It can be proved that formula (36) (Mott-Nabarro relationship) for a *force acting on the unit length of a dislocation* is true for the movement of screw and mixed dislocations. Since the Burgers vector is an invariant of a dislocation and since, with uniform shear stresses, τ is constant over the whole slip plane, the force acting on the unit length of dislocation is the same in magnitude (but not in direction) in any portion of a curvilinear dislocation and is directed perpendicular to the dislocation line in any its point towards the portion of the slip line which is still not involved in shear.

Relationship (36) can be obtained by a somewhat different method which turns out to be effective for determining the force of interaction between dislocations. Let us derive formula (36) by using the method of sections known from the strength of materials.

Let an edge dislocation be formed under the action of an external force F (Fig. 23a). The work of external forces Fb is equal to the

work of internal forces (stresses), i.e. to the energy of the dislocation. The work of external forces in the formation of a dislocation is spent to form the stress field [see formula (27)]. In order to determine the force f acting in the slip plane in direction x_1, let us make a section and remove the shaded portion (Fig. 23*b*). The effect of the removed portion can be replaced by external loads which should be balanced so that any point of the section and of the external contour of the crystal remained in its original position. In that case the system of external loads must be distributed so as to correspond fully to the stress diagram $\sigma_{12}(x_1)$ along the section surface [for the system represented in Fig. 23*b* and *c*, the stresses σ_{11} are internal ones and, according to (27), $\sigma_{22} = 0$]. The diagram in Fig. 23*b* is equivalent to that in Fig. 23*a*, but implies a different version of formation of dislocations: a section is made in the form shown in Fig. 23*b*, the top portion of the crystal is displaced relative to the bottom one by the Burgers vector **b**, and external forces are applied to the section surface, which are distributed by the same law as the stresses $\sigma_{12}(x_1)$ in formula (27). In that case, only the shear stresses σ_{12} will perform work on the path **b** of displacement of the top portion of the crystal (the stresses σ_{22} are normal to the displacement vector **b**). Along the path *ab*, a unit length of dislocation will be acted upon by the resulting force $N = \int_s \sigma_{12}\, ds = \int_s \sigma_{12}\, dx_1$ (see Fig. 23*c*), which performs on **b** the work $A_1 = b\int_s \sigma_{12}\, dx_1$ equal to the internal energy W of the system. The force f_{x_1} acting on the dislocation along x_1 is determined as $f_{x_1} = \partial W/\partial x_1$ or

$$f_{x_1} = \frac{\partial W}{\partial x_1} = \frac{b\int \sigma_{12}\, dx_1}{\partial x_1} = \sigma_{12} b = \tau b \qquad (37)$$

Expression (37) is analogous to (36).

As a dislocation approaches the free surface of the crystal, the strain energy of the crystal decreases, since the free surface causes no stresses which might inhibit dislocation movement. The smaller is the distance from a dislocation to the free surface, the smaller is the dislocation energy and the higher is its attraction to the free surface. This is why a dislocation will be attracted to the surface until it emerges onto the surface and forms a jog of a width of one atomic spacing. The force of attraction of a dislocation to the free surface of crystal is identical to the force with which this dislocation would be acted upon in an infinite crystal by an imaginary dislocation of opposite sign appropriately oriented relative to the crystal surface. In the case of a screw dislocation approaching the crystal surface, the imaginary dislocation is the mirror image of the origi-

nal dislocation from the crystal surface. The force with which a dislocation is attracted to the surface is respectively called the *image force*. In particular, if a screw dislocation is parallel to the free surface and lies at a distance r from it, the image force per unit length of this dislocation is

$$f_1 = \frac{\partial E_s}{\partial r} = \frac{\partial}{\partial r}\left(\frac{Gb^2}{4\pi} \ln \frac{r_1}{r_0}\right) = \frac{Gb^2}{4\pi r} \tag{38}$$

A thin layer of oxides (an oxide film on aluminium, for instance) on the surface of a crystal can offer resistance to the passage of a dislocation onto the surface, which leads to noticeable surface

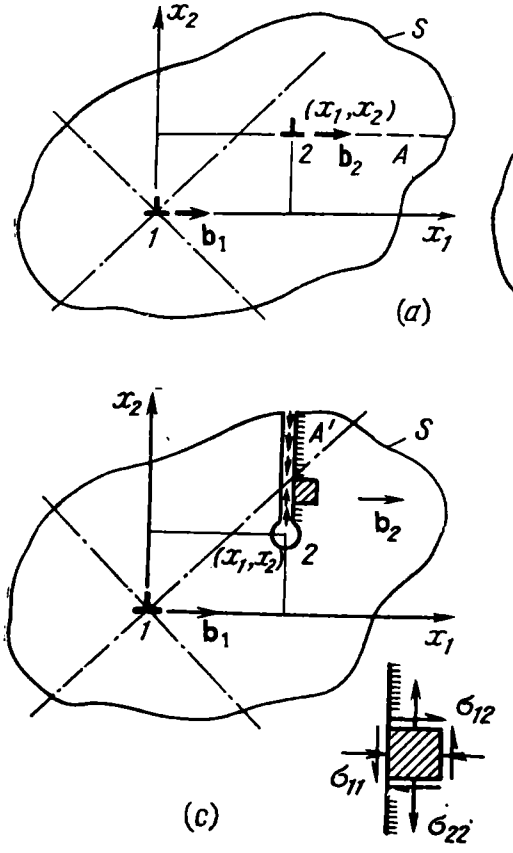

Fig. 24. Diagrams for determining the force of interaction between two edge dislocations; (*b*) f_{x_1}; (c) f_{x_2}. In (*b*), the work on the path of displacement $\mathbf{b}_2$ is performed by stresses σ_{12} which are external on the surface A. Stresses $\sigma_{22} \perp b_2$ and thus perform no work. In (c), the work on displacement $\mathbf{b}_2$ is performed by stresses σ_{11} external on the A' surface; stresses $\sigma_{12} \perp b_2$ and perform no work

hardening. It can be expected that the mechanical properties of the material will thus change appreciably. As has been indicated by A. H. Cottrell, the yield limit of some soft metals can be raised by a factor of three in this way.

Interaction forces between dislocations. Suppose that a dislocation *2* in a crystal limited by surface S is in the field of an immobile dislocation *1* (Fig. 24*a*). The energy of the system is composed of the energy E_1 of the first dislocation, the energy E_2 of the second dislocation, [which are determined by formula (30)], and the energy of interaction between these dislocations, E_{1n}. If E_{1n} is known, the

vector components of the interaction forces will be determined as $f_{x_i} = \partial E_{in}/\partial x_i$ ($i = 1, 2, 3$). In particular, for the plane problem considered, we have:

$$f_{x_1} = \partial E_{in}/\partial x_1; \quad f_{x_2} = \partial E_{in}/\partial x_2 \tag{39}$$

Dislocation *2* can be introduced into the field of dislocation *1* with the Burgers vector $\mathbf{b}_1$ by the scheme shown in Fig. 24*b*, i.e. by cutting along the surface A and subsequent shear through $\mathbf{b}_2$*. Note that the stresses acting in the plane of section are the sum of the stresses due to dislocations *1* and *2*. We however are not interested in superposition of elastic stress fields. To determine the energy of interaction of dislocations, it is essential to know the stress field due to dislocation *1* in points of the section surface A (Fig. 24*b*). As in the previous example, when dislocation *2* forms, work is performed by the stresses σ_{12} due to dislocation *1*, which are distributed over the surface A in path b_2. For that reason,

$$E_{in} = b \int \sigma_{12}\, dx_1$$

and

$$f_{x_1} = \sigma_{12} b_2 \tag{40}$$

Another vector component of the force of interaction between dislocations, $f_{x_2} = \frac{\partial}{\partial x_2}\left(b_2 \int\limits_A \sigma_{12}\, dx_1\right)$, can be found in an easier manner by the above technique if we make a vertical section in the crystal up to the point (x_1, x_2) (Fig. 24*c*). In that case the external forces which perform work on b_2 are the stresses σ_{11} distributed over the surface A'. The force performing work in A', related to a unit length of dislocation, will be

$$\int\limits_{A'} \sigma_{11}\, dS' = \int \sigma_{11}\, dx_2$$

Using (39), we can find:

$$f_{x_2} = \frac{\partial E_{in}}{\partial x_2} = \frac{\partial}{\partial x_2}\left(b \int \sigma_{11}\, dx_2\right) = \sigma_{11} b \tag{41}$$

Substitution of (27) into (40) and (41) gives formulae for *the force of interaction of two parallel edge dislocations*:

$$f_{x_1} = \frac{Gb_1b_2}{2\pi(1-\nu)} \frac{x_1(x_1^2 - x_2^2)}{\rho^2} = K \frac{\varkappa_1(\varkappa_1^2 - 1)}{(\varkappa_1^2 + 1)^2}$$

$$f_{x_2} = \frac{Gb_1b_2}{2\pi(1-\nu)} \frac{x_2(x_2^2 + 3x_1^2)}{\rho^2} = K \frac{3\varkappa_1^2 + 1}{(\varkappa_1^2 + 1)^2} \tag{42}$$

where $K = \dfrac{Gb_1b_2}{2\pi(1-\nu)x_2}$ and $\varkappa_1 = x_1/x_2$.

* The technique used here is similar to that by which the Mott-Nabarro relation (37) has been derived.

In polar coordinates, we have

$$f_r = f_{x_1}\cos\theta + f_{x_2}\sin\theta = \frac{Gb_1b_2}{2\pi(1-\nu)}\frac{1}{r}$$
$$f_\theta = f_{x_2}\cos\theta - f_{x_1}\sin\theta = \frac{Gb_1b_2}{2\pi(1-\nu)}\frac{\sin\theta}{r} \qquad (43)$$

With screw dislocations, the stresses $\sigma_{z\theta}$ due to the first dislocation ($\mathbf{b}_1$) perform work on introduction of the second dislocation ($\mathbf{b}_2$) into the field of the first one (Fig. 25). The energy of interaction of these dislocations is $E_{in} = \int \sigma_{z\theta} b \, dA$ (A = section surface) and the *force of interaction of two parallel screw dislocations is*

$$f_r = \frac{\partial}{\partial r}\int b\sigma_{r\theta}\, dr = \frac{Gb_1b_2}{2\pi r} \qquad (44)$$

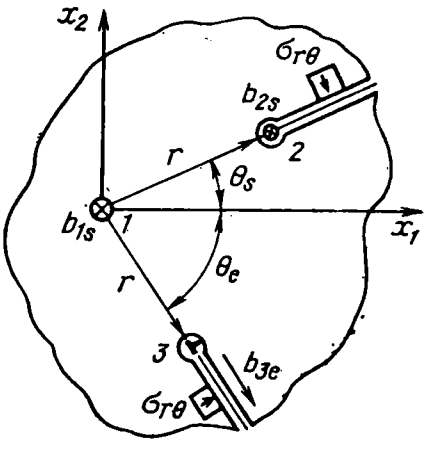

Fig. 25. Diagrams for determining the force of interaction between dislocations

When two screw dislocations *1* and *2* interact, the Burgers vector and the direction of external stresses $\sigma_r\theta$ on the surface are parallel to the x_3 axis and $\sigma_r\theta$ performs work in $\mathbf{b}_2$. When a screw dislocation (*1*) and an edge dislocation (*3*) interact, external stresses $\sigma_r\theta$ are directed along x_3, the Burgers vector of the edge dislocation lies in $x_1 x_2$ plane, i.e. $\sigma_r\theta \perp b_e$ and $\sigma_r\theta$ performs no work in b_e

When using formulae (42) through (44), one should consider the sign of stresses due to the first dislocation and the direction of Burgers vector of the second dislocation. It is assumed that the interaction energy is positive if the dislocations are of the same sign and negative if they are of opposite signs.

The results obtained offer the following conclusions:

1. Screw dislocations interact like electric charges, i.e. like dislocations are repulsed and unlike ones, attracted.

2. Interaction forces between dislocations are of the long-range type and vary proportional to $1/r$ [see formulae (42) through (44)].

3. An edge and a screw dislocation, if parallel to each other, do not interact (see Fig. 25), since the external force determined by the stress $\sigma_{z\theta}$ due to the screw dislocation, according to formula (25), is perpendicular to the Burgers vector $\mathbf{b}_e$ of the edge dislocation.

4. The stress field of an edge dislocation is asymmetrical, resulting in a complicated relationship $f_{x_1}(x_1, x_2)$ (Fig. 26). For two like dislocations of the same magnitude ($b_1 = b_2 = b$)

$$f'_{x_1} = f_{x_1}/K = [x_1(x_1^2 - 1)]/(x_1^2 + 1)^2 \qquad (45)$$

with repulsion taking place at $f'_{x_1} > 0$ and attraction, at $f'_{x_1} < 0$*.

* The diagrams $f'_{x_1}(x_1)$ are symmetrical relative to the axis of ordinates.

Like dislocations are repulsed at $x_1 > x_2$ ($\varkappa_1 > 1$), see curve *1* in Fig. 26, and attracted at $\varkappa_1 < 1$; the value $\varkappa_1 = 1$ corresponds to $f'_{x_1} = 0$. This position of the second dislocation is, however, unstable; its slight displacement to the right will cause the appearance of repulsion forces (the dislocations move apart), while a displacement to the left involves attraction. At $\varkappa_1 = 0$, the force of interaction of like dislocations f'_{x_1} is zero and the second dislocation is in a stable position, since only attraction forces will act irrespective of whether the dislocation is displaced slightly to the right or to the left. Thus, like dislocations occupy a stable dislocation configuration and form an array (Fig. 27*a*). The energy E_n of an array composed of n dislocations is smaller than the sum of the energies, nE_d, of n individual dislocations. By comparing Figs. 27*a* and 23, it is clear why a dislocation array has a reduced energy: the compression fields of individual dislocations are superposed on the tension field of all the dislocations located above the array, while the tension

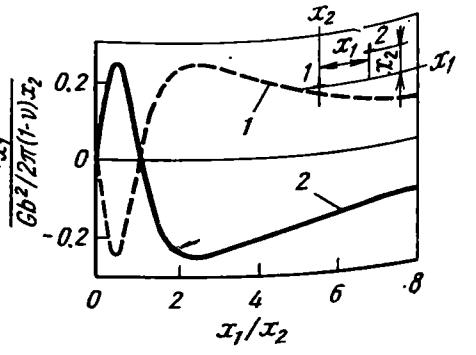

Fig. 26. Effect of the relative distance x_1/x_2 between dislocations on the force f_{x_1} with which dislocation *1* acts on dislocation *2* in the slip plane of the latter (see Fig. 24*a*)
1 — like-sign dislocations; *2* — unlike-sign dislocations

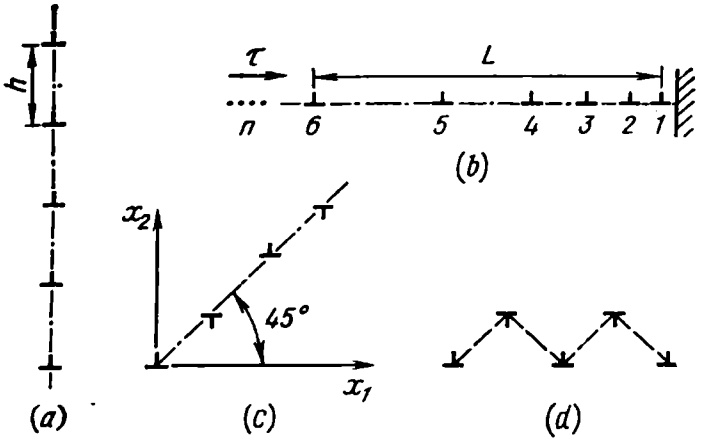

Fig. 27. Dislocation configurations formed by int eraction of edge dislocations
(*a*) dislocation array; (*b*) dislocation pile-up on an obstacle; (*c*, *d*) stable configurations in a pile-up of unlike dislocations

fields are superposed on the compression field of all the dislocations located below the array. Stress compensation takes place along the array and thus E_n is lower compared with nE_d. Stable arrays may be low-angle grain boundaries, i.e. boundaries of subgrains (blocks). The formation of dislocation arrays has found an experimental

evidence in polygonization occurring in high-temperature annealing of plastically deformed crystals.

5. It follows from formula (43) that for dislocations with the Burgers vector $\mathbf{b}_1 = \mathbf{b}_2 = \mathbf{b}$ in the slip plane ($x_2 = 0$)

$$f_{x_1} = \frac{Gb^2}{2\pi(1-\nu)} \frac{1}{x_1} \tag{46}$$

so that like dislocations are repulsed. Dislocations accumulated in the same slip plane on an obstacle form an unstable dislocation pile-up (Fig. 27*b*) whose energy is $E_{\text{con}} > n_{\text{con}} E_{\text{d}}$. Since the stress field of a dislocation is a long-range field, it can be assumed that at distances r less than L, the dislocation pile-up behaves as a superdislocation with the Burgers vector $\mathbf{B} = n_{\text{con}}\mathbf{b}$, where n_{con} is the number of dislocations in the pile-up. Since the energy of a dislocation is proportional to the square of Burgers vector, $(n_{\text{con}}b)^2$ of a superdislocation is substantially greater than Σb^2 of n_{con} individual dislocations.

6. It follows from what has been said under 4 and 5 that the energy E_n of a configuration composed of n dislocations differs substantially from the sum of the energies of individual dislocations, nE_{d}, which is due to the interaction of the long-range stress fields. Depending on the kind of configuration, cases are possible when $E_n > nE_{\text{d}}$ or $E_n < nE_{\text{d}}$, this difference being greater at a larger number of dislocations. This is why at the early stages of plastic deformation when the dislocation density is still low, the main part is played by the properties of individual dislocations associated with the structure of their core. As deformation proceeds, the dislocation density increases and the main contribution to the energy of the system is now made by the long-range stress fields of dislocations. In this connection the main part must be played by the properties and interactions of large dislocation groups, with the structure of the dislocation core having a weaker effect.

7. For unlike dislocations, a minus sign should be written before K in formula (42) for f_{x_1}; expressions (45) and (46) will then take the form:

$$f'_{x_1} = \frac{f_{x_1}}{K} = -\frac{\varkappa_1(\varkappa_1^2-1)}{(\varkappa_1^2+1)^2}$$

and

$$f_{x_1} = -\frac{Gb^2}{2\pi(1-\nu)} \frac{1}{x_1} \tag{47}$$

It follows from formula (47) that unlike dislocations are attracted at $\varkappa_1 > 1$ (curve *2* in Fig. 26) and repulsed at $\varkappa_1 < 1$. Thus, at $\varkappa_1 = 1$ and $f_{x_1} = 0$, there forms a stable dislocation configuration (Fig. 27*c* and *d*). On the contrary, at $\varkappa_1 = 0$ and $f_{x_1} = 0$ the position of dislocation *2* (see Fig. 24) is unstable; with its slight displa-

cement to the right or to the left repulsion forces become operative which displace dislocation *2* into a stable position at $\varkappa_1 = 1$. As earlier, the energy of a stable dislocation configuration, E_n, is smaller than the sum of the energies, nE_d, of individual dislocations.

8. According to formula (47), unlike dislocations in the same slip plane are attracted to one another and annihilate: two extra-planes merge into a single complete atomic plane. If unlike dislocations are in adjacent slip planes separated by an atom spacing (Fig. 28*a*), then a chain of vacancies or interstitial atoms will form on their closure (Fig. 28*b*), which has turned out to be 'superfluous'

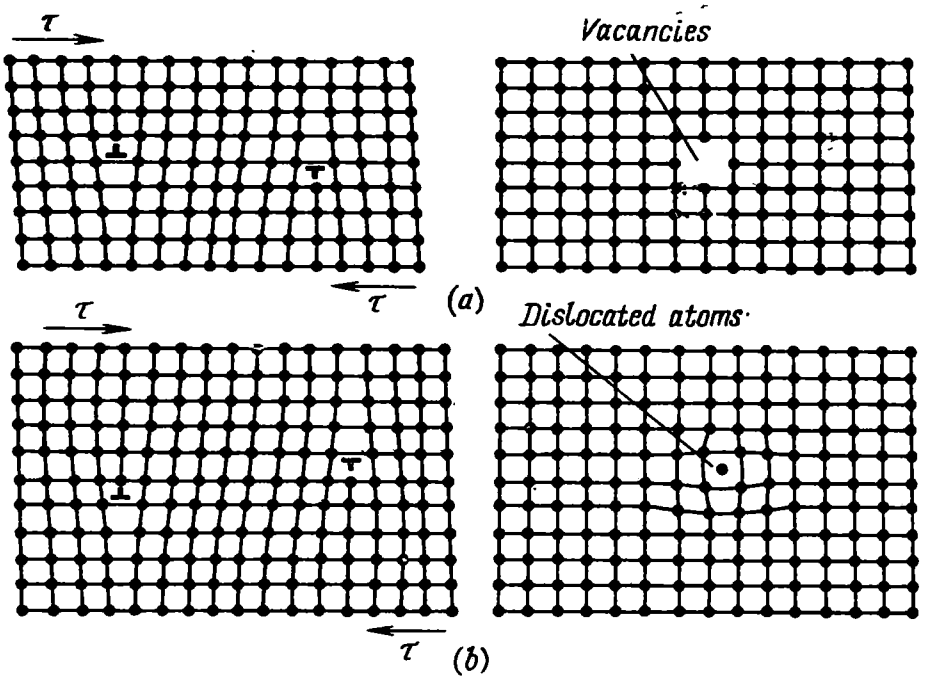

Fig. 28. Annihilation of linear unlike dislocations located in parallel slip planes leading to the formation of (*a*) a chain of vacancies and (*b*) dislocated atoms

when two extra-planes merged into a single complete plane. With an increase in the spacing between slip planes, attraction of unlike dislocations at short distances along the slip plane changes to repulsion (see Fig. 26, curve *2*).

Forces acting between dislocations and solute atoms (point defects) possess a spherical symmetry. The energy of interaction between an edge dislocation and a solute atom is:

$$E_{in} = \frac{4}{3}\frac{1+\nu}{1-\nu}\frac{Gber^3 \sin\alpha}{R} \tag{48}$$

where R and α are the polar coordinates of the solute atom relative to a positive linear dislocation. The radius of atoms of the base metal differs from that of the dissolved impurity, which is $r' =$

$= (1 + \varepsilon) r$. The interaction forces

$$f_\alpha = -\frac{1}{R}\frac{\partial E_{in}}{\partial \alpha} \text{ and } f_R = -\frac{\partial E_{in}}{\partial R}$$

are found by differentiation of E_{in} (48) with respect to α and R.

It follows from analysis of variations of f_α and f_R that a solute atom is repulsed from compressed regions of the dislocation field and attracted into tensioned regions.

Since the average stress in the stress field of a screw dislocation is zero, a screw dislocation does not interact with solute atoms.

Movement of a dislocation. An important property of dislocations is their mobility. An edge dislocation (see Fig. 14) can move easily

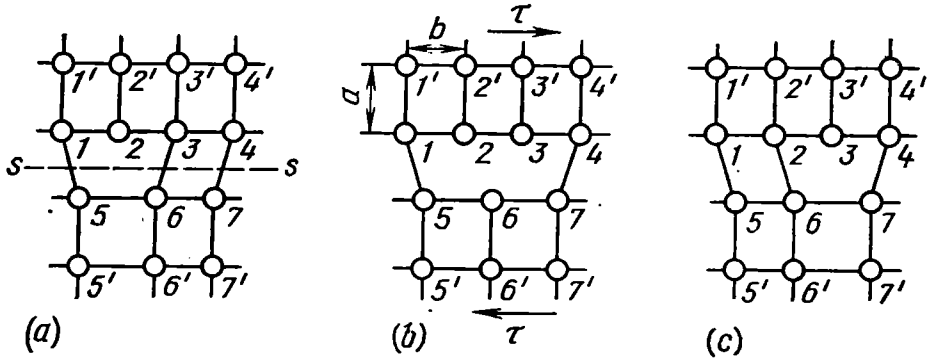

Fig. 29. Interaction of atoms in the core of a dislocation when the latter is displaced through one atomic spacing

(*a*) original position; (*b*) intermediate position of unstable equilibrium; (c) final position, which is energetically identical to the original one, but with the extra-plane displaced by **b**

in the slip plane *ABCD* under the action of light stresses. The magnitude of these stresses is characterized by short-range distortions in atomic arrangement or by the structure of the dislocation core.

Let us consider the movement of an edge dislocation in the slip plane *ss* (Fig. 29*a*) and clarify why dislocations can move easily. In the original position, the extra-plane is formed by atoms *2-2'*. Let us assume for clarity that the attraction forces between atoms decrease rapidly with increasing distance. For that reason, the bonds between atoms *2-5* and *2-6* can be regarded negligible and mutually balanced, while those between atoms *1-5* and *3-6* are somewhat weakened. Let a shear stress τ be applied to the lattice (Fig. 29*b*). It will increase the distance between atoms *3-6* and decrease that between atoms *2-6*. As the upper portion of the crystal (relative to line *ss*) moves further over the lower portion under the action of shear stresses, the distance between atoms *3* and *6* will increase so that the bond between them will weaken sharply. On the contrary, the distance *2-6* will decrease (Fig. 29*c*), leading to a stronger bond. As a result, the former half-plane (extra-plane) *2-2'* (Fig. 29*a*) will combine with the lower half-plane *6-6'* to form a complete plane *2'-2-6-6'* and a new extra-plane *3-3'* (see Fig. 29*c*).

This *slip* (or *conservative movement*) *of a dislocation* in the slip plane *ss* is characterized by the fact that the total number of weakened bonds existed before slip is retained at all stages of the movement. In the example considered, there were two weakened bonds in the initial state: *2-5* and *2-6*. Though the extra-plane has moved from position *2-2'* to *3-3'*, i.e. the dislocation has moved through **b**, the number of weakened bonds has remained unchanged. These are the bonds *3-6* and *3-7*. Thus, as the dislocation has moved through **b**, the *2-6* bond has been restored and the *3-6* bond, weakened. Consequently, *dislocation movement is a process by which crystal lattice bonds are periodically weakened and restored in the dislocation core.*

The initial state represented by the diagram in Fig. 29*a* corresponds to the minimum of potential energy of interaction of atoms. The final configuration (Fig. 29*c*) is identical to the original, since all atoms are similar and therefore undistinguishable. For that reason, the energy E_0 in the example considered is the same in the original and the final state. In an intermediate state, the system energy $E > E_0$, so that a minimum of energy should be expected for the symmetrical intermediate state shown in Fig. 29*b*. Thus, variations of the energy $E(x)$ depending on the displacement x of a dislocation in slip direction are described by a periodic function with the period b. The same is true of the force of interaction between atoms in the dislocation core [since $F(x) = \partial E(x)/\partial x$] and of stresses $\tau(x)$. This circumstance served as the basis for developing various models of dislocation core proposed, for instance, by Frenkel and Kontorova, Peierls and Nabarro, et al. All these models are rather approximate, with their formulae being derived under rather crude assumptions. For that reason, the solutions obtained are valid only qualitatively.

Mobility of dislocations is usually analysed by using Peierls' solution, who has proposed formulae for determining the energy $\Delta E = E - E_0$ of *the start of dislocations and of the critical shear stress required for a dislocation to start to move and overcome a potential barrier* ΔE:

$$\tau_{P\text{-}N} = \frac{2G}{q} \exp\left(-2\pi a/qb\right) \tag{49}$$

where $q = 1$ for a screw dislocation and $q = 1 - \nu$ for an edge dislocation. The stress $\tau_{P\text{-}N}$ is called the *Peierls-Nabarro stress*, or *stress to move a dislocation.*

Peierls used in his formula (49) one of the possible kinds of periodic stress function

$$\tau(x) = \frac{G}{2\pi} \frac{b}{a} \sin \frac{2\pi\varphi(x)}{b}$$

which is identical with the function used in the analysis of the theoretical strength by Frenkel. An essential difference here is in

the determination of $\varphi(x)$ which varies within the limits $\pm b/2$. This function describes the mutual displacement of two atoms opposing one another at both sides of the slip plane in the dislocation core, i.e. the function describes the displacement of atoms in the dislocation core from the portion of the slip plane where slip has taken place to another portion where it still has not. The width of this transition along the slip plane within which the displacement exceeds $b/4$, i.e. 50 per cent of the total displacement, is called the *dislocation width* and is the measure of smoothness of this transition. If this transition occurs within the interval $(1\text{-}2)b$, the dislocation is called *narrow*; with an interval more than $5b$, the dislocation is *wide*. Wide dislocations are typical of metals and narrow ones of covalent crystals of the type of diamond, in which bonds are oriented. Wide dislocations are characterized by a smaller displacement of atoms above the slip plane relative to the positions of atoms below that plane, which results in a lower misfit energy and a lower energy ΔE spent for overcoming the bonding forces in the dislocation core. Consequently, *the mobility of dislocations increases with increasing dislocation width.*

In formula (49), the dislocation width is $\omega = a/(1 - \nu)$. Since Peierls stresses vary periodically during dislocation movement, they have been called on these grounds 'the friction forces of the lattice in dislocation movement'.

Analysis of formula (49) and of schemes of dislocation movement (see Fig. 29) suggests the following conclusions:

1. A moving dislocation is transferred in relay-race manner, as it were, from one plane to another; at the same time, bonds in the crystal lattice are weakened and restored again, not instantaneously over the whole slip plane in the crystal, but only in the dislocation core. In that connection, the stress $\tau_{P\text{-}N}$ is much lower than the theoretical shear stress $\tau_t = G/2\pi$ in an ideal lattice. For instance, for a simple cubic lattice with $a = b$, $\nu = 1/3$ and $q = 2/3$ (an edge dislocation), $\tau_{P\text{-}N} = 2.5 \times 10^{-4}\, G \ll \tau_t$. The order of magnitude of $\tau_{P\text{-}N}$ agrees well with the available experimental data.

2. The critical shear stress $\tau_{P\text{-}N}$ is lower at a lower Burgers vector $\mathbf{b}$ and a greater distance a between the planes in the direction normal to the slip plane. Even a slight increase in the a/b parameter may have a strong effect on $\tau_{P\text{-}N}$. For instance, for the case considered under (1), $\tau_{P\text{-}N} = 2.5 \times 10^{-4}\, G$ at $a/b = 1$ and roughly $2.1 \times \times 10^{-6}\, G$ at $a/b = 1.5$, i.e. decreases almost by a factor of 100. This is why the highest mobility is shown by dislocations with a low Burgers vector, lying in atomic planes with the largest distance a between them. In particular, $\tau_{P\text{-}N}$ is the lowest and the interplane distance is the highest for close-packed planes which for this reason are *easy glide planes.*

3. Under identical conditions, edge dislocations have a higher mobility than screw type. Indeed, with $a/b = 1$, $\tau_{P\text{-}N} = 2.5 \times$

$\times 10^{-4} G$ for an edge dislocation and $4 \times 10^{-3} G$ for a screw dislocation*.

4. The forces which tend to eliminate misfit of atoms in adjacent planes are the weakest between close-packed planes, since the distance between such planes is greater than between any other planes in the lattice. For that reason, the widest dislocations lie in close-packed planes and the mobility of a dislocation increases with an increase in its width.

5. The movement of a dislocation is an elementary act of plastic deformation. Plastic deformation takes place in the elastic stress field around a dislocation.

The highest gain in the lattice energy on passage of a dislocation into the most unstable state—the Peierls stress (the friction forces of the lattice)—depends on the nature of bonding and the width of dislocation. Peierls stress is higher in crystals with covalent (oriented) bonds and lower in those with metallic and ionic (unoriented) bonds.

If a dislocation has moved through the whole length of the crystal l_1 (see Fig. 14) and formed a jog of width b on its left-hand face, the amount of plastic deformation will be $\varepsilon = b/l_1$ on movement of one dislocation and $\varepsilon_n = nb/l_1$ on movement of n dislocations. A case is possible however that not all n dislocations will move through the whole crystal, i.e. some of them will be arrested by obstacles and cover only a path $l_{fp} < l_1$, which is called the *free-path length of a dislocation.* Accordingly, the deformation ε_n will be smaller by a factor of l_{fp}/l_1, i.e.

$$\varepsilon_n = bl_{fp}\frac{n}{l_1^2} = N_m b l_{fp} \tag{50}$$

where $N_m = n'/l_1^2$ is the density of mobile dislocations whose number is $n' < n$.

Differentiation of (50) with respect to time gives an expression for the rate of deformation:

$$\dot{\varepsilon}_n = N_m b v + \dot{N}_m b l_{fp} \tag{51}$$

where $v = \mathrm{d}l_{fp}/\mathrm{d}t$ is the rate of dislocation movement and $\dot{N}_m$ is the time variation of the density of mobile dislocations.

Let us find $\dot{\varepsilon}_n$ under the following assumptions: the stresses are high, and therefore, $N_m \approx N$ and $\dot{N}_m$ is low, so that the second term in (51) can be neglected. Then, with $N = 10^{11}$ cm^{-2}, $b = 3 \times 10^{-8}$ cm, and $v = 10^5$ cm/s (it is practically the speed of sound

* This statement is valid for a simple cubic lattice considered here and for f.c.c. lattices; in b.c.c. metals at low temperatures, screw dislocations are more mobile.

in the metal), we have $\dot{\varepsilon}_n \approx 3 \times 10^8$ s^{-1}. The highest deformation rates $\dot{\varepsilon}$ usually do not exceed 10^3-10^5 s^{-1}. This suggests a conclusion that the density of dislocations is so high that always ensures the highest rates of plastic deformation.

Multiplication of dislocations. The intrinsic energy of dislocations is quite high: 30-50 eV for a dislocation length $L = 10b$. For that reason, there should be no thermodynamically stable dislocations in a crystal. Therefore, other causes should be responsible for the initiation and multiplication of dislocations, in particular, the conditions of growth and cooling of a crystal and even more so, the conditions of plastic deformation of the crystal.

The nucleation of dislocations of length L (see Fig. 14) in portions of a perfect crystal requires a very high stress τ which must perform the work $A = FL = \tau b l_{fp} L$ (l_{fp} = free-path length of a dislocation) equal to the energy of formation of a dislocation $E_d = Gb^2L/2$. Consequently, $\tau = 0.5Gb/l_{fp}$. For the formation of a dislocation in a perfect crystal, l_{fp} must not exceed (1-2)b, i.e. the stress for nucleation of a dislocation in a perfect crystal $\tau = G/2$-$G/4$ is quite appreciable and is of the order of the theoretical strength of the crystal. Since usually $\tau \ll G/2\pi$, it may be concluded that dislocations should preferably nucleate in distorted portions of a crystal, in particular where other dislocations already exist. To prove this assumption, let us make use of the earlier concepts of the force f acting per unit length of a dislocation and the force f_0 of linear dilatation of a dislocation [see formula (35)]. Consider the problem of equilibrium of a dislocation section fixed at the ends, in the field of a constant stress τ (Fig. 30). An elementary arc δL is acted upon by a force $F_1 = f\delta L = b\tau\delta L$ directed with x. An opposing force F_2, which appears due to the linear dilatation f_0, is directed towards the centre of curvature O against x: $F_2 = 2f_0 \sin 0.5\delta\theta \approx f_0\theta = f_0\delta l/R$ (for small angles, it can be taken that $\sin 0.5\delta\theta = 0.5\delta\theta$ and $\delta\theta = \delta l/R$). Noting formula (35) for f_0, the force preventing the dislocation line from bending into an arc of radius R_d is $F_2 = 0.5Gb^2\delta L/R_d$ and the corresponding stress is found from the condition of equilibrium $F_1 = F_2$ or $b\tau\delta L = 0.5Gb^2\delta L/R_d$, whence we have

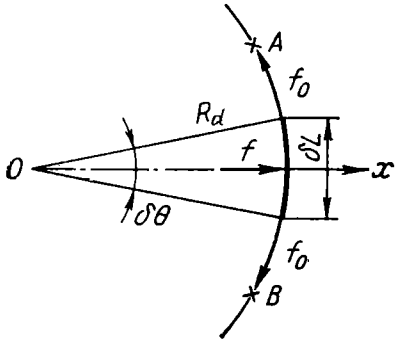

Fig. 30. Dislocation section fixed at ends A and B in the field of a constant stress τ. The slip plane is in the plane of drawing

$$\tau = 0.5Gb/R_d \qquad (52)$$

As may be seen from (52), the highest stress τ for a dislocation fixed at points A and B ($AB = L$) is attained at $R_d = R_{min}$. In

the Frank-Read model of initiation of dislocations (Fig. 31), $R_{min} = L/2$, and therefore, the shear stress $\tau_{F\text{-}R}$ required for operation of a Frank-Read dislocation source of length L, i.e. for bending of a dislocation line up to $L/2$, is:

$$\tau_{F\text{-}R} = Gb/L \qquad (53)$$

i.e. $\tau_{F\text{-}R}$ is lower at a higher length of the fixed dislocation portion. With $L = 1$ μm (roughly $3 \times 10^3 b$), which corresponds to a dislocation density $N = 10^8$ cm^{-2}, $\tau_{F\text{-}R} = 3 \times 10^{-4} G$, which agrees well with the yield limit of pure metals.

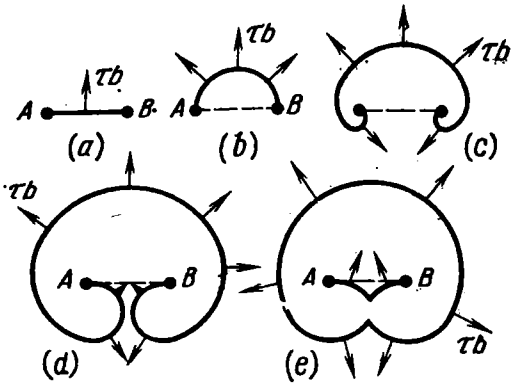

Fig. 31. Operation of a Frank-Read source schematically (the slip plane of dislocation AB is in the plane of drawing)

(a) the originally straight dislocation is bent by a normal force $f = \tau b$ arising from the stress applied; (b) the curvature of the dislocation line is at a maximum when $\tau = \tau_{cr}$; the dislocation becomes unstable; this leads to an increase of the dislocation loop (c, d), resulting in unit shear-finally (e), the two portions of the shear region combine and form a closed dislocation loop. The portion AB is now prepared for creation of a new loop

A dislocation line AB* is restored at the end of each cycle of loop formation and for that reason can generate an unlimited number of loops. Each loop performs a unit shear when propagating in the slip plane. Thus, a Frank-Read source generates repeatedly and can form an enormous number of dislocation loops, which fact explains well why displacements up to a thousand of atomic spacings are often observed in plastically deformed crystals.

Such is the simplest way of multiplication of dislocations in the course of plastic deformation. There are however more intricate cases, such as multiplication of dislocations by multiple cross slip; spatial and helical Frank-Read sources; etc.

3. Dislocations in Typical Crystal Structures

We have described the principal types of dislocation (edge, screw, and mixed) using a simple cubic lattice as an example. This lattice has the Burgers vectors $a\langle 100\rangle$ or $a\langle 110\rangle$ or else $a\langle 111\rangle$ and can contain only *unit dislocations* (of unit power). These vectors coincide with the translation vectors of the lattice which characterize an identical translation, i.e. a transfer of the lattice when its final

* A dislocation AB is usually held at both ends by nodes of a spatial dislocation network (see Fig. 19b) and is then called a segment AB.

state is undistinguishable from the original. In our earlier discussion, such dislocations have been termed *perfect.*

In f.c.c., b.c.c. and c.p.h. crystal lattices typical of metal, there exist dislocations whose Burgers vectors are not coincident with the translation vectors. Such *partial dislocations* with the Burgers vector $\mathbf{b}_r = n\mathbf{b}$ $(0 < n < 1)$ can combine into a perfect dislocation: $\mathbf{b}_{1r} + \mathbf{b}_{2r} = \mathbf{b}$ or recombine to form other partial dislocations by the equation $\mathbf{b}_{1r} + \mathbf{b}_{2r} = \mathbf{b}_{3r} + \mathbf{b}_{4r}$. A perfect dislocation can dissociate (extend) into partial dislocations: $\mathbf{b} = \mathbf{b}_{1r} + \mathbf{b}_{2r}$. Dislocation reactions of other types are also possible.

Dislocation reactions are governed by the *Frank criterion* based on the statement that a reaction must reduce the energy of the system.

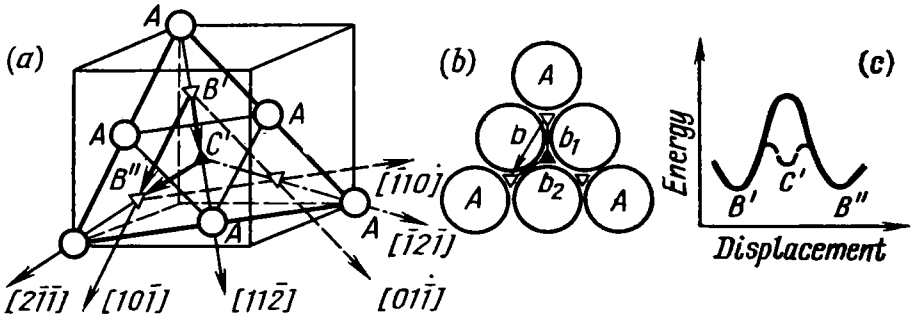

Fig. 32. Dissociation of a complete dislocation b into partial dislccationos b_1 and b_2 in (111) plane of an f.c.c. lattice. The layer of closest packing of atom with pits for layer B (bright triangle) at the top and pits for layer C (dark triangle) from layer A at the bottom

a) tridimensional diagram; (*b*) projection onto (111) plane; (c) energy variation on displacement of atoms in the closest-packed layer: solid line—for the displacement from pit B' into B'' along **b**; dashed line—displacement from B' into B'' through C' along $\mathbf{b}_1$ and **b**

Since the energy of a dislocation is proportional to the square of the Burgers vector, Frank's criterion is formulated as follows: a dislocation reaction is possible if the sum of squares of the Burgers vectors of the original dislocations is greater than the sum of squares of the Burgers vectors of the dislocations formed. With $\mathbf{b}_1 > \mathbf{b}_2 + \mathbf{b}_3$, a dislocation dissociates. If $\mathbf{b}_1 < \mathbf{b}_2 + \mathbf{b}_3$, dissociation is impossible and two dislocations combine into a single one. This explains well why a perfect dislocation of n-multiple power, $n\mathbf{b}$, is unstable and dissociates into n unit dislocations with the Burgers vectors **b** [since $(nb)^2 > nb^2$]. It is easy to note that the angle between two dissociating dislocations should always be greater than 90°.

In addition to Frank's power principle, the formation of partial dislocations is determined by the crystallography of the lattice (f.c.c., b.c.c. or c.p.h.) Since the Peierls-Nabarro force attains a minimum in close-packed slip planes, the spatial arrangement of atoms in closest packings is of extreme importance.

Partial dislocations. Stacking faults. In a close-packed f.c.c lattice (Fig. 32*a* and *b*), the smallest atomic spacing constitutes half

of the diagonal of the face of the unit cell, $a/\sqrt{2}$, and the distance between close-packed {111} planes is $a/\sqrt{3}$ (see Fig. 6*b*, distances BB' and CC'). The sequence of close-packed layers in Fig. 32*a* is the same as in Figs. 4 and 6, i.e. *ABCABC...*, with bright triangles denoting the projections of atoms of layer B, which lies above layer A, onto the (111) plane, and dark triangles, the projections of atoms of layer C, which is below layer A. The extra-plane of an edge dislocation with the Burgers vector **b** (see Fig. 32) is perpendicular to the slip plane (111), i.e. to layer A (it is perpendicular to the plane of Fig. 32 and at the same time to vector **b**), and can move in direction $[10\bar{1}]$. A perfect dislocation, say $\overrightarrow{B'B''} = \mathbf{b} = 0.5a\,[\bar{1}0\bar{1}]$, dissociates into two partial dislocations: $\overrightarrow{B'C'} = \mathbf{b}_1 = (a/6)\,[112]$ and $\overrightarrow{C'B'} = \mathbf{b}_2 = (a/6)\,[2\bar{1}1]$, obeying the condition $b^2 = (a^2/2) > b_1^2 + b_2^2 = (a^2/6) + (a^2/6)$, i.e. the Frank criterion. Besides, the passage of atomic layers through the intermediate C' position in the zig-zag path $B' \rightarrow C' \rightarrow B''$ alternately in $\mathbf{b}_1$ and $\mathbf{b}_2$ corresponds to overcoming a lower energy barrier than in the direct transition from B' to B''. During shear along **b** (see Fig. 32*b*), a sphere of layer B, which occupies a pit B' (see Fig. 6*b*), rolls over a sphere A and overcomes a high energy barrier (see Fig. 32*c*), since this transition involves lifting of the extra-plane and therefore, requires an additional substantial amount of energy. For sphere B in pit B', it is energetically more favourable to move not in a straight path along the vector **b**, but first to slip along the 'chute' into an adjacent pit C' along the vector $\mathbf{b}_1$ and then along another 'chute' in pit B'' along the vector $\mathbf{b}_2$ (see Fig. 32*b*). The position of the sphere in the intermediate pit C' is mechanically stable. The sphere of layer B is in dense contact with three spheres of layers A, which corresponds to a relative minimum of energy (the dashed line in Fig. 32*c*). The absolute minimum of energy is not attained here, since the position of layer B in C pits is not inherent in f.c.c. crystals, and the stacking of atomic layers becomes *CACA . . .*, which is typical of c.p.h. crystals. Thus, an interlayer with disturbed sequence of close-packed layers, i.e. a *stacking fault*, appears in an f.c.c. lattice, and this is associated with an excess of energy. The stacking fault energy per unit area may be denoted E_{sf}, erg cm^{-2}. The formation of two partial dislocations of one sign and of the power $b_1 = b_2$ leads to their repulsion with an energy $Db_1^2 \ln R/d$*. Thus, two partial dislocations $\mathbf{b}_1$ and $\mathbf{b}_2$ turn out to be spaced a distance d apart, with a stacking fault between them; the total energy of this combination must be smaller

* Obtained by integration of repulsion forces $F = Db_1^2/r$

$$E_{1n} = -\int_R^d F(r)\,dr = Db_1^2 \ln R/d$$

than the energy of a single perfect dislocation **b**. A combination of two partial dislocations with a stacking fault between them is called an *extended dislocation*. As the spacing d between partial dislocations increases, the energy gain per unit length of dislocation, dE_{sf}, increases. Since the system tends to minimize its energy, the partial dislocations are drawn together by the tension of the stacking fault which thus opposes their repulsion force. Therefore, the maximum value of d will be limited and is determined from the condition that $\partial E_{ex}/\partial d = 0$ which is the condition of the least energy E_{ex} of an extended dislocation:

$$E_{ex} = 2\left[\frac{1}{2}\frac{Gb_1^2}{2}\ln\frac{R}{r} + Z\right] + E_{sf}\,d + Db_1^2\ln\frac{R}{d} \qquad (54)$$

The first term in this expression is the energy of two partial dislocations. Differentiating (54) with respect to d and equating the result to zero, we obtain the equilibrium width (equilibrium separation) d_0 of an extended dislocation:

$$d_0 = \frac{Db_1^2}{E_{sf}} = \frac{Ga^2}{24\pi(1-\nu)E_{sf}} \qquad (55)$$

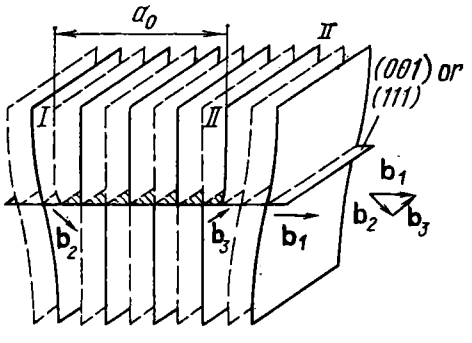

Fig. 33. Extended edge dislocation in an f.c.c. lattice; d_0 — width of the stacking fault; $b_1 = a/3\ [\bar{1}2\bar{1}0]$ or $a/2\ [10\bar{1}]$

Taking that $G = 3 \times 10^4$ MPa, $d_0 = 10a$, $\nu = 1/3$, and $a = 3 \times 10^{-8}$ cm, we find that $E_{sf} = 1.8 \times 10^{-6}$ J cm^{-2}. Experimental values of the stacking fault energy are of the same order of magnitude but vary appreciably. For instance, E_{sf} (mJ/cm^2) is equal to $(10 \pm 5) \times 10^{-4}$ for silver, $(20 \pm 10) \times 10^{-4}$ for gold, $(40 \pm 10) \times 10^{-4}$ for copper, $(200 \pm 20) \times 10^{-4}$ for aluminium, $(140 \pm 40) \times 10^{-4}$ for iron, 150×10^{-4} for nickel, and more than 300×10^{-4} for chromium.

The stacking fault energy can be changed substantially by alloying. In copper-base solutions, E_{sf} decreases with increasing concentration of aluminium. For instance, in bronzes with 4.5 per cent and 7 per cent Al, $E_{sf} = 20 \times 10^{-4}$ erg/cm^2 and 2×10^{-4} erg/cm^2, respectively. The relative width d_0/b_1 of a stacking fault may vary within 1 to 60 or even more.

Stacking faults can form in various ways: by shear in the closest packed plane, by removal or, on the contrary, by insertion of a close-packed plane or its portion, and by other mechanisms.

We have discussed earlier the formation of a stacking fault by shear which forms two extra-planes (Fig. 33) with partial dislocations $\mathbf{b}_1$ and $\mathbf{b}_2$. The unit dislocation **b** is an edge dislocation, but the

partial dislocations are not of the edge type, since their Burgers vectors are not perpendicular to their lines (for more clarity, this is not shown in Fig. 32). Between the extra-planes, there is a stacking fault where the regular sequence *ABCABC*... has changed to *ABCACABCA* . . . . Thus, a thin interlayer of c.p.h. lattice *CACA* has appeared in the f.c.c. lattice between the Shockley partial dislocations $\mathbf{b}_1$ and $\mathbf{b}_2$. During glide of an extended dislocation, the moving partial head dislocation displaces atoms in front of it into irregular positions, while the tail partial dislocation returns the atoms in the region of the stacking fault into their normal positions.

An extended screw dislocation forms in a similar manner and there is complete analogy with glide of an extended edge dislocation.

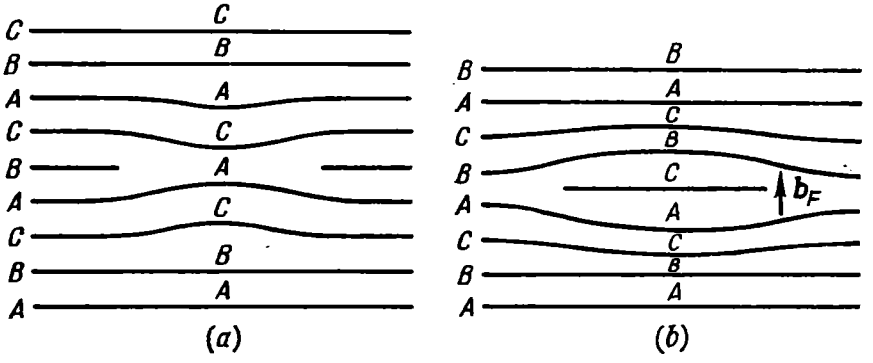

Fig. 34. Intrinsic (*a*) and extrinsic (*b*) stacking faults in an f.c.c. lattice; $\mathbf{b}_F$ = Burgers vector of a Frank dislocation

The dissociation (splitting) of a screw dislocation into two Shockley partials, however, changes substantially the pattern of its glide. As has been noted earlier, a purely screw dislocation can be characterized by its capability for gliding in any crystallographic plane. An extended dislocation can glide only in the plane of a stacking fault, since the slip plane must contain the Burgers vector of the gliding dislocation, whereas two partial screw dislocations do not lie on the same straight line. Thus, the plane to which both partial screw dislocations belong is the sole plane in which slip is possible.

A stacking fault can also form on removal of a portion of a close-packed layer and closure of the adjacent close-packed layers along the normal (Fig. 34*a*). This forms an intrinsic stacking fault. If an incomplete close-packed layer is introduced between {111} layers, there appears an extrinsic stacking fault. The Burgers vector of such partial dislocations (called *Frank dislocations*) is oriented normal to a {111} plane and perpendicular to the dislocation line, i.e. a Frank dislocation is an edge dislocation. Its power is $b = a/3\ \langle 111 \rangle$ and $b_F = a/\sqrt{3}$, i.e. the length of vector $\mathbf{b}_F$ is numerically equal to the spacing between close-packed planes. Thus, the vector $\mathbf{b}_F$ does not lie in the closest-packed plane (nor in a stacking

fault plane) and therefore, a Frank dislocation cannot move by slip in contrast to edge dislocations which can glide easily. A Frank dislocation can move by climb in developed diffusion processes. A climbing dislocation moves normally to the Burgers vector, i.e. climb of a Frank dislocation is effected in the stacking fault plane with reconstruction of an incomplete atomic layer or with removal of atoms from its edge. For that reason, Frank partial dislocations are called sessile, or semilocked.

Dislocation reactions in an f.c.c. lattice. Dislocation reactions in an f.c.c. lattice can be described conveniently by using a special

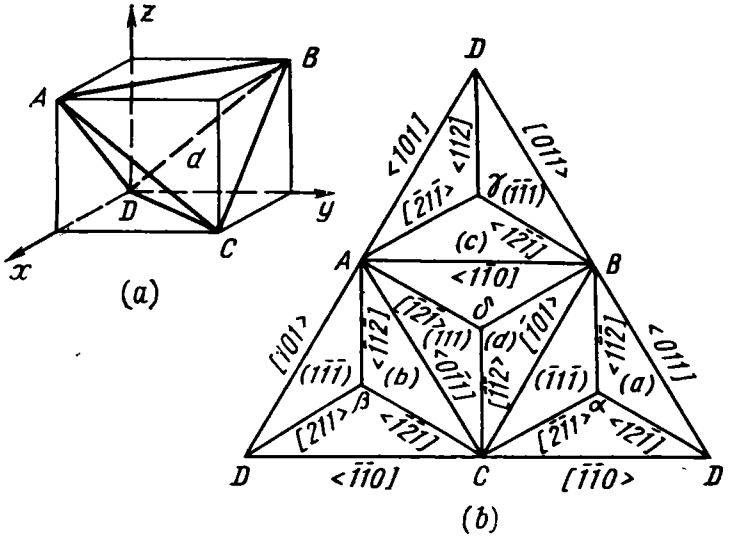

Fig. 35. Geometrical construction to describe dislocation reactions in an f.c.c. lattice

(*a*) tetrahedron *ABCD* with the length of faces $0.5a\sqrt{2}$ for the eighth portion of an elementary f.c.c. lattice; (*b*) opened-up Thompson's tetrahedron. The designation [1̄10] etc. instead of the common designation [1̄10] is introduced to mark the vector direction

geometrical construction, *Thompson's reference tetrahedron.* The faces of this tetrahedron (Fig. 35*a*) are the four possible slip planes of the type {111}. (The planes (111) and (1̄11̄) are parallel to each other, so that only four planes will be non-parallel of the total number of eight.) The edges of the tetrahedron correspond to six slip directions of the type ⟨110⟩, or to twelve directions, if we consider their sign. The mid-points of the faces opposing atoms *A*, *B*, *C*, and *D* are denoted respectively as α, β, γ, and δ, and the planes are denoted (*a*), (*b*), (*c*), and (*d*). Thompson's reference tetrahedron can be opened out relative to point *D* (Fig. 35*b*), which then represents a {111} plane coincident with the plane of the figure, and a perfect dislocation with the Burgers vector $0.5a$ ⟨110⟩ can be denoted by two Latin letters.

For instance, a $0.5a$ [10$\bar{1}$] dislocation is written as *BC*; a respective dislocation of an opposite direction, $0.5a$ [$\bar{1}$01], is denoted *CB*.

Partial dislocations of a power (1/6) a ⟨112⟩ are denoted by a Latin and a Greek letter. For $\mathbf{b}_1 = (1/6)\, a\, [11\bar{2}]$ (see Fig. 32), Thompson's notation is δC (or $C\delta$ for an opposite vector $\mathbf{b}_1 = (1/6)\, a\, [\bar{1}\bar{1}2]$). The class of all ⟨011⟩ directions is denoted DC/AB.

Thompson's tetrahedron is a convenient tool for analysis of complex dislocation reactions.

1. The reaction represented in Fig. 32: $(a/2)\, [10\bar{1}] = (a/6)\, [11\bar{2}] + (a/6)\, [2\bar{1}\bar{1}]$ can be written in the form:

$$BC = B\delta + \delta C \tag{56}$$

or, if the Burgers vectors change direction, as $CB = C\delta + \delta B$.

2. A Frank partial dislocation has its Burgers vector perpendicular to a (111) plane and is denoted αA or δD. These vectors connect the mid-point of a face with the opposite corner. Thus, the reaction of a Frank dislocation with a Shockley partial dislocation

$$A\alpha + \alpha B = AB \tag{57}$$

forms a unit dislocation and eliminates the stacking fault.

3. Cross slip of an extended screw dislocation, for instance $A\gamma + \gamma D$ from a γ $(\bar{1}\bar{1}1)$ plane into β $(1\bar{1}\bar{1})$ plane, takes place by drawing a portion* of the stacking fault into a unit dislocation with the Burgers vector AD, which then dissociates into partial dislocations $A\beta$ and βD in plane β, i.e.

$$A\gamma + \gamma D = AD = A\beta + \beta D \tag{58}$$

An additional energy is required to constrict a partial dislocation, since the reaction $A\gamma + \gamma D = AD$ is inverse of reaction (56) and, by Frank's criterion, the energy of the system should be raised. Therefore, an additional energy must be spent to realize this reaction. Reaction (58) is favoured by thermal activation and high stresses in crystals with a large width of extended dislocations. The probability of cross slip is higher with a lower width of an extended dislocation. Experiments show that cross slip is found most often** in aluminium which has a high stacking fault energy and a low width of stacking faults (around 1-2 atomic spacings).

In Figure 36*a*, the hatched area of a stacking fault is shown for an extended screw dislocation AD in the original position *1* and in the original slip plane $(\bar{1}\bar{1}1)$. The boundaries of that zone are partial dislocations (in position *2*, hatching is omitted for greater clarity). Suppose that in the zone of constriction l_1 (see Fig. 36*a*), dislocation movement in the slip plane $(\bar{1}\bar{1}1)$ is locked by a barrier (impurity atoms, disperse particles, other dislocations, etc.). Under the stress applied, the width of the extended dislocation diminishes, so that

* This portion is called the constriction of stacking fault.

** F.c.c. metals can be divided into those having a low stacking fault energy (Cu, Ag, Au, γ-Fe) and those with a high stacking fault energy (Al, Ni, Pb).

a unit dislocation $a/2$ [101] forms in l_1 (position *3* in Fig. 36*a* and position *4* in Fig. 36*b*). At stage *5* (see Fig. 36*b*), this unit dislocation moves by cross slip onto a new plane $(1\bar{1}1)$, dissociates again here (stage *6* in Fig. 36*c*), and glides, thus increasing the area involved in shear. When locked at the ends of the constriction, a dislocation bows out at stage *7* and the length of the constriction increases (Fig. 36*d*). The movement of the dislocation and plastic deformation in the new $(1\bar{1}\bar{1})$ plane can be facilitated, since a dislocation loop formed in this process (see Fig. 36*d*) opens possibilities for creation

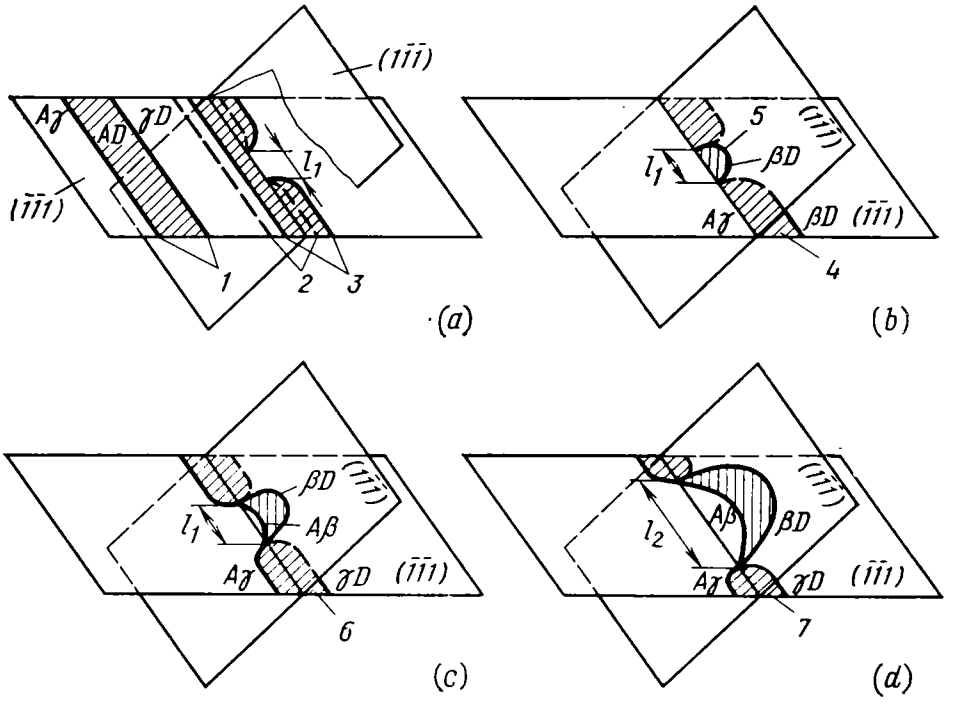

Fig. 36. Stages *1-7* of cross slip of an extended screw dislocation AD in an f.c.c. lattice (l_1— constriction length of stacking fault). Upon unlocking in plane $(\bar{1}\bar{1}1)$, the constriction length $l_2 > l_1$ increases in plane $(1\bar{1}\bar{1})$ (*d*)

of a Frank-Read source. The width of extended dislocations and accordingly the tendency to cross slip is different in various metals and alloys, which fact is of extreme importance for the formation of dislocation structures (cell structures, see Ch. 3) in deformation and for structural changes in subsequent recovery and recrystallization.

4. The formation of a stair-rod dislocation by the reaction

$$\beta A + A\delta = \beta\delta \tag{59}$$

can be imagined as follows. Suppose that plane (*b*) (see ADC in Fig. 35) contains an extended dislocation $AD = A\beta + \beta D$ which consists of Shockley partial dislocations connected by a stacking fault (hatching in Fig. 37*a* shows the width of the stacking fault).

In plane ABC, i.e. in plane (d) or (111), there is an extended dislocation $AC = A\delta + \delta C$ composed of two partials and a stacking fault between them. The slip planes intersect along line AC indexed $[0\bar{1}1]$ (see Fig. 35). The moving head portions of dislocations βA and $A\delta$ meet on the line AC and form a new partial dislocation $\beta\delta$. The section $\beta\delta$, which connects the mid-points of the two faces, is parallel to edge DB (see Fig. 35a) and equal to (1/3) DB. Thus, the

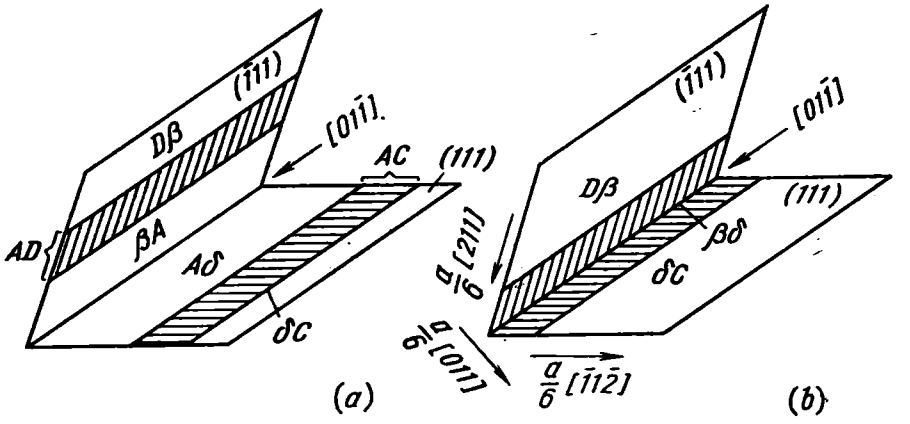

Fig. 37. Formation of a Lomer-Cottrell dislocation by meeting of extended dislocations moving in intersecting slip planes

(a) before meeting; (b) after meeting. The sections $D\beta$, βA, $A\delta$ and δC are dislocation lines proper. The Burgers vector of these lines has the same designation and is determined on Thompson's reference tetrahedron (see Fig. 35b)

power of the stair-rod dislocation $\beta\delta$ is $b_{\beta\delta} = (1/3)\,(a/2)\,[011]$ and $\mathbf{b}_{\beta\delta} = a\sqrt{2}/6$. The combination of two head dislocations into a partial dislocation by a reaction of the type (59) or by the reaction $(a/6)\,\langle 112\rangle + (a/6)\,\langle 112\rangle = (a/6)\,\langle 011\rangle$ gives a large gain in energy, since

$$2\left(\frac{a\sqrt{6}}{6}\right)^2 > \left(\frac{a\sqrt{2}}{6}\right)^2 \text{ or } \frac{a^2}{3} > \frac{a^2}{18}$$

Since line $[01\bar{1}]$ and vector $\frac{a}{b}[011]$ lie in the same (100) plane and are perpendicular to each other, the stair-rod dislocation is of purely edge type. The new extended dislocation formed by the meeting of two extended dislocations (see Fig. 37b) has the shape of a wedge. The wedge-shaped stacking fault in each of the slip planes is bounded by Shockley partial tail dislocations $D\beta$ and δC. The combination of three partial dislocations in a wedge-shaped stacking fault is termed the *Lomer-Cottrell dislocation.* For this dislocation, the plane [100] in which the dislocation line $\beta\delta$ and its Burgers vector lie is not the slip plane and does not contain Shockley tail dislocations. For that reason, all the three dislocations, $\beta\delta$, $D\beta$ and δC, which form a Lomer-Cottrell dislocation are immobile and locked firmly along the whole length, since this is a rigid bond of the two slip

planes. Accordingly, the Lomer-Cottrell dislocation is called *sessile*. Using Thompson's notation, reaction (59) for the formation of a Lomer-Cottrell dislocation can be written in the following stages:

$$(D\beta + \beta A) + (A\delta + \delta C) = D\beta + (\beta A + A\delta) + \delta C$$
$$= D\beta + \beta\delta + \delta C$$

A Lomer-Cottrell dislocation consisting of a stair-rod dislocation and two Shockley dislocations can be formed by dissociation of a unit dislocation by reaction of the type (see Fig. 35*b*)

$$DC = D\beta + \beta\delta + \delta C$$

Neglecting the energy for the formation of a stacking fault, this dissociation reaction proceeds with reduction of energy:

$$\left(\frac{a\sqrt{2}}{2}\right)^2 > \left(\frac{a\sqrt{6}}{6}\right)^2 + \left(\frac{a\sqrt{2}}{6}\right)^2 + \left(\frac{a\sqrt{6}}{6}\right)^2$$

and

$$\frac{a^2}{2} > \frac{7a^2}{18}$$

Lomer-Cottrell dislocations are often observed in plastically deformed stainless steels and other f.c.c. metals and alloys.

Unit and partial dislocations in c.p.h. and b.c.c. lattices. The closest-packed plane in c.p.h. crystals is most often the basal plane, with atoms in each layer arranged as in f.c.c. crystals (see Fig. 32*b*), but with a stacking sequence *ABABAB*... (see Fig. 7). The smallest unit vector of this lattice is $(a/3)[1\bar{2}10]$, with the magnitude *a*. With Burgers vectors as in Fig. 32*b*, the dislocation reaction of dissociation of a unit dislocation into two Shockley partial dislocations can be written as follows: $(a/3)[1\bar{2}10] = (a/3)[01\bar{1}0] + (a/3)[\bar{1}100]$.

As in an f.c.c. lattice, two Shockley partial dislocations are connected in the c.p.h. lattice by a stacking fault which forms an interlayer *ABC* typical of the f.c.c. lattice. The stacking fault energy and the width of an extended dislocation can be found by a method similar to that given earlier [see formulae (54) and (55)].

An extended dislocation in the c.p.h. lattice moves in a single plane, so that *there are no favourable conditions for the formation of sessile dislocations.*

A Frank dislocation with the Burgers vector directed normal to the basal plane is formed by analogy with the f.c.c. lattice.

In a b.c.c. lattice, a unit dislocation with the vector $\mathbf{b}_1 = 0.5a\langle 111\rangle$ has the lowest magnitude. The direction $\mathbf{b}_1$ is coincident with the closest-packed direction (see Fig. 38*a*). A unit dislocation $\mathbf{b}_2 = a[010]$ of an energy higher than that of $\mathbf{b}_1$ cannot dissociate into two dislocations $0.5a\langle 111\rangle$, since $b_2^2 < b_1^2 + b_3^2$

($a^2 < 1.5a^2$). According to Frank's criterion: $2a^2 > 1.5a^2$, a recombination reaction $\mathbf{b}_2 + \mathbf{b}_4 = \mathbf{b}_1 + \mathbf{b}_5$ is energetically favourable (see Fig. 38*a*).

In b.c.c. metals, slip is often observed in {112} planes (see Fig. 38*b*) in ⟨111⟩ direction. The geometry of formation of typical dislocations in the b.c.c. lattice is somewhat more complicated than in c.p.h. and f.c.c. lattices, owing to a more complicated sequence of atomic layers than in closer-packed lattices.

In a (112) plane (see Fig. 38*b*), atomic layers *A* and *B* (Fig. 39*a*) differ in their atom arrangement; in particular, the close-packed

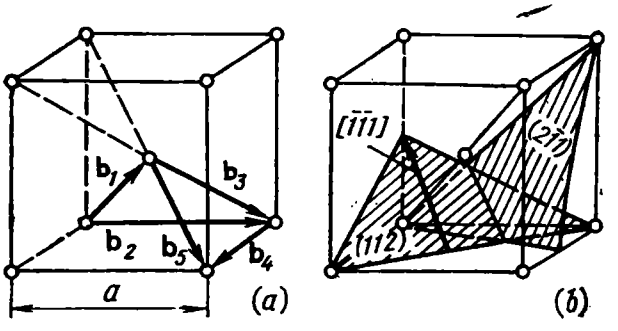

Fig. 38. Unit cells of a b.c.c. lattice in which Burgers vectors of unit dislocations are marked

(*a*) $\mathbf{b}_1 = 0.5a\ [111]$, $\mathbf{b}_2 = a\ [010]$, $\mathbf{b}_3 = 0.5a\ [\bar{1}1\bar{1}]$, $\mathbf{b}_4 = a\ [100]$, $\mathbf{b}_5 = 0.5a\ [11\bar{1}]$; (*b*) slip planes (112), $(2\bar{1}1)$ and their intersection in the $[\bar{1}11]$ slip direction

atomic row B_2 (B_2, B_2', B_2'') is displaced relative to the close-packed atomic row A_2 (A_2, A_2', A_2'') by $0.5a$ [110] (Fig. 39*c*). This is true of any atomic row A_m and B_m (m = number of a close-packed atomic row in Fig. 39*a*). Considering the projections of close-packed atomic layers *A*, *B*, etc. on a $(1\bar{1}0)$ plane, we can prove (Fig. 39*b*) that each next atomic layer is displaced relative to the previous one by $(1/3)\ a\ [\bar{1}11]$.

Thus, a third layer *C* is displaced (the spacing between atoms A'' and C'' in Fig. 39*b*) by $(2/3)\ a\ [\bar{1}11]$ and a fourth layer, *D*, by $(3/3)\ a\ [\bar{1}11] = a\ [1\bar{1}1]$ relative to layer *A*. This gives a sequence *ABCD* . . .; when projected on a [112] direction, i.e. in a (112) plane, atomic rows close-packed in ⟨111⟩ direction will be displaced successively by $0.5a$ $[1\bar{1}0]$ (Fig. 39*c*). For that reason, the close-packed atomic rows in layers *A* and *C*, *B* and *D* coincide with each other. Though the layer *D* in $(1\bar{1}0)$ plane is displaced by $a\ [\bar{1}11]$ relative to *A* (i.e. the two layers seem in Fig. 39*b* to be fully coincident), these layers in (112) plane are displaced relative to one another by $0.5a$ [110] (see Fig. 39*c*), i.e. layer *D* is arranged not identically to layer *A*, and therefore, the notation of the layers must be continued: *ABCDEFGH* . . . . In that case, ⟨111⟩ close-packed atomic rows *A*, *C*, *E*, *G* are displaced by $(2/3)\ a\ [\bar{1}11]$ in $(1\bar{1}0)$

plane (Fig. 39*b*) and coincident in (112) plane (Fig. 39*c*). Atomic rows B, D, F, H, which are close-packed in $[1\bar{1}1]$ direction, are displaced relative to one another by (2/3) a $[\bar{1}11]$ in $(1\bar{1}0)$ plane (see Fig. 39*b*) and coincident in (112) plane (see Fig. 39*c*), but are displaced relative to the close-packed atomic rows A, C, E, G by

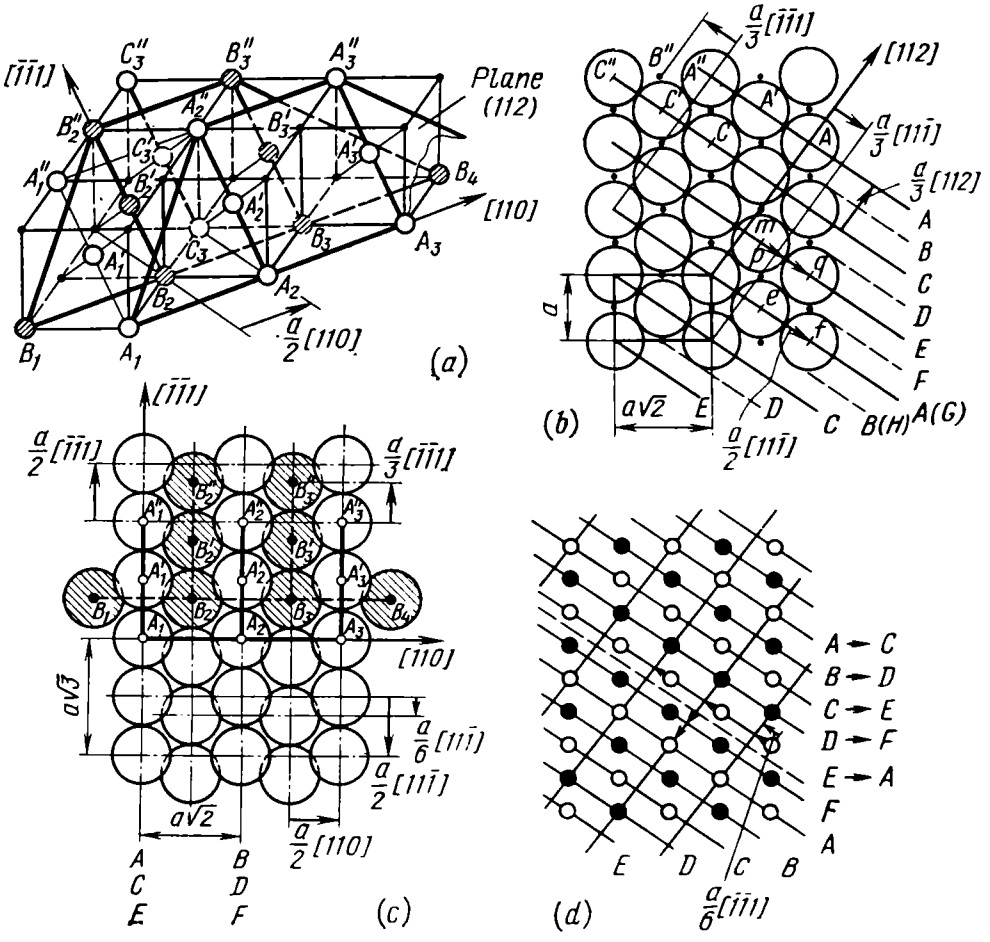

Fig. 39. (*a*) (112) planes in a b.c.c. lattice in which atomic layers A, B and C are indicated; (*b*) position of $ABCDEF$ layers in a projection onto $(1\bar{1}0)$ plane; (*c*) sequence of close-packed atomic rows in layers A and B in the (112) plane; (*d*) displacement of one atomic layer above layer E by $a/6$ $[1\bar{1}\bar{1}]$

0.5a [110]. On passage from layer A to layer C by (2/3) a $[1\bar{1}1]$ (see Fig. 39*b*), from layer C to layer E by (2/3) a $[\bar{1}11]$, and from layer E to layer G by (2/3) a $[1\bar{1}1]$, A and G will coincide in $(1\bar{1}0)$ plane (see Fig. 39*b*) and the close-packed layer G, which belongs to the combination A, C, E, G (see Fig. 39*c*), will be located in plane (112) just beneath layer A. Thus, layer G repeats the arrangement of layer A, layer H repeats that of B, etc. and the sequence of layers will be $ABCDEFABCDEF$ . . . .

Suppose that, when a unit screw dislocation with the Burgers vector 0.5a $[11\bar{1}]$ (vector ef in Fig. 39*b*) is formed, the top portion of the

crystal, beginning from an arbitrary layer, say layer C, is displaced relative to the bottom portion. Since $\mathbf{b} = 0.5a\,[11\bar{1}]$ coincides with the translation vector, the lattice after displacement will remain perfect and will have the same layer sequence $ABCDEFAB\ldots$. Thus, by analogy with the formation of a screw dislocation in a simple cubic lattice (see Fig. 17*c*), the two perfect portions of the crystal will be separated here by a zone of displacements of atoms in layer C and above it relative to layer E and below (see Fig. 32*b*) in direction $[11\bar{1}]$ by a magnitude less than $0.5a\,[11\bar{1}]$. The regular stacking sequence of atomic layers in that zone will be violated, as in the case of a screw dislocation in a simple cubic lattice (see Fig. 17*c*).

A unit screw dislocation of magnitude $0.5a\,[\bar{1}1\bar{1}]$ may dissociate into two partial dislocations. In that case a portion of the crystal beginning, say, from row E and above it, is displaced relative to the portion beginning from row F* and below (see Fig. 39*b*), but not through the whole length of the translation vector $0.5a\,[11\bar{1}]$ as was the case earlier, but only through one-third of it, i.e. $(a/6)\,[11\bar{1}]$ (vector mp). Let all the layers beginning from E and above it be displaced by $(a/6)\,[\bar{1}\bar{1}1]$ (vector pm). The layer F will then occupy in plane (110) a position identical to that of layers A and D in the original lattice (see Fig. 39*d*). But the close-packed rows of layer A coincide with the new position in plane (112), so that, when displaced by $(a/6)\,[\bar{1}\bar{1}1]$, the layer E will now carry the features of layer A and, similarly, the layer C will have the features of layer E (see Fig. 39). Beginning from layer E and above it, there will be no further distortions of the crystal lattice, so that the sequence of layers in the stacking fault (see Fig. 39) will be $CDEFA\,|\,FABC\ldots$. Thus, a screw dislocation of power $\mathbf{b}_1 = (a/6)\,[\bar{1}11]$ (vector pm) represents a boundary of a stacking fault. Another boundary of this fault is formed by a Shockley dislocation $\mathbf{b}_2 = (a/3)\,[\bar{1}11]$ (vector qp), which, according to the dissociation reaction

$$(a/2)\,[\bar{1}\bar{1}1] = (a/6)\,[\bar{1}\bar{1}1] + (a/3)\,[\bar{1}11] \qquad (60)$$

will set atoms of an upper layer into a fully stable position relative to those of a lower layer, with the total vector $\mathbf{b} = (a/2)\,[\bar{1}\bar{1}1]$ equal to the unit translation vector. The resulting sequence of layers in plane (112) is characteristic of an ideal b.c.c. lattice. Upon a displacement by $\mathbf{b}_2 = (a/3)\,[\bar{1}11]$, the Burgers vector closes the stacking fault boundary.

According to Frank's criterion, reaction (60) is favourable energetically, since

$$\left(\frac{a\sqrt{3}}{2}\right)^2 > \left(\frac{a\sqrt{3}}{6}\right)^2 + \left(\frac{a}{\sqrt{3}}\right)^2 \text{ or } \frac{3a^2}{4} > \frac{5a^2}{12}$$

* Similar considerations hold true for any sequence of planes $ABCDEF$.

The difference in the energies of the perfect and two partial dislocations is low, so that this type of dissociation can only be realized if the stacking fault formed has a low energy.

Shockley partial dislocations formed by dissociation of a screw dislocation in a b.c.c. lattice possess a property of high importance. The Burgers vectors $\mathbf{b}_1$ and $\mathbf{b}_2$ of the partial dislocations are parallel to the Burgers vector $\mathbf{b}$ of the unit dislocation (in contrast to this case, extended dislocations $\mathbf{b}_1$ and $\mathbf{b}_2$ in an f.c.c. lattice are not parallel to each other nor to the vector $\mathbf{b}$ of perfect dislocation). For that reason, a unit screw dislocation in a b.c.c. lattice dissociates into two purely screw partial dislocations: an extended screw dislocation can pass easily from one plane onto another; for an extended screw dislocation in an f.c.c. lattice, this is impossible without constriction of stacking fault (see Fig. 36). For constriction of a stacking fault, an additional external force or thermal activation of the process is required.

Thus, extended screw dislocations in a b.c.c. lattice can be characterized by the capacity of cross slip. Planes $(\bar{1}21)$ and $(2\bar{1}1)$ intersect plane (112) along line $11\bar{1}$. Figure 38*b* shows the intersection of planes $\{112\}$: $(2\bar{1}1)$ and (112) along line $[\bar{1}\,\bar{1}1]$, and, as may be seen, a screw dislocation can move easily from one slip plane onto another.

As in f.c.c. and c.p.h. lattices, violations of the regular sequence *ABCDEFAB* . . . in the b.c.c. lattice can produce intrinsic and extrinsic stacking faults. For instance, an extrinsic stacking fault can be characterized by a sequence *ABCDEDEF* or *ABCFABCD* and an intrinsic one, by *ABCFAB* . . . or *ABCBCDEFA* . . . .

4. Movement and Intersection of Dislocations. Interactions Between Dislocations and Point Defects

Dislocation movement leads to irreversible displacements of atoms in the crystal lattice, i.e. to elementary acts of plastic deformation. The elastic interaction of dislocations increases the total energy of the system, and therefore, the resistance to plastic deformation. We have discussed earlier the idealized cases of movement and interaction of parallel dislocations due to long-range stress fields. The actual picture of movement and interaction of dislocations with one another and with other crystal lattice defects is however much more complicated.

Intersection of dislocations. Up to this point, we discussed the interaction of parallel dislocations. The main contribution to such interactions is due to long-range stress fields. Analysis of long-range stress fields and interaction forces between dislocations may show that orthogonally oriented dislocations do not interact. Therefore, such dislocations can approach one another quite closely when mov-

ing and the main contribution to the energy of interaction of these dislocations will be made by dislocation cores.

Let a moving dislocation *1* (Fig. 40*a*) with the extra-plane *1cd1'* and the slip plane *qvtr* intersect a stationary dislocation *2* whose Burgers vector $\mathbf{b}_2$ is perpendicular to $\mathbf{b}_1$. The dislocation line *11'* will move by slip from left to right and the top portion of the crystal will be displaced by $\mathbf{b}_1$ relative to the lower portion (Fig. 40*b*).

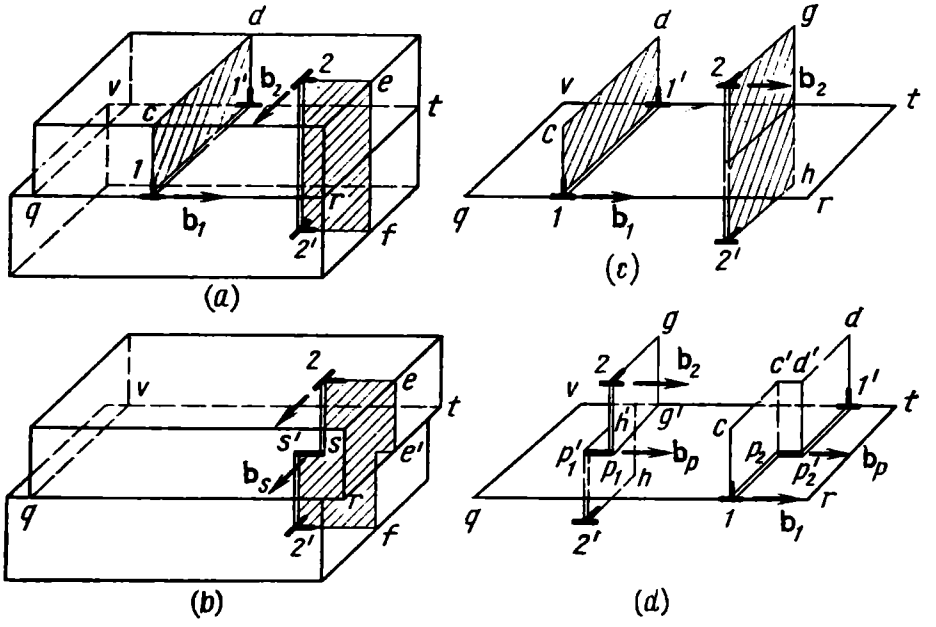

Fig. 40. Intersection of orthogonally oriented edge dislocations *1* and *2* with mutually perpendicular (*a*, *b*) and parallel (*c*, *d*) Burgers vectors $\mathbf{b}_1$ and $\mathbf{b}_2$ (*a*) and (*c*) before intersection; (*b*) and (*d*) after intersection

Since a dislocation line cannot be interrupted within a crystal, there forms a *jog ss'* between the lower portion *2's'* and the upper portion *s2* of the dislocation. The jog is a portion of the dislocation line *2ss'2'*. Due to invariance property of the Burgers vectors, the vector $\mathbf{b}_2$ is constant along the dislocation line and has the same direction. This results in the Burgers vector of the jog $\mathbf{b}_s = \mathbf{b}_2$ being perpendicular to $ss' = |b_1|$, i.e. the jog has an edge orientation. Upon intersection, dislocation *1* has increased its length by the magnitude b_2 of the Burgers vector, since there have been n atomic planes along *11'* and *cd* before intersection (Fig. 40*a*) and there are now $(n + 1)$ planes to the right of dislocation line *22'*.

If the Burgers vector of a stationary dislocation *2* is parallel to the x axis, i.e. the directions of vectors $\mathbf{b}_1$ and $\mathbf{b}_2$ are coincident (Fig. 40*c*), intersection will result in *kinks pp'* being formed on each dislocation (Fig. 40*d*), the length of the kink on the dislocation line $1p_2p_2'1'$ being $b_p = b_2 = p_2p_2'$ and that on $2p_1p_1'2'$ being $b_p = b_1 = p_1p_1'$. Both vectors $\mathbf{b}_p$ lie in the slip plane of one or another dis-

location and are parallel to pp', i.e. the kinks have a screw orientation.

Thus, it follows from comparison of Fig. 40*a*, *b* and *c*, *d* that intersection of edge dislocations may give a different result depending on the mutual orientation of dislocation lines and their Burgers vectors. The following rules for the intersection of edge dislocations can be formulated.

1. If the Burgers vector $\mathbf{b}_1$ of a moving dislocation lies in the slip plane of a stationary dislocation (Fig. 40*c* and *d*), a kink is formed

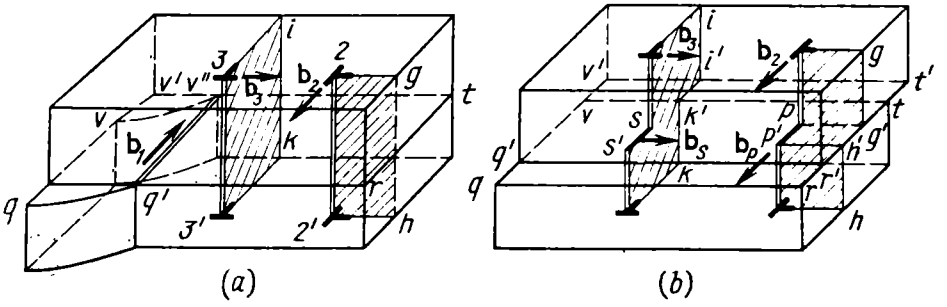

Fig. 41. Formation of a kink (dislocation with vector $\mathbf{b}_2$) and a jog (dislocation with vector $\mathbf{b}_3$) on edge dislocations by movement of a screw dislocation with the Burgers vector $\mathbf{b}_1$
(*a*) before intersection; (*b*) after intersection

in the latter; if the vector $\mathbf{b}_1$ does not lie in the slip plane of the second dislocation (Fig. 40*a* and *b*), there forms a jog.

2. Upon intersection of two dislocations, the length of a jog or kink on one dislocation is equal to the Burgers vector of the other dislocation.

These rules hold also true when moving screw dislocations intersect edge dislocations (Fig. 41). Indeed, the Burgers vector $\mathbf{b}_1$ of a moving screw dislocation coincides with the slip plane of dislocations with the Burgers vector $\mathbf{b}_2$. Upon their intersection, there forms a kink $pp' = b_1$ of screw orientation and $\mathbf{b}_p = \mathbf{b}_1$. Here, $\mathbf{b}_1 \parallel \mathbf{b}_2$, as in Fig. 40*c* and *d*. If $\mathbf{b}_1 \perp \mathbf{b}_3$ (see Fig. 41), the intersection of a moving screw dislocation with an edge dislocation will produce a jog $\mathbf{b}_s = \mathbf{b}_1$ of edge orientation.

If a moving edge dislocation intersects a stationary screw dislocation (Fig. 42), the dislocation line $22'$ is in the slip surface which is a helical surface produced by the screw dislocation. The edge of the extra-plane $2gh2'$ becomes curved on approaching the screw dislocation. For the twisting direction of the planes of the screw dislocation as shown in Fig. 42, the portion $s_2'2$ of the edge dislocation turns out upon the intersection to be below the portion $2s_2$ by the magnitude of the Burgers vector $\mathbf{b}_1$ of the screw dislocation. The jog s_2s_2' thus formed is a portion of the edge dislocation with the magnitude and direction of the Burgers vector characteristic for

the whole dislocation $2s_2s_2'2'$. Since $\mathbf{b}_2 \perp s_2s_2'$, the jog has an edge orientation. The jog slides in the direction of movement of the edge dislocation. The hatched area in Fig. 42 is the area described by the moving jog. As the edge dislocation moves from right to left, the upper portion of the crystal displaces to the left by $\mathbf{b}_2$, which results in a jog $s_1s_1' = \mathbf{b}_2$ appearing on the screw dislocation. The jog is a portion of the screw dislocation with the same Burgers vector $\mathbf{b}_1$. Since $s_1s_1' \perp \mathbf{b}_1$, the jog s_1s_1' has an edge orientation. The above-formulated rule for intersection of dislocations is valid here too.

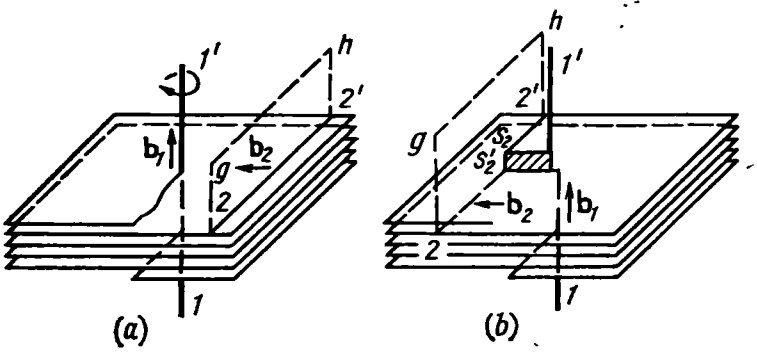

Fig. 42. Intersection of an immobile screw dislocation *1* by moving edge dislocation *2*

(*a*) before intersection, planes are twisted by the screw dislocation and slip of the edge dislocation occurs in a single plane; (*b*) after intersection, the edge dislocation slips in two planes at a distance $\mathbf{b}_1$ from each other

Indeed, the vector $\mathbf{b}_2$ of the moving dislocation does not lie in the slip plane of the stationary one and, according to that rule, a jog must form. It should be clear that two orthogonally oriented screw dislocations produce two jogs on intersection. Each of the jogs will have an edge orientation, i.e. the Burgers vector will be perpendicular to the jog line.

Thus, two intersecting dislocations form either a jog or a kink and the length of a dislocation increases by the magnitude of the Burgers vector $\mathbf{b}$. The radius R at which stresses from a jog (or kink) of length b are sensitive is of the order of a few b: $R = (2\text{-}4)\,b$. Substituting this for R in the formula for the dislocation energy, we find that the energy of each dislocation increases upon intersection by

$$\Delta E = \frac{Db^3}{2} \ln (2\text{-}4) \approx Db^3 \qquad (61)$$

i.e. intersection of dislocations requires an additional expenditure of energy.

Thus, a moving dislocation has to overcome an additional energy barrier ΔE associated with an increased elastic distortion of the crystal lattice directly in the dislocation core, i.e. the external stress must be increased. It is said in such cases that the crystal (metal)

is hardened. An increased external load leads to an increase in shear stresses in the slip plane by $\Delta\tau$, and therefore, in a higher force acting per unit length of the moving dislocation, F, which increases by $\Delta F = \Delta\tau b$. On the path $s = b$ of intersection of the stationary dislocation, this force ΔF performs an additional work $\Delta A = \Delta Fs = \Delta\tau b^2 L$, where L is the length of the moving dislocation.

An essential condition for intersection of moving dislocations is:

$$\Delta A = \Delta\tau b^2 L > \Delta E \approx Db^3 \quad \text{or} \quad \Delta\tau > Db/L \tag{62}$$

With $\Delta\tau < Db/L$, the increment of external stress is insufficient for intersection of stationary dislocations ('forest' dislocations) by moving ones and the latter will be locked by the former. As the

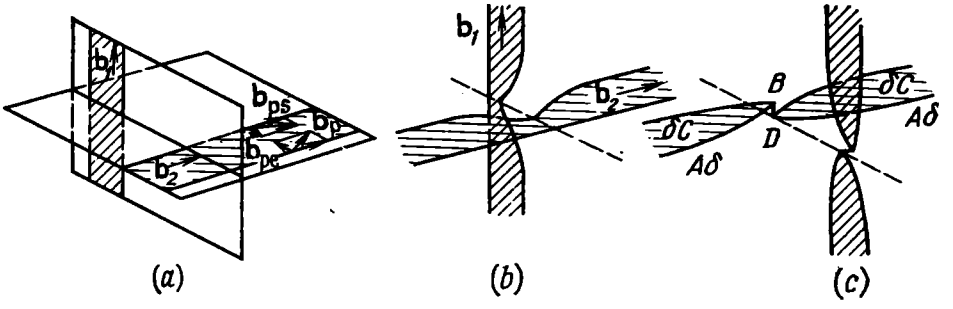

Fig. 43. Intersection of extended dislocations
(*a*) extended dislocations with Burgers vectors $\mathbf{b}_1$ and $\mathbf{b}_2$ before intersection, $\mathbf{b}_2 = \mathbf{b}_h + \mathbf{b}_t$, where $\mathbf{b}_h = \mathbf{b}_{he} + \mathbf{b}_{hs}$; $\mathbf{b}_t = \mathbf{b}_{te} + \mathbf{b}_{ts}$ are Burgers vectors of the head and tail partial dislocations each of which consists of an edge ($\mathbf{b}_{pe}$) and a screw ($\mathbf{b}_{ps}$) component;(*b*) formation of a stacking fault constriction; (*c*) dislocations with unextended jog *BD* after intersection

stress increment increases to a value determined by (62), dislocations begin to move, i.e. plastic deformation proceeds further, with a corresponding increase in external stresses. This phenomenon, i.e. an increase in external stresses required to continue plastic deformation, is called *strain hardening*, or *cold work*. In the case considered, strain hardening is associated with the movement through a dislocation 'forest', i.e. with intersection of stationary dislocations by moving ones. In that case, the interaction of dislocations is of short-range order and is determined by the structure of the dislocation core.

Intersection of extended dislocations (Fig. 43) involves bending of the dislocation lines of partial head dislocations towards partial tail dislocations. For partial dislocations, the Burgers vector, which lies in the slip plane, is inclined relative to the dislocation line (Fig. 43*a*), so that their Burgers vectors ($\mathbf{b}_p$ of a partial head dislocation or $\mathbf{b}'_p$, of a partial tail dislocation) can be imagined to consist of two components: an edge component $\mathbf{b}_{pe}$ and a screw com-

ponent $\mathbf{b}_{ps}$: $\mathbf{b}_p = \mathbf{b}_{pe} + \mathbf{b}_{ps}$. For the screw dislocation illustrated in Fig. 43*a*, the components $\mathbf{b}_{pe}$ are directed opposite each other and the components $\mathbf{b}_{ps}$ are directed in the same sense. In that case the stress tensor contains all stress components, so that the introduction of the second dislocation into the field of the first will produce long-range elastic interaction. Thus, bending of partial head dislocations is the result of elastic long-range interaction of stress fields. It is natural that additional energy must be consumed to overcome this interaction and bend the dislocation line with the formation of a stacking fault constriction (Fig. 43*b*). The consumption of energy increases even more when the dislocations intersect and begin to interact in the short-range order which is determined by the structure of the dislocation core. The jogs formed on constriction of stacking faults and intersection of dislocations may be either unextended, i.e. unit dislocations of a small length, including stair-rod type, or extended dislocations. Figure 43*c* shows an extended dislocation $AC = A\delta + \delta C$ lying in the plane ABC (see Fig. 35*b*). This dislocation can be intersected by other dislocations: AD, CD, BD which lie in other planes. As has been noted, the direction of a jog on a dislocation coincides with the Burgers vector of the intersecting dislocation. Therefore, the extended dislocation AC may produce unextended jogs whose lines follow along AD, CD or BD. A jog directed along BD (see Fig. 43*c*) is a portion of the dislocation AC and has the Burgers vector of AC (see Fig. 35*b*). The jog can lower the free energy if it dissociates by the reaction $AC = A\gamma + \gamma\alpha + \alpha C$. Further slip of such a jog will only be possible when it is constrained into a unit dislocation length under the action of the stresses applied. The higher is the energy for dissociation of a jog, the more energy must be spent for its constraint for further movement. If the stresses applied are insufficiently high, a jog remains extended. Such a jog cannot slip and locks substantially dislocation movement.

Elevated stresses for dislocation movement are also needed in cases when the metal has a low stacking fault energy, i.e. a large width of extended dislocations.

Interaction between dislocations and point defects. The elastic fields around a dislocation and a point defect can interact with each other. The energy of interaction of an edge dislocation with an impurity atom [see formulae (48)] is higher at a higher misfit factor ε.

Since there is a hydrostatically compressed zone at one side of an extra-plane and dilated zone at the other, interstitial and substitutional impurity atoms whose diameter is larger than that of the base metal are attracted into the dilated zone and occupy positions beneath the extra-plane. Atoms of a substitutionally dissolved element with the size less than that in the base metal are attracted into the compressed zone and concentrated above the edge of the

extra-plane. This concentration of impurity atoms ('impurity atmospheres' or 'clouds') leads to a lower stress level and lower energy of the system composed of dislocations and impurity atoms. Interstitial atoms, i.e. those occupying interstices, distort the crystal lattice more appreciably than substitutional atoms which occupy lattice sites, and therefore, form stronger stress fields and are attracted to dislocations much more substantially than substitutional atoms. This attraction of interstitial impurity atoms results in their 'condensation' around a dislocation line or in what is called *Cottrell atmospheres.* Besides, the formation of Cottrell atmospheres is favoured by the fact that interstitial impurities have a higher diffusion mobility than substitutional ones.

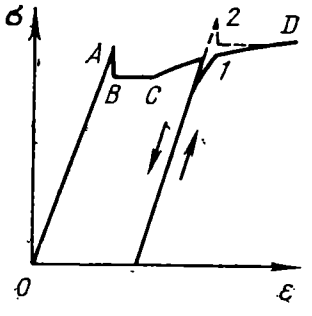

Fig. 44. Yield stress peak (*A*) and yield elongation zone (*BC*) in the σ-ε diagram of soft polycrystalline steel

1 — immediate repeated loading; *2* — repeated loading after ageing which has caused precipitation of Cottrell atmospheres around dislocations

The greater was the reduction in the energy of the system on the formation of a Cottrell atmosphere, the higher the external load that must be applied to break away a dislocation from the atmosphere for further movement, i.e. for plastic deformation. As soon as a dislocation breaks away from a Cottrell atmosphere, no such a high stress is needed for its further movement, so that the external stress can be reduced. This fact can explain, in particular, why some metals, say, low-carbon steel, exhibit in tension a sharp yield stress peak in the stress-strain diagram (Fig. 44).

Cottrell atmospheres may disappear with an increase of temperature. With lowering temperature, the concentration of impurity on a dislocation increases and can reach the solubility limit near the dislocation core, after which precipitates of a disperse secondary phase can form. In that case, dislocation movement and plastic deformation will be largely inhibited.

In contrast to an edge dislocation, a screw dislocation does not form zones of hydrostatic compression and dilatation and therefore, cannot attract point defects. An interstitial atom may however distort the crystal lattice unevenly in various directions, so that the distortion and the elastic stress field of the crystal lattice will cease to have purely spherical symmetry. Such a stress field of point defect can interact with shear stresses of the stress field around a screw dislocation. For instance, carbon atoms in α-iron can occupy octahedral voids amid the edges and in the centres of faces. An interstitial atom in the centre of a (110) face is at a distance of $0.5a$ from its two neighbours in the direction [010] and at a distance of $a/\sqrt{2}$ from four neighbours in other directions. Carbon atoms intersticed into the centre of (010) faces increase the size of the elementary cell

in the [010] direction. An interstitial atom, which occupies an octahedral void in the centre of a {100} face or amid a ⟨100⟩ edge of a b.c.c. lattice, distorts the elementary cell tetragonally by elongating it in the ⟨100⟩ direction. Owing to this tetragonal distortion, an interstitial impurity atom in a b.c.c. lattice can interact with the shear stress field of a screw dislocation. This interaction can result in lower shear stresses and in attraction of interstitial atoms to a screw dislocation.

When being attracted to a dislocation, interstitial atoms (carbon or nitrogen in α-iron) fill in the octahedral voids in the mid of edges of a unit cell with the same probability. An external stress applied increases the distance between two atoms along one of the possible directions. In that case, interstitial atoms become orderly arranged preferably along the dilated edges of the unit cell. This effect, i.e. ordering of interstitial atoms concentrated around an edge or screw dislocation, is called the *Snoek atmosphere*. Snoek atmospheres form at higher speeds than Cottrell atmospheres, and reduce the free energy of a crystal.

For an extended dislocation, say, in an f.c.c. lattice, a stacking fault is essentially an interlayer of the c.p.h. lattice for which the solubility of impurity atoms is different from that in the f.c.c. lattice. At a high temperature, diffusion redistribution of atoms occurs similarly to redistribution of elements between two phases. This type of atom redistribution has been termed chemical interaction of an extended dislocation with solute atoms. A change in the concentration decreases the energy of a stacking fault and increases its width. A change in the concentration of impurity atoms or atoms of alloying elements in a stacking fault of an extended dislocation is called the *Suzuki atmosphere*. The energy of a common stacking fault, E_{sf} is higher than that of a stacking fault in the Suzuki atmosphere, E_{sfS}, i.e. $E_{sf} > E_{sfS}$. Substituting the equilibrium width of stacking fault (55) in (54), we obtain expressions for the energy of an extended dislocation without and with a Suzuki atmosphere:

$$E_{ed} \approx Db^2 [5 + \ln RE_{sf}/(Db^2)]$$

and

$$E_{edS} \approx Db^2 [5 + \ln RE_{sfS}/(Db^2)]$$

i.e. the energy of a dislocation decreases in the latter case by

$$\Delta E_S \approx Db^2 \ln E_{sf}/E_{sfS}$$

Suzuki atmospheres lower the energy of the system and lock dislocations, i.e. make them less mobile. As with Cottrell atmospheres, additional energy must be spent to move a dislocation from a state of a higher extension (E_{sfS}) to that of a lower (E_{sf}). In other words, the external stress must be increased in order to initiate dislocation movement.

5. Surface and Volume Defects

A surface defect is an imperfection in the crystal lattice having an appreciable extent in two directions. This group includes low-angle boundaries between sub-grains (sub-boundaries) misoriented through small angles relative to one another; high-angle grain boundaries; interphase boundaries; stacking faults; twin boundaries; dislocation

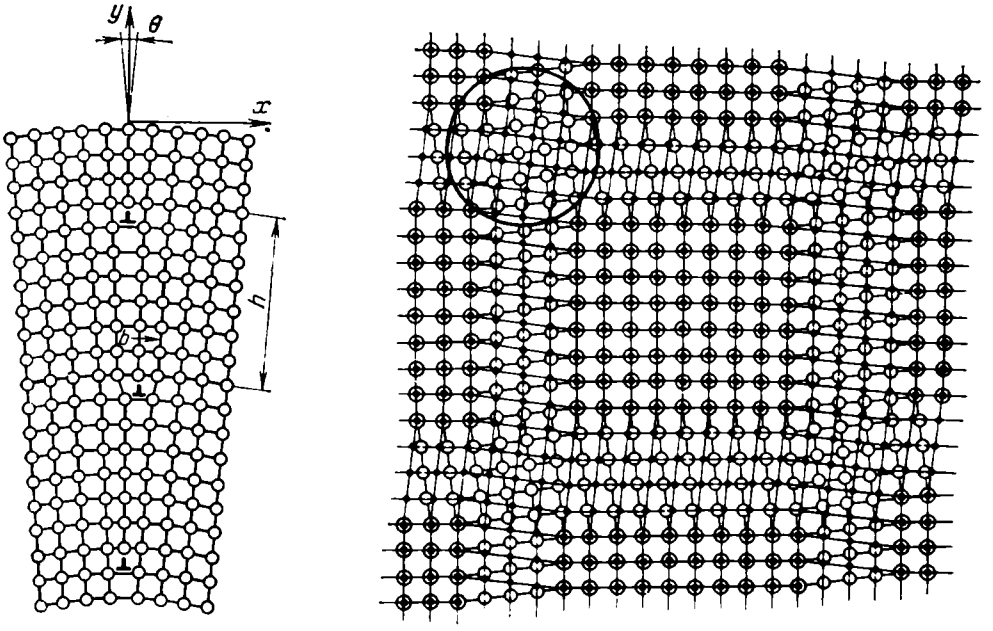

Fig. 45. (*left*) Schematic of a boundary between sub-grains with small misorientation angles in a simple cubic (primitive) lattice

Fig. 46. Schematic of a 'twist boundary'. The boundary is parallel to the plane of drawing. Black dots are atoms of the lower boundary atomic plane, bright ones belong to the upper boundary plane. Grains adjoin closely one another, except for the regions near the two series of screw dislocations with Burgers vectors $a/2\,[011]$ and $a/2\,[01\bar{1}]$ which form closed circuits

pile-ups in a single slip plane; and some other combinations of linear defects. Let us consider, as an example, the structure of boundaries between sub-grains.

A distinction is made between high-angle and low-angle boundaries of sub-grains, depending on the angle of misorientation between two adjacent grains (sub-grains). In the dislocation model of low-angle boundaries (Fig. 45), it is assumed that two sub-grains of a simple cubic lattice are tilted one relative to the other in the plane xOy about the z-axis through equal and opposite angles $\theta/2$. The misorientation angle is $\theta = 2 \arctan (b/2h)$ or $\theta \approx b/h$. A boundary consists of a number of parallel edge dislocations of one sign. The misorientation angle θ is not more than 5° and $h_{\min}$ exceeds ten lattice para-

meters. Since the distance between dislocations is large, individual dislocations in a sub-boundary are easily discernible. In an etched microsection of a metal, sub-grain boundaries are seen as 'etch pits', provided that h is a few micrometers and therefore, angle θ is small. Dislocations are readily observed microscopically if N_d is of the order of 10^3 cm^{-2}.

The sub-boundary just described is of the simplest type. In the general case, a sub-boundary has five degrees of freedom. Three of them are responsible for the relative rotation of adjacent crystals about three mutually perpendicular axes, while the other two determine the orientation of the surface of the boundary proper relative to the crystal. The boundary illustrated in Fig. 45 uses a single degree of freedom, that of symmetrical rotation of the crystals about the z-axis. By a similar independent rotation about the y-axis due to a number of dislocations whose lines are parallel to the y-axis, we can obtain two crystals tilted in the plane xOy relative to the y-axis. To obtain tilting about the x-axis, one has to introduce screw dislocations (Fig. 46). This diagram illustrates a 'twist boundary'. In that case, the boundary plane between the crystals of a simple cubic lattice has an axis of rotation a [100] (x-axis) and contact plane (100) which lies in the plane of the figure. The twist boundary shown circled in Fig. 46 has been formed by two intersecting, mutually perpendicular rows of screw dislocations equidistant from one another with the pitch $h = b/\theta$. The directions of the screw dislocations are [011] and [01$\bar{1}$] and the Burgers vectors are equal to (a/2) [011] in the former case and to (a/2) [01$\bar{1}$] in the latter. As has been noted by A. H. Cottrell, a network of parallel screw dislocations is unstable, since it can cause shear deformation which will propagate over the whole crystal. Introduction of another dislocation network will prevent propagation of shear and form a stable boundary between two oppositely tilted crystals.

A more complicated structure of a boundary with a small misorientation angle θ can be formed by two series of linear dislocations whose extra-planes are perpendicular to each other (Fig. 47). This grain boundary has two degrees of freedom: one is realized by rotation of one grain relative to the other through an angle θ (see Fig. 45) and the other, by rotation of the boundary proper about the common axis of the cubic lattice of both grains. Angle φ is the angle between the boundary plane and the midline between [100] directions of the two grains. The boundary makes an angle $\varphi + \theta/2$ with the [100] direction in one grain and an angle $\varphi - \theta/2$ with the [100] direction in the other. Figure 45 shows a particular case when $\varphi = 0$ or 90°. As may be seen from Fig. 47, $CE = AC \cos(\varphi - \theta/2)$ is greater than $AB = AC \cos(\varphi + \theta/2)$ by nb, where n is the number of dislocations in the boundary AC with the Burgers vector $\mathbf{b}_1$.

Taking that $AC = 1$, we can write that the number n of vertical planes

which terminate in the unit length of the grain boundary AC is:

$$n = \frac{CE-AB}{AC}\frac{1}{b} = \frac{1}{b}\left[\cos\left(\varphi-\frac{\theta}{2}\right)-\cos\left(\varphi+\frac{\theta}{2}\right)\right]$$
$$= \frac{2}{b}\sin\frac{\theta}{2}\sin\varphi \approx \frac{\theta}{b}\sin\varphi$$

The edge of each such plane terminates in a dislocation $\mathbf{b}_\perp$. Similar considerations are true for determining the density of dislocations $\mathbf{b}_\dashv$. Thus, a sub-boundary consists of two series of equidistant dislocations, the distances h between them being: $\mathbf{h}_\perp = \mathbf{b}/\theta \sin\varphi$ and $\mathbf{h}_\dashv = \mathbf{b}/\theta \cos\varphi$.

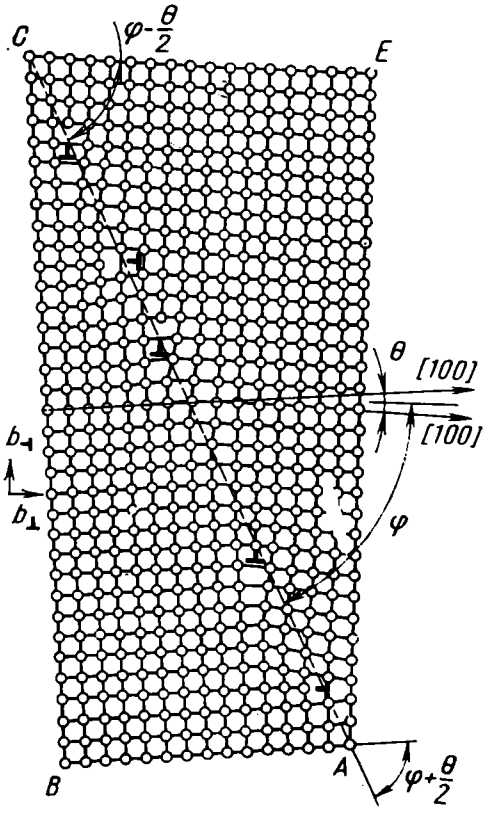

Fig. 47. Schematic of a sub-boundary with a small misorientation angle. The scheme is similar to Fig. 45, except for the plane AC of the boundary, which forms an arbitrary angle φ between the grain boundary and the midline between (010) planes of the two grains. The boundary is formed by two series of linear dislocations whose Burgers vectors are denoted $\mathbf{b}_\perp$ and $\mathbf{b}_\dashv$

For low-angle boundaries, the dislocation density increases with increasing angle θ, so that at $\theta \approx \approx 15°$, dislocations are separated by an interval of the order of two lattice parameters. With $\theta > 15°$, a boundary becomes high-angle and the regions it separates are grains.

Grain boundaries possess a higher energy compared with the bulk of grains, owing to a difference in atomic bond forces at the two sides of a boundary resulting from different atomic structures of contacting planes of adjacent grains. An excess energy of atoms on the boundaries (grain-boundary energy E_{gb}) is analogous to an elevated surface energy E_s which is the work spent for the formation of unit area of a new surface. An elevated surface energy appears due to the difference in the atomic bond forces at the two sides of an interface. The ratio E_{gb}/E_s for most metals is 0.25 to 0.4 and E_{gb} can be one order of magnitude higher than the energy of a coherent twin boundary E_{tw}, which is indicative of high mobility of grain boundaries.

The dislocation structure of grain boundaries may be different depending on the type of contact of grains and sub-grains and is characterized by the size and misorientation of grains (Table 5).

Table 5. Structure of Grain Boundaries

Structural elements	Size, mm	Misorientation angle, degrees	Dislocation structure of boundary and models of grain boundaries	Degrees of freedom
Sub-grains	10^{-5}-10^{-3}	5-2	Array of like dislocations (see Fig. 45)	One
Low-angle grains in polycrystal				
symmetrical	10^{-3} and more	Less than 5	Ditto	One
unsymmetrical	10^{-3} and more	5-15	Dislocations with noncomplanar Burgers vectors (see Fig. 47)	Two
High-angle grains in polycrystal	10^{-3} and more	12-25	*Models*: 1. Mott islet model with boundaries of good and bad conjugation 2. Coincidence site model with singular (special) and random (arbitrary) boundaries * 3. Model of structural units or 'repetition segments' 4. Model of grain-boundary dislocations	Five

* Special boundaries are called partially conjugate; the term 'superlattice boundaries' is also in use.

A sub-grain boundary is the surface of conjugation of two practically undistorted crystallites (see Fig. 45, *AC* in Fig. 47). Some atoms of this boundary can belong to both lattices (the region of 'good conjugation'), and others to none of them; there also can exist empty or compressed regions of 'bad conjugation' of a width not more than 1-2 interatomic spacings.

The type of the boundary described is determined by the orientation of its surface relative to one of the two crystals [two degrees of freedom determined by angle φ (see, for instance, Fig. 47)] and by the minimal angle of rotation to match the two lattices (three degrees of freedom for three angles: θ_1, θ_2 and θ_3). As has been noted by W. T. Read, boundaries with five degrees of freedom are too complicated, so that in most cases analysis is limited to the simplest boundaries with one degree of freedom (which are called symmetrical dislocation tilt boundaries, see Fig. 45) or with two degrees of freedom (symmetrical twist boundaries, see Fig. 47). Characteristic of symmetrical tilt and twist dislocation boundaries is that there are no long-range stress fields, i.e. stresses decrease sharply with increasing distance from a boundary.

For a simple boundary with one degree of freedom, W. T. Read and W. Shockley have found the relationship between the angle of

misorientation and the grain boundary energy per unit surface, by summing up the stress fields of dislocations arranged in an array:

$$E_{gb} = E_0\theta\,(A - \ln\theta) \tag{63}$$

where $E_0 = b\tau_0/2$; $\tau_0 = G/[2\pi\,(1-\nu)]$; $A = 1 + \ln\theta_m$ (θ_m is a constant).

In equation (63), the first term, $E_0\theta A$, includes the elastic energy of a dislocation, E_0, which is proportional to the dislocation density

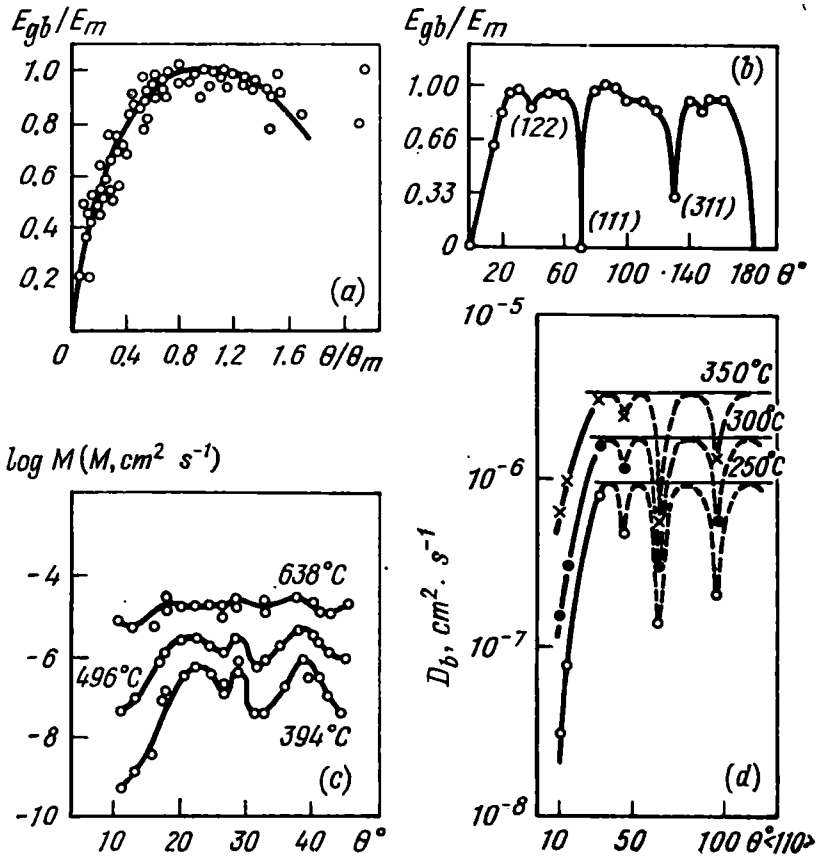

Fig. 48. Effect of the misorientation angle on the properties of grain boundaries (*a*) theoretical formula (63) as compared with experimental data; (*b*) E_{gb} (θ) at large misorientation angles around ⟨011⟩ for aluminium; (c) mobility of grain boundaries at various temperatures; (*d*) rate of boundary diffusion at misorientation around ⟨011⟩ in aluminium

$1/h = \theta/b$; it indicates that the energy increases proportional to the misorientation angle θ. The second term, $\theta E_0 \ln\theta$, shows that, as the angle θ increases and the distance h between dislocations in an array decreases, the field of compressive stresses of one dislocation is superposed on the field of tensile stresses of an adjacent dislocation, leading to stress compensation and reduction of the boundary energy (Fig. 48*a*).

For boundaries with two degrees of freedom, equation (63) retains essentially its form, but E_0 and A depend on $\cos\varphi = a$ and

$\sin \varphi = c$:

$$E_0 = 0.5\tau_0 b\,(a + c); \quad A = A_0 - ac\,(a \ln a + c \ln c)/(a + c) \tag{64}$$

With $\varphi = 0$ or $\pi/2$, expressions (64) relate to simple boundaries with a single degree of freedom.

A curve of $E_{gb}(\theta)$ constructed by equation (63) has a maximum which depends only on the energy of the dislocation core $E_m = E_0\theta_m$ at $\theta_m = \exp(A - 1)$, or $\ln \theta_m = A - 1$. In dimensionless units, equation (63) takes the form:

$$E_{gb}/E_m = [1 - \ln(\theta/\theta_m)]\,\theta/\theta_m \tag{65}$$

A good correlation between the theory and experimental data (see Fig. 48) is observed for many metals: $\theta_m = 35$-$45°$ (Cu); $\theta_m = 25$-$36°$ (Fe-Si, Ag and Pb); $\theta_m = 12°$ (Sn).

As may be seen from these data and Fig. 48*a*, equations (63) and (65) for low-angle boundaries agree quite well with experimental data for boundaries with misorientation angles $\theta < \theta_m$; θ_m may reach quite a high value. With $\theta > \theta_m$, however, experimental points do not fall on Read-Shockley's theoretical curve. It has also been established that some properties of grain boundaries, such as their mobility (Fig. 48*c*) or rate of diffusion (Fig. 48*d*) vary non-monotonically depending on misorientation angle θ, which has given a key for explaining the complex nature of the function $E_{gb}(\theta)$ at large misorientation angles (see Fig. 48*b*). The studied properties of grain boundaries (see Fig. 48*c* and *d*) vary most substantially at twinning misorientations. As has been established by W. Burgers and P. Lacombe, twin boundaries and boundaries between very closely oriented grains possess the lowest mobility. L. S. Schwindlerman et al. have found that the dependence of boundary mobility M on temperature in the coordinates log M-$(1/T)$ (Fig. 49) has a stable linear pattern at any misorientation angles studied, which is indicative of the activation nature of the process. The functions $M(\theta)$ and $Q(\theta)$ (Q = activation energy of a process) are, however, essentially non-monotonic and have many extrema (see Fig. 48).

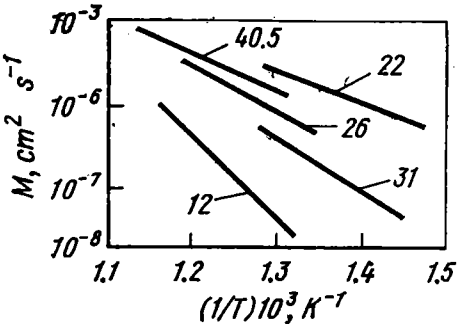

Fig. 49. Effect of temperature on mobility of tilt boundaries at various angles of tilt (indicated at curves) around ⟨100⟩

The maximum rate of migration in various lattices is observed at different orientations between adjacent grains; in f.c.c. metals, for instance, it is found at misorientation by rotation through 20°

and 30-40° around ⟨001⟩. The lowest mobility corresponds to rotation through 60° around ⟨111⟩.

If the lattices of two identical crystals are matched together and one of them is then rotated relative to the other around a particular crystallographic direction, some atoms in both lattices will occupy common positions at definite angles of rotation; these are called 'coincidence sites'. The common positions of the atoms form a spatial

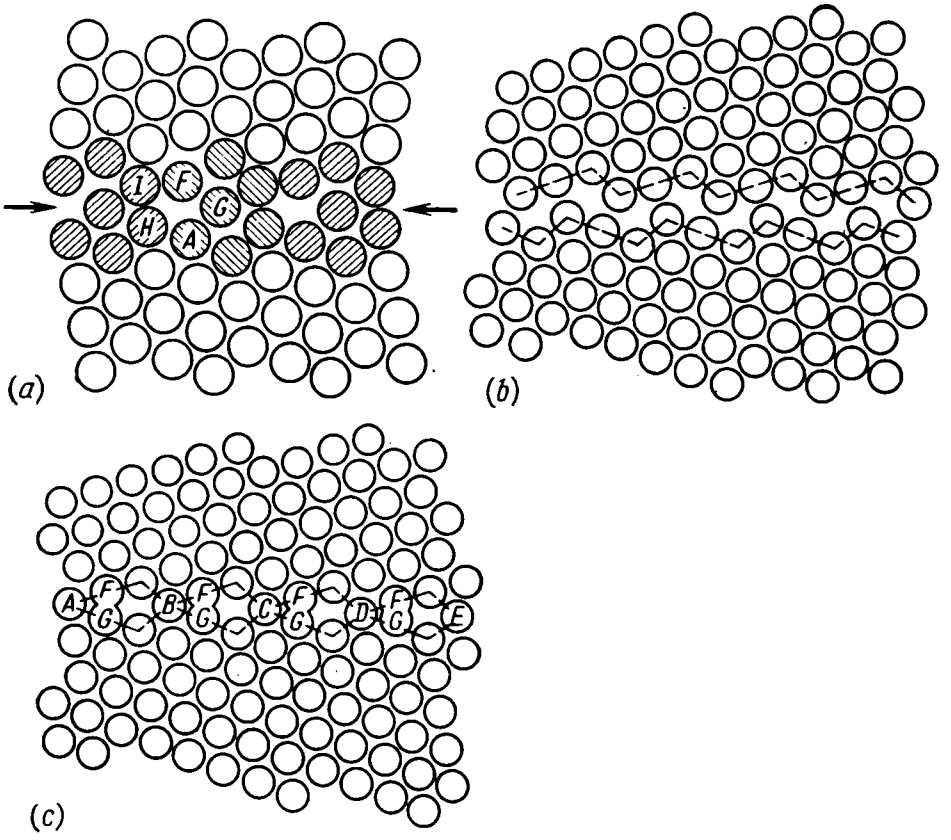

Fig. 50. Mutual position of atoms in {111} planes belonging to two f.c.c. lattices tilted by 38.2° around ⟨111⟩ relative to each other and the atomic structure of a boundary between two crystals tilted by 38° relative to each other

(*a*) variation of positions of atoms which reduces the free energy; (*b*) crystallites are displaced relative to each other; (*c*) crystallites are moved closer to each other and form coincidence sites, but the positions of atoms in the undistorted lattice remained unchanged (as in *b*)

'superlattice'. In particular, a 'superlattice' can be obtained by rotation of an f.c.c. lattice relative to another such lattice about the common ⟨111⟩ direction through an angle of 38.2°. In that case, the position of every seventh atom in the new orientation coincides with that it had before rotation (Fig. 50*a*), i.e. every seventh atom will belong to both lattices. Other atoms move through distances less than the atomic spacing. Such a boundary, which forms a 'superlattice' (or coincidence site lattice), is called partially conjugate. A 'superlattice' can be characterized by the number of sites in the main lattice per coincidence site, Σ, which may be termed the misfit

factor or the degree of coincidence of lattice sites. In Fig. 50*a*, $\Sigma = 7$; the lowest possible value of Σ is three. The values of Σ and θ (θ = = angle of mutual misorientation) depend on the type of crystal lattice and are different for various axes of rotation (Table 6). The

Table 6. The Degree of Coincidence of Lattice Sites, Σ, and Angles of Mutual Misorientation, θ, in B.C.C. and F.C.C. Lattices

Rotation axis	θ	Σ	Rotation axis	θ	Σ
⟨100⟩	36.9	5	⟨211⟩	180	3
	28.1	5		101.6	5
	22.6	5		135.6	7
⟨110⟩	70.5	3	⟨311⟩	146.4	3
	38.9	9		154.2	5
	50.5	11		67.1	9
⟨111⟩	60.0	3	⟨411⟩	180	9
	38.6	7		129.6	11

lowest values correspond to the lowest boundary energy. Twin boundaries relate to those having the lowest Σ; their energy is low, only 0.03-0.10 of the energy of 'random' high-angle boundaries; for that reason, twin boundaries are practically immobile. The energy of partially conjugate high-angle boundaries is (0.2-0.25) $E_{s\{100\}}$ ($E_{s\{100\}}$ is the surface energy of {100} plane) and that of random boundaries, $0.32E_{s\{100\}}$.

The model of coincidence sites, in which special boundaries are strictly distinguished from random ones, has been further developed into a grain boundary model composed of structural units, or 'repetition segments'.

As in the previous model, this concept is based on the fact that the strength of atomic bonds between atoms in a boundary is of the same order as in the bulk of a crystal. For that reason, atoms on a grain boundary should be arranged in such a manner and at such distances so as to ensure the lowest energy and high strength of the boundary. In that case, the structure of a boundary with the least free energy (Fig. 50*b*) consists of periodically arranged groups of atoms. This structure is obtained from the original ideal structure by slight displacement of one crystallite relative to the other, followed by slight displacement of individual atoms in the boundary proper. These groups contain a small number of atoms and are called structural units, or repetition segments (Fig. 51*a* and *b*). With a deviation from the ideal orientation, a boundary is a mixture of repetition segments taken in a particular proportion. This model of random grain boundaries can explain the fact why the properties of boundaries vary gradually, rather than abruptly as their orienta-

tion deviates from the special. This structure of random boundaries causes the appearance of long-range stress fields owing to elastic distortions (deformations) near individual repetition segments. Long-range stress fields have an essential role in the interaction of random boundaries. This model also explains well why vacancies may be present in elevated concentrations at boundaries.

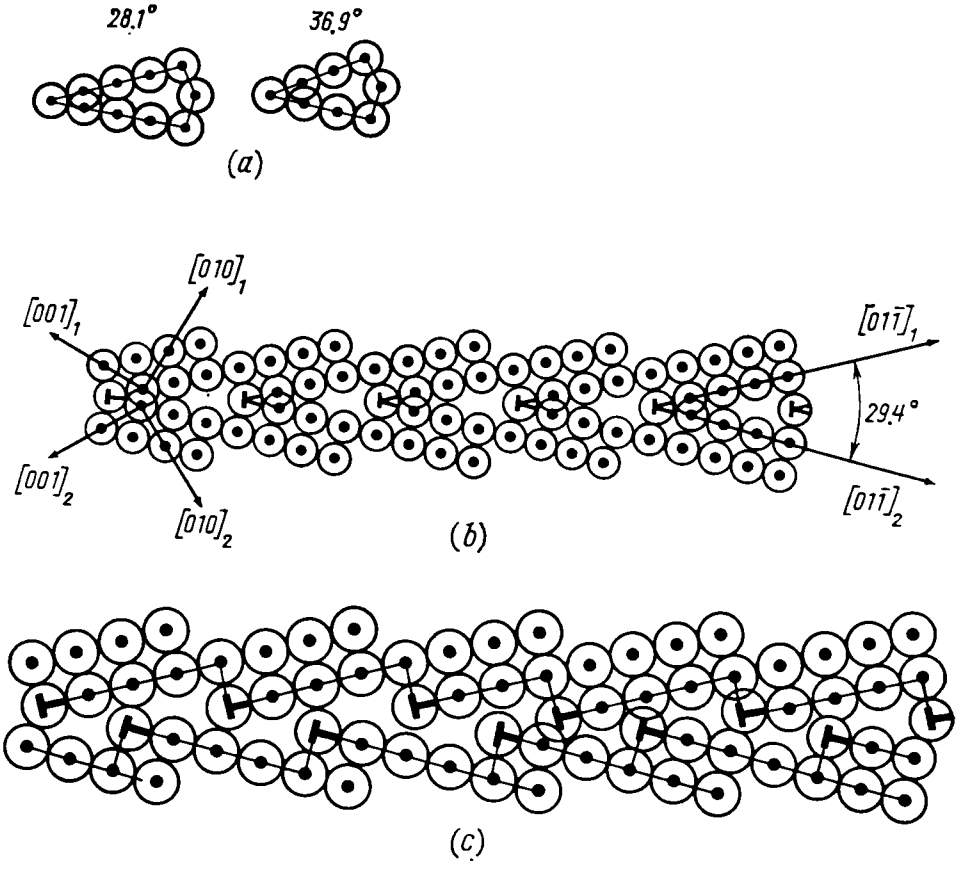

Fig. 51. Repetition segments (structural units)
(*a*) for orientation 28.1° and 36.9°; (*b*) the structure of a boundary constructed from repetition segments of different type; its misorientation angle does not correspond to the ideal conditions of coincidence sites; (c) grain-boundary dislocations schematically

A further stage in the development of the theory of structure of grain boundaries was the discovery of grain-boundary dislocations existing on grain boundaries, including high-angle ones (Fig. 51*c*). In that case, a boundary consists of portions with coincidence sites and of grain-boundary dislocations. These may be either mobile or sessile. Mobile grain-boundary dislocations can move along the boundary and play an important part in grain-boundary sliding whose rate increases with increasing density of grain boundary dislocations. The existence of grain-boundary dislocations has been confirmed by electron-microscopic examination of specially grown bicrystals.

The oldest dislocation theory of structure of grain boundaries can also be used for explaining the specific of deformation in polycrystals. In particular, Mott's grain boundary model presumes that dislocations in boundaries with large misorientation angles are so close to one another that they lose their individual characteristics and thus cannot be regarded as separate defects. For that reason, *Mott's islet model of high-angle* ($\theta > 10$-$15°$) *boundaries* is based on the assumption that grain boundaries consist of islets of good conjugation separated by regions with a strongly distorted structure.

Thus, it is assumed in the theory of dislocation structure of grain boundaries that the structure of a boundary depends on misorientation angles, and therefore, the properties of grain boundaries (in particular, their energy) must also depend on these angles. Experiments have confirmed this fact and thus have shown that grain boundaries have a dislocation nature.

The *chemical properties of grain boundaries* depend on their structure and misorientation angle:

1. Grain boundaries can be etched easily. The rate of etching does not decrease if a purer metal is taken, i.e. impurities play only a subordinate role in etching.

2. The rate of etching is higher with a higher angle of misorientation of two neighbouring grains.

3. Sub-boundaries with low misorientation angles are revealed by etching not as continuous lines, as is the case in etching of grain boundaries, but consist of separate etch pits. Their density depends on the mutual orientation of sub-grains and the distance between pits coincides quite well with the calculated values of h (see Fig. 45) of dislocation arrays constituting the wall of a sub-grain.

The *preferable diffusion on grain boundaries* also depends on their structure, since it has been established that:

1. The coefficient of diffusion in a polycrystal exceeds that in a single crystal of the same metal at temperatures $T < 0.75T_{\text{m.p.}}$ and increases with decreasing grain size.

The activation energy in diffusion at grain boundaries E_{gb} is roughly one-half of the activation energy E_g in the bulk of grains, so that D_{gb} diminishes more slowly than D_g with decreasing temperature, i.e. the relative contribution of diffusion at grain boundaries is higher at lower temperatures. This is typical of all systems.

2. Grain-boundary diffusion depends substantially on the angle of misorientation of adjacent grains (Fig. 52*a*).

3. The anisotropy of diffusion, expressed as the ratio of the coefficient of self-diffusion along dislocation cores ($D_{\parallel}$) to the coefficient of diffusion perpendicular to dislocation cores ($D_{\perp}$), which depends on the distance between dislocations, i.e. on misorientation angle, is also a function of misorientation angle (see Fig. 52*b*).

Segregation of impurities on boundaries (Fig. 52*c*) is different for low- and high-angle boundaries, which is indicative of different

structures of these boundaries. Greater segregation for high-angle boundaries should be attributed to the existence of strongly distorted regions in them.

All these facts are an evidence that plastic flow on grain boundaries is a structure-sensitive characteristic and should depend strongly on the angle θ.

By analogy with point, linear and surface defects, one can outline a group of *volume defects*, i.e. those having an appreciable size in all

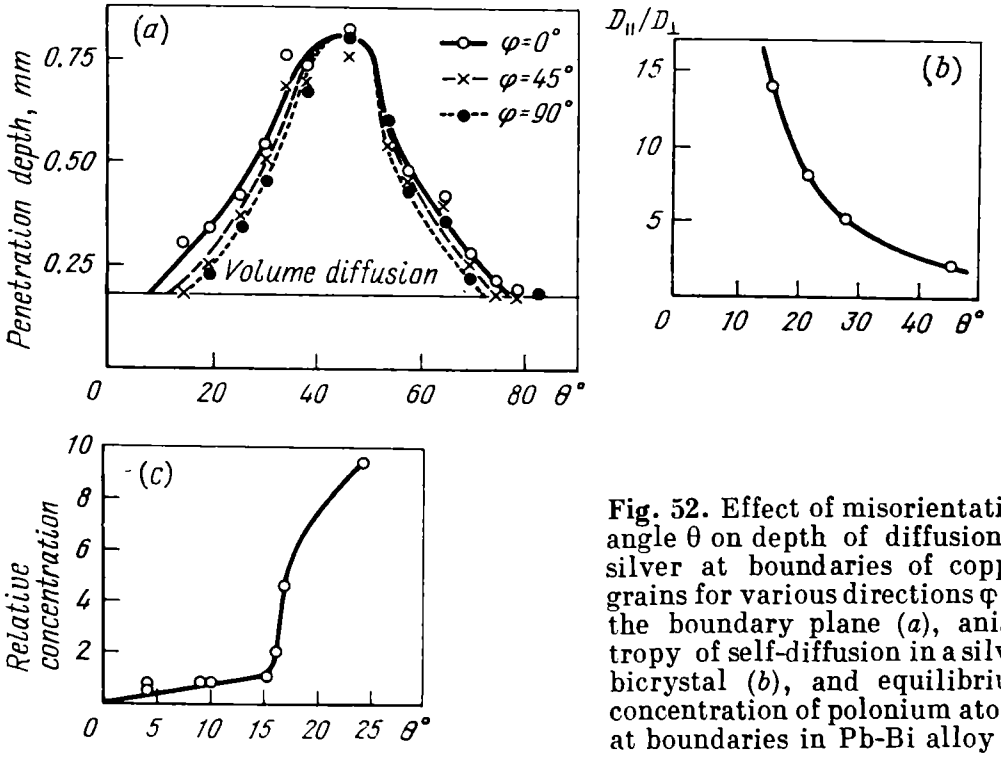

Fig. 52. Effect of misorientation angle θ on depth of diffusion of silver at boundaries of copper grains for various directions φ in the boundary plane (*a*), anisotropy of self-diffusion in a silver bicrystal (*b*), and equilibrium concentration of polonium atoms at boundaries in Pb-Bi alloy (*c*)

three dimensions. They include colonies of point defects of the type of pores or dislocation systems distributed in the volume of a crystal. Fine crystals of a structure and orientation different from the base lattice, when present in a single crystal, can also be regarded as volume defects. Thus, second phases, disperse precipitates, various inclusions (say, non-metallic), and non-uniformly distributed stresses and strains in macrovolumes of a body are related to volume defects.

6. Methods for Detection and Examination of Dislocations

At present, there are several experimental methods for examining the type, number and distribution of crystal structure defects in deformed and undeformed materials. Since 1953, such studies have been carried out systematically and provided ample data in support of the theory of structural defects in metals, which appeared and

developed long before its validity has found direct evidence. It is now an unquestionable fact that dislocations do exist and can move by slip and climb. Edge, screw, mixed, extended, prismatic, curvilinear and stair-rod dislocations have been discovered experimentally in full conformity with the theoretical predictions. One can observe experimentally the sub-structure of boundaries, the effects of cross slip, the operation of Frank-Read sources, dislocation reactions, and plane dislocation pile-ups, also in full accordance with the theory.

Of the greatest interest are direct methods for observation and examination of dislocations, dislocation pile-ups, and point defects. They include observations in a field-ion microscope, X-ray topography and light and electron microscopy. Direct methods provide us with the most valuable information on defects in crystals, but are, however, inapplicable for quantitative estimations in the studies of metals subjected to an appreciable plastic deformation or of commercial alloys of a complex composition. In such cases, use is made of indirect methods: X-ray structural analysis based on examining the shape and intensity of interference maxima, mechanical tests, and measurements of internal friction and electric and magnetic characteristics.

Field-ion microscopy. The arrangement of atoms around a dislocation line can be analysed directly only with a very high resolution. At present, such a high resolution is offered only by a field-ion microscope which operates by the following principle. The surface of a specimen which is a needle with a very small radius of curvature of the end (less than 10^{-5} cm) emits electrons when placed into a high-voltage electric field. Owing to the polarization effect, molecules of an inert gas precipitate on the needle. On impinging the metal surface, gas molecules diffuse to the needle end. When a molecule enters a region of locally intensified high-voltage field, it is ionized and the ion thus produced moves onto a fluorescent screen under the action of accelerating high voltage. This method, which has the highest resolution among all the known direct methods for studying the structure of metals, makes it possible to detect individual atoms in crystals. The magnification of the instrument is determined by the ratio of the radius of curvature of the needle end to the distance between the object and screen and may be as high as a few millions.

Using this method, it has been possible, for instance, to obtain photographs of an almost perfect platinum crystal oriented in the [001] direction (Fig. 53). Each spot in the photograph represents an atom. A vacancy corresponds to a missing spot in a symmetrical row and an interstitial atom, to an extra or a larger spot. By successive evaporation of atomic layers, it is possible to obtain information on the concentration and distribution of defects. For instance, in experiments with platinum hardened from 1 800 K, 71 atomic

layers in (102) plane were examined successively and it was found that there were 5 vacancies in the total number of 8 500 atoms counted. Thus, the concentration of vacancies determined by direct counting was $n/N = 5.9 \times 10^{-4}$.

Interstitial atoms and dislocations can be counted in a similar way. Because of certain limitations, in particular, difficulties in making needles of a very small radius of curvature, etc., field-ion

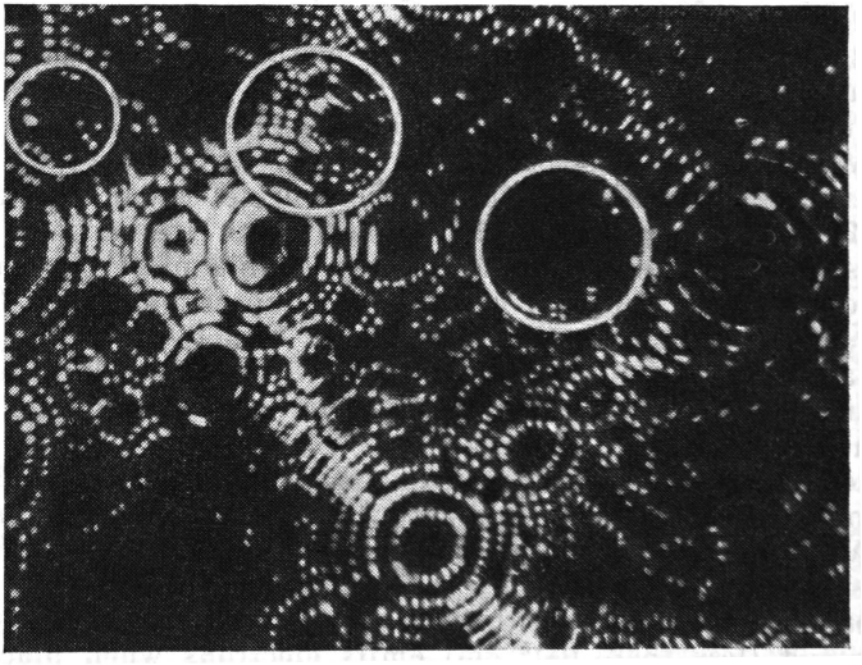

Fig. 53. Field-ion micrograph of a platinum crystal, 10 000 000 ×

microscopy is applicable only for examining high-melting metals (molybdenum, tungsten, platinum, iridium, etc.).

Field-ion microscopy has also given photographs of atom arrangement around edge dislocations, for instance, the atomic structure of a dislocation core with the Burgers vector $b = 0.5a$ [100] in molybdenum. Analysis of micrographs has revealed the existence of an extra half-plane as an evidence of the validity of the above-described model of atomic arrangement around an edge dislocation.

Transmission electron microscopy. An electron beam passing through a thin metal foil is diffracted partially by the crystal lattice, being reflected from its atomic planes according to the Wulff-Bragg reflection condition and thus deviating from the original direction. The intensity of beams passing through the foil and a narrow aperture (which cuts off deflected beams) is equal to the difference of intensities of the original beam incident on the foil and the diffracted beam. Due to diffraction contrast, there appears an image of a distorted portion of the lattice, resulting in a dark image of that portion

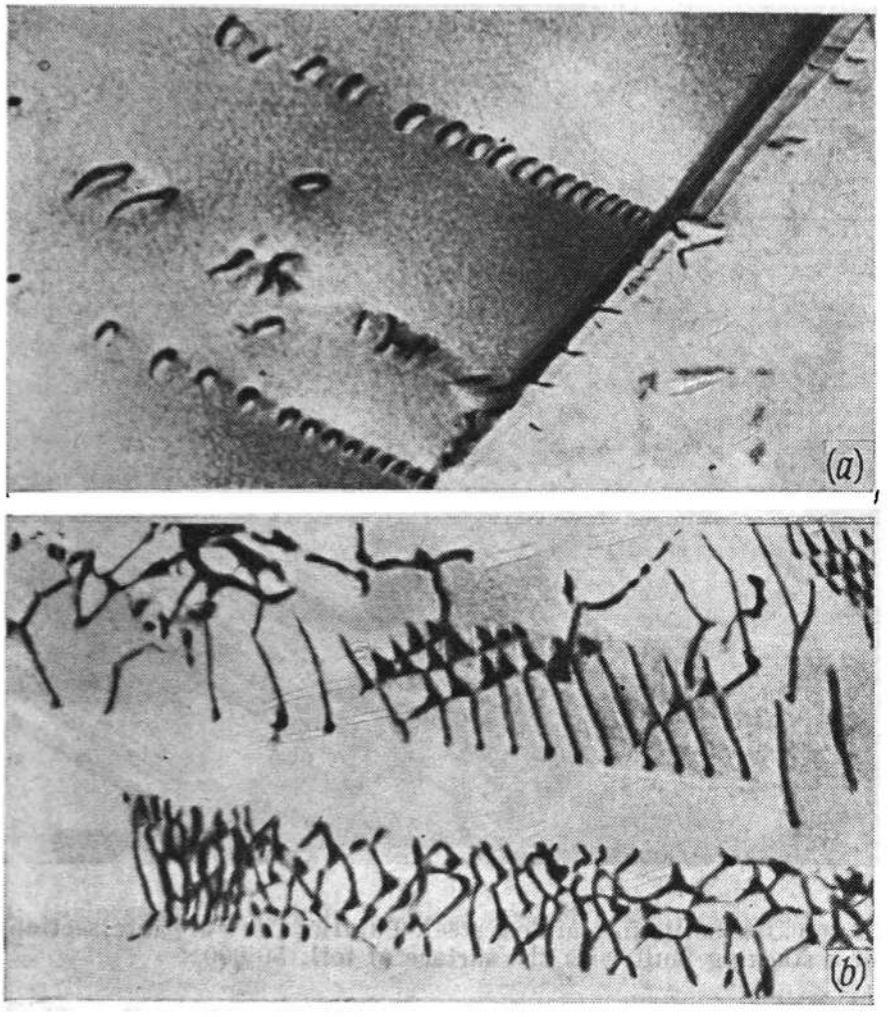

Fig. 54. Dislocation lines
(*a*) dislocation pile-up in slightly deformed austenitic stainless steel, revealed by thin-foil transmission electron microscopy, 22 000×; (*b*) dislocations and slip lines in stainless steel deformed 10% by tension, 40 000×

being produced on a screen as a pattern of lines of a width of 5-20 nm.

A dislocation can be represented by continuous, interrupted or wavy lines depending on the conditions of diffraction. Wavy or interrupted lines in the image can be amended by tilting the foil slightly.

An image of an edge dislocation is usually wider than that of a screw dislocation. Dislocations more inclined to the foil plane give narrower images.

The image of a dislocation disappears fully if the foil is oriented to the original electron beam so that the Burgers vector of the dislocation lies in the plane of reflection. This circumstance is made use of to determine the Burgers vector. The foil is tilted until the image of a dislocation disappears. The electron microscope is then set to

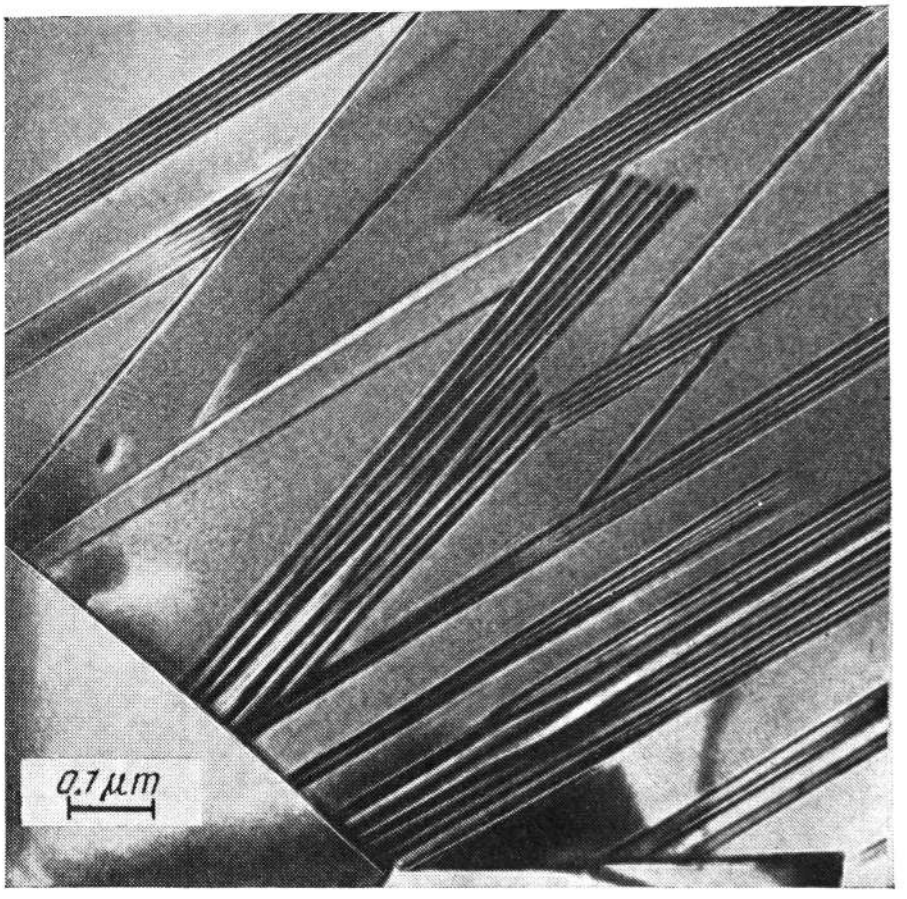

Fig. 55. Stacking faults in stainless steel. Parallel lines are intersections of the plane of a stacking fault with the surface of foil, 50 000×

electronographic mode of operation to produce an electron micrograph, after which the indices of the reflection plane, in which the Burgers vector lies, can be measured.

An image of dislocation lines (Fig. 54) is essentially the projection of their spatial arrangement in the foil onto the screen plane. The end points of the lines which represent dislocations are points of emergence of dislocations onto the upper and lower surfaces of the foil (or onto a single surface), rather than points of interruption of dislocations inside the foil (which is utterly impossible).

A stacking fault in thin-foil electron microscopy gives a typical pattern of bright and dark streaks (Fig. 55). The number and spacing of streaks depend on the thickness and orientation of foil and the inclination of the stacking fault plane. An image of a stacking fault band is limited at two sides by dark or bright lines of partial dislocations and at two other sides, by lines of intersection of the fault plane with the foil plane.

Owing to a relatively small width of images of unextended dislocations, transmission electron microscopy can be used with success

for examining metals and alloys with a local dislocation density up to 10^{12} cm^{-2} and average density up to 10^{11} cm^{-2}. It is the sole technique suitable for direct observation of individual dislocations and their distribution in heavily work-hardened metal (Fig. 56).

The foil for examining dislocation structures must be transparent for electrons. The smaller is the atomic number of an element and the greater the accelerating voltage, the higher may be the thickness

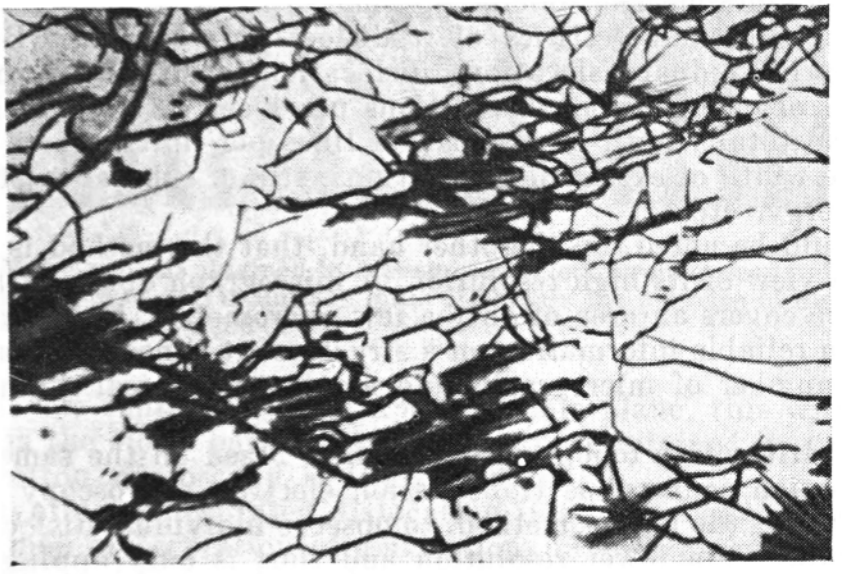

Fig. 56. Dislocation network in stainless steel deformed by tension, 30 000 ×

of foil. Usually, the foil thickness is 0.1-10 μm. It is obtained by electrolytic or chemical polishing of a rolled foil or a thin platelet cut out from a massive specimen under study.

Great potentialities are offered by the use of a high-voltage microscope for an accelerating voltage of 1 000 kV, which makes it possible to use foils of a thickness of a few micrometres (for instance, 10 μm for aluminium).

Electron transmission of metal foils can be used for examining the shape of dislocation lines, formation of kinks, dipoles, helicoids, loops, etc. The method can provide us with information on distribution of dislocation in the volume of a foil, reveal a dislocation network and the shape of its nodes, dislocation pile-ups and tangles, tilt and twist sub-grain boundaries, dislocation pairs in the superstructure, etc. Some typical examples of dislocation structure are illustrated in Figs. 54-56.

Thin-foil transmission microscopy can also be employed for studying the interaction of dislocations with one another and with disperse inclusions, the behaviour of dislocations in a stress field

applied to the foil and in post-deformation heating, i.e. during polygonization and recrystallization.

Useful information can be collected when studying the dislocation cell structure in deformed metals and alloys, their sub-grain structure, polygonized and recrystallized metals, in particular various texture components. It is also possible to observe and photograph redistribution of dislocations during heating and deformation of the foil directly in the electron microscope.

Transmission electron microscopy makes it possible to determine the principal characteristics of a dislocation structure: Burgers' vectors of individual dislocations, dislocation density (by the number of points of emergence of dislocations per 1 cm^2 of the foil surface or by the total length of dislocation lines per unit volume of the foil), the width of extended dislocations, size of subgrains, stacking fault energy, etc.

It should be noted, on the other hand, that the method is highly local, in view of its high resolution. A micrograph obtained by this technique covers an area of only a few micrometres. Thus, in order to obtain reliable information on a structure, it is needed to analyse a large number of micrographs and employ statistical methods of analysis.

X-ray diffraction topography, which is based on the same effect of diffraction contrast as transmission electron microscopy, makes it possible, as the former method, to observe individual dislocations. It has however a lower resolution and thus is only applicable to single crystals with the dislocation density not more than 10^5-10^4 cm^{-2}. For that reason, the method cannot be used widely for studying dislocation structures in metals and alloys. Its main application is for the analysis of dislocation structures in perfect single crystals of semiconductors (silicon, germanium, etc.).

Electron microscopy with crystal lattice resolution. The direct proof of existence of dislocations in crystals was obtained by J. Menter in 1956 when he studied a crystal with a high interplane spacing (around 1.2 nm) in a transmission electron microscope. He managed to obtain directly images of individual atomic planes and detected portions with incomplete atomic planes. The low resolution of the microscope did not allow him to observe directly atomic planes in metals since their interplane distances measured only a few angstroms (a resolution of 0.05 nm has been attained quite recently). For that reason, the existence of incomplete atomic planes in metals was verified indirectly by using the Moiré method. If a thin layer of a crystal is superposed on another and their lattices are oriented parallel but have slightly different interplane distances a_1 and $a_2 = a_1 + \Delta a$, transmission view will produce a typical interference (Moiré) pattern which is essentially an image of interplane spacings enlarged $a_1 a_2/\Delta a$ times. Moiré effect can even be produced by superposing two quite identical but slightly misoriented lattices. If one

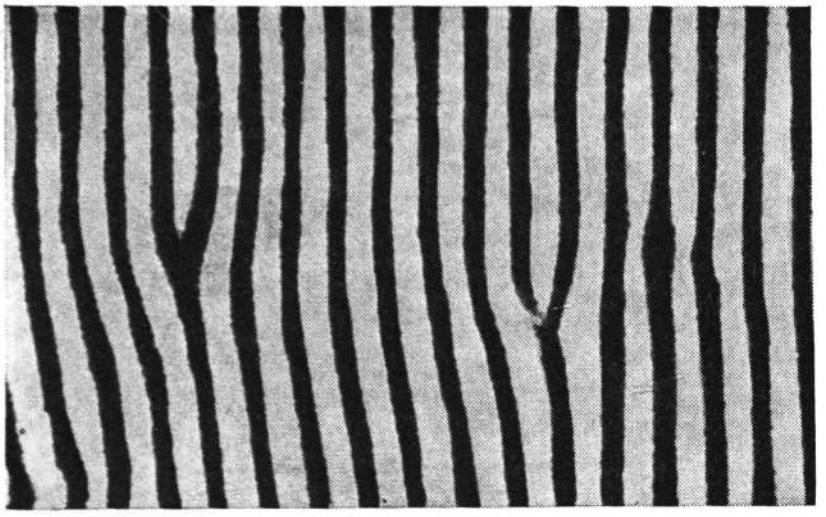

Fig. 57. Moiré pattern obtained by transmission electron microscopy of overlapping (111) layers of palladium and gold; it reveals the presence of dislocations in one of the layers, 1 800 000 ×

of the layers contains an incomplete atomic plane, this will be reflected in the Moiré pattern. A Moiré pattern obtained by transmission electron microscopy is illustrated in Fig. 57.

Observation of decorated dislocation lines in a light microscope. The method of decoration of dislocations in transparent crystals is essentially as follows. A crystal is doped, during growth or by diffusion, with an impurity whose atoms are attracted to dislocations. On proper heat treatment, the region around a dislocation line turns out to be supersaturated with the impurity which precipitates in the form of finest particles along the dislocation line. These opaque particles scatter light and make the dislocation line visible though the diameter of its core is beyond the resolution of a common light microscope. This method was used to observe dislocations in sodium chloride, potassium chloride, silver halides and some other crystals transparent in the visible range of spectrum. In silicon, which is transparent to infra-red light, decorated dislocations can be seen in an infra-red microscope. Figure 58 illustrates dislocation loops created by a Frank-Read dislocation source in a silicon crystal containing copper as impurity; the original position of the dislocation is not seen in the figure, since it was out of focus when photographed. A hexagonal dislocation network was readily revealed in a crystal of potassium chloride upon decoration with silver.

The decoration method has provided good possibilities for detailed examination of the geometry of dislocation networks, the shape of dislocation lines (helicoids, rings, etc.) and other characteristic features of dislocation structures in the volume of transparent crystals. In age-hardening alloys, it is sometimes possible to observe in a light or electron microscope (on replicas) the dislocation lines

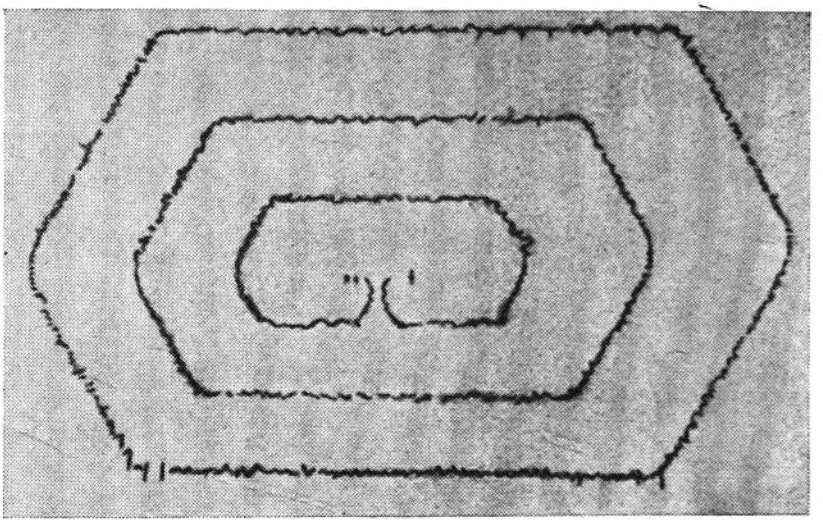

Fig. 58. Frank-Read source in a silicon crystal. The silicon crystal was heated in contact with copper up to 900°C and then cooled in order to decorate dislocations by copper precipitates. Infra-red light photography

in metals which were located immediately under the surface of a section and have been decorated by disperse particles precipitated from a supersaturated solid solution.

The etch pit method. In this method, the polished surface of a microsection is etched by an appropriate etchant which leaves etch pits in points of emergence of dislocations onto the surface. The appearance of etch pits is due to the fact that the free energy in the dislocation core is higher than otherwise and dissolution proceeds here more quickly than at a distance from a dislocation. The dislocation core acts as a dissolution nucleus. An etch pit becomes visible in the microscope when it reaches a size many orders of magnitude

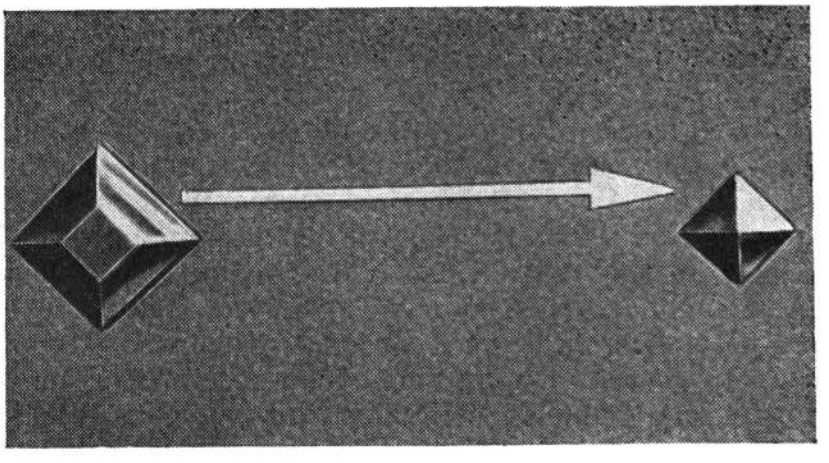

Fig. 59. Movement of a dislocation in the {100} plane of lithium fluoride, revealed by etch pit technique, 4 000 ×

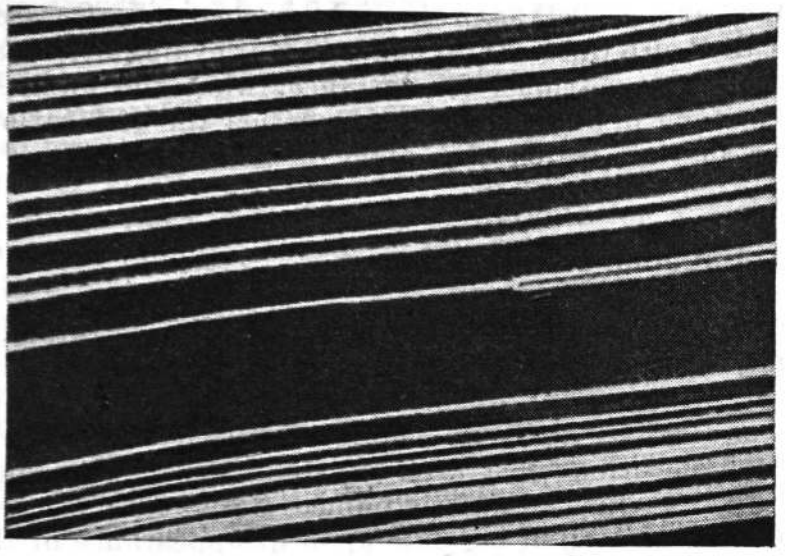

Fig. 60. Electron micrograph of slip lines in deformed α-brass, 10 000 ×

larger than the width of the dislocation core. Since the rate of dissolution in a crystal depends on orientation, etch pits often (but not always) have distinct crystallographic faces. For instance, etch pits in cubic lattice crystals have a triangular shape in plane {111} and a square shape in plane {100} (Fig. 59). On deviations of the metal plane from these crystallographic planes, distorted triangles and squares form. The dislocation origin of etch pits has been proved by comparing the distance between etch pits in a low-angle boundary in germanium with the distance h between dislocations calculated by the results of radiographic examination of misorientation angle θ. The results were quite coincident. This is indicative both of the validity of the dislocation model for the structure of low-angle boundaries and of the dislocation origin of etch pits in it.

The etch pit method is used for determining the dislocation density (by the number of etch pits per unit area of metal surface) and the pattern of dislocation distribution. Defects of non-dislocation origin may also produce their own etch pits and distort the actual picture of the dislocation structure. For that reason, it is essential to employ multiple polishing and repeated etching in order to be sure that the same etch pit pattern is reproduced repeatedly. Since dislocation lines pass from the metal surface into the depth, their pattern will be reproduced almost exactly upon repeated polishing and etching.

Dislocations can also be detected by *indirect methods*, for instance, by examining slip lines. Moving dislocations leave steps where they emerge onto the free surface of a crystal. The width of a step is one Burgers vector per each dislocation (Fig. 60). A surface step left by a unit dislocation is undiscernible, but if it has been produced by a group of dislocations (dislocation avalanche) it may be visible

by the naked eye, as well as in the light or electron microscope. Such steps are called slip lines or slip bands. Their examination can clarify many important questions, for instance, what the number of dislocations moving in an avalanche is; whether the dislocation sources are flat or spatial; which slip plane is preferable, etc.

7. Initiation of Dislocations

The dislocation energy is a few electron-volts per atom, so that, in contrast to the formation of point defects, thermal activation is helpless in initiation of dislocations.

Single- and polycrystals of metals usually contain a very high number of dislocations just after crystallization. This suggests an idea that dislocations can appear immediately at the crystallization front or during cooling of crystals upon disappearance of the liquid phase. Some probable mechanisms for initiation of dislocations are discussed below.

1. A crystal free of dislocations grows by attachment of a nucleus to an existing step, since a nucleus attaches to a crystal better when there are more neighbour atoms. In this way, the layer on a crystal will be finally completed. To form a new atomic layer on the smooth surface of the crystal, it is essential that a 'two-dimensional' nucleus should appear on that surface; this is the most critical stage in the growth of perfect crystals and requires a high supersaturation (undercooling). This stage is inessential however if the growing crystal contains a screw dislocation. As atoms are attached to a step on its surface, the latter rotates. Since atoms are laid onto a helical surface, the step continues to exist all the time and thus facilitates the attachment of atoms to the crystal, i.e. the crystal growth.

A crystal containing a screw dislocation represents an atomic plane twisted along a helical path. A question then arises: what causes twisting at the initial moment of growth, on the formation of a nucleus? As is well known, crystals nucleate on a ready substrate, such as mould walls or finest solid particles suspended in the melt. Such substrates always have ready steps to which atoms from the solidifying melt can attach. Thus, a screw dislocation 'grows' into a nucleating crystal, as it were.

2. The nucleation of dislocations during solidification of the metal can also be explained by the appearance of stresses. When oriented growth (epitaxy) of a crystal on a substrate takes place, a slight misfit between two conjugate lattices (which exists always) produces elastic stresses both in the substrate and epitaxial layer. As the epitaxial layer attains a critical thickness, it becomes energetically favourable to release the elastic stresses by the formation of a dislocation at the boundary between the substrate and the growing crystal. The gain in energy due to the formation of disloca-

tions is compensated for by a decrease of the energy of elastic deformation of the conjugate lattices.

3. Segregation of impurities during crystallization can result in the formation of adjacent layers of different composition, with slightly different atomic spacings. This difference may cause the appearance of elastic stresses. At a certain difference in atomic spacings, it becomes energetically favourable for a dislocation to appear on the boundary between two adjacent layers.

4. Dislocations may appear due to various occasional reasons during growth of crystals in solidifying metal. This may result in the formation of a mosaic structure, i.e. a crystal will consist of mutually misoriented sub-grains (blocks). One of the probable causes for the formation of misoriented sub-grains is bending of very 'fine' dendritic branches due to convective currents, temperature gradient or other factors acting in solidifying metal. When slightly misoriented dendritic branches grow together, dislocations appear on boundaries between them, the surface of contact being essentially an array of edge dislocations.

5. Dislocations can initiate in fully solidified metal in direct vicinity of the solidification front or at a distance from it. It is assumed that this occurs mainly by the vacancy mechanism. The equilibrium concentration of vacancies decreases sharply as the temperature decreases below the melting (solidifying) point. With fast cooling, a crystal may be strongly supersaturated with vacancies. Excess vacancies condensate in the form of discs parallel to the closest-packed plane. The thickness of a disc may be one, two or three vacancy layers. When the diameter of a vacancy disc attains a critical value, interatomic attraction forces draw the two sides of the disc together, the disc collapses, and its sides join. The phenomenon is called the collapse of vacancy discs.

If a vacancy disc lying in a {111} plane of f.c.c. lattice collapses as the two layers separated by it join along the normal, it leaves an extrinsic stacking fault. Figure 34*a* shows the stacking sequence of close-packed {111} layers upon collapse of a vacancy disc. Before collapse, the disc was located in the middle of atomic layer *B*. Upon collapse of the disc, the adjacent layers *A* and *C* joined along the normal and formed a stacking fault *CACA* in the f.c.c. lattice *ABCABC* . . . . Such stacking faults are usually not round or oval in shape, but are bounded by close-packed atomic rows, i.e. there forms a Frank dislocation having a hexagonal shape. Such hexagons have been observed in quenched aluminium foils.

A Frank dislocation cannot glide by itself. If however there is a Shockley partial dislocation in its stacking fault, the Frank dislocation and the Shockley dislocation can combine into a unit dislocation capable of gliding [see the dislocation reaction (57)]. This reaction is energetically favourable, since it eliminates the stacking fault associated with Frank dislocation.

Dislocations can form by collapse of vacancy discs not only during cooling of solidified metal, but also in hardening from a high temperature, when the metal becomes highly supersaturated in vacancies and these can condensate into discs.

6. Dislocations can also initiate due to thermal stresses, plastic deformation, secondary phases, etc.

RECOMMENDED LITERATURE

1. Amelinckx S., *The Direct Observation of Dislocations.* New York-London, Academic Press, 1964.
2. Cottrell A. H., *Dislocations and Plastic Flow in Crystals.* Oxford, Clarendon Press, 1953.
3. Friedel J., *Dislocations.* London, Pergamon Press, 1964.
4. Gorelik S. S., *Recrystallization in Metals and Alloys.* Moscow, Mir Publishers, 1981.
5. Hirth J. P., Lothe J., *Theory of Dislocations.* New York, McGraw-Hill, 1968.
6. Mirkin L. I., *Physical Principles of Strength and Plasticity.* Moscow, Moscow State University Press, 1968 (in Russian).
7. Novikov I. I., *Crystal Lattice Defects of Metals.* Moscow, Metallurgiya, 1968 (in Russian).
8. Read W. T., *Dislocations in Crystals.* New York, McGraw-Hill, 1953.
9. *The Theory of Creep and Long-term Strength of Metals.* Moscow, Metallurgizdat 1959. Authors: N. A. Oding, V. S. Ivanova, V. V. Burduksky, and V. N. Geminov (in Russian).

3 Plastic Deformation of Single Crystals

The mechanisms of plastic deformation of single crystals and the associated variations in the dislocation structure are analysed by means of stress-strain curves. Such a curve gives the shear stress that must be applied to cause further plastic deformation. It has been demonstrated that the behaviour of pure metals in deformation cannot be represented by a single stress-strain (τ-γ) curve. The shape of a τ-γ curve may depend on many factors, such as the type of crystal lattice, metal purity, orientation of a crystal relative to the deforming stress, solute impurities, particles of other phases, temperature and rate of deformation, the size and shape of crystal, and the state of its surface. The diversity of factors affecting the shape of τ-γ curves has resulted in different concepts of the deformation mechanism and different dislocation models explaining various portions of the τ-γ diagram. The validity of these theories and hypotheses is checked experimentally.

The principal mechanism of plastic deformation in metals and alloys is intragranular shear displacement of some portions of a crystal (or crystallite) relative to other portions, which can be effected by various kinds of dislocation movement. This is what is called *intragranular plastic deformation.* The shear mechanisms of plastic deformation are quite diverse, but the principal ones are slip (glide), twinning, and kinking.

In many cases, the processes of plastic deformation may be simultaneously realized by more than one mechanism. A particular contribution of some or other mechanism to the process is determined by many factors, such as the type of crystal lattice, chemical and phase composition, the structure of the metal (alloy), the amount, rate and temperature of deformation, etc.

1. Deformation by Slip

Since the lowest Peierls stress corresponds to the lowest Burgers vector and closest-packed planes (see Ch. 2), single crystals and polycrystals deform by slip in close-packed planes along directions of

Table 7. Slip Systems for Selected Metals and Alloys

Metal or alloy	Preferable slip systems * (plane and direction) at		τ_{cr}, MPa, at room temperature	Metal purity, %, for determination of τ_{cr}
	room temperature	high temperature		
Face-centred cubic (f.c.c.) lattice				
Cu	{111} ⟨110⟩	{100} ⟨110⟩	0.35	99.999
Au	{111} ⟨110⟩	{100} ⟨110⟩	0.50	99.999
Ag	{111} ⟨110⟩	{100} ⟨110⟩	0.40-0.70	99.999
Ni	{111} ⟨110⟩	{100} ⟨110⟩	3.30-7.50	99.98
Al	{111} ⟨110⟩ and {100} ⟨110⟩	{100} ⟨110⟩	0.55-1.00	99.994
Body-centred cubic (b.c.c.) lattice				
Fe	{110} ⟨111⟩ **	{123} and {*hkl*} ⟨111⟩	15.00	99.96
	{112} ⟨111⟩			
	{123} ⟨111⟩			
Fe+3% Si	{110} ⟨111⟩	{123} and {*hkl*} ⟨111⟩	—	—
	{112} ⟨111⟩			
Nb	{110} ⟨111⟩	—	34.0	Zone-refined
V, Mo, Mo-Re	{110} ⟨111⟩ and {112} ⟨111⟩	—	—	—
W	{110} ⟨111⟩ and {112} ⟨111⟩	{112} ⟨111⟩	—	—
Cr	{123} ⟨111⟩	—	—	—
Close-packed hexagonal (c.p.h.) lattice				
Cd ($c/a=1.886$)	$\langle 11\bar{2}0\rangle$ {0001} and {1101}	$\langle 11\bar{2}0\rangle$ $\{10\bar{1}0\}$ and {0001}	0.13	99.999
Zn ($c/a=1.856$)	$\langle 11\bar{2}0\rangle$ {0001} and $\{11\bar{2}2\}$	$\langle 11\bar{2}0\rangle$ $\{10\bar{1}0\}$ and $\langle 11\bar{2}3\rangle$ $\{11\bar{2}2\}$	0.30	99.999
Mg ($c/a=1.624$)	$\langle 11\bar{2}0\rangle$ {0001} and $\{1\bar{1}00\}$	$\langle 11\bar{2}0\rangle$ $\{10\bar{1}1\}$ and {0001}	0.50	99.99
Co ($c/a=1.621$)	$\langle 11\bar{2}0\rangle$ {0001}		6.5	99.999
Ti ($c/a=1.59$)	$\langle 11\bar{2}0\rangle$ {1010}	$\langle 11\bar{2}0\rangle$ {0001}	14.0	99.99
Zr ($c/a=1.59$)	$\langle 11\bar{2}0\rangle$ $\{10\bar{1}0\}$	$\langle 11\bar{2}0\rangle$ {0001}	7.0	99.0

* Where more than one slip system is indicated, the most preferable one is written first.

** Below room temperature, the sequence of preferable slip systems may change.

closest packing. The slip plane and the direction of slip that lies in that plane form what is called the *slip system.*

Slip systems. *F.c.c. metals* deform in close-packed octahedral {111} planes along a close-packed ⟨110⟩ direction. For each of the four differently oriented {111} planes (see Fig. 35*b*), there are three ⟨110⟩ directions with the Burgers vector of a perfect dislocation $0.5a$ [110]. The total number of slip systems which can participate in slip is $4 \times 3 = 12$. Cases when the slip plane is other than an octahedral plane are rare and are more likely to occur at elevated temperatures. For instance, slip in aluminium can be observed in three {100} planes, with two ⟨110⟩ directions in each of them being slip directions, i.e. there are $3 \times 2 = 6$ additional slip systems. At elevated temperatures, this combination of slip systems is responsible for around 40 per cent of slip lines in aluminium.

In *b.c.c. metals,* slip almost always takes place along a ⟨111⟩ direction which corresponds to the lowest Burgers vector of perfect dislocation, $0.5a$ [111]. The closest-packed planes are here {110} planes, while the {112} plane is the main plane of stacking faults. Depending on the stacking fault energy, some or other slip systems may be operative (Table 7). Further, slip planes with indices {123} and other {*hkl*} planes with higher indices are encountered in b.c.c. structures; slip in these planes may take place at high temperatures or at any temperature but low deformation rate. This type of slip is usually attributed to cross slip of screw dislocations. As has been proved experimentally, with an increase of the relative temperature of deformation $T/T_{\text{m.p.}}$, the existing slip systems become operative in the following sequence: {110}, {112}, {123}, and {*hkl*}. The possibility of existence of another sequence: {112}, {110}, {123}, is not excluded. This can be explained by the fact that the Peierls energy condition and the stacking fault energy are not the sufficient criteria to explain exhaustively the appearance of slip. An important role is also played by the temperature relationships for Peierls stress and stacking fault.

If slip takes place in a {112} ⟨111⟩ system, there are four ⟨111⟩ directions each of which is the line of intersection of three {112} planes (see Fig. 38), so that 12 physically different slip systems are possible. With slip in {110} and {123} planes along a ⟨111⟩ direction, there are also 12 physically different slip systems (Fig. 61). The large number (48) of possible slip systems for a number of b.c.c. metals sometimes results in a substantially wavy form of slip bands observed on the metal surface (Fig. 62). A slip surface is the surface of a prism whose every face coincides with the slip plane, while the edges are intersections of these planes with the slip direction. This type of slip resembles longitudinal shear in a bundle of pencils and is called accordingly *pencil glide.*

In *c.p.h. metals,* the probable slip systems are very diverse (see

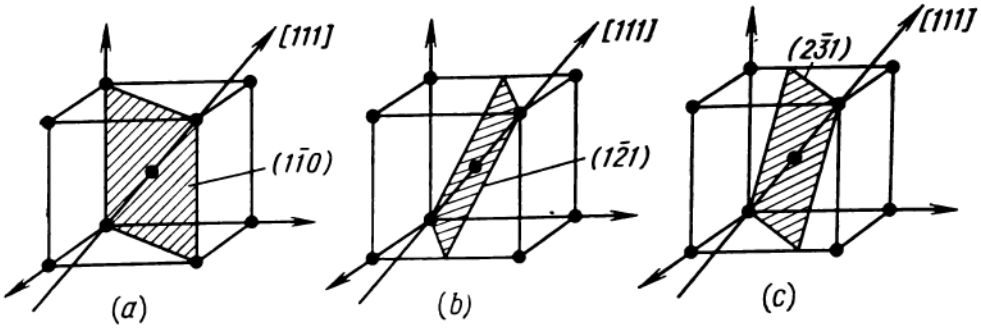

Fig. 61. Typical slip systems in a b.c.c. structure

Table 7) and depend on the c/a ratio. The ratio $c/a = 1.633$ in c.p.h. lattices corresponds to an ideal structure of close-packed spheres. The lowest Burgers vector, $a/3\ \langle 11\bar{2}0 \rangle$, lies in a close-packed basal $\{0001\}$ plane which contains three probable slip systems. The occurrence of extended dislocations in the (0001) plane often observed in Co, Zn, Cd, and Mg is an evidence of a low stacking fault energy in that plane. For Cd and Zn, $c/a > 1.633$ (see Table 7), so that slip takes place in the basal plane. Though the c/a ratio for Mg and Co is less than 1.633 (=1.62), slip in the (0001) plane does however occur, due to their low stacking fault energy. For Ti and Zr, c/a is still lower: the distance between $\{10\bar{1}0\}$ planes in these metals is smaller than that between basal planes. According to Peierls' formula, slip in these metals is effected in $\{10\bar{1}0\}$ planes which are called prismatic.

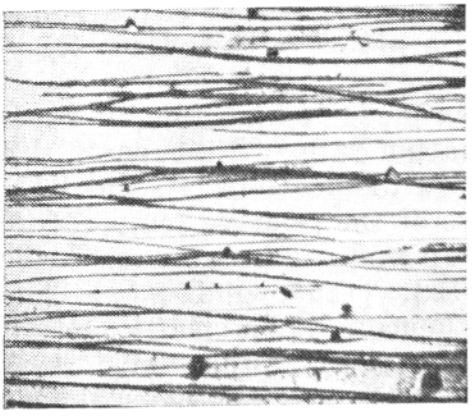

Fig. 62. Slip lines in (110) plane in a crystal of Fe + 3% Si alloy deformed at room temperature, 100×

Apart from basal plane slip, slip in $\{11\bar{2}2\}$ plane and along $(a/3)\ \langle \bar{1}\bar{1}23 \rangle$ direction is also observed in c.p.h. metals (Fig. 63). Dislocations can extend into partial dislocations in pyramidal $\{10\bar{1}1\}$ and $\{11\bar{2}2\}$ planes.

The resolved shear stress for slip in single crystals. If a number of randomly oriented crystals of a metal are deformed in tension, the stress-strain (σ-ε) curves obtained will be substantially different, which can be explained by different orientation of their slip planes and directions relative to the external load. Anisotropy of the flow stress, ultimate tensile strength and maximum relative elongation is noticeable even in cubic crystals whose other physical properties

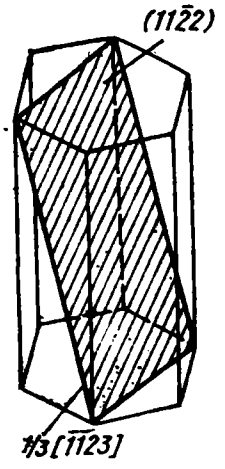

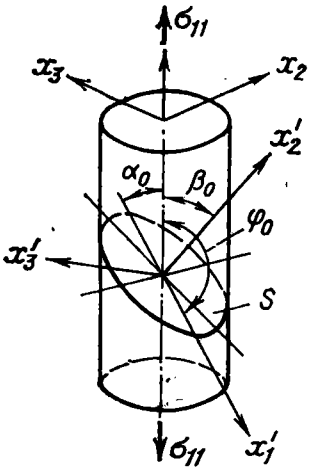

Fig. 63. (*left*) Slip system ⟨$\bar{1}\bar{1}$23⟩ {11$\bar{2}$2} in a c.p.h. lattice

Fig. 64. Coordinate system x_1', x_2', x_3 related to the geometry of slip in a single crystal deformed by simple tension. The angle $\varphi_0 = 180° - \alpha_0$ and $\cos \varphi_0 = -\cos \alpha_0$ (see Fig. 66)

(for instance, electric resistivity) are essentially isotropic. In tension of hexagonal crystals, the flow stress may change as much as by a factor of six at a change of orientation. The relative elongation measured in tensile tests may vary from a few per cent to a few hundred per cent.

This can be explained by the fact that the measurement of flow stress is not the best way for measuring stresses in the course of slip, which is effected by shear. The same is true of the measurement of elongation in the direction of tension. The generally adopted definition of deformation does not suit properly for description of deformations which occur in a distinct system of crystallographic planes. It should be recognized that the shear test is the best method of testing, though the tensile test is practically more convenient. In order that the stress-strain (σ-ε) curves obtained for crystals of different orientation could be compared with one another, the stresses and strains determined in the tests are usually recalculated to those operative along the shear direction in the slip plane. Let us determine these stresses and strains.

Let a single crystal be in a state of simple tension (Fig. 64) under the action of a stress σ_{11} in the direction of the axis x_1. The component σ_{11} is the sole component of tensor σ_{ij} in the system of coordinates x_1, x_2, x_3.

Let us take a new system of coordinates x_1', x_2', x_3' with the x_2' axis directed along the normal to the slip plane S. The angle between the axis x_2' and the direction of tension x_1 is β_0, with $\cos \beta_0 = \lambda_{2'1}$ being the direction cosine between the axes x_2' and x_1. The slip direction in the new system x_1', x_2', x_3' is coincident with the x_1' axis and the direction cosine between the x_1' and x_1 axes is $\lambda_{1'1} =$

$= \cos \alpha_0$. The stresses in the given slip system, which is fixed by the coordinate axes x_1', x_2', x_3', can be found by transformation of the stress tensor σ_{ij} from the old system of coordinates by the formula $\sigma_{i'j'} = \lambda_{i'i}\lambda_{j'j}\sigma_{ij}$.

Since slip takes place under the action of shear stresses τ, we are interested only in the stress tensor component $\sigma_{i'j'}$: $\tau = \sigma_{1'2'}$ which causes the displacement of one plane, S, relative to another plane, S', in the slip direction x_1':

$$\tau = \sigma_{1'2'} = \lambda_{1'i}\lambda_{2'j}\sigma_{ij} = \lambda_{1'1}\lambda_{2'1}\sigma_{11} = \cos \alpha_0 \cos \beta_0 \sigma_{11} \quad (66)$$

Equation (66) was first derived by E. Schmid and the coefficient $\cos \alpha_0 \cos \beta_0 = m$ is accordingly called the Schmid factor. As may be seen from equation (66), the stress τ is equal to zero when the axis of tension is either parallel to the slip plane ($\beta_0 = 90°$) or normal to that plane ($\beta_0 = 0$ and $\alpha_0 = 90°$). Thus, slip deformation in the indicated extreme orientations is impossible since the shear stress τ in the direction of slip is zero. The highest shear stress is obtained when the Schmid factor $m = 0.5$, which corresponds to the angles α_0 and β_0 of 45°. Hence, $\tau_{max} = 0.5\sigma_{11}$. If the stress applied causes plastic flow in a single crystal, τ attains the critical value τ_{cr} causing crystallographic shear displacement of plane S relative to S' (see Fig. 66). The critical stress τ_{cr} is independent of the orientation of the slip plane and slip direction relative to the stress applied, and therefore, is a constant for a given metal and particular type of slip system. Taking τ_{cr} as the limiting value of stress, i.e. the stress that causes plastic flow in the metal (in the case considered $\sigma_{11} = \sigma_y$), we have

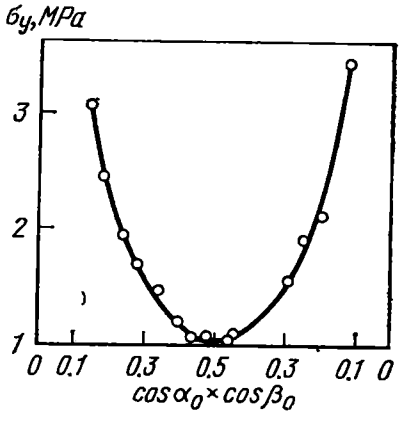

Fig. 65. Effect of the Schmid factor m on flow stress σ_y in tensioned zinc crystal (99.999% Zn)

$$\sigma_y = \tau_{cr}/(\cos \alpha_0 \cos \beta_0) = \tau_{cr}/m \quad (67)$$

i.e. the yield limit σ_y of a single crystal is determined by the crystal orientation and the Schmid factor m (Fig. 65). The experimental points of σ_y in Fig. 65 correlate well with the curve σ_y (m) plotted by formula (67), which is indicative that Schmid's law (67) is perfectly true. This correlation has been verified experimentally for cadmium, zinc and magnesium crystals (all having a c.p.h. lattice).

The results for f.c.c. and b.c.c. metals are less convincing, since the multitude of probable slip systems in them does not allow the Schmid law (67) to be verified in a wide range of m factor. Notwithstanding this fact, the magnitude of τ_{cr} is a fundamental cha-

racteristic of the mechanical properties of any metal, since it is associated with the main kind of plastic shear strain along the existing slip planes.

The critical stress τ_{cr} may depend substantially on the metal purity, the concentration of alloying elements, deformation rate, temperature, etc. Values of τ_{cr} for some high-purity metals may be found in Table 7. The magnitude of τ_{cr} is usually much lower than the yield limit obtained in shear tests of commercially pure metals and alloys on their base. For instance, $\tau_{cr} = 15$ MPa for 99.96% pure iron, against $\tau = 105$ MPa for steel Grade Ст.3. The cause for this substantial difference will be discussed later in the book.

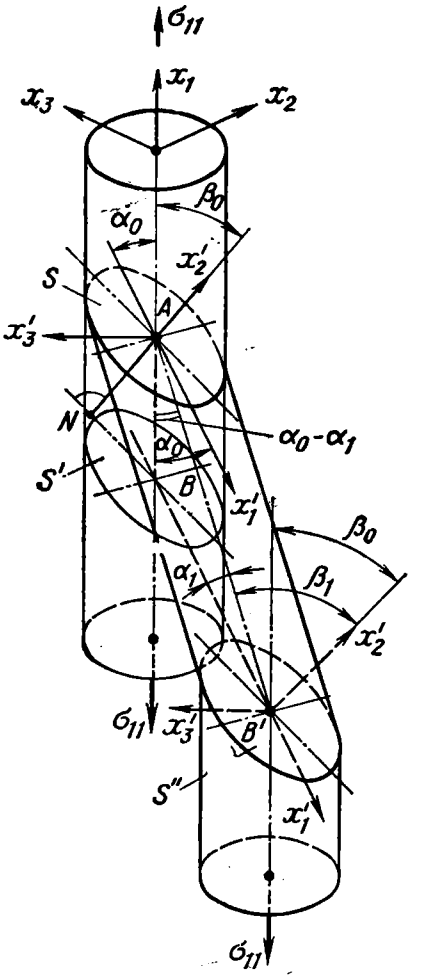

Fig. 66. Diagram to determine the shear strain in slip plane S' relative to plane S in the direction of x_1' axis on the path BB'

The shear strain in slip. Stress-strain curves. Like shear stress, shear strain is a more appropriate measure of deformation in slip than is the relative elongation in tension. Shear strain can be determined in terms of the relative displacement of two adjacent slip planes S and S' (Fig. 66). The geometry of a specimen varies during slip; if, for instance, the specimen was originally round in cross section, it becomes oval when being elongated. In the course of shear, plane S' is displaced by slip relative to plane S in the direction x_1' (along BB') and occupies a new position S''. The angle β_0 between the normal to S (S') and the axis of the specimen at the initial moment of deformation (see Fig. 66) increases to β_1 as extension proceeds (i.e. as plane S' slips to new position S''), whereas the angle α_0 between the specimen axis and the slip direction (prior to deformation) decreases to α_1, i.e. the direction of slip (axis x_1' or BB') rotates towards the axis of tension*. In the course of extension, the length of the specimen in the region of displacing planes S and S' is equal to the distance l_0 between these planes, i.e. $l_0 = AB$. Upon deformation, the distance between planes S and S'' is AB', since

* Figure 66 shows an equivalent but inverse diagram: the slip direction (axis x_1' or BB' direction) is shown fixed, while the axis AB' of the specimen rotates towards the slip axis x_1'.

exactly this distance is measured in the course of extension. Therefore, $l_1 = AB'$.

The distance AN between the planes S and S' can be determined by considering the triangle ABN: $AN = l_0 \cos \beta_0$. Connecting the point N with B', we can note that NB and BB' lie in the plane S', and therefore, NB' also lies in plane S' and the angle ANB' is a right angle. It may be seen from the triangle ANB' that $AN = AB' \cos (\angle NAB')$. Noting that $\angle NAB' = \beta_1$, we have from triangles ABN and $AB'N$:

$$AN = l_0 \cos \beta_0 = l_1 \cos \beta_1 \tag{68}$$

Considering the triangle ABB', we can find the shear BB':

$$BB' = l_1 \cos \alpha_1 - l_0 \cos \alpha_0 \tag{69}$$

and, noting that $\angle BAB' = \alpha_0 - \alpha_1$ and $\angle ABB' = 180° - \alpha_0$, we obtain the relationships

$$l_1/l_0 = \sin \alpha_0/\sin \alpha_1 \text{ or } l_1/\sin \alpha_0 = l_0/\sin \alpha_1$$
$$= BB'/[\sin (\alpha_0 - \alpha_1)]$$

whence we have

$$BB' = l_1 [\sin (\alpha_0 - \alpha_1)]/\sin \alpha_0$$
$$= l_0 [\sin (\alpha_0 - \alpha_1)]/\sin \alpha_1$$

Assuming $\gamma = BB'/AN$ to be the measure of shear deformation, we write

$$\gamma = l_1 : l_0 = [\sin (\alpha_0 - \alpha_1)]/\cos \beta_0 \sin \alpha_0$$

or, cancelling out α_1 from the last equation, we obtain the expression for the shear strain:

$$\gamma = \frac{1}{\cos \beta_0} \left(\sqrt{\left(\frac{l_1}{l_0}\right)^2 - \sin^2 \alpha_0} - \cos \alpha_0 \right) \tag{70}$$

whose right-hand side contains terms which can be determined experimentally, i.e. the length of a specimen before and after deformation and the angles α_0 and β_0 of the original orientation of the crystal.

Stress-strain (σ-ε) curves of crystals can be more conveniently represented in the coordinates: *resolved shear stress* τ [formula (66)]—*resolved shear strain* γ [formula (70)]. This construction can diminish (though not eliminate fully) the difference in the shape of curves for crystals with different orientation of slip planes and slip directions relative to the external stress. For all metals, the resolved shear stress increases with increasing strain (Fig. 67), the phenomenon being known as *strain* (work) *hardening*, or *cold work*. The strain hardening effect in f.c.c. metals is however much stronger than for instance in such c.p.h. metals as cadmium, magnesium or zinc. C.p.h. metal can withstand very high shear deformations, but only

when their crystals are oriented properly. To clarify this difference, let us analyse in detail the geometry of slip in f.c.c. and c.p.h. crystals.

Geometry of slip in f.c.c. and c.p.h. crystals. The axis of a monocrystalline specimen usually does not coincide with the rational crystallographic axis, i.e. with the direction with low indices. The usual way for designating the orientation of a crystal is to use a stereographic projection. The normals for various planes of a crystal are drawn to intersect a sphere. The latter with all its intercepts ('traces') is projected onto a plane surface to form a circular plot which contains the intercepts of all the plane normals, called 'poles' of these planes. The angles between these are then measured with a stereographic net which is subdivided into degrees and represents a projection of a sphere ruled to provide angular relationships.

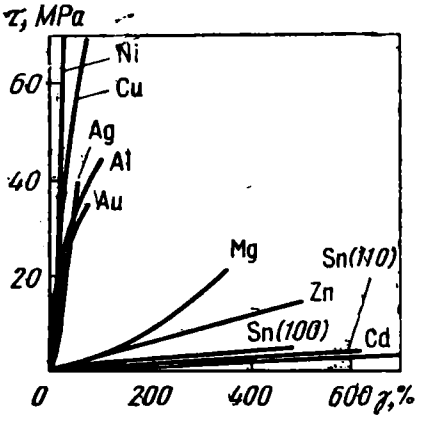

Fig. 67. Resolved shear stress —resolved shear strain (τ-γ) curves for selected metals

Crystal structures and orientations are usually represented by means of a standard projection (Fig. 68). This type of projection is obtained by orienting the crystal with a plane of low indices in the plane of projection. For a cube face, for instance, the centre of projection is the normal to the cube plane, i.e. the [001] direction. In such a projection, the symmetry of a crystal is fully revealed. In the case of a cubic crystal (f.c.c. or b.c.c.), the projection is divided by intersecting great circles into 24 stereographic unit triangles which are crystallographically identical (Fig. 68*b*). In each case, the three corners of the triangles represent equivalent directions, ⟨001⟩, ⟨011⟩ and ⟨111⟩ making always the same angles with each other. In the standard projection, however, these triangles vary in shape due to variations in the angular and linear elements in various portions of the projection.

In the specification of the orientation of a crystal in uniaxial tension, only one triangle need to be used, commonly the triangle with corners [001], [011], [$\bar{1}$11] located in the centre of the projection. All possible orientations of crystals of cubic structure can then be specified by certain points (e.g. of the tension axis) within this triangle or along its boundaries. Consequently, in practice, if one wishes to represent the orientations of a number of single crystal specimens, the angles between the specimen axis and at least two of the [001], [011] and [$\bar{1}$11] directions are measured, and the axis is plotted in the standard triangle using a stereographic net.

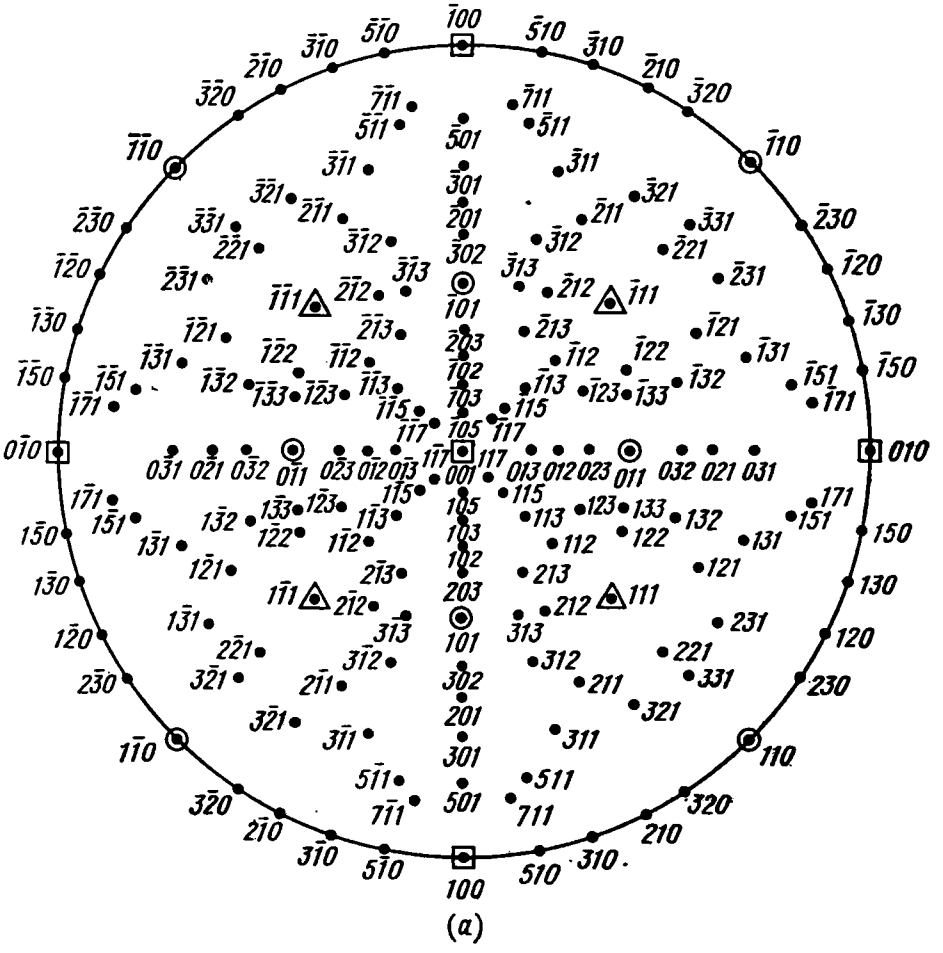

Fig. 68. Standard cubic projection (*a*) and cubic stereographic projection showing 24 basic triangles (*b*)

Each of the unit triangles in the stereographic projection defines the region in which a particular slip system is operative (see Fig. 68*b*). There are four poles ⟨111⟩ (designated by the letters *A*, *B*, *C*, and *D*) which correspond to traces of the normals on octahedral slip planes, and six slip directions, from *I* to *VI*. Taken a common standard triangle *WAI*, it may be seen that the system *BIV* is operative within its boundaries: this means that, in tensile deformation with the axis of tension lying in this triangle, the slip plane is plane *B*, i.e. (111), and the slip direction is *IV*, i.e. $[\bar{1}01]$.

The stereographic projection makes it possible to follow the rotation of a crystal during deformation. In tensile tests, the direction of slip tends to rotate towards the axis of tension or, which is equivalent, the tension axis *I* [i.e. (011) in the example considered] tends to rotate towards the slip direction *IV*.

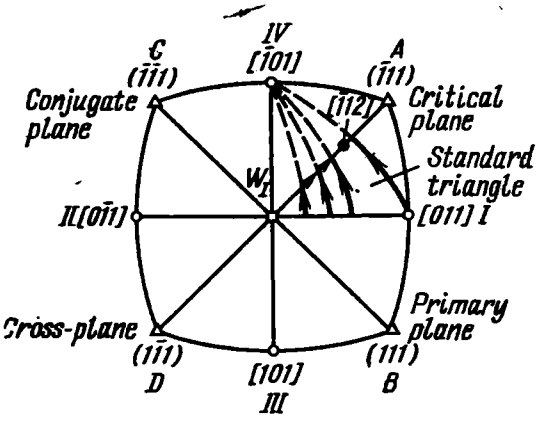

Fig. 69. Rotation of crystal axes in slip with the axes of tension oriented initially along W_I *I* line and the effect of secondary systems

Figure 69 gives the signs of rotation for the region of orientations within the standard stereographic triangle. As rotation proceeds, however, the tension axis may finally come to the boundary W_IA between two stereographic triangles, with an utterly different slip system *CI* being operative in one of them (see Fig. 68*b*). Deformation in such a point usually takes place in two systems, i.e. double, or conjugate, slip occurs.

The system in which deformation commences (*BIV* in the case considered) is called *primary*; it is always the system having the highest resolved shear stress. Once the crystal orientation is known, we can measure on the stereographic projection the angles α_0 and β_0 for all twelve possible slip systems and thus calculate the Schmid factor *m*. The operative slip system will have the highest Schmid factor.

As illustrated in Figs. 68*b* and 69, the system (111) [011] is a conjugate slip system and (111) $[\bar{1}01]$ is primary. Double slip can cause further movement of the specimen axis along the boundary [001]—$[\bar{1}11]$ of the triangle towards the $[\bar{1}12]$ pole which is half-way between the slip directions $[\bar{1}01]$ and [011] and lies within the great circle connecting these poles. The tension axis retains this orientation up to local necking and fracture of the specimen. Thus, owing to double slip, the axis of a cubic crystal ceases to rotate towards the slip direction. This is why cubic crystals can be extended much less

appreciably than hexagonal in which the rotation of the axis towards the slip direction (with slip occurring in one system only) may be as high as a few degrees. In cubic crystals, the resolved shear strain only rarely attains 100 per cent, while hexagonal crystals, say, zinc, cadmium or magnesium, can be deformed up to 400 per cent or more.

We have considered the behaviour of crystals with the tension axis within the stereographic triangle. Crystals with their axes lying on boundaries of the triangle constitute a special group, since the critical shear stress for them is the same in more than one slip system and plastic deformation begins in more than one slip plane.

Figure 70 presents data on the number of expected operative slip systems. The most complicated case is that of the [001] orientation for which at least four slip systems are equally favourable. The orientation in the centre of the projection is indicative of the operation of eight slip systems, which corresponds to four planes with two slip directions in each. Of these two directions, only one can be used at a time, since simultaneous slip in one plane in two or more directions is impossible.

The capacity of cubic crystals for deforming simultaneously in more than one slip systems is responsible for the experimentally established fact of higher rates of strain hardening in these metals compared with metals of a hexagonal crystal structure.

The essence of the problem on the nature and number of operative slip systems consists in that the number of simultaneously operating slip systems determines the type of the dislocation structure formed on deformation, which can influence the resistance to slip (to dislocation movement) or strain hardening in the course of deformation, and on the conditions of subsequent recrystallization. For that reason, the study of stress-strain curves (see Chs. 3 and 4), whose pattern is closely associated with the dislocation structure, is of extremely high significance.

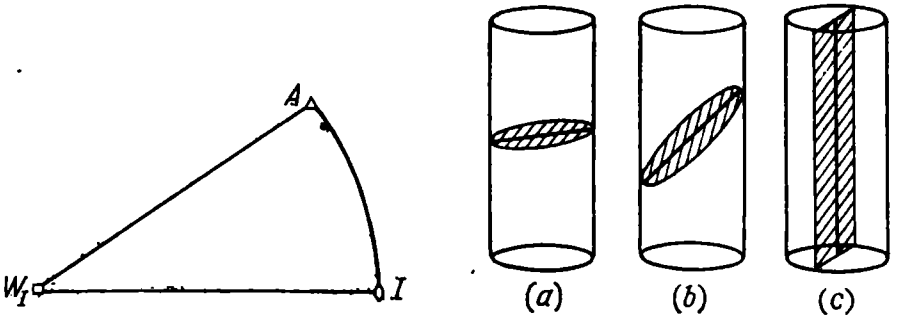

Fig. 70. (*left*) Operative slip systems at particular orientations of the crystal relative to the operative stress

W_I—four planes, with two directions in each; *A*—three planes with two directions in each; *I*—two planes with two directions in each; along W_IA and W_II—two planes with one direction in each; along *AI*—two directions in one plane

Fig. 71. Various possible orientations of basal plane in a tensioned c.p.h. crystal

At room temperature, cadmium, zinc and magnesium crystals are deformed mainly by slip in the basal plane, i.e. only one slip system is operative in the course of deformation. The pattern of the stress-strain curve obtained depends very strongly on the orientation of the basal plane relative to the axis of tension prior to deformation, which determines to an appreciable extent the amount of plastic deformation that a crystal can withstand before fracture.

Since the slip plane rotates in such a manner that the slip direction moves towards the tension axis, the resulting plastic deformation is higher on a greater rotation of the slip plane. As has been demonstrated earlier, in f.c.c. crystals this rotation is limited. It is clear that a crystal oriented as shown in Fig. 71*a* will have the highest plastic deformation, while that with the orientation as in Fig. 71*c* will be incapable of slip in the basal plane; with an orientation as in Fig. 71*b*, the resolved shear stress is at a maximum and the shear deformation is moderate.

The expression for the resolved shear stress, (66), assumes that the tensile stress applied, σ_{11}, for crystals of different orientation may vary within wide limits for the same deformation, both at the beginning of plastic deformation (stress τ_0) and at any later stage (stress τ). This means that, for limiting values of angles β_1, an appreciable tensile stress must be applied to attain the required resolved shear stress in an unfavourably oriented basal plane. Under such conditions, slip often takes path along other planes: pyramidal or prismatic, or twinning may occur; for that reason, the behaviour of such crystals cannot be related in a simple manner to the behaviour of crystals deformed exclusively by slip in basal planes. In the general case, crystals with the angle β_0 within 10-80 degrees may be expected to exhibit an 'ideal' behaviour.

The problem becomes even more complicated if the rotation of the slip plane and the direction of slip vary in time during plastic deformation, i.e. if the angles α_1 and β_1 are variable. Let us suppose for clarity that there is no strain hardening and that the crystal is deformed all the time at a constant critical shear stress τ_{cr}. Using expressions (67) and (68), we can then write the equation of the stress-strain curve with variable angles α_1 and β_1 in the following form:

$$\sigma_y = \sigma_{11} = \tau_{cr}/(\cos\alpha_1 \cos\beta_1) = \tau_{cr}\lambda^2/\cos\beta_0 \sqrt{\lambda^2 - \sin\alpha_0}$$

where $\lambda = l_1/l_0$.

Assuming, for simplicity, that $\alpha_0 = 90° - \beta_0$, we obtain a series of stress-strain curves for various values of the angle β_0 between the slip plane and tension axis (Fig. 72). These curves reflect the anisotropy of the flow stress in tension and also show that, as the yield limit is attained, deformation often occurs with decreasing stress, the drop in stress being greater at a smaller β_0.

The large drop in stress in the range of β_0 angles from 0 to 30° can be understood easily if we recall that for a crystal with the basal plane oriented initially almost normal to the tension axis, a high tensile stress is required to attain τ_{cr} in the slip plane. When deformation commences, however, the basal plane will rotate to more favourable positions where the resolved shear stress is higher, so the tensile stress needed to continue deformation will be lower. In practice, these stress drops are often hidden by the occurrence of work hardening; however, they are observed in hexagonal crystals of a low melting point (low work hardening at room temperature) when properly oriented. The phenomenon is called '*geometrical softening*' because it arises from the changing geometry of the crystal, and does not reflect structural softening of the metal. By analogy, the hardening effect observed at $\beta_0 > 45°$ and τ_{cr} = constant can be called '*geometrical hardening*'. Like 'geometrical softening', it has no relation to structural work hardening, but results from rotation of the slip plane to a position unfavourable for slip.

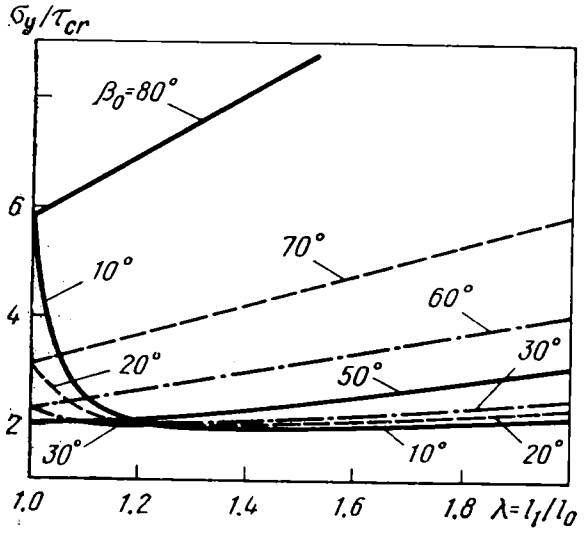

Fig. 72. Theoretical σ_y/τ_{cr}-λ curves at $\lambda_0 = 90° - \beta_0$

Thus, a large difference in the pattern of stress-strain curves for crystals of different orientation can be avoided if these are plotted in the coordinates: resolved shear stress—resolved shear strain. In contrast to the critical resolved shear stress τ_{cr}, however, the values of the resolved shear stress τ at deformation ε will be different for all such crystals. This is caused, first of all, by different strain hardening in them, which depends on the structural changes in the metal. Neglecting, however, the extreme orientations, i.e. very low and very high angles β_0, the behaviour of most crystals of a given metal can be approximated by a single curve in the coordinates: resolved shear stress—shear strain, which can be characterized by the following:

(1) slip deformations are high (in favourable orientations);

(2) the rates of strain hardening (at room and higher temperatures) are low in the greatest portion of the stress-strain curve;

(3) the stress-strain curve exhibits a noticeable dependence on temperature.

Dislocation movement in slip. We have described earlier the sim-

plest cases of movement of screw, edge and mixed dislocations, movement and intersection of extended dislocations, and operation of a Frank-Read dislocation source. Double cross slip has also been considered. The discussion below will deal with movement of dislocations with jogs, double kinks, singular points, etc.

A dislocation line can be regarded either as a line curved smoothly in space or as a combination of a number of straight sections. In the latter case and with an insufficient magnification, it will be seen as a smoothly curved line of a mixed dislocation composed of straight sections of edge and screw dislocations. The points B, C, D and E (Fig. 73) at which the straight sections join with each other are called singular points. If singular points are at small distances from one another [BC, $DE \approx (1\text{-}2)\ b$], it follows from the earlier discussion (see the section on intersection of dislocations) that BC is a jog, since it is at an angle (perpendicular in Fig. 73) to the slip plane, and DE is a kink, since it is in the slip plane.

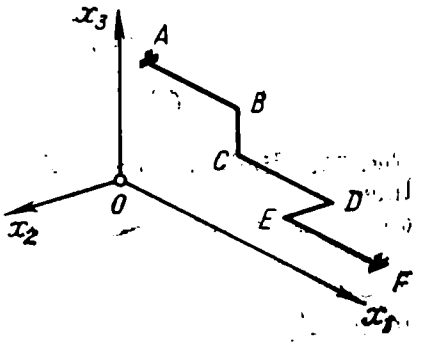

Fig. 73. Singular points B, C, D, E in a broken dislocation line $ABCDEF$

ABC—kink; BC—jog; DE—kink. Portions AB, CD and EF are parallel to bx_1; $BC \parallel Ox_3$; $ED \parallel Ox_3$; the Burgers vector of the whole dislocation, $\mathbf{b} \parallel Ox_2$. The slip plane is parallel to the x_1Ox_2 plane

The movement of a kink (or a jog) along a dislocation (Figs. 74 and 75) per one atomic spacing is an elementary act of dislocation slip. The movement of a dislocation line from the initial state AB to the final state CD at a distance $AC = BD \approx b$ can be effected as a series of successive displacements (drift) of the kink EF. An elementary act of such displacement is the movement of EF to position $E'F'$ with $EE' = FF' = b$ (see Fig. 74). A moving kink, as a linear dislocation moving in the slip plane, has to overcome a certain energy barrier which is usually called Peierls' secondary barrier E_{P_2}. As has been demonstrated by calculations and experi-

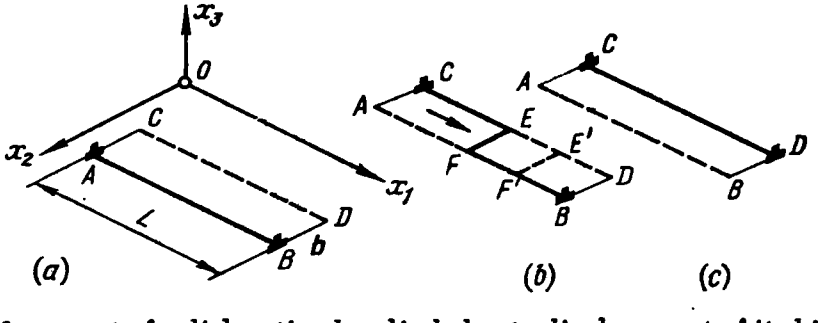

Fig. 74. Movement of a dislocation by climb due to displacement of its kink along the dislocation axis (AB and $CD \parallel Ox_1$, $\mathbf{b} \parallel Ox_2$)

(a) original position; (b) intermediate configuration; (c) final position (arrow indicates the displacement of the kink)

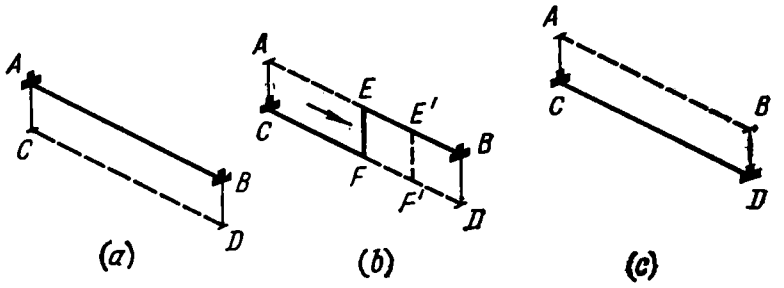

Fig. 75. Climb of a dislocation due to movement of its jog along the dislocation line
(*a*) original position; (*b*) intermediate position; (*c*) final position

mentally, a kink can move much more easily than a whole dislocation which has to overcome a greater Peierls barrier E_{P1}, i.e. $E_{P2} \ll E_{P1}$.

Thus, *slip with participation of climb* occurs not by movement of a dislocation as a whole per one atomic spacing, but by unit displacement of a kink along the dislocation line. For that reason, a dislocation of length L can move as a whole through one atomic distance by n successive jumps ($n \approx L/b$) of a kink. Since the potential barrier for movement of a kink, E_{P2}, is much lower than that for movement of a whole linear dislocation, $E_{P2} \ll E_{P1}$, the stress to initiate its movement is also much lower. Therefore, it can be expected that dislocation movement will be limited by the rate of formation of new kinks on a dislocation.

Climb of an edge dislocation can also be effected as a series of successive displacements of a jog from EF to $E'F'$ with $EE' = FF' \approx b$ (see Fig. 75). The direction of climb in each elementary act, i.e. a unit displacement of the jog by b, is determined by whether it absorbs a vacancy or leaves behind an interstitial atom.

It is known that, as plastic deformation proceeds, the dislocation density increases, as also does their curvature, i.e. there form more jogs and kinks per unit dislocation length. In this process, reactions between individual singular points are possible (for instance, a screw dislocation can slip in more than one plane). If there are two such planes (Fig. 76), kinks can form in each of them and, on collision, can react with each other and form a jog. Movement of a dislocation with a jog is strongly impeded and should be assisted by diffusion processes. Thus, an increase in the concentration of kinks and their reactions with the formation of jogs result in strain hardening.

It should be noted that a smoother transition from one direction of a dislocation line to another is more favourable energetically for a kink, i.e. a rectangular kink $CEFB$ (Fig. 77) is actually an oblique (dashed line) and can be replaced by a kink $CE'F'B'$. The energy of a rectangular kink, E_{rk}, and that of an oblique kink, E_{ok}, can be estimated if we note the following points:

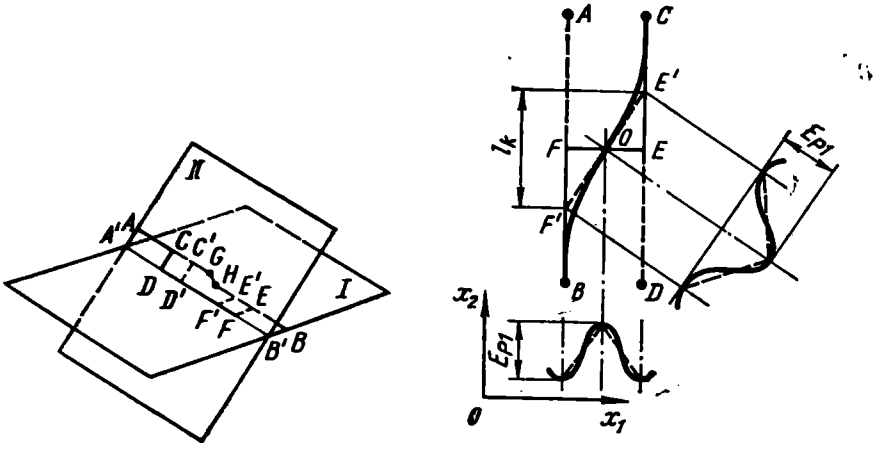

Fig. 76. (*left*) Movement of kinks: CD in plane II and EF in plane I, to meet each other (elementary acts are displacements of CD to $C'D'$ and of EF to $E'F'$) with the formation of jog GH

$A'B'$—original position of the dislocation; $ACDFEB$—intermediate position; $AGHB$—final position of the dislocation, with portion AG in plane II; BH—in plane I and with a jog between planes I and II

Fig. 77. Smooth kink BOC

The slip plane of dislocation coincides with the plane of drawing; $CEFB$—rectangular kink; $CE'F'B$—oblique kink which conditionally replaces the actual smooth kink BOC

(1) the portion EF ($l_{EF} = b$) or $E'F'$ of a dislocation lies in the region of elevated energy proportional to E_{P1}. With a simplifying assumption that the Peierls energy $E_{P1}(x)$ is distributed linearly, we have:

$$\left.\begin{aligned} E'_{rk} &= 0.5E_{P1}l_{EF}/b = 0.5E_{P1} \\ E'_{ok} &= 0.5E_{P1}l_{E'F'}/b \end{aligned}\right\} \qquad (71)$$

(2) a rectangular kink increases the length of a dislocation by $l_{EF} = b$, i.e. increases its energy by

$$\Delta E_{rk} = 0.5Gb^2l_{EF} = 0.5Gb^3 = E_{d1}$$

while an oblique kink increases the dislocation energy by

$$\Delta E_{ok} = 0.5Gb^2\,(l_{E'F'} - l_{EE'} - l_{FF'}) = E_{d1}\,(l_{E'F'} - l_k)/b \qquad (72)$$

where l_k is the length of the kink.

In expression (72), sections EE' and FF' do not belong to the total length of the dislocation $CE'F'B$; they do not contribute to ΔE_{ok}.

Thus, the total energy of an oblique kink is the sum of (71) and (72):

$$E_{ok} = E'_{rk} + \Delta E_{ok} = \frac{E_{d1}}{b}\,(\sqrt{l_k^2 + b^2} - l_k) + \frac{E_{P1}}{2b}\sqrt{l_k^2 + b^2} \qquad (73)$$

The equilibrium width of a kink, l_{eq}, can be found by minimizing E_{ok} (73); $\partial E_{ok}/\partial l_k|_{l=l_{eq}} = 0$:

$$l_{eq} = b\sqrt{2E_{d1}/E_{P1}} \qquad (74)$$

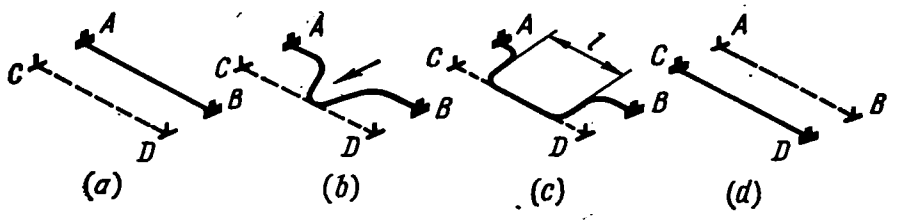

Fig. 78. Schematic of slip caused by movement of a dislocation due to double kinks

(*a*) original position; (*b*) ejection of a double kink into an adjacent position *CD* of minimal energy; (*c*) expansion of double kink; (*d*) final position corresponding to displacement of the dislocation through an atomic spacing

In expression (74), we can neglect values of the order of unity or less, since, as is known (see Ch. 2), $E_{d1} \gg E_{P1}$ for any dislocation, and therefore, $\sqrt{E_{d1}/E_{P1}} \gg 1$. Substituting (74) into (73), we obtain the minimal energy of a kink:

$$E_{ok.\,min} = \sqrt{0.5E_{P1}E_{d1}} = E_{P1}\sqrt{E_{P1}/E_{d1}} = E_{P1}b/l_{eq} \qquad (75)$$

Thus, with $E_{d1} \gg E_{P1}$, we have that $l_{eq} \gg b$ and $E_{rk} = E'_{rk} + \Delta E_{rk} = 0.5E_{P1} + E_{d1} \approx E_{d1} \gg E_{ok.min}$, i.e. the real kink is actually oblique.

Dislocation movement by means of double kinks can be regarded as the transition of a dislocation into a potential pit *CD* of Peierls' relief in two stages (Fig. 78). The first stage is the nucleation of a double kink on a straight dislocation and the second is its propagation in two directions. Intermediate states (Fig. 78*b* and *c*) possess an excess energy ΔE, since, firstly, the length of the dislocation increases and, secondly, a portion of the dislocation, namely, a kink, lies in the region of an elevated potential energy of the Peierls barrier. For that reason:

$$\Delta E = 2E_{ok.min} - \tau b^2 l - \alpha D b^4/l \qquad (76)$$

where $E_{ok.min}$ is the equilibrium minimal energy of kink (75); $\tau b^2 l$ is the work of the force $f = \tau b$ due to an external stress τ for movement of a dislocation of length l through distance b when an area bl is involved in slip; and $\alpha D b^4/l$ is a term which describes the interaction of kinks with the distance l between them ($\alpha \approx 1$ is a constant).

The distance $l = l_0$ between the kinks which corresponds to the maximum value of ΔE (76) can be found from the condition

$$\left.\frac{\partial \Delta E}{\partial l}\right|_{l=l_0} = 0$$

whence

$$l_0 = b\sqrt{\alpha D/\tau} \approx b\sqrt{D/\tau} \gg b \qquad (77)$$

Since $\left.\frac{\partial^2 \Delta E}{\partial l^2}\right|_{l=l_0} < 0$, the length l_0 corresponds to the maximal energy of a double kink (76). Substituting (77) into (76), we can estim-

ate ΔE_{max}:

$$\Delta E_{max} = 2E_{ok.\,min} - 2b^3\sqrt{\alpha D\tau}$$

With $l < l_0$, the energy of a double kink decreases due to the interaction of the kinks; with $l > l_0$, it decreases owing to the work of an external force. Since $\tau \ll D$ and $E_{ok.min} = E_{P1}b/l_{eq}$, we find that $E_{ok.min} \gg 2b^3\sqrt{\alpha D\tau}$ and it can be taken, as a first approximation, that

$$\Delta E_{max} \approx 2E_{ok.min} \tag{78}$$

i.e. an intermediate configuration (of the type shown in Fig. 78*b* and *c*) possesses a certain excess energy whose maximal value is roughly twice the energy of a single kink. Since the work of the external force has been considered in the derivation of formulae (76)-(78), the sole energy source for initiation of a double kink is the fluctuation of the energy of thermal motion of atoms. With a constant stress applied to each dislocation section of length l (l is the length of a double kink) and the frequency of thermal oscillations $\nu \approx 10^{12}$ s^{-1}, the frequency of formation of double kinks is $P_{dk} = \nu \exp(-\Delta E/kT)$ or, noting (78):

$$P_{dk} = \nu \exp(-2E_{ok.\,min}/kT) = \nu \exp(-\sqrt{2E_{P1}E_{d1}}/kT) \tag{79}$$

Analysis of expression (79) suggests the following conclusions.

1. As has been shown by calculations and experimentally, the energy $E_{ok.min} \approx 0.08$-2 eV, i.e. is quite low, in particular, lower than the Peierls energy E_{P1}. For that reason, the formation and movement of double kinks requires thermal activation and the stress σ to move double kinks depends on temperature and is lower than the Peierls-Nabarro stress σ_P:

$$\sigma = \sigma_P\left(1 - \frac{T}{AT_0}\right)^2 \text{ at } T \ll T_0 \tag{80}$$

$$\sigma = \sigma_P \exp\left(\frac{T_0}{T} - \frac{1}{A}\right) \text{ at } T \approx T_0 \tag{81}$$

where $kT_0 = 2b^2\sqrt{E_0\sigma_P}$, $E_0 = 0.5Gb^2$ is the minimal energy for initiation of a double kink at a stress equal to zero, and A is a monotonous function of σ, T and $\dot{\varepsilon}$, i.e. the stress σ to ensure a given deformation rate $\dot{\varepsilon}$ at given temperature T must not vary noticeably with variations of $\dot{\varepsilon}$.

The temperature dependence for stress, $\sigma(T)$, is parabolic up to $T_c = AT_0$ in accordance with (81) and becomes exponential at $T_c > AT_0$ (Fig. 79).

2. In metals with a low Peierls barrier, double kinks form at rather low temperatures. For instance, in Al [$2E_{ok.min} \approx 0.1$ eV, $T_c \approx 100$ K, and $\sigma < 7.5$ MPa ($kT = 1/120$ eV)], the probability

(frequency) of formation of double kinks is:

$$P_{dk} = 10^{12} \exp\left(-\frac{0.1}{1/120}\right) \approx 10^7 \text{ s}^{-1}$$

which ensures the velocity of dislocation movement

$$v_d = bP_{dk} \approx 3 \times 10^{-8} \times 10^7 \approx 0.3 \text{ cm/s}$$

With a high stress applied, a dislocation can move as a whole without the aid of double kinks. On the contrary, in crystals with high Peierls barriers, temperature variations can influence substantially the rate of deformation.

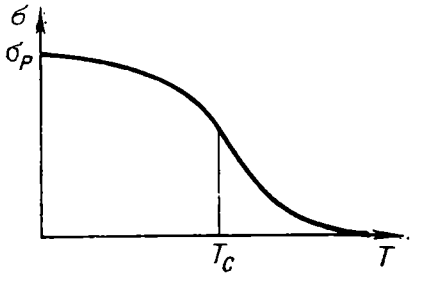

Fig. 79. Effect of temperature $T_c = AT_0$ on stress at constant deformation rate

3. Suppose that the rate of plastic deformation $\dot{\varepsilon}$ and the density of mobile dislocations ρ_m are constant. It then follows from the formula $\dot{\varepsilon} = \rho_m b v_d$ (see Ch. 2) that the dislocation velocity $v_d = v_0$ is constant too. If the temperature is reduced, the stress σ applied to the body must be increased in order to maintain the constant velocity (see Fig. 79). At low temperatures, $P_{dk} b < v_0$, so that the intensity of thermal motion is insufficient for maintaining the desired frequency of formation of double kinks and the constant dislocation velocity v_0. At temperatures $T < T_c = AT_0$, the stress σ is close to the Peierls stress σ_P.

At $T > T_c$, the frequency of formation of double kinks increases, so that even a negligible stress is sufficient to maintain a constant dislocation velocity v_0; these stresses vary according to (81) and the effect of Peierls barriers becomes insignificant.

Thus, plastic flow by slip in close-packed planes along closest-packed directions occurs by the mechanism in which dislocations overcome Peierls barriers, the process being assisted by thermal fluctuations when $\sigma < \sigma_P$. The thermofluctuational mechanism is most effective at $T > T_c$ where the influence of the Peierls barrier on the commencement of plastic flow becomes inessential.

2. Deformation by Twinning

Deformation twinning is one of the mechanisms of shear deformation. Deformation twinning can be characterized by high rates and the evolution of energy in the form of sound (typical cracking of deformed crystal). Twinning is accompanied by a jumpwise variation of the deforming stress, with corresponding tooth-shaped or saw-shaped twinning portions appearing on the stress-strain curves (Fig. 80). Metallographic examination of twinned specimens reveals

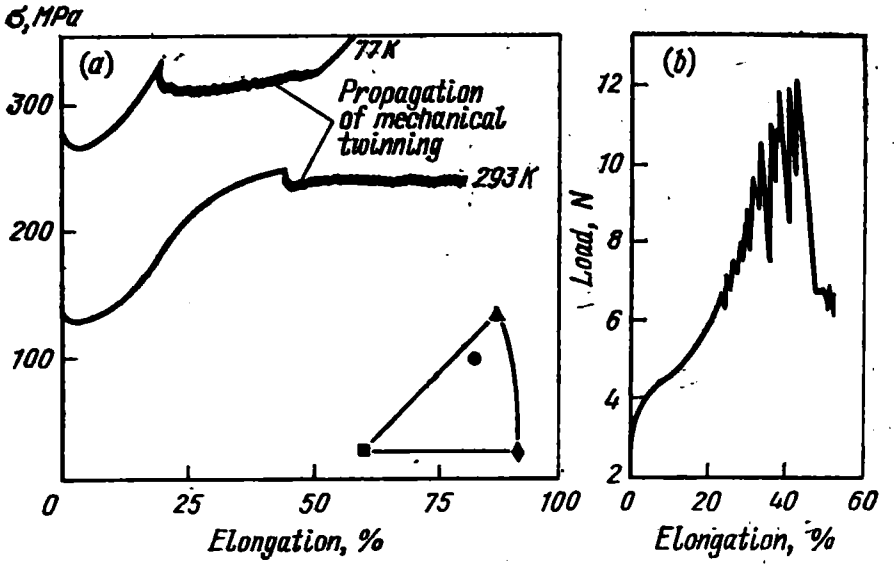

Fig. 80. Stress-strain curves for (*a*) crystals of Cu + 10 at.% In alloy and (*b*) cadmium crystals

regions which are etched differently from the surrounding matrix metal. These regions are characterized by linearity and strict crystallographic orientation of two parallel boundaries. As has been established by X-ray diffraction and like methods, these regions differ regularly in their orientation and arrangement of atoms in the matrix. The atomic arrangement in such a region is a mirror image of that in the matrix crystal (see Figs. 81 and 82). The mirror-image planes whose intersection with the plane of the microsection has the form of rectilinear boundaries are called *twinning planes*. In Fig. 82*a* and *b*, for instance, the twinning plane is (112). The reoriented regions are called *twins* and are formed by the process called *twinning*. Twins in crystals are classified as *annealing twins* (formed during growth of crystals from the melt or in recrystallization and annealing) and *deformation twins*.

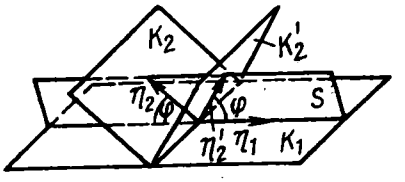

Fig. 81. Diagram to explain elements of twinning
S—shear plane; K_1—twinning plane; η_1—shear direction

Crystallography of twinning. Unlike random boundaries, twinning planes are *coherent* boundaries, since atoms in them occupy the sites which are common to the twinned region and the matrix crystal (see Fig. 82*a*). X-ray or other radiation scattered by atoms of the two crystal portions is regularly phase-shifted, i.e. coherent.

The end boundaries of a twin, which terminate within a grain or at its boundaries, are incoherent.

The process of twinning is a cooperative movement of atoms in which individual atoms move only a fraction of the atomic spacing

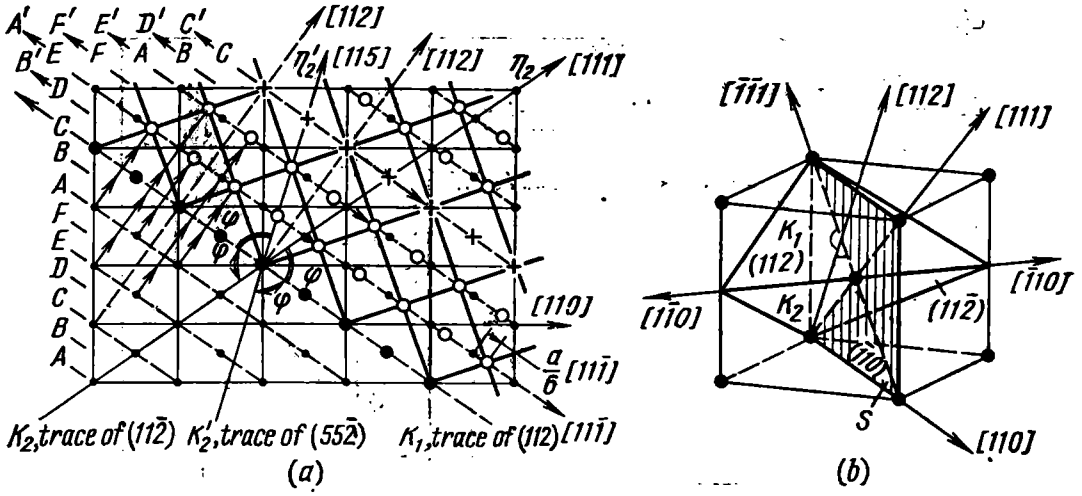

Fig. 82. Geometry of twinning

(*a*) diagram of atom rearrangement in twinning in α-iron; (*b*) positions of twinning elements in a unit cell. Designations in Fig. 82*a*: ● —position of atoms before twinning; ○—twinned positions of atoms; + —atoms in coincident positions. Thin lines indicate atomic layers lying in the same [112] direction in one plane, i.e., according to Fig. 39, designated by the same symbols: *A*, *B*, *C*, etc. before twinning and *A'*, *B'*, *C'*, etc., after twinning

relative to each other, but the total result is macroscopic shear which can often be visible to the naked eye. In contrast to slip, in which atoms are displaced through one or more atomic spacings, twinning is the result of smaller displacements which occur successively in adjacent planes. These displacements (Fig. 81) take place in a *shear plane S in a particular slip direction* η_1. In the b.c.c. lattice illustrated in Fig. 82*a*, $[11\bar{1}]$ is the slip direction and $(\bar{1}10)$, the shear plane. Twinning can be characterized completely by the following twinning elements (see Fig. 81).

1. The twinning plane K_1 and the shear direction (slip direction) η_1 whose vector lies in the plane K_1. In Fig. 82*a*, plane (112) corresponds to K_1 and $[11\bar{1}]$ direction, to η_1. Atoms lying in the plane K_1 are not displaced and the plane is called accordingly the first undistorted plane.

2. The planes K_2 (before deformation) and K_2' (after deformation), which intersect K_1 along a line perpendicular to the shear direction η_1 (see Fig. 81) and make equal angles with the plane K_1 before and after shear in the shear plane S, also undergo no distortion in twinning. In a b.c.c. lattice, for instance (see Fig. 82*a*), plane $(\bar{1}10)$ corresponds to the shear plane S, plane $(11\bar{2})$ to K_2, and plane $(55\bar{2})$ to K_2', the line $[1\bar{1}0]$ being the line of intersection of the planes K_1 and K_2.

3. The directions η_2 and η_2' oriented along the lines of intersection of the shear plane S with the planes K_2 and K_2', respectively, are important characteristics in the geometry of twinning. In the example illustrated in Fig. 82*a*, the vector η_2 coincides with the [111] direction and η_2', with [115].

4. The amount of shear s and the shear strain in the shear plane S are important criteria of the twinning transformation. In this transformation, the orientation of a twin band changes, but the symmetry and structure of the crystal do not. For that reason, the angle φ between the first, K_1, and second, K_2, undistorted planes is the same both before and after the transformation and the amount of shear s is proportional to the distance from the mirror-image plane. In particular, for a b.c.c. crystal (see Fig. 82*a*), $s = (na\sqrt{3})/6$, where $n = 0, 1, 3 \ldots$ is the number of the (112) plane considered as counted from the mirror-image plane ($n = 0$). (In Fig. 82*a*, only the atoms of every second such plane are shown, i.e. the atomic layers *A*, *C*, *E*, *A*, etc., while the atomic layers *B*, *D*, *F*, *B*, which do not lie in the plane of the drawing (see also Fig. 39), are not indicated.)

Since the distance from an nth parallel plane to the mirror-image plane ($n = 0$) is $d = nd_{(112)} = (na\sqrt{6})/6$, the shear deformation in a twin band $\gamma = s/d = 2 \tan (90° - \varphi) = 2 \operatorname{cotan} \varphi = \sqrt{3}/\sqrt{6} = 1/\sqrt{2} = 0.707$, i.e. is constant and determined by the structure of the crystal. Therefore, if the two undistorted planes have been determined, the shear deformation can be found by measuring the angle φ between these planes. Some typical crystallographic characteristics of twinning are given in Table 8.

Table 8. Some Crystallographic Characteristics of Twinning (after R. Honeycombe, J. Hirth)

Crystal structure (metal)	Twinning indices				Shear γ
	K_1	η_1	K_2	η_2	
F.c.c. (Cu)	(111)	$[11\bar{2}]$	$(11\bar{1})$	[112]	0.707
B.c.c. (Cr, Na, α-Fe)	(112)	$[1\bar{1}1]$	$(1\bar{1}2)$	[111]	0.707
C.p.h. (Mg, $c/a = 1.624$; Zn, $c/a = 1.856$; Cd, $c/a = 1.866$)	$(10\bar{1}2)$	$[10\bar{1}\bar{1}]$	$(10\bar{1}1)$	$[10\bar{1}1]$	$a(3 - c^2/a^2)/c\sqrt{3}$

Geometry of twinning in b.c.c., f.c.c. and c.p.h. metals. If α-iron is subjected to impact loading during high-rate plastic deformation which can be effected, for instance, by explosion, there form very thin crystallographically regular oriented platelets; these are twins. They can also form in deformation of many other b.c.c. metals, such as molybdenum, tungsten, chromium, niobium or tantalum. Twins are usually long and thin and only seldom attain a thickness of 5×10^{-4} cm, since twinning is associated with a heavy plastic deformation ($\gamma = 0.707$), see Table 8. Planes {112} are the twinning planes (in Fig. 82*a*, they are perpendicular to the plane of the draw-

ing). Planes {112} are packed in a sequence

$$ABCDEFABC... \tag{82}$$

If a layer A in this structure is let to displace by $a/6\,[\bar{1}\bar{1}1]$ relative to the previous layer F, there will form a stacking fault $ABCDEFEFABC\ldots$ (see Ch. 2, Fig. 39) for which the plane F is the mirror image of planes E, i.e. the stacking fault is a twin band of a thickness $a/3\,[112]$, i.e. a thickness equal to the distance between (112) planes.

To obtain a twinned crystal, the operation of shear of the layer A relative to the layer F must be performed layerwise for each (112) plane following A, so as to obtain the configuration (82) every time by the scheme:

$$\begin{array}{l} ABCDEFABCDE \\ \quad\downarrow\downarrow\downarrow\downarrow\downarrow \\ \quad EFABC \\ \quad\downarrow\downarrow\downarrow\downarrow \\ \quad DEFA \\ \quad\downarrow\downarrow\downarrow \\ \quad CDE \\ \quad\downarrow\downarrow \\ \quad BC \rightarrow A \end{array} \tag{83}$$

Thus, we obtain a stacking sequence $ABCDEFEDCBA$. This transformation produces a shear 0.707, whose value has been found experimentally and confirmed by calculations (see Table 8). This transformation has been properly fixed in Fig. 82*a* by the sequence of layers $CDEFABCB'A'F'E'D'C'$, where the primed symbols relate to the twin band. The described variation in orientation can also be obtained by a large shear of layer C' relative to the middle layer C in the opposite direction, i.e. by a distance $a\,[111] = -a\,[\bar{1}\bar{1}1]$ (see Fig. 82*a*). This however is energetically unfavourable for the formation of a twin band of thickness $a\sqrt{6}$ equal to the distance $a\,[112]$ between two planes with identical indices before deformation.

The formation of twins can be explained by using the pole mechanism of twinning. The tendency to twinning in b.c.c. metals increases with increasing deformation rate and decreasing temperature. For instance, pure iron subjected to tension at 4 K deforms by twinning. Twins are not usually found in pure iron deformed by tension at room temperature, but impact deformation at room temperature can cause twinning. Impurities may have a substantial effect on twinning: additions of silicon produce more active twinning in iron; on the other hand, interstitial impurities (oxygen, nitrogen, carbon) in niobium in concentrations each of the order of 2×10^{-4}-2×10^{-3} can fully suppress twinning in slow deformation. Alloys of the types

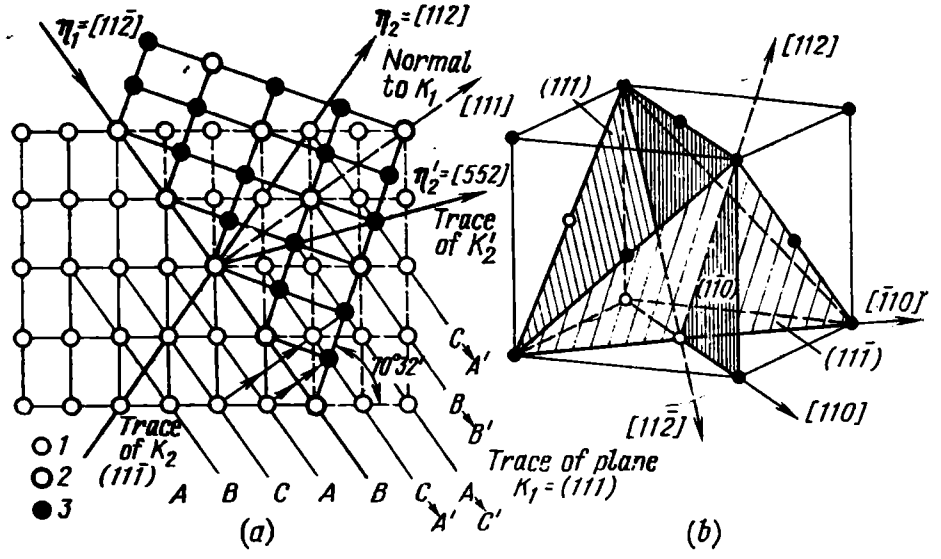

Fig. 83. Geometry of twinning in f.c.c. lattice (*1*—position of atoms before twinning; *2*—atoms in coincident positions; *3*—twinned positions of atoms)

(*a*) view in the plane (1$\bar{1}$0) with *A'*, *B'*, *C'* being planes belonging to twins; (*b*) elements of twinning in unit cell

Mo-Re, W-Re, Nb-V, which are essentially solid solutions, are twinned easily at room temperature and slow rates of deformation.

The energy of a coherent twin boundary is $E_{tw} = 0.5E_{sf}$, so that the tendency to twinning increases with decreasing stacking fault energy. For instance, deformation twins are not found in f.c.c. aluminium crystals, but have been observed in copper crystals deformed at 4 K and in silver, gold and nickel deformed at high stresses. For copper, the shear stress is 150 MPa, against 3 MPa for nickel. Such stresses can be attained at low temperatures or high deformation rates.

Twinning in f.c.c. metals results in serrations appearing on the stress-strain curve (see Fig. 80). The crystallographic characteristics and geometry of twinning are represented in Table 8 and Fig. 83. The twinning planes are {111} planes, i.e. those most closely packed. Shear takes place along ⟨112⟩ directions in {111} planes. The crystallographic characteristics shown in Fig. 83 correspond to those given in Table 8. In twinning, a regular stacking sequence *ABCABCABC* . . . changes to *ABCABA'C'B'A'*. The layer *B* is the boundary (plane) of a twin. On passage through that plane, the crystal has an opposite stacking sequence relative to that in the untwinned region.

Solid-solution alloys of f.c.c. metals (for instance, Ag + Au, Cu + Zn, Cu + Al, Cu + In, etc.) are more liable to twinning than the pure metals. Alloys are observed to have a lower resolved shear stress for twinning. For copper-base alloys, these stresses do

not exceed 0.4-1.2 MPa. As a rule, the shear stress in twinning decreases with decreasing stacking fault energy (Fig. 84). The stacking fault energy of the solvent metal can be lowered substantially by the presence of atoms of a solute metal, which is associated with a change in the number of valency electrons per atom. Multivalent metals reduce the stacking fault energy more effectively than univalent ones (such as nickel). Since twinning in f.c.c. metals is essentially a change in the sequence of close-packed {111} planes in which stacking faults appear on extension of dislocations, it is natural to suppose that in f.c.c. metals there is a correlation between the stacking fault energy and the stress for twinning; this has been verified experimentally (see Fig. 84).

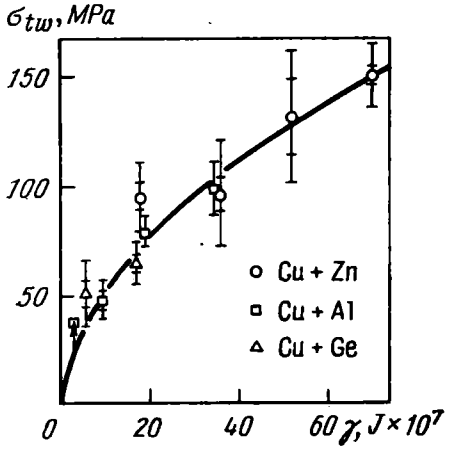

Fig. 84. Correlation between twinning stress and stacking fault energy in Cu-base alloys

In c.p.h. metals, twinning is the most common mechanism of plastic deformation, since the possibilities for slip are limited (slip in c.p.h. metals occurs, as a rule, in basal planes only). If a crystal is oriented unfavourably for basal slip (the axis of tension is at an angle of 5-10° to the basal plane), twinning can occur at an appropriately high stress. For pure cadmium, the shear stress for twinning is 1.0-7.0 MPa, whereas basal slip can occur at a stress of only 0.2-0.3 MPa. Zinc crystals with the basal plane parallel to the direction of tension are twinned at a shear stress of 25.0-50.0 MPa, after slip in pyramidal $\{11\bar{2}2\}$ planes (Fig. 85*a*).

Observations show that nucleation of twins is associated with the presence of stress concentrators. Poorly finished crystals (with scratches and other machining defects) can twin at appreciably lower stresses than those well finished. Twinning is facilitated by preliminary slip, which is a source of stress concentrators. As a single twin has been formed, a multitude of other twins appear explosively, the twinning stress drops down, and serrations appear on the stress-strain curve.

The type of deformation (whether tension or compression) may have a strong effect on the formation of twins in c.p.h. metals. For instance, a zinc crystal ($c/a = 1.856$), with the basal plane oriented parallel to the axis of the specimen, can be twinned in tension, since the plane K_2 $(\bar{1}012)$ (Fig. 85*a*) moves in deformation to position $\overline{K}_2'$ by rotation clockwise relative to the twinning plane $(10\bar{1}2)$. Having imagined the left-hand portion of the crystal (Fig. 85*b*) to be clamped

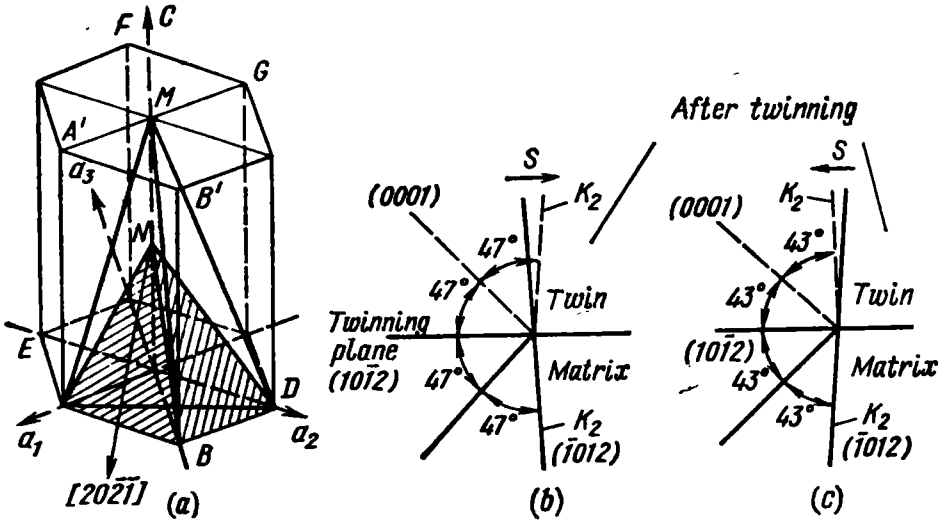

Fig. 85. Crystallographic characteristics of twinning in an elementary c.p.h. lattice for twinning plane ANB $(10\bar{1}2)$ and probable pyramidal twinning planes (*a*) AMB $(10\bar{1}1)$, AMD $(11\bar{2}1)$, AND $(11\bar{2}2)$; (*b*) twinning geometry in zinc; (*c*) in magnesium. $A'B'BA$—$(10\bar{1}0)$—prismatic plane. AM—$[\bar{1}\bar{1}23]$; BD—$[1\bar{1}20]$; BB'—[0001]; G—$[0\bar{1}10]$; $AEFM$—prismatic $(10\bar{1}1)$ plane

in the fixed grip of the testing machine, we can verify that shear s is only possible in tension. In compression, a zinc crystal will be deformed by kinking. On the other hand, a Mg crystal ($c/a = 1.624$) has a smaller angle between the basal plane and twinning plane (43° against 47° for Zn). Considering in a similar way, i.e. placing the left-hand portion of the single crystal with its basal plane parallel to the operative force, we can prove by Le Chatelier's principle that twinning is only possible in compression when the vector s of transition from plane K_2 to K_2' is directed counterclockwise relative to the fixed grip. Thus, the formation of twins should be expected to occur in compression for magnesium and in tension for zinc. In metals with a still lower axial ratio than that of magnesium (such as titanium or zirconium), twinning is more complicated and is observed not only in $\{10\bar{1}2\}$ planes, but also in $\{11\bar{2}2\}$ and other pyramidal planes (see Fig. 85*a*).

The dislocation mechanism of twinning. Twinning usually requires a higher shear stress to initiate it than does slip, though these stresses are still well below the theoretical strength of a crystal. Consequently, a mechanism involving the simultaneous movement of all atoms in the twin is unrealistic, and preference should be given to dislocation mechanisms of twinning. To produce homogeneous shear typical of twinning, it is essential that twinning dislocations, which can form stacking faults in b.c.c. (f.c.c. or c.p.h.) crystals, were present in each plane without exception and operated successively [see reaction (83)]; this seems to be improbable. The process can also be realized by regular movement of a dislocation through each

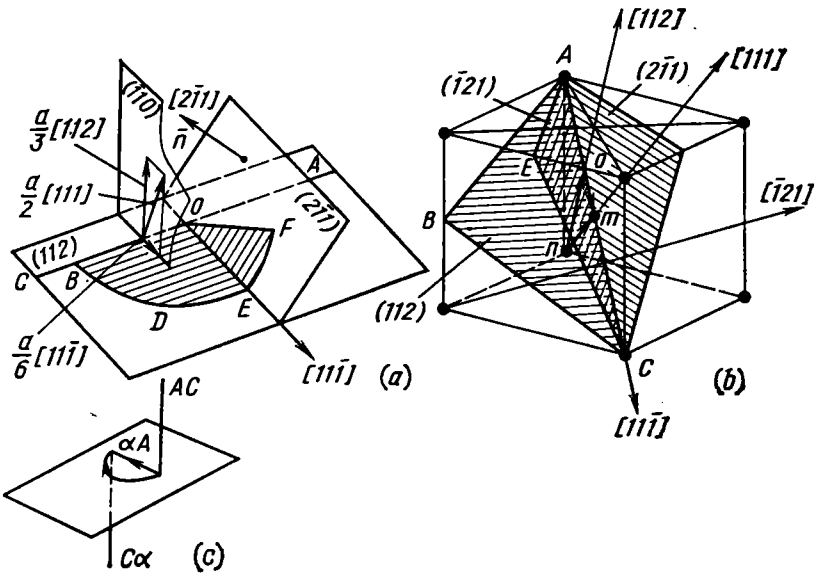

Fig. 86. Dislocation model of pole mechanism
(*a*) formation of twins in b. c. c. lattice; (*b*) dislocation reaction and possible twinning planes for $a/2$ [111] and $a/2$ $[\bar{1}\bar{1}\bar{1}]$ dislocation; (*c*) model of pole mechanism of twinning in f.c.c. lattice

plane of a family of parallel planes. A number of dislocation mechanisms of twinning have been proposed and some of them will be discussed below.

The *Cottrell-Bilby pole mechanism* assumes that the twinning (112) plane of a b.c.c. lattice contains a dislocation *AOBC* with the Burgers vector $0.5a$ [111] (Fig. 86*a*). Under the action of an external stress, the dislocation *AOBC* can dissociate in point *O* into *OBC* and *BDE* (see Fig. 86) by the reaction:

$$(a/2)\,[111] = (a/3)\,[112] + (a/6)\,[11\bar{1}] \qquad (84)$$

As a first approximation, the change of elastic energy in reaction (84) is zero; the reaction is possible only at appreciable stresses. The dislocation *OBC* is a Frank sessile dislocation whose Burgers vector $(a/3)$ [112] is directed along the normal to the slip plane (112) (see Fig. 86*a*). This partial dislocation cannot glide in plane (112). The other partial dislocation, $(a/6)$ $[11\bar{1}]$, glides in the (112) plane and forms a stacking fault *OBDE*. The dislocation section *OE* is parallel to the Burgers vector $(a/6)$ $[11\bar{1}]$, i.e. is a screw dislocation which can move by cross slip onto any of the planes (112), $(\bar{1}21)$ or $(2\bar{1}1)$ containing the $[11\bar{1}]$ direction (Fig. 86*b*). Suppose that it moves onto plane $(2\bar{1}1)$ (see Fig. 86*a*); it then forms again a stacking fault region *OFE* and the section *OF* rotates around point *O* of the sessile $(a/3)$ [112] dislocation and forms a faulted layer or a two-dimensional twin. The sessile dislocation *OB* with the Burgers vector $(a/3)$ [112] contains a screw component perpendicular to plane $(2\bar{1}1)$.

The projection of this vector on the $[2\bar{1}1]$ direction, i.e. on the normal to $(\bar{2}11)$, is equal to the distance $(a/6)$ $[\bar{1}21]$ between the close-packed (112) planes*. Thus, the dislocation OF, on having made a complete revolution, will move forward in the direction OB; during a second revolution, it will add another layer to the two-dimensional twin. This mechanism allows the possibility of formation of twins of an appreciable thickness. The dislocation reaction described has not been confirmed experimentally for b.c.c. metals, except for niobium, so that the proposed pole mechanism can only be regarded as a probable among other mechanisms.

It is essential to note the following. Though reaction (84) is realized at appreciable stresses, such high stresses are not needed for the formation of stacking faults $OBDE$ and EFO and for rotation of the dislocation OF around O and its subsequent movement along OB. It can be taken therefore that the pole mechanism explains satisfactorily why the stress to move a twin is lower than that needed for its nucleation.

The pole mechanism for f.c.c. metals can be represented by using the possibility of a perfect dislocation AC to dissociate into a Frank partial sessile dislocation $A\alpha$ and a twinning dislocation αC (see Thompson's opened-up tetrahedron) by the reaction:

$$\frac{a}{2}[00\bar{1}] \rightarrow \frac{a}{3}[\bar{1}\bar{1}1] + \frac{a}{6}[2\bar{1}\bar{1}] \qquad (85)$$

The dislocation αC (Fig. 86*c*) rotates around the point at the end of dislocation AC. Having made a revolution, it meets $A\alpha$ and forms a twin layer. The recombined dislocation $A\alpha + \alpha C = AC$ then glides on a next plane, dissociates by reaction (85), widens the stacking fault, and recombines after a second revolution. Thus, layers are grown successively one onto the other and form a twin band. A similar pole mechanism of twinning can be imagined for c.p.h. metals.

The minimal stress to initiate twinning by the pole mechanism must be such as to compensate for the stacking fault energy in the initial period of operation of the source, i.e.

$$\sigma = E_{sf}/b \qquad (86)$$

For iron, whose stacking fault energy is $E_{sf} \approx 2 \times 10^{-2}$ mJ/cm^2, equation (86) gives: $\sigma \approx 0.02G$. The real stresses at which twinning occurs are usually of an order of $10^{-3}G$, i.e. additional stress concentration is needed for nucleation of twins.

* Vectors $\overline{V} = [112]$ and $\overline{W} = [2\bar{1}1]$ are equal in magnitude: $|V| = |W| = \sqrt{6}$, so that the projection of the unit vector $\hat{v} = \overline{V}/|V| = 1 \cdot i + 1 \cdot j + 2 \cdot k$ on the unit vector $\hat{w} = \overline{W}/|W| = 2 \cdot i - 1 \cdot j + 1 \cdot k$ is equal to $\hat{v}\hat{w} = v_i w_i = (2 - 1 + 2)/6 = 1/2$, i.e. the projection of the unit vector [112] on the unit vector $[2\bar{1}1]$ is 1/2 and that of vector $a/3$ [112] is $a/6$ $[\bar{1}12]$.

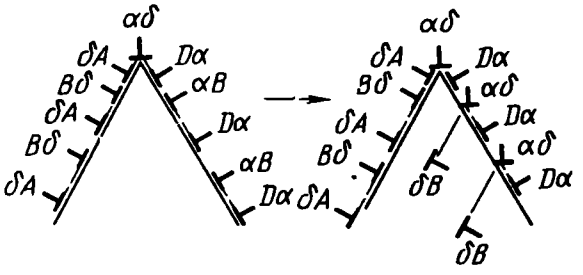

Fig. 87. Twinning dislocations δB formed by slip of dislocations behind a Lomer-Cottrell lock in an f.c.c. crystal

Another mechanism of twinning is associated with movement of a *single partial dislocation.* A partial dislocation can break off from an extended configuration if the stress applied is $\sigma > E_{sf}/b$. Such dislocations may come from the following sources:

(1) barriers produced by partial dislocations (for instance, Lomer-Cottrell barriers);

(2) centres of locking of extended dislocations by Suzuki atmospheres; and

(3) two partial dislocations extended by the stress applied.

Having broken off, a partial dislocation can twist around any 'forest' dislocation containing a screw component of the Burgers vector, i.e. perpendicular to the slip plane of the twinning dislocation. On meeting a screw dislocation, one branch of the partial dislocation moves in the upper plane and the other, in the lower, thus forming a helix around the screw dislocation. The partial dislocation moves successively through each parallel plane and forms a twin.

Another probable mechanism of twinning may be by *cross slip near obstacles.* It is assumed that twinning in f.c.c. structures can be initiated as dislocation pile-up behind a Lomer-Cottrell barrier (Fig. 87). Partial dislocations δB in a pile-up dissociate into $\delta\alpha$ and αB in the twinning plane and form twinning dislocations. This mechanism might be operative at any pile-up behind an obstacle, but elastic interaction limits the emission of twinning dislocations in twinning planes, so that additional mechanisms (say, pole mechanism) are needed.

A probable explanation to the mechanism of twinning may be the concept of *'emitted' gliding dislocations.* These are essentially perfect dislocations emitted from an incoherent peak of the twinning front. The twinning front formed by partial dislocations gliding successively in each plane (see Fig. 88*a*) can be regarded as a twin boundary composed of partial dislocations. Such configuration possesses a long-range stress field. The energy of a twin boundary can reduce on a change to a configuration of the type shown in Fig. 88*b* where every third partial dislocation has reacted and produced an

emitted dislocation and a partial dislocation of an opposite sign:

$$\frac{1}{6}[11\bar{1}] \rightarrow \frac{1}{3}[\bar{1}\bar{1}1] + \frac{1}{2}[11\bar{1}] \qquad (87)$$

Reaction (87) is energetically unfavourable and is only possible with stress concentration on the incoherent twin front, which actually is the case. Reaction (87) gives a set of dislocations emitted from incoherent twin boundaries with the zero long-range stress field. Thus, the length of a twin band increases due to emission of dislocations from an incoherent boundary. The shear deformation produced by the emitted dislocations is equivalent to the deformation due to the original twin boundary from which they have been emitted. The existence of emitted dislocations in b.c.c. and c.p.h. metals has been confirmed experimentally; in particular, transmission electron microscopy has revealed travel of subboundaries in front of twins.

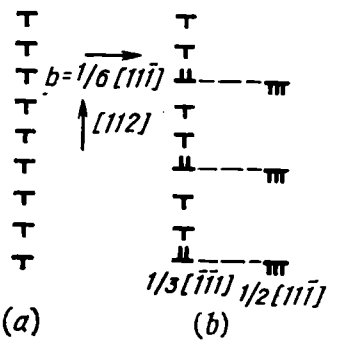

Fig. 88. Schematic of reaction of a twin boundary composed of edge dislocations (*a*), with the formation of an incoherent twin boundary without long-range stress field (*b*)

Interaction of twins with other defects. The role of twinning in plastic flow. Twinning causes appreciable local deformations in a twin proper (see Table 8), in the surrounding matrix, and especially near obstacles met by the twin. These deformations can strongly influence the nature of strain hardening and fracture of metals.

Obstacles appearing on the path of a twin can lock the movement of twinning dislocations and cause them to pile up, i.e. the Stroh model of dislocation pile-up on obstacles is also true for the interaction of twins with obstacles. There is a difference, however, which consists in that the stress concentration on an obstacle turns out to be lower than in the case of locking of a slip band. This is supported by direct observations such as in Fig. 89*a* where a fan of slip bands propagates from the head of a locked twin into the depth of grain or in Fig. 89*b* showing a complex-deformed region (strain torch). It has also been observed that the intersection of two twins (Fig. 89*c*) can cause local displacement of one or both twins, with subsequent fracture in the twin proper or at its joints with obstacles. The amount of this displacement may sometimes exceed the width of intersecting twins. If both twins are displaced, high local deformations may appear in the joint and the dislocation density in the twins proper increases substantially, thus increasing sharply the resistance to deformation and tendency to fracture. The magnitude of local deformations in a twin-to-twin joint may be different and depends on (1) the conditions of twinning; (2) the nature of twin

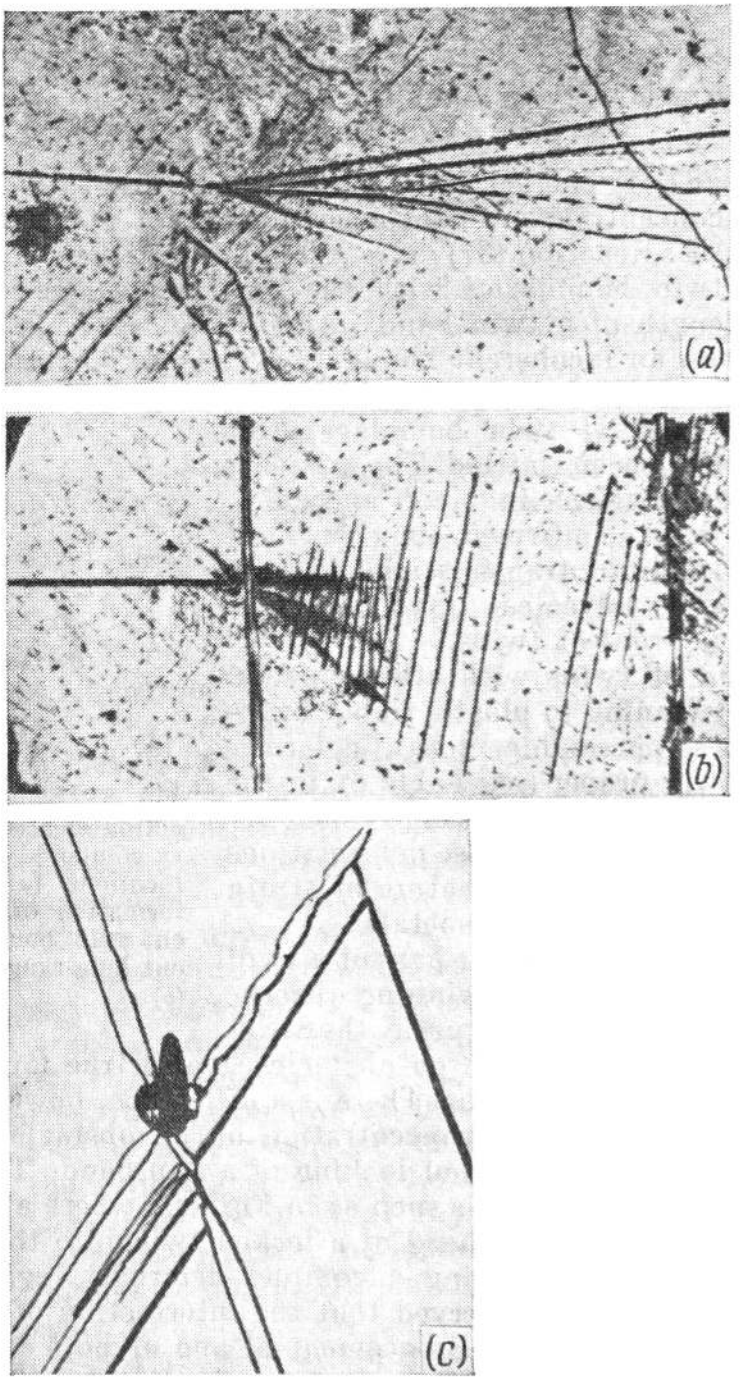

Fig. 89. Fan-like slip bands produced by locking of a twin, 300 × (*a*); deformation torch formed on locking of a twin by a twin-type barrier, 200 × (*b*); and local shear and fracture produced by intersection of two twins, 350 × (*c*)

boundaries and twin bands; and (3) the angle at which the twins meet.

Twin boundaries can act as barriers for gliding dislocations. Besides, if gliding dislocations intersect twin boundaries, they can form twinning dislocations and form a new twin. The last mechanism of the formation of new twins is most probable in crystals of a high symmetry.

According to J. P. Hirth, the intersection of a twin with a gliding dislocation can be the cause of the growth (or constriction) of that twin. Since the resulting dislocation dissociation reactions are energetically unfavourable, a twin can grow only at a higher external stress applied than that needed for slip. Gliding dislocations, which interact with a twin, can widen or contract its boundaries or can bow out and pass through the twin, leaving kinks and jogs in it. In cases when the dislocation reactions associated with these phenomena do not take place, the twin boundary must act as a barrier, resulting in a pile-up of gliding dislocations, strong strain hardening, and subsequent fracture.

Twinning can contribute substantially to the total plastic deformation of a metal. The maximal contribution has been estimated by E. Schmid and W. Boas for a single crystalline specimen. According to them, the relative elongation ε on complete twinning of a single crystal can be described by the expression:

$$1 + \varepsilon = (1 + 2s \sin \beta \cos \alpha + s^2 \sin^2 \beta)^{1/2} \tag{88}$$

where s is the relative unit shear in twinning; β is the angle between the specimen axis and twinning plane; and α is the angle between the specimen axis and twinning direction.

For twinning in {112} planes in b.c.c. alloys, the highest value of ε is 41.4 per cent at $\alpha = \beta = 54.7°$. Thus, the lowest possible contribution of twinning to plastic deformation may be quite high.

It should be noted in conclusion that twinning is an important kind of plastic deformation in b.c.c. metals (especially at low temperatures and high deformation rates) and in c.p.h. metals, but is immaterial in deformation of f.c.c. metals.

3. The Shear Mechanisms of Plastic Deformation Associated with Intercrystalline Reorientation

The distribution of dislocations in deformed crystals is highly non-uniform and, when there is an excess of dislocations of one sign, dislocation networks and sub-boundaries cause microscopic inhomogeneities and local misorientations up to a few degrees. In simplest kinds of deformation (tension, compression), the resulting misorientations can be quite appreciable. In macroscopically inhomogeneous and non-uniform stress and strain fields (produced, for instance,

in rolling, torsion, bending, pressing, etc.), the appearance of substantial misorientations is unavoidable.

An experimental evidence of misorientation is the phenomenon of *asterism* observed in the Laue pattern, i.e. photographs taken by the X-ray Laue technique. An undeformed perfect crystal gives a pattern of sharp spots on a Laue pattern and if the crystal is then uniformly deformed (there is no excess of one-sign dislocations), the spots will remain sharp. For instance, with proper orientation of the slip systems relative to the external stress, single crystals of zinc and cadmium give sharp Laue patterns on elongations up to 100 per cent. If, however, the elongated crystals are bent (i.e. when there is an excess of one-sign dislocations), the sharp diffraction spots will be smeared out into arcs. This phenomenon is referred to as asterism; it shows that a unique orientation in the crystal has been replaced by a range of orientations.

In aluminium single crystals, for instance, asterism becomes noticeable after an elongation of 1 per cent, i.e. already at the easy glide stage, but is more pronounced at stage 2. Such evidence suggests that the deformation of crystals in tension is not uniform microscopically.

In macroscopically non-uniform deformation (rolling, bending, etc.), variations in orientation can be revealed easily by etching when the changes in orientation show up as differently etched bands.

Apart from misorientations associated with dislocation movement, reoriented regions of the lattice are often observed in crystals. They appear as bands in micrographs and are often termed *deformation bands.* Many researchers studied the phenomenon, gave different names to it, and suggested various mechanisms for the formation of these bands. As has been established by A. H. Cottrell and R. Honeycombe, there should exist two main types of lattice reorientation in crystals and accordingly two mechanisms of plastic deformation which are referred to as *kinking* and *rotational slip.*

Kinking has been observed in compressed single crystals of zinc, cadmium and titanium and in tensioned crystals of iron, aluminium, tin, zinc, bismuth, magnesium, titanium, copper, and other metals and alloys.

According to R. Honeycombe and other researchers, a rod-shaped crystal of cadmium or zinc, with the ⟨0001⟩ axis almost parallel to the rod axis, undergoes local collapse (kink) when compressed along that axis and forms a *kink band* (Fig. 90). It has been shown that kink bands form gradually during compression of the crystal by a progressive rotation of the lattice, which may be as little as a few degrees or as large as 80°. Kinking occurs easily in compression when the angle β between the slip plane (basal plane) and the compression axis is within the range of 35-24°. Kinking does not occur if the angle β is less than 2.5°. With $\beta > 24°$, the form of kink bands is not well-defined.

The structure of a kinked region (Fig. 91) represents two regions, *ADE* and *CFB*, of severe lattice curvature, which are separated from each other and from the unkinked crystal by well-defined *kink planes* *AB* and *CD* which are essentially walls of edge dislocations. The curved regions, *ADE* and *CFB*, have excess dislocations of one sign and are responsible for the marked X-ray asterism observed in Laue photographs; on annealing they are also the preferred sites where polygonization and recrystallization take place. A kink band proper consists of a rotated, but initially not curved portion *ABCD* of the crystal. In the course of deformation, this portion of the crystal also becomes curved.

In iron, kink bands form when the crystal is tensioned in a [111] direction and the stress applied drops sharply at the moment as a kink band appears. The boundaries of kink bands roughly coincide with the (111) plane; the angle of lattice rotation in a kink band relative to the unkinked portion of the crystal increases with increasing deformation. Traces of slip in the (112) plane appear within a kink band.

The characteristic features of kinking are as follows.

1. The crystal lattice in a kink band rotates around a direction lying in the slip plane and perpendicular to the slip direction.
2. The boundary of a kink band is almost perpendicular to the slip planes operative in the matrix.
3. The formation of kink bands is associated with movement of edge dislocations, with the dislocations nucleating within a future

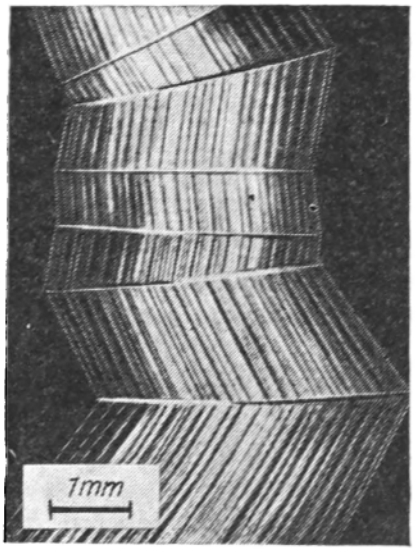

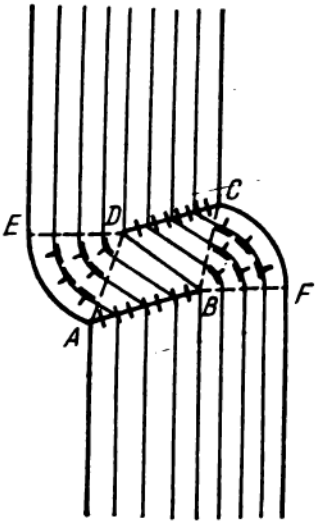

Fig. 90. (*left*) Kink band in a zinc crystal on compression

Fig. 91. Schematic structure of a kinked region and distribution of dislocations in a crystal with kink band

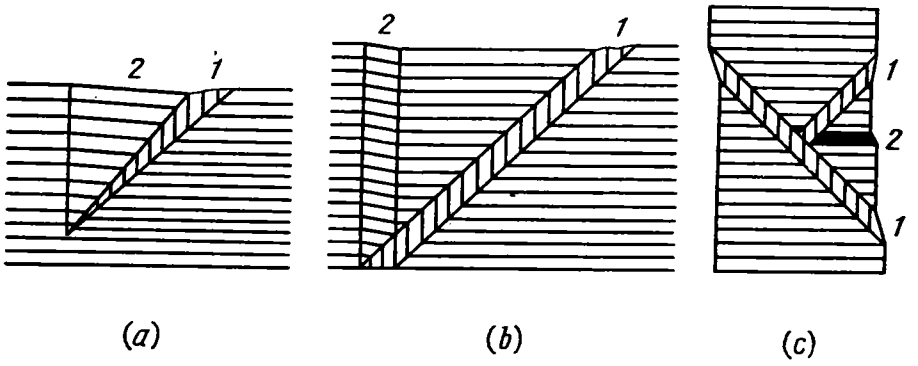

Fig. 92. Various schemes of accommodation kinking on a twin (*1*—twin; *2*—accommodation region) in a zinc crystal
(*a*) accommodation to a wedge-shaped twin band by bending of basal planes; (*b*) scheme for a case when a twin has spread over the whole crystal by bending of basal planes; (*c*) near two twin bands by slip in the basal plane

kink band, after which like dislocations move apart and form boundaries of the kink band.

Kinking, as a mechanism of plastic deformation with the characteristic features given above, explains well the earlier proposed mechanisms of formation of platelets (A. V. Stepanov) and of irrational twinning (i.e. twinning in arbitrary planes rather than in crystallographic planes of low indices).

The appearance of *accommodation bands* can also be regarded as a kind of kinking. The formation of accommodation bands has been called *accommodation kinking* by R. Honeycombe. Accommodation bands adjoin twin bands and thus accommodate the surrounding lattice to the existence of the twin and compensate for the deformation of the lattice caused by the twin. Accommodation can be effected either by curvature of the slip planes or by glide of dislocations (Fig. 92). For instance, the presence of two accommodation bands was detected experimentally in deformed zinc.

Deformation bands which were observed by L. Pfeil and C. S. Barrett in single and polycrystals of α-iron can also be attributed to the mechanism of kinking. N. F. Mott explains this phenomenon by a dislocation mechanism by which edge dislocations (as in kinking) move to future deformation bands from the outside (as in the formation of kink bands). The two other characteristic features of the formation of deformation bands remain the same as in kinking.

The dislocation model of the formation of deformation bands or kink bands can be imagined in a simpler form.

The shear stresses caused by an edge dislocation

$$\tau_{r\theta} = \frac{Gb}{2\pi(1-\nu)} \frac{\cos\theta\cos 2\theta}{r}$$

are equal to zero at $\theta = \pi/2$ and $\theta = \pm\pi/4$. For the latter case, a diagonal position of unlike dislocations is the position of equilib-

rium (see Ch. 2). If the external stresses do not exceed the maximal value $\tau_{max} = Gb/8\pi\,(1-\nu)\,h$ (h = distance between slip planes), unlike dislocations will move one past another without stopping in the diagonal equilibrium position. With a lower stress, they will stop in the diagonal position and will further retain all the like dislocations which move behind them. These dislocations will also inhibit dislocation slip in adjacent planes and promote the appearance of new pile-ups (Fig. 93). In such a pile-up, positive dislocations arrange themselves in a vertical row and negative ones, in another vertical row which is parallel to the former. In this way, a *deformation band* is formed (we describe the mechanism of dislocation movement from the main portion of a crystal to a deformation band and not the other way, as is the case in kinking), with positive dislocations being arranged at its one side and negative ones, at the other. If dislocations come quickly by this mechanism, it may be supposed that substantial shears must appear in the reoriented region and that the curved regions *ADE* and *CBF* (see Fig. 91) may serve as accommodation elements, so that dislocations in these regions are partially redistributed and their concentration in a wall is reduced.

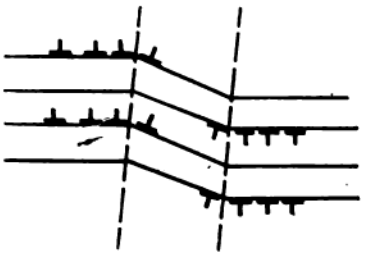

Fig. 93. Formation of deformation bands (kink bands) by mutual locking of groups of unlike dislocations

Rotational slip. In contrast to kinking which is associated with curvature of the operative slip planes, the crystal lattice may also be observed to rotate irregularly and form bands in which slip has taken place in a system of planes different from the slip system operative in other portions of the crystal. R. Honeycombe has called them *bands of secondary slip*. The axis of rotation of the lattice in a secondary slip band is perpendicular to the operative slip planes. Thus, the appearance of bands of secondary slip is associated with slip in a secondary system of slip planes and involves rotation of

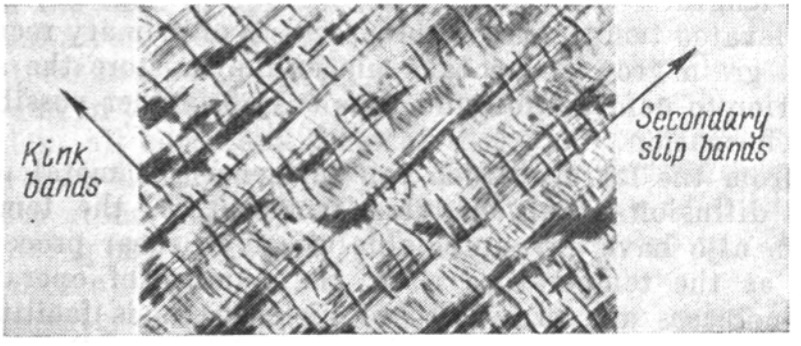

Fig. 94. Secondary slip

the slip planes around the normal to them. This mechanism of plastic deformation has been called *rotational slip* by H. Wilman. As distinct from kinking, rotational slip occurs by movement of screw dislocations and can be characterized by that the bands of secondary slip are arranged roughly parallel to the main slip traces (Fig. 94).

4. The Mechanisms of Diffusion Plasticity

Diffusion processes may play an important part in plastic deformation of metals at high temperatures. Diffusion may have a double role. On the one hand, it can influence substantially the shear mechanisms of plastic deformation and on the other, diffusion processes proper can cause the effects of plastic flow. This is why the *mechanism of diffusion plasticity is essentially the mechanism of residual shape variation due to diffusion processes.*

A few examples illustrating the indirect effect of diffusion on plastic deformation will be considered below.

1. Diffusion causes non-conservative movement of dislocations due to the directed inflow of vacancies to the compressive zone or of dislocated atoms, to the tensile zone. In both cases, a dislocation will move from one slip plane onto another parallel plane and can glide in the new plane, as well as in the old plane if it has been locked there for some or other reason. In that case, the dislocation source in the old plane is 'freed' and begins to generate new dislocations.

2. Diffusion causes migration or dissolution of obstacles in the surrounding matrix and thus opens path for dislocation movement. Examples of such obstacles are point defects whose mobility increases strongly with temperature. At high temperatures, diffusion processes may lead to coagulation (enlargement of larger particles at the expense of smaller ones which are dissolved) and spheroidization (rounding-off of initially stretched inclusions of an excess phase). Spheroidization and coagulation lead to a decrease in the length of interphase boundaries by unlocking pinned dislocations and increasing their free-path length.

3. At elevated temperatures, the processes of primary recrystallization and grain growth can take place; they restore the structure existed prior to deformation and thus ensure further possibility for plastic deformation.

Apart from the factors which can influence the metal plasticity owing to diffusion at an elevated temperature, the temperature proper can also have an appreciable effect on shear processes. For instance, as the temperature rises, the number of operative slip systems increases and cross slip of dislocations is facilitated. In a c.p.h. lattice, for example, an increase of temperature results in an intensive development of slip in pyramidal planes, and these

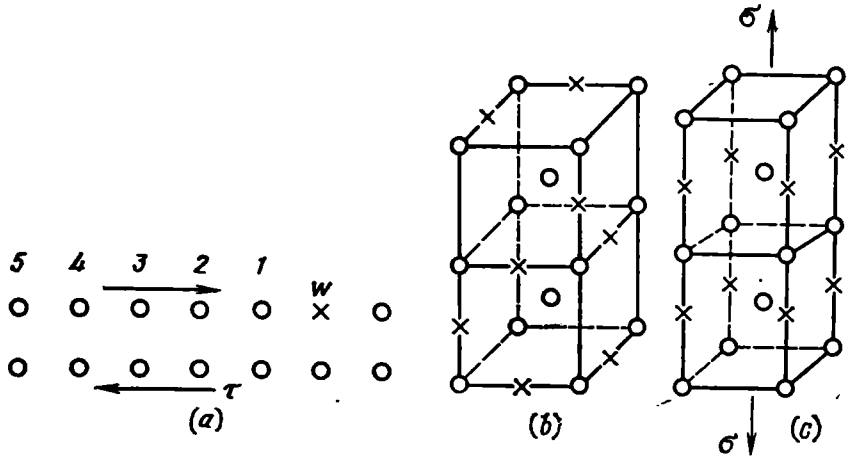

Fig. 95. Oriented diffusion of a vacancy w in the field of applied shear stresses (*a*); formation of oriented solution (*b* and *c*) in the stress field σ (× —interstitial atom in α-iron)

systems are very convenient for multiple and complex slip without substantial strain hardening.

The phenomena mentioned above, notwithstanding their importance and the large, sometimes principal, contribution to the total deformation in single and polycrystals, do not relate to mechanisms of diffusion plasticity proper.

The diffusion occurring in an elastic stress field is oriented, i.e. atoms are displaced selectively, most intensively in the direction of the highest shear strains (γ_{max}) or highest shear stresses (τ_{max}) (Fig. 95*a*). A vacant site *w* will be occupied by atom *1* (Fig. 95*a*), the newly formed vacant site will be occupied by atom *2*, and so on, i.e. there will be an *oriented flow of atoms in the direction of the highest shear stresses and a flow of vacancies in the opposite direction.*

Upon stress release, the oriented displacement of atoms will stop and change to common diffusion (self-diffusion) which occurs with the same intensity in all directions.

One of the mechanisms of plastic deformation in the presence of diffusion is associated with oriented displacements of interstitial atoms in the field of applied stresses. In a stressed crystal lattice, interstitial atoms are arranged randomly in interstices. For instance, carbon atoms in an α-iron solid solution occupy the sites in the centre of faces and in the mid of edges of the cube (Fig. 95*b*). Before stress application, all edges and faces of the cube are equivalent. In the presence of an elastic stress σ, this uniformity is disturbed (Fig. 95*a*) and solute atoms concentrate preferably on extended edges. Thus, the dissolving power of the lattice becomes different in various directions (anisotropic).

Consequently, before stress application, solute atoms (interstitial or substitutional) were distributed statistically in the solvent metal lattice (disordered solid solution). On stress application, there forms

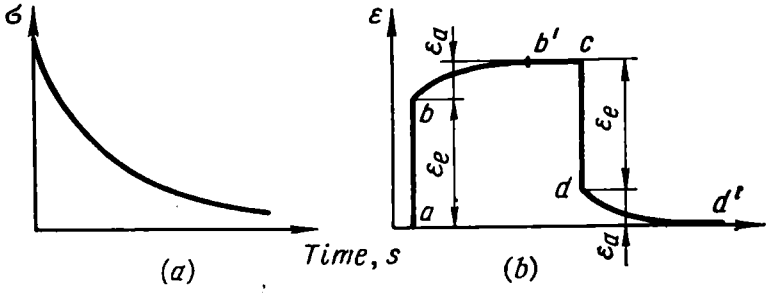

Fig. 96. Relaxation curve (*a*) and time dependence of deformation (ε) with the aftereffect portion *dd′*, which illustrates anelasticity associated with diffusion

a solid solution with solute atoms positioned preferably in accordance with the deformation of the crystal lattice. The formation of such a solid solution is inevitably associated with a change in the lattice shape and deformation of the whole specimen. If the solid solution thus formed (let it be called oriented-ordered solution) can be fixed by locking of the lattice by dislocations or grain boundaries, there will appear an oriented plastic deformation.

The discussed mechanism of plastic deformation by the formation of oriented-ordered interstitial or substitutional solid solution is used for explaining the phenomenon of *stress relaxation* in metals, i.e. *a loss of stress with time*, $\sigma = \sigma(t)$, *owing to the transition of a part of elastic deformation to plastic deformation at a given constant total deformation* $\varepsilon = \text{const}$. With $\varepsilon = \text{constant}$, residual deformations ε_0 can appear on the formation of an oriented-ordered solid solution, provided that the sum of elastic (ε_e) and residual (ε_0) deformations remains constant: $\varepsilon_e + \varepsilon_0 = \varepsilon = \text{const}$. As ε_e decreases, the level of elastic stresses (whose effect is in reducing the rate of formation of oriented-ordered solid solution) also decreases, the total result being that stresses decrease exponentially (Fig. 96*a*).

If there are no factors that might fix the solid solution, all stresses in the crystal lattice upon removal of the load (stress release) become equivalent and the residual deformation disappears. Indeed, if a specimen is loaded by a constant stress at a strain of the order of 10^{-5}, an elastic deformation ε_e will appear (Fig. 96*b*, section *ab*). The deformation increases with time (section *bb′*) at a constant decrease of the deformation rate. This gain in deformation, ε_a, is associated with the diffusion process of formation of oriented-ordered solid solution. The deformation ε_a is referred to as *anelastic deformation*. Upon stress release, the elastic deformation ε_e disappears (Fig. 96*b*, line *cd*) and the anelastic deformation varies slowly with time (owing to the fact that all directions in diffusion are equivalent) and restores the specimen to the original length. The variation of deformations in the section *dd′* with subsequent restoration of the specimen size is called the aftereffect. The phenomenon is observed not only at deformations of the order of 10^{-5}, but also in the presence

of residual deformations. In this case, the decrease of deformation dd' by ε_a will not restore fully the size of the specimen*.

P. G. Shewmon has made use of the phenomenon of anelasticity and of the tests by the scheme in Fig. 96*b* to determine the coefficient of diffusion of a dissolved or intersticed substance in terms of the rate with which ε_a decreases.

Ya. I. Frenkel, and later F. R. N. Nabarro and C. Herring have developed a model and *mechanism of intragranular diffusion plasticity*** based on oriented flows of vacancies. In this mechanism, use is made of the fact that diffusion processes occur most intensively at grain boundaries, i.e. in places of the highest distortion of the crystal lattice. Grain boundaries serve as sources and sinks for oriented movement of vacancies in the field of the stress applied, the vacancy flow passes through the volume of a grain in the direction from transverse to longitudinal boundaries (Fig. 97), and the flow of atoms moves in the opposite direction. Thus, mass transfer and plastic flow take place in the process. These flows result in that the grain is stretched in the longitudinal direction and contracted laterally (since the grain volume is not changed). Due to the low mobility of grain boundaries, the new shape of the grain is fixed and deformations become irreversible. This mechanism of plastic deformation is used to explain all time-dependent processes, i.e. relaxation, aftereffect, and creep***.

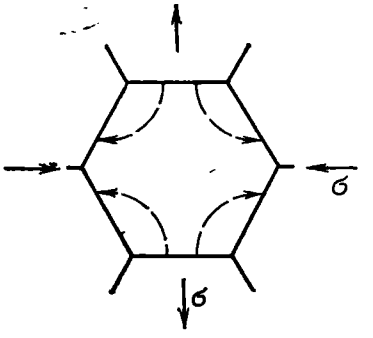

Fig. 97. Directed flows of vacancies in a grain during deformation (σ — applied stress)

Diffusion-dislocation mechanisms of plastic deformation are associated with oriented diffusion in the elastic stress field of dislocations, dislocation tangles and their complexes.

Apart from climb (non-conservative movement), other types of dislocation processes are possible in the presence of diffusion. When moving dislocations intersect one another or pass through a dislocation 'forest', jogs form on the dislocation lines. For screw dislocations, movement of jogs is nonconservative and is accompanied by the formation of vacancies which lock the movement of jogged dislocations until a possibility arises for their disappearance. In this case, the mechanism of plastic deformation which controls the deforma-

* The aftereffect dd' is sometimes (especially in rheology) associated with the 'memory' of a metal of its state in point *a* (see Fig. 96*b*), i.e. prior to deformation.

** This mechanism is often referred to as 'diffusion creep' which is characterized by a combination of various mechanisms discussed in Ch. 2, Sec. 5.

*** Creep is a process in which part of the elastic deformation changes to plastic, i.e. the total deformation increases with time [$\varepsilon = \varepsilon(t)$] at a constant stress level ($\sigma = \text{const.}$).

ion rate is, as earlier, associated with the rate of vacancy diffusion and the activation energy of plastic deformation is equal to the activation energy of self-diffusion.

Due to the stress field existing around a dislocation, the diffusion of vacancies along the dislocation occurs at a higher rate than in the bulk of grain. In this case, dislocation climb and the nucleation and movement of jogs are facilitated by 'feeding' vacancies to them.

The mechanism of plastic deformation by diffusion through dislocation cores (i.e. along a dislocation) can explain the elevated mobility of single and double kinks under the stress applied, which promotes more intensive slip by overcoming the Peierls barrier.

In particular, for a kink on a screw dislocation, an external force F produces an opposing stress σ in the slip plane along the direction **b**.

In that case the force acting on the kink along the dislocation is

$$F_k = \sigma b_k \tag{89}$$

Using Einstein's relation between the force F and the velocity v of oriented drift of a defect in diffusion:

$$v = DF/kT \tag{90}$$

we find that the rate of movement of a kink along a dislocation is

$$v_k = D_k \sigma b_k / kT \tag{91}$$

where $D_k \approx \nu a^2 \exp(-Q_k/kT)$ is the coefficient of diffusion of the kink ($\nu \approx 10^{12}$-10^{13} s^{-1} = oscillation frequency, a = length of jump, and Q_k = activation energy for movement of the kink).

The rate of deformation for a kink of width Δ is found from formula (91):

$$\xi = v_k/\Delta = D_k \sigma b_k / \Delta kT \tag{92}$$

and, as may be seen, increases with temperature.

The diffusion-dislocation mechanisms explain a number of phenomena occurring in metals, such as the yield stress peak, strain ageing, or blue brittleness. These phenomena can be explained by the appearance of irreversible deformations due to oriented diffusion of atoms, which form the solid solution, in the stress field around a dislocation. The inflow of these atoms decreases the stresses around the dislocation, and therefore, the dislocation energy. The energy of interaction of a dislocation with an atom of the solid solution at a point with the coordinates r and θ from the dislocation centre is found by the formula:

$$E_{ss} = 4Gb\varepsilon (R^3 \sin\theta)/r$$

where $\varepsilon = (R' - R)/R$ and R' is the radius of a foreign atom.

For α-iron, for instance, E_{ss} is equal to 0.5-1.0 eV. This energy is the driving force for the formation of a 'cloud' of solute atoms around a dislocation. The average concentration of atoms in the

'cloud' will vary by the law $c = c_0 \exp(E_{ss}/kT)$ until E_{ss} begins to change with concentration. At room temperature, $E_{ss} \gg kT$ and the 'cloud' is supersaturated with foreign atoms. In dislocation glide, a 'cloud' can move only by diffusion, because of which 'clouds' lock dislocation movement at room temperature. At low stresses, the rate of dislocation movement may be commensurable with the rate of diffusion, so that dislocations can move together with their 'clouds'. At higher stresses, when a cloud lags behind a dislocation, the latter can break off and acquire mobility. The appearance of a yield stress peak is explained by the presence of these 'clouds' which are called 'Cottrell atmospheres'. Using the mechanism of the formation of Cottrell atmospheres, F.R.N. Nabarro has clarified the phenomenon of blue brittleness*. At moderate diffusion rates (below the rate of dislocation movement), dislocations cannot break off beyond a 'cloud'. Such diffusion rates are called 'critical'. A moving dislocation drags behind a 'cloud' of impurities and its movement is impeded substantially, resulting in higher values of ultimate strength and yield limit and in lower plasticity. At a higher temperature, the mobility of a 'cloud' increases, resulting in a higher plasticity. In impact tests, i.e. at high deformation rates, the critical rate of movement of a 'cloud' should shift to a region of higher temperatures, i.e. the temperature limit of brittleness increases. This has been supported experimentally: in impact tests of low-carbon steels, the effect of blue brittleness is observed in the temperature range of 400-500°C.

5. Deformation of F.C.C. Crystals

Face-centred cubic crystals exhibit in deformation three distinct hardening stages, *I-III*, i.e. three different portions appear in the τ-γ curve. These portions of the curve can be characterized by the following hardening parameters:

1. The *critical shear stress* τ_0 is the stress at which plastic deformation begins. The transition from elastic to plastic deformation is rather smooth, so that τ_0 is determined by extrapolating the linear Stage *I* up to $\gamma = 0$ (Fig. 98, point *A*).

2. The *hardening coefficients* θ_i at each stage ($i = I, II, III$): $\theta_i = d\tau_i/d\gamma$.

3. The *parameters* τ_{II} and θ_{II} (or τ^*_{II} and θ^*_{II}) which characterize the end of Stage *I* and the beginning of Stage *II*; the parameters τ_{III} and θ_{III} which characterize the end of Stage *II* and the begin-

* In static tests of steel, its plasticity has been observed to drop down substantially in the range of 250-300°C and restore at higher temperatures. At $t =$ = 250-300°C, a blue temper colour appears due to oxidation. For that reason, the loss of plasticity in the temperature range indicated has been called 'blue brittleness'.

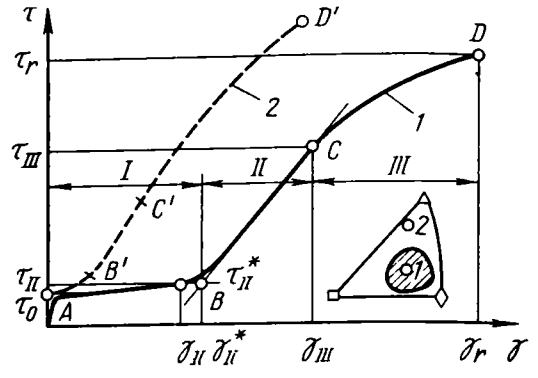

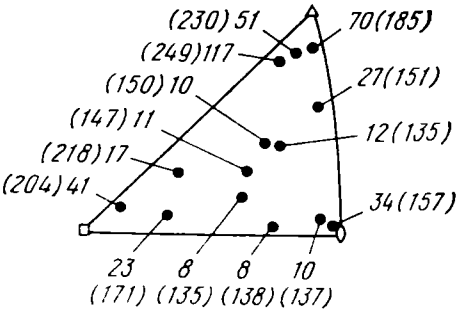

Fig. 98. (*left*) Typical hardening curves in the coordinates τ-γ (resolved shear stress — shear strain) for f.c.c. single crystals with orientations *1* and *2*. The shaded region in the stereographic triangle is the region of 'soft' orientations, the remaining portion representing 'hard' orientations

Fig. 99. Hardening coefficients θ_I for copper crystals (99.98% Cu), MPa, at different orientations. Values of θ_{II} are given in parentheses

ning of Stage *III*; and the parameters τ_r (rupture stress) and γ_r (rupture strain) which characterize the end of the τ-γ curve.

Stage *I* hardening. At this stage, only one slip system is operative and the hardening effect is observed to be slight; for that reason, it is called the '*easy glide*' *stage*.

Crystal orientation. The values γ_{II} and θ_I of differently oriented crystals may vary at the *linear Stage I* within wide ranges. Crystals oriented favourably for slip in a single system at a low resolved shear stress are referred to as 'soft' (Fig. 98, crystal *1*). 'Hard' orientations of crystals lie near or at the boundaries of the stereographic triangle, where two or more slip systems have close values of the resolved shear stress and slip is of the multiple type from the very beginning.

The steepest hardening curves are obtained for crystals with orientation [001] and [$\bar{1}$11] where four or respectively three slip systems are operative (see Fig. 70). In the case of the 'hardest' orientation, Stage *I* is absent and deformation begins just from Stage *II*. Crystals of a 'soft' orientation can exhibit shear deformations of the order of 15-50 per cent at Stage *I*. The coefficient θ_I increases with a decrease of the length of Stage *I* and constitutes roughly $G \times 10^{-4}$— $G \times 10^{-3}$. The highest values of θ_I are obtained for orientations near directions [$\bar{1}$11] and [001] and the lowest, near [011] (Fig. 99).

The length of Stage *I* hardening is determined by the possible amount of rotation of the crystal axis during tension. The end of Stage *I* does not correspond to the coincidence of the tension axis with the symmetrical [001]-[$\bar{1}$11] boundary in the stereographic triangle, since other slip systems become practically operative before this point is attained, which varies substantially the rate of hardening.

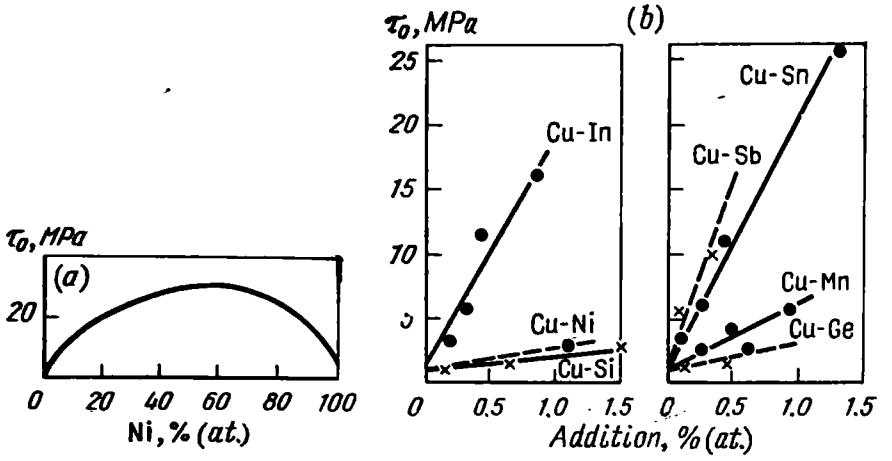

Fig. 100. Critical shear stress τ_0 in solid solution crystals
(*a*) Cu-Ni alloys; (*b*) in crystals of dilute solid solutions of copper depending on the content of dissolved element

The length of Stage *I* depends on the *nature and purity of the metal.* Besides, the stacking fault energy E_{sf} can also have an essential effect. For instance, E_{sf} of aluminium crystals at room temperature is high and γ_{II} does not exceed 4-5 per cent, whereas E_{sf} of copper is low and γ_{II} exceeds 20 per cent. Impurities can have a noticeable effect on the length of Stage *I*, an essential point being the shape in which they are present in a crystal. If impurities form a secondary phase, Stage *I* is observed to become shorter or disappear completely even at a low concentration of impurities. An explanation is that inclusions of other phases cause local slip in other slip systems, rather than in the primary slip system, and thus eliminate Stage *I* hardening.

Dissolved impurities lower the stacking fault energy and increase the width of extended dislocations, which inhibits double cross slip and increases the critical shear stress relative to its value in the pure metal (Fig. 100*a*). Thus, the length of Stage *I* (parameter γ_{II}) increases and θ_I decreases. Experiments with dilute solutions have demonstrated that impurities produce especially marked effect in low concentrations (Fig. 100*b* and *c*). As the concentration of impurities varies from 10^{-5} to 10^{-4}, τ_0 increases roughly by a factor of 2 or 3. The effect of solute additions on the flow stress is stronger when the size of their atoms differs more appreciably from that of atoms of the base metal (compare the effect of Ni and Si, on the one hand, with that of Sb, In, and Sn, on the other, as illustrated in Fig. 100*b* and *c*).

Temperature. At a lower temperature, the length of Stage *I* hardening and the critical shear stress τ_0 increase (Fig. 101). The ratio θ_I/G varies insignificantly: it increases slightly with increasing temperature, with the purity of the metal having an essential effect on the θ_I (T) relationship.

Two types of the temperature relationship for τ_0/G have been obtained: one for Cu and Al single crystals with inflections and the other for Ag and Ni single crystals with $\tau_0\,(T)$ decreasing monotonously with increasing temperature (Fig. 102).

The size of crystal and the state of its surface. The length of 'easy glide' Stage *I* increases as the size of grains decreases. According to R. Honeycombe, crystals of copper (99.98% pure) of a diameter of 1.78 mm had $\gamma_{II} = 16$ per cent and those 0.21 mm in size, $\gamma_{II} = 40$ per cent. The magnitude of θ_{II} did not change. An increase of γ_{II} should be attributed to a greater path of dislocation movement in slip. In fine crystals, dislocations cannot be locked in the bulk of metal, but emerge to the crystal surface and form jogs. In larger crystals, they can be locked in the metal bulk. The shape of crystals can also influence the process of deformation. For instance, in aluminium single crystals of a rectangular cross section, the system with the lowest resolved shear stress is not necessarily the primary operative slip system.

Crystals with a thin oxide film on their surface exhibit an appreciably lower length of the easy glide stage, since the oxide layer is an obstacle for emergence of dislocations onto the surface.

The fact that the length of the easy glide stage depends on the length of the path of dislocation glide and on the state of the crystal surface suggests a conclusion that dislocations in crystals can cover at this stage appreciable distances without meeting obstacles.

The microstructure at Stage I. Dislocations in the primary slip system only rarely interact with the stress fields of dislocation networks existing in the original (prior to deformation) state. Thus, only few of them can be locked, and therefore, the free-path length of dislocations is relatively large. At Stage *I*, there appear long thin

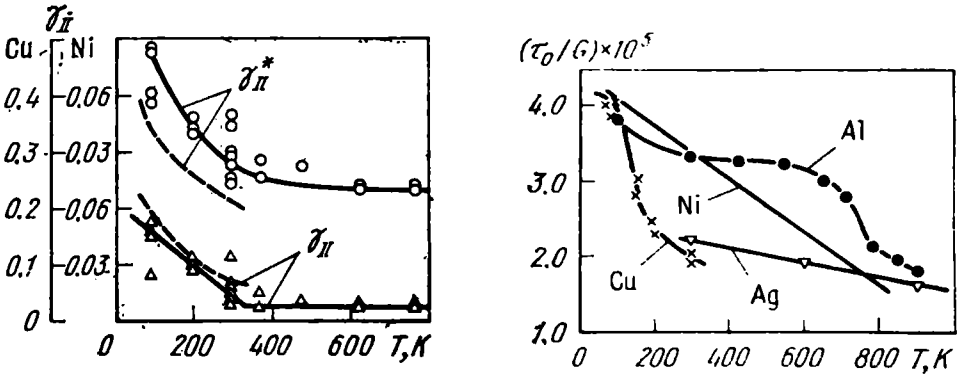

Fig. 101. (*left*) Effect of temperature on the length of Stage *I* hardening (γ^*_{II} and γ_{II}, see Fig. 98) for Ni single crystal (solid lines, with experimental points shown at the curves) and for copper single crystal (dashed line, experimental points are not shown)

Fig. 102. Effect of temperature on τ_0/G of single crystals of selected metals with different stacking fault energy (after R. Berner, H. Kronmüller)

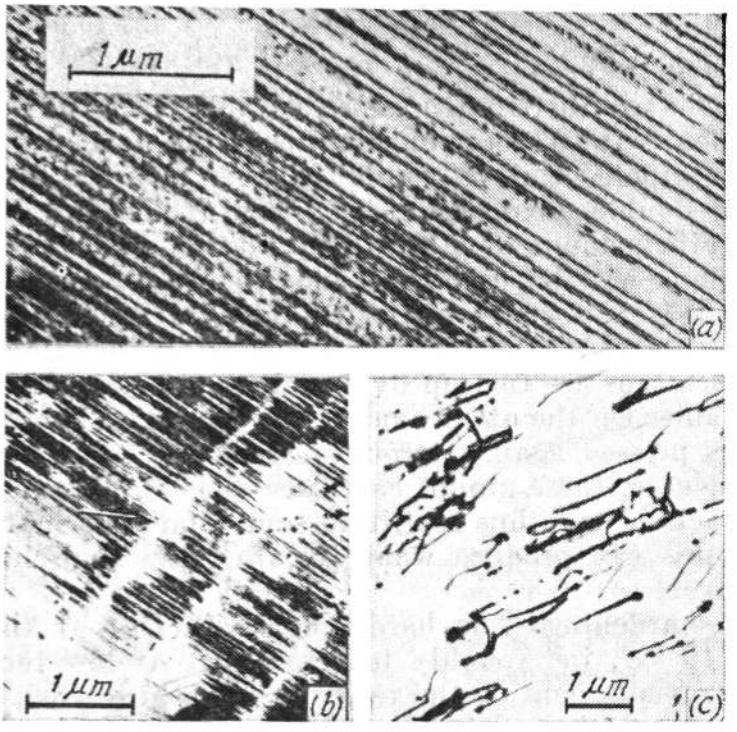

Fig. 103. Electron micrographs (replicas) of slip lines at Stage *I* of deformation in copper crystal (*a*); kink bands in aluminium single crystal (*b*); and dislocation dipoles in magnesium at the stage of easy glide (*c*)

slip lines uniformly covering the surface of a crystal (Fig. 103*a*). According to V. A. Pavlov, the average distance between slip lines in copper at $\gamma = 9$ per cent is 40-65 nm and the amount of shear (the height of jog) is from roughly 3 nm (94 per cent of all slip lines) to roughly 6 nm (6 per cent of all slip lines). Near the end of the easy glide stage, it is possible to reveal slip traces in other slip systems. At the end of Stage *I*, some irregularities in the microstructure can be observed: in addition to slip traces in other slip systems in core portions of a specimen, one can observe kink bands (Fig. 103*b*) and bands of secondary (rotational) slip. The etch pit method has established dislocation pile-ups at sub-boundaries in primary slip planes. The dislocation density increases with increasing deformation. As a first approximation, the following relationship is true for Stage *I*:

$$\tau = 0.5GbN_d^{0.5} \tag{93}$$

where N_d is the dislocation density; τ is the flow stress; and G is the shear modulus.

The average free-path length L of a dislocation, as found from the formula $\gamma = N_d bL$, is equal to 1-2 mm (in experiments, $L \approx 0.5$ mm) and the dislocation density increases linearly with increasing plastic

deformation:

$$N_d = 2.8 \times 10^8 \gamma \qquad (94)$$

Dislocations are distributed non-uniformly over the cross section of a specimen, with dislocation pile-ups being formed periodically. Dislocation dipoles can be found between sub-boundaries as an evidence of double cross slip (Fig. 103*c*). If the stress is released upon a certain amount of plastic deformation, an appreciable part of dislocations will be unable to move on their paths backward. One of the reasons for irreversibility of slip is associated with dislocation dipoles. A labyrinth of a spatial dislocation tangle in which dislocations are tied up by a multitude of dipoles, is practically invariable. On the other hand, there can exist denser groups of dislocations pressed against strong obstacles by the stress applied. On stress release, these groups can cause plastic deformation in the reverse direction and thus facilitate somewhat deformation in this direction; this can produce what is called the Bauschinger effect (see Ch. 4).

Stage *II* hardening. The hardening coefficient at this stage is $\theta_{II} \approx 2 \times 10^{-3} G$, i.e. roughly ten times θ_I. At low temperatures, Stage *II* is predominant on the τ-γ curve. It begins when the tension axis of the crystal is still inside the stereographic triangle at a certain distance from its [001]-[$\bar{1}$11] boundary.

Crystal orientation. The orientational relationship for θ_{II} is not so pronounced as that for Stage *I*, but the general tendency remains the same: for crystals with the tension axis close to [011], θ_{II} is smaller than that for crystals oriented close to the [001]-[$\bar{1}$11] boundary (see Fig. 99).

The nature and purity of metal. The effect of stacking fault energy is noticeable at Stage *II*, as well as at Stage *I*. In aluminium at room temperature, Stage *II* hardening is expressed quite feebly, so that Stage *I* seems to pass immediately into Stage *III*. At cryogenic temperatures, all the three stages are quite distinct. On the contrary, copper crystals at $t = 20°C$ exhibit clearly Stage *II*. Depending on the orientation, it begins at $\gamma_{II} = 5$-20 per cent and ends at $\gamma_{III} = 15$-35 per cent. The beginning of Stage *III* is associated with intensive cross slip which in copper (having a rather low stacking fault energy) can occur less easily than in aluminium. For solid solutions, the increased length of Stage *II* is explained by the effect of additions on the stacking fault energy which drops down in copper and silver from $(0.30\text{-}0.40) \times 10^{-2}$ mJ/cm^2 to 0.2×10^{-3} mJ/cm^2 on addition of 15 at.% Al.

Temperature. An increase in temperature shortens the length of Stage *II* and makes Stage *III* more pronounced. In some cases, Stage *II* may disappear fully and the τ-γ curve then practically consists of Stage *III* only. With all other factors being constant, the hardening coefficient is insensitive to temperature (Fig. 104). In all known

ases, the dimensionless hardening coefficient θ_{II}/G, which characterizes the slope of the τ-γ curve at Stage *II*, exhibits practically no dependence on temperature. This parameter is roughly the same for all f.c.c. metals and alloys examined to this time.

In most studies made up to now, the temperature relationship for τ_{II} is similar to τ_0 (T), or in other words, the temperature relationship for the τ_{II}/τ_0 ratio is a monotonous curve without inflections. Most often, $\tau_{II}/\tau_0 = \text{const} \neq f(T)$.

The size and surface state of crystals. These factors are at Stage *II* less essential than at the easy glide stage. As has been established, finer crystals are hardened more quickly than larger ones only when oriented close to [001]. In the remaining portion of the stereographic triangle, no noticeable effect of the size and shape of crystals on the pattern of the τ-γ curve at Stage *II* has been established.

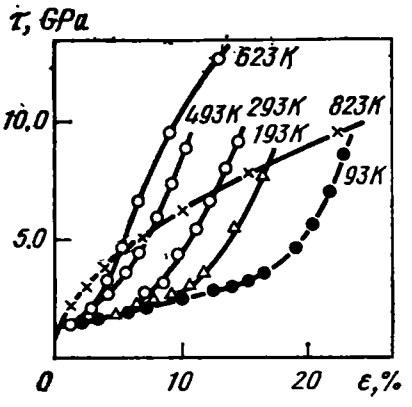

Fig. 104. Effect of temperature on τ-γ curves of identically oriented copper crystals. The slope of all the curves at Stage *II* is the same at any given temperature, except for the curve at $T = 823$ K which has no Stage *II*, but only Stage *III*

The microstructure at Stage II. The pattern of slip lines depends appreciably on crystal orientation, especially if the tension axis is close to a symmetrical boundary of the stereographic triangle. In that case, slip in one or more secondary slip systems {111} can be observed. Such crystals exhibit a higher rate of hardening than 'soft' ones.

The dislocation density, measured by the etch pit method, increases with increasing plastic deformation more quickly than would be expected by a linear law. For that reason, the average free-path length of gliding dislocations diminishes. The average length of slip lines ($L \approx$ 20-40 μm) decreases with increasing deformation at Stage *II* and can be found by the formula:

$$L = K/(\gamma - \gamma_{II}) \tag{95}$$

where γ is the total deformation and $K \approx (4\text{-}6) \times 10^{-4}$ cm is a constant.

The dislocation picture typical of Stage *I* remains essentially the same at the beginning of Stage *II*; one can observe a coarse dislocation sub-structure which is obviously associated with deformation bands and with more complex dislocation pile-ups. The formation of a dislocation cell structure begins at this stage (Fig. 105), but there are regions free of dislocations and surrounded by dislocation dipoles. Dipoles and edge dislocations of the primary slip system

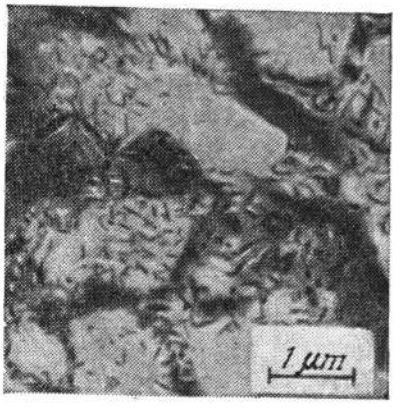

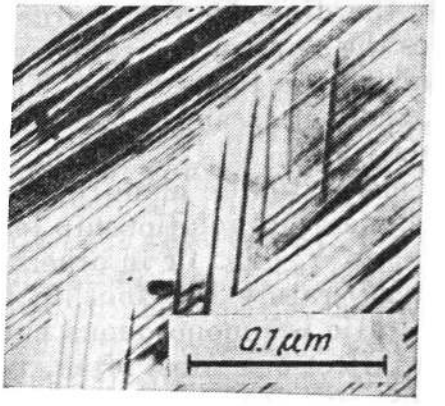

Fig. 105. (*left*) Cell structure of aluminium deformed 10% at 77 K

Fig. 106. Structurized slip at Stage *II* and bands of secondary shear at $\gamma = 0.43$

are the typical structural formations, especially at the beginning of Stage *II*.

At Stage *II*, dislocations of a secondary slip system (Fig. 106) begin to react with those of the primary system and form Lomer-Cottrell dislocations, i.e. dislocations with the Burgers vector lying in neither of the probable slip planes (Fig. 107). These dislocations are 'sessile' and strongly inhibit slip: they embrace the dislocations in the primary slip plane and form configurations like those shown schematically in Fig. 108. Lomer-Cottrell dislocations appearing on lines of intersection of {111} planes, and therefore, positioned along ⟨110⟩ direction, are barriers on which dislocation loops are

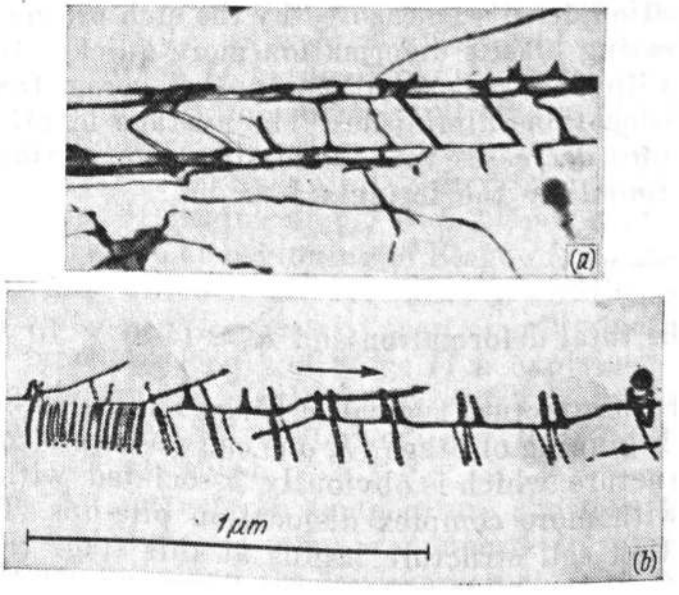

Fig. 107. Lomer-Cottrell locks in stainless steel (*a*) and in Cu + 8% Al alloy (*b*)

piled up in groups of 10-100 dislocations. The stress fields of such pile-ups are responsible for a sharp rise of hardening at Stage *II*. The *S* zones (Fig. 108) bounded by 'sessile' dislocations are referred to as *slip zones*.

The combinations of slip systems which can form Lomer-Cottrell barriers in the primary slip plane are as follows:

Orientation of sessile dislocations	[011] *	[110] *	[101] *
Slip system pairs	*B*IV-*C*I	*B*IV-*A*VI	*B*V-*D*I
	*B*II-*C*III	*B*V-*A*III	*B*II-*D*VI

Due to the formation of Lomer-Cottrell sessile dislocations, dislocation dipoles (formed by meeting of dislocation loops gliding in closely oriented slip planes) and complex dislocation networks, the hardening effect at Stage *II* is quite strong. In view of the complex picture of dislocation configurations formed at this stage, analytical calculation of τ_{II} involves certain difficulties.

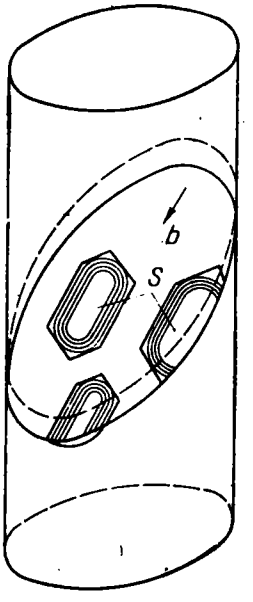

Fig. 108. Slip zones (*S*) in a deformed crystal

Stage *III* hardening. This stage corresponds to the parabolic portion of the τ-γ curve and can be characterized by gradual decrease of the hardening coefficient. The main mechanism of deformation at this stage is thermally activated cross slip, because of which the beginning of Stage *III* is determined primarily by temperature. As has been established, the stress at the beginning of Stage *III*, τ_{III}, decreases rapidly (by a logarithmic law) with an increase of temperature (Fig. 109):

$$\ln (\tau_{III}/G) = \ln (\tau_{III0}/G_0) - BT \qquad (96)$$

where τ_{III0} and G_0 are the stress and shear modulus at 0 K.

The principal factors discussed for Stages *I* and *II*, have an inessential effect at this stage of hardening.

The extent of portion *III* of the curve increases at the expense of portion *II* with an increase of temperature. At low temperatures of deformation (below 100 K), Stage *III* in aluminium single crystals disappears completely and, since Stage *II* is predominant, high characteristics of hardening are attained. At room temperature, on the contrary, Stage *II* is hardly noticeable, with Stage *III* being predominant. At high temperatures, the τ-γ curve for aluminium begins with the parabolic portion.

* The reader is invited to write the indices of the planes and directions for each of the systems by reference to Figs. 68 and 69.

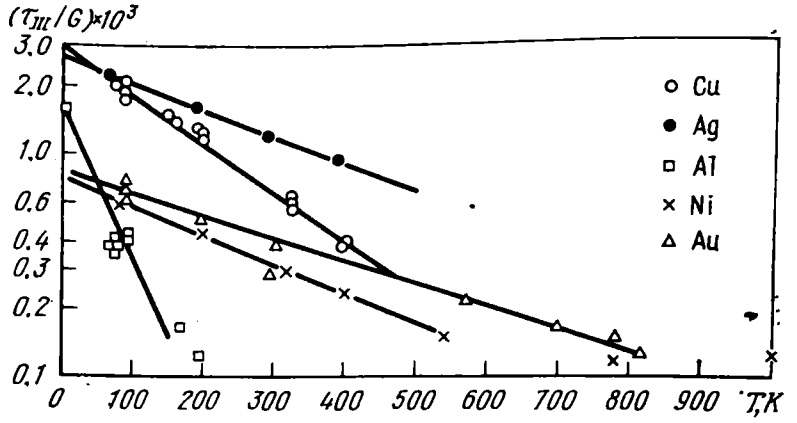

Fig. 109. Effect of temperature on τ_{III}/G in selected metals

The transition to Stage *III* in aluminium requires a lower temperature than that needed for copper. At the same temperature, the transition to Stage *III* occurs in aluminium at a lower stress than in copper.

The parameters τ_r and γ_r correspond to necking (see Fig. 98). For f.c.c. single crystals, the total deformation to rupture, γ_r, decreases with increasing temperature (Fig. 110*a*), as also does the rupture stress τ_r (Fig. 110*b*).

The microstructure at Stage III. The gradual decrease of the hardening coefficient at Stage *III* can only be explained by that the dislocation pile-ups formed at Stage *II* should partially disappear in a certain way. This is caused by *cross slip of screw dislocations.* Since the Burgers vector of screw dislocations is parallel to the dislocation line, i.e. they are not 'tied up' to a particular slip plane, screw dislocations can easily bow around obstacles and move onto other planes of the same {111} family, i.e. onto *cross-slip planes* (see Ch. 2) and further onto a plane parallel to the original plane where the influence of the obstacles is largely attenuated. Thus, cross slip is one of the mechanisms by which gliding dislocations can overcome obstacles. This is why θ_{III} at Stage *III* diminishes with increasing deformation

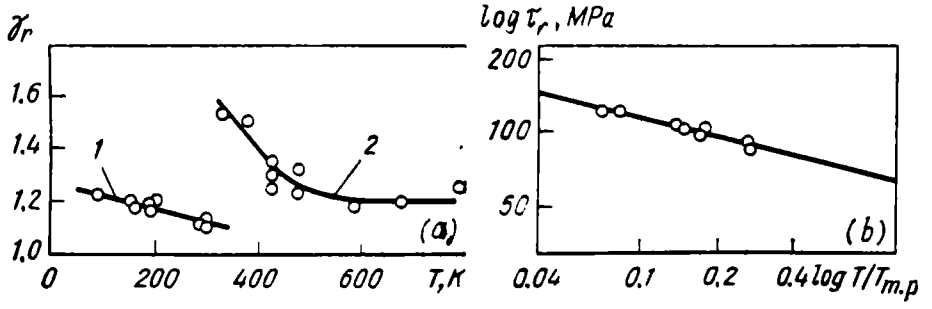

Fig. 110. Temperature relationships for
(*a*) γ_r (T) in copper (*1*) and in Ni + 50% Co alloy (*2*); (*b*) log $\tau_r = f(\log T/T_{m.p.})$ for copper

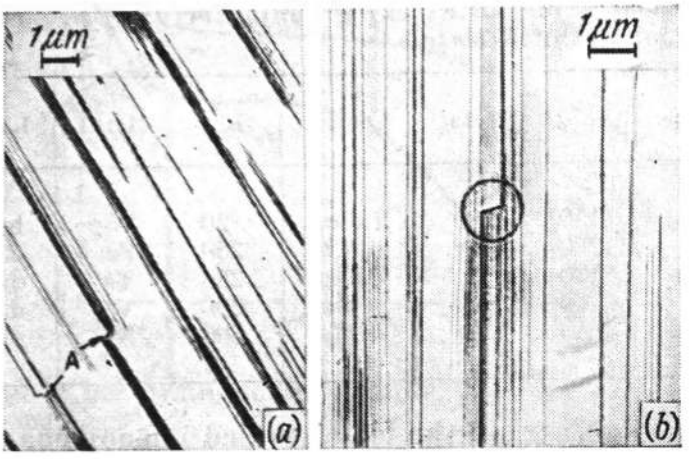

Fig. 111. Distinct coarse slip bands at Stage *III*
(*a*) bands due to double cross slip (marked by '*A*'); (*b*) jog due to cross slip (encircled) at the beginning of Stage *III* in copper single crystal

This *double cross slip* has been observed experimentally between slip bands (Fig. 111). Cross slip of extended dislocations becomes possible only when the surrounding partial dislocations combine into a perfect dislocation with a constriction of length *BD* (see Fig. 43).

A constriction on an extended dislocation, which is needed for initiation of cross slip in another plane, is formed due to the shear stress applied and to thermal oscillations of the lattice, since the recombination reaction is energetically unfavourable. Constriction of an extended dislocation and its movement in a cross slip plane require the activation energy whose magnitude depends on the size of the constriction and the width of the extended dislocation. The calculated activation energy for aluminium has turned out to be close to 1.0 eV. For copper, however, which has a greater width of extended dislocations, an appreciably higher energy is needed. Therefore, cross slip in copper requires a higher stress and higher temperature. Since the width of a stacking fault depends on the stacking fault energy E_{sf}, the stress τ_{III} is also dependent on the stacking fault energy.

A. Seeger has proposed the following formula to determine τ_{III} for a model of a flat pile-up of n dislocations:

$$\tau_{III} = \frac{1}{n}\left(\frac{\sqrt{2}}{4\pi}G - \frac{2E_{sf}}{b}\right) \tag{97}$$

This formula explains well why aluminium and copper, which differ substantially in the stacking fault energy E_{sf} (Table 9), have different lengths of Stages *II* and *III* hardening.

The dislocation structure observed at Stages *I* and *II*, degenerates with increasing deformation into a cell structure (see Fig. 105) in which cell walls contain tangled dislocation pile-ups whose density increases with deformation.

Table 9. Averaged Values of Stacking Fault Energy, E_{sf}, 10^4 mJ cm^{-2}, for Selected Metals

Metal	Lattice	E_{sf}	Metal	Lattice	E_{sf}	Metal	Lattice	E_{sf}
Ni	f.c.c.	150	Ag	f.c.c.	20	W	b.c.c.	300
Al	ditto	200	Mg	c.p.h.	250	Fe	ditto	140
Pt	ditto	120	Zn	ditto	250	Ta	ditto	110
Cu	ditto	60	Cr	b.c.c.	300	V	ditto	140
Au	ditto	40	Mo	ditto	300	Nb	ditto	30

Necking and rupture are the least studied phenomena in deformation of single crystals. However the slope of the straight line describing the dependence of log τ_r on log $(T/T_{m.p.})$ (see Fig. 110*b*) for single crystals of copper, gold, lead, and other f.c.c. metals is proportional to A/Gb^3, where $A = 2.7\text{-}2.8$ is a constant. The relationship between τ_r and A suggests the idea that the processes occurring at the formation of a rupture neck and in cross slip at Stage *III* are largely similar, i.e. the rupture stress τ_r, which is readily reproducible in experiments, characterizes the state of a whole crystal, rather than the development of a rupture neck, which takes place more or less at random. This idea has found support in the fact that if the remaining piece of a ruptured crystal is deformed again, a neck will form in a certain arbitrary point again at the same (i.e. initial) stress.

The effect of temperature and deformation rate on flow stress. As has been established (Fig. 112), the ratio of flow stresses $(\tau_T/G_T^*)/(\tau_0/G_0)$ for Ag, Cu, Ni, and Al, which is independent of deformation, remains essentially constant in the temperature range of 200 to 400 K. This ratio, however, increases at $T < 200$ K and decreases at $T > 500$ K.

As has been indicated by A. N. Cottrell and R. J. Stokes, if an aluminium crystal deformed heavily at Stage *II* at a low temperature (say, 90 K) is again deformed at an appreciably higher temperature (say, 293 K), the low-temperature hardening effect will be partially eliminated, with the appearance of a sharp yield stress peak. The phenomenon has been called *strain softening*. It has been demonstrated for this case that the dislocations locked by barriers in primary planes can bow around these barriers by cross slip.

Variations of the deformation rate can produce effects similar to those caused by temperature variations. With a higher deformation rate, there is less time for the occurrence of thermally activated

* The terms τ_T and G_T are found at a definite temperature T, and τ_0 and G_0, at $T = 0$ K. The ratio of flow stresses $(\tau_T/G_T)/(\tau_0/G_0)$ is independent of deformation at Stages *II* and *III* of the τ-γ curve; in the specialist literature, this circumstance is referred to as Cottrell-Stokes' law.

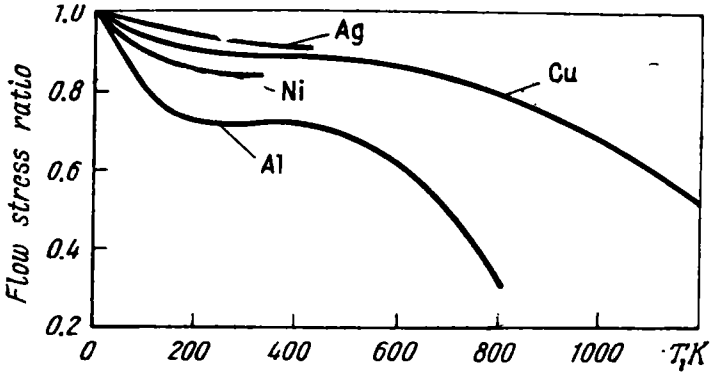

Fig. 112. Effect of temperature on the ratio of flow stresses $(\tau_T/G_T)/(\tau_0/G_0)$ for selected f.c.c. metals

processes, which is equivalent to a drop of temperature. As may be seen from the expression for the energy of thermally activated processes

$$E = kT \ln (\dot{\gamma}_0/\dot{\gamma}) \tag{98}$$

(where $\dot{\gamma}_0$ is a constant depending on the geometrical configuration of dislocations), the temperature and the shear rate $\dot{\gamma}$ have opposite effects on the activation energy. Since expression (98) is logarithmic, the rate of deformation must be changed by a few orders of magnitude to produce a sensible effect. It has been established experimentally that τ_0, τ_{II} and τ_{III} increase with increasing deformation rate; the parameter θ_{III} is however insensitive to deformation rate (Fig. 113*a* and *b*).

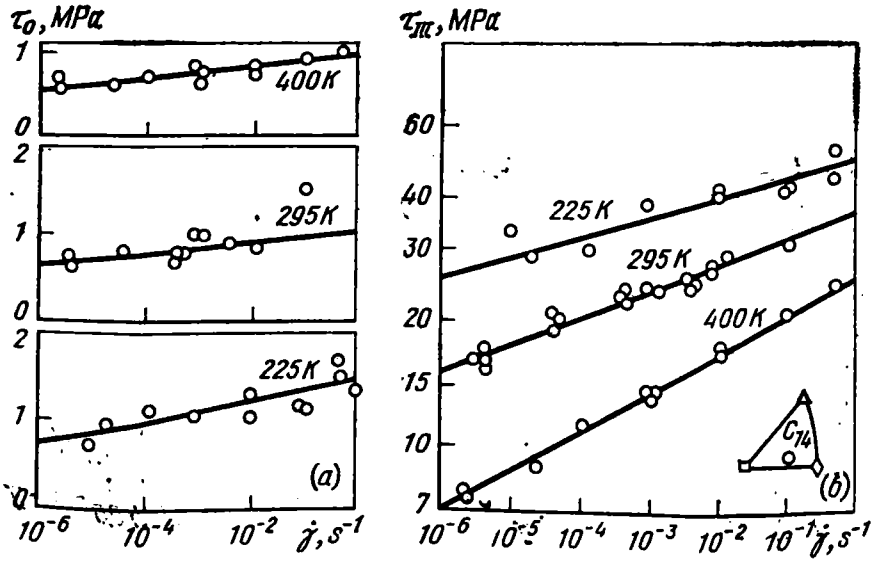

Fig. 113. Effect of rate of deformation $\dot{\gamma}$ of a copper single crystal on (*a*) τ_0 and (*b*) τ_{III} in the τ-γ curve

6. Deformation of B.C.C. Crystals

The pattern of the τ-γ curve of b.c.c. crystals is similar to that for f.c.c. crystals. It also has three stages of hardening, but all curves are obtained on crystals of high purity as regards interstitials (Fig. 114*a*).

The rate of hardening (parameter θ_{II}) at Stage *II* hardening is smaller compared with θ_{II} for f.c.c. single crystals where θ_{II} is not temperature-sensitive. In b.c.c. single crystals, on the contrary, θ_{II} depends on temperature (decreases with increasing temperature). Interstitial impurities can have an essential effect on the pattern of τ-γ curves. For instance, θ_{II} of α-iron is sensitive to crystal orientation and equals in magnitude to θ_{II} of f.c.c. crystals (Fig. 114*b*). The onset of Stage *II* in niobium corresponds exactly to the appearance of double slip and the length of Stage *I* increases on moving farther from the symmetrical [001]-[101] boundary of the stereographic triangle. In iron, for instance, all the three stages can be revealed only in 'softly' oriented crystals. A parabolic τ-γ curve is obtained with slip occurring in two slip systems (Fig. 114*b*).

The flow stress or the resolved shear stress of b.c.c. single crystals depends on temperature more substantially than in f.c.c. crystals, especially at reduced temperatures. The temperature sensitivity of flow stress can be explained by the following: (a) a more pronounced effect of temperature-dependent Peierls-Nabarro forces; (b) more efficient locking of dislocations by interstitial impurity atoms at low temperatures; the effect is eliminated at higher temperatures as impurity atmospheres are dissolved; and (c) the contribution from non-conservative movement of dislocation jogs and cross slip.

Analysis of dislocation structure in iron with 3 per cent Si has shown that edge dislocations cover appreciably longer distances than do screw dislocations, since the latter have a greater length. Screw dislocations can easily move by cross slip. A simple disloca-

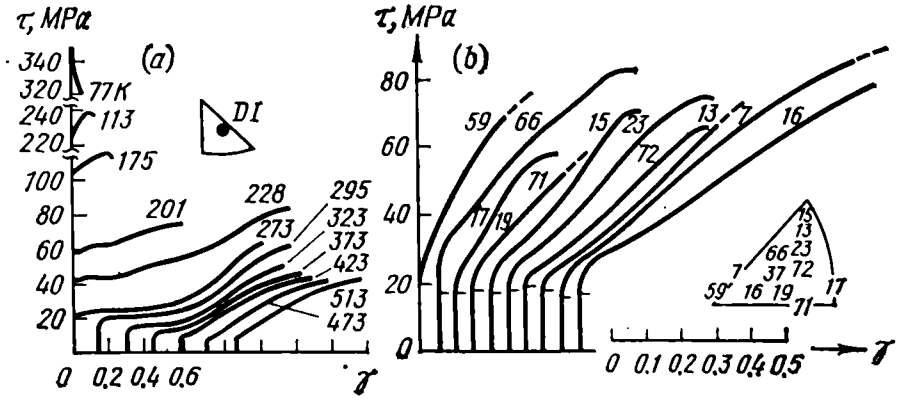

Fig. 114. The τ-γ curves for zone-refined Nb at various temperatures (*a*) and for iron single crystals at various orientations (*b*). Numbers at curves are orientations. θ_{II} depends on orientation

tion structure obtained on deformation of 1-2 per cent quickly degenerates at a heavier deformation into a cell structure in which cell walls contain tangled dislocation pile-ups whose density increases with deformation.

7. Deformation in Hexagonal Metal Crystals

In most hexagonal metals, the axial ratio, c/a, is different from that of the ideal close-packed lattice ($c/a = 1.633$), and therefore the relative packing density is different in various planes, and therefore, has a certain influence on the slip characteristics in plastic deformation (Table 10).

In hexagonal-lattice metals, slip in basal planes is predominant, especially when $c/a > 1.633$. With $c/a < 1.633$, slip in pyramidal $\{10\bar{1}1\}$ and $\{\bar{1}122\}$ planes and also in prismatic $\{10\bar{1}0\}$ planes can also occur (see Table 10).

Table 10. Packing Density in Various Planes of Hexagonal Lattice and Preferable Slip Planes in It

Metal	c/a	Packing density in planes			Observed slip planes in order of ease of activation
		{0001}	$\{10\bar{1}0\}$	$\{10\bar{1}1\}$	
Cd	1.886	1.000	0.918	0.816	(0001), $(\bar{1}100)$, $(10\bar{1}1)$
Zn	1.856	1.000	0.933	0.846	(0001), $(1\bar{1}00)$, $(\bar{1}\bar{1}22)$
Mg	1.624	1.000	1.066	0.940	(0001), $(10\bar{1}1)$, (1100)
Ti	1.587	1.000	1.092	0.959	$(1\bar{1}00)$, (0001), $(10\bar{1}1)$

In addition to slip, twinning can also take place in plastic deformation of hexagonal metals (see Ch. 2), in particular when the deformation axis makes small angles with the hexagonal axis and the basal plane. If the crystal axis is oriented close to the basal plane, the shear stress in that plane is very low, but may be quite high in the prismatic and pyramidal planes, depending on their orientation. In that case, slip in pyramidal and prismatic planes may develop in addition to twinning, though the shear stress in these planes exceeds substantially (by one or more orders) the critical shear stress in the basal plane. Thus, the behaviour of hexagonal metals in deformation and their τ-γ curves depend substantially on crystal orientation.

The effect of orientation. In his analysis of the effect of orientation on plastic behaviour of hexagonal crystals, A. Seeger divides all possible orientations into four groups (Fig. 115).

Group 1. It includes all orientations in the vicinity of the greater circle $\langle 10\bar{1}0\rangle$-$\langle 11\bar{2}0\rangle$. In this region, slip in prismatic and pyramidal planes is observed and twinning can also take place if the axial

ratio $c/a > \sqrt{3}$ (Fig. 115, *1*), as follows from the Schmid-Boas formula (see Table 7) for shear in twinning:

$$s = a\,[(c/a)^2 - 3]/(c\sqrt{3}) \qquad (99)$$

which implies that shear s changes sign at $c/a = \sqrt{3}$.

Group 2 contains all orientations close to the axis c. This group is characterized by orientational (geometric) softening (see Fig. 72), twinning for crystals with $c/a < \sqrt{3}$ and brittle fracture for those with $c/a > \sqrt{3}$ (Fig. 115, *2*).

Group 3 contains orientations near the symmetrical $\langle 0001\bar{1}\rangle$-$\langle 10\bar{1}0\rangle$ boundary where the two basal slip systems are almost equivalent which results in double slip (Fig. 115, *3*).

Group 4 includes all orientations far from the corners $[0001]$ and $[11\bar{2}0]$ and the symmetrical $[0001]$-$[10\bar{1}0]$ boundary of the orientational triangle. When oriented in this manner, crystals with the normal or elevated c/a ratio are deformed by single slip in basal planes (Fig. 115, *4*).

The pattern of the τ-γ curve, the number and extent of hardening stages, and the value of θ in each stage may be different depending on crystal orientation (Fig. 116). In crystals oriented favourably for single slip, all the three stages of hardening are usually observed (Fig. 116, curves *1* and *2*). With the crystal orientation close to the standard (Fig. 116, curve *9*) in which basal slip is predominant, the τ-γ curve consists practically of Stage *I* hardening up to deformations of 200 per cent. Stage *I* is substantially smaller or even absent in crystals oriented favourably for double slip (Fig. 116, curves *8* and *7*). All τ-γ curves of hexagonal crystals exhibit typically high deformations at fracture (γ_r = 150-280 per cent).

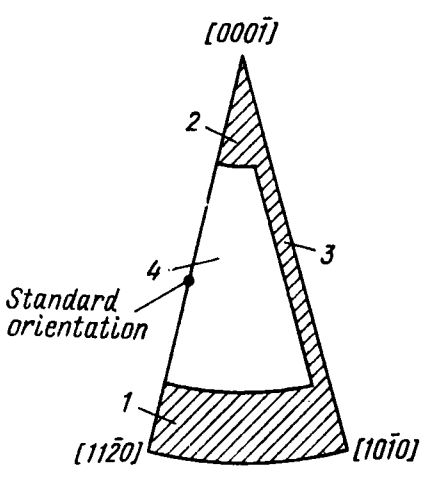

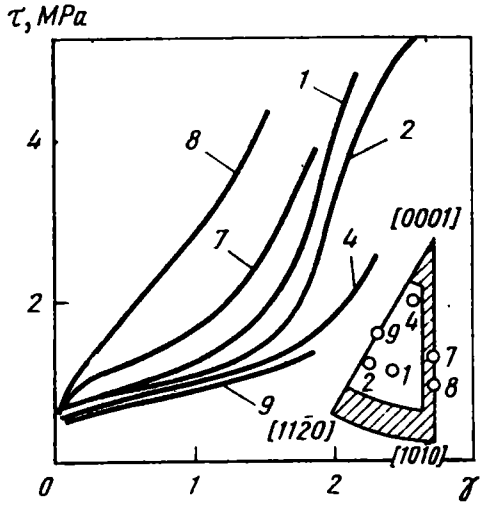

Fig. 115. (*left*) Orientation triangle for hexagonal crystals. *1-4*—orientation groups

Fig. 116. Hardening τ-γ curves for zinc crystals at room temperature. Curves of particular orientations are numbered

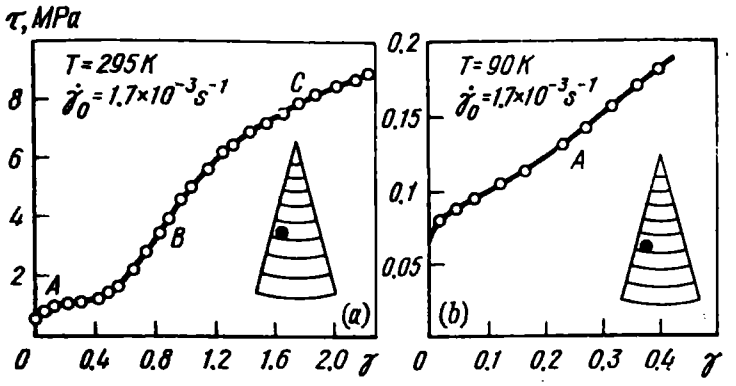

Fig. 117. Hardening τ-γ curves for zinc single crystals deformed at (*a*) room and (*b*) low temperature

Effect of temperature and strain rate on the pattern of hardening curves. In the general case, the hardening curve of hexagonal metals has all the three stages of hardening (Fig. 117). They will be called *A*, *B* and *C*, to distinguish them from Stages *I*, *II* and *III* of f.c.c. metals, since the processes occurring at these stages may differ substantially from those which take place in f.c.c. metals.

The general characteristic of Stages *A*, *B* and *C* is essentially the same as that for f.c.c. metals (see Fig. 116 and its description in the text). The behaviour of hexagonal metals in deformation has however some peculiarities. One of them consists in that the hardening at room temperature in metals having a relatively low melting point (such as Zn, Cd or Mg) occurs in parallel with the thermally activated process of recovery. Since the activation energy of self-diffusion of these metals is low*, point defects appearing during the plastic deformation can migrate at a relatively low temperature and change substantially the dislocation structure. Cobalt has a higher melting point and a higher activation energy of self-diffusion (2.94 eV). Notwithstanding this fact, Stage *A* in this metal, as in zinc (see Fig. 117), has a very large extent at any temperature.

The value of γ at Stage *A* may attain 200 per cent. The τ-γ curve in this portion is characterized by a very low hardening coefficient, $\theta_A \approx G \times 10^{-4}$, which should be attributed to slip in basal planes. Dislocations meet very few obstacles and can pass through a crystal quite easily. Only a small fraction of the generated dislocations remains in the crystal upon deformation and they can be annihilated readily by recovery annealing, which occurs without recrystallization.

The results of quantitative analysis of photographs with slip traces in basal planes have shown that the average distance δ be-

* The activation energy of self-diffusion at room temperature along the hexagonal axis (where the diffusion coefficient is anisotropic, in contrast to cubic crystals) constitutes 0.95 eV for Zn, 0.79 eV for Cd, and 1.4 eV for Mg.

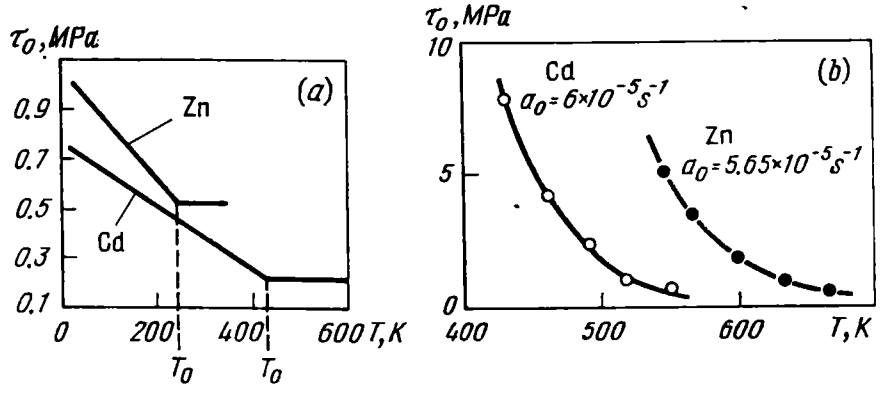

Fig. 118. Effect of temperature on critical shear stress for (*a*) basal and (*b*) prismatic slip in zinc and cadmium

tween slip lines and the length L of dislocation lines remain essentially constant at Stage A. Accordingly, the number n of dislocations emerged on the crystal surface per slip step increases linearly with γ at reduced temperatures and remains practically constant at room temperature. For Zn at room temperature, the average value of δ varies from 300 nm at $\gamma = 0$-5 per cent to 45 nm at $\gamma = 0$-16 per cent and the length of slip lines is 20 mm and 3 mm, respectively. The number of dislocations $n \approx$ 22-25.

At Stage B, the length of slip lines decreases with increasing shear from 0.56 mm (at $\gamma = 0.4$-0.5) to 0.1 mm at $\gamma = 1.8$-1.9 and the number of dislocations per step is not practically changed. The length of slip lines decreases by the law (95) given earlier for f.c.c. metals. For Zn, however, $K = 1.75 \times 10^{-2}$ cm, i.e. roughly 40 times the value of K for copper.

At Stage B, slip traces are observed to smear out, i.e. clear slip lines branch into many finer lines, the number of finer lines and the smeared out area being greater at heavier deformation.

The effect of temperature on critical shear stress τ_0. The temperature relationship for the critical shear stress τ_0 has two portions: in one, τ_0 decreases up to a temperature T_0 which is definite for a particular metal (see Fig. 118*a*); in the other, τ_0 remains constant at $T > T_0$. For pure prismatic slip in Zn and Cd crystals at room temperature, τ_0 is 10-20 times that needed for slip in the basal plane and the τ (T) relationship is somewhat different (see Fig. 118*b*). The value θ_A (T) of hexagonal metals drops quickly from its constant value at low temperatures down to practically zero at elevated temperatures, the only exception being cobalt (Fig. 119*a*). The temperature relationships for θ_B and θ_C still have not been studied properly. At high temperatures, θ_A is strongly temperature-dependent, which is evidence of an appreciable role of thermally activated processes. This is seen most clearly in a strain rate curve, θ_A ($\dot{\gamma}$)

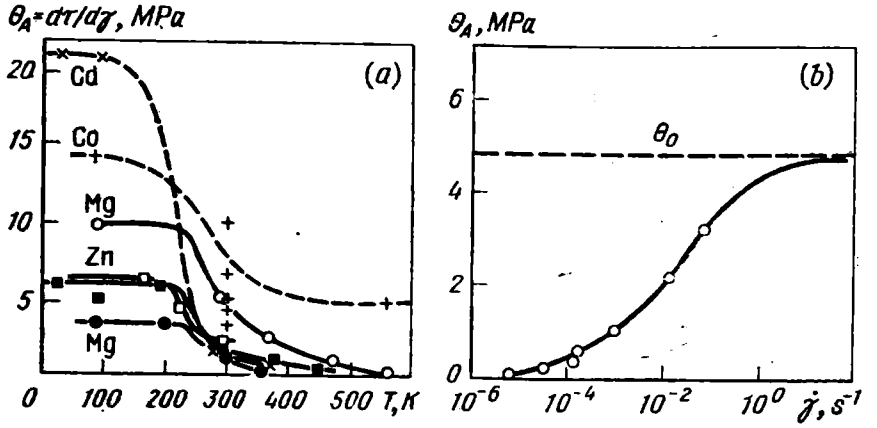

Fig. 119. Effect of temperature on θ_A in Cd, Co, Mg, and Zn (*a*) and effect of deformation rate at room temperature on θ_A in Zn single crystal (*b*)

(Fig. 119*b*). At low shear rates, recovery processes can occur in a crystal already during deformation, resulting in release of internal stresses.

Explanation of hardening effects. According to A. Seeger the deforming stress is

$$\tau = \tau_G + \tau_S \qquad (100)$$

where τ_G accounts for the processes of elastic interaction and depends on temperature only indirectly, i.e. through the elastic constant G which only slightly depends on temperature; for that reason τ_G is practically temperature-insensitive; τ_S accounts for the contribution of the processes of dislocation intersection to hardening and is strongly temperature-sensitive.

Dislocations moving in a slip plane intersect a *dislocation forest.* Acts of intersection of individual dislocations with a dislocation forest involve constriction of extended dislocations; the energy for this process depends on temperature.

The problem on which of thermally activated processes controls τ_S can be solved by using a $\tau\,(T)$ relationship. At $T > T_0$ intersection acts practically do not contribute to τ and the latter is determined only by τ_G. At $T < T_0$, τ_S increases with decreasing temperature. By producing the curve $\tau\,(T)$ further into the region of lower temperatures, we can expand the function $\tau_{T=0} = \tau_0$ into τ_{0S} and τ_{0G}. The relationship $\tau\,(T)$ is similar to that for f.c.c. metals. According to Seeger, only the processes of intersection of edge dislocations of the primary slip system with forest screw dislocations are essential in aluminium, which has a high E_{sf}/Gb ratio.

For hexagonal metals with a relatively high E_{sf}/Gb, such as Mg, Zn or Cd, this relationship is observed to be the same as in f.c.c. metals with a high stacking fault energy.

The considerations given above for the critical shear stress τ_0 are equally true of the *deforming stress* τ_d at low temperatures, i.e. when recovery cannot take place. At higher temperatures, point defects can diffuse more actively and influence the dislocation structure. For that reason, one should distinguish between low- and high-temperature hardening.

Similarly, it can be written for the total hardening coefficient: $\theta = \theta_S + \theta_G$. With low-temperature deformation, which occurs by slip in basal planes, the dislocation density of a dislocation forest remains constant ($\theta_S = 0$) and the hardening effect reduces to an increase of internal stresses. As at Stage *I* of f.c.c. metals, the hardening coefficient θ_G in hexagonal crystals should be calculated by accounting only for the elastic interaction of dislocations, since the distance δ between the operative slip planes is much smaller than the extent L of slip zones.

High-temperature hardening. In contrast to low-temperature hardening, the coefficient θ_S in this case is other than zero and may be either positive or negative (note for comparison that $\theta_G > 0$ always), depending on whether the plastic deformation increases or decreases the number and extent of thermally activated acts. Two processes are essential here.

1. When point defects coagulate, they form prismatic loops which can, on the one hand, increase the number of intersection acts and, on the other, diminish the free-path length of dislocations. The actual occurrence of these two processes has been confirmed by transmission electron microscopy.

2. Point defects promote dislocation climb, which leads to internal stress release and probably to dislocation annihilation. An evidence to this is the appearance of smeared out slip traces on heavier deformations.

Stage A. It has been established experimentally that:

1. The hardening coefficient θ_A of zinc upon deformation at Stage *A* is restored entirely at room temperature in 24 hours. A short-term recovery at Stage *A* results in a slight increase of θ_A compared with its initial value.

2. At Stage *B*, θ_B restores at room temperature only partially.

3. The temperature curves $\theta_A(T)$ exhibit a sharp drop with increasing temperature (see Fig. 119*a*).

These phenomena should be attributed to diffusion of point defects which precipitate on dislocations and cause climb of edge dislocations in which unlike dislocations can probably annihilate one another. The relationship of θ_A on strain rate, $\theta_A(\dot{\gamma})$, can be explained in a similar manner (see Fig. 119*b*): at low strain rates, point defects have enough time to annihilate on dislocations and thus cause internal stress release, whereas at higher strain rates the strength of stress fields increases so quickly that there is no time for diffusion of point defects.

In addition to the sink of vacancies to dislocations, which produces softening, other softening processes can also occur at Stage *A*, in particular those resulting from the formation of prismatic dislocation loops due to coagulation of point defects and shorter free-path length of dislocations. The relation between the two opposing processes, i.e. softening (due to dislocation climb) and hardening (due to the formation of prismatic loops), depends on the concentration of point defects and the dislocation density. With a low concentration, point defects will precipitate on dislocations; with a higher concentration of point defects and not a too high dislocation density, prismatic dislocation loops formed by point defect coagulation will be predominant. At heavier deformation, the number of prismatic loops increases so that they will inhibit the mobility of gliding dislocations and Stage *A* changes to Stage *B*.

Stage B. As has been established experimentally, the effect of prismatic loops at this stage results in a shorter free-path length of dislocations, in accordance with formula (95). The result is that $\theta_B > \theta_A$. Prismatic loops act here like Lomer-Cottrell locks in f.c.c. metals and influence mainly the temperature-insensitive component of the hardening coefficient, i.e. θ_G. For that reason, an increase of θ_B should be attributed to the action of long-range stress fields.

Stage C. At this stage, the hardening coefficient diminishes, which can be associated, as in Stage *A*, with precipitation of point defects on dislocations. The dislocation density at this stage becomes so high that point defects interact with dislocations before they coagulate. At Stage *C*, smeared out slip traces are found more often on photographs. This is an evidence that dislocations have moved onto new slip planes by their interaction with point defects. Experiments have shown that the contribution of τ_S to the deforming stress at Stage *C* is greater than at Stages *A* and *B*. At these two stages, cross slip, as well as prismatic dislocation loops, can probably contribute to τ_S.

It should be emphasized in conclusion that there is an essential difference between hexagonal and f.c.c. crystals deformed at room temperature. In zinc, for instance, recovery processes can take place already at room temperature and influence substantially the hardening effect which results mainly in a rearrangement of the dislocation structure occurring already during the deformation.

Effects of other factors on τ-γ curve. Oxide films and coatings on the metal surface can influence substantially the shape of the τ-γ curve. The rate of deformation of a zinc crystal at a constant stress increases when an oxide film has been removed from its surface, say by hydrochloric acid. On the other hand, the deformation rate will be much lower if a copper layer is applied on the surface.

Experiments with surface films have confirmed the standpoint that dislocations emerge on the crystal surface in a large number at

Stage *A*. Surface films oppose this process, which results in dislocations piling up on the metal-film interface.

Impurities can also influence the shape of the τ-γ diagram. As the concentration of impurities in zinc increases up to 0.05 at.%, the critical shear stress increases by a factor of 3.5, while θ_A may diminish by 75 per cent at room temperature and by 23 per cent at $T = 90$ K. According to R. Berner, an increase in the concentration of impurities above 0.05 at.% has no substantial effect on hardening parameters.

8. The Theories of Work Hardening

Many theories of work hardening, based on direct electron-microscopic observations of dislocations, have been proposed in recent years, but none of them has been recognized as the generally acceptable one. The reason should be sought in the fact that the processes associated with plastic deformation are highly complicated and diverse. All these theories are however important and essential, since they, firstly, can provide the basis for more purposeful experimenting; secondly, make it possible to calculate the characteristics of the τ-γ curve and answer exhaustively what the mechanisms of plastic deformation and the processes which control them are; and, thirdly, can be a scientifically substantiated basis for developing plastic working technology and high-strength materials.

During plastic deformation, dislocation movement is impeded by a number of factors, the principal among them being as follows:

(1) stress fields produced by other dislocations;

(2) boundaries of grains and sub-grains, solute atoms, particles of other phases, and surface films.

Following Seeger's view, the theoretical calculation of the hardening curve must answer the following questions.

1. What is the dislocation arrangement in a plastically deformed single crystal? Having answered this question, we can determine the critical stress at each stage of hardening.

2. How do the parameters of the original dislocation structure vary with deformation and what factors (T—temperature, γ and $\dot{\gamma}$—strain and strain rate, etc.) can cause these variations? Having answered this question, we can calculate $d\tau/d\gamma = \theta\ (T, \gamma, \dot{\gamma})$.

3 What is the stress to move a dislocation in a crystal? The deforming stress can be found in this case by integration of $\theta\ (\gamma)$ with respect to γ between the known boundary conditions: τ_0, τ_{II}, τ_{III} at each stage.

Work hardening due to long-range stress fields. The *theory of interaction of individual dislocations* (Taylor's theory, 1934) proceeds from the assumption that a long-range stress field exists around a dislocation. Other principal assumptions in the theory are as

follows: many dislocations do not reach the surface of a crystal, but interact elastically with other dislocations within the crystal and become anchored, forming a network; deformation is effected by movement of individual dislocations.

Taking that L is the average distance a dislocation moved before it was stopped and N_d is the dislocation density after a given deformation γ, the strain is given by:

$$\gamma = N_d L b \tag{101}$$

Let the distance between two slip planes be l. Then the internal stress τ necessary to force two dislocations past each other can be found, considering the stress field around an edge or a screw dislocation, by the formulae:

$$\tau = Gb/2\pi\,(1 - \nu)\,l \quad \text{and} \quad \tau = Gb/2\pi l \tag{102}$$

The spacing of the dislocations and the dislocation density are interrelated by the expression $l = 1/\sqrt{N_d}$. Substituting this in (102) and determining N_d from (101), we obtain a parabolic relationship between τ and γ:

$$\tau = kG\,(\gamma b/L)^{0.5} \tag{103}$$

The *theory of interaction of dislocation complexes* (Mott's theory) has been developed to modify Taylor's theory for more conformity with experimental evidence. In particular, the second hypothesis has been corrected. The Mott theory considers the interaction of dislocation groups emanating from a source (say, a Frank-Read dislocation source), rather than of individual dislocations. Dislocations moving in a slip plane become piled up against obstacles (sessile dislocations), resulting in an increase of the internal stress at the head of a pile-up. A dislocation pile-up consisting of n dislocations is considered as a superdislocation with the Burgers vector nb. The separation distance is $2L$ (each section of dislocation line moves a distance L), the distance between the slip planes is δ, the density of pile-up groups is $\rho = 1/(L\delta)$, and the average distance between them is

$$l = \frac{1}{\sqrt{\rho}} = (L\delta)^{0.5}$$

Substituting the value of δ for a superdislocation of strength nb, we have:

$$\tau = Gnb/2\pi\,(L\delta)^{0.5} \tag{104}$$

The plastic strain γ is found by summing up the strains from each pile-up, i.e.

$$\gamma = nbL/L\delta = nb/\delta \tag{105}$$

Substituting δ from (105) into (104), we finally obtain, as in (103), a parabolic relationship between τ and γ:

$$\tau = (G/2\pi)\,(\gamma nb/L)^{0.5} \tag{106}$$

As has been shown by experimental work, however, in most crystals the relationship between τ and γ at Stage *A* or *I* is linear, rather than parabolic. This is the principal drawback of the earlier theories of work hardening.

A. Seeger has assumed in his theory that hardening at Stage *I* or *A* is due to the long-range interaction of dislocation loops moving in the primary slip system a large distance one behind another. When the stress τ is reached, N dislocation sources per unit volume will have emitted n dislocation loops. By experimental evidence, each loop moves a large distance L through the crystal, while loops on adjacent slip planes are at a distance $\delta \ll L$.

An increment in stress $d\tau$ will result in an increase of the number of loops by dn, which will give rise to an increment in strain $d\gamma$. Using (101), we obtain:

$$d\gamma = Lb\,dN_d = Lb\,d\,(NLn) = bNL^2\,dn \tag{107}$$

From the definitions for N, δ and L, we have:

$$N\delta L^2 = 1 \tag{108}$$

so that

$$d\gamma = (b/\delta)\,dn \tag{109}$$

The generation of dn new dislocation loops will increase the back stress τ_b by $d\tau_b$ which can be determined from (102):

$$d\tau_b = \frac{Gb}{2\pi}\,d\left(\frac{1}{\delta}\right) = \frac{Gb}{2\pi}\,d\left(\frac{n}{L}\right) = \frac{Gb}{2\pi L}\,dn \tag{110}$$

When $d\tau = d\tau_b$, no further loops are generated. Substituting (109) into (110), we get:

$$\theta_I \doteq \theta_A = d\tau/d\gamma = G\delta/2\pi L \tag{111}$$

A more detailed treatment made by A. Seeger gives a similar expression

$$\theta_I = \theta_A = \frac{8G}{9\pi}\left(\frac{\delta}{L}\right)^{0.75} \tag{112}$$

Substituting typical values for δ (30 nm) and L (0.5 mm), we obtain a work-hardening rate $\theta_I \approx 3 \times 10^{-4}\,G$ which is close to the experimentally measured value.

Thus, Seeger's theory is satisfactory in describing the hardening at Stage *I* or *A*.

Seeger's theory is also fairly applicable to Stage *II* hardening where an increase in θ_{II} and in deforming stress is attributed to the

temperature-insensitive contribution from the stress fields of dislocations on primary slip planes, rather than to the component due to interactions with dislocation forest, which is temperature-dependent. Slip lines become progressively shorter as a result of increasing concentration of the Lomer-Cottrell locks. Seeger has proposed the following relationship for Stage *II*:

$$d\tau/d\gamma = \theta_{II} \approx \beta G/6\pi^2 \qquad (113)$$

where $\beta \approx 0.5$ is a constant.

As may be seen from (113), hardening is independent of the slip line length.

At Stage *III*, the deforming stress is determined by formula (97).

Hardening due to short-range stress fields. By the theory due to J. J. Gilman, a moving dislocation leaves behind dislocation dipoles (Fig. 120), each of which is essentially a pair of parallel dislocations of opposite signs. The existence of dislocation dipoles has been confirmed by electron-microscopic examination. Dislocation dipoles interact with subsequent dislocations and inhibit their movement. At heavier deformation, more dipoles are left and more strongly they inhibit dislocation movement.

D. Kuhlmann-Wilsdorf assumes in her theory that hardening is due to intersection of dislocations with dislocation tangles; these also have been detected by electron microscopy. The mechanism by which dislocation tangles form may be referred to as 'branching'.

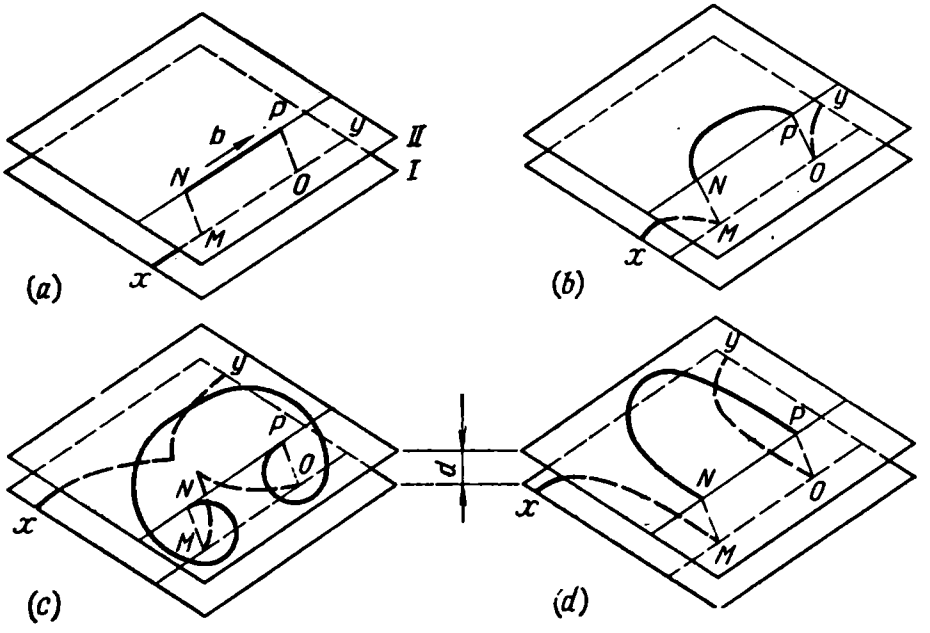

Fig. 120. Stages of double cross slip and formation of two dislocation dipoles
(*a*) passage of a screw dislocation from plane *I* to plane *II* by cross slip; (*b*) cross slip of section *NP* in plane *II*; (*c*) formation of a new dislocation loop at a considerable stress; (*d*) formation of dipoles *NM* and *PO* in cases when stress is insufficient to form a loop as in (*c*)

It consists essentially in that, as dislocations move, they leave behind the defects they have intercepted, which leads to the formation of dislocation dipoles, vacancies, and small dislocation loops appearing due to vacancy precipitation. These defects cause the originally straight dislocations to curve, the process being also favoured by cross slip. The final result is that straight dislocations become curved into tangles. Dislocation tangles are distributed non-uniformly. For that reason, dislocations at Stage *I* hardening fill in spaces between tangles, i.e. free regions in a crystal, thus producing a quasi-uniform density of tangles. Later, at Stage *II*, the density of tangles increases due to their intersection with moving dislocations and the distance between them decreases, resulting in a higher deforming stress. In this theory, Stage *III* hardening is explained by predominant occurrence of cross slip.

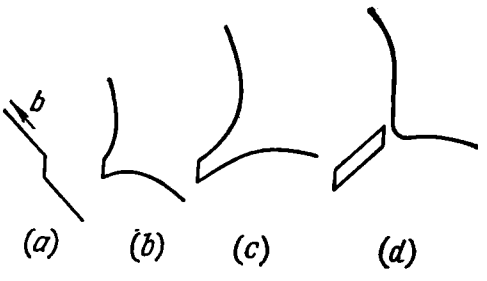

Fig. 121. Various stages of formation of a dislocation dipole by a moving jog

The theory proposed by P. B. Hirsch and N. F. Mott is based on the assumption that hardening at Stage *II* is mainly due to jogs on dislocation lines (see Ch. 2). Jogs are assumed to form by intersection of a dislocation line with a 'forest' of sessile dislocations. In f.c.c. metals, jogs on moving dislocations can lead to the formation of a row of point defects or dislocation dipoles (Fig. 121). Jogs can move along with the rest of the dislocation, provided that this is of the edge type. With screw dislocations, non-conservative movement of a jog together with the dislocation line is energetically unfavourable (see Ch. 2). In that case, vacancies and interstitial atoms are created behind a moving dislocation. Jogs reduce the dislocation mobility and thus promote hardening. As the number of dislocations increases, the density of jogs increases too, resulting in a higher deforming stress.

The theories of hardening just discussed, as also the earlier theories, establish a quantitative relationship between τ and γ, but each of them is based only on a few among the many phenomena observed experimentally in deformation processes.

The theory of temperature-sensitive deforming stress in c.p.h. and f.c.c. single crystals. Among the thermally activated processes associated with intersection of moving dislocations, the most important ones are as follows:

(1) formation of jogs on constrictions of extended dislocations;
(2) formation of jogs by intersection of dislocations;
(3) generation of point defects by jogs on moving dislocations, preferably of screw orientation.

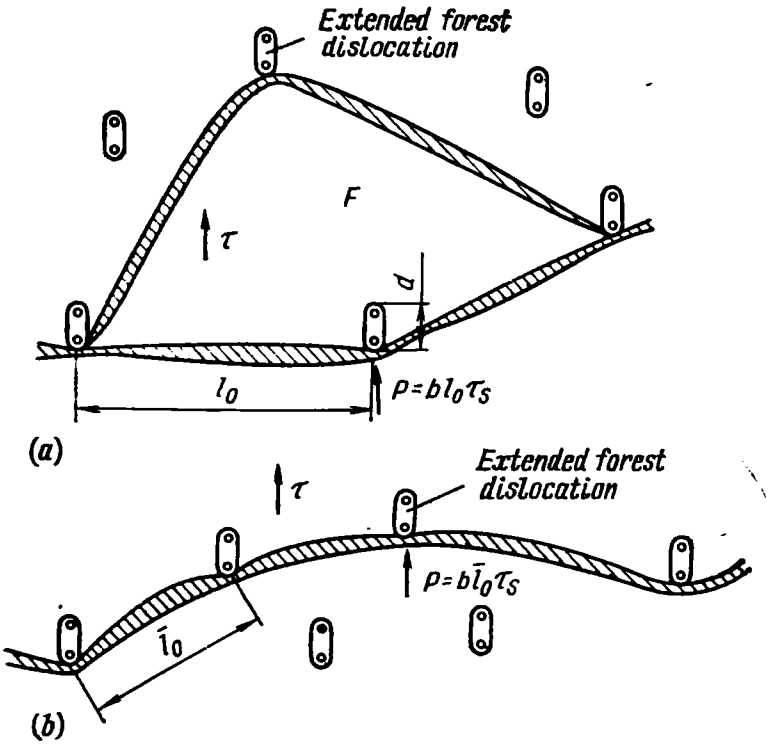

Fig. 122. Intersection of extended dislocations and main intersection parameters

The temperature relationship for the flow stress due to the processes under (1) and (2) will be discussed below and is applicable for the analysis of plastic deformation in c.p.h. and f.c.c. metals.

The total energy U necessary for a dislocation to cut through a dislocation forest is a function of the force P which acts on the dislocation in the point of intersection. The number of cutting (intersecting) acts, and therefore, the total strain rate, depend on temperature by Arrhenius' equation:

$$\dot{\gamma} = \dot{\gamma}_0 \exp\left[-U\,(P)/kT\right] \tag{114}$$

and

$$\dot{\gamma}_0 = NFbv_0 \tag{115}$$

where N is the number of intersections per unit volume; F is the area swept off by the dislocation line during cutting through under a low stress (Fig. 122*a*); b is the Burgers vector of the dislocation; and ν_0 is the frequency two orders of magnitude lower than the Debye frequency.

The force P lowers the total energy $U\,(P)$ required for cutting through. Expanding $U\,(P)$ into a Taylor series and taking only the first two terms, we obtain:

$$U\,(P) = U_0 - dP \tag{116}$$

The product dP in this equation is the work performed by the force P on a dislocation line in a unit cutting act through the dislocation forest. The activation energy U of the process thus decreases by dP. The remaining energy U_0 must be provided by thermal fluctuations (d is the average effective diameter of the 'obstacle' that is surmounted by the combined action of thermal fluctuations and applied stress).

The force P is a function of the shear stress component τ_S acting locally on the obstacle. The magnitude of τ_S is equal to the difference between the applied shear stress τ and the long-range stress τ_G due to elastic interaction:

$$\tau_S = \tau - \tau_G \tag{117}$$

Denoting by l_0 the length of individual dislocation segments (see Fig. 122*a*), the relationship between τ_S and P will be expressed by the formula:

$$P = \tau_S l_0 b \tag{118}$$

Substitution of (118) in (116) gives:

$$U = U_0 - v\,\tau_s \tag{119}$$

where $v = bdl_0$ is referred to as the activation volume of the process.

The simplest supposition according to equation (117) is that, as a first approximation, v is independent of τ_S. We then have a linear dependence of τ_S on temperature which agrees well with the experimental data (see, for instance, Fig. 118*a*):

$$\tau = \tau_S + \tau_G = \tau_G + \frac{U_0 - kT \ln \dot{\gamma}_0/\dot{\gamma}}{v} \quad \text{for } T < T_0 \tag{120}$$

and

$$\tau = \tau_G \quad \text{for } T_0 = \frac{U_0}{k \ln \dot{\gamma}_0/\dot{\gamma}} < T$$

The dislocations arrested by individual forest dislocations will be bent by a higher shear stress than that in the case considered above. This will increase the probability for a dislocation to meet a forest and decrease the effective spacing between forest dislocations. As a dislocation is curved, the distance between two intersection points decreases (Fig. 122*b*). Calculations give the following expression for the average effective spacing:

$$l_{av} = 1.5 \sqrt[3]{l_f^2 Gb/\tau_S} \tag{121}$$

where l_f is the average spacing between individual forest dislocations in any direction along the slip plane.

It follows from equation (118) that the force acting in an intersection point is:

$$P = 1.5b \sqrt[3]{Gbl_f^2\tau_S^2} \tag{122}$$

The activation energy for dislocations to cut through a forest is:

$$U = U_0 - 1.5\, db \sqrt[3]{Gbl_f^2\tau_S^2} \tag{123}$$

If the activation volume [see equation (119)] depends on shear stress τ_S, it is reasonable to introduce the differential activation volume:

$$v' = \frac{dU}{d\tau}\Big|_{T=\text{const}} = v(\tau) + \tau_S \frac{dv(\tau)}{d\tau} \tag{124}$$

Noting equation (123), we then have:

$$v' = db \sqrt[3]{Gb/\rho_f \tau_S} \tag{125}$$

In our discussion l_f is the average spacing between forest dislocations, which in turn is associated with the density of the dislocation forest by the equation:

$$\rho_f = 1/l_f^2 \tag{126}$$

Finally, the temperature relationship is found from equations (114) and (115):

$$\tau_S = \left[\frac{U_0 - kT \ln(\dot\gamma_0/\dot\gamma)}{1.5bd\sqrt[3]{Gb/\rho_f}}\right]^{\frac{3}{2}} \tag{127}$$

The temperature relationships by equations (120) and (127), which correspond to two different assumptions on the activation volume, are illustrated in Fig. 123.

Under the assumption used, τ_S is infinitely small at temperatures above

$$T_0 = U_0/k \ln(\dot\gamma_0/\dot\gamma) \tag{128}$$

At temperatures $T > T_0$, the total flow stress is $\tau = \tau_G$, i.e. the deforming stress is determined by long-range stress fields only and the temperature relationship is associated with thermal activation indirectly, i.e. through the elastic constants. The formulae derived above agree satisfactorily with the temperature relationships of the deforming stress in f.c.c. and c.p.h. metals.

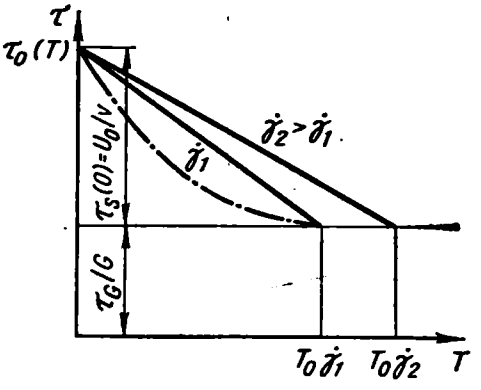

Fig. 123. Effect of temperature on deforming stress (flow stress) as determined by formulae (120) (solid lines) and (127) (dot-and-dash line)

The general concept of hardening and plastic strain resistance in single crystals. The contributions of two or more processes, each of which may be thermally activated, to the macroscopic flow stress T_S are additive, i.e. T_S can be represented in the form:

$$T_S = \tau_{P-N} + \tau_f + \tau_{im} + \tau_{dp} + \tau_{pd} \tag{129}$$

where τ_{P-N} is the resistance to dislocation movement from the crystal lattice proper, defined as the Peierls-Nabarro stress; τ_f is the resistance to movement of a gliding dislocation from other dislocations, in particular, 'forest' dislocations; τ_{im} is the resistance due to interaction of dislocations with solute impurity atoms; τ_{dp} is the resistance due to interaction with disperse particles of secondary phases; and τ_{pd} is the resistance due to interaction of dislocations with point defects.

Resistance of the crystal lattice to dislocation movement (τ_{P-N}); the opposing force to dislocation movement from the crystal lattice proper is termed the Peierls-Nabarro stress τ_{P-N}; it is due to the presence of periodic potential barriers with the period equal to the atomic spacing. Dislocations can surmount potential barriers by means of thermal activation (for instance, by the mechanism of double kinks) in the following manner. If a stress τ, which is smaller than τ^0_{P-N}, the Peierls-Nabarro stress at 0 K, is applied to a dislocation, the latter will be displaced elastically from its original position $A_0B_0C_0$ in a potential relief pit into a parallel position ABC (Fig. 124). Under the action of thermal fluctuation, the dislocation will form a dislocation loop $AB'C$ containing two kinks, AB' and $B'C$. When the size of the loop exceeds the critical, the kinks will move apart and the dislocation will jump past a new equilibrium state $A'_0B'_0C'_0$ (without load) into a next loaded equilibrium position $A''B''C''$.

The energy of formation of a double kink by thermal fluctuation without stress, $2U_{dk}$, is correlated with the Peierls-Nabarro stress τ^0_{P-N} and the energy of formation of double kink E_{dk} at a stress $\tau < \tau^0_{P-N}$.

For all kinds of barriers, $E_{dk} = 2U_{dk}$ at $\tau = 0$. The ratio $E_{dk}/2U_{dk}$ depends relatively slightly on the shape of a potential barrier and can be approximated quite well by a straight line: $E_{dk}/2U_{dk} = 1 - \tau/\tau^0_{P-N}$, which can be written in a more convenient form

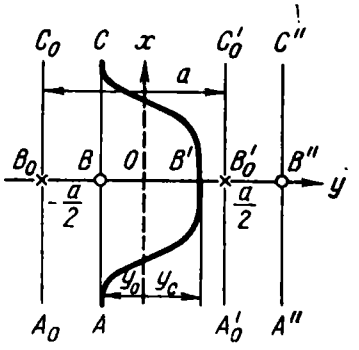

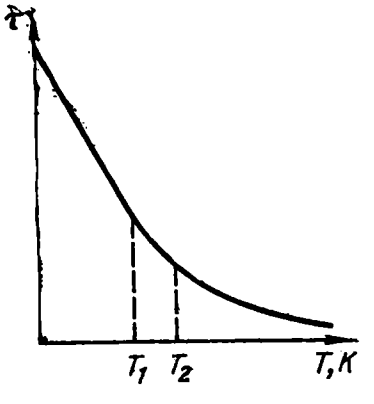

Fig. 124. (*left*) Formation of double kink on a dislocation

Fig. 125. Theoretical temperature relationship for critical shear stress

$E_{dk} = 2U_{dk} - v\tau$, where $v = 2U_{dk}/\tau^0_{P-N}$ is the activation volume.

In the formation of a double kink, a potential barrier $2U_{dk}$ can be overcome much more easily at an increase of temperature (due to thermal fluctuation), so that the process becomes possible at a stress τ lower than τ^0_{P-N}. For that reason, the Peierls mechanism gives a sharp temperature dependence for the shear stress τ which may vary from τ^0_{P-N} at 0 K to

$$\tau = [2U_{dk} - kT \ln (M/\dot{\gamma})]/v$$

where $\ln M$ is slightly temperature-dependent.

The relationship τ (T) is linear at temperatures below T_1 and exponential at higher temperatures (above T_2) (Fig. 125). According to V. I. Trefilov, these results agree quite well with experimental data for a wide class of crystals.

The main causes for dislocation locking by the crystal lattice are the ability of a screw dislocation to dissociate into partial dislocations occupying several planes of the type {112} or {110} in b.c.c. metals, and the formation of sessile dislocation configurations. In that case, an extended dislocation must constrict and then recombine and form new constrictions which can glide in the crystal lattice; all these processes require an appreciably higher dislocation energy and are therefore responsible for the high resistance to dislocation movement. The model of dissociation and recombination of screw dislocations explains satisfactorily the temperature dependence of the crystal lattice resistance to dislocation movement, the high level of flow stress at 0 K in b.c.c. metals, and a lower mobility of screw dislocations compared with edge type. Interstitial atoms can stabilize a sessile dislocation configuration and lower the probability of formation of a constriction on an extended dislocation, which leads to a higher Peierls stress at a higher concentration of interstitial impurities.

The resistance to slip due to other dislocations in a crystal, τ_f. It can be caused either by 'forest' dislocations lying in the planes which are intersected by a gliding dislocation or by the elastic interaction of the latter with other dislocations in planes parallel to the slip plane.

In accordance with theoretical and experimental results, τ_f is described satisfactorily by the relationship:

$$\tau_f = \mu G b \eta_n \sqrt{\rho}$$

where ρ is the total dislocation density; μ is a coefficient usually equal to 0.2-1.0, it can be determined experimentally.

The coefficient μ is observed to decrease with increasing temperature, since thermally activated processes are intensified at a higher temperature, so that a moving dislocation can cut more easily through a dislocation forest.

The parameter η_n characterizes the distribution of dislocations. With uniform distribution, $\eta_n = 1$. If a cell structure has formed, $\eta_n < 1$; in more distinct cell structures, it decreases more appreciably.

As has been first indicated by A. Seeger, the slip resistance τ_f is responsible for the critical shear stress in c.p.h. and f.c.c. metals being dependent on temperature. The resistance τ_f contains a temperature-insensitive component (τ_G) and a component depending on temperature (τ_S), with τ_G being usually identified with resistance to dislocation movement in parallel slip planes (long-range stress fields) and τ_S, as the resistance due to intersection of 'forest' dislocations. The movement of dislocations through a dislocation forest is facilitated appreciably by thermal activation. In b.c.c. metals, the dependence of τ_f on temperature is much weaker than that of τ_{P-N}, and, in contrast to the case with c.p.h. and f.c.c. metals, can practically be neglected.

The resistance to dislocation movement from solute impurity atoms, τ_{1m}. Three principal types of interaction between dislocations and solute impurity atoms are as follows.

1. Dislocations are mobile and solute atoms are stationary; this results in friction resistance.

2. Dislocations are stationary, while solute atoms are mobile. This results in locking of dislocations by impurity atoms. At low temperatures and under the action of an appropriate stress, solute atoms become stationary and the dislocations can break away from them and begin to glide in the crystal.

3. Both dislocations and solute atoms are mobile. This situation can result in the phenomena of dynamic strain ageing, interrupted flow in tension, etc.

The strain hardening effect of the first type is usually attributed to the influence of elements forming substitutional and interstitial solutions. The interaction of dislocations with impurities is then analysed by considering the misfit of atomic sizes which is determined by the parameter

$$r = (1/a)\, da/dc$$

where a is the lattice parameter and c is the concentration of an impurity element, and the difference of the elastic moduli which is determined by the parameter

$$R = (1/G)\, dG/dc$$

Interactions of this type can be analysed within the frame of the theory of elasticity, since they are due to long-range stress fields. Interactions of the short-range type are also possible; they are determined by electrostatic interaction between the dislocation core and solute atoms. The stress τ_{1m} in the region where it is temperature-insensitive, i.e. is determined by the long-range, can be found by the

relationship

$$\tau_{1m} = zG\varepsilon_{\alpha}^{3/2}c^{1/2}$$

where $z = 1/760$ and $\varepsilon_{\alpha} = R' + \alpha_0 r$ is the misfit parameter ($\alpha_0 = 3$ for an edge dislocation and $\alpha_0 = 16$ for a screw; $R' = R/1 + |R|/2$).

The relationship τ_{1m}-$c^{0.5}$ is satisfied quite well for metals with low concentrations of impurity elements.

The rate of formation of double kinks on dislocation lines, N, in the presence of solute impurity atoms can be found by the formula:

$$N = \omega_1 \nu_0 \exp[-U_1(\tau)/RT] + \omega_2 \nu_0 \exp[-U_2(\tau)/kT]$$

where $U_1(\tau)$ is the energy for the formation of a double kink in a crystal lattice free from impurities; $U_2(\tau)$ is the energy required to form a double kink near a solute atom; ν_0 is the frequency factor; and ω_1 and ω_2 are the probabilities of double kink formation at a distance from and near an impurity atom.

If there is at least one impurity atom near a dislocation line of length L, so that $U_2(\tau) < U_1(\tau)$, the local probability of double kink formation increases and the dislocation will move through a distance b. If at least one impurity atom is present in each next atomic row, a double kink will form near it and the activation energy of the process will be determined by $U_2(\tau)$. If $L = 10^{-4}$ cm and $b = 2 \times 10^{-8}$ cm, the required concentration of the impurity will be $b/L = 0.02$ per cent. In this case, the crystal lattice resistance (τ_{P-N}) can drop down substantially.

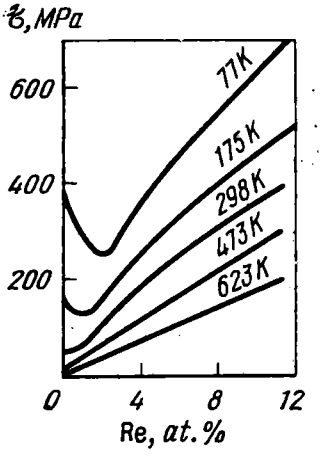

Fig. 126. Alloy softening in single crystals

In association with the process just described, it is of interest to consider the phenomenon which is referred to as alloy softening. Its essence is that the critical shear stress in b.c.c. crystals decreases on addition of a small concentration of an alloying element. Alloy softening is usually observed at room and lower temperatures, i.e. in the temperature range where the critical shear stress depends substantially on the thermally activated processes by which Peierls barriers are overcome (Fig. 126).

Strain hardening due to the presence of secondary phase disperse particles (τ_{dp}) may be either direct or indirect. The direct effect is due to immediate interaction of gliding dislocations with disperse particle barriers in the course of plastic deformation. The indirect effect is associated with the fact that disperse particles of secondary phases can increase the stability of inequilibrium structural states and raise the temperature of recrystallization. Only the direct effect

will be discussed below. In Orowan's model, dislocations move in a soft tough matrix containing hard equi-axed particles of a strengthening phase. According to Orowan, the stress is determined by the necessity to bend a dislocation between adjacent particles into a semicircle of the diameter λ (λ is the spacing between particles). Thus, $\tau_{dp} = 2F/b\lambda$, where $F = Gb^2/2$ is the linear tension. We then have: $\tau_{dp} = Gb/\lambda$.

Introducing the volume concentration of the strengthening phase, f_v, and noting that

$$\lambda = r\sqrt[3]{4\pi/3f_v}$$

where r is the particle radius, we finally obtain

$$\tau_{dp} \approx 0.6Gb^3\sqrt[3]{f_v/r}$$

Thus, the hardening effect depends substantially on particle size and less so, on the total concentration of the secondary phase.

Interaction of dislocations with point defects. The hardening effect produced by atomic (point) defects in solid solutions may be qualitatively different. Atomic defects can be divided into those which interact only weakly with edge and screw dislocations and those whose interaction is quite strong. The former produce slow hardening. As the atomic concentration c of defects increases, the hardening effect, $d\sigma/dc$, may constitute (0.1-0.01) G. On the other hand, defects which interact strongly with dislocations can produce a sharper hardening effect (roughly by two orders of magnitude).

Interstitial atoms in b.c.c. metals and interstitial atoms of copper in its own lattice can cause an appreciable tetragonality, leading to sharp hardening. On the other hand, substitutional atoms and univalent ions in b.c.c. metals and interstitial atoms in f.c.c. metals can produce only a slight hardening effect.

A number of the principal physical processes are known to be responsible for the interaction between point defects and dislocations. For instance, elastic interaction causes impurity atoms to migrate in regions of a dislocation core, which leads to the formation of segregates (Cottrell clouds). The energy of interaction between dislocations and interstitial impurities is high in b.c.c. lattices ($E \approx 0.55$ eV for carbon and nitrogen in α-iron) and low in f.c.c. lattices ($E \approx 0.08$ eV for hydrogen in nickel). In cubic-lattice metals, vacancies produce no noticeable volume distortions of the lattice, and therefore, no long-range shear stress fields. For that reason, the interaction between vacancies and dislocations in such metals is weak ($E \approx 0.02$ eV).

In b.c.c. metals, the energy of *electrostatic interaction* is relatively high and roughly equals the Cottrell energy. Impurity atoms interact electrostatically with a dislocation since the dislocation core possesses a strong electric dipole charge, which is screened off in

metals by conduction electrons and becomes effective only in close vicinity of the dislocation core.

The nature of electrostatic interaction of impurities with a dislocation is determined by the sign and magnitude of the charge of impurity ions.

Chemical interaction (Suzuki atmosphere) is due to different solubility of impurity atoms in a perfect lattice and in stacking faults on extended dislocations. This type of interaction is typical of metals with close-packed lattices and is substantially weaker ($E \approx 0.1$ eV) than the elastic and electric interactions.

A kind of interaction due to ordering can appear in the elastic stress field of dislocations (Snoek atmospheres). As is known, interstitial atoms in b.c.c. solid solutions can occupy octahedral voids corresponding to the three possible directions of tetragonality: [100], [010], and [001]. In the stress field of a dislocation, the originally equal probability of filling all the three types of voids is disturbed, since the energy of distortion depends on the kind of filling. The probability for filling voids with a low energy increases, thus leading to a certain kind of ordering. The stress required to break dislocations from a Snoek atmosphere is independent of temperature.

The resistance produced by point defects, τ_{pd}, is associated with the type of hardening and their concentration. In b.c.c. metals strengthened by interstitial impurities, τ_{pd} is proportional to $c^{0.5}$.

RECOMMENDED LITERATURE

1. Berner R., Kronmüller H., *Plastische Verformung von Einkristallen.* Berlin, Springer-Verlag, 1965.
2. Cottrell A. H., *Dislocations and Plastic Flow in Crystals.* Oxford, Clarendon Press, 1953.
3. Gorelik S. S., *Recrystallization in Metals and Alloys.* Moscow, Mir Publishers, 1981.
4. Hirth J. P., Lothe J., *Theory of Dislocations.* New York, McGraw-Hill, 1968.
5. Honeycombe R.W.K., *The Plastic Deformation of Metals.* London, Edward Arnold, 1968.
6. Kaibyshev O. A., *Plasticity and Superplasticity of Metals.* Moscow, Metallurgiya, 1975 (in Russian).
7. McLean D., *Mechanical Properties of Metals and Alloys.* New York-London, John Wiley, 1962.
8. Pavlov V. A., *Physical Principles of Plastic Deformation of Metals.* Moscow, USSR Academy of Sciences Publishing House, 1962 (in Russian).
9. *Physical Metallurgy.* Ed. by R. W. Cahn. Amsterdam, North-Holland Publ. Co., 1965.
10. Read W. T., *Dislocations in Crystals.* New York, McGraw-Hill, 1953.
11. Schmid E., Boas W., *Kristallplastizität.* Berlin, Springer-Verlag, 1935.
12. Schwindlerman L. S., Aristov V. V., Fridman E. M., *Fizika Metallov i Metallovedenie* 35, 4: 859-63 (1973).
13. *Selected Physical Aspects of Plasticity of Crystals.* Moscow, USSR Academy of Sciences Publishing House, 1960 (in Russian).
14. Shewmon P. G., *Diffusion in Solids.* New York, McGraw-Hill, 1963.
15. Trefilov V. I., Mil'man Yu. V., Firstov S. A., *Physical Principles of Strength of High-melting Metals.* Kiev, Naukova Dumka, 1975 (in Russian).

4 Plastic Deformation of Polycrystals

When deformed plastically, polycrystals behave differently from single crystals, since their grains may have diverse orientations. More than one independent slip system must be operative at a time in each grain so as not to disturb the continuity at grain boundaries. The number of slip systems may reduce (by von Mises rule, there must be five of them) if grain-boundary sliding takes place or in some particular cases of misorientation between individual grains. The presence of grain boundaries, however, always results in that simple slip cannot occur, so that deformation in every crystallite commences by multiple slip. For that reason, polycrystals are hardened more intensively than single crystals.

At temperatures $T \geqslant 0.5T_{\text{m.p.}}$ and low deformation rates, up to 20 per cent of the total plastic deformation may be associated with grain-boundary sliding. An important part can be played here by diffusion processes which facilitate essentially both *transgranular* and *intergranular plastic deformation.* At such temperatures, the concentration and mobility of vacancies increase substantially, thus enabling diffusion movement (slip) of individual crystallites.

1. Mechanisms of Grain-boundary Plastic Deformation

Grain-boundary sliding is a mechanism of plastic deformation inherent in polycrystals. The micromechanism of grain-boundary sliding has not yet been fully clarified. The hypothesis of viscous flow by slip along grain boundaries, which is based on the theory of amorphous structure of boundaries and on experiments on internal friction, has found no proper confirmation.

The equi-cohesive temperature, i.e. the temperature at which the strength of boundaries is the same as that in the bulk of grains, constitutes roughly $0.4T_{\text{m.p.}}$. Grain boundaries are somewhat more stronger than the bulk of grains at $T < 0.4T_{\text{m.p.}}$ and less so, at $T > 0.4T_{\text{m.p.}}$. It then follows that the atomic bond forces in boundaries (and therefore, atomic spacings) must be of the same order as

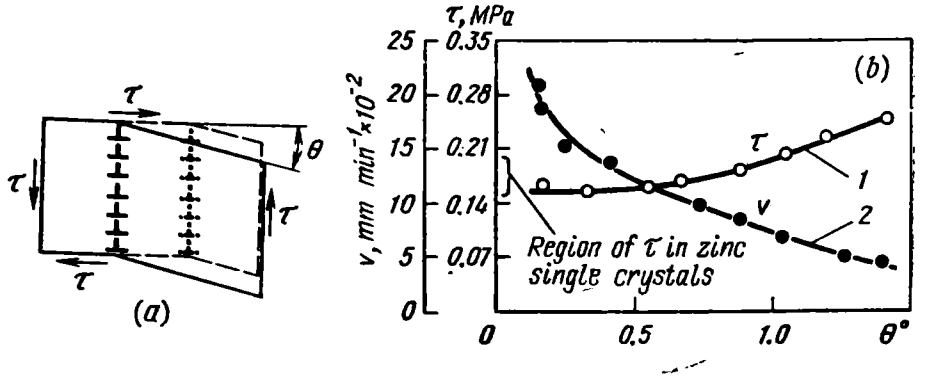

Fig. 127. Movement of a low-angle grain boundary under the action of stress τ
(*a*) movement of a boundary having one degree of freedom; (*b*) effect of misorientation angle θ on stress τ and rate of boundary movement *v*

in the bulk of grains. In view of this, the modern theory of grain-boundary processes of plastic deformation is based on modern concepts of grain-boundary structure which agree well with the experimental data.

Stress-induced movement of grain boundaries. Grain-boundary sliding. There are two alternative mechanisms of movement of low-angle tilt boundaries under the action of stress: (1) by simultaneous movement of all dislocations of a boundary in their slip plane and (2) by dislocation movement normally to the slip plane (dislocation climb), which is associated with diffusion displacements and 'viscous' behaviour of boundaries.

Both processes result in that a boundary moves as a whole parallel to its original position, i.e. a macroscopic deformation $\gamma = \theta$ is produced (Fig. 127*a*). The former process, however, is athermal, while the latter can occur only at elevated temperatures. As θ increases, the critical stress increases too (Fig. 127*b*). If a stress τ is operative in the slip plane in the direction of slip, the force acting per unit length of a dislocation is τb and is directed normally to the boundary. Summation of all the forces gives the pressure P exerted on the boundary, which is the product of τb by the dislocation density θ/b. The pressure $P = \tau\theta$ tends to move the boundary by simple slip (Fig. 127*a*). The work performed by the stress τ per unit of the volume described by the boundary in its movement is also equal to $\tau\theta$. As the operative stress changes its sign, the direction of movement of boundaries varies and the critical stress reduces. This phenomenon, similar to the Bauschinger effect in single crystals, is associated with the fact that the reverse movement of dislocations along the paths they have passed can be effected more easily than the direct movement. At a constant stress, the rate of boundary migration is higher at a smaller misorientation angle (Fig. 127*b*).

With a boundary having two degrees of freedom (see Fig. 47), dislocations move away from it by pure glide in their slip planes.

In that connection, some particular types of boundary migration are possible. For instance, if $\varphi = 45°$ and all ⊥ dislocations in the portion CEA of the crystal move rightwards and ⊢ dislocations in the portion CBA move upwards by the same distances, the whole boundary will migrate rightwards by pure slip.

Uniform migration of boundaries with two degrees of freedom is possible without their splitting not only due to glide of dislocations moving in their planes, but also due to a normal displacement of dislocations away from their planes, i.e. dislocation climb which is assisted by diffusion processes. A moving dislocation is then a source or sink of vacancies, so that atoms will move from the edge of the constricting plane to the growing extra-plane due to diffusion of vacancies in the opposite direction. The successive positions of a grain boundary determine: (1) the amount of macroscopic deformation; and (2) the driving forces for diffusion of vacancies from one series of dislocations to another. This complicated uniform movement of dislocations, assisted by diffusion processes, will result in a lower rate of boundary migration which depends on the structure of boundaries proper, i.e. on misorientation angles between grains. These effects, i.e. the reducing rate of boundary migration and its dependence on misorientation angle, explain the viscous properties of grain boundaries. According to W. T. Read, the driving force of diffusion in this type of grain boundary migration is the stress applied, i.e. the pressure exerted on the boundary which, as in the previous case, is $P = \tau\theta$.

Boundaries with low angles θ are less mobile than high-angle ones, since the latter have a higher concentration of vacancies. The rate of slip on an arbitrary high-angle boundary is roughly 10 times that on a low-angle one.

A stress τ applied to a grain boundary increases the flow rate in its direction by $\tau n a \omega$, where a is the length of an elementary shear and ω is the area per atom. With certain assumptions, the rate of slip can be described by the formula:

$$v = 2\nu\alpha \exp\left[-\frac{nL(1-T_{\text{m.p.}}/T)}{kT}\right] \sinh \frac{an\omega\tau}{2kT} \tag{130}$$

where ν is the frequency of atomic oscillations.

With low stresses (as in creep), expression (130) takes the form:

$$v = \nu a^2 n \omega \tau \exp\left(nL/kT_{\text{m.p.}}\right) \exp\left(-nL/kT_{\text{m.p.}}\right)/kT \tag{131}$$

Grain-boundary sliding becomes especially noticeable at temperatures above $0.5T_{\text{m.p.}}$. Most experiments relate to grain-boundary sliding in creep; their results are represented in the coordinates of grain-boundary displacement—time in Fig. 128. The curves have an interrupting, rather than smooth, pattern (see for instance, curve I in Fig. 128), which is indicative of substantial variations of the shear rate on a boundary. The relative shear can be measured by

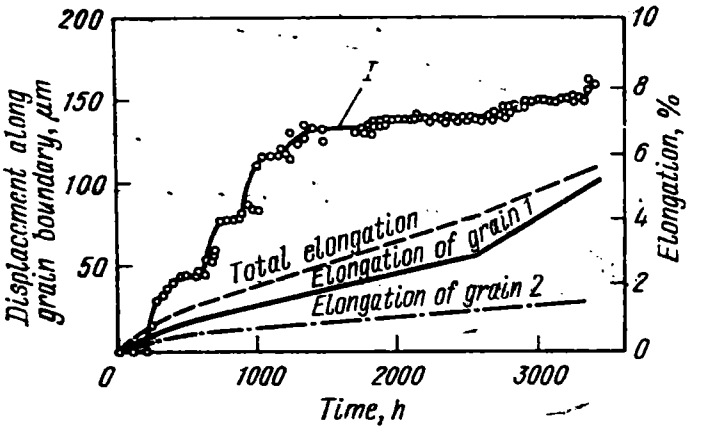

Fig. 128. Time variations of displacement along grain boundary in aluminium bicrystal ($\tau = 0.70$ MPa, $t = 300$°C) (curve *I*). The elongation of each grain in the bicrystal and the total elongation (including the contribution of the grain boundary which, as may be seen, is quite insignificant, up to 6%) are given as a percentage

means of reference marks made on the surface of a bicrystal. A direct logarithmic relationship of the shear rate in the initial portion of the creep curve on $1/T$ makes it possible to calculate the activation heat of macroshear depending on misorientation angle θ. The activation heat of macroshear increases as the angle θ increases from 0 to 90°. It has also been established that the activation heat of migration diminishes with increasing θ.

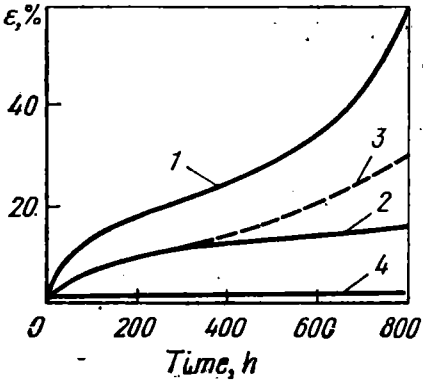

Fig. 129. Strain components in creep of aluminium at t=200°C (according to D. McLean)
(*1*) total strain; (*2*) strain due to coarse slip; (*3*) strain due to fine shears between coarse slip bands; (*4*) strain at grain boundaries

Grain-boundary sliding can be observed on the surface of microsection of deformed metal as a characteristic relief of recesses and ridges formed along grain boundaries. Displacements of grains normal to the microsection surface can be measured by means of an interference microscope, after which the plastic deformation caused by intergranular displacement can be calculated. The results of such measurements (Fig. 129) suggest that the contribution of grain-boundary sliding to the total deformation should be relatively low, not above 10 per cent, i.e. $\varepsilon_{gb}/\varepsilon_{\Sigma} \approx 0.1$, and depends on misorientation angle θ, temperature, deformation rate, applied stress, and grain size. For instance, displacement is higher, and $\varepsilon_{gb}/\varepsilon_{\Sigma}$ is higher too, at a smaller grain size and higher stress for a given temperature (Fig. 130*a*). With an increase of temperature, $\varepsilon_{gb}/\varepsilon_{\Sigma}$ can increase due to diffusion processes up to 0.3 (Fig. 130*b*). D. McLean has de-

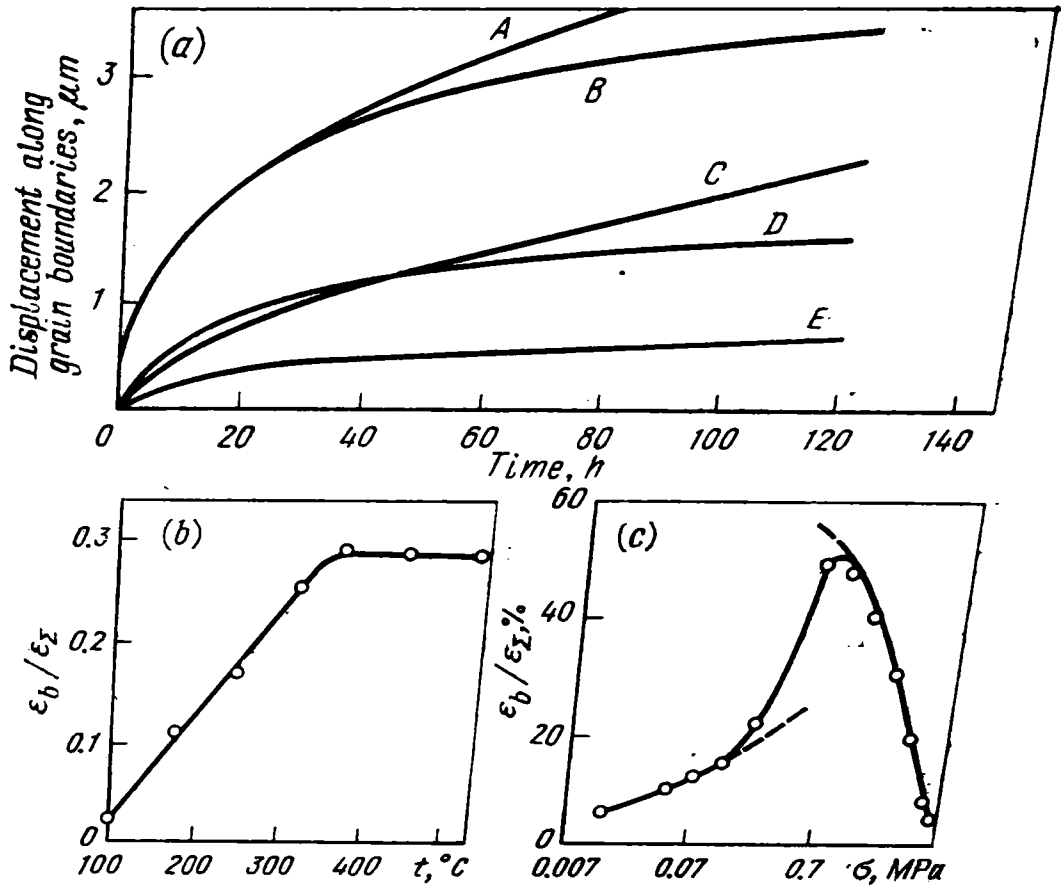

Fig. 130. Effect of various factors on grain-boundary deformation
(*a*) time curves of displacement along grain boundaries in aluminium (*A*, *D* and *E*—4.5 grain/mm, σ = 11.5 MPa, 7.7 MPa, and 5.25 MPa, respectively; *B* and *C*—σ = 7.7 MPa for 1.0 and 9.2 grain/mm, respectively); (*b*) effect of temperature; (*c*) effect of stress σ at t = 300°C on the fraction due to grain-boundary sliding

monstrated by theoretical analysis that the contribution of grain-boundary displacements to the total deformation cannot be more than 33 per cent. It can be higher only in cases when the deformation process is associated with boundary migration. As the flow stress increases, the ratio $\varepsilon_{gb}/\varepsilon_\Sigma$ first increases (Fig. 130*c*) and then diminishes. This is an evidence that at least two mechanisms can be responsible for relative displacement of grains along boundaries. The results shown in Fig. 130*c* are indicative of limited development of grain-boundary deformation in plastic working processes performed at high stresses and high deformation rates.

It has been established for a number of metals that there is a linear relationship between grain-boundary sliding and total deformation (Fig. 131). Noting that intragranular deformation is the greatest component of total deformation, the considerations given above suggest the following. Suppose that there is a system of interfaces (slip planes) in which shear is allowed and another system of such planes possessing different properties (grain boundaries). The ratio of shears in these two systems should then be perfectly defi-

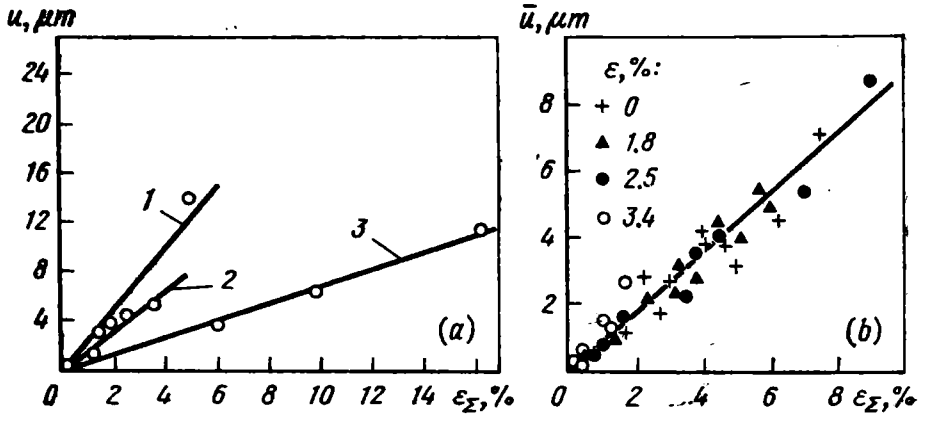

Fig. 131. Effect of ε_Σ on average displacement u on grain boundaries in nickel (*a*) at $t = 800°C$ and various stresses: *1*—20 MPa; *2*—30 MPa; and *3*—40 MPa; (*b*) at $t = 700°C$ and $\sigma = 25$ MPa in specimens with different amount of prior deformation

nite and constant (in view of the linear relationship in the coordinates: displacement—total deformation ε_Σ in Fig. 131) to retain continuity of the metal and continuity of stress and strain. For that reason, slip and deformation of grains in polycrystals are interrelated. McLean has proved that the processes which inhibit shear deformation also produce a retarding effect on grain-boundary sliding. Since the contribution of transgranular deformation is greater, shear in grains seems to be the process that controls total deformation. Experiments have shown that the relative displacement is smaller for grains which have been strengthened more appreciably by prior deformation. Should the processes of deformation of grains and of their relative displacement be independent of each other, the relative deformation of prestrained grains due to grain boundaries would increase. As may be seen from Fig. 131*b*, however, the ratio s/ε_Σ is independent of prior deformation. This suggests the reasonable conclusion that grain-boundary sliding is the result of transgranular deformation, but not the other way.

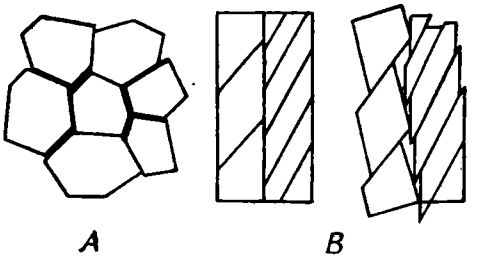

Fig. 132. Two models (*A* and *B*) of a polycrystal

The role of accommodation and transgranular flow in grain-boundary plastic deformation. Let us consider the behaviour of two extremely idealized models (Fig. 132). Suppose that a polycrystalline metal is described by a set of hard polyhedra which are capable only of 'rigid' sliding along their boundaries. In this model (let it be *A*) with hard polyhedra, transcrystalline slip and variations in the shape of polyhedra are impossible. Suppose, on the contrary, that

only transcrystalline slip is allowed in another model (*B*); with grain-boundary sliding being excluded. Analysis of simple two-dimensional versions of these models can show (see Fig. 132) that, with the assumptions made above, slip is possible in neither of them. For model *A*, an additional strain component normal to the boundary is required; in model *B*, slip is impossible unless grain-boundary sliding is allowed.

These models show that transcrystalline and intercrystalline slip cannot be treated as unrelated processes contributing independently to the total deformation. When each of the models is analysed separately, it becomes clear that there is a definite linear correlation between grain-boundary sliding and transgranular slip, i.e. grain boundaries should displace in order to accommodate themselves to slip within grains. This exactly is the result obtained experimentally by D. McLean (see the previous section).

Grain boundaries in polycrystals are not flat, i.e. sliding is effected over rough surfaces (Fig. 133*a*). Protrusions on the surface, even of atomic size, preclude direct grain-boundary sliding, since this would require a high stress to shear off them. For that reason and as has been indicated in the previous section, grain-boundary sliding is not an elementary act of plastic deformation. Its realization depends on the probability of development of accommodation processes which can make a boundary flat like a crystallographic slip plane; only after that, grain-boundary sliding will be allowed.

In turn, accommodation is controlled by: (a) elastic displacements; (b) diffusion mechanisms of plasticity; and (c) transgranular dislocation glide.

At low stresses and temperatures, only elastic accommodation of boundary sliding is observed; it can occur unless the internal stresses counter-balance the external ones (Fig. 133*b*). At low stresses and a high temperature, diffusion accommodation is possible: stresses on a boundary cause diffusion flow which makes the boundary flat (Fig. 133*c*). At high stresses, accommodation can result from

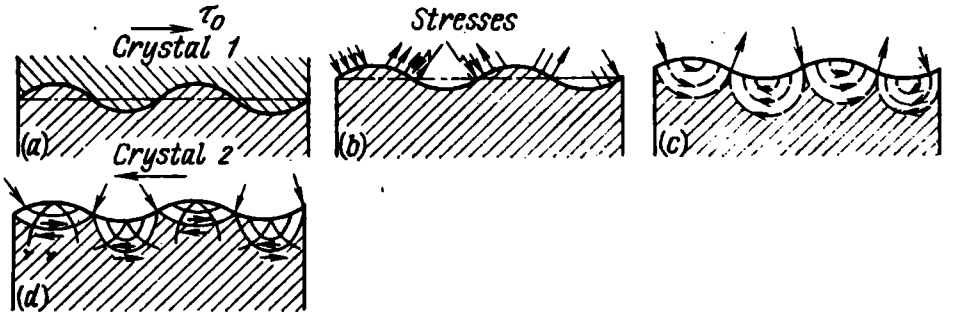

Fig. 133. Scheme of grain-boundary sliding over rough surface of a bicrystal (*a*); elastic accommodation (*b*); diffusion accommodation in the bulk or on grain boundary (*c*); and plastic accommodation due to intergranular slip (*d*)

plastic deformation, i.e. from slip and climb of dislocations at the two sides of a boundary; this ensures removal of substance from some portions of the boundary (protrusions) and addition to recesses (Fig. 133*d*).

With plastic accommodation, the rate of grain-boundary sliding depends on the deformability and structure of grains, since the process can result in work hardening. It is impossible to predict numerical parameters (stress and deformation temperature) which would make it possible to differentiate between the first and the second mechanism of plastic accommodation. Under particular real conditions, both mechanisms may be simultaneously operative. It is also not always clear which of the processes controls the rate of slip: whether accommodation or grain-boundary sliding.

As has been demonstrated by M. F. Ashby, sliding and migration of arbitrary grain boundaries are closely interrelated and proportional, since only then slip is possible without variations in the structure of boundaries. With grain-boundary sliding on a high-angle boundary, migration is the process which ensures continuous accommodation (flattening) of the boundary on atomic scale by movement of grain-boundary dislocations. This type of migration should be distinguished, however, from the migration occurring in plastic accommodation (observed in local plastic deformation) which is not directly associated with grain-boundary sliding. This irregular migration can inhibit grain-boundary sliding, since it can prevent a boundary to become flat in the course of slip. To effect continuous sliding over the surface of a grain boundary, an operative source of grain-boundary dislocations is essential. It is supposed that Frank-Read dislocation sources operating on a grain boundary can serve as such. Spiral formations detected on grain boundaries are essentially sources of grain-boundary dislocations which multiply by climb, rather than by slip. Grain-boundary dislocations can also form due to the interaction of lattice dislocations with structural defects in a boundary.

The model of grain-boundary sliding described above is based on really established facts, for instance, on existence of grain-boundary dislocations and jogs. This is, however, not the sole model of grain-boundary sliding. In other models, grain-boundary sliding is attributed to processes of dislocation climb in boundary regions and diffusion creep.

It is probable that different mechanisms of grain-boundary sliding can be operative under various structural and temperature-rate conditions of deformation. It should be emphasized that grain-boundary sliding, whatever its micromechanism may be, is not an elementary act of plastic deformation, but the result of a certain combination of other elementary processes: plastic accommodation; slip along grain boundaries matched with boundary migration effected by dislocation slip and climb; and diffusion creep.

Since the deformation of individual grains in a polycrystal must be continuous and matched with that of other grains, other deformation mechanisms must be operative in addition to grain-boundary sliding. This can well be illustrated by Fig. 134. Suppose that the stress applied causes a grain boundary AB to slide a distance Δ. The sliding contributes to grain-boundary deformation (ε_{gb}), but causes stress concentration at point B. To relax this stress, plastic flow should develop in the adjacent grain along BC (ε_g). This means in reality that, as a dislocation reaches point B, it must cause slip in the adjacent grain in the direction to C, then along CD and so on (this is what is called the relay-race mechanism). This movement is possible if the dislocation is capable both of gliding and climbing, since BC and CD are not necessarily parallel.

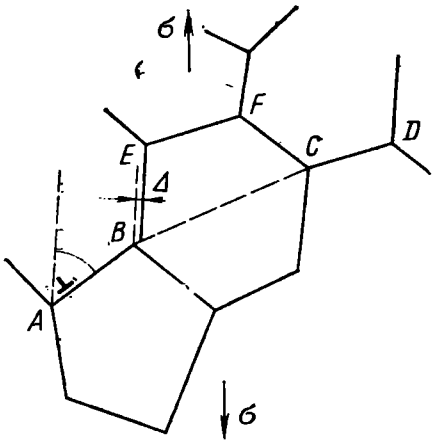

Fig. 134. Scheme of combined plastic deformation by grain-boundary sliding and intragranular slip

Since however the distance for climb is small, $\varepsilon_{gb}/\varepsilon_g = AB/AC = 1/3$ (hexagonal grains of equal size are considered in the model). If we consider another possibility, say grain-boundary sliding along $BEF \ldots$, the $\varepsilon_{gb}/\varepsilon_g$ ratio will be equal to 0.6, i.e. the contribution of grain-boundary sliding to total deformation cannot exceed 60 per cent. The correlation between grain-boundary deformation ε_{gb} and accommodation sliding (in terms of displacement) can be expressed as

$$\varepsilon_{gb} = 0.5 s_v g \tag{132}$$

where s_v is the relative surface of grain boundaries participating in sliding.

The deformation rate will then be found as

$$\dot{\varepsilon}_{gb} = 0.5 s_v \dot{g} \tag{133}$$

where $\dot{g}$ is the rate of transgranular slip.

Since $s_v = 2\sqrt{\pi}/d$, where d is the size of grains, we finally have:

$$\dot{\varepsilon}_{gb} = \dot{g}\sqrt{\pi}/d \tag{134}$$

In the case considered, diffusion movement of atoms, or diffusion-gliding movement of dislocations, is essential to ensure matched deformation and prevent fracture. McLean has demonstrated that his accommodation movement causes plastic deformation in the direction of the force applied. With these conditions satisfied, one

can expect that plastic deformation will be practically unlimited and occur at a rather high rate, depending on grain size. It should be noted that grain-boundary sliding can contribute appreciably to the total deformation only at sufficiently high temperatures at which the diffusion mechanisms of deformation can usually operate too.

In the Herring-Nabarro model (see Fig. 97), the resulting deformation rate $\dot{\varepsilon}$ ensured by a flow of vacancies is

$$\dot{\varepsilon} = C_1 \frac{D_v \Delta\mu}{kTd^2} = 2C_1 \frac{D_v \sigma b^3}{kTd^2} \tag{135}$$

where D_v is the coefficient of volume diffusion, and C_1 is a constant roughly equal to 10; b is the lattice parameter; and d is the grain diameter.

This expression has been derived under the assumption that a flow of vacancies passes through a grain. In some cases, the main contribution to deformation may be due to a diffusion flow along grain boundaries. According to Coble's model of diffusion creep, the rate of deformation is

$$\dot{\varepsilon} = C_2 \frac{D_{gb}}{kT} \frac{\Delta\mu}{d^3} = \frac{2C_2 D_{gb} b^3 \omega \sigma}{d^3 kT} \tag{136}$$

where D_{gb} is the coefficient of grain-boundary diffusion; ω is the effective width of a boundary; and C_2 is a constant roughly equal to 30.

For the general case when diffusion creep can take place both along boundaries and in the bulk of grains, we have:

$$\dot{\varepsilon} = 20 \frac{\sigma \Omega D_v}{kT d^2} \left(1 + \frac{\pi \omega D_{gb}}{d D_v}\right) \tag{137}$$

where Ω is the volume involved in deformation.

Since a polycrystal contains many grains, their shape must vary in a matched manner as diffusion creep takes place. Diffusion creep in polycrystalline materials can result in grain-boundary sliding which then appears to be an accommodation process. Diffusion creep and grain-boundary sliding can also be interrelated processes: when diffusion creep develops, grain-boundary sliding can be regarded as an accommodation process and, on the contrary, as grain-boundary sliding proceeds, diffusion creep becomes an accommodation process for it. In cases when the rate of plastic deformation is limited by the rate of diffusion creep, it is determined by formula (137). It may however be less than the value given by the formula, since grain boundaries may cease to play the part of perfect sources and sinks of vacancies. A combination of diffusion creep and grain-boundary sliding represents a deformation mechanism which can principally ensure a heavy deformation without fracture.

Plastic flow can be realized in various ways. Without knowledge of the operative mechanisms of plastic deformation, it is practically impossible to conclude reliably on the best utilization of the plasticity of a metal. The situation is especially complicated in hot plastic working, when more than one deformation mechanism or their combinations may be operative. The physical theory of plasticity establishes the limiting parameters (structure, temperature-rate conditions of deformation) at which one mechanism or a combination of mechanisms may be observed to change to another mechanism (or combination).

Under these circumstances, the decisive role may be played by experimental studies into the mechanisms of deformation of metals under various conditions. Such studies can clarify the effect of external (temperature-rate conditions of deformation) and internal factors (microstructure, alloying additions) on the operation of various deformation mechanisms and thus help in selecting the conditions of plastic working in which the plastic properties of a metal can be utilized most fully.

2. Effect of Grain Boundaries on Deformation Process and the Pattern of τ-γ Curve

If an increasing tensile stress σ is applied to a polycrystal, plastic deformation will occur initially in the most favourably oriented grains, i.e. in those with the highest resolved shear stress in one of the slip systems. Other grains will not be deformed beyond the elastic region. Thus, the strain distribution becomes non-uniform, with some grains being deformed only elastically and others having local microdeformations of the order of $\varepsilon_m = 10^{-4}$-10^{-5}.

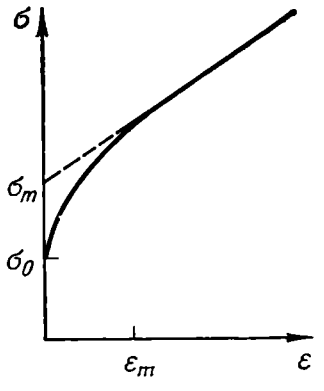

Fig. 135. Microdeformation in a portion, $0 \geqslant \varepsilon \geqslant \varepsilon_m$, and macroscopic elastic limit σ_m of a polycrystal

Let the stress at which all grains are plastically deformed be conditionally called the microscopic elastic limit σ_m. Grain boundaries in a polycrystal restrict easy glide and thus raise the microscopic elastic limit as compared to the critical stress in a single crystal, and therefore, increase the work hardening coefficient. At stresses below σ_m, local plastic microdeformations may be observed, with individual grains being gradually involved in the process of plastic deformation. At $\sigma < \sigma_m$, deviations from Hooke's law take place.

At the stage of microdeformation, the σ-ε relationship is usually parabolic (Fig. 135). The length of the parabolic portion depends on grain size, i.e. $\varepsilon_m \approx Ad^3 (\sigma - \sigma_0)^2$, where A and σ_0 are roughly constants; σ is the applied stress; and d is the average grain size.

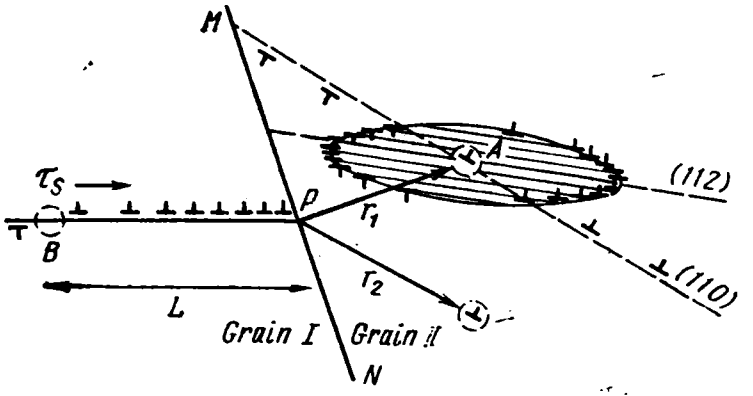

Fig. 136. Initiation of slip (or twinning) in an adjacent grain of polycrystal in a certain point *A* at distance r_1 from the top *p* of a flat dislocation pile-up

At deformations ε above ε_m, contact on grain boundaries is retained. It then follows that individual crystallites are deformed in a matched manner, i.e. with the conditions of *microscopic* and *macroscopic continuity* being satisfied.

The first condition of continuity, i.e. *microscopic continuity*, consists essentially in the following. When an external force is applied (at not too high a temperature), a dislocation cannot move beyond a grain by forming a jog, since this is prevented by an adjacent grain. Dislocations can only approach grain boundaries. Thus, dislocations from an operative dislocation source *B* in grain *I* (Fig. 136) move close to a boundary of grain *II* (which is favourably oriented for slip), are arrested there and produce internal stresses in that and neighbouring grains which oppose the stress applied and thus harden the metal efficiently.

As the stress applied increases further, more dislocations concentrate at the boundary *p*. The local stresses produced by them increase to a level sufficient to initiate another dislocation source *A* in an adjacent grain (see, for instance, grain *II* in Fig. 136). In the first place, this will induce the operation of sources whose dislocations come to the grain boundary roughly in the same place as the dislocation group in grain *I*.

Thus, dislocations cannot move directly from one grain into another (as has been shown by F. R. N. Nabarro, the shear stress required for this is very high, of the same order as the theoretical shear resistance), so that slip can propagate from one grain to another only by initiation of dislocation sources in an adjacent grain *II* under the action of stress concentration at the tip of the slip band in grain *I* (see Fig. 136). In that case, the stresses produced by the dislocation pile-up in grain *I* are neutralized most efficiently. As this stress is reached, the shear intersects the boundary and the stress field around the dislocation pile-up is relieved (stress relaxation), thus providing favourable conditions for further plastic deformation. In the diagram shown in Fig. 136, grain boundaries serve as specific barriers

for dislocation movement, so that the case considered is referred to as the barrier effect of grain boundaries, or *barrier work hardening.*

In single-phase b.c.c. and f.c.c. polycrystals, slip in adjacent grains can occur relatively easily, since among many slip systems in adjacent grains there is always one with a favourable orientation for slip. The barrier effect in such metals is not operative until the stress is raised to a rather high level. The difference in work hardening and plasticity of single and polycrystals will not be very sharp. Barrier work hardening is essential for hexagonal metals deformed at room temperature. In this case, there is only one plane for easy glide and only few of surrounding grains are oriented favourably relative to the stress applied. For that reason, hexagonal single crystals oriented for basal slip are work-hardened slowly up to rather heavy deformations, whereas polycrystalline specimens (Fig. 137) are hardened much more quickly. The plasticity of polycrystals is substantially lower than that of single crystals. At higher temperatures, slip in other planes, in addition to the basal plane, becomes possible, so that polycrystals exhibit greater plasticity and lower tendency to work hardening.

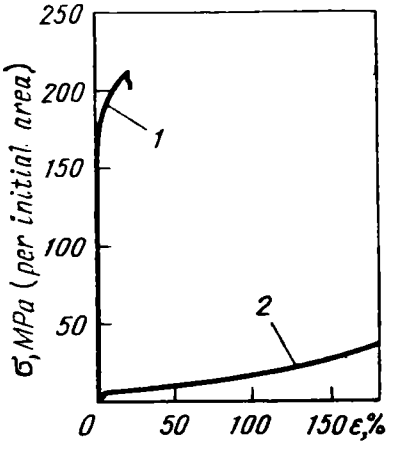

Fig. 137. The σ-ε curves of (*1*) polycrystal and (*2*) single crystal of magnesium. Here, σ is a conditional stress related to the initial cross-sectional area

In a metal containing a hard, practically undeformable phase, shear can never cross a grain boundary; barrier work hardening results here in an appreciable increase of stress.

A typical characteristic of barrier work hardening is that grain boundaries produce short-range forces acting on a dislocation. A. H. Cottrell and D. McLean refer to the calculations according to which a unit dislocation acted upon by a shear stress $10^{-5}G$ is arrested at a distance of five atomic spacings from a grain boundary. It should be noted that a dislocation at a grain boundary is acted upon by two oppositely directed forces. On the one hand, the dislocation is attracted to the boundary, since atoms here are far from being in perfect order, so that the misfit energy of the boundary will not change much by distortions present in the dislocation core. On the other hand, it is repulsed by the opposing forces on the other side of the boundary in an adjacent grain, which are due to different orientations of the two grains separated by the boundary.

Under the action of a shear stress τ, the dislocations will be retained in front of the boundary at a distance s, with $\tau = G(\beta/s)^4/6\pi^2$, where β is of the order of atomic spacing.

The second condition of continuity, i.e. *macroscopic continuity*, can be explained as follows. Upon deformation, adjacent grains must contact one another without disturbing the continuity of their boundaries. By von Mises condition, up to five slip systems must be operative in a grain so that individual grains in a polycrystal match in shape to one another along their boundaries. Multiple slip observed in polycrystals results in substantial work hardening. The contribution of multiple slip to work hardening in b.c.c. and f.c.c. polycrystals is much higher than the contribution from barrier work hardening. As has been established experimentally, polycrystals of the same purity are work hardened five times more intensively than single crystals oriented favourably for easy glide and twice as those oriented for multiple slip (Fig. 138). This indicates that multiple slip is responsible roughly for 50 per cent of work hardening in single and polycrystals.

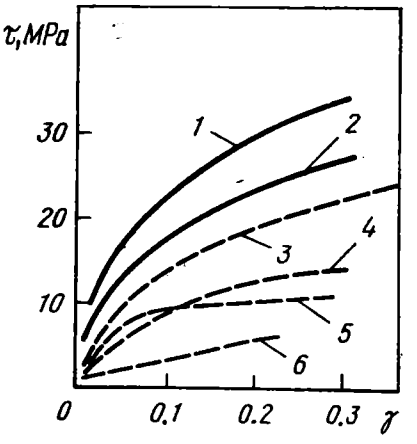

Fig. 138. The τ-γ curves for aluminium (99.99%)
1, 2—polycrystals with different grain size; *3-5*—single crystals with different orientation for multiple slip; *6*—single crystal oriented for ordinary slip

Observations on the behaviour of bi- and polycrystals of hexagonal metals have shown that strain hardening in them is determined mainly by the probability of slip in non-basal planes. At 77 K, zinc polycrystals break perfectly brittle, magnesium polycrystals on a deformation $\varepsilon \approx 0.03$-0.05, and cadmium polycrystals, on a deformation $\varepsilon \approx 0.15$-0.20. Even at room temperature, zinc and magnesium polycrystals withstand only a slight plastic deformation, while cadmium monocrystals fracture at $\varepsilon \approx 0.35$. An explanation to this is that non-basal slip in magnesium is restricted and found in prismatic planes only. Notwithstanding the developed twinning which facilitates plastic deformation by reorientation of individual regions into positions favourable for glide, the total deformation and plasticity remain low owing to chaotic orientations. In cadmium, substantial non-basal slip in the pyramidal $\{11\bar{2}2\}\langle 11\bar{2}3\rangle$ system is observed, and the combination of basal and pyramidal slips satisfies the von Mises condition of five independent slip systems. As a result, polycrystalline cadmium exhibits substantial plastic deformation before fracture and has a higher plasticity than magnesium or zinc.

3. Locality of Deformation in Polycrystals

In the absence of cracks between grains, each grain in a polycrystal deforms so that the deformation at each of its boundaries matches with that in an adjacent grain. For that reason, local deformations must

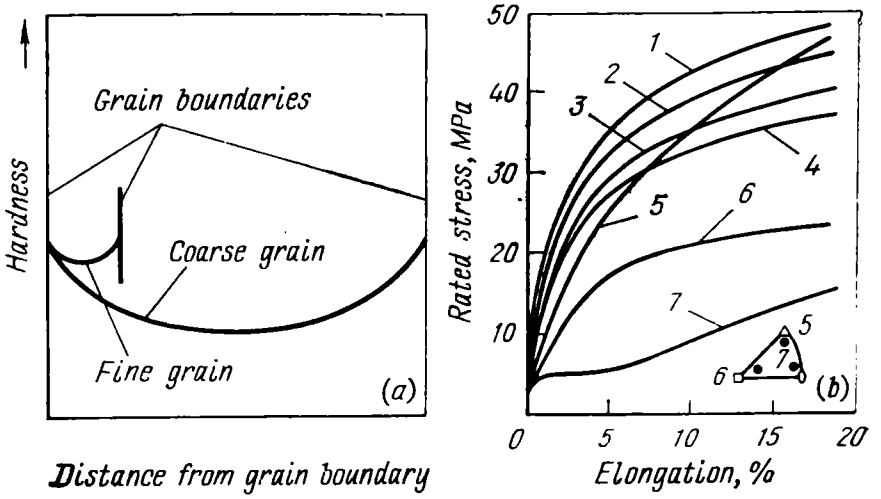

Fig. 139. Variation of hardness along the length of fine and coarse grains (*a*) and the effect of grain size on the form of the σ-ε curves for pure aluminium (*1-4*— 0.034 mm, 0.088 mm, 0.24 mm and 0.5 mm, respectively) and of orientation of single crystals (curves *5-7*, respectively) (*b*)

vary from grain to grain due to their different orientation relative to the external action, as well as within each grain.

The amount of deformation within a grain may vary by a factor of 10. With coarse grains and low deformations, a region may often appear in the core of grain where deformation is effected in a single slip system only, i.e. the core is deformed like a single crystal. This behaviour of grains in a polycrystallite, similar to the behaviour of an isolated single crystal of the same orientation, is more noticeable in coarser grains. At distances closer to a boundary, the barrier effect of the boundary is more sensible and multiple slip is more likely to occur. Thus, core portions of a grain are deformed less strongly than those near boundaries and the hardness (work hardening, strain resistance) of the metal is higher at grain boundaries where multiple slip takes place (Fig. 139*a*). This is why fine-grained metal will have a higher hardness than coarse-grained one. In addition, a fine-grained polycrystalline specimen can be work hardened more appreciably than a coarse-grained one (Fig. 139*b*).

The deformation in core portions does not however differ regularly from that at boundaries. It may be non-uniform owing to non-uniform distribution of strain between grains. If, for instance, two adjacent grains are separated by a common boundary and the average strain in the second is lower than in the first, the strain in the first grain at the common boundary will be lower than in its core. If, on the contrary, the second grain is deformed more strongly, the strain in the first grain will be greater at the boundary and lower in the core. Thus, additional deformations appear at boundaries of adjacent grains, which ensures the equality of strains at boundaries. For that reason, if strains at a boundary are increased additionally relative

to the average value over the grain, the hardness at the boundary will also be higher. In the opposite case, i.e. if the additional deformations at a boundary diminish the average strain over the grain, the hardness at the boundary may either increase or decrease, depending on two opposing factors: (1) reduction of deformation resulting in lower hardness and (2) multiple slip which increases hardness. Thus, deformation of a polycrystal can be affected both by multiple slip and barrier effect.

The barrier effect of grain boundaries is more pronounced in deformation of two-phase alloys. D. McLean has analysed the results of numerous experiments and resumed as follows.

1. When a softer phase is continuous, deformation proceeds mainly in that phase. Due to the equality of deformations at phase boundaries, deformations diminish fastly with distance from a boundary. Since the deformation of the softer phase at the boundary is smaller than the average value, recrystallization in this phase is observed naturally to commence far from the boundary. On the contrary, the harder phase will start recrystallization at the boundary.

2. When the concentration of the harder phase is such that the softer phase ceases to be continuous, the deformation of the softer phase will be lower than in the previous case and the plasticity of the two-phase alloy will be lower.

In b.c.c. metals, the barrier mechanism of relay-race transfer of strain from grain to grain is additionally impeded by the tendency of these metals to strong segregation of impurities (carbon, nitrogen, oxygen) on grain boundaries. Their hardness is substantially greater near grain boundaries. On the contrary, such high variations in hardness are not observed, for instance, in copper or aluminium which are not so liable to segregation as b.c.c. metals. The barrier effect can explain the appearance of a sharp yield stress peak typical of b.c.c. metals.

4. The Pattern of Deformation and the σ-ε Curves for Some Polycrystalline Metals

The contribution of barrier effect and multiple slip (complicating effect) to work hardening varies with increasing deformation and depends on the type of crystal lattice, structure of crystals, grain size, temperature, and rate of deformation. All these factors may have an appreciable effect on the shape of the σ-ε-curve and plasticity of polycrystals.

Polycrystals of f.c.c. metals. The initial hardening in f.c.c. polycrystals proceeds mainly due to multiple slip, since barrier effect cannot contribute substantially to hardening in pure metal possessing many favourable slip systems. For that reason, hardening follows a parabolic law.

A typical stress-strain (σ-ε) curve can be approximated differently:

(1) by a parabola (in the whole strain range, see Fig. 138, curves *1* and *2*):

$$\sigma = \sigma_0 + A\varepsilon^n \tag{138}$$

(2) by a parabola at Stage *I* hardening with $\varepsilon_I \geqslant \varepsilon \geqslant 0$:

$$\sigma = \sigma_0 + A\varepsilon^n \tag{139}$$

a linear portion at Stage *II* hardening with $\varepsilon_{II} \geqslant \varepsilon \geqslant \varepsilon_I$ (Fig. 140):

$$\sigma = \sigma_0' + A'\varepsilon \tag{139a}$$

and finally, a parabola at Stage *III* hardening with $\varepsilon > \varepsilon_{II}$:

$$\sigma = \sigma_0'' + A''\varepsilon^{n'} \tag{139b}$$

where n = const, n' = const or $n = n(\varepsilon)$, $n' = n'(\varepsilon)$ are hardening indices; ε_I and ε_{II} are the extents of Stages *I* and *II*; σ_0, σ_0' and σ_0'' are the yield limit and the deforming stresses at the end of Stages *I* and *II*, respectively; and A, A', A'' are constants or strain-dependent functions*. In contrast to single crystals where single slip is observed at Stage *I*, in this case multiple slip takes place at that stage. The linear portions of the curves at Stage *II* hardening for single and polycrystals are practically parallel to each other. There is also much similarity in Stages *III*.

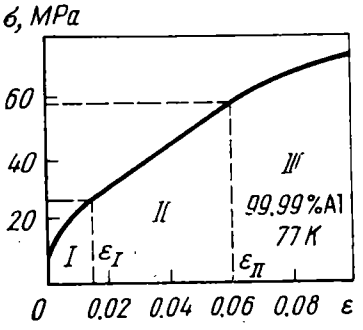

Fig. 140. Stress-strain curve for polycrystalline aluminium at 77 K

In a curve obtained for polycrystalline aluminium, Stage *II* is hardly noticeable, i.e. $\varepsilon_I \approx \varepsilon_{II}$. This is similar to the behaviour of aluminium single crystals at room temperature which exhibit Stage *III* hardening already on slight deformations ($\varepsilon < 2$ per cent). As has been given earlier (Ch. 3), the extent of Stage *II* of single crystals depends on the ease with which dislocations can overcome obstacles by cross slip. For that reason, Stage *II* hardening is longer for metals with a low stacking fault energy and its extent increases with reducing temperature. Using these facts for interpreting the stress-strain curves for single crystals, we can conclude that the extent of Stage *II* for silver polycrystals is longer than that for copper or aluminium. This agrees perfectly with the experimental data given by R.W.K. Honeycombe. For instance, the extent of Stage *II* turned out to be 1.5 to 20 per cent for Ag, 1.5 to 8 per cent for Cu and was practically absent for aluminium, with $\varepsilon_I = \varepsilon_{II} = 1.6$ per cent.

---

* In formulae (138) and (139), A and n are called rheologic constants or, if strain-dependent, rheologic variables.

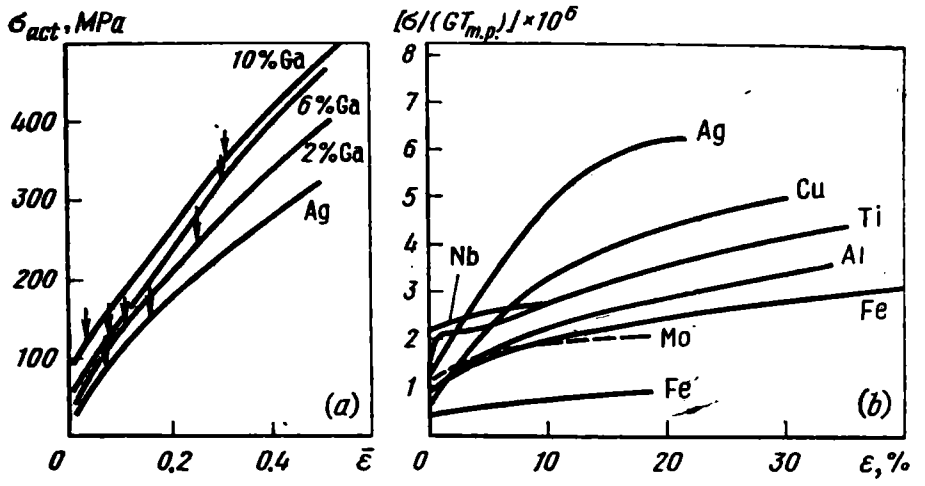

Fig. 141. (*a*) The σ-ε curves of polycrystals of silver and silver-gallium solid solution alloys with the same grain size at 77 K. Arrows indicate beginning and end of Stage *II*. The stacking fault energy of alloys, erg cm^{-2}: Ag—36; Ag + + 2% Ga—32; Ag + 6% Ga—20; Ag + 10% Ga—10; (*b*) the σ-ε curves for polycrystalline metals: Ag 99.97%, grain size 0.04 mm; Cu 99.999% (0.03 mm); Ti 99.9% (0.10 mm); Al 99.99% (0.11 mm); Fe 99.96% (0.075 mm); Mo 99.98% and zone-refined Fe (0.09 mm). The difference in melting points and elastic moduli is accounted for by the ratio, $\sigma/GT_{m.p.}$

The effect of stacking fault energy on the pattern of σ-ε curves is analysed by comparing the behaviour of a pure metal and a number of its solid solutions with increasing concentrations of a second component, and therefore, decreasing stacking fault energy, resulting in a corresponding increase of the deforming stress (or strain resistance) (Fig. 141*a*). As with single crystals, Stage *III* begins to dominate with an increase of temperature. At this stage, the dislocations which have been locked by barriers in their slip planes, turn out to be capable of cross slip, which results from the combined effect of stress and thermal activation. This allows further plastic deformation to occur and at the same time diminishes the strain hardening coefficient.

B.C.C. polycrystals. In contrast to f.c.c. single crystals, the barrier effect in b.c.c. polycrystals is more pronounced. The plastic deformation prior to overcoming an obstacle is very low, which results in the appearance of a sharp yield stress peak on the stress-strain curve. For that reason, many b.c.c. polycrystals exhibit a yield stress peak (see Fig. 44) whose appearance is attributed to the presence of low concentrations of interstitial impurity atoms of carbon and nitrogen which lock dislocations (Cottrell atmospheres) and enhance the barrier effect.

Zone-refined iron is hardened by deformation at room temperature only slightly more intensively than aluminium 99.99 per cent pure. The σ-ε curves for b.c.c. metals, with corrections for the shear modulus and melting point, pass lower than those for f.c.c. metals. The hardening effect in b.c.c. metals is lower than in f.c.c. metals,

mainly because there are more slip systems. The σ-ε curves of b.c.c. polycrystals (Fig. 141*b*), like those of f.c.c. ones (see Fig. 139*b*), are sensitive to grain size; a more fine-grained metal has a higher yield limit and can be hardened more intensively by deformation.

The appearance of the yield stress peak and upper and lower yield limits on the σ-ε curves of b.c.c. metals is attributed to dislocation locking by interstitial impurity atoms. These phenomena disappear in a purer (for instance, zone-refined) metal. The upper yield limit usually corresponds to a plastic deformation of 0.02-0.5 per cent. The difference between the upper and the lower yield limit may be as high as 100 per cent. A yield stress peak on a curve is followed by a horizontal yield elongation zone within which plastic deformation propagates in the metal as moving fronts of Lüders-Chernov bands. When these bands cover the whole specimen, the yield elongation zone ends and a portion of strain hardening appears on the σ-ε curve. With an increase of the test temperature, a serrated portion appears on the σ-ε curve in place of the yield stress peak and yield elongation zone (the Portevin-Le Chatelier effect). In a temperature range roughly 0.2 to $0.6T_{m.p.}$, the intensity of work hardening at increasing temperatures becomes substantially higher than at lower temperatures, since impurity atoms can diffuse quickly and follow behind a moving dislocation. This locking of moving dislocations increases $d\sigma/d\varepsilon$, so that the stress applied has to overcome this locking by breaking away the locked dislocations or generating new ones.

In contrast to f.c.c. and c.p.h. metals, b.c.c. metals exhibit a strong temperature dependence of the yield limit below $0.2T_{m.p.}$. Deformation rate can also have a noticeable effect on the yield limit at temperatures above $T = (0.3\text{-}0.4)\,T_{m.p.}$. In polycrystals of b.c.c. metals, the yield limit is usually more pronounced than in single crystals, since grain boundaries inhibit dislocation movement, while segregation of impurities to grain boundaries enhances the barrier effect.

The σ-ε curves in repeated and alternating loading. In most practical cases, especially with heavy deformations, it is assumed that the elastic lines of unloading, DdD_0, beginning from the point D in a σ-ε diagram (Fig. 142*a*) and of subsequent loading, D_0dD, are coincident, so that the portion DE of the diagram coincides with $ABCDE$ without unloading. If, however, the strains are measured by a sensitive instrument, it may be noticed that the lines of loading, B_0cB, and unloading, BbB_0, do not actually coincide (Fig. 142*a*), but form a mechanical hysteresis loop of width cb. This behaviour in unloading and subsequent loading is typical of any plastically deformed metal. *Mechanical hysteresis* is especially marked on slight deformations when the width cb of the hysteresis loop is commensurable with the total deformation. In Fig. 142*a*, the hysteresis loop is shown with an exaggerated width, while actually the elastic deformation ε_{el} is many times the anelastic deformation ε_{an}. The pheno-

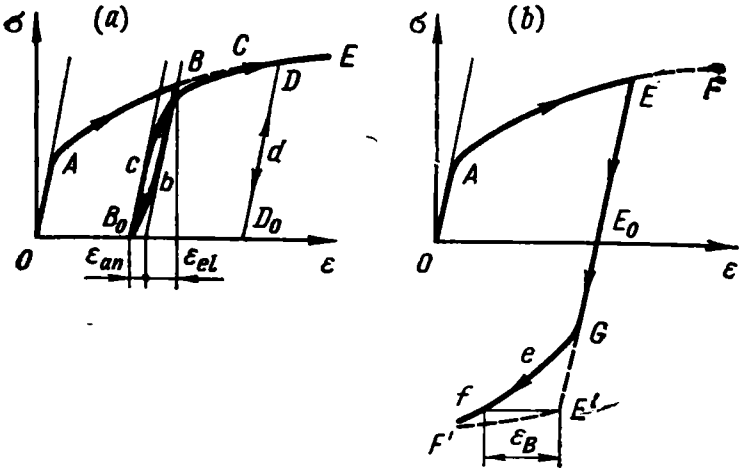

Fig. 142. The σ-ε diagram with indicated (by arrows) directions of loading and unloading (*a*) and a scheme to illustrate the Bauschinger effect (*b*)

menon described is a special case of the Bauschinger effect whose essence consists in that if the sign of stress is altered (loading along E_0G in the reverse direction to prior deformation along AE in Fig. 142*b*), plastic deformation will commence at a lower stress than that required for repeated loading without stress sign alteration, i.e. a change of stress sign facilitates plastic deformation. In Fig. 142*b*, reverse loading follows the line E_0Gef, which differs from $E_0E'F'$ and is a reflection of the portion E_0EF. As may be seen, $E_0G < EE_0 = E_0E'$ and the loading curve E_0Gef moves away from curve $E_0E'F'$; the distance $E'f$ between the two curves, as measured from point E', is called the Bauschinger strain ε_B.

The *Bauschinger effect* can be observed both in single and polycrystals, the magnitude of the Bauschinger strain ε_B being larger in the former. For that reason, the Bauschinger effect cannot be explained by the influence of residual stresses remaining in the metal after stress release*, though, undoubtedly, this effect plays a definite part in polycrystals too. It would be improper to explain the Bauschinger effect by this cause only, since the Bauschinger strain may exceed several times the strain at the beginning of plastic flow.

The suggested mechanisms explain the Bauschinger effect by the formation of dislocation pile-ups on obstacles and dislocation locking by thick portions of dislocation 'forest'. It is supposed that 'trees' of a dislocation 'forest' are bowed in front of a moving dislocation, and therefore, the density of 'forest' dislocations which pierce through the slip plane of the moving dislocation is thus increased

* By this hypothesis, tensile deformation of various grains in a polycrystal is non-uniform, so that additional compressive stresses appear in more strained grains and tensile stresses in those less strained. As the stress changes sign, the compressive stresses are added with the operative compressive stresses, thus causing earlier plastic flow.

(Fig. 143). When the sign of the operative stress is changed, 'forest' dislocations will meet less obstacles at the initial portion of their reverse path. Calculations show that the deformation associated with the arrest of gliding dislocations in regions of their elevated concentration (say, on sub-grain boundaries) may reach a few per cent. For instance, using the relationship $\gamma = N_d L b$ (N_d = dislocation density; L = free-path length of a dislocation, which according to Fig. 143 is the distance between positions *1* and *2*, i.e. the sub-grain size) and the typical values of N_d, L and b ($N_d = 10^{10}$ cm^{-2}, $L = 10^{-4}$ cm, and $b = 2.5 \times 10^{-8}$ cm), we can find that $\gamma = 2.5 \times 10^{-2} = 2.5$ per cent.

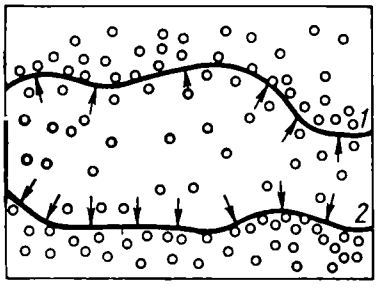

Fig. 143. Anisotropy of resistance to slip on variation of slip direction, leading to the Bauschinger effect

1—dislocations stopped before barriers of high density at the end of loading (in point E in Fig. 142*b*); *2*—a dislocation is stopped again at barriers of the initial density when movement from position *1* to *2* involves passage through the yield limit (point G), so that point f (see Fig. 142*b*) is within portion $E'F'$ of the diagram

The Bauschinger effect can also be attributed to *anelasticity*, i.e. the property of a metal to dissipate the strain energy stored in elastic deformation. Anelasticity is associated with thermal effects. For instance, the temperature of a metal may rise quickly under the action of elastic compressive stresses and decrease in a zone of tensile stresses. Owing to thermal fluctuations and stress concentrators, dislocations can always move and produce new locally dilated or compressed zones. The resulting heat flow leads to energy dissipation and the appearance of temperature-induced internal friction. With fast heating (in loading of a specimen) and slow heat transfer (in unloading), the deformation will lag behind the stress compared with the common Hooke's relationship. In this process, the amount of energy transformed into heat is proportional to the mechanical hysteresis loop in the σ-ε diagram. Thermoelastic effects can also appear due to inhomogeneous structure of the metal. In a polycrystal, where adjacent grains have different elastic constants in the direction of applied stress, each grain will therefore show a different adiabatic temperature variation. Internal friction can be produced not only by thermal effects, but also by microscopic deformations at stresses below the macroscopic yield limit. All these phenomena can influence the formation of a hysteresis loop, which is of extreme practical importance in the theory and calculations of long-term strength and fatigue strength on alternating deformations.

It is essential to account for the Bauschinger effect in calculations of various structures and technological processes where plastic deformations are expected, especially when they will be commensurable with the Bauschinger strain.

Stress-strain diagrams on heavy deformations. The bonding between adjacent grains in deformed metal is retained due to multiple slip. Twinning is also favourable in this respect. Interacting grains can produce bending moments, even when a tensile or shear stress is applied from the outside. These moments can be relieved by the formation of kink bands. Kinking and twinning lead to stress relaxation which favours further plastic deformation. If this relaxation is insufficient, cracks can appear on grain boundaries.

Multiple slip in f.c.c. polycrystals results in fast formation of the Lomer-Cottrell locks, so that the linear Stage *II* and parabolic Stage *III* are observed to follow quickly after the parabolic Stage *I*. As in single crystals, the stress at which Stage *III* begins decreases rapidly with increasing temperature. Cross slip develops at Stage *III*, so that grain boundaries play no essential part at heavy deformations, since the hardening is determined by the processes occurring within grains and the bonding between grains is retained due to accommodation processes in regions close to grain boundaries: local multiple slip, kinking, twinning, grain-boundary sliding, etc.

5. Calculation of Stress-strain Curves for Polycrystals from the Data on Single Crystals

In polycrystals, the orientation factor $m = 1/\cos\alpha_0 \cos\beta_0$ varies from grain to grain and the applied tensile stress $\sigma = m\tau$ is therefore different for every grain, even if the shear stress τ acting in a given slip plane is the same. Multiple slip and other deformation mechanisms different from simple slip, which can take place in polycrystals, make it difficult to calculate the σ-ε diagrams of polycrystals from the known τ-γ diagrams of respective single crystals. G.I. Taylor has used for such calculations the von Mises principle by which five independent slip systems must exist in each grain for plastic deformation of a polycrystalline aggregate. In Taylor's calculation for f.c.c. metals, five systems satisfying the minimum work principle are selected from the total number of 12 crystallographically equivalent octahedral slip systems. It is assumed that all grains undergo the same amount of deformation. In that case, the averaged orientation factor $\bar{m}$ for a polycrystal is found for these five systems from the condition that the work $\sigma\, d\varepsilon$ performed by a macroscopic stress σ in deformation $d\varepsilon$ is the sum of the works performed by the critical stress τ_0 in an infinite increment of shear deformation $d\gamma$:

$$\sigma\, d\varepsilon = \sum_{1}^{5} \tau_0\, d\gamma \qquad (140)$$

Taylor has made the assumption that the critical shear stress τ_0 is the same for all the five slip systems and that the work hardening is not changed from grain to grain. Expression (140) then takes the form:

$$\sigma/\tau_0 = \Sigma d\gamma/d\varepsilon = \overline{m} \qquad (141)$$

According to G. I. Taylor, J. F. W. Bishop and R. Hill, for randomly oriented grains in an f.c.c. polycrystal, $\overline{m} = 3.06\text{-}3.1$.

Calculations show that a theoretical σ-ε curve for a polycrystal, calculated from the data on a single crystal oriented in the centre of the stereographic triangle, should pass much lower than the experimental curve. If, however, the calculation is made for τ and γ of a single crystal oriented favourably for multiple slip (in the case of tension of an f.c.c. single crystal, in directions ⟨111⟩ and ⟨100⟩), the calculated σ-ε curves will practically coincide with the experimental one (Fig. 144).

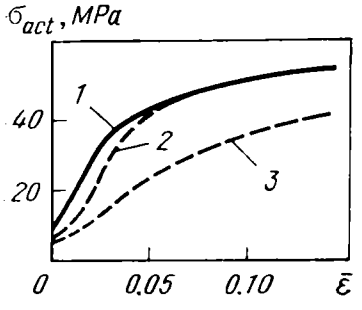

Fig. 144. Comparison of an experimental σ-ε curve (*1*) for polycrystalline aluminium with theoretical curves for single crystals with the orientation in the centre of stereographic triangle (*3*) and with ⟨111⟩ orientation (*2*)

Thus, Taylor's method gives good results only when the slip mechanisms in poly- and single crystals are the same.

B.c.c. metals which have a high stacking fault energy can be characterized by relative ease of cross slip. The macroscopic slip plane is close to the surface formed by portions of the planes of region ⟨111⟩ in which the critical resolved shear stress is at its maximum. For that reason, it is unclear which of the curves for b.c.c. single crystals of different orientation should be used as the original one in calculations. By analogy with f.c.c. crystals, it may be recommended to use such orientations of b.c.c. single crystals in which multiple slip is observed. In particular, for a single crystal with the orientation ⟨100⟩ and with four slip systems, the calculated and experimental σ-ε curves are in fairly good agreement.

For c.p.h. crystals, calculation by Taylor's method is impossible, since single crystals and grains in a polycrystal are deformed by different mechanisms; in polycrystals, in particular, twinning, kinking and non-basal slip have a predominant role.

6. Effect of Grain Size on Plasticity and Flow Stress of Polycrystals

Grain size can influence all elements of the σ-ε curve (see Figs. 138, 139*b*, and 145), but most markedly, the elastic limit and yield limit (Fig. 146*a*). The elastic limit of aluminium may vary depending on

grain size from 1.5 MPa to 3.5 MPa, whereas its value for a single crystal is 0.9 MPa.

The dependence between grain size and the stress to initiate plastic flow, σ_y^*, or the deforming stress σ_d, obeys the Hall-Petch relation**:

$$\sigma_y = \sigma_0 + k_y d^{-n}, \quad \sigma_d = \sigma_{0\varepsilon} + k'_y d^{-n} \tag{142}$$

where d is the average grain size (if there is no developed network of sub-boundaries) or the average size of sub-grains*** (for metals with a strongly fragmented structure). The exponent n in formula (142) is equal to 0.5 for b.c.c. polycrystals, but cannot be determined as clearly for f.c.c. polycrystals; σ_0 is the friction stress which is independent of grain size and represents the stress needed to move unlocked dislocations in slip planes of a single crystal. The value of σ_0 can be determined by extrapolation of the linear relationship σ_y-$d^{-0.5}$ to d=0 (see Fig. 146*b*). The stress $\sigma_{0\varepsilon}$ has the same meaning as σ_0 but for an arbitrary deformation ε.

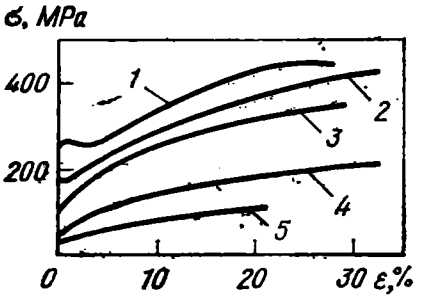

Fig. 145. Effect of grain size on the shape of curves of decarburized Armco iron

1 —1 100 grains/mm²; *2*—200 grains/mm²; *3*—40 grains/mm²; *4*—coarse-grained metal; *5*—single crystal

In the Hall-Petch formula, k_y and k'_y are constants associated with propagation of deformation across grain boundaries.

The propagation of plastic deformation from grain to grain can be explained by Cottrell's model (see Fig. 136): several dislocations emanating from source B in grain I move in the slip plane and pile

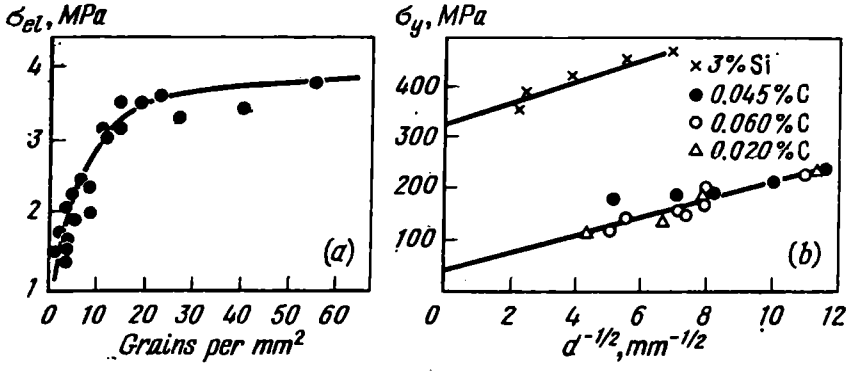

Fig. 146. Effect of grain size on elastic limit of aluminium (99.99%) at room temperature (*a*) and the lower yield limit of iron alloys (*b*)

* The lower yield limit for b.c.c. metals.

** The σ-d relationship is different for superplastic flow of an ultrafine-grained material (see Ch. 15).

*** More strictly, d or $2L$ should be understood as the length of the slip plane along which a dislocation can move without obstruction (free-path length).

up at the grain boundary. A stress concentration appears at the tip p of the leading dislocation. Cottrell has found that dislocations will be created, say, by a Frank-Read source B until the stress τ_y operative in the vicinity of that source (which increases due to n dislocations locked in the slip plane) is counter-balanced fully by opposing stresses τ_d.

If the dislocation source begins to function at a limiting stress τ_0, dislocations will pile up until $\tau_d = \tau_{dB}$ (for source B) becomes equal to $n(\tau_y - \tau_0)$, i.e.

$$\tau_d = n(\tau_y - \tau_0) = \tau_{dB} \tag{143}$$

If source B has generated n dislocations with the Burgers vector **b**, this results in a displacement nb on the length $d = 2L$, with the shear deformation being $\gamma = nb/2L = \tau/G$. If the source generates dislocations at a limiting stress τ_0 below the operative stress τ, then $\tau = \tau_y - \tau_0$ and

$$n = 2L\tau/Gb = d(\tau_y - \tau_0)/Gb \tag{144}$$

Substituting (144) into (143), we obtain:

$$\tau_d = d(\tau_y - \tau_0)^2/Gb$$

or

$$\tau_y = \tau_0 + d^{-0.5}\sqrt{\tau_{dB}Gb} = \tau_0 + k_y d^{-0.5} \tag{145}$$

The factor n in formula (143) can be regarded as the concentration coefficient which attains its maximum at grain boundaries. As r_1 increases, the stress concentration in grain II diminishes, which can cause generation of dislocation source A (see Fig. 136), the stress required for this being $\tau_d = \tau_{dA}$. The concentration coefficient in places where a slip band ends in a crystal has been determined by the theory of elasticity for a case when the slip band is considered as a freely gliding crack with the stress normal to it being zero. According to B. Chalmers,

$$q = \sqrt{L/r_0} \tag{146}$$

where r_0 is the radius of the crack tip, which is equal to atomic spacing. The concentration coefficient diminishes down to $\sqrt{L/r_0}$ as the distance r_1 to A increases. The stress concentration produced by the pile-up of dislocations emitted from source B can initiate slip in grain II when τ_d attains τ_{dA}, i.e. the stress for initiation of dislocation source in A. Then we have

$$\tau_{dA} = (\tau_y - \tau_0)\sqrt{d/2r_1}$$

or

$$\tau_y = \tau_0 + \tau_{dA}\sqrt{2r_1}\, d^{-0.5} = \tau_0 + k_y d^{-0.5} \tag{147}$$

Thus, according to (145), $k_y = \sqrt{\tau_{dB} Gb}$ at the head of a flat dislocation pile-up and $k_y = \tau_{dA}\sqrt{2r_1}$ for a dislocation source A at a certain distance from the head p of a flat dislocation pile-up.

Since the slip direction and slip plane in an adjacent grain are different from the grain considered, the critical stress τ'_{dA} at point r_1 should be higher, i.e. $\tau'_{dA} = m\tau_{dA}$, where m is the orientation factor, and $k'_y = m\tau_{dA}\sqrt{2r_1}$. Therefore

$$\sigma_y = m\tau_y = m(\tau_0 + k'_y d^{-0.5}) = m\tau_0 + mk'_y d^{-0.5}$$
$$= \sigma_0 + k_y d^{-0.5}$$

where $\sigma_0 = m\tau_0$; $k_y = m^2\tau_{dA}\sqrt{2r_1}$.

The theoretical model described above, which explains the effect of grain size on the deforming stress (the flow stress at a given strain ε) and the yield limit, establishes the relationship between grain size and stress concentration in individual slip bands. By this theory, the grain size d limits the length of a flat dislocation pile-up and the number of dislocations, n, in it.

Another theoretical model is based on the supposition that the dislocation density in individual grains increases sharply with decreasing grain size. In that case, the shear stress τ_y is associated with the density of homogeneously distributed dislocations ($\eta_h = 1$) by the relationship

$$\tau_y = \tau_0 + \alpha\eta_h Gb\sqrt{N_d}$$

Assuming that the dislocation density at a given strain ε is inversely proportional to grain size d, i.e.

$$N_d = N_{d0} + N'_d\varepsilon/d$$

where $N'_d \approx$ constant and $N_{d0} \ll N'_d\varepsilon/d$ (the dislocation density increases upon deformation by two or three orders compared with N_{d0}), we find that

$$\tau_y = \tau_0 + \alpha\eta_h Gb\sqrt{N'_d\varepsilon/d} = \tau_0 + kd^{-0.5} \qquad (148)$$

where $k = \alpha Gb\sqrt{N'_d\varepsilon}$, i.e. we have come to the Hall-Petch relationship.

In formulae (142), (145), (147) and (148), σ_0 or τ_0, accounts for the resistance to dislocation movement in the bulk of a grain. This stress depends on Peierls-Nabarro forces and on the presence of obstacles (dislocation forest, foreign atoms, disperse phase particles, etc.) to dislocation movement in the slip plane. These factors may be thought to produce friction opposing the movement of a dislocation in the bulk of grain and for that reason are referred to as 'friction stresses'. The parameter σ_0 (or τ_0) can be represented as the sum of particular components. The factor characterizes the resistance to the transfer of slip, i.e. to relay-race propagation of strain from one

grain to another, and therefore, depends on the state of the boundary. In particular, a higher degree of locking of dislocation sources near the boundary by segregated interstitial impurities in b.c.c. polycrystals is associated with an increase of τ_d, and therefore, of k_y. For that reason, τ_d and k_y of b.c.c. metals are quite high (see Table 11), though m in these metals is lower than in f.c.c., owing to certain specifics of slip in their lattice. Since k_y is high, σ_y should depend strongly on grain size.

In f.c.c. metals, m and τ_d are not high; the former due to the large number of probable slip systems and the latter, also due to this factor and to an easier transfer of strain by the relay-race mechanism. Hence, k_y is low (see Table 11), and therefore, τ_d and k_y depend only slightly

Table 11. Constants in Hall-Petch Equation (142) for Determining the Yield Limit and Deforming Stress at a Given Strain

Metal	Constants in (142) determined for	σ_0, $\sigma_{0\varepsilon}$, MPa	k_y, k'_y, N/mm$^{3/2}$	k_y/G, k'_y/G, 10^{-3} mm$^{1/2}$
		B.c.c. lattice		
Low-carbon steel	σ_y	72	23.9	0.28
	$\varepsilon = 0.01$	300	12.6	1.15
Iron	σ_y	48	22.8	0.27
Iron, partially decarburized	σ_y	46	9.9	0.12
Molybdenum	σ_y	110	57	0.42
	$\varepsilon = 0.01$	400	17	0.12
		F.c.c. lattice		
Copper	$\varepsilon = 0.005$	26	3.6	0.08
Aluminium	$\varepsilon = 0.005$	16	2.2	0.08
Silver	$\varepsilon = 0.005$	38	2.2	0.08
Brass 70/30	σ_y	46	10	0.25
	$\varepsilon = 0.2$	344	11.0	0.27
		C.p.h. lattice		
Zinc	$\varepsilon = 0.005$	33	7.1	0.19
	$\varepsilon = 0.175$	73	11.7	0.32
Magnesium	$\varepsilon = 0.002$	7	0.9	0.50
Titanium	σ_y	80	13	0.29

on grain size. For that reason, the dependence of τ_y (or σ_y) on grain size at heavy deformations is hardly noticeable. In the presence of alloying elements capable of dislocation locking (as in α-brass), τ_d increases, which causes an increase of k_y and a greater dependence of σ_y on grain size.

In c.p.h. metals, k_y is high due to the limited number of slip systems and an appreciable value of m. The value of τ_d is high too and

controls the relay-race transmission of strain between grains. High values of m and τ_d are indicative of a strong dependence of σ_y on grain size (see Table 11).

Thus, the yield limit σ_y and the flow stress σ_d (the deforming stress, or strain resistance) increase with decreasing grain size. This effect should be attributed not simply to the presence of a boundary, but to the interaction of the grains separated by that boundary. If dislocations are locked firmly by a boundary and relay-race transfer of strain is restricted, as is the case observed in c.p.h. polycrystals, deformations are localized in microvolumes and the flow stress (strain resistance) increases. If deformations are localized substantially, this can result in elevated stress concentration and premature fracture, i.e. in a lower plasticity of the metal.

The possibility for relay-race transfer of strain is higher with smaller grain size. Ultrafine-grained metals (of the grain size index 14-15 by the standard scale) have been observed to have a noticeably higher strength with an amply high plasticity, which should be attributed to a reduced stress concentration, since dislocations cannot pile up substantially during slip in very fine grains. The favourable effect of ultrafine grain is utilized for increasing the whole complex of mechanical characteristics and producing the high-strength state in alloys (hardening and low tempering).

7. The Role of Twinning in Plastic Deformation of Polycrystals

The relative elongation ε_{tw} in a completely twinned single crystal is determined by expression (88). For twinning in a {112} plane in a b.c.c. crystal the highest value $\varepsilon_{tw.max} = 41.4$ per cent is attained at $\alpha = \beta = 54.7°$. Only a fraction of the total volume, however, changes to the twinning orientation ($f_{tw} < 1$), so that

$$\varepsilon'_{tw} = \varepsilon_{tw.max} f_{tw} \tag{149}$$

and, according to V.O. Moiseev and V.I. Trefilov, ε'_{tw} drops down to 4-5 per cent.

In a b.c.c. polycrystal, a twin band of a thickness δ forms by movement of a combination $n = \delta/c$ of twinning dislocations with the Burgers vector $b = a/6\ \langle 111 \rangle$ ($c = a/\sqrt{6}$ is the spacing between parallel {112} planes).

The relative shear γ is limited by grain size d:

$$\gamma = Anb/d = A\delta b/cd$$

and the corresponding relative elongation of the grain is

$$e = \gamma/m = \delta/2\sqrt{2}\,dm$$

where $A \approx 0.5$ is a coefficient depending on the mean free-path length of a dislocation and $m = 1 : (\cos \alpha \cos \beta)$ is the orientation factor for a given twinning plane and twinning direction.

With N twin bands observed in a grain, the deformation due to twinning is

$$\varepsilon''_{tw} = \bar{\delta} N / 2 \sqrt{2 \bar{d} \bar{m}}$$

where $\bar{d}$ is the average grain size; $\bar{m}$ is the average orientation factor ($\bar{m} \approx 3.1$ for a $\{112\}\langle 111 \rangle$ twinning system); and $\bar{\delta}$ is the average thickness of twin bands.

With $\bar{\delta}$, $\bar{d}$ and N determined experimentally by microstructure analysis, the above formula gives $\varepsilon''_{tw} = 1\text{-}4$ per cent, which is substantially lower than the total deformation to fracture. Thus, the contribution of twinning deformation to the total plasticity of a polycrystal turns out to be not high, notwithstanding the circumstance that there is a stress concentration in places where dislocations have piled up against various obstacles (say, where they intersect slip bands), which is favourable for twinning, and an additional stress concentration in polycrystals which favours twinning more with a larger grain size. Reduced temperature and increased deformation rate inhibit relay-race slip and stress relaxation, and therefore, are favourable for the development of twinning. As has been shown by analysis and experiment, the contribution of twinning to the deformation of a single crystal is substantially lower than would be expected by formulae (88) and (149). As has been given earlier, a finer grain gives a lower stress concentration, resulting in that the high stress to initiate a twinning source, $\sigma_{tw} = E_{sf}/b$, is not achieved (for iron, the stacking fault energy $E_{sf} = 1.4 \times 10^{-2}$ mJ/cm^2 and $\sigma_{tw} = 2000$ MPa). It may be stated in a similar manner that the division of an as-grown grain in a polycrystal into 'fragments' confined in a framework of twin platelets produces a peculiar 'self-locking' effect (V.I. Trefilov and co-workers), which is enhanced as twinning proceeds further.

The critical stress for twinning $\sigma_{cr.tw}$ is associated with the effective grain size d_e (or the size of fragments) by the Petch-Stroh equation:

$$\sigma_{cr.tw} = \sigma_{0tw} + k_{y.tw} d_e^{-0.5} \qquad (150)$$

where σ_{0tw} is the resistance to movement of partial twinning dislocations and $k_{y.tw}$ is a parameter.

Plastic deformation can proceed by slip at the same time as twinning. Which type of plastic deformation will be realized depends on the ratio between the critical shear stress for slip, σ_0, and that for twinning, σ_{0tw}, within fragments. The grain size (or the size of fragments) d_x corresponding to the equality of these two stresses is found by combined solution of the Hall-Petch equation for shear

and the Petch-Stroh equation for twinning:

$$d_x^{-0.5} = \frac{\sigma_0 - \sigma_{0tw}}{k_{y.tw} - k_y} \qquad (151)$$

With an increase of grain size (at $d > d_x$) (Fig. 147), the contribution of twinning increases sharply but remains relatively small. When N twins have been formed in a grain, the effective grain size diminishes to $d_e \approx d/\sqrt[3]{N}$ and when $d_e = d_x$ is attained, which is determined by relationship (151), the twinning process turns out to be suppressed and further deformation will occur exclusively by slip.

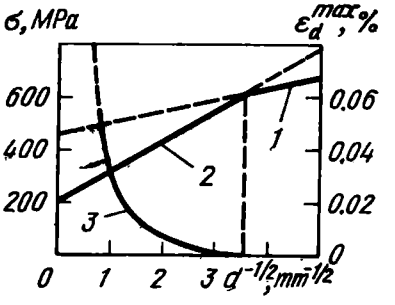

Fig. 147. Effect of grain size on the deforming stress σ_d in shear (*1*) and twinning (*2*). Curve *3* gives the highest possibe plastic deformation by twinning

It should be noted in conclusion that, notwithstanding its low contribution to the total deformation in polycrystals and the occurrence of the 'self-locking' effect, twinning, which takes place at early stages of plastic deformation, is favourable for increasing the plasticity of the metal. In addition, it results in grain reorientation, which favours the development of slip, the main process of plastic deformation.

8. The Structure and Properties of Plastically Deformed Polycrystals

The stored strain energy. The energy spent in plastic deformation is not converted entirely to heat. A fraction of it, associated with crystal lattice defects (dislocations, vacancies, deformation twin boundaries, etc.) is left in the deformed metal as stored (latent, or absorbed) strain energy, which causes changes in the physical properties of the crystal. In particular, it increases the strain resistance and electric resistivity, accelerates diffusion processes, etc. The stored strain energy is determined as the difference between the work performed in the deformation and the amount of heat evolved, or by measuring the heat liberated during annealing of the deformed metal. The latter method makes it possible to determine simultaneously the distribution of crystal lattice distortions in their thermal stability.

The amount of stored energy increases with deformation first quickly and then slowly (Fig. 148*a*) and the relative absorbed energy (related to the work performed) decreases with increasing deformation (Fig. 148*b*), which indicates that energy is absorbed more intensively in slight deformations (10 per cent in Fig. 148*b*) while heat evolution is more substantial on heavier deformations when

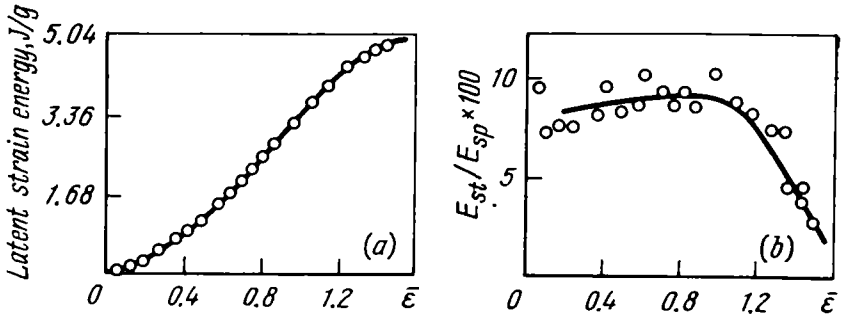

Fig. 148. Effect of deformation in torsion on (*a*) stored (latent) strain energy and (*b*) the ratio of stored energy E_{st} to spent energy E_{sp}

only 3 per cent fall on the energy absorbed. The decrease of the relative absorbed energy with increasing deformation can be explained by the formation of defects in the crystal lattice at the early stages of deformation, which are stable at a given temperature. These defects annihilate partially as deformation proceeds and liberate free energy in the form of heat. In further deformation, the density of defects increases, and therefore, defects of opposite signs are more likely to meet one another and annihilate and ever greater portion of the distortions will disappear in the course of deformation. It is not excluded that a state of saturation will be attained, i.e. the number of distortions formed will be equal to the number of distortions which disappear and the entire energy of deformation will be converted to heat. A state close to saturation can be achieved, for instance, in machining or drilling when the metal is subjected to a heavy plastic deformation. In that case, the energy absorbed is only 1 per cent, while 99 per cent are converted into heat and the work of fracture. The state of full saturation cannot be attained in view of the development of microscopic cracks.

The fraction of stored energy relative to that spent is 20-25 per cent in dynamic plastic working and only 10-15 per cent in static (Fig. 149). This is an extra indication that lattice distortions appearing in the course of plastic deformation are partially annihilated during this process due to recovery. The effect of elimination

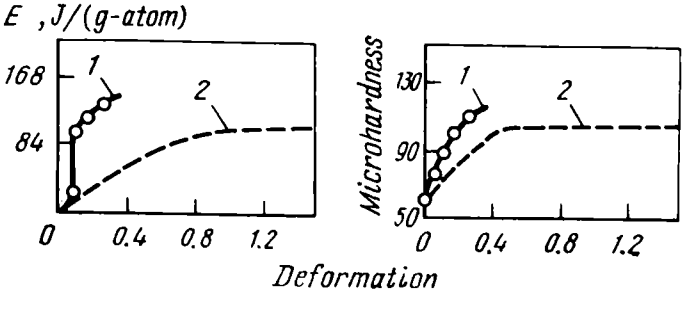

Fig. 149. Effect of amount of deformation in (*1*) high-speed and (*2*) static plastic working on the stored energy and microhardness of Au-Ag alloy

of crystal lattice distortions by recovery is substantially lower at low temperatures and slight deformations. Under such conditions, almost the entire energy spent in deformation (or at least its greater fraction) is absorbed by the metal and spent for the formation of crystal lattice distortions (Fig. 150).

The latent strain energy is liberated during heating of the deformed metal within a quite wide range of temperatures, with a single extremum being observed in pure metals (Fig. 151) and two or sometimes three extrema, in alloys. The higher-temperature maximum observed in alloys and the maximum in pure metals fall into the temperature range of recrystallization and depend on the amount of prior deformation (Fig. 152). As the energy is liberated during heating, the electric resistivity and hardness of a metal decrease (see Fig. 151*b* and *c*).

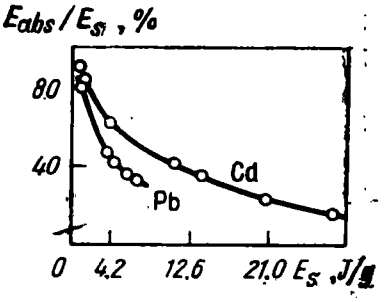

Fig. 150. Variation of the ratio of absorbed to spent energy in low-temperature (77 K) plastic working of cadmium and lead

Thus, it has been established experimentally that the energy absorbed in plastic deformation characterizes variation in the dislocation (fine) structure of a crystal. In this connection, direct examination of the fine structure of plastically deformed metals is essential for understanding the problems associated with variation of their properties on deformation.

The fine structure and dislocations in deformed polycrystals. Grains of deformed metals show up groups of slightly misoriented regions (cells) with a low density of dislocations surrounded by spatial dislocation networks (cell walls). The size of a cell may be 1-2 μm and the thickness of its wall, a few tenths of a micrometre. The structure is said to be a cell structure (Fig. 105).

An important feature in the formation of a cell structure is that the size of cells is only slightly dependent on the original grain size and decreases to a certain limit with increasing deformation. Even in deformed single crystals, the size of cells is roughly the same as in deformed fine-grained metal.

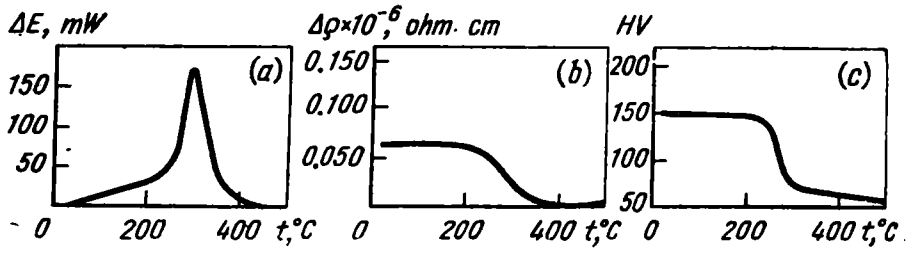

Fig. 151. Variations in liberated energy (*a*), electric resistivity (*b*) and hardness (*c*) during annealing of copper

Another feature typical of a cell structure is that the crystal lattice has quite strong distortions at cell boundaries which depend on the misorientation angle θ.

Dislocation movement is impeded by grain boundaries, secondary phase particles, concentration inhomogeneities, structural imperfections (in particular, other dislocations), and crystal lattice fluctuations due to non-uniform distribution of energy or impurities. For that reason, as deformation proceeds, the total dislocation density increases and dislocations are redistributed and form dislocation arrays which divide a crystal (or grain) into volumes which are relatively free from dislocations, i.e. a cell structure is formed. The initial stage of plastic deformation is associated with the appearance of macroinhomogeneities in the distribution of deformations over the volume of a crystallite. At this stage, kink bands and secondary slip bands appear, in which deformation occurs in slip planes different from the main portion of the crystallite (rotational slip). Subsequently, kink bands and secondary slip bands become obstacles for dislocation movement. A cell structure can also form due to kinking and twinning which impede the movement of dislocations and cause them to pile up against obstacles in their slip planes.

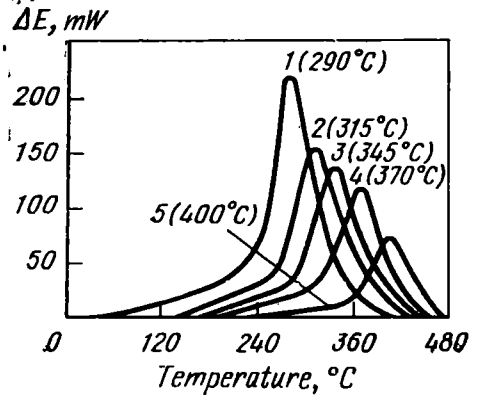

Fig. 152. Effect of temperature on the position of the maximum of liberated energy ΔE during annealing of copper deformed by torsion. (The amount of prior deformation: *1*—3.03; *2*—2.15; *3*—1.41; *4*—0.94; *5*—0.47. The temperatures of recrystallization are given in parentheses)

With a sufficiently heavy deformation ($\varepsilon > 80$-90 per cent), the maximum misorientation between adjacent cells may exceed 5-10°, with the average misorientation being 2-3°. There is a definite critical angle θ_{cr} for misorientation at a boundary between cells. With θ_{cr} between 0 and 2-5°, cell boundaries offer resistance to dislocation movement by the type of 'forest' dislocations. If, however, $\theta > 2$-5°, cell boundaries become as effective barriers for propagation of slip as grain boundaries are, and thus increase the deforming stress. The propagation of plastic deformation through such boundaries involves piling up of dislocations. In contrast to various other stages of plastic deformation in which the length of the pile-up plane is limited by the size of a metallographically detectable grain, the length of that plane in heavy deformations is limited by the size of a cell. The formation of cellular dislocation structures depends on the conditions of plastic working, the principal among them being the temperature, the amount and rate of deformation and the kind of stres-

sed state. Numerous experimental data make it possible to state that a lower temperature of deformation, a high stacking fault energy, alloying or contamination of the metal increase the flow stress and at the same time are unfavourable for the formation of a cell structure. The latter can have a direct effect on the properties of as-deformed metal, with the structure-sensitive mechanical properties being dependent on the angle θ between adjacent cells, as well as on the size of cells.

Studies into the evolution of the dislocation structure in plastic deformation have established that this structure is in close relation to the stacking fault energy.

In f.c.c. metals with a low stacking fault energy (silver, gold, cobalt, stainless steel, copper alloys), wide extended dislocations and flat dislocation pile-ups are usually observed. A cell structure begins to form in these metals only on heavy deformations, with cells having thicker walls.

In f.c.c. metals with moderate values of the stacking fault energy (copper, nickel, platinum) and especially in those which have a high stacking fault energy (aluminium and aluminium alloys), where cross slip and climb of dislocations can occur easily, cell structures can form even on slight deformations (Fig. 153) and cell walls are thinner.

In b.c.c. metals, for instance in deformed iron, where cross slip develops progressively, the cell structure formed is much like that in f.c.c. metals with a high stacking fault energy.

The formation of a misoriented ($\theta > 2$-$5°$) cell structure leads to an appreciable improvement of the complex of mechanical properties: the metal is strengthened and at the same time its ductile-brittle transition temperature T_b decreases. The formation of such misori-

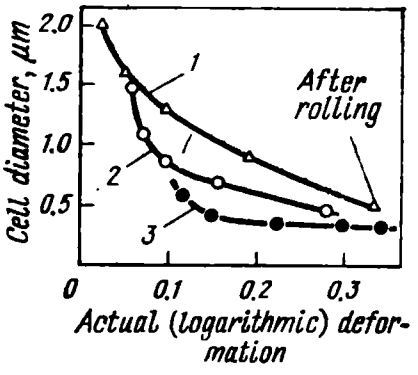

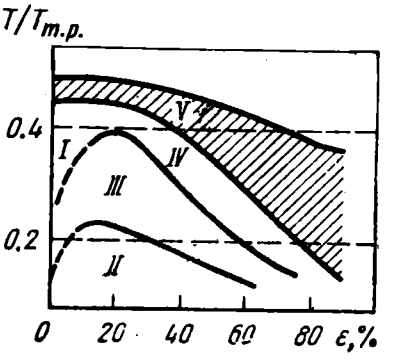

Fig. 153. (*left*) Effect of deformation on the size of cells of sub-structure
1—Ag, room temperature; *2*—Ag + 2% Ga (variations of the stacking fault energy of the alloy see in Fig. 141), room temperature; *3*—Ag + 2% Ga, $t = -196°C$

Fig. 154. Diagram of structural states for metals of group VIA
I—region of existence of tangles and weakly misoriented cells; *II*—chaotic distribution of dislocations; *III*—region of intermediate structural states; *IV*, *V*—existence of misoriented cell structure; region of optimal conditions of plastic working is shown cross-hatched

ented cell structures has been detected in high-melting b.c.c. metals on deformation in the low-temperature range ($T_{def} \leqslant 0.2T_{m.p.}$) in uniform compression, in particular, in hydroextrusion. Experiments have shown that the process of formation of misoriented perfect cell structure in hydrostatic compression occurs more fully than under common conditions. As under common conditions, an increase of the temperature of deformation is favourable for the formation of a more homogeneous cell structure. In that case, misorientation turns out to be rather high (3-4°), resulting in an appreciable improvement of the mechanical properties of a metal.

The results of electron-microscopic examination of the evolution of the dislocation structure formed on plastic deformation in a wide range of temperatures have been systematized by V.I. Trefilov and co-workers and represented in the form of structural-state diagrams (Fig. 154).

Slight plastic deformation (1-2 per cent) at $T < (0.2\text{-}0.3)\ T_{m.p.}$ leads to an increase in the dislocation density from 10^8 cm^{-2} in the original recrystallized state to 10^9 cm^{-2}, with their distribution over the volume being relatively homogeneous.

With further deformation, variations in the structure are determined by non-uniform distribution of the operative dislocation sources with the maximum stress for their initiation, as well as by obstacles existing in the slip plane. When meeting obstacles, dislocations form tangles stretched in the direction of slip. Such dislocation tangles are oriented along traces of slip planes. With increasing deformation, spaces between dislocation tangles are filled in by relatively uniformly distributed dislocations and only later on, a misoriented cell structure will form.

A special role in the formation of cell structures is played by polygonization processes. At temperatures close to the recrystallization temperature, polygonization processes control the formation of misoriented cell structures, with continuously increasing misorientation and thinning of cell boundaries being observed (see Ch. 7).

In low-temperature plastic deformation, i.e. when polygonization processes are suppressed, spaces between dislocation tangles formed at early stages of plastic deformation are quickly filled in by dislocations, their distribution being the more uniform, the lower the temperature is. Further plastic deformation is associated with an exceptionally high concentration of point defects, since moving dislocations intersect thick dislocation 'forests' ($N_d = 10^{10}\text{-}10^{11}$ cm^{-2}) and form numerous jogs which in the further movement create vacancies and interstitial atoms. After a low-temperature deformation of only 10 per cent, the concentration of point defects can rise up to $10^{19}\text{-}10^{20}$ cm^{-3}, i.e. $n/N = (10^{-3}\text{-}10^{-4})$. Thus, the concentration achieved is equal to the concentration of vacancies at the melting point (10^{-4}). Under such conditions, vacancy complexes are very likely to form. An increase in the concentration of point defects, and espe-

cially of vacancies leads to an increase of the metal volume on plastic deformation up to 0.25 per cent. The formation of misoriented cell structure in the low-temperature range (0.2-0.3) $T_{m.p.}$ is favoured by chaotic distribution of dislocations with their density being quite high, which leads to the appearance of point defects. An increased concentration of point defects is favourable for climb of edge dislocations, and therefore, a misoriented cell structure can form, as in the case of polygonization with developed non-conservative dislocation movement. Plastic deformation at a low temperature is associated with a decrease of the size of cells in the direction of the deforming force and its increase in the direction of dilatation in rolling, pressing and drawing. This leads to the appearance of an anisotropic *lamellar cell structure*, which has a characteristic feature that the dislocation density in such cells does not vary substantially, i.e. the dislocations which cause a change in the shape of a lamellar cell emerge to its surface or to the surface of the grain.

Interstitial impurities can have an essential effect on the formation of cell structures. In particular, the processes of dynamic strain ageing observed in b.c.c. metals are due to the interaction of moving dislocations with impurity atoms. The high energy of bond of interstitial impurity atoms with dislocations in a b.c.c. lattice (0.5-1 eV) is due to their elastic interaction and leads to the formation of impurity atmospheres capable of diffusion at an appreciable speed in the range of dynamic strain ageing, so that dislocations move together with such an atmosphere.

Impurity atmospheres decrease substantially the dislocation mobility and the possibility for polygonization processes to take place. According to Snoek and Cottrell, the formation of impurity atmospheres lowers the elastic energy of dislocations and thus decreases the driving force for polygonization. With stress relieving around atmospheres, diffusion of point defects along dislocations is slowed down, and therefore, the rate of climb of edge dislocations is decreased. All these factors retard the formation of a cell structure during deformation and this may appear in subsequent annealing. Dynamic strain ageing is observed in various b.c.c. metals in the following temperature ranges: 200-400°C and 600-800°C in Cr; 150-400°C and 650-800°C in Mo; and 350-550°C and 800-900°C in W. The effect of dynamic strain ageing in the indicated lower temperature ranges is attributed to the interaction of moving dislocations with impurity atoms by the Snoek mechanism due to local ordering of impurity atoms in the stress fields of dislocations for which a displacement of impurity atoms within an elementary cell is sufficient. At higher temperatures, dynamic strain ageing is attributed to the Cottrell mechanism of interaction between moving dislocations and impurity atoms.

The formation of a cell structure during plastic deformation may occur differently depending on the temperature of deformation.

The most complete rearrangement of the dislocation structure can probably occur at temperatures suitable for the realization of non-conservative dislocation movement—diffusion climb. As is known, cross slip of screw dislocations takes place at relatively low temperatures, and therefore, cannot be decisive for rearrangement of the dislocation structure.

Climb of edge dislocations is a process which controls the extent of distortion of the crystal lattice and the dislocation structure in as-deformed metal. Self-diffusion is essential for climb of edge dislocations. Using the expression for the self-diffusion coefficient

$$D = a^2/\tau = D_0 \exp(-E_{sd}/kT)$$

where a is the atomic spacing (the length of diffusion jump); τ is the averaged time of an atomic jump which determines the development of self-diffusion at a given temperature T, K; and $E_{sd} \approx \approx 38T_{m.p.}$ is a semi-empirical dependence of the activation energy of self-diffusion on the melting point, we can determine approximately the temperature limit above which dislocation climb is possible:

$$T_{cl} = 38T_{m.p.}/k \ln(\tau D_0/a^2)$$

In particular, M.L. Bernstein has found for the typical values $D_0 \approx 0.1$ cm^2/s, $\tau \approx 10^3$ cm^2/s, and $a = 10^{-8}$ cm that $T_{cl} \approx 0.5T_{m.p.}$. It is assumed that cold deformation takes place below this temperature limit ($T < 0.3T_{m.p.}$).

Plastic deformation in the temperature range $T = (0.3\text{-}0.6)\ T_{m.p.}$ ('warm' deformation) involves rearrangement of the dislocation structure by climb of edge dislocations, but without essential migration of grain boundaries by diffusion.

In hot deformation, i.e. at $T > (0.6\text{-}0.7)\ T_{m.p.}$, the dislocation structure is rearranged intensively. The process is characterized by retention of dislocation structures which are stable at high temperatures and by migration of boundaries of grains and sub-grains associated with the development of dynamic recrystallization (see Ch. 8)..

The principal scheme of controlled formation of sub-structures. Let us consider the formation of a sub-structure with desired characteristics, i.e. the desired size of sub-grains (cells) δ and their misorientation angles θ. Such a controlled formation of a sub-structure can be carried out by using the available experimental data on the dependence of the principal characteristics of sub-structures on the amount of deformation, temperature, time of holding between successive stages of deformation, etc.

An increase in the amount of deformation results in greater misorientation angles and smaller size of sub-grains in a cell structure (Fig. 155*a*). As follows from the experimental data, the size of substructural elements varies insignificantly with deformations above 10 per cent, but increases with increasing temperature. The amount

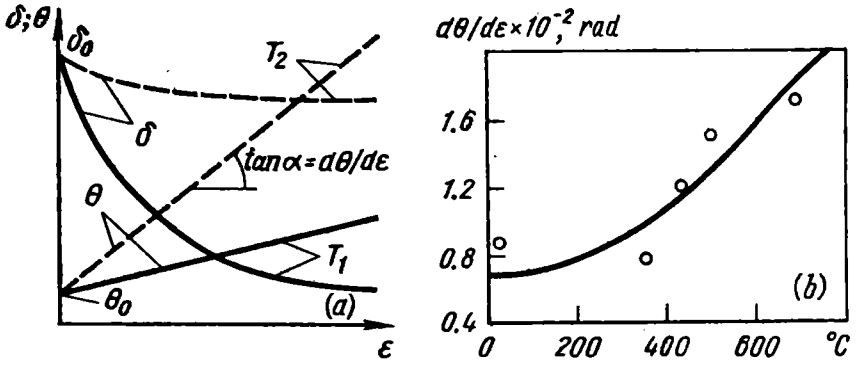

Fig. 155. Dependence of principal characteristics of substructure on deformation at two temperatures ($T_2 > T_1$) (*a*) and of relative misorientation of sub-grains, $d\theta/d\varepsilon$ in deformed nickel on temperature (*b*)

of deformation and temperature have a strong effect on misorientation of a cell structure; a temperature rise by a factor of two can change the relative misorientation of sub-grains (Fig. 155*b*), i.e. the magnitude of $d\theta/d\varepsilon$. At 700°C, the relative misorientation in nickel attains one degree per each per cent of deformation (see Fig. 155*b*). The increase in the relative misorientation with temperature of deformation can be explained by the development of cross, double cross and multiple slip. Thus, it is essential to select properly the amount (and rate) of deformation and temperature to obtain a sub-structure with the desired characteristics. Variation in the characteristics of a sub-structure can be described by a $\bar{\delta}$-$\bar{\theta}$ diagram as in Fig. 156, where curves AB and AB' represent variations of $\bar{\theta}$ and $\bar{\delta}$ with increasing deformation at two temperatures: T_1 and T_2 ($T_2 > T_1$). In sections from A to B or B', deformation increases. The relationship between $\bar{\theta}$ and $\bar{\delta}$ can be changed by varying the amount of deformation along curves of the type AB, varying the temperature of deformation, selecting a particular one from a set of AB curves, selecting properly the temperature and time of annealing or post-deformation isothermal holding (curves CMD and EK). During annealing, the average misorientation angle $\bar{\theta}$ will increase together with an increase of $\bar{\delta}$. Using diagrams of the type given in Fig. 156, it is possible to recommend various schemes for obtaining a sub-structure with the specified characteristics. For instance, a sub-structure with the values of $\bar{\delta}$ and $\bar{\theta}$ at point M can be obtained by deformation

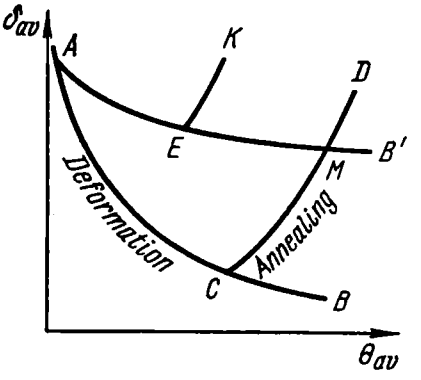

Fig. 156. The δ-θ diagram for two various schemes of deformation and annealing

up to point C along curve AC and subsequent annealing along CM. The same characteristics can be obtained at higher temperatures (curve AB') and higher amount of deformation by following along AM; in that case, annealing will be needless.

Systematic studies of variations of $\overline{\delta}$ and $\overline{\theta}$ depending on the conditions (amount, temperature and rate) of deformation, on the temperature and time of subsequent annealing, and on the time of holding between successive stages of plastic deformation can outline ways for controlled plastic working of metals and alloys aimed at obtaining the specified microstructural characteristics and a higher complex of mechanical and other properties.

RECOMMENDED LITERATURE

1. Bernstein M. L., *The Structure of Deformed Metals.* Moscow, Metallurgiya, 1977 (in Russian).
2. Chalmers B., *Physical Metallurgy.* New York, Wiley, 1959.
3. Honeycombe R.W.K., *The Plastic Deformation of Metals.* London, Edward Arnold, 1968.
4. Moiseev V. O., Trefilov V. I., *Plasticity in Twinning.* In: *Physical Nature of Plastic Deformation and Fracture of Metals.* Kiev, Naukova Dumka, 1969 (in Russian).
5. Trefilov V. I., Mil'man Yu. V., Firstov S. A., *Physical Principles of Strength of High-melting Metals.* Kiev, Naukova Dumka, 1975 (in Russian).

5 Deformation Textures

1. General Concepts. Classification of Textures

An anisotropic arrangement of components of a solid which are orderly oriented relative to an external system of coordinates is referred to as a *texture*.

In practice, metals and alloys are often found to consist of grains having a stretched fibrous shape. Some alloys may have a lineage arrangement of particles of one or more of their phases. Textures of this type are often called '*mechanical*'. The term implies that the shape of particles of a body and/or their arrangement are anisotropic.

Much more common and practically important are *crystallographic textures*. In such a texture, some crystallographic orientations are preferred or, in other words, crystal lattices of some components of a solid have a definite regular orientation in space.

Crystallographic textures are most often found in polycrystalline solids, where some crystallites (grains) or their microvolumes may have a preferable crystallographic orientation.

The term 'texture' becomes senseless when applied to a single crystal if there is only a single orientation in it. If, however, plastic deformation of a single crystal has changed the crystallographic orientation of some of its microvolumes, with new preferable orientations being formed, this is an evidence of the formation of a texture.

Crystallographic and mechanical textures are far from being always interrelated. As a rule, grains in recrystallized materials, which are characterized by a distinct crystallographic texture, have an isotropic shape. On the other hand, grains whose shape is anisotropic for some or other reasons, may be characterized by random crystallographic orientations.

Textures can form due to an oriented action of external or internal forces in a body. These forces can be caused by mechanical stresses, magnetic, electric or thermal fields, etc. Textures appear in various technological processes: solidification of molten metal, plastic working, preparation of thin films and precipitates, packing of powders with particles of anisotropic shape, etc.

Practically any type of plastic deformation, except for uniform compression, is associated with the formation of a crystallographic texture of a particular type and intensity.

Crystallographic textures to be discussed in the book can appear on plastic deformation or subsequent recrystallization. They will be referred to simply as 'textures'.

The practical significance of textures lies in the anisotropy of the properties of a metal they produce, which is utilized effectively in some cases and is undesirable in others.

The problem of textures and their control requires knowledge of the mechanism of texture formation.

Classification of textures. In texture classification, a class of textures comprises all textures having similar regularities in the spatial arrangement of particular crystallographic orientations and/or planes, or of symmetry elements. Textures in which some crystallographic directions have a preferable spatial orientation are referred to as '*axial*', *conical* and *ring*; those in which their crystallographic planes are preferably oriented are called *planar*; and finally, textures with preferable orientation of both planes and directions in them are called *complete*.

Axial texture. In this type of texture, all grains (or a group of grains) in a polycrystal are oriented with a particular direction ⟨*uvw*⟩ parallel to one another and to a definite direction in the polycrystal. This direction is called the *axis of an axial texture*, or simply the *texture axis*. Grains can be rotated randomly around the texture axis *F* (Fig. 157). Therefore, with an axial texture present in a polycrystal, the orientation of its grains has one degree of freedom.

Examples of axial texture are textures formed in drawn wire and those produced by extrusion and upsetting.

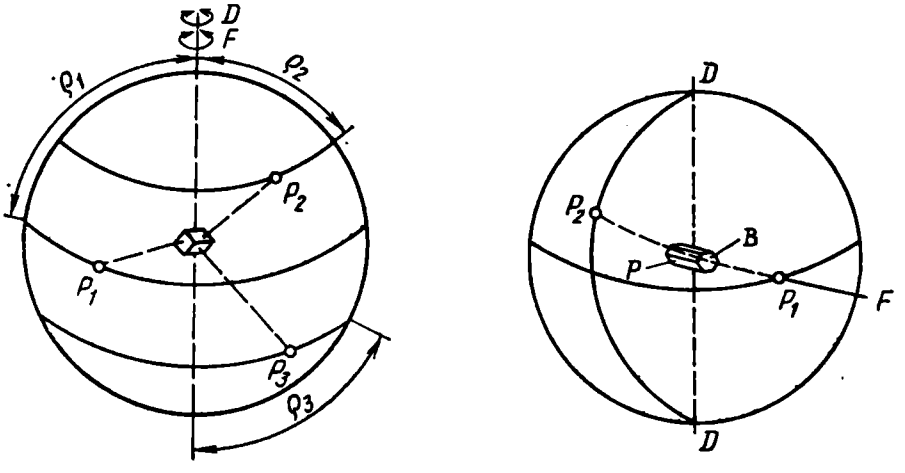

Fig. 157. (*left*) Axial texture. Spherical projections of normals onto planes of two systems. *F*—texture axis; *D*—specimen axis (schematic)

Fig. 158. Ring texture in hexagonal symmetry. The ⟨0001⟩ axis is perpendicular to *D*-*D* axis of the specimen (schematic)

In drawn wire, the crystallographic axis F of the texture coincides, as a rule, with the wire axis D.

Conical texture is characterized by that the crystallographic $\langle uvw \rangle$ direction is at an angle φ to the axis of the specimen, thus forming a conical surface. If $\varphi = 0$, a conical texture degenerates into an axial.

Ring texture may be regarded as a particular case of the conical texture when the angle $\varphi = 90°$. The specifics of this texture may well be illustrated by the orientation of particles in a hexagonal lattice (Fig. 158).

Let a hexagonal basal plane B be parallel to the wire axis D-D. As the plane B rotates around the hexagonal axis F, the projection of this plane onto the circles of projections (point P_1) is not displaced, but describes a circle when rotated around the wire axis D-D.

The prismatic planes P, which are parallel to the hexad axis, behave differently. When rotated around the axis F, the projections of these planes (one of them is point P_2) describe a great circle perpendicular to the circle of projections and, with simultaneous rotation around the axis D-D, the projections P_2 will cover the whole sphere.

Thus, with a ring texture, the planes parallel to the texture axis (the hexad axis in the case considered) turn out to be oriented randomly around that axis, whereas the basal plane is oriented anisotropically.

This case serves to illustrate that a random arrangement of crystallographic planes of a particular type is by no means a sufficient basis for concluding that there is no texture; it is essential to check the orientation of some other types of planes.

Planar, or *upsetting*, *texture* is essentially an axial texture. The fixed $\{hkl\}$ plane can be rotated in various grains randomly around the normal to that plane.

Complete, or *rolling*, *texture* can be characterized by a fixed orientation of a particular crystallographic $\{hkl\}$ plane and a particular $\langle uvw \rangle$ direction in that plane in the specimen.

The principal and most common example of this texture is the texture formed in rolled sheets of metals. Grains in a rolled metal are arranged with their $\{hkl\}$ planes parallel to the rolling plane and with the $\langle uvw \rangle$ rolling direction lying in an $\{hkl\}$ plane. Rolling texture is symbolized as $\{hkl\}$ $\langle uvw \rangle$.

As follows from the foregoing, the spatial orientation of grains in a complete, or rolling, texture turns out to be strictly fixed, i.e. has zero degrees of freedom.

Some most common rolling textures with particular orientations have been given general names in the literature. For instance, the texture in which cube $\{100\}$ planes are parallel to the surface of rolled sheet and $\langle 001 \rangle$ edges of the cube are directed along the sheet length (along the rolling direction) is called the *cube texture*

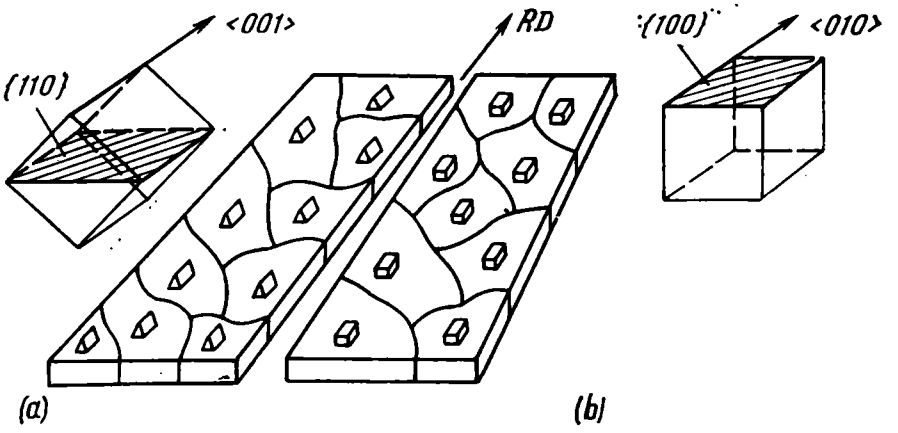

Fig. 159. Schematic of orientations of crystallites in metal sheets with cube texture (right) and rib texture (left)

(Fig. 159*b*) and symbolized {100} ⟨001⟩. The texture in which the {110} plane (the plane of rhombic dodecahedron) is parallel to the sheet plane and the ⟨001⟩ edge of the cube, lying in that plane, is directed along the sheet, is referred to as *rib texture*, or *Goss texture* (Fig. 159*a*). Its notation is {110} ⟨001⟩.

If all grains in a specimen have the same orientation, more strictly, an orientation described by a single symbol, this is a *single-component texture*. If, however, some grains have one orientation and others another, etc., the specimen has a *multi-component texture*. In the latter case, the notation of the texture includes the symbols of all or principal orientations (all texture components) written in a definite sequence. The symbol of the most intensive orientation, i.e. of the texture component occupying the largest relative volume (possessed by the greatest number of grains), is written first; then follow other orientations in the sequence of decreasing intensity, or 'weight'*.

For instance, the texture of iron upon cold rolling with a high reduction contains the following three principal texture components written in the order of decreasing intensity: {112} ⟨110⟩, {100} ⟨011⟩; and {111} ⟨112⟩.

The axial texture of drawn wire for some f.c.c. metals is written: ⟨111⟩, ⟨100⟩, which implies that it has two orientations, of which the ⟨111⟩ component is more frequent (appears in a greater number of grains).

---

* The 'weight' of an ith orientation $P_i = V_i \Big/ \sum_{i=0}^{i=n} V_i$ is understood as the ratio of the volume (or area in a microsection) possessing the orientation of the given (ith) texture component (together with the volume contributing to its 'scatter') to the total volume. It is clear that the data on the 'weight' of a particular component will be more reliable with a greater total volume (area) of the material investigated.

It should be emphasized that the multi-component texture described relates to cases where adjacent microvolumes in a macrovolume of a specimen possess different orientations, for instance, individual grains which have had different orientations originally (prior to deformation). The deformation texture is very often, practically always, not the same even within the volume of one and the same original grain. Various microvolumes, such as boundary regions and those in the bulk, strain bands and microbands, may differ in the type of dislocation slip and, as a consequence, in the type of texture. This case should not be mixed with that where textures differ in macrovolumes of metal. This case represents textural macroinhomogeneity which may be due to different conditions of metal flow in various sections of the workpiece. Most often it appears owing to friction between the metal and deforming tool (rolls, drawhole, etc.). In that case, textures of different nature may be found in outer and inner layers of the metal (see later for examples). In manufacture of articles of intricate shape, the conditions of metal flow may be different in various sections.

Symbols of a texture component refer to an ideal orientation. Under real conditions, however, the actual orientation of a texture component may differ statistically from the ideal, this difference being called *texture scatter*. The amount of scatter depends on many factors and may vary from a few degrees to 10-15 degrees. Texture scatter is especially strong on slight deformations and decreases on heavier deformations. Texture scatter is promoted by particles of other phases present in the metal, a higher temperature of deformation, etc.

2. Methods of Texture Analysis. Pole Figures

The principal methods for texture examination are X-ray, electron and neutron diffraction analyses. These methods are based on the same diffraction principles, but differ in the depth of penetration of diffraction rays into the object being studied, i.e. in the thickness of the layer where texture is analysed.

Among these methods, X-ray diffraction analysis is the simplest and most popular. It gives information on textures in layers a few fractions of a millimetre. Electron diffraction analysis is suitable for texture examination in very thin surface layers and films of micrometre thickness, since electrons are absorbed more strongly than X-rays. The principal advantage of diffraction analysis over other methods of texture examination is that it makes it possible to reveal easily the presence or absence of texture and establish its symmetry without destruction of the specimen, and also in that it establishes the crystallographic symbols of texture components.

Along with diffraction analysis, some physical methods (optical, magnetic and ultrasonic) are employed for texture examination.

Let us discuss in more detail the *X-ray diffraction analysis* of textures. First of all, the method determines easily whether a texture is present in a metal. If there is no texture, lines (or rings) on an X-ray powder photograph are blackened uniformly (Fig. 160*a*). In X-ray photographs of a textured material, these lines cease to be uniformly black, but exhibit individual maxima of blackening at regular intervals along a line. The more distinct a texture is (i.e. the lower the texture scatter), the less stretched are the blackening maxima along the Debye rings. An example of X-ray photograph of a textured material is shown in Fig. 160*b*.

A multi-component texture gives a more complicated pattern of Debye rings, since each of the texture components present produces its own system of interference maxima. All other conditions being identical, the intensity of these maxima (the density of blackening on a photograph) is the greater, the larger the relative volume occupied by a given component (or the 'weight' of that component).

Apart from solving this simplest problem, X-ray diffraction analysis can also determine the type of texture, i.e. the number of texture components, their crystallographic symbols, and the proportion of the material possessing the orientation of a given component.

Essential progress in X-ray diffraction analysis of textures and in quantitative estimation of the 'weight' of various components and the extent of texture scatter has been achieved in recent years due to the use of *ionization methods* for recording diffracted X-rays. Quantitative analysis of textures, especially of multi-component ones, is rather complicated and is based on the construction of 'pole figures' by the data obtained by X-ray diffraction analysis.

Pole figures. A pole figure of a polycrystal is the stereographic projection (see Ch. 2) of the normals (poles) to particular atomic planes $\{h_i k_i l_i\}$ constructed for all grains of a polycrystal, more strictly, of the volume in it for which a diffraction pattern is available.

If there is no texture, any orientations of planes in various grains are equally probable. In that case, the pole figure of these planes is a

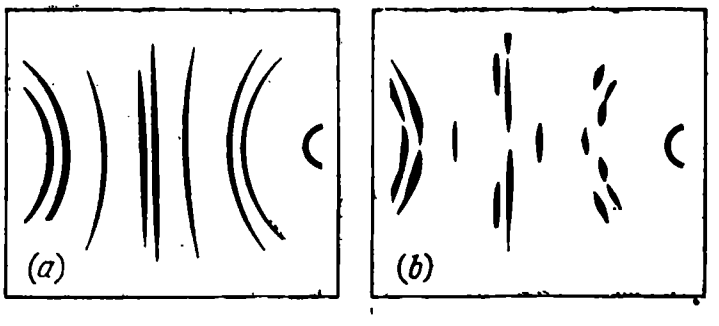

Fig. 160. Debyegrams of (*a*) untextured and (*b*) textured material

projection circle with uniformly distributed $\{h_i k_i l_i\}$ poles, which is represented graphically by even hatching of the whole projection circle (Fig. 161*a*). In a textured polycrystal, $\{h_i k_i l_i\}$ planes of various grains are oriented regularly in space, all planes of a particular texture component being arranged so that the corresponding crystallographic parameters are oriented strictly in the same sense (if there is no texture scatter) or only with a slight misorientation (with scatter).

In that case, poles will be distributed unevenly in the projection circle (see Figs. 161*b-d*, 162, and 163). The pattern of pole distribution depends on the type of texture, its scatter, and naturally, on the particular $\{h_i k_i l_i\}$ planes for which the pole figure has been constructed. With an ideal single-component rolling texture, a polycrystal becomes a single crystal, as it were, with the poles positioned in definite regular points of the projection circle (there are no degrees of freedom of orientations).

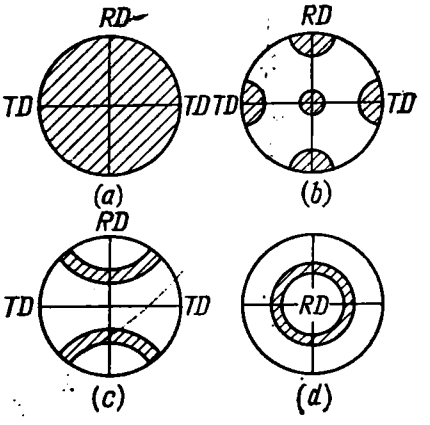

Fig. 161. Poles in pole figures of various textures (schematic)
(*a*) no texture; (*b*) ideal single-component rolling texture (cube texture, pole figure {100}); (*c*) axial texture (with axis in the plane of projection); (*d*) axial texture (with axis perpendicular to the plane of projection)

For an ideal multi-component texture (such as axial texture), grain orientations have one degree of freedom, so that the poles will be distributed along lines (arcs). With real multi-component textures, the picture is more complicated. Their pole figures contain more than one system of points (lines) according to the number of texture components. Under real conditions, where texture scatter is always present, points and arcs of a pole figure are smeared into spots.

The foregoing may well be illustrated by schematic and real pole figures given in Figs. 161-163.

Regions in a pole figure related to texture components of various intensity (various 'weight'), which have produced interference maxima of various intensity on an X-ray powder photograph, are usually hatched differently, as in Fig. 163, thicker hatching being used for more intensive components.

In recent time, when ionization methods have come into use for recording diffracted X-rays and quantitative estimation of the 'weight' of various texture components and the nature of texture scatter, lines of equal intensity of pole distribution are additionally drawn on pole figures. Numbers at these lines give the relative 'weights' of pole density in a given region of a pole figure (see Fig. 162).

Orientations on pole figures are determined by means of standard

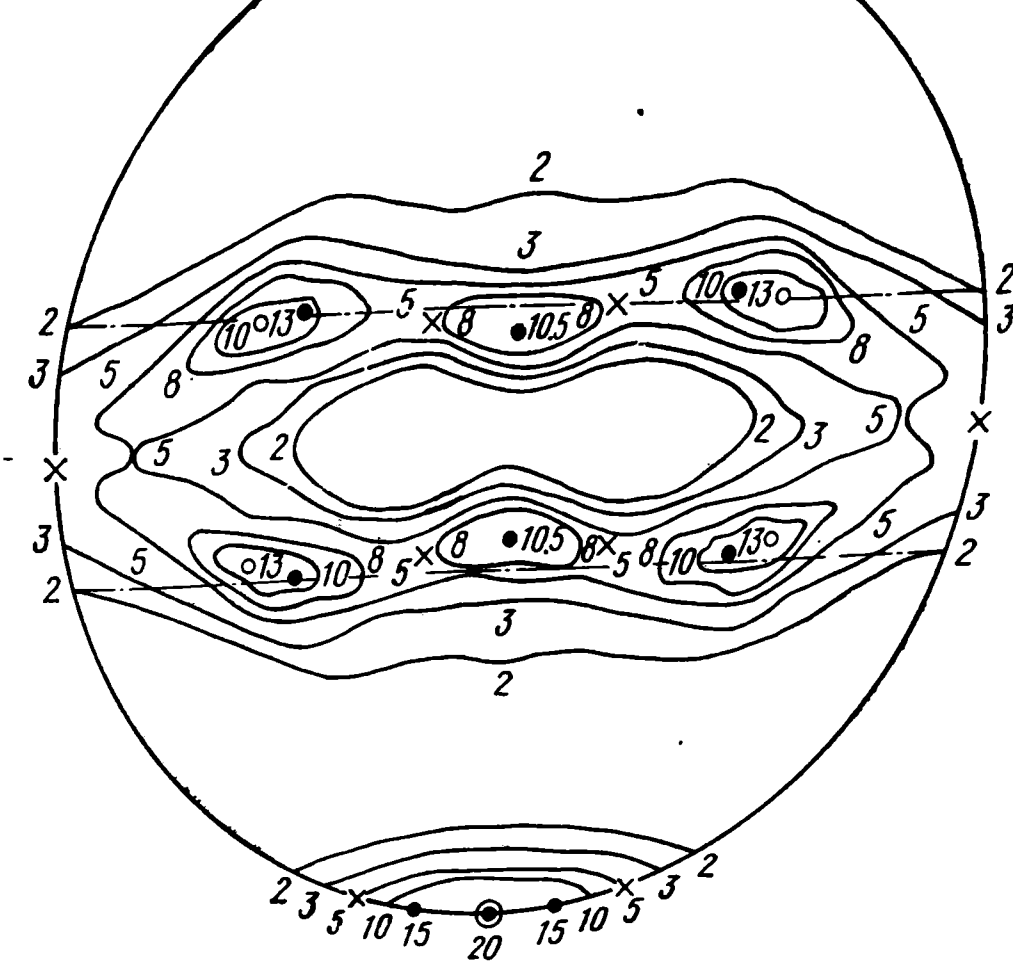

Fig. 162. The {111} pole figure of a multi-component texture in 50% F + 50% Ni f.c.c. alloy. Numbers are relative 'weights' of pole density

projections (Sachs' grids) which represent the stereographic proje tions of poles of various (*hkl*) planes in a single crystal oriented a definite manner relative to the projection circle.

Let us consider this procedure taking a rolling texture as an exam ple.

A pole figure is laid on various Sachs' grids (standard projections) and rotated to find the grid in which the projections of normals to the $\{h_i k_i l_i\}$ planes, for which the pole figure has been constructed, are coincident with the maxima on that figure.

When made coincident, the indices of the central spot of the selected Sachs' grid are those of the atomic plane which is parallel to the direction of rolling. The indices of the normals on the grid which coincide with the ends of the direction *RD* (rolling direction) and *TD* (transverse direction) on the pole figure determine the crystallographic directions of the lattice which coincide respectively with *RD* or *TD*. With a multi-component texture, some grains may be oriented with one crystallographic plane, and others with a different plane, parallel to the rolling direction, and therefore, not all the maxima of the pole figure can be made coincident with the poles of $\{h_i k_i l_i\}$ planes in a single Sachs' grid. In that case, one has to

find another grid in which the poles of the same $\{h_i k_i l_i\}$ planes will be coincident with the remaining undetermined maxima of the pole figure. This grid will give new additional indices of planes and directions parallel to *RD* or *TD*.

As an example, Fig. 163 shows the {110} pole figure of an Fe + 3% Si alloy after cold rolling.

Different hatching of regions in a pole figure implies different density of normals in density units of a pole figure for an untextured specimen, i.e. denotes the relative 'weights' of corresponding orientations (see numbered rectangles at the bottom of the figure).

As may be seen from that pole figure, a multi-component texture has formed in the iron-silicon cold-rolled alloy, which comprises a number of scattered orientations, the scatter regions being 15-20° wide and overlapping. The density maxima fall on the orientations {001} ⟨110⟩; {112} ⟨110⟩; and {111} ⟨112⟩.

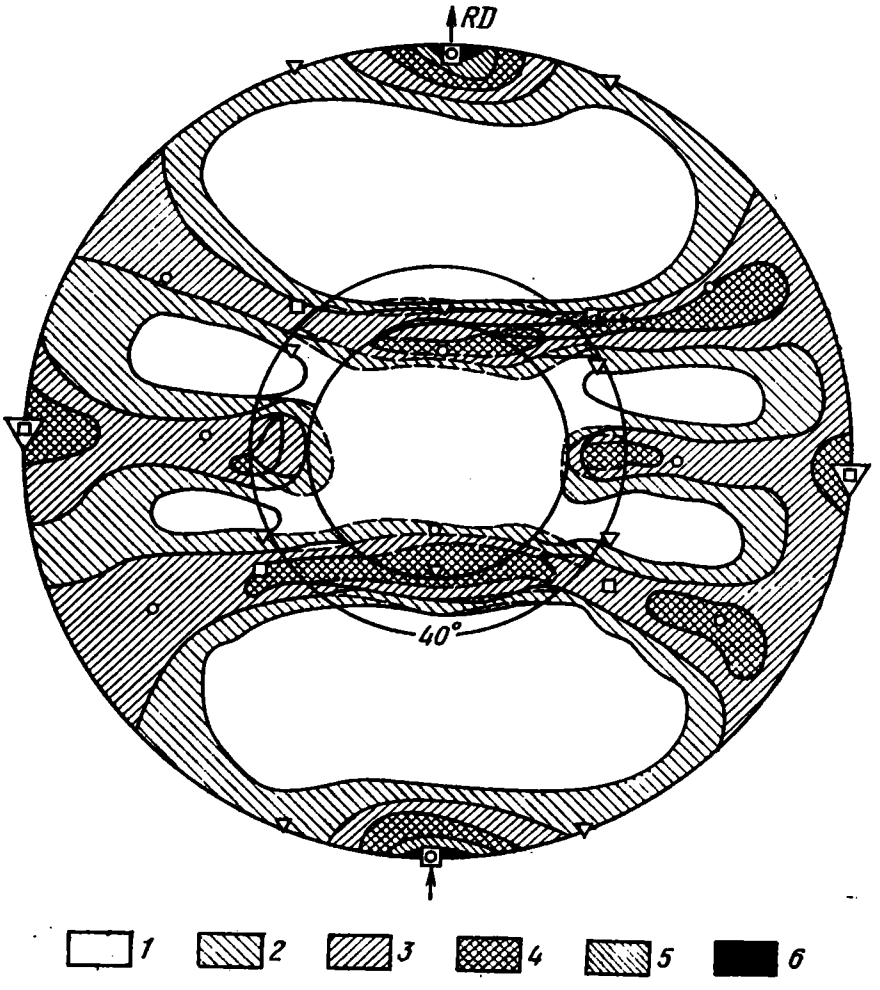

Fig. 163. Pole figure in [110] planes of Fe-Si alloy
Variously hatched regions define different densities of normals in density units of the pole figure of a specimen without preferable orientation (*1*—less than 1/2; *2*—1/2 to 1; *3*—1 to 2; *4*—2 to 4; *5*—8; *6*—above 8; *RD*—rolling direction)

It follows from this notation that a group of grains (most numerous) is oriented with their {100} planes parallel to the rolling plane and with their ⟨110⟩ direction parallel to the rolling direction (*RD*). The projections of normals to {110} planes of this group of grains are marked by squares in the pole figure.

Two other groups of grains (less numerous than the first one) have their {112} or respectively {111} planes parallel to the rolling plane and the ⟨011⟩ or ⟨112⟩ directions, parallel to the rolling direction. The projections of normals to {110} planes of these grains are marked respectively by circles and triangles in the pole figure.

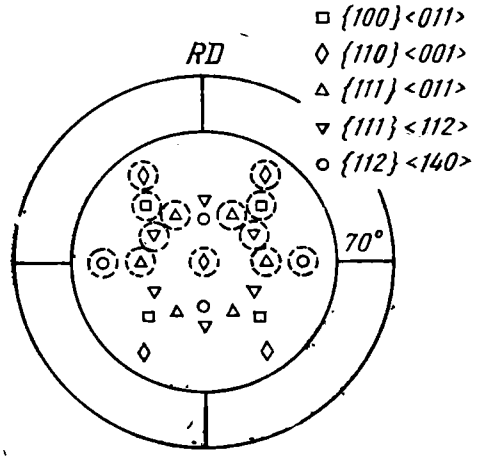

Fig. 164. Pole figure of coarse-grained polycrystalline transformer iron constructed by Laue photographs of individual crystallites

As can be concluded from analysis of this pole figure and from the extent of hatched scatter regions, rolling has produced essentially a continuous series of preferred orientations from {001}⟨110⟩ to {111}⟨112⟩.

When making texture analysis on pole figures constructed by the data of X-ray diffraction analysis, one should consider certain limitations of the method associated with its insufficient sensitivity. The intensity of diffracted rays from the texture components whose 'weight' is low will be low too and may be overlooked by the recording device on the strong background of scattered X-rays. As a result, these weak texture components will not be represented on the pole figure. On the other hand, their role is often decisive, especially in texture formation during recrystallization. Thus, when weak texture components can be expected to have an essential role, they should be revealed by special local methods (for instance, by electron diffraction analysis or etch pit methods).

If a coarse-grained material is to be analysed for textures, pole figures are constructed by the data obtained from Laue photographs of individual large grains on which their orientation in space can be determined. The orientations of various planes (with various $\{hkl\}$ indices) are then marked by points on the corresponding pole figures (Fig. 164). These points will form a pattern of varying density in the pole figure and thus can characterize the texture. It should be clear that the number of Laue photographs of individual grains should be sufficiently high to obtain pole figures of appropriate reliability.

Coarse-grained materials can also be examined in a diffractometer with an attachment for texture analysis. It is essential to use a spe-

cial device to move the specimen being photographed at a sufficient speed, so that a greater number of grains could be 'placed' into reflecting position.

As follows from the foregoing, common pole figures are essentially the two-dimensional projections of distribution of the orientations of normals to particular crystallographic planes of grains in a polycrystal in three-dimensional space. To obtain a more ample information on a texture, one has to use a few pole figures constructed for several planes with different indices.

In recent time, a method of three-dimensional analysis of orientations has been proposed. It uses three-dimensional functions of distribution of orientations of grains, which express the probability of the presence of crystallites with orientations described by the so-called Euler angles which correlate the coordinate systems of crystallites and specimen [in the general case, *RD* (rolling direction), *TD* (transverse direction), and *ND* (normal to rolling direction)]. The initial data for the method are several pole figures constructed for various $\{hkl\}$ planes. The minimal required number of pole figures depends on the lattice symmetry of a metal (at least three for cubic lattices).

The method is rather labour-consuming, involves a large body of mathematics and requires a mass-storage electronic computer. The description and possibilities of the method can be found in the specialist literature.

Etch pit technique can also be used successfully for rough estimations of textures in coarse-grained materials.

The *optical method* of texture analysis is based on the crystallographic anisotropy of the rate of chemical dissolution. With proper etching conditions, etch pits can be produced in the surface of grains which are readily visible in the light microscope. The shape of etch pits and their orientation in the section plane depend on which of $\{h_i k_i l_i\}$ planes of a grain is oriented parallel to the section plane and how this $\{h_i k_i l_i\}$ plane has been rotated around the normal to the section plane.

Figure 165 illustrates typical shapes of etch pits for some crystallographic planes.

Etch pit method is used with success for examination of changes in orientations in the course of deformation and recrystallization of single crystals and coarse-grained polycrystals of aluminium, transformer iron, etc.

Interesting data on grain orientation can be obtained by analysing the positions of slip lines and coherent twin boundaries in grains and also by colour etching. Grains oriented differently in the section plane can be coloured differently. This is achieved by various methods: by thermal etching in various gaseous media or by application of oxide films which are then examined in polarized light, etc.

Some optical methods are based on measuring the angles at which

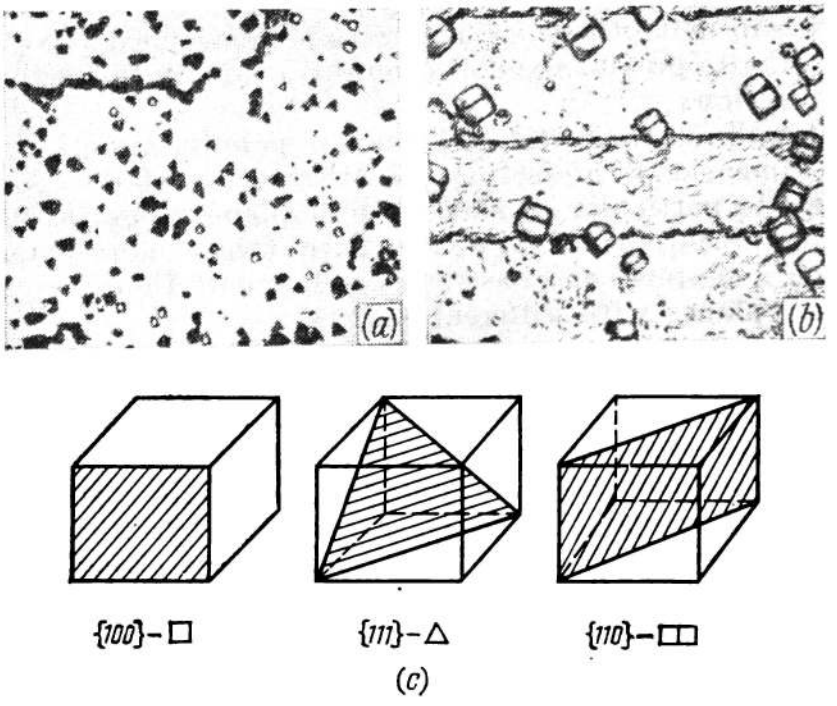

Fig. 165. Etch pits (*a*, *b*) found in most common crystallographic planes (*c*) of cubic lattice crystallites

the reflected light has the highest intensity (so-called 'maximum lustre method').

The *magnetic method* for texture analysis is not as widely applicable as the former ones, but is used successfully for examination of many ferromagnetic materials possessing anisotropic magnetic properties (transformer and dynamo steel, etc.). It is based on the tendency of a magnetically anisotropic material, when magnetized, to orient itself with the easy magnetization direction along the magnetic field applied, which produces a torque whose magnitude depends on the position of the specimen. Measurements of this torque at various positions of the specimen can give information on the anisotropy of its magnetic properties (the constant of magnetic anisotropy). The method is quite effective for analysis of texture scatter but cannot be used for determining the particular crystallographic indices of a texture. The method is quite simple and is used widely as a production control method. It can be applied for texture examination when combined with X-ray diffraction analysis.

3. General Principles of the Influence of Stressed-strained State on the Type of Deformation Texture

The number of the factors which determine the type of texture formed in a body on application of an external force field will be different depending on how the body behaves relative to the field

applied: either as a continuous isotropic medium (continuum) or as a medium in which only discrete displacements are allowed (discontinuum). The texture formation in crystalline bodies in plastic deformation which is realized by dislocation movement in particular crystallographic planes and directions furnishes an example of discontinuum.

In all cases, the symmetry typical of a given texture is determined by the symmetry of the external field. If the external action is complicated and represents a combination of several elementary actions with different symmetry*, the symmetry of the medium resulted from this action is determined by the principle of superposition of symmetry groups which has first been formulated by P. Curie.

A *symmetry group* (or, by the terminology adopted in crystallography, a *point group*) is understood as a combination of the least number of symmetry elements which can characterize a given symmetry class.

Before explaining this on an example, let us recall the symbols used for denoting the principal symmetry elements. Axes of symmetry are denoted by numbers 1, 2, 3, 4, 6 and ∞ ('infinity'), the number of an axis indicating how many states appearing during full rotation around that axis are identical with the initial state (before rotation). Dashed numbers indicate axes of mirror rotation. A plane of symmetry is denoted by letter *m*. A dot between the symbols of two elements implies that these elements are parallel to each other, a colon, that they are perpendicular, and a stroke (/), that they are tilted relative to each other. The symbol for a symmetry group (point group) includes only the minimal number of symmetry elements which is sufficient for designation of the symmetry class. For instance, the symmetry of a doubled cone is denoted by the symbol $\infty : m$, though, in addition to the ∞th order axis and a perpendicular symmetry plane, the figure also has the centre of symmetry.

The principal types of oriented action on materials are mechanical actions and those due to electric and magnetic fields.

As has been shown by P. Curie, the symmetry of an electric field is described by a group $\infty \cdot m$ (its geometrical analogue is a stationary cone) and that of a magnetic field, by $\infty : m$ (rotating cylinder). The mechanical stress fields which form in the most popular types of plastic working (rolling, pressing, drawing, stamping) are described in the general case by a symmetrical second-order tensor. As regards their symmetry, they can be related to one of the three groups as follows: $\infty/\infty \cdot m$; $m \cdot \infty : m$; or $m \cdot 2 : m$. The stress fields appearing in uniaxial deformation (pressing, drawing, etc.) belong to the symmetry $m \cdot \infty : m$, with one or more crystallographic directions oriented along the axes of compression or tension (axial

* Examples of complicated action may be found on p. 238.

textures). The stress fields typical of rolling result in a symmetry $m \cdot 2 : m$, i.e. some crystallographic planes are parallel to the rolling plane and some crystallographic directions in them coincide with the rolling direction.

Torsional deformation gives an $\infty : 2$ texture.

The principle of superposition of symmetry groups can be illustrated by the examples which follow.

(a) Articles of barium ferrite which has a hexagonal lattice (the symmetry of mechanical action is $m \cdot \infty : m$) are pressed in a magnetic field applied along the axis of pressing ($\infty : m$ symmetry). With such type of complicated action, the superposition of symmetry groups leads to the basal {0001} plane being oriented parallel to the pressing axis.

(b) If narrow platelets are cut out from a rolled sheet (symmetry $m \cdot 2 : m$) so that they are randomly oriented relative to a second-order (diad) axis, and then subjected to drawing, the symmetry in the wire specimens thus obtained will be $2 : m$. Subsequent deformation by torsion of these wires will reduce their symmetry to a single diad axis.

Though being important, symmetry is only a general characteristic of a texture. It is quite clear that an infinite number of particular textures, including multi- and single-component, may have one and the same texture symmetry. This may well be seen in the pole figures of rolled metals illustrated in Figs. 162 and 163. All of them belong to the symmetry $m \cdot 2 : m$, though represent quite different types of texture.

In real conditions, this is caused by differences in the type and number of operative slip systems on a particular external action, i.e. is associated with discrete nature of atom displacements in a body which thus behaves as a discontinuum. This behaviour in turn depends on a large number of factors, including the type of lattice, stacking fault energy, phase composition, orientation of external forces relative to operative slip systems, etc.

Thus, one should realize the limitations of the symmetry analysis of textures. The method can provide information only on the symmetry of a texture, in particular, of a multi-component one, but fails to determine the particular type of texture and therefore, the angular relationships characterizing the anisotropy both crystallographically and as regards the anisotropy of the properties, gives no data on the contributions of various texture components, etc.

On the other hand, the symmetry of action undoubtedly determines what may be called the macroscopic anisotropy of properties and structure, which is quite essential.

The kind of stressed-strained state is responsible for variations in the shape of specimens, whatever the crystal structure of the material may be.

In deformation of polycrystals, individual grains are subjected

to the same shape variation as the whole specimen. The crystal structure of a deformed body can be characterized by variation in the orientations of the crystal lattice, as well as by a desired variation in its shape. This variation is associated with the symmetry of the stressed-strained state and results finally in that a particular crystallographic plane and/or crystallographic direction are oriented parallel to the direction of the external deforming forces.

As has been noted in Ch. 2, the crystallographic direction of shear in tensioned single crystals is rotated with increasing deformation towards the axis of tension up to coincidence with the latter (on heavy deformations) and in compression, up to coincidence with the plane normal to the direction of compression. An important point is that, as the final stable orientation has set in, it is not changed by further deformation.

The direction of shear may be one of the slip directions belonging to the slip systems which exist in a particular type of crystal lattice.

Let us demonstrate what is the role of the type of lattice and of the symmetry of stressed-strained state in the formation of selected textures.

Axial texture. The principal slip system in b.c.c. metals is {110} ⟨111⟩. In any plane of the type {110}, there are two equivalent directions of the family ⟨111⟩ (Fig. 166), which are the directions of shear in b.c.c. lattices. Due to the symmetry of stressed-strained state, slip in these two directions, say $[11\bar{1}]$ and $[1\bar{1}1]$ in Fig. 166, is equivalent to slip along their resultant. In a state of stable orientation, these two directions must therefore be arranged symmetrically relative to the axis of wire (the direction of the external deforming force). This condition will be satisfied if one of the two crystal-

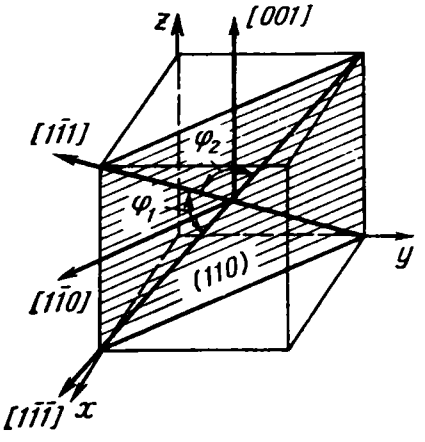

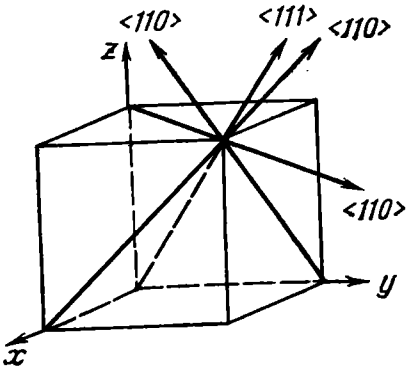

Fig. 166. (*left*) Diagram to establish ⟨110⟩ direction parallel to the axis of axial drawing texture in b.c.c. metals

Fig. 167. Diagram to establish ⟨111⟩ direction parallel to the axis of axial texture in f.c.c. metals

lographic directions of the type ⟨100⟩ or ⟨110⟩ is oriented along the wire axis. For the case illustrated in Fig. 166, these directions are [001] and [1$\bar{1}$0]. In practice, the ⟨110⟩ direction will be realized, since the angle between it and ⟨111⟩ (angle $\varphi_1/2$ in Fig. 166) is smaller than that between ⟨100⟩ and ⟨111⟩ (angle $\varphi_2/2$).

Similarly, in f.c.c. metals, where the slip system is {111} ⟨110⟩, three slip directions of the type ⟨110⟩ are symmetrical relative to the direction of the type ⟨111⟩, as illustrated in Fig. 167. The resultant of these three directions is the ⟨111⟩ direction and it will be oriented along the wire axis.

Under particular conditions, an axial ⟨100⟩ texture can also form in f.c.c. metals.

Rolling texture. The complex deformation in rolling can be imagined as superposition of two simpler deformations: tension along the rolling axis and compression perpendicular to the surface of metal.

In compression, owing to the symmetry of the cubic lattice, pairs of equivalent mutually perpendicular planes of the {110} family participate in slip. In each of these planes, slip can occur along two directions of the type ⟨111⟩, so that the resultant is a ⟨100⟩ direction.

In a pair of equivalent planes of the type {110}, slip can take place along two mutually perpendicular directions ⟨100⟩. This means however that it must occur in a plane containing two directions of the ⟨100⟩ family and one ⟨110⟩. This condition is satisfied by a plane of the type {100} which will therefore be perpendicular to the direction of compression.

These conditions should be favourable for the formation of a stable {001} ⟨110⟩ rolling texture which is actually observed in b.c.c. metals.

B. V. Molotilov and co-workers studied systematically how various original orientations of Fe + 3.5% Si single crystals were changed in rolling. It turned out that only the {001} ⟨011⟩ orientation was not changed in deformation. Moreover, many other orientations of single crystals changed to this orientation upon rolling.

It is clear that the transition from a given original to the final (stable) orientation passes through a number of intermediate states. The nature and sequence of this transition depend on the original orientation and the type of stressed-strained state, as well as on the type of crystal lattice. These factors determine the sequence in which various slip systems become operative during plastic deformation and, as a consequence, the type of re-orientation.

Numerous studies have demonstrated that several slip systems must operate in order to produce a noticeable re-orientation of the lattice. Figure 168 (after Boas and Schmid) shows how f.c.c. metals can re-orient during plastic deformation from one to another crystallographic direction parallel to the axis of tension (compression). Depending on the original orientation, one can distinguish four regions in which different slip systems are operative. In tension,

in particular, the final orientation may be either ⟨111⟩ (regions *a* and *c*) or ⟨100⟩ (regions *b* and *d*).

In compression (where orientations are reversed against the directions indicated by arrows), a ⟨110⟩ direction is the final orientation for all original orientations.

Plastic deformation of polycrystals involves additional rather complicating factors.

Some of them are associated with the fact that the number and types of operative slip systems and respectively the sequence of reorientation may be different owing to different original orientation of grains. For this mere reason, a multi-component texture is always existent during plastic deformation in which the number of components begins to diminish noticeably on appreciable deformations.

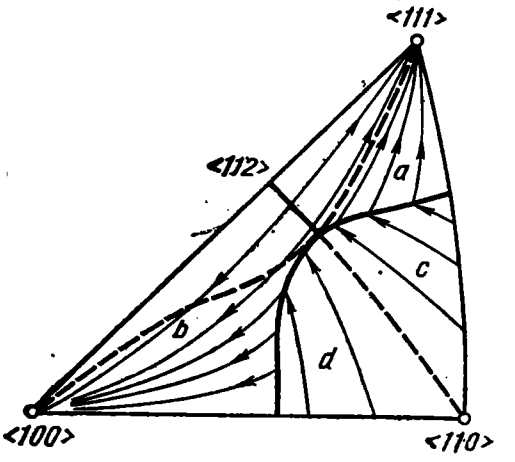

Fig. 168. Rotation of crystallographic direction to the axis of tension during deformation of f.c.c. metals (schematic)

The picture changes somewhat if the metal has been textured in the original state (prior to the deformation considered).

Another complicating factor is the presence of grain boundaries. The complications laid on by grain boundaries on plastic deformation and dislocation structure were discussed in Ch. 4. It should only be noted here that boundary regions, where slip is more turbulent, can be characterized by different orientations from those in the bulk of grains and by greater texture scatter than as dictated by the type of stressed-strained state.

4. Effect of Deformation, Crystallochemical Nature of Materials and Alloying on the Type of Deformation Texture

The number of factors which can determine the particular type of deformation texture is quite large, the principal ones being the conditions of deformation (type of deformation, rate, temperature, lubrication, etc.), the nature of the material being deformed (type of crystal lattice, nature of bonding, stacking fault energy, original texture and grain size, etc.), type of alloying (the nature of alloying addition, concentration, phase state), etc.

A systematic discussion of the main types of deformation texture is given below.

Drawing textures. In the general case, f.c.c. metals upon drawing contain two texture components: ⟨111⟩ and ⟨100⟩ in various pro-

portions. The ⟨111⟩ component is the first to appear in plastic deformation (on deformations of 20-30 per cent) and the ⟨100⟩ component forms on heavier deformations (roughly 40 per cent in copper and above 98 per cent, in aluminium).

Notwithstanding the enormous amount of data obtained by many researchers and for many materials, the principal factor responsible for variations in the proportion between these components remained for a long time unclear.

In recent time, a viewpoint based on the dislocation concepts has become popular and seems to be the most consistent.

According to it, the probability for the formation of some or other of these two orientations and the numerical proportion between them are determined by the tendency to cross slip, and therefore, in the first place by the stacking fault energy E_{sf} of the material. With a lower stacking fault energy and lower tendency to cross slip, the ⟨100⟩ axial texture component is more likely to form and in a greater amount, at the expense of the other component, ⟨111⟩.

This approach can explain well the majority of experimental facts, in particular the fact that pure aluminium (a high E_{sf}) upon drawing has practically only the ⟨111⟩ orientation and that the ⟨100⟩ orientation becomes stronger in the order aluminium-nickel-copper-brass-silver, i.e. in the same sequence as the stacking fault energy decreases from one of these metals to the next. After drawing deformation, the proportion of the ⟨100⟩ component in these metals decreases consistently and constitutes 8 per cent in aluminium (99.5% pure), 27 per cent in nickel, 34 per cent in copper, and 54 per cent in silver.

This agrees well also with the fact that the proportion of the ⟨100⟩ component in aluminium increases with increasing temperature of deformation and decreasing purity of the metal.

An essential role is played by the original orientation of grains. For instance, if a copper wire has had the ⟨111⟩ or ⟨100⟩ orientation prior to drawing, this orientation remains stable up to $\varepsilon = 80$ per cent. A second orientation appears on heavier deformations. With any other original orientation, the ⟨111⟩ component, as has been noted earlier, appears at $\varepsilon \leqslant 40$ per cent.

In all cases mentioned in the literature, b.c.c. metals (Fe, Nb, Ta, Mo, W, β-brass, single-phase iron alloys) form a single type of drawing texture: ⟨110⟩.

The results obtained for c.p.h. metals and alloys are less unique. For instance, the texture formed in titanium wire, which is characterized by a very low axial ratio: $c/a = 1.587$, is of the axial ⟨1010⟩ type with the basal plane parallel to the wire axis.

In magnesium ($c/a = 1.624$), a ring texture appears on drawing, with the basal plane parallel to the wire axis, i.e. the hexad axis is perpendicular to the axis of the wire, but the lattice can rotate about the hexad axis through any angle.

In zinc, whose axial ratio is still greater (1.856), a simple axial texture forms upon a relatively slight drawing deformation (20-30 per cent), with the basal plane being however not parallel but perpendicular to the wire axis; upon heavier deformations, a conical texture sets in, in which the basal plane makes an angle of 18° and respectively the hexad axis, an angle of 72°, with the wire axis.

Thus, a clear correlation can be traced between the *c/a* ratio of hexagonal metals and the type of axial texture that forms in them on drawing deformation. According to the material given in Ch. 3, a change in the axial ratio should involve a change in the operative slip systems, and therefore, in the type of deformation texture.

In recent time, the list of materials whose manufacture includes plastic deformation has been widened noticeably; this relates, in particular, to extrusion which also forms an axial texture.

Of large importance is the inhomogeneity of the axial textures formed by drawing, pressing and extrusion, which may appear in a number of forms.

Firstly, the inhomogeneity may be associated with scatter of texture orientations. Since a particular ideal orientation is set in not jumpwise, but by gradual re-orientation of the lattice in the course of plastic deformation, the amount of scatter depends, primarily, on the amount of deformation. It may decrease from tens to a few degrees with increasing deformation. In multi-component textures, the scatter of various texture components turns out to be different for the same amount of total deformation. Analysis of this phenomenon in copper wire has shown that the scatter of the ⟨100⟩ orientation is roughly twice that of ⟨111⟩, the reason of this effect still being not known uniquely. It is most natural to assume that the ⟨100⟩ orientation forms later than ⟨111⟩. If various texture components are formed not simultaneously, the one that forms on a heavier deformation should generally be more scattered.

Secondly, the texture may be inhomogeneous over the cross section. As a rule, texture scatter in surface layers is substantially higher than in the core*. In extreme cases, the surface layer may remain almost untextured. The depth of the layer in which the texture is different from the core decreases sharply with increasing deformation. In some cases of heavy deformations, thin surface layers may have a texture qualitatively different from that existing in the core. For instance, external layers of cold-drawn thin aluminium wire may have a conical texture with an angle of tilt up to 10° instead of the normal axial texture in the core.

Variations in the type of texture between outer and inner layers are especially frequent in hexagonal metals and alloys. Texture variations over the cross section of wire may be associated with tem-

* The difference can be reduced by reverse drawing.

perature differences over it, caused, for instance, by the conditions of deformation (heat evolution due to friction forces) or cooling. Which of these causes is prevailing determines whether texture variations will take place during deformation (due to temperature effect on deformation conditions) or during cooling (due to more intensive recrystallization in deeper layers of the wire).

The foregoing is associated closely with the problem on the effect of the rate and temperature of deformation on the type of axial texture, which has not been elucidated properly in the literature. In the general case, an increase in the rate or temperature of deformation provokes the formation of inhomogeneous and multi-component textures. Analysis of the laws and causes of this effect is however aggravated by the superposition of recrystallization processes which have time to occur to some or other extent during the deformation proper or in subsequent cooling.

Let us describe briefly other deformation processes which can form axial textures.

Tensile textures are, as a rule, similar to those formed on drawing. A more distinct tensile texture forms on heavy deformations typical of the formation of a neck just before fracture.

Compressive (upsetting) textures relate to the group of axial textures but differ substantially from those formed on drawing. The causes for this difference should be clear from the general principles of the effect of stressed-strained state on symmetry textures given in Sec. 3 of this Chapter. As has been given there, the direction of shear tends to set in parallel to the deforming force in tension and perpendicular to that force, in compression.

As a consequence, in upsetting of f.c.c. metals, the ⟨110⟩ crystallographic direction is preferably oriented parallel to the axis of compression. The texture formed is not however as distinct as that on drawing. In addition to the ⟨110⟩ orientation, other orientations can also be present in substantial proportions. For aluminium, these are the orientations lying between the ⟨110⟩ corner and the ⟨100⟩-⟨111⟩ side of the stereographic triangle.

In b.c.c. metals, such as iron, molybdenum, etc., compressive deformation most often forms a double axial ⟨111⟩ + ⟨100⟩ texture. In compressed hexagonal metals, the ⟨0001⟩ axis sets in either parallel to the compression axis, as in magnesium, or at a certain angle (15-30°), as in metals with a different c/a ratio (titanium, hafnium, etc.).

Complete textures (rolling textures). The types and sequence of orientations depend on the slip systems typical for a given crystal lattice and on how these systems are arranged in the original state relative to the deforming forces.

For a given type of lattice, the tendency to cross slip may have an additional role.

Important information for understanding the laws of lattice re-

orientation in rolling can be gained from results of rolling of single crystals of various original orientation.

Face-centred cubic metals and alloys. As has been demonstrated by experiments on single crystals and enormous number of various polycrystalline f.c.c. metals, the principal component of rolling texture in them is {110} ⟨112⟩, with the {112} ⟨111⟩ component being less frequent and the weak cubic {100} ⟨001⟩ component, even less so.

The general regularity is as follows. If cross slip is not easy, a simple single-component {110} ⟨112⟩ texture forms. When easy cross slip is allowed, a {112} ⟨111⟩ component appears and contributes more and more to the texture. This is why only the {110} ⟨112⟩ texture, often referred to as 'brass texture', or 'alloy texture', usually forms in f.c.c. metals and alloys of low stacking fault energy E_{sf}, such as silver, α-brass, and many solid solutions of f.c.c. metals.

Metals with a higher stacking fault energy E_{sf}, such as aluminium, nickel or copper, give a {110} ⟨112⟩ + {112} ⟨111⟩ texture which is called 'metal texture', or 'copper texture', though high-purity copper develops even a more intricate texture.

The term 'alloy texture' can be explained as follows. The formation of a substitutional solid solution usually lowers E_{sf}, especially at a higher valency of the alloying impurity. For that reason, if an original pure metal develops a copper texture, its solid solution of a noticeable concentration, i.e. an alloy on its basis, will form a simple {110} ⟨112⟩ texture. Thus, alloying can be used to control rolling texture in f.c.c. metals.

This explains well the phenomenon of what is called 'texture transition', which essentially consists in the following. As the temperature of deformation increases and thus allows easy cross slip, the texture maxima are shifted from the position corresponding to an 'alloy texture' towards that of a 'metal texture'. Texture transition has been found to occur in many alloys. In Cu + 2% Ge and Cu + 32% Zn alloys it is observed on raising the deformation temperature from −196°C to +20°C; in Cu + 15% Al alloys, from −196°C to +270°C; in Co + 30% Ni alloys, from +20°C to +600°C, etc.

Only materials of a very low stacking fault energy E_{sf} (such as silver) can retain a brass texture up to rather high temperatures of rolling (roughly 0.5 $T_{m.p.}$).

From the standpoint of symmetry, these two texture components can be explained by regarding the rolling process as a combination of tension and compression.

Under the effect of tensile forces, slip in f.c.c. metals occurs along ⟨110⟩. For every three symmetrical axes of the type ⟨110⟩ intersecting in a single point (see Fig. 167), the resulting slip direction is one of the type ⟨111⟩ which is oriented along the axis of tension. In com-

pression, a particular slip direction must set in perpendicular to the direction of compression, i.e. perpendicular to a direction of the type ⟨111⟩.

It follows from the condition of perpendicularity of two directions in a cubic lattice ($u_1u_2 + v_1v_2 + w_1w_2 = 0$, where $\langle u_1v_1w_1\rangle$ corresponds to ⟨111⟩) that directions of the types ⟨112⟩ and ⟨110⟩ can serve as $\langle u_2v_2w_2\rangle$. This means however that planes of the types {112} and ⟨110⟩ can set in perpendicular to the compression axis, i.e. parallel to the rolling plane.

By a similar consideration, a ⟨112⟩ direction can be the resulting one for two, but not three, directions of the type ⟨110⟩. For this direction, the probable $\langle u_2v_2w_2\rangle$ direction is ⟨110⟩, which gives an orientation {110} ⟨112⟩.

In addition to these two main orientations, a weak cube texture component {100} ⟨100⟩ can often be detected in copper and aluminium sheets upon a rather heavy deformation. This texture component in f.c.c. metals can be characterized by an extremely high stability in rolling. If an originally textured material containing a {100} ⟨001⟩ component is subjected to rolling, this component will be retained up to very heavy deformations (50 per cent or more).

There is certain evidence in the literature that, with particular original orientations ({112} ⟨111⟩, etc.), twinning may have an important role in texture variations.

Body-centred cubic metals and alloys. The most stable orientation in rolled b.c.c. metals and alloys is the {001} ⟨110⟩ texture. In this case, as with axial textures, various b.c.c. metals behave practically in the same manner.

The type of texture formed on rolling of differently oriented single crystals has been studied most systematically on silicon iron (Fe + 3.5% Si). It has turned out that the {100} ⟨001⟩ orientation separates in rolling into {100} ⟨001⟩ + {100} ⟨011⟩ and {110} ⟨001⟩ crystals are deformed by slip and twinning on the {112} ⟨111⟩ system and by the lattice rotation around {110}, which results in a change to a {111} ⟨112⟩ texture which, however, is unstable.

In rolling of originally textured polycrystalline silicon iron with the orientation {110} ⟨001⟩, a noticeable variation of texture begins on rather heavy deformations (50-70 per cent) and proceeds in the sequence: {110} ⟨001⟩ → {111} ⟨112⟩ → {112} ⟨110⟩ → {100} ⟨011⟩.

With finer size of original grains, the transition begins on slighter deformations.

It should not be concluded, however, from the sequence of texture transitions given above that a stable single-component {100} ⟨011⟩ texture will set in b.c.c. polycrystals on a heavy deformation. These textures are always scattered and multi-component. The most typical texture in b.c.c. metals is {100} ⟨011⟩ + {112} ⟨110⟩ + {111} ⟨112⟩, which has been first discovered in cold-rolled iron (on defor-

mation approximately 98 per cent). In addition to these main orientations, some weaker components may sometimes be observed in b.c.c. metals (Mo, etc.).

Hexagonal metals and alloys. Rolling textures in these metals are close to the {0001} ⟨1120⟩ orientation, but deviate from this ideal texture depending on the *c/a* ratio.

In metals with $c/a = 1.633$, i.e. that of the closest packing (magnesium, cobalt), the basal plane is practically parallel to the plane of rolled sheet, but the ⟨1120⟩ direction is strongly scattered around the rolling direction.

In metals with $c/a < 1.633$ (beryllium, hafnium, zirconium, titanium), the basal plane is tilted to the sheet plane and rotated around the rolling direction (*RD*) through an angle of 15 to 40°. Besides, the prismatic slip direction ⟨1010⟩ often sets in along the rolling direction.

Finally, in metals with $c/a > 1.633$ (zinc, cadmium), the basal plane is also tilted to the sheet plane, but it is rotated around the transverse direction (*TD*).

Tube texture. The scarce data available on this subject can be reduced to the following. If the scheme of deformation is such that only the wall thickness d is reduced and the tube diameter D remains unchanged, the orientation formed on the deformation will be essentially a rolling texture. If, however, both d and D are reduced roughly to the same extent, a drawing texture will appear. The drawing texture observed in rolled copper tubes, however, differs somewhat from the axial texture. Among the two orientations ⟨111⟩ + ⟨100⟩ the latter differed in that the rotation around ⟨100⟩ was limited. With $\Delta d/\Delta D > 2.5$, the rolling texture is again prevailing.

Cross-sectional inhomogeneity and texture scatter, which have been noted to occur in axial textures, are even more inherent in rolling textures. The effect of friction forces results in different stressed states in the surface layers and the core, and therefore, in inhomogeneous texture across the thickness of rolled sheets.

In many f.c.c. metals, a single-component texture, corresponding to the {100}⟨011⟩ orientation, forms in the surface. In addition, the distribution of textures across the thickness of sheets may often be unsymmetrical owing to different conditions of cooling or heating of the metal by the upper and the lower roll.

A typical feature of rolled b.c.c. and f.c.c. metals is also that the planes with the highest and most pronounced texture scatter are oriented definitely (but in a different manner) relative to the rolling direction (*RD*).

In b.c.c. metals and alloys, these planes are perpendicular to *RD* (Fig. 169), while in f.c.c. metals they are tilted symmetrically at an angle of approximately 30-40° to *RD* (see Fig. 162). Traces of these planes are shown in the figures by dot-and-dash lines. Another typical feature of texture scatter can also be seen in the figures:

they almost always exhibit three maxima of pole distribution density, which are denoted respectively by A, B, and C.

These maxima begin to appear on appreciable deformations (50-60 per cent); with further deformation, the distance between them diminishes, but the width of each maximum remains almost unchanged.

Generally, the scatter of rolling textures diminishes with increasing deformation, but remains stable beginning roughly with $\varepsilon \approx 90$ per cent.

In addition to inhomogeneity of textures across the thickness, a noticeable inhomogeneous lateral deformation may appear in narrow strips, caused by inhomogeneous transverse flow of the metal. In widened portions, the direction of the highest deformation will no more be the same as in the middle of the strip and will involve a change in the texture type.

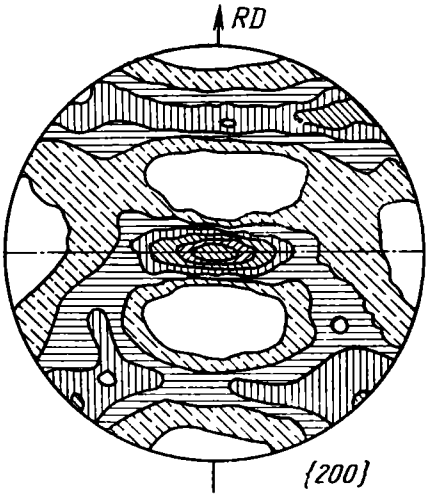

Fig. 169. Orientation of planes with the maximum scatter relative to rolling direction (*RD*) in rolled b.c.c. metals

A special case of texture formation is that when the rolling direction is changed by 90° (cross rolling) or 180° (reverse rolling).

Cross rolling of carbonyl iron and generally of b.c.c. metals has been found to reduce substantially texture scatter. In f.c.c. metals, in particular, in copper, the texture obtained on cross rolling was essentially a combination of two common rolling textures rotated through 90° relative to each other. Some other orientations can also appear, which results in a noticeably lower anisotropy of the mechanical properties.

The effect of reverse rolling should be most marked in metals of low symmetry, but the available data are very scarce. In copper, texture scatter increases on reverse rolling.

Effect of alloying and secondary phases on texture formation. Texture formation in single-phase alloys is determined by a number of factors, the most essential among them (in addition to deformation conditions) being the type of crystal lattice which determines the number and type of slip systems, and the stacking fault energy which characterizes the tendency to cross slip. The effects of these factors should be clear from the earlier discussion.

The situation is much more complicated with heterophase alloys. The peculiarities of texture formation in heterophase alloys are of double interest. On the one hand, heterophase alloys are extremely popular and important in engineering. On the other, particles of

secondary phases can be introduced intentionally for control of deformation textures, and especially of recrystallization textures (see Ch. 10). The laws governing this process are essentially the same for various types of deformation.

The effect of secondary phases on texture formation depends on the nature, size, shape and concentration of their particles.

When both phases are sufficiently plastic, the texture that forms in each of them is typical for a given phase in single-phase state and the given type of deformation. This has been demonstrated on binary alloys: Ag + Cu (28%), Cd + Zn (17%), and α + β-brass.

Anisotropy of Principal Properties in Textured Materials

The practical significance of textures is associated with the fact that they produce anisotropy of metal properties which may be substantial not only in metals with lattices of low symmetry, but even in cubic-lattice metals.

Among the properties which are especially texture-sensitive are the mechanical properties of metals, in the first place their elastic constants, and the magnetic properties of ferromagnetics. Besides, the coefficient of thermal expansion, electric and thermal conductivity and some other properties of materials with other than cubic lattice may be anisotropic.

Specialists in plastic working of metals are interested in the problem since, on the one hand, it is essential in many cases to know what properties and how can be changed by plastic deformation. There is however another, sometimes more important, aspect of how a texture can influence the process of plastic deformation proper. This influence can be produced, first of all, by the mechanical properties and the coefficient of thermal expansion.

The highest possible anisotropy of the properties in a given material due to crystallographic textures can be determined by analysing the anisotropy of these properties in single crystals of the material. Comparison of these data with experimental data on the anisotropy in textured polycrystals often gives substantially different results which may be due to a number of factors, the principal ones among them being the following two: (a) frequent superposition of a mechanical texture on the crystallographic (stretched shape of grains, and therefore, different distances between grain boundaries along and across grains) and (b) lineage structure formed by disperse phase particles.

As regards theoretical calculation of anisotropy of properties in real materials, it involves additional difficulties associated with the fact that the textures are multi-component and scattered.

For that reason, the following discussion of the anisotropy of properties of single crystals will be complemented by a brief survey

of experimental data on the properties of textured polycrystals.

Anisotropy of mechanical properties. The closest correlation with texture is found in the properties which can be described by fourth-order tensors. Among the mechanical properties, these include the elastic characteristics. As a rule, the characteristics associated with the flow stress correlate only qualitatively with texture. It is however difficult to establish unique relationships for elastic properties. In some cases, materials with the same type of crystal lattice texture may exhibit different anisotropy.

Figures 170 and 171 give orientational relationships for the elastic modulus E in sheets of copper and Fe + 48% Ni alloy (f.c.c. lattice) and Fe and Mo (b.c.c. lattice) after cold rolling and after

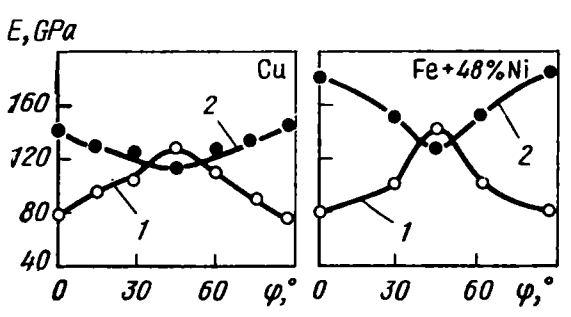

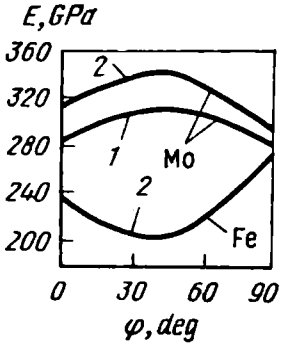

Fig. 170. (*left*) Orientation relationship for the elastic modulus E of f.c.c. metals and alloys (Cu and Fe + 48% Ni) after recrystallization (*1*) and cold rolling (*2*)

Fig. 171. Orientation relationship for the elastic modulus E of b.c.c. metals (Mo and Fe) after cold rolling (*2*) and recrystallization (*1*)

recrystallization. In all the cases, the extremal values correspond to an angle $\varphi = 45°$ to the rolling direction, but the types of extrema are different.

In the f.c.c. cold-rolled materials, the value of E is at a minimum in the direction at 45° to RD, but rises to a maximum upon recrystallization when a cube texture forms. The b.c.c. metals behave in a different manner. In iron, the angle of 45° corresponds to a minimum of E both in cold-rolled and recrystallized state, whereas in molybdenum sheets E is at its maximum in this direction. It should be considered that E can be affected by the presence of dislocations, as well as by texture. Dislocations lower the value of E. For that reason, E often decreases on slight deformations owing to an increase in the dislocation density and then begins to rise again as the role of texture becomes more substantial.

Anisotropy of the elastic modulus is made use of in springs whose maximum energy may be determined as follows:

$$A_{max} = (V/6)\,(\sigma_E^2/E)$$

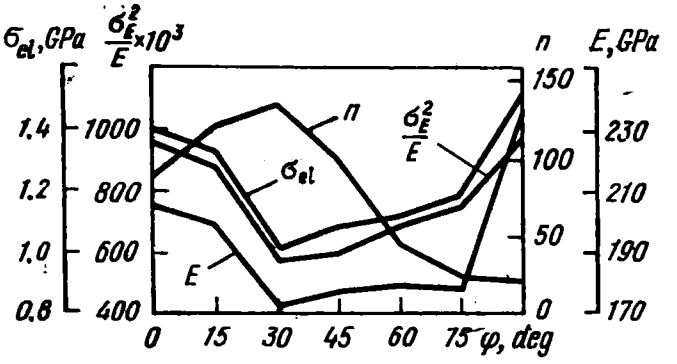

Fig. 172. Anisotropy of σ_{el}, E, σ_E^2/E and n (number of bends to fracture) in patented and cold-rolled steel sheets

where V is the volume of a spring, σ_E is the elastic limit, and E is the bulk modulus. The maximum energy A_{max} can be attained in materials of a high σ_E, i.e. high E.

As an example, Fig. 172 shows the anisotropy of σ_E, E, σ_E^2/E, and n (number of bends to fracture) for patented and cold-rolled steel sheets. As may be seen, the *RD* and *TD* (angles 0 and 90° respectively) are characterized by the maximum values of elastic characteristics, whereas n has a maximum at an angle 30° to *RD* and a minimum in *TD*. This regularity can well be explained crystallographically. The direction ⟨112⟩ is close to the ⟨111⟩ direction along which E is at a maximum. The direction ⟨100⟩ along which E has a minimum in textured f.c.c. metals (Al, Cu) is at an angle close to 45° relative to ⟨111⟩ and ⟨112⟩. The nature of this anisotropy in f.c.c. metals should change upon recrystallization which forms a cube texture. In rolled sheets of b.c.c. metals, the anisotropy of σ_t, σ_y and δ is not very pronounced. The general law is that the strength (σ_t and σ_y) is the highest in *TD*, while the maximum elongation is obtained in *RD*.

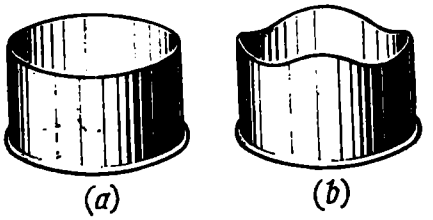

Fig. 173. 'Earing' formed upon deep drawing of cube-texture copper sheets (due to anisotropy of plasticity)
(*a*) untextured; (*b*) textured

Of special importance is the effect of texture on the capacity of sheet materials for deep drawing without fracture. The presence of a texture can result in 'earing' (Fig. 173), which can result in uneven thickness of walls, loss of metal with 'ears', and higher cost of deep-drawn articles. Earing can be characterized by the height of an 'ear' or the depth of a recess between 'ears', expressed in millimetres or as $(H_{max} - H_{min})/H_{min} \times 100\%$, and also by the number and arrangement of 'ears' around the perimeter. Earing may be especially pronounced in sheets of copper and other f.c.c. metals if a

cube texture is present. In that case, four 'ears' form, at angles 0 and 90° to *RD*. In addition, for copper sheets there has been established a linear relationship between the height of 'ears' and the concentration of grains with a cube texture component. Thus, avoidance of cube texture is the principal measure to avoid 'earing'. Steel sheets with the cube {100} plane oriented parallel to the sheet plane have been found to have a reduced drawability. Sheets with a {111} texture turn out to be much more plastic. With the rolling texture {110} ⟨112⟩ + {112} ⟨111⟩, which is typical of copper and aluminium, 'ears' appear at angles of 45° to *RD*.

The extent and type of 'earing' depend on many factors.

Textures are responsible for the phenomenon known as extrusion effect: under particular conditions of pressing of aluminium alloys, their strength properties in the direction of pressing turn out to be substantially higher than in the direction of metal flow in other types of deformation, say, in rolling. Hexagonal single crystals which have a lower symmetry than the cubic ones can be characterized by respectively stronger anisotropy of their properties. This is also true of textured hexagonal polycrystals. In this case, however, there are no unique regularities and the results may be different in metals and alloys with various *c/a* ratios. In this respect, zinc and its alloys have been studied most thoroughly and less so, magnesium, beryllium and titanium.

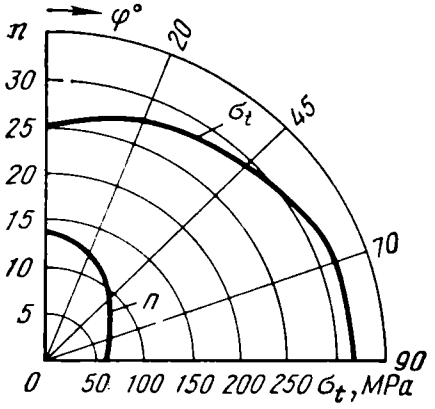

Fig. 174. Effect of angle φ to rolling direction on σ_t and number of bends *n* in the plane of zinc sheet (c.p.h. lattice)

As a rule, the bulk modulus of elasticity, *E*, is the highest in the basal plane and the lowest along hexad axes. For that reason, the direction of the highest *E* in a specimen will depend on how the basal plane has been oriented in deformation. In the rolling plane *E* is the highest in the direction *RD* and lower in *TD*. The strength is higher in *TD* and the plasticity (the number of bends to fracture), in *RD* (Fig. 174). This is associated with the fact that the strength is the highest in specimens in which the basal plane is oriented longitudinally, i.e. where the angle between a hexad axis and the specimen's longitudinal axis is close to 90°. Since the basal plane in zinc sheets is rotated around the *TD* direction, specimens cut across the rolling direction are stronger than those cut along the direction of rolling. The same regularity (a higher strength in *TD* than in *RD*) has been established for magnesium and magnesium alloys. Generally, magnesium is more anisotropic than zinc. An inverse relationship might be expected for metals with $c/a < 1.633$, but

a direct evidence to this is still unavailable. In rolled titanium, no anisotropy of the strength and elongation in the basal plane has been found.

Many hexagonal metals and alloys exhibit a distinct anisotropy of plasticity (deformability). For instance, beryllium wire is most plastic when the hexad axis is perpendicular to the wire axis; beryllium sheets show up the greatest plasticity when the basal planes are parallel to the sheet plane.

An interesting effect of texture strengthening has been detected in a number of metals of hexagonal symmetry. This is understood as strengthening due to the formation of a texture that is hard to deform. The effect of texture strengthening must be more pronounced in metals with $c/a \leqslant 1.633$ (Mg, Ti, Zr), in which $\{0001\}\langle 10\bar{1}0\rangle$ is an ideal rolling texture. In tension of a strip with such a texture, all shears will be in the strip plane (basal plane), in which three slip directions are operative, corresponding to prismatic $\{10\bar{1}0\}$ and hexagonal $\{10\bar{1}1\}$ slip. The resistance against thinning which is estimated in terms of the parameter R ($R = \varepsilon_w/\varepsilon_{th}$, where ε_w and ε_{th} is the deformation across the width and thickness respectively), can also characterize the degree of strengthening of a material. In a perfectly isotropic polycrystal, $R = 1$. In an ideal hexagonal texture with the orientation $\{0001\}\langle 10\bar{1}1\rangle$, $R = \infty$. In real cases where the orientation deviates from the ideal, R may take on values from 1 to ∞. The common values of R in hexagonal metals are 3 to 7 and depend slightly on direction in the basal plane. In deformation by two-dimensional tension (which can be regarded as a combination of hydrostatic tension and uniaxial compression), plastic flow begins only when the tensile stress exceeds the compressive stress which is perpendicular to the sheet plane. In strongly textured hexagonal materials where there is no suitably oriented slip system for thinning, the yield limit in compression increases, resulting in noticeable strengthening on two-dimensional tension. This strengthening by texture may be of interest for practical utilization in making impact-resistant vessels from sheets. In this respect, alloys based on titanium, beryllium and some other metals are promising.

For specialists in plastic working of metals, of much value are data on the effect of texture on the behaviour of a metal in plastic deformation, in particular, on such parameters as spread, shape of blank, pressure of metal onto rolls, etc. The available information in the literature is rather limited but there is undoubtful evidence of the existence of such an effect.

It has been reported on a study into the behaviour of iron and Fe + Si (2.16%) alloy with an axial $\langle 100\rangle$ texture and of artificial quasi-bicrystals made by argon-arc welding and consisting of strips of electric steel Grade ЭИ330 with a perfect $\{110\}\langle 001\rangle$ rib texture, cut out at different angles from the sheet.

Analysis of anisotropy of plastic flow in ⟨100⟩ grains for a case when {110} ⟨111⟩ is the principal slip system suggests that the most favourable direction for deformation should be the ⟨100⟩ cube edge and the least favourable, ⟨110⟩, other directions being intermediate. The experimental data are explained well from these concepts.

In hot rolling of differently oriented specimens with an axial ⟨100⟩ texture, it has been demonstrated that the greatest spread takes place in specimens with the ⟨100⟩ axis transverse to the rolling direction (across the width). Specimens in which the ⟨100⟩ axis was directed longitudinally had a lower spread (47% and 36%, respectively). The difference in spread diminishes with increasing reduction.

Cold rolling of specimens with the original flat cube texture (plane {100} parallel to the specimen surface and ⟨001⟩ direction tilted through various angles α relative to the rolling direction) has shown that strips are bent in the plane of rolling, but differently depending on the angle α. At $\alpha = 0$, there was no bending; at $\alpha = 30°$ bending was the highest (the specimen axis deviated at exit from rolls by 25° from the original direction). The cause of bending should be sought in that, at $\alpha \neq 0$, the direction of metal flow in the deformation region is not coincident with the axis of rolling. If the ⟨100⟩ direction is tilted to the rolling plane, the strip will be bent in the vertical plane (the bending plane will not coincide with the rolling plane).

Different orientation of slip systems relative to the operative stresses results in a different strain resistance, i.e. different pressure of metal onto rolls.

For that reason, rolling of {110} ⟨001⟩ specimens along the cube edge requires the lowest force for deformation. Rolling of welded quasi-bicrystals in which slip systems in one portion are oriented differently from the other portion leads to the main deformation vectors in these portions being non-parallel; furthermore, the elastic deformations of the rolls will be different. This causes distortions in the orientation and shape of strip at the exit from the rolls, in particular, uneven thickness across the width, longitudinal and horizontal bending, camber, buckling, and twisting. The particular type of distortion is determined by the mutual orientation of the preferred slip systems and respectively of the main deformation vectors in two portions of a bicrystal. Some types of deviation from the flat shape of strip having differently textured macroportions are illustrated in Fig. 175.

Anisotropy of thermal expansion. This type of anisotropy may lead to substantial changes in the structure, and therefore, the properties of a body if this is subjected to cyclic heating. Cyclic heating with a low number of cycles may take place in some procedures of plastic deformation.

The coefficient of thermal expansion α in non-cubic crystals is

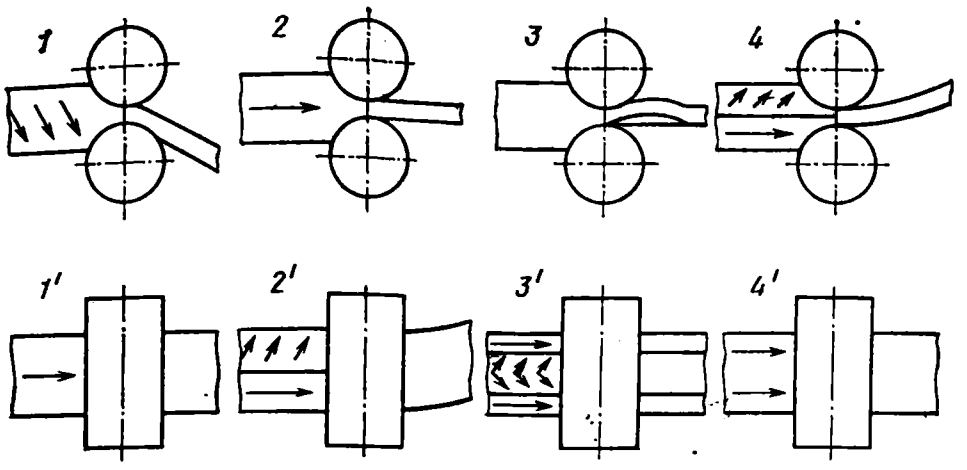

Fig. 175. Typical deviations from plane shape in rolled strips due to different textures in different macrovolumes of original blanks
1-4—side views; *1'-4'*—top views

substantially anisotropic. In hexagonal crystals, anisotropy is stronger when the axial ratio deviates more from the ideal $c/a = 1.633$. The coefficient of thermal expansion ($°C^{-1}$) for some c.p.h. metals in the directions parallel and perpendicular to the c axis is as follows: 25×10^{-6} and 25.4×10^{-6} for Mg ($c/a = 1.624$); 63.9×10^{-6} and 14.1×10^{-6} for Zn ($c/a = 1.856$); and 30.5×10^{-6} and 15.5×10^{-6} for Sn ($c/a = 1.546$).

Heating of non-cubic lattice polycrystals produces substantial local internal stresses which are greater at a higher anisotropy of the coefficient of thermal expansion. The appearance of local stresses is due to the fact that the expansion of a grain is opposed by neighbouring differently oriented grains. These stresses can cause plastic deformation of some grains, increase the density of dislocations and point defects and, under particular conditions, even lead to cracking.

A characteristic feature of these effects in textured materials is that cyclic heating can cause anisotropic macroscopic changes in the size of a specimen.

RECOMMENDED LITERATURE

1. Borodkina M. M., Spektor E. N., *X-ray Diffraction Analysis of Textures in Metals and Alloys.* Moscow, Metallurgiya, 1981 (in Russian).
2. Bunge H. J., *Z. Metallk.* 56, No 12: 872-874 (1975).
3. Honeycombe R.W.K., *The Plastic Deformation of Metals.* London, Edward Arnold, 1968.
4. Kudryavtsev I. P., *Textures in Metals and Alloys.* Moscow, Metallurgiya, 1965 (in Russian).
5. Smirnov V. S., Durnev V. D., *Texture Formation in Metal Rolling.* Moscow, Metallurgiya, 1971 (in Russian).
6. *Theory of Texture Formation in Metals and Alloys.* Ed. by N.V. Ageev. Moscow, Nauka, 1979 (in Russian).
7. Wassermann G., Grewen J., *Texturen metallischer Werkstoffe.* Berlin, Springer Verlag, 1962.

6 Characteristics and Driving Forces of Softening Processes (Recovery, Polygonization and Recrystallization) in Deformed Metals and Alloys

The free energy of as-deformed (cold-worked) metal is higher than that of annealed due to the distortion energy brought about by dislocations and point defects which have been formed by deformation. For that reason, a cold-worked metal is thermodynamically unstable at any temperature and its transition to a stabler state of a lower free energy is not strictly associated with a particular temperature. In that respect, this transition differs principally from phase transformations.

On the other hand, the deformed state is nonetheless quite stable ('frozen') at reduced temperatures. This can be explained by the fact that the transition to an undeformed state requires a certain thermal activation (activation energy Q) to overcome the potential energy barriers. The time τ for this process to set in is shorter at higher temperatures T and varies by an exponential law: $\tau = \tau_0 \exp(Q/RT)$.

As has been given in Ch. 3, the type and nature of distribution of crystal structure defects produced by deformation are quite diverse. These defects are eliminated on heating by way of various elementary processes which have a different activation energy and therefore, occur in different temperature intervals and at different rates. This is the principal difference between the processes of transition from work-hardened to undeformed state and phase transformations.

The activation energy Q of softening processes may vary depending on the associated elementary processes: from the activation energy of duffusion of vacancies to that of boundary and volume diffusion. If a number of elementary processes are superimposed on one another, the activation energy Q usually increases and becomes the 'effective', rather than the actual activation energy of the process.

The elementary processes which can occur in heating of a deformed metal and decrease the activation energy are as follows (in the sequence they appear during heating):

(1) diffusion of point defects and their disappearance in dislocations and boundaries, accompanied by partial annihilation of vacanc-

ies with interstitial atoms and by the formation of point defect complexes;

(2) redistribution and partial annihilation of unlike dislocations and narrowing of dislocation loops;

(3) redistribution of dislocations by climb, which, in combination with dislocation slip, results in 'flattening' or sometimes, on the contrary, in 'unraveling' of dislocation arrays and sub-boundaries;

(4) formation of low-angle boundaries associated with redistribution of dislocations by simple and cross slip and climb;

(5) migration of low-angle and high-angle grain boundaries into the deformed matrix, accompanied by consumption ('sweeping-out') of defects; and

(6) migration of grain boundaries between recrystallized grains and coarsening of these grains.

It should be noted, however, that the classification given above is only conditional and that the atomic mechanisms of a number of the elementary processes mentioned still have not been studied thoroughly, especially the mechanism of formation of low-angle boundaries.

The above-mentioned elementary processes can occur either one after another or simultaneously, depending on the amount and kind of deformation, the rate and time of heating, the nature and purity of the metal and some other factors. As a consequence, the effects of cold work on the structure and properties of a metal (alloy) can be eliminated in different ways and to a different extent. The following principal stages of structural changes during heating upon work hardening can be distinguished (written in an order of increasing activation energy, and therefore, increasing temperature for their realization)*: (1) recovery; (2) polygonization; (3) recrystallization, which includes: (a) primary recrystallization; (b) grain growth (uniform); and (c) secondary recrystallization, often called 'exaggerated', or anomalous, grain growth.

1. The Mechanisms and Temperature Levels of Recovery and Polygonization

a) Recovery. In the general sense, *recovery* should be understood as the process of structural perfection of cold-worked metal by redistribution and annihilation of point defects and redistribution of dislocations by conservative slip without formation of new boundaries. Thus, the stage of recovery involves no visible changes in the microstructure of the metal.

The detailed list of the elementary processes which occur at the recovery stage is not unique and generally adopted. This is associat-

* This classification has been proposed by S. S. Gorelik and differs somewhat from his earlier classification.

ed with the fact that the direct detection of point defects, the main type of defects eliminated in recovery, is still practically impossible, whereas indirect analysis (by a change in the metal properties) is usually ambiguous.

A partial way out from the situation has been found by using certain methods (particle irradiation or hardening from a higher temperature*) which produce only point defects in the material. By analysing the changes in the physical properties of such irradiated or hardened materials, it is possible to determine the temperature intervals, kinetics and activation energy for annihilation of these defects. The results obtained are then applied to deformed materials.

When studying recovery in deformed materials, useful information on the course of a particular elementary process can be obtained by analysing in parallel the changes in resistivity, enthalpy (by calorimetric measurements), density, hardness, elastic and yield limit, internal friction, and the pattern of X-ray interference maxima.

When analysing the results obtained by various methods, the effect of a particular type of defect on a given property should be considered. For instance, the concentration of point defects has the strongest influence on resistivity; the density and distribution of dislocations, on the mechanical properties and the pattern of X-ray lines; the type of dislocation locking by point defects, on yield limit and internal friction; the concentration of vacancies, on density; etc.

Using the methods indicated, it has been demonstrated that some elementary processes of recovery require a very low activation energy and can therefore occur at quite low temperatures, only a few hundredths of the absolute melting point ($T_{m.p.}$). In that connection, studies of recovery should be done on specimens deformed at as low a temperature as possible and then heated gradually. Otherwise, there is a risk to miss the part of the stored energy of cold work that is released already in the course of plastic working or after it but before the measurements are made.

H. G. Van Bueren has generalized the data of a number of studies on irradiated, hardened and deformed copper and gold and proposed a classification of the stages of recovery, polygonization and recrystallization. His classification (with slight modifications) is given in Table 12.

Though Van Bueren's classification is not exhaustive and true for other metals and alloys, it still has not lost its significance.

As has been demonstrated in later works, the number of recovery stages can be influenced substantially by impurities, the stacking fault energy, and the conditions of deformation. It has been shown that the number of recovery stages may vary from two to six.

* The method of hardening is less reliable, since hardening can lock thermal vacancies and produce dislocations (owing to high thermal stresses).

Table 12. Elementary Processes of Restoration of Electric Resistivity in Copper and Gold

Process	Stage	Temperature range, K (fraction of $T_{m.p.}$)	Activation energy, eV	Supposed mechanism of elementary process
Recovery	I	30-40 (0.03-0.4)	0.1	R.P.
Ditto	II	90-200 (0.1-0.15)	0.2-0.5	M.M.
Ditto	III	210-320 (0.16-0.20)	0.7	M.V.
Polygonization	IV	400 (0.27-0.35)	1.2	M.R.
Primary recrystallization	V	around 500 (0.35-0.40)	2.1	C.T.S.

Note: R.P. – recombination of interstitial atom-vacancy pairs; M.M. – migration of interstitial atoms, migration of vacancy groups (bivacancies, etc.); M.V. – migration of vacancies to traps, migration of bivacancies; M.R. – migration of vacancies to dislocations promoting redistribution of dislocations, with the formation of low-angle boundaries and partial annihilation; C.T.S. – climb and thermally activated slip of dislocations, resulting in partial annihilation of dislocations and formation of high-angle mobile boundaries.

The first three stages of recovery are undoubtedly associated with movement and annihilation of point defects. It is still difficult to relate more strictly and uniquely a particular stage of recovery to a definite type of point defects (vacancies, interstitials, bivacancies, complexes of the type vacancy-impurity, vacancy-interstitial atom, etc.).

The main portion of restored electric resistivity is due to recovery caused by point defect annihilation*. In deformed metals, the electric resistivity is restored at the stage of recovery (at the expense of point defects) roughly by 20-30 per cent.

The available data on the effect of point defect annihilation on the mechanical properties are controversial and ambiguous. It has been found that the yield limit of gold and aluminium increases at the stage of recovery; the effect has been attributed to the formation of vacancy clusters which can inhibit dislocation movement. It is still unclear whether the dislocation structure proper, which has a decisive effect on the mechanical properties, remains unchanged in this process.

There are, however, certain specific conditions of deformation after which the properties of annealed metal can be restored fully at the recovery stage. This is possible, for instance, in cases when the defor-

* In view of the fact that partial restoration of a property occurs without any noticeable changes in the microstructure, the stage considered has been termed 'recovery'.

mation has been limited to the stage of easy slip (in a single slip system). The most typical example is the deformation of hexagonal crystals oriented favourably for basal slip.

If more than one slip systems have participated in slip, the properties of the metal at the recovery stage will be restored only partially.

The kinetics of recovery can be characterized by the fact that the process has no incubation period. Its rate is at a maximum at the initial instant ($\tau = 0$) and then decreases exponentially.

Denoting by X the restored fraction of a property, we have:

$$X = 1 - \exp\left[-k'\tau \exp\left(-Q/RT\right)\right] \tag{152}$$

where T and τ are respectively the absolute temperature and time of heating; Q is the activation energy; R is the gas constant; and k' is a coefficient.

For an isothermal process:

$$X = 1 - \exp\left(-k'\tau\right) \tag{153}$$

$$dX/d\tau = k'/\tau$$

i.e. the rate of variation of the property which is restored by recovery is inversely proportional to the time of heating and has a maximum at the beginning of the process.

Polygonization. Among the processes which can noticeably change the structure of a deformed material on heating, polygonization is the most low-temperature one.

Polygonization is understood as the process of formation and coarsening of sub-grains during heating of cold-worked metals and alloys. Sub-grains are formed by redistribution of individual dislocations and/or by 'flattening' of spatial dislocation pile-ups due to dislocation slip and climb, with the formation of low-angle dislocation sub-boundaries. Coarsening of sub-grains is realized by their coalescence or by migration of sub-boundaries.

The phenomenon of polygonization was first observed by S. T. Konobeevsky and I. I. Mirer in rock salt crystals*. They found that radially extended spots (asterism streaks) in Laue photographs of a salt crystal deformed by bending were separated on annealing into discrete single fine spots. This effect implies that a plastically bent crystal disintegrates on annealing into a number of structurally perfect blocks which are discretely tilted through small angles relative to one another, with the total misorientation of the crystal remaining unchanged. In that case, each spot is a trace of an interference beam 'reflected' from an individual block.

Similar results have been later obtained by many workers on various single crystals and coarse-grained polycrystals and the

* The term 'polygonization' was proposed later by E. Orowan.

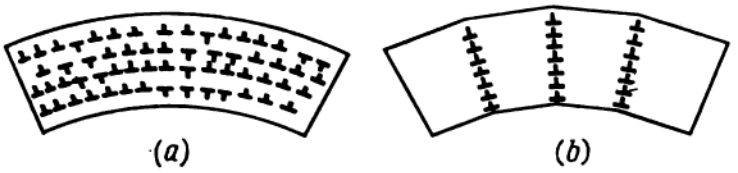

Fig. 176. Distribution of dislocations in a crystal deformed by bending
(a) before polygonization; (b) after polygonization

atomic mechanism of the phenomenon has been explained on the basis of the modern concepts of dislocation theory.

The dislocation mechanism of polygonization can be described most clearly by considering a single crystal deformed by bending (i.e. by easy slip corresponding to Stage *I* work-hardening), which has an excess of like edge dislocations (Fig. 176).

During annealing, dislocations are re-grouped under the effect of long-range elastic fields. Unlike dislocations annihilate and excess like dislocations are rearranged into energetically more favourable dislocation arrays perpendicular to the planes in which the dislocations were arranged prior to annealing (Fig. 176*b*). The process, which includes dislocation slip and climb, results in the formation of new flat tilt boundaries perpendicular to the slip planes, which were absent before heating. Such boundaries possess no long-range stress fields and are characterized by a low curvature and therefore, low mobility. The regions of the crystal separated by these low-angle boundaries and free of dislocations, represent, as it were, crystallite blocks, or polygons (hence the name 'polygonization').

Dislocation arrays are readily revealed matallographically as a series of etch pits arranged perpendicular to the slip planes. Each etch pit appears in the point where a dislocation comes to the surface of a microsection. A dislocation array formed on polygonization is illustrated in Fig. 177.

Thus, an important feature of the simplest mechanism of polygonization considered earlier is that boundaries of polygons are form-

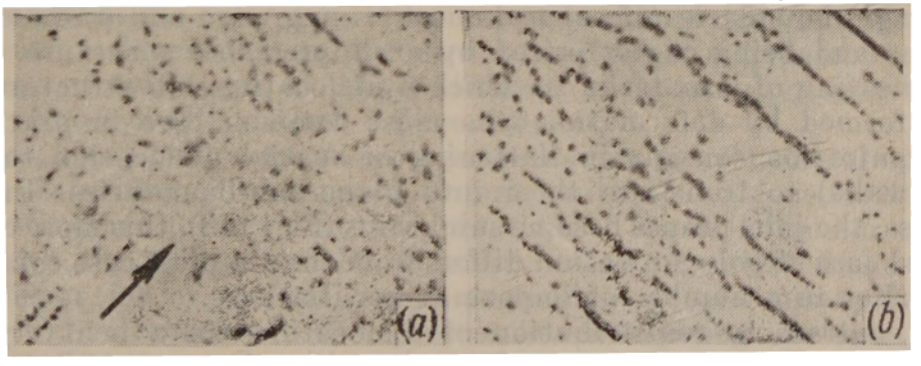

Fig. 177. Low-angle dislocation boundaries (arrays) formed on polygonization of Fe + 3.5% Si single crystal and revealed by etch pit method
(a) before polygonization, (arrow indicates slip direction); (b) after polygonization

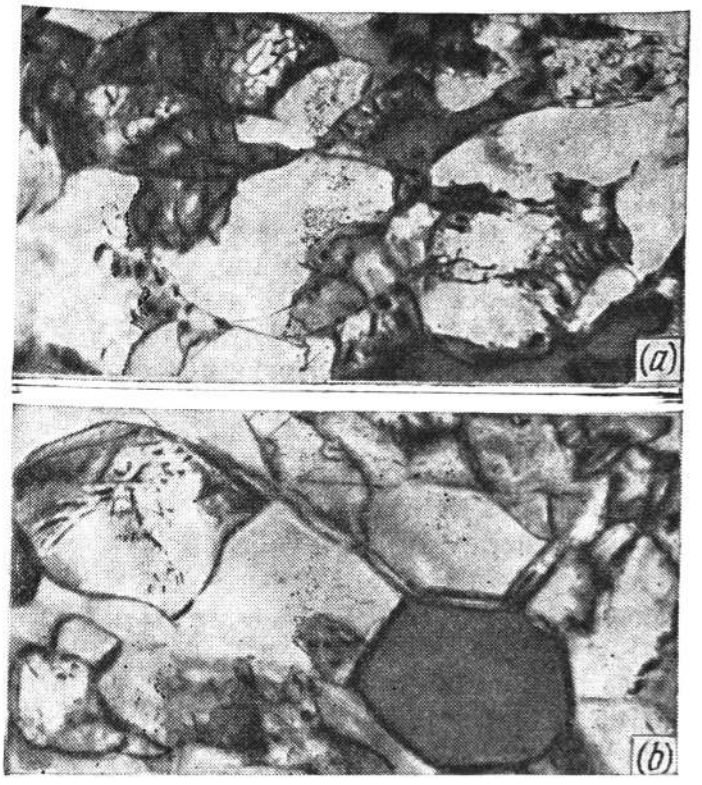

Fig. 178. Dislocation cell structure in aluminium deformed 70% at —50°C by rolling (*a*) and then heated at 270°C in salt-petre to induce polygonization (*b*). 1200×

ed anew in the course of polygonization proper. Neither these boundaries nor their contours were present in as-deformed metal.

Later, the concept of polygonization has been given a broader interpretation. It is described as a complicated process of redistribution and interaction of dislocations resulting in the formation of subgrains in single and polycrystals deformed by multiple slip, with low-angle boundaries of subgrains containing edge and screw dislocations and being characterized by an appreciable curvature.

In heating of a material in which a dislocation cell structure has been formed by deformation (the most common case in practice), polygonization consists in flattening of spatial dislocation tangles (cell walls) to transform them into plane sub-boundaries. In this process, the cells proper become sub-grains (Fig. 178), this more complicated case of polygonization differs from the simplest case considered earlier in a number of important peculiarities.

In contrast to redistribution of dislocations in a bent crystal, complex polygonization includes cross slip of screw dislocations, as well as conservative slip and climb. Further, in polygonization of deformed metal by multiple slip, the boundaries of polygons formed in the process have been outlined in as-deformed state by walls of

dislocation cells. Sub-boundaries formed by flattening of cell walls are characterized by an appreciably higher curvature and mobility than dislocation arrays formed anew in polygonization upon slight deformation.

The final important difference is that the structure of polygons and their boundaries in a cell structure is practically independent of temperature. With an increase of temperature, the process is simply accelerated, but the contributions of various mechanisms of dislocation redistribution and the paths of these redistributions are changed only weakly with temperature. Slightly deformed crystals, in which the cell structure has not yet been formed distinctly, behave in a different way. A change in the heating temperature varies the contribution of various mechanisms of dislocation redistribution, and therefore, the paths of these redistributions and the type of the polygonized structure formed. At relatively low temperatures, dislocations move by slip and climb and form stable boundaries of a low curvature. At higher temperatures, cross slip plays ever greater part, increasing the probability of formation of polygons with boundaries of greater curvature and mobility and the probability of migration of the original boundaries which consume dislocations.

This difference in the nature of polygonization depending on the nature of the original (prior to annealing) dislocation structure of deformed material is essential for understanding the relation between polygonization and recrystallization, in particular, for clarifying the problem of whether polygonization is a process which competes with recrystallization or merely the initial stage of the latter. This problem, which was disputed for a long time, is of high practical significance. If these processes are competing, polygonization can be used to prevent recrystallization in cases when this is unwanted.

Should the paths of redistribution of dislocations in polygonization be the same as at the initial stages of recrystallization, it will then be clear that polygonization is only the initial stage of recrystallization; otherwise, the two processes can be competing.

In view of the foregoing, it seems reasonable to differentiate polygonization depending on the structure formed and introduce the concept of two types of polygonization: stabilizing polygonization and prerecrystallizational polygonization.

Stabilizing polygonization is a process of redistribution of dislocations on heating of a deformed material with a homogeneous dislocation structure formed through operation of a small number of slip systems; the process results in annihilation of unlike dislocations and formation of new stable low-angle (low-mobile) sub-boundaries of a slight curvature. The process is a competing one relative to recrystallization.

Prerecrystallizational polygonization is a process of redistribution of dislocations on heating of a deformed material, which results in partial annihilation of dislocations in walls of dislocation cells and

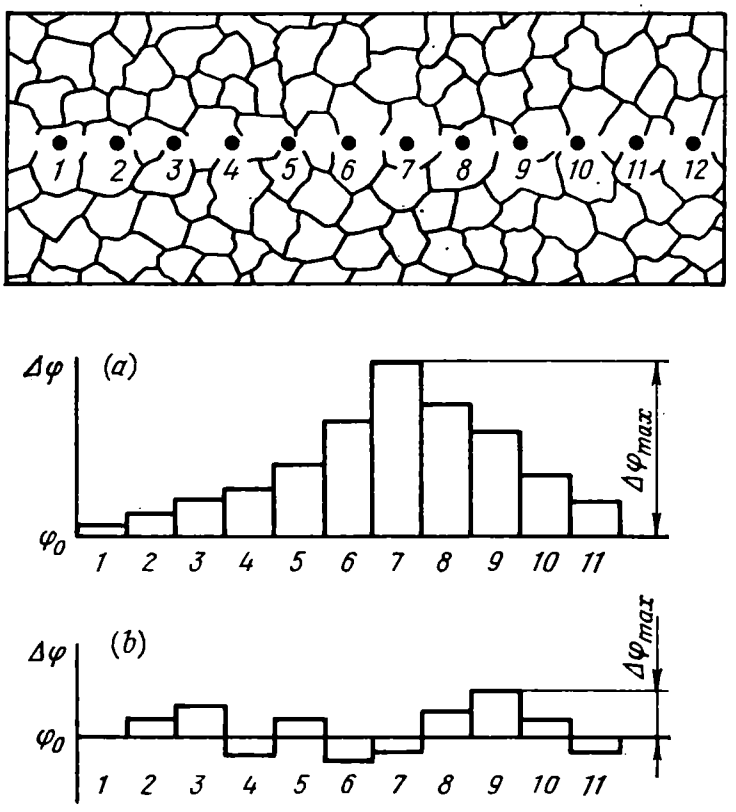

Fig. 179. Various types of sub-grain misorientation (schematic)
(*a*) misorientations increase regularly from one grain to another; (*b*) irregular variation of misorientation; the algebraic sum of misorientations on a large length is close to zero

in flattening of these cells into sub-boundaries of a relatively high curvature and high mobility. In this process, cells are transformed into sub-grains with different misorientation relative to one another. The process is essentially the initial stage of primary recrystallization.

Apart from the stage of formation of sub-grains, polygonization also includes the stage of their coarsening which can occur by two mechanisms: (1) by migration of sub-boundaries due to the trend of the system to diminish and balance the boundary tension or to reduce the volume energy of adjacent polygons and (2) by coalescence of adjacent polygons with unravelling of the dislocation sub-boundary between them (the mechanism of coalescence will be discussed in the section on the mechanisms of formation of recrystallization nuclei).

If misorientation angles ($\Delta\varphi$) increase regularly from one sub-grain to another (Fig. 179), their misorientation relative to the matrix will increase during their growth at the expense of the matrix. At the moment when a sub-boundary becomes a high-angle boundary, the respective sub-grain becomes a nucleus of actual primary recrystallization.

If the algebraic sum of the misorientation angles between sub-grains at appreciable distances from one another is equal to zero, sub-grains will increase to an appreciable size (a few micrometres) in the course of their growth by boundary migration, without any noticeable increase in their misorientation relative to the surrounding matrix. This case has been called in-situ recrystallization. The term, however, seems to be inappropriate, since recrystallization relates to processes associated with high-angle boundaries. It would be more correct to call the process 'collective polygonization'.

Since polygonization includes a number of elementary processes (conservative slip, cross slip, climb), the rate of the process as a whole should be limited by the slowest elementary process. Diffusion climb is most often such a process, though the processes of dislocation slip may turn out to be the slowest if there are strong barriers for dislocation movement.

For that reason, polygonization is impeded by all the factors which can retard the diffusion of vacancies and diminish their concentration, lock dislocation movement, favour the formation of impurity atmospheres around dislocations, diminish the stacking fault energy E_{sf} and thus inhibit cross slip of screw dislocations.

2. The Mechanism and Temperature Level of Recrystallization

Recrystallization is a process in which grains of a given phase are replaced fully or partially by the same-phase grains having a lower energy. The process can occur through the appearance and motion of high-angle boundaries (primary recrystallization) or only through the motion of such boundaries (grain growth and secondary recrystallization).

Thus, recrystallization, like recovery, is a multi-stage process. The first, most low-temperature, stage is called *primary recrystallization.* It can occur either immediately after polygonization or at the same time with polygonization occurring in neighbouring portions. This stage reduces most radically the number of crystal structure defects introduced by prior deformation and accordingly the stored volume energy of deformation, up to full restoration of the structure and properties the material has had before the deformation.

The essence of primary recrystallization consists in the following. As the metal is being heated, portions form and grow in the deformed matrix, which have an undistorted or appreciably less distorted lattice than the matrix. These portions are separated from the matrix by high-angle boundaries and called recrystallization nuclei. The growth of nuclei at the expense of the matrix is realized by migration of their high-angle boundaries.

Primary recrystallization is completed (but not recrystallization in the general sense) as the deformed matrix disappears.

The most important role of recrystallization is in that it not only restores the structure of undeformed material (in primary recrystallization), but also can produce further substantial changes in the structure and texture of the material, and therefore, in its properties (in subsequent recrystallization stages).

Thus, recrystallization is a powerful tool which can influence the properties of metals and alloys. For this influence to be controllable, it is essential to know the mechanism of the process at all its stages.

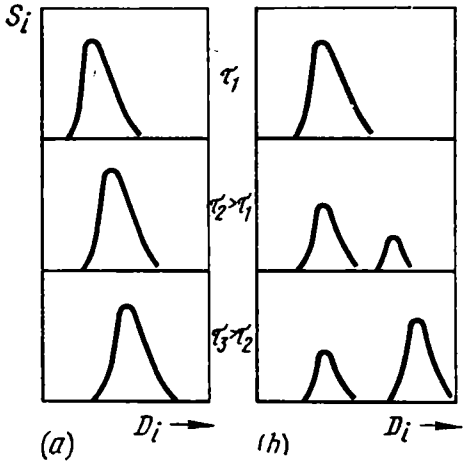

Fig. 180. Variations in grain size distribution during (*a*) grain growth and (*b*) secondary recrystallization

S_i —area occupied by grain of ith size; D_i—diameter of ith size grains; τ—time of annealing

If a material in which primary recrystallization is completed is heated further at the same or a higher temperature, it will pass through the stage of grain growth and/or *secondary recrystallization.* In this process, grains which have grown from primary recrystallization nuclei will grow further at the expense of their neighbours by migration of their high-angle boundaries. The size of grains and their distribution in size can vary up to the formation of single crystals (a rare but principally possible case), with their crystallographic orientation being also changed (recrystallization texture).

These stages of recrystallization are also associated with reduction of the free energy of the system, though not so intensive as in primary recrystallization.

The difference between grain growth and secondary recrystallization consists in that the former process occurs uniformly whereas the latter does not since there are some grains which, for certain reasons, can grow at an appreciably higher speed than others and thus serve as secondary 'nuclei'.

This difference may be clearly seen from the curves of grain size distribution given in Fig. 180. In addition to the above classification of recrystallization stages, one should also distinguish between *static* and *dynamic recrystallization.* These concepts of recrystallization have been introduced relatively recently in association with a sharply increasing interest to recrystallization in hot deformation and some specifics of the mechanism of recrystallization under these conditions.

Static recrystallization is understood as recrystallization that takes place upon completion of deformation, irrespective of whether

this has been cold or hot. If the deformation has been cold, static recrystallization, beginning with the stage of formation of primary recrystallization nuclei, is realized during heating after deformation. If it has been hot, but recrystallization nuclei have not fully formed directly in the course of deformation, static recrystallization can be realized during cooling after hot deformation or during isothermal annealing immediately after it (without intermediate cooling) or else during heating of the material cooled after the deformation.

If primary recrystallization nuclei have completely formed directly in the course of hot deformation, the process is called dynamic recrystallization (for more detail see Ch. 8).

Let us discuss the mechanisms operative at various stages of recrystallization.

Primary recrystallization. The mechanism of nucleation is the most important in the theory of recrystallization. The following observations seem to be most essential.

Recrystallization nuclei always appear in portions where the crystal lattice has been distorted most severely by deformation and are thus misoriented appreciably relative to the surroundings. Since misorientations in the lattice are produced by an excess of like dislocations, this means that the appearance of an excess of dislocations and respectively the distortion of the lattice in local regions is an indispensable condition for the formation of recrystallization nuclei.

Direct experiments on aluminium have demonstrated that recrystallization nuclei appear only in regions which have been misoriented relative to the surrounding matrix by angles not less than 15-20° in the course of deformation. Such misorientations can appear due to intensive multiple slip. The most favourable places for their appearance are first of all triple joints at grain boundaries (*a*), grain boundaries in the general, less frequently, microbands and twins (*b*), and matrix regions near particles of secondary phases (*c*), see Fig. 181. It has been demonstrated on deformed single crystals that recrystallization occurs in them during heating only in portions in which the deformation has been within Stage *III* of the stress-strain curve. In cases when the deformation has been within Stage *I* or even Stage *II*, only stabilizing polygonization occurred during heating.

The smallest size of recrystallization nuclei formed in deformed material is of the order of a micrometre or a few tenths of a micrometre. Small concentrations of dissolved impurities and undissolved particles of disperse phases retard sharply the formation of recrystallization nuclei in all cases, without any exception. Recrystallization nuclei have the same orientation as that of the local region in the deformed matrix where they have appeared.

The kinetics of primary recrystallization differs from that of

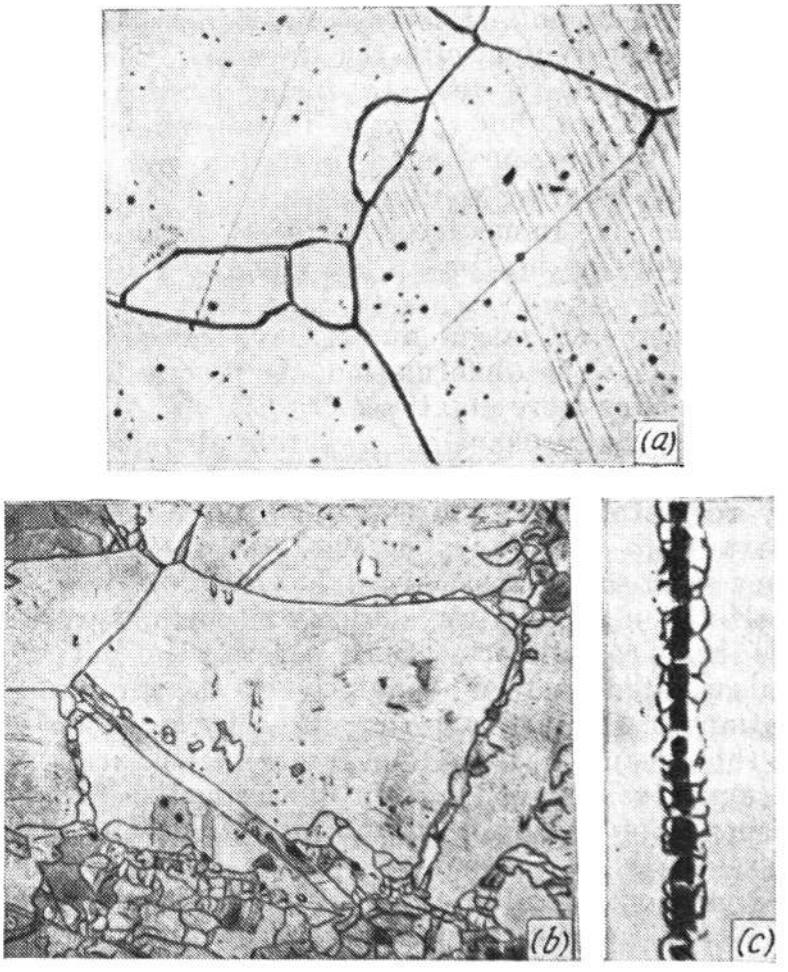

Fig. 181. Sites of preferable formation of primary recrystallization nuclei (*a*) triple joints of original grains; (*b*) grain boundaries and twins; (*c*) particles of secondary phases

recovery. Primary recrystallization begins after a certain incubation period. Its rate first increases to a maximum and then diminishes, i.e. the process is described by a sigmoid curve.

After unsuccessful attempts to explain the mechanism of nucleation in recrystallization by analogy with the mechanism of the formation of nuclei of a new phase in phase transformations (known as the fluctuational theory), the modern dislocation theory of nucleation in recrystallization has been developed. It explains well the phenomena described above, though many important details of the process still remain unclear.

In the most general form, the dislocation concepts reduce to the statement that the formation of recrystallization nuclei is associated with regrouping of dislocations resulting in prerecrystallizational polygonization. This leads to the appearance of sub-grains, i.e. undistorted or slightly distorted regions of the lattice tilted through

certain angles relative one another, which are initially rather small, i.e. separated from one another by low-angle boundaries. Since the deformed structure is inevitably inhomogeneous, there are always regions (sub-grains) which are larger than the surrounding grains and are misoriented more appreciably. Such subgrains grow more intensively than others, their low-angle boundaries consume new dislocations in their migration and become high-mobile high-angle boundaries, which is characteristic of the end of nucleation in recrystallization.

As the misorientation angle of a boundary increases, its energy also increases until the boundary becomes a high-angle one. The concept of the critical radius of a nucleus is untrivial in the case of recrystallization. The critical radius of a primary recrystallization nucleus is the local radius of curvature which varies from one point to another. For a nucleus to grow at the expense of the deformed matrix, it should not be separated from the latter by high-angle boundaries on all sides. If a portion of a recrystallization nucleus, no matter how small, differs substantially in its orientation from the surrounding deformed matrix, the radius of curvature of that portion turns out to be greater than the critical, since the growth of the nucleus in that portion causes no increase in the grain boundary energy.

In that case the incubation period includes the time required for redistribution of dislocations, formation of subgrains and transformation of their boundaries into high-angle boundaries at least in a small local portion. All the factors which retard redistribution of dislocations and migration of sub-boundaries (impurity 'atmospheres', disperse phase particles, etc.) should increase the incubation period and inhibit recrystallization.

Minor details of the mechanism of primary recrystallization depend on many factors, especially on the conditions of plastic working and the nature of the material.

On relatively slight deformations, when the cell structure formed is still not distinct, the dislocation density at both sides of the original boundaries of adjacent grains often turns out to be substantially different. This can be explained by inhomogeneous deformation of differently oriented grains in a polycrystal. In that case, some of the original grains can grow during heating at the expense of adjacent ones by migration of local portions of their high-angle boundaries. This results in the appearance of protrusions, or 'tongues', on a migrating boundary. Typical examples are illustrated in Fig. 182. The driving force of this process is the local difference in volume energies (dislocation densities) on the two sides of the migrating portion of a boundary, which is due to inhomogeneous deformation. The boundary (its local portion) migrates into a region of an adjacent grain with a higher dislocation density. The migrating portion of the boundary 'sweeps out', as it were, all defects on its path (in

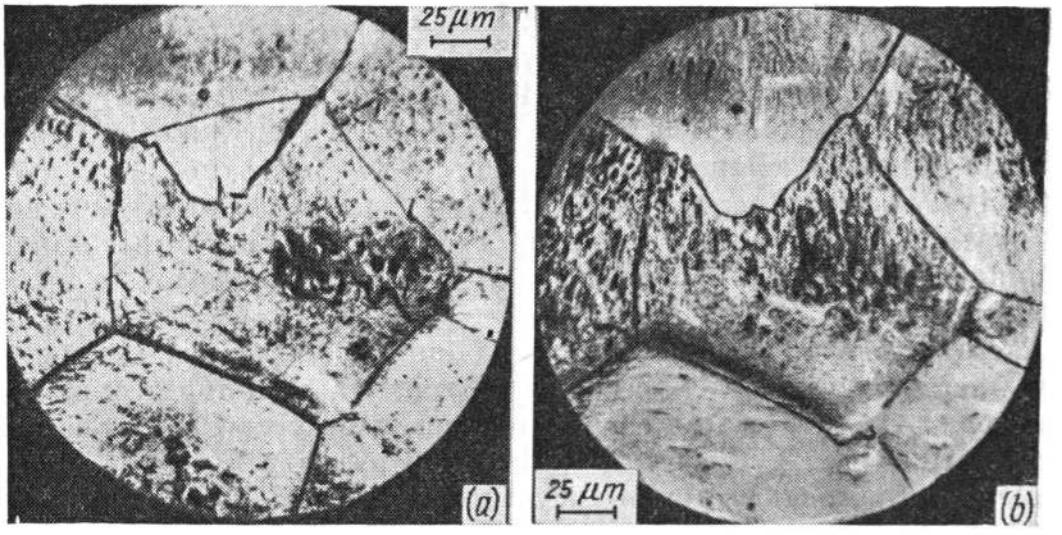

Fig. 182. Recrystallization in electrolytic iron by formation of tongues of a high-angle boundary, stimulated by different dislocation density at both sides of the boundary
(*a*) before repolishing; (*b*) after repolishing

Fig. 182, regions with different dislocation density can be distinguished by different etchability).

This mechanism of primary recrystallization, which has been first discovered by P. A. Beck and P. R. Sperry, is quite common, especially in hot deformation (see Ch. 8). It may be called the mechanism of recrystallization by migration of original grain boundaries due to a gradient of cold work, or shortly, by strain-induced migration.

A gradient of cold work can form in cases when a cell structure has formed at grain boundaries, but the size of cells and respectively of sub-grains is sharply different on both sides of the boundary. The boundary will then migrate into a grain containing smaller subgrains.

It is essential that the migration mechanism considered, which is initially of local nature, can in the course of further heating cause an appreciable rearrangement of the whole microstructure, since the 'tongues' disturb the balance of boundary energy in triple joints. Under certain conditions (upon plastic working to the critical deformation) this can lead to noticeable coarsening of grains. On heavier deformations, when a cell structure forms, the subsequent recrystallization occurs in a different way—through the stage of prerecrystallizational polygonization.

The most probable process of formation of recrystallization nuclei with a dislocation cell structure being present before annealing can be imagined schematically to consist of three stages. The first stage is the formation of low-angle sub-boundaries by flattening of cell walls and the transformation of cells into sub-grains. Dislocations flow from the bulk of cells (subgrains) into the flat sub-boundaries

thus formed. As a result, sub-grains turn out to have a lower dislocation density than the surrounding deformed matrix. The second stage is the growth of sub-grains and an increase of their misorientation relative to the surrounding matrix, up to the formation of high-angle boundaries. The moment when boundaries become high-angle ones marks the completion of formation of recrystallization nuclei. The third stage is quick migration of highly mobile high-angle boundaries into the deformed matrix. Since the structure is inhomogeneous, this process cannot naturally occur simultaneously over the whole volume of the metal. For that reason, growth of recrystallization nuclei in some portions may occur at the same time with polygonization in others. The role and the temperature-time extent of each of these stages may be different depending on the conditions of deformation, the stacking fault energy, phase composition and other factors which determine the type of dislocation structure.

Studies made on materials with different stacking fault energy deformed at temperatures above and below the room temperature have demonstrated a large role of cross slip. With all other conditions being identical, the factors which inhibit cross slip (a low stacking fault energy or a low temperature of deformation) are favourable for the formation of a finer cell structure, but with less distinct ('thicker') cell walls and a higher excess of like dislocations, i.e. with greater angles of misorientation between cells. Conditions favourable for dynamic recovery (cross slip) produce an inverse effect, i.e. make cell walls thinner, increase the size of cells, and diminish their misorientation angles.

Therefore, in cases when dynamic recovery is impeded, flattening of spatial dislocation arrays can result in the formation of sub-boundaries with greater misorientation angles and in the end, even of high-angle boundaries. The second stage will then be very short or even absent.

If dynamic recovery is realized easily and the excess of like dislocations is not high, cell walls will be thin already before annealing. When flattened, they will only form a low-angle dislocation boundary. In that case, the second stage is prolonged substantially. Furthermore, a sub-grain can grow to a large size (a few tens or hundreds micrometres), but will remain surrounded by low-angle boundaries. This essentially is the above-mentioned case of collective polygonization (in-situ recrystallization).

It should be noted that in materials with a high stacking fault energy (small width of extended dislocations), cross slip can occur easily not only during deformation, but also in subsequent annealing. The material will soften noticeably at the stage of recovery, as well as in recrystallization. Typical examples are aluminium and copper (respectively with a high and a low stacking fault energy E_{sf}). The former softens noticeably at the recovery stage, whereas copper soft-

ens only in recrystallization. Coarsening of sub-grains (the second stage of formation of nuclei) can be realized by two mechanisms: either by migration of low-angle boundaries of subgrains or by coalescence of adjacent sub-grains, with disappearance of the separating sub-boundaries.

The migration mechanism is the principal one and obviously more common. In recent time, however, coarsening of sub-grains by coalescence has been observed in a number of materials, as a rule, with a high stacking fault energy (aluminium, molybdenum, silicon iron, vanadium). In this process, sub-grains can coalesce in pairs and in larger groups.

Coalescence of sub-grains is associated with 'unravelling' of unstable sub-boundaries and the passage of dislocations from them into nearest more stable sub-boundaries. An apparent condition for this to occur is that the attraction forces between dislocations and an 'unravelling' boundary should be weaker than the forces with which these dislocations are attracted by the stress fields of nearest sub-boundaries into which these dislocations move. An indirect evidence to this is that the disappearance ('unravelling') of a boundary

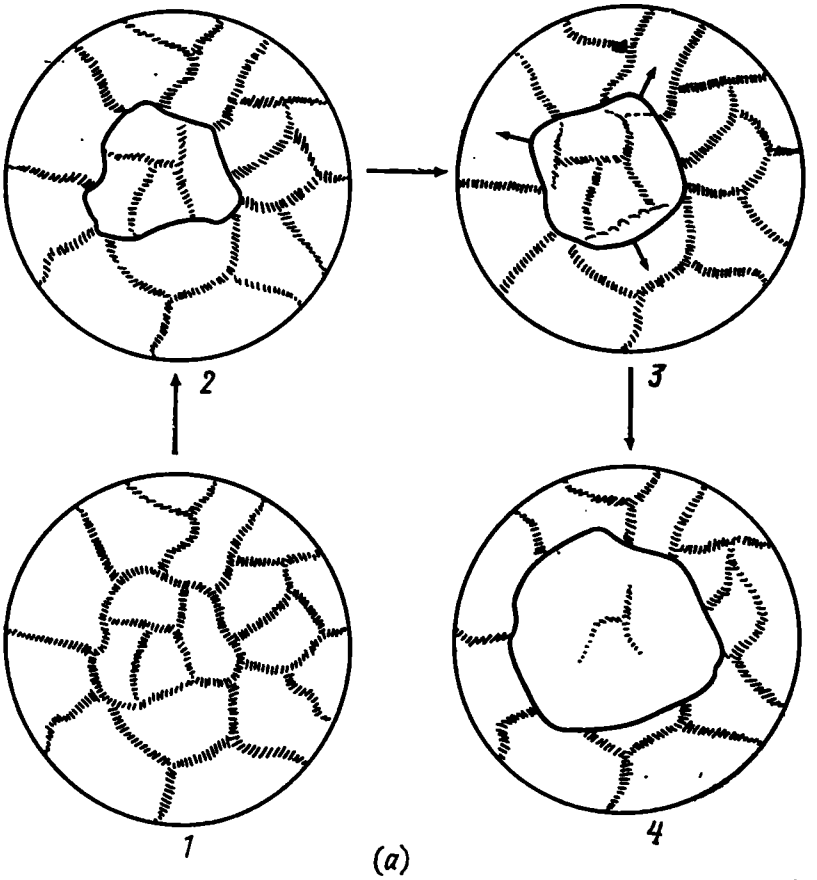

Fig. 183. Sub-grain coalescence, beginning with disappearance of peripheral portions of sub-boundaries
(*a*) schematic (*1-4*—successive stages of coalescence);

usually begins in portions in direct contact with stable sub-boundaries (Fig. 183).

It can be supposed by the results of observations in a high-voltage electron microscope that unravelling boundaries are characterized by a lower dislocation density than stable ones.

Coalescence occurs more often under conditions of hot deformation and/or during heating of deformed materials with a high stacking fault energy, which enables us to suppose that cross slip plays an important part in forming favourable conditions for coalescence of sub-grains.

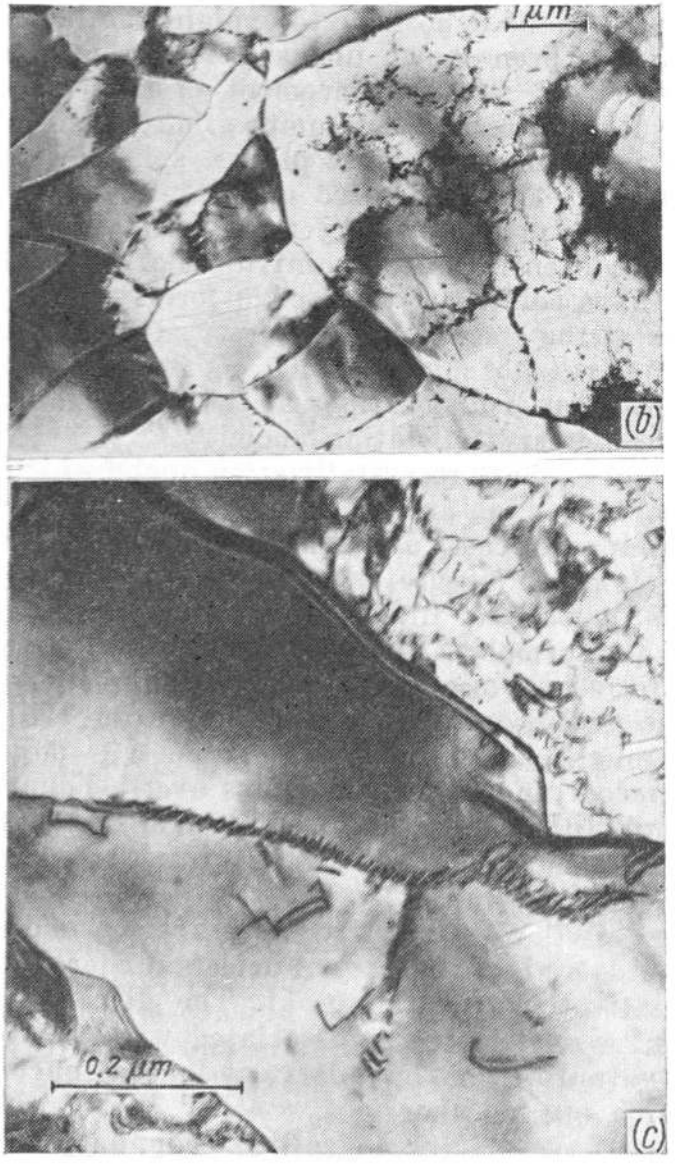

(*b*) and (*c*) transmission electron microscopy of aluminium and transformer iron

The mechanism of sub-grain coalescence is obviously one of the mechanisms responsible for the fact that recrystallized grains are often not structurally perfect, but contain dislocations and low-angle dislocation boundaries (see Fig. 183). These dislocations and low-angle boundaries may be remnants of unravelled sub-boundaries. A high-angle boundary of a recrystallization nucleus may form and start to migrate intensively when the nucleus still retains in its volume part of dislocations belonging to an unravelled sub-boundary, provided that the dislocation density in the surrounding matrix is substantially higher than in the bulk of the growing nucleus.

The above-discussed concepts of the mechanism of nucleation in recrystallization make it possible to explain another important phenomenon. As has been shown in many works, primary recrystallization is associated with enhancement of diffusion processes. In particular, such processes as decomposition of supersaturated solid solutions, coagulation of disperse phases, spheroidization of lamellar cementite, etc. are accelerated upon the onset of recrystallization. This can imply that primary recrystallization involves an increase in the concentration of point defects. A number of special experiments have confirmed the fact of formation of vacancies and their clusters at the stage of primary recrystallization.

This obviously takes place in the course of redistribution and partial annihilation of dislocations at the first and second stages of the formation of recrystallization nuclei.

The growth of primary recrystallization nuclei which are separated from the matrix by high-angle boundaries, can occur only by boundary migration, as in cases of grain growth and secondary recrystallization. Coalescence of grains separated by common high-angle boundaries is impossible. In special cases, the growth of grains can occur due to the formation and growth of annealing twins, but even then it is effected by migration of incoherent boundaries of twins.

The atomic mechanism of boundary migration still has not been clarified thoroughly. By the most popular viewpoint, it consists in separate uncoordinated atomic jumps over a boundary (in crosswise direction). In some cases of migration of special-type boundaries, the mechanism of cooperative coordinated displacements of atomic groups can obviously be realized.

During the growth of primary recrystallization nuclei, a boundary migrates towards a higher density of defects (dislocations) and leaves behind a relatively perfect material. The direction of motion of a boundary of a nucleus is not associated with the position of the centre of curvature of that boundary, as long as nuclei do not start to collide with one another.

When nuclei have started to collide, boundary tension and the tendency of the system to balance this tension in triple joints begin to play a noticeable part. At the stages of grain growth and secondary

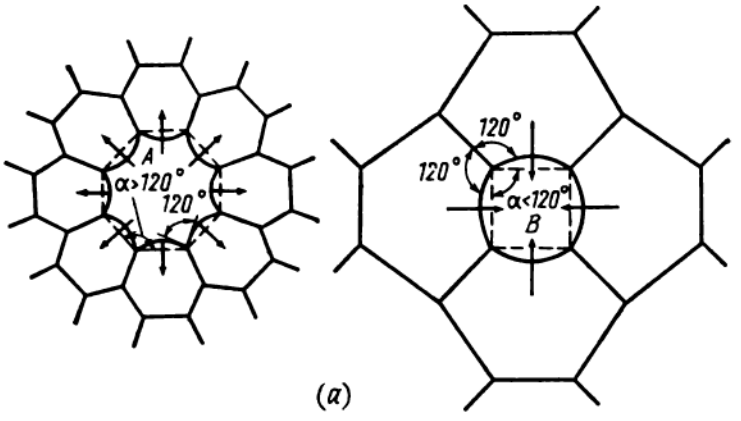

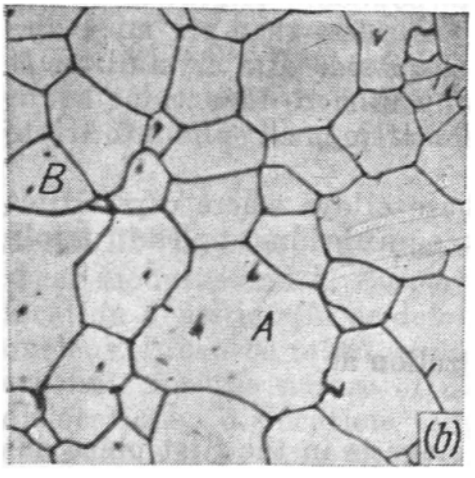

Fig. 184. Concave boundaries of grain *A* (more than six faces) and convex boundaries of grain *B* (less than six faces)
(*a*) schematic (arrows indicate the direction of boundary migration); (*b*) microstructure of nickel alloy, 300×

recrystallization, the role of unbalanced boundary tension in triple joints becomes very high.

In the general case, the effect of surface tension σ on the equilibrium shape of particles may be seen in the fact that the sum of products of σ_i for various surfaces of a particle by the area of the respective surface (face), s_i, tends to a minimum, i.e.

$$\sigma_{tot} = \Sigma \sigma_i s_i \rightarrow \min$$

In polycrystals, their crystallites will have an equilibrium shape when the vector sum of the coefficients of boundary tension, laid off in the plane normal to the common edge of three intersecting grains, is equal to zero.

On the basis of these considerations, it can be shown for an isotropic material, i.e. the one in which the anisotropy of grain-boundary energy can be neglected, that the equilibrium angle in triple joints should be equal to 120°. For that reason, the sides of equilibrium grains in single-phase isotropic metals and alloys should meet at angles of 120° in points of junction at the surface of a microsection.

Therefore, in single-phase alloys having practically an isotropic grain-boundary energy and straight boundaries, the only grains that can be in metastable equilibrium are those in which the number of sides in a section is equal to six. Grains with the number of sides less than six must have convex boundaries in order to form angles of 120° in triple joints, and grains where the number of sides is more than six must have concave boundaries (Fig. 184).

Since the position of atoms on the concave side of a boundary is more stable than on the convex one, the frequency of atomic jumps onto the concave side is greater than in the opposite direction. As a result, boundaries between grains of the same phase, which tend to reduce their energy, usually migrate at the stage of grain growth to the centres of their curvature. This is why grains with the number of sides more than six must grow due to boundary migration to the outside and those with the number of sides less than six must disappear as their boundaries migrate to the inside of a crystallite. It also follows from the foregoing that joints of more than three boundaries are unstable and, if formed occasionally, must split into triple joints.

In anisotropic materials and two-phase alloys where crystallites of the two phases are close in size, the equilibrium angles in triple joints should differ from 120°.

3. Driving Forces of Recrystallization at Various Stages

The rate of recrystallization at any stage is in the first place determined by the gain in free energy ΔF which essentially is the driving force of the process. When related to a unit of volume or surface, this gain is denoted as P_{dr}.

As has been noted, the principal driving force of primary recrystallization is the gain in volume energy P_v. The principal driving force of grain growth is the reduction of the grain-boundary energy P_b, which appears due to shortening of grain boundary extent and to the tendency to balance the boundary tension. Secondary recrystallization can be stimulated by various factors depending on particular conditions, which leads to a gain in the volume, surface or grain-boundary energies. Thus, the driving force of recystallization can be written in the general form as follows:

$$P_{dr} = P_v + P_b + P_s$$

All stages of recrystallization, except for the formation of recrystallization nuclei, are realized by migration of high-angle boundaries. The rate of boundary migration, and therefore, the rate of the whole process, depend on P_{dr} which determines the direction in which a boundary will migrate, and also on the mobility M of the boundary proper, which is determined by the atomic structure of

that boundary. On the other hand, some factors operative in real metals and alloys and under real conditions of heating can produce retarding effect on recrystallization. First of all, they include dissolved impurities and disperse phase particles, thermal etch pits, etc. The force that retards recrystallization can be denoted as P_{ret}. The rate of recrystallization can then be written in the following general form:

$$V = M(P_{dr} - P_{ret})$$

Quantitative estimation of P_{dr} and P_{ret} and of their relationship at various stages of recrystallization can be essential for understanding many regularities of the process. It should be noted however that, with the modern state of the art, such quantitative relationships can only be used for rough estimations.

The driving force of primary recrystallization is the excess volume energy stored in the course of plastic deformation and practically entirely localized in stress fields around dislocations. This energy can be found by the relationship

$$P_{dr}^{pr} = k\Delta N_d G b^2$$

where Gb^2 is the energy per unit length of dislocation (G being the shear modulus and b, Burgers vector); ΔN_d is the difference of dislocation densities (in as-deformed material and in recrystallization nucleus, it can be taken equal to 10^{12} cm^{-2}); k is a coefficient which accounts for the nature of distribution of dislocations (individual dislocations, dislocation tangles, dislocations in sub-boundaries, etc.) and varies from 0.1 to 1.

Taking $G = 10^7$ N cm^{-2}, $b = 3 \times 10^{-8}$ cm and $k = 1$, we obtain:

$$P_{dr}^{pr} = 10^7 \times 10^{12} \times 9 \times 10^{-16} \approx 10^3 \text{ N cm}^{-1}$$

For the case of primary recrystallization realized by migration of original grain boundaries due to a cold work gradient (strain-induced migration), the reduction of the volume energy due to 'sweeping-out' of defects must exceed the gain in grain-boundary energy due to an increased length of a boundary upon the formation of a 'tongue'. This is the driving force of the process which can be determined as

$$P_{dr}^{pr.mig} = \Delta E_{def} - E_b \frac{ds}{dv}$$

where ΔE_{def} is the difference in the stored energy of deformation on the two sides of a boundary; E_b is the unit grain-boundary energy; and ds/dv is the relative increase of the area of the boundary per unit volume of the 'tongue'. As has been calculated, the smallest length of a portion of a boundary in which the formation of a 'tongue' is energetically favourable is around 10^{-4} cm on moderate deformations (10-30 per cent).

The driving force of grain growth (as has been given earlier) is the trend of the system to reduce the boundary energy and balance the boundary tension by forming grain boundaries of an equilibrium configuration. An important point is that the stability of a structure is determined, in the first place, not by absolute dimensions of grains, but by the curvature of boundaries, the angles in triple joints, the number of sides in sections through grains, and the uniformity of their size.

If the edge angle in a grain is greater than 120°, the edge will move in the direction away from the grain. The edge angle will thus decrease and the grain will grow. If the edge angle is less than 120°, the edge will migrate inside the grain, the angle will increase and the grain will be 'consumed' by its neighbours.

A boundary tends to migrate towards its centre of curvature. Thus, a convex boundary migrates to the inside of the grain and diminishes the surface of that grain, while a concave boundary migrates away from its grain and increases the grain surface. In the process of grain growth when grains differ only slightly in size, the effect of deviation of angles in triple joints from 120° and the effect of boundary curvature can cause identical grains to grow at the expense of neighbouring grains in some portions and be 'consumed' by surrounding grains in others. This situation is impossible in primary and secondary recrystallization where recrystallization 'centres' always grow in all directions at the expense of surrounding grains.

If grains are unequal in size, the energy of grain boundaries per unit volume will be different. This difference in the unit grain-boundary energy $\Delta E_{\text{b.un}}$ is essentially the driving force of grain growth.

Assuming, for simplification, that grains are of a cubic shape with the edge length D, the driving force of the growth of a grain of size D_2 at the expense of the one of size D_1 will be:

$$P_{\text{dr}}^{gg} = \Delta E_{\text{b.un}} = 3E_{\text{b}} (1/D_1 - 1/D_2) = 3E_{\text{b}} (\Delta D/D_1 D_2)$$

As may be seen, the driving force is greater when grains differ more in their size and their absolute size is smaller.

Assuming that $E_{\text{b}} = 5 \times 10^{-5}$ J cm^{-2} and that grains differ in their sizes by a factor of three (with a larger difference, the conditions would be close to secondary recrystallization) and taking that the size of the smaller grain (D_1) is equal to 1, 10 and 100 μm, the driving force P_{dr}^{gg} will be equal respectively to 10^0, 10^{-1}, and 10^{-2} N cm^{-1}. Thus, with a very small size of grains (around 1 μm), the driving force for grain growth may turn out to be only slightly less than the driving force of primary recrystallization.

If the size of grains is a few tens micrometres, as is often the case in grain growth, and the difference in their sizes is not large, the

driving force of grain growth, P_{dr}^{gg} is four or five orders of magnitude smaller than that of primary recrystallization.

As has been noted earlier, secondary recrystallization can be caused by various factors, which requires a differentiated approach to determining the driving force of the process. For instance, secondary recrystallization can take place under the conditions when the size of the main mass of grains is stabilized, say, by disperse phase particles, so that only some individual large grains (centres of secondary recrystallization) can grow. Assuming that the size of secondary recrystallization nuclei is hundred times the linear size of the main mass of grains and that $E_b = 5 \times 10^{-5}$ J cm^{-2}, we find that P_{dr}^{r} is equal to 1.5×10 N cm^{-1} at $D_1 = 10^{-5}$ cm and 1.5 N cm^{-1} at $D_1 = 10^{-4}$ cm.

In thin sheets and films, whose thickness is commensurable with the size of grains, secondary recrystallization can be stimulated by a gain in the surface energy. This can occur if there is a noticeable difference in the surface energy of the faces of grains which pass onto the surface of the sheet (film). Grains having the lowest surface energy and which are few in number will become centres of secondary recrystallization.

Faces most closely filled with atoms and respectively characterized by the highest interplane spacings have usually the lowest values of surface energy. These are {110} planes in b.c.c. lattices, {111} planes in f.c.c. lattices, etc. The difference in surface energy between various planes is roughly 0.3-0.1 J cm^{-2}. For instance, the surface energy of {110}, {111} and {100} faces in iron is respectively $1.3 \times \times 10^{-4}$ J cm^{-2}, 1.5×10^{-4} J cm^{-2} and 1.6×10^{-4} J cm^{-2}.

A circumstance of practical importance is that the ratio of surface energies of various faces can be varied by selective adsorption of various surface-active additions on these faces. This is a useful tool for controlling the texture. It is used, in particular, in the manufacture of transformer steel.

If the size of secondary recrystallization nuclei is equal to or greater than the thickness H of a sheet, these may pass with their least-energy faces onto both sides of the sheet. In that case, the driving force of secondary recrystallization is

$$P_{dr} = 2\Delta\sigma_s/H$$

where $\Delta\sigma_s$ is the difference in the surface energies of secondary recrystallization nuclei and of grains of a different orientation which are consumed by these nuclei. If we take that $\Delta\sigma_s = 1.5 \times 10^{-5}$ J cm^{-2} and the thickness of sheets is 100 μm and 1000 μm, the driving force P_{dr} will be equal respectively to 3×10^{-3} N cm^{-1} and $3 \times \times 10^{-4}$ N cm^{-1}, i.e. four-six orders of magnitude smaller than that of primary recrystallization.

RECOMMENDED LITERATURE

1. Gorelik S. S., *Recrystallization in Metals and Alloys.* Moscow, Mir Publishers, 1981.
2. Larikov L. N., in: *Physical Principles of Strength and Plasticity of Metals.* Moscow, Metallurgizdat, 1963.
3. *Physical Metallurgy.* Ed. by R. W. Cahn. Amsterdam, North-Holland Publ. Co., 1965.

7 Recrystallization in Heating After Cold Deformation (Static Recrystallizaiton)

1. Effect of the Conditions of Deformation and Heating on the Mechanism of Recrystallization and Type of Microstructure

The rate of primary recrystallization is characterized by variation of the relative amount of recrystallized volume in the deformed matrix with the time of annealing τ (Fig. 185).

The recrystallized volume of the material increases during annealing owing to two processes: the nucleation and the growth of nuclei. The rate of these processes is determined by the rate of nucleation, N (the number of nuclei formed per unit time, $\Delta n/\Delta\tau$), and the rate of growth, G (an increase in the average linear size of nuclei per unit time, $\Delta D/\Delta\tau$). New grains appear and grow after a definite incubation period τ_0 which is shorter at a higher temperature T of annealing and a heavier prior deformation ε. It is clear that the type of the microstructure that forms on recrystallization is determined by the relation between N and G. An increase of N results in grain refinement, while an increase of the rate of growth G gives a coarser microstructure. As the time of isothermal annealing increases, N first increases to a maximum and then decreases. The average rate of growth of nuclei G (up to the beginning of mutual collisions) during the time of annealing τ is

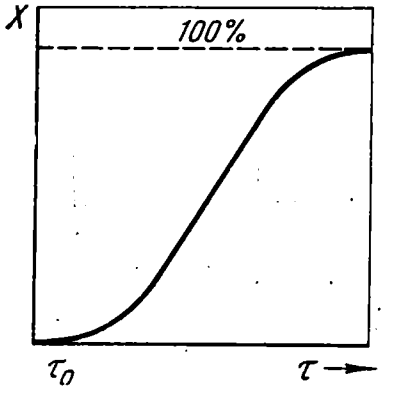

Fig. 185. Diagram of recrystallized volume X versus annealing time τ

$$G = \Delta D/(\tau - \tau_0)$$

A number of relationships have been proposed to describe the kinetics of isothermal recrystallization. The most generalized among them is that proposed by M. Avrami:

$$X = 1 - \exp(-B\tau^k)$$

where X is the relative amount of recrystallized material and B and k are the coefficients depending respectively on the temperature

and the nature of nucleation as well as on the growth of grains. For three-dimensional recrystallization (massive specimens), k is within the range $3 \leqslant k \leqslant 4$; for a two-dimensional process (thin sheets), $2 \leqslant k \leqslant 3$, and for one-dimensional (thin wire), $2 \leqslant k \leqslant 1$.

Let us analyse the available data on the effect of various factors on the mechanism of the process, the parameters N and G, and the type of microstructure formed on recrystallization.

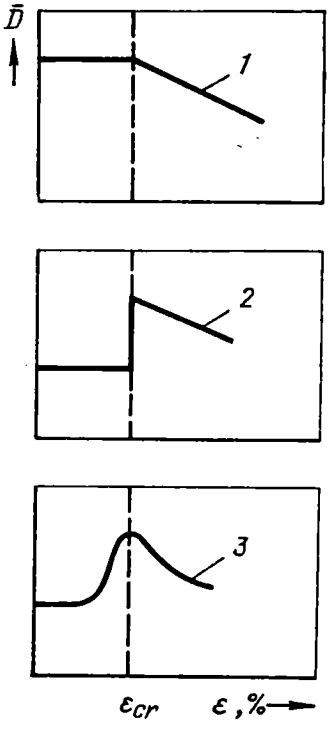

Fig. 186. Variations of grain size $\bar{D}$ in recrystallization depending on prior deformation
1—single crystal; *2* and *3*—polycrystals

The amount of deformation ε. The dependence of the size D of a recrystallized grain on the amount of deformation ε for a constant time of isothermal annealing τ after cold deformation is not monotonous. For polycrystalline solids, it is described by a curve with one or more (up to three) maxima. The amount of deformation at which the first maximum of grain size appears in the curve during annealing is called the critical deformation ε_{cr}. Let us specify more exactly the critical deformation ε_{cr}, since this term is sometimes given a different sense.

A small amount of deformation (less than ε_{cr}) corresponds to the first stage or the beginning of the second stage of the hardening curve. Heating after such a low deformation, as a rule, causes only the stabilizing polygonization which impedes subsequent structural changes. Heating after such a deformation causes no grain coarsening. The process is limited to polygonization occurring within grains. As the amount of deformation increases to the end of the second or the beginning of the third stage of hardening, this forms favourable conditions for recrystallization to occur during heating either by the mechanism of migration of original boundaries under the effect of strain gradient (strain-induced migration) or by the mechanism of initiation and growth of actual recrystallization nuclei.

Strictly speaking, the critical deformation ε_{cr} should be understood as the lowest amount of deformation on which recrystallization nuclei can appear and grow in heated metal. In that case, the curves relating the average size of a recrystallized grain, $\bar{D}$, to the amount of prior deformation, $\bar{D} = f(\varepsilon)$, will show a different effect of deformation on ε_{cr} in single crystals and polycrystals. With single crystals, the appearance of new grains will result in a decrease of $\bar{D}$, so that ε_{cr} will be essentially the lowest deformation causing a decrease

of $\overline{D}$ in heating (curve *1* in Fig. 186). With polycrystals, the appearance of a small number of recrystallized nuclei and their growth at the expense of the deformed matrix must cause an increase in the size of recrystallized grains $\overline{D}$ compared to the original size (prior to deformation) and ε_{cr} represents a maximum on the curve $\overline{D} = f(\varepsilon)$ (Fig. 186, curve *2*).

As has been given earlier, however, coarsening of the structure can also take place under the effect of strain-induced migration. Special experiments with tapered specimens deformed by tension in which the region of low deformation could be widened conveniently (i.e. a low strain gradient $d\varepsilon/dx$ could be formed) revealed two maxima of grain size (but not one) in the region of low deformations (Fig. 187). The first of these maxima was associated with migration of the original grain boundaries and the second, with the appearance and growth of a small number of actual recrystallization nuclei. The deformations corresponding to these two maxima were however very close to each other in magnitude. This is why a single maximum is usually detected under common conditions of experiment and the $\overline{D} = f(\varepsilon)$ curve most often has no peaks in the range of low ε, i.e. to the left of ε_{cr}.

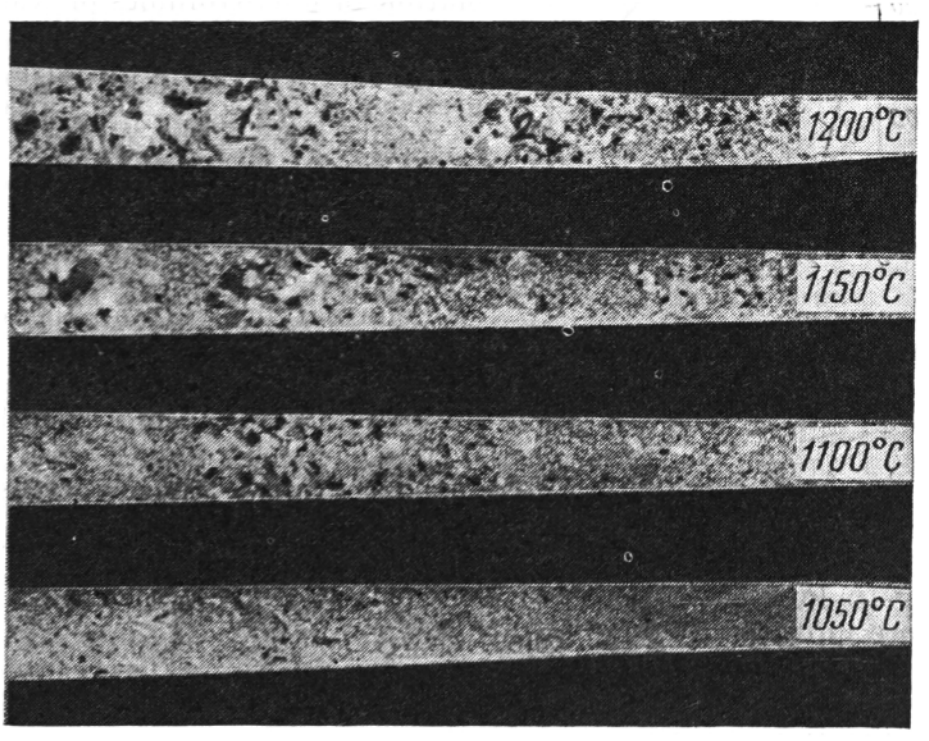

Fig. 187. Microstructure of tapered specimens of nickel alloy after tensile deformation and recrystallization. As may be clearly seen, the maximum of grain size of recrystallized grains formed by heating after the 'critical' deformation has split into two maxima: (*1*) due to growth of individual original grains and (*2*) due to the formation of a small number of recrystallization nuclei

In that connection for polycrystals the critical deformation ε_{cr} is generally accepted to be the lowest deformation under which the first maximum of grain size appears on the $\overline{D} = f(\varepsilon)$ curve, irrespective of the actual causes of its appearance.

If the time of heating does not exceed 1-2 hours and the temperature of heating is not higher than $0.9T_{m.p.}$, the degree of structure coarsening, $\overline{D}_{cr}/\overline{D}_{or}$, varies within 4 to 10. If an alloy contains disperse phases and the heating after ε_{cr} is carried out to a temperature at which the disperse phases can be dissolved (though not very intensively), $\overline{D}_{cr}$ may turn out to be very high, a few tens of times the size of original grains.

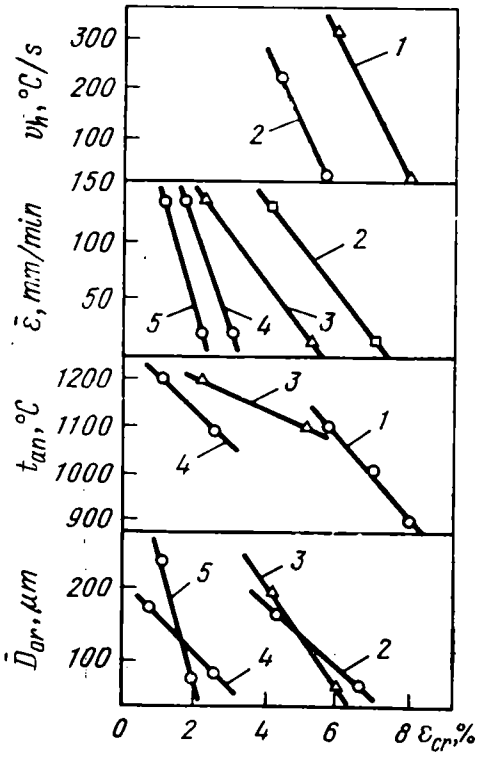

Fig. 188. Effect of various factors on critical deformation ε_{cr}
1—Fe-Si alloy; *2*—iron; *3*—steel 12X18H9T; *4*—Ni-Cr alloy; *5*—XH88BT alloy

The magnitude of ε_{cr} depends on a great number of factors and may range from 1 per cent to 15 per cent or even more. The most important among these factors are the degree of uniformity of deformation in microvolumes of various grains, the rate and temperature of heating, original grain size, and presence of disperse phase particles. All factors which increase nonuniformity of deformation have a reducing effect on ε_{cr}. Here, the rate of deformation should be named first. An increase in the rate of deformation within the common range makes deformation less uniform, and therefore, decreases the critical deformation (Fig. 188). With a change to high-speed pulse methods of deformation (explosion deformation), various grains are deformed much more uniformly (see Ch. 2), ε_{cr} increases, and the material is less liable to coarsening of its structure, i.e. $\overline{D}_{cr}/\overline{D}_{or}$ is relatively low.

More uniform deformation in local volumes of the metal can be obtained by an intermediate polygonizing procedure (between deformation and recrystallization annealing). Indeed, prior stabilizing polygonization sharply decreases the extent of structure coarsening in recrystallization after ε_{cr} and increases slightly ε_{cr} (Fig. 189). The temperature of heating for polygonization should be relatively high (only slightly less than that of the beginning of recrystallization). The mechanism of this effect of stabilizing polygonization

consists obviously in that it diminishes the long range of the elastic fields of dislocation networks, i.e. decreases the ability of dislocations to attract grain boundaries. The formation of new sub-boundaries of a low curvature, on the other hand, impedes dislocation migration and their transformation into high-angle boundaries.

An increase of deformation temperature (within the range of what is called 'warm' deformation) gives an effect similar to stabilizing polygonization.

An increase of the temperature of recrystallization annealing acts in inverse direction. The number of new recrystallization nuclei increases as the temperature of annealing is raised. As a result, ε_{cr} is shifted to lower values of ε. Besides, the ratio $\overline{D}_{cr}/\overline{D}_{or}$ increases sharply owing to the higher rate of growth, i.e. a higher value of $\overline{D}$ corresponds now to ε_{cr}.

The role of non-uniform deformation of grains is closely associated with the effect of the original grain size. With an increase of $\overline{D}_{or}$, various grains are deformed more non-uniformly and ε_{cr} is thus shifted towards lower values of ε (see Fig. 188).

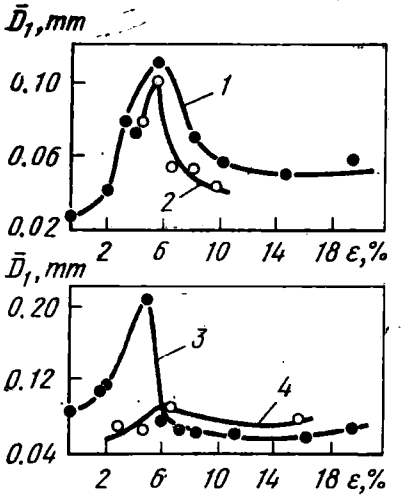

Fig. 189. Effect of polygonization on the shape of $\overline{D} = f(\varepsilon)$ curves and the position of ε_{cr} for aluminium. Heating for 30 min at various temperatures, °C
1—500; *2*—300+500; *3*—550; *4*—400+550

The rise of ε_{cr} due to refinement of original grain can be enhanced effectively by introducing a large quantity of disperse particles of secondary phases. For instance, chrome bronze (Cu + 0.5% Cr) was subjected to cold rolling before recrystallization annealing which was carried out for 30 minutes at 1000°C. In coarse-grained ($D = 0.7$ μm) single-phase state of the metal which was formed by hardening from a high temperature prior to deformation, ε_{cr} turned out to be equal to 2 per cent. When a fine-grained structure ($D = 0.02$ mm) was formed prior to deformation and the metal contained a large percentage of chromium precipitated from the solid solution, ε_{cr} was appreciably higher (18-20 per cent).

Generally, disperse particles produce an inhibiting effect on grain coarsening which however appears only in cases when the temperature of recrystallization annealing is below the temperature of dissolution of disperse phases. If these temperatures coincide, disperse particles lose their inhibiting role, but the effect will be different depending on the rate of dissolution of particles. With a low rate of dissolution, annealing after ε_{cr} will result in very vigorous coarsen-

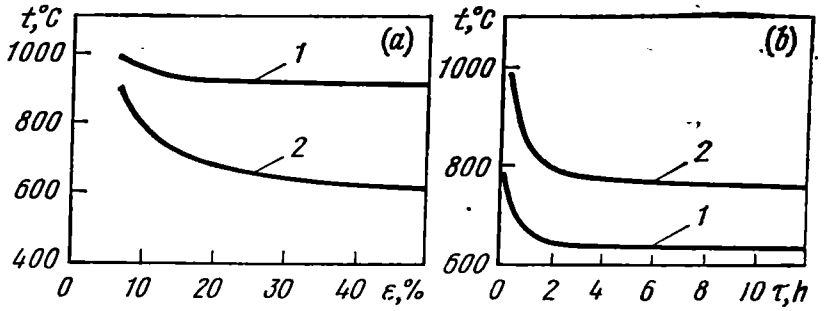

Fig. 190. Effect of plastic deformation (*a*) and annealing time (*b*) on t^s_r (*1*) and t^f_r (*2*)
(*a*) alloy H-5Г12; (*b*) Ni + 13% Cr alloy, ε = 40%

ing of grains, much more intensive than in the absence of such particles (see the recrystallization diagram in Fig. 193*f*). With a high rate of dissolution, disperse particles will have only a slight effect on ε_{cr}.

An increase of the heating rate up to tens or hundreds degrees per second acts in an opposite sense to stabilizing polygonization, i.e. shifts ε_{cr} to lower values of ε, provided that the high rate is used only to approach the isotherm. If however high-speed heating is employed without subsequent isothermal curing, the maximum of grain size in annealing after ε_{cr} can be reduced sharply or even suppressed fully. With an increase of the amount of deformation above ε_{cr}, grain size decreases monotonously to the end of primary recrystallization. This is attributed to the fact that, as ε increases, both N and G increase, but N increases more quickly than G. The function $D = f(\varepsilon)$ decreases monotonously only with the following conditions being observed: (a) the time of recrystallization annealing must not be long (not more than 30 minutes to 1 hour); (b) the alloy must not contain disperse phases which would be dissolved at the temperature of recrystallization annealing.

If these conditions are not observed, a long heating in the range of medium deformations can produce a second maximum of grain size. The amount of deformation at which this maximum appears is fixed less rigidly and may vary within very wide limits (from ε = 20 per cent to 50 per cent) depending on the original grain size, concentration and dispersity of particles, temperature and rate of their dissolution, etc. The appearance of that maximum is associated with the phenomenon of secondary recrystallization and will be discussed in more detail in Ch. 9.

Since N and G at the primary recrystallization stage increase with increasing deformation, the temperature of the beginning of recrystallization t^s_r diminishes sharply. This is most noticeable up to deformations of 50-60 per cent after which t^s_r remains practically constant (Fig. 190), more strictly, approaches asymptotically to a definite temperature limit t^s_{rl}. For that reason, the temperature of

recrystallization on heavy deformation, t^s_{r1}, is taken conditionally as the temperature limit of recrystallization for a given alloy. Thus, this limit is understood as the temperature below which a given alloy, when annealed for a practically reasonable time, will not recrystallize upon any amount of deformation.

The dependence of t^s_r on ε and τ can be described by functions of the type $t^s_r = a\varepsilon^{-b} + t^s_{r1}$ or $t^s_r = c\tau^{-d} + t^s_{r1\tau}$, where a, b, c and d are constants for a given composition of an alloy and the conditions of deformation and heating.

Deformation rate $\dot{\varepsilon}$. The effect of deformation rate $\dot{\varepsilon}$ on recrystallization turns out to be different in cold and in hot deformation.

In hot deformation (see Ch. 8), the rate of deformation has the decisive effect while in cold deformation, the amount of deformation is decisive.

In cold deformation, the effect of deformation rate is not monotonous. At heavy deformations ε, an increase in the deformation rate first accelerates recrystallization, but at very high rates (explosion deformation), when deformation becomes more uniform owing to a greater number of operative slip systems and deformation mechanisms, the conditions for subsequent recrystallization become less favourable and t^s_r increases.

The temperature and time of heating. The nucleation and growth of recrystallization nuclei are thermally activated processes. For a given strain, the effect of temperature on N and G is described by Arrhenius' equations:

$$N = N_0 \exp(-Q_N/RT) \text{ and } G = G_0 \exp(-Q_G/RT)$$

where Q_N and Q_G is respectively the effective activation energy of nucleation and growth.

These expressions are strictly valid only in temperature ranges where Q_N, Q_G and the pre-exponential factors, G_0 and N_0, are constant. Since, however, Q_G decreases with increasing temperature, this increases additionally the rate of growth. This is why at common heating rates (furnace heating) the size of grains formed at the end of primary recrystallization increases noticeably with an increase of annealing temperature. Nonetheless, the size of grains depends more on the amount of deformation than on annealing temperature. The effect of heating temperature proper is often masked in practice by the fact that heating is done relatively slowly. An increase in heating temperature then involves a longer time during which the metal is held at a high temperature.

In most practical cases, recrystallization annealing is carried out for a rather long time, so that grain growth has time to occur all the same, at least partially. This is why the size of grain on recrystallization annealing turns out to be even more dependent on temperature ($\overline{D}$ is greater at a higher temperature of annealing). It should be

noted, however, that this is true only of cases when no structural recrystallization takes place in the metal. Otherwise, the recrystallized metal will have a finer grain. This may be clearly seen in recrystallization diagrams of carbon steel where the $\alpha \rightarrow \gamma$ transformation involves grain refinement.

It has been established by direct observations on the growth of grains that, unlike the average rate, the actual rate of growth does vary in time. The growth proceeds jumpwise, with maximal rates (at the moment of a jump) being at least one order of magnitude greater than the average rate. The causes are still unclear but are most probably associated with the structure of boundaries and the effect of impurities and thermal etch pits.

Prior recovery has different effect at $\varepsilon > \varepsilon_{cr}$ and $\varepsilon \leqslant \varepsilon_{cr}$. Recovery and polygonization after supercritical deformations increase somewhat the incubation period τ_0, diminish N, and have only an insignificant effect on G. As a consequence, recovery after $\varepsilon > \varepsilon_{cr}$ results in a slight increase of D.

The rate of heating. With a higher heating rate, recrystallization proceeds quicker, with finer grain being formed at the end of primary recrystallization. This can be explained by two circumstances as follows.

Firstly, with high-speed (say, induction) heating, recovery has no time to proceed before the onset of recrystallization. As a result, recrystallization begins at a higher concentration of defects, including point defects, which facilitate nucleation and growth of recrystallization nuclei.

Secondly, in high-speed heating, point defects (vacancies and their complexes) which form at the early stages of primary recrystallization due to dislocation annihilation, should have a greater influence on the process. At very high heating rates, the number of point defects appearing per unit time should be appreciably greater. Besides, dissociation of vacancies at high temperatures favours further climb and redistribution of dislocations and migration of boundaries.

As has been established experimentally, in high-speed induction heating nucleation is enhanced much more intensively (3-5 times) than growth of nuclei, which explains well why high-speed (induction) heating produces fine grain. In induction heating, which is usually carried out without isothermal holding of the metal, the temperature of the beginning of recrystallization (t_r^s) rises substantially and grain is refined as the heating temperature is reached. For instance, t_r^s of Armco iron deformed 60 per cent and heated without isothermal holding turned out to be 500 °C on furnace heating, 700°C on heating at a rate of 500°C/s and 900°C on heating at a rate of 650 °C/s. Of significance here is the time during which the metal is held in the temperature region where the processes of recovery and recrystallization occur most intensively. The sharp effect

of high-speed heating can be used advantageously for obtaining a finer microstructure and varying the properties of the metal.

High-speed heating is especially effective with metals subjected to light or moderate deformations, provided that the strain is non-uniform over the volume of the article, and the length of the incubation period of the formation of recrystallization nuclei, τ_0, is noticeably different in various portions. These differences are greater at a lower temperature of annealing. With slow (common) heating, recrystallization nuclei appear in portions with the lowest values of τ_0 much earlier than elsewhere. In portions where τ_0 is the highest, recrystallization nuclei will not be realized at all, since the corresponding regions are consumed by the growing nuclei of low τ_0, or, if realized, will be much smaller in size. In high-speed heating, the metal is heated up to a high temperature before the realization of recrystallization nuclei of low τ_0, when the difference in τ_0 between various portions is still small. The result is that an appreciably larger number of potential nuclei are realized and the final structure is much finer and more homogeneous than on slow (furnace) heating.

The size of original grain $\overline{D}_{or}$. The size of grain can influence not only the critical deformation ε_{cr}, but also the rate (the temperature of beginning) of primary recrystallization at deformations $\varepsilon > \varepsilon_{cr}$.

At smaller $\overline{D}_{or}$, primary recrystallization begins earlier and at a lower t_r^s, mainly due to quicker nucleation at boundaries of original grains. This effect is more pronounced in hot deformation. Should however this effect be due only to easier formation of recrystallization nuclei at grain boundaries, t_r^s of coarse-grained metal would be the same as that of fine-grained and the two would differ only in the number of nuclei formed at the earliest stage. Actually, however, a noticeable decrease of t_r^s is observed on grain refinement. A probable explanation is that, as the original grain is refined, favourable conditions for the appearance of recrystallization nuclei at grain boundaries are formed on a lower amount of deformation than in a coarse-grained material. This agrees well with the available experimental data which show that grain refinement results in more intensive work hardening due to quicker onset of multiple slip near grain boundaries and triple joints and quicker complication of the dislocation structure.

2. Effect of Atomic Structure of Alloy, Solute Impurities and Disperse Phases of Recrystallization

Since recrystallization occurs in several stages and includes various elementary mechanisms, it is impossible to find a single parameter which would characterize the effect of the atomic structure of the base substance and of alloying additions on recrystallization.

One of the most stable parameters which can characterize the liability of a metal (alloy) to recrystallization is the temperature t_r^s of the beginning of recrystallization of heavily deformed metal (alloy) after a relatively long (for one hour or more) annealing. This parameter can be called the temperature limit of recrystallization. It should be understood as the temperature of the beginning of recrystallization after heavy deformation (at least 50 per cent) and annealing for not less than one hour. This parameter will be taken in this book as the principal one for analysis of the effect of various factors (atomic structure, alloying, etc.) on liability of metals to recrystallization.

Useful information can also be derived from the data on the activation energy of recrystallization Q_r which enters expression (152). It should however be considered in that case that Q_r can be affected by many factors and its value, as found experimentally, is usually the effective activation energy of a combination of elementary processes occurring in deformed metal during heating. The physical essence of Q_r cannot be interpreted easily, since the softening processes (redistribution and partial annihilation of dislocations, etc.) occurring in alloys during recrystallization may be accompanied by processes of decomposition of supersaturated solid solutions, coagulation and reverse dissolution of disperse phases, etc. All these factors can have a certain effect on the behaviour of dislocations and the formation of recrystallization nuclei, and therefore, on the value of Q_r. In analysis of the effect of alloying on the effective activation energy of recrystallization, it is therefore essential to consider the nature of the processes which can take place in the temperature interval in which Q_r has been determined and their probable effect on the conditions of recrystallization.

The temperature level of recrystallization of metals and brittle compounds. A. A. Bochvar was first to notice a certain correlation between the absolute temperature of the beginning of recrystallization, T_r^s, or the temperature limit of recrystallization, and the absolute melting point $T_{m.p.}$. He has found that T_r^s makes up a definite constant fraction of $T_{m.p.}$: $T_r^s = \delta T_{m.p.}$. The absolute magnitude of δ is not however strictly constant, and, as has been demonstrated by Bochvar, may vary from 0.35 to 0.40 for commercial pure metals.

It has been established in later studies that δ of high-purity metals is substantially lower and is only 0.2-0.3. Apart from the degree of purity, the temperature level of recrystallization can be influenced by the structure of deformed metal, which in turn is associated with the conditions of deformation, the type of crystal structure (the number of operative slip systems and the nature of atomic bonds) and the stacking fault energy. In the general case, with all other conditions being identical, a decrease of the number of slip systems in polycrystals results in less homogeneous work hardening, a greater

local surplus of like dislocations, and therefore, in easier recrystallization.

The role of stacking fault energy is associated with dynamic recovery in deformation. In materials having a high stacking fault energy, a decrease of the temperature of deformation can inhibit cross slip and dynamic recovery more substantially than in those with a low stacking fault energy. Accordingly, a change from deformation at room temperature to that at a lower temperature can change more appreciably the structure in deformed state (increase work hardening) in metals of the former group, with a high stacking fault energy, and therefore, can reduce more substantially the temperature of the beginning of recrystallization in them.

In metals with impeded cross slip (a low stacking fault energy E_{sf}), t_r^s diminishes only slightly at a lower temperature of deformation. This has been confirmed by experimental data obtained on aluminium, iron, nickel (metals with a high E_{sf}) and copper (low E_{sf}). For instance, commercially pure aluminium deformed 20 per cent at room temperature and at 78 K recrystallized respectively at 520°C and 390°C, i.e. t_r^s was decreased in the latter case by 130 degrees. High-purity iron and nickel, deformed heavily at the same two temperatures, recrystallized at 450°C and 20°C and respectively at 325°C and 20°C, i.e. the reduction of t_r^s was 430 degrees for iron and 305 degrees for nickel. On the other hand, for copper deformed 20 per cent under the same conditions, the reduction of t_r^s was only 35 degrees (from 450°C to 415°C).

Irrespective of the embrittling factor (excess phase precipitates at boundaries in some metals, such as chromium, molybdenum, tungsten, tantalum, etc., or an appreciable concentration of a covalent-bond interstitial phase in semiconductors) brittle metals and compounds are characterized by a substantially higher lever of T_r^s, even in a relatively pure state; their T_r^s can constitute 0.5-0.6 of $T_{m.p.}$ or more. For instance, the $T_r^s/T_{m.p.}$ ratio is equal to 0.5-0.45 for chromium, tantalum and tungsten and 0.55-0.6 for TaC and WC carbides and their solid solutions.

An explanation to this fact is that work hardening of such metals, even to a high degree (by surface roughing, grinding, etc.) is actually associated with dispersion of the structure, so that the dislocation density in the bulk of grains (sub-grains) varies only insignificantly. The main driving force of recrystallization in such materials is the tendency to minimize the grain boundary energy, while the volume energy does not actually contribute to primary recrystallization. Peierls-Nabarro locks can also play a definite part. Higher locks inhibit more appreciably the distribution of dislocations by slip, and therefore, the formation of recrystallization nuclei.

The temperature level of recrystallization in single-phase alloys. The higher temperature level of recrystallization in commercially

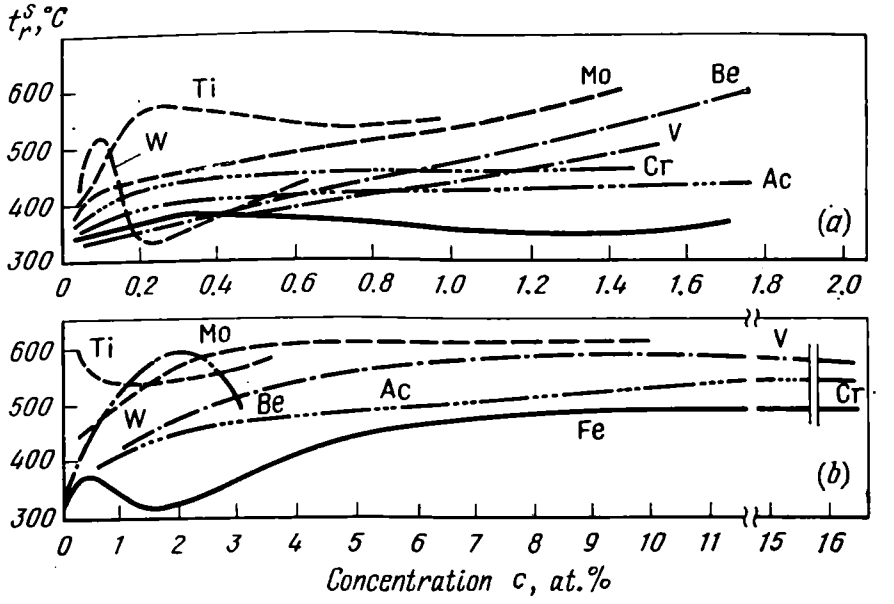

Fig. 191. Effect of concentration of a second component on t^s_r of binary nickel-base alloys ($\varepsilon = 50\%$)
(*a*) alloys with a low concentration: (*b*) alloys with a high concentration

pure metals compared to high-purity metals is associated with the effect of minor additions. Soluble minor additions (in concentrations of tenths, hundredths or sometimes thousandths of an atomic per cent) almost always raise the temperature limit of recrystallization. The higher is the purity of the original metal, the greater will be the effect of soluble minor additions.

Atoms of an addition interact with dislocations and vacancies, decrease the elastic energy and mobility of dislocations and thus impede the formation of recrystallization nuclei. The effect of minor additions is greater with a larger difference in the atomic radii of the base metal and impurity, lower solubility of the impurity, and higher purity of the original metal. Under proper conditions, 0.01-0.1 at.% of an impurity can raise t^s_r by hundreds degrees. The effect of minor additions in nickel-base solid solutions is illustrated by the curves given in Fig. 191.

With a further increase in the concentration of a solute impurity, metal portions near dislocations become saturated and the difference in the concentrations of the impurity in these portions and in the bulk of crystallites diminishes. This results in a lower energy required for redistribution of dislocations and formation of recrystallization nuclei, i.e. t^s_r rises further less steeply or even can become lower compared with alloys of a lower concentration. In that case, the curve relating the concentration of an impurity with t^s_r will have a maximum in the range of low concentrations. Such maxima can be revealed distinctly on dissolution of tungsten, iron and titanium in

nickel (see Fig. 191); they appear respectively at concentrations of 0.1 per cent, 0.2 per cent, and 0.3 per cent.

The influence of impurities on t_r^s of a solid solution containing an impurity in a concentration above the respective maximum is determined by two factors. Firstly, by the effect that the impurity dissolved in the volume of crystallites produces on the structure of the deformed state and secondly, by its effect on the strength of interatomic bonds and therefore on the diffusion mobility in undeformed state. The effect on the structure appears as a change in the stacking fault energy. Impurities which can lower this energy and thus inhibit cross slip of dislocations (dynamic recovery), also lower t_r^s. The reducing effect of impurities on the strength of atomic bonds acts in the same sense. With an increase in the strength of bonds, t_r^s increases.

The effect of impurities on the stacking fault energy E_{sf} and the structure in deformed state appears obviously at lower concentrations than their effect on the strength of atomic bonds. Thus, if an impurity decreases E_{sf} and the strength of atomic bonds, t_r^s attains the first maximum and then falls off monotonously as a function of impurity concentration. If an impurity decreases E_{sf} but raises the strength of atomic bonds, the curve of t_r^s will fall off after the first maximum and then rise again. Finally, if the effect of an impurity on E_{sf} is insignificant, the curve $t_r^s = f(c\ \%)$ will have no maximum at all in the range of low concentrations, but will rise more monotonously. This behaviour is characteristic of molybdenum, chromium and aluminium additions in nickel (see Fig. 191).

In the range of high concentrations in a solid solution, t_r^s of single-phase alloys depends only weakly on composition. A change of concentration of an impurity by 1 per cent varies t_r^s only by a few degrees in the positive (if atomic bonds become stronger) or negative (if they become weaker) direction. As a result, the $T_r^s/T_{m.p.}$ ratio of single-phase alloys cannot be raised above 0.55-0.60 even by complex alloying. A higher relative temperature level of recrystallization can only be attained in supersaturated solid solutions.

The temperature level of recrystallization of supersaturated solid solutions. Figures 191, 192 and 193 give the temperatures of the beginning of recrystallization (t_r^s) for selected age-hardening and single-phase alloys with the compositions near the solubility limit. As may be seen from the curves, t_r^s increases sharply by 200-300 degrees on a change from single-phase to age-hardening alloys. The $T_r^s/T_{m.p.}$ ratio of age-hardening alloys is as a rule greater than 0.60 and can attain 0.75-0.80 in some cases. The highest relative level of recrystallization is found in alloys in which a new phase, isomorphous with the matrix (such as in Nimonic alloys), precipitates from the supersaturated solid solution on heating of deformed metal (or

in the course of hot deformation, see Ch. 8) and is coherent with the matrix, and also in some alloys in which the transition temperature from two-phase to single-phase region is very close to the melting point.

Another feature characteristic of supersaturated solid solutions in which heating after deformation is associated with decomposition or pre-decompositional processes, is that their t_r^s is far less dependent on deformation than that of single-phase alloys (see Fig. 192). This is why the higher value of t_r^s of age-hardening alloys is especially noticeable upon heavy deformations. This sharp rise of the temperature limit of recrystallization in age-hardening alloys should be attributed to the fact that, when a deformed supersaturated solid solution is being heated (and partially in the course of deformation), it undergoes decomposition (ageing) which inhibits the nucleation and/or the growth of recrystallization nuclei. Decomposition of a solid solution and the associated structural work hardening vary the conditions of redistribution of dislocations and of migration of boundaries.

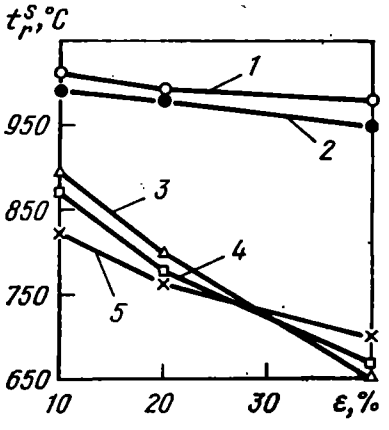

Fig. 192. Effect of deformation on t^s_r of nickel-base alloys

1, *2*—age-hardening alloys, Ni-Cr-Al-Ti-Co and Ni-Cr-Al-Ti; *3*, *4*, *5*—single-phase alloys Ni-Cr, Ni-Cr-W, and Ni-Cr-Co

The temperature level of recrystallization in heterophase alloys. Most commercial alloys are heterophase. Most often they consist of a plastic polycrystalline matrix with inclusions of hard disperse particles. All carbon and alloy steels, aluminium alloys, high-temperature nickel and iron alloys and composite alloys containing a metal and a high-melting disperse phase belong to the group of heterophase alloys.

Supersaturated solid solutions, when in the state of decomposition, are also heterophase alloys. In the following discussion, we shall only consider heterophase alloys in which the second phase is not dissolved in the course of heat treatment and is practically present in the alloy prior to deformation.

Secondary-phase particles may have a different effect on an alloy. In some cases, they accelerate recrystallization of the matrix; in others, they decelerate it. In this respect it is of interest to consider the data on recrystallization of ferrite in carbon steel. Primary recrystallization nuclei form in excess ferrite at boundaries of pearlitic colonies and at a greater speed than in carbonless ferrite, while ferrite of the pearlite colonies does not recrystallize up to rather high temperatures at which spheroidization of cementitic platelets begins.

A special effect is produced when high-disperse particles are present in a high concentration. They weaken the degree of texture formation in the matrix during deformation and increase sharply the stability of the metal against recrystallization (softening).

In order to understand these results and predict reliably the probable effect of disperse particles on recrystallization in the matrix, one has to analyse the principal factors determining the liability to recrystallization which can be affected by the presence of disperse particles in the matrix prior to deformation.

Disperse particles can change the type of dislocation structure and texture forming during deformation. This variation may be different depending on the size of particles and the volume occupied by them (the mean distance between particles). If the size of particles is a few tenths of a micrometre or more and the distance between them is sufficiently large, at least greater than the particle size (which corresponds to a few volume per cent), they will mainly serve as barriers for dislocations which move in the matrix under the effect of deforming forces. This results in local pile-up of dislocations in microvolumes of the matrix near particles and in an increased distortion of the lattice in these volumes. During heating, these portions become sites of preferable nucleation in recrystallization. A typical case of this kind is illustrated in Fig. 181*c*. A group of recrystallization nuclei in transformer steel has formed at a non-metallic inclusion.

If disperse-phase particles are smaller than the size indicated and are located at smaller distances from one another (i.e. their volume concentration is respectively higher than in the former case), the dislocation structure will be utterly different. In alloys containing such disperse particles, the dislocation density, already on light deformations ($\varepsilon \approx 5$ per cent) turns out to be substantially higher than in the pure metal, but dislocations are distributed more uniformly and chaotically over the matrix. Features of a cell structure appear on appreciably heavier deformations than in pure metals.

The presence of disperse oxide particles may have an essential effect on the texture, which in this case is multi-component and less distinct.

It is supposed that such alloys have a large number of internal dislocation sources; disperse particles proper obviously serve as such sources. Particles are always surrounded by an elastic stress field which is due to the different unit volume and different coefficients of thermal expansion of particles and of the matrix (structural strain hardening). When an external stress is superposed on these internal fields, this may raise the dislocation density and activate dislocation slip in many slip systems already at light deformations. This should result in a less distinct texture being formed and a more uniform distribution of dislocations. But a more uniform distribution of dislocations and smaller angles of misorientation between

cells imply that there is a smaller surplus of like dislocations. For sub-boundaries to become high-angle boundaries and for sub-grains to become recrystallization nuclei under such conditions, sub-boundaries should pass through an appreciably greater distance than in a material with a less uniform distribution of dislocations. Thus, recrystallization in this case will be retarded. Besides, secondary-phase particles can alter the conditions of redistribution of dislocations during heating and the migration of boundaries by the barrier mechanism, i.e. can change the conditions of formation and growth of recrystallization nuclei and grains.

If the size of particles is within 0.05-0.3 μm or more and the distance between them, 0.1-1.0 μm or more, their effect on the type of the dislocation structure formed on deformation ceases to be critical, but they now play a decisive part in redistribution of dislocations during heating and in boundary migration. Their effect on redistribution of dislocations is similar to the mechanism for age-hardening alloys discussed earlier. Their effect on boundary migration can be described as follows. Zener and Smith have demonstrated that the force with which disperse particles retard boundary migration is

$$P_{\text{ret}} \approx \frac{3f}{d} E_{\text{b}} \qquad (154)$$

where f is the volume concentration of particles; d is their diameter, and E_{b} is the boundary energy.

It follows from this formula that the retarding effect is greater at a higher volume concentration of inclusions, smaller size of particles, and greater boundary energy.

It follows, however, from the expression $V = M(P_{\text{dr}} - P_{\text{ret}})$ (see Ch. 6) that the effect of particles is greater at a lower driving force of the process, since migration of a boundary is only possible when $P_{\text{dr}} > P_{\text{ret}}$. This implies that, to retard the enlargement of nuclei in primary recrystallization, which is stimulated by the different density of defects at a nucleus and in the deformed matrix, the volume concentration of undissolved particles should be greater and the particle size should be smaller than when it is required to retard grain growth stimulated by boundary migration, which is stimulated only by the trend of the system to minimize its boundary energy.

For instance, as follows from relationship (154), 1 per cent of particles 0.5 μm in diameter can form a retarding force of 1.0 N cm^{-1} at a grain boundary of an energy of 5×10^{-5} J cm^{-2}. This concentration of particles cannot inhibit the growth of primary recrystallization nuclei since its driving force exceeds 10^2 N cm^{-1}, but can inhibit grain growth beginning from the particle size 10 μm (see Ch. 6).

In the course of grain growth, as the size of grains increases, the effect of disperse particles becomes more and more pronounced, with the result that grain growth comes to an end. According to C. Zener,

grains in a matrix containing disperse particles of an average size $\bar{d}$ and volum. concentration f can grow t the maximum size $D_{max} = \bar{d}/f$. The parameters $\bar{d}$ and f can be replaced by a generalized parameter, the distance between particles, $\bar{\lambda} = \bar{d}(4\pi/3f)^{1/3}/2$. Thus, to retard grain growth, particles need not form a continuous barrier; it suffices to have the distance between them equal to about 50-100 atomic spacings.

Thus, the temperature level of recrystallization and the maximum grain size can be controlled by varying the concentration and dispersity of secondary-phase particles.

Disperse particles can also mask the actual beginning of recrystallization and softening, since they often are disintegrated into smaller particles in plastic deformation.

When analysing the effect of disperse phases, it should be considered that disperse phases proper can be disintegrated at heavy deformations. Should this occur, their size $\bar{d}$ diminishes for the same volume concentration and their effect on boundary migration becomes stronger than prior to deformation. Disintegration of secondary-phase particles will be stronger when their original size is larger and their shape is less round.

This has as a consequence a number of important particularities. For instance, the hardening effect in deformed steel turns out to be stronger when the original metal has more carbides. Upon 80-per cent deformation, the Vickers hardness increased by 100 units in commercial iron, by 120 units in steel Ст. 3, and by 150 units in steel Grade ШХ15. For the same composition, a steel containing lamellar cementite can be hardened more appreciably than that with globular cementite. The hardness of a steel rich in carbides varies in a peculiar manner during heating. In steel ШХ15, the hardness, up to the end of primary recrystallization, is higher upon heavier prior deformation. The difference in hardness may be substantial, up to roughly 40 HV. This difference can be explained by disintegration of carbide particles and, as a consequence, by disintegration of recrystallized ferritic grains. The effect described should be considered when developing the technology of intermediate softening annealing procedure for steels having different concentrations of carbides.

3. First-order Recrystallization Diagrams

Average grain size, degree of inequigranularity and structure are among the most important characteristics of a material. In many cases, some of these structural parameters are standardized, along with chemical composition of metals. The size of grain and the type of structure are essential for selecting the optimal conditions of metal treatment procedures.

The most common and convenient form for representing graphically the effect of deformation and heating on the microstructure of recrystallized material is what is called the recrystallization diagram. Recrystallization diagrams of cold-deformed material are called first-order recrystallization diagrams. The structure of recrystallized material upon hot deformation is depicted in second- and third-order diagrams which will be discussed in the next chapter.

A first-order recrystallization diagram is usually a three-dimensional diagram representing the dependence of the average grain size $\bar{D}$ (vertical axis) on deformation ε (horizontal axis in the plane of drawing) and annealing temperature t, °C (the axis normal to the plane of drawing). Some typical first-order recrystallization diagrams are shown in Fig. 193.

Common recrystallization diagrams which contain data on the average grain size $\bar{D}$ give only limited information, especially in view of ever increasing requirements laid on the properties and structure of metals and alloys. For instance, if the main quantity of grains in a specimen is of index 8, but the structure contains a few very large grains, the structure may be estimated on a recrystallization diagram by index 2 or 3, which is far from being its actual characteristic. In that connection, some authors have proposed to use special marks at lines of recrystallization diagrams to characterize the type of structure (inequigranularity, texture, twins, etc.). Examples of such diagrams are given in Ch. 8.

By another method, inequigranularity in first-order recrystallization diagrams is characterized by two factors: the average grain size of fine-granular matrix and the average size of large grains. Accordingly, two experimental lines instead of one are drawn in respective portions of a recrystallization diagram. In order to define more clearly the conditions of deformation and heating which cause inequigranularity, the portions of a diagram between the two lines mentioned (which correspond to inequigranular structure) can be hatched, as shown in Fig. 193. An advantage of this method of presentation of recrystallization diagrams is that it makes it possible to reveal more distinctly the second maximum of grain size.

A disadvantage of common recrystallization diagrams is that they are not always based on actual deformation. Recrystallization diagrams are most often constructed by using flat or cylindrical specimens. Upon rolling (upsetting) and heat treatment of specimens, the size of grain is determined as an average over the height of cross section of a specimen (in the point of intersection of diagonals). The relative reduction is found by the formula $\bar{\varepsilon} = [(h_0 - h_1)/h_0] \times$ $\times$ 100% and the actual deformation, by the formula $\varepsilon = \ln (h_1/h_0)$, where h_0 and h_1 are the original and the final height of the cross section. It should be noted that the values of actual deformation

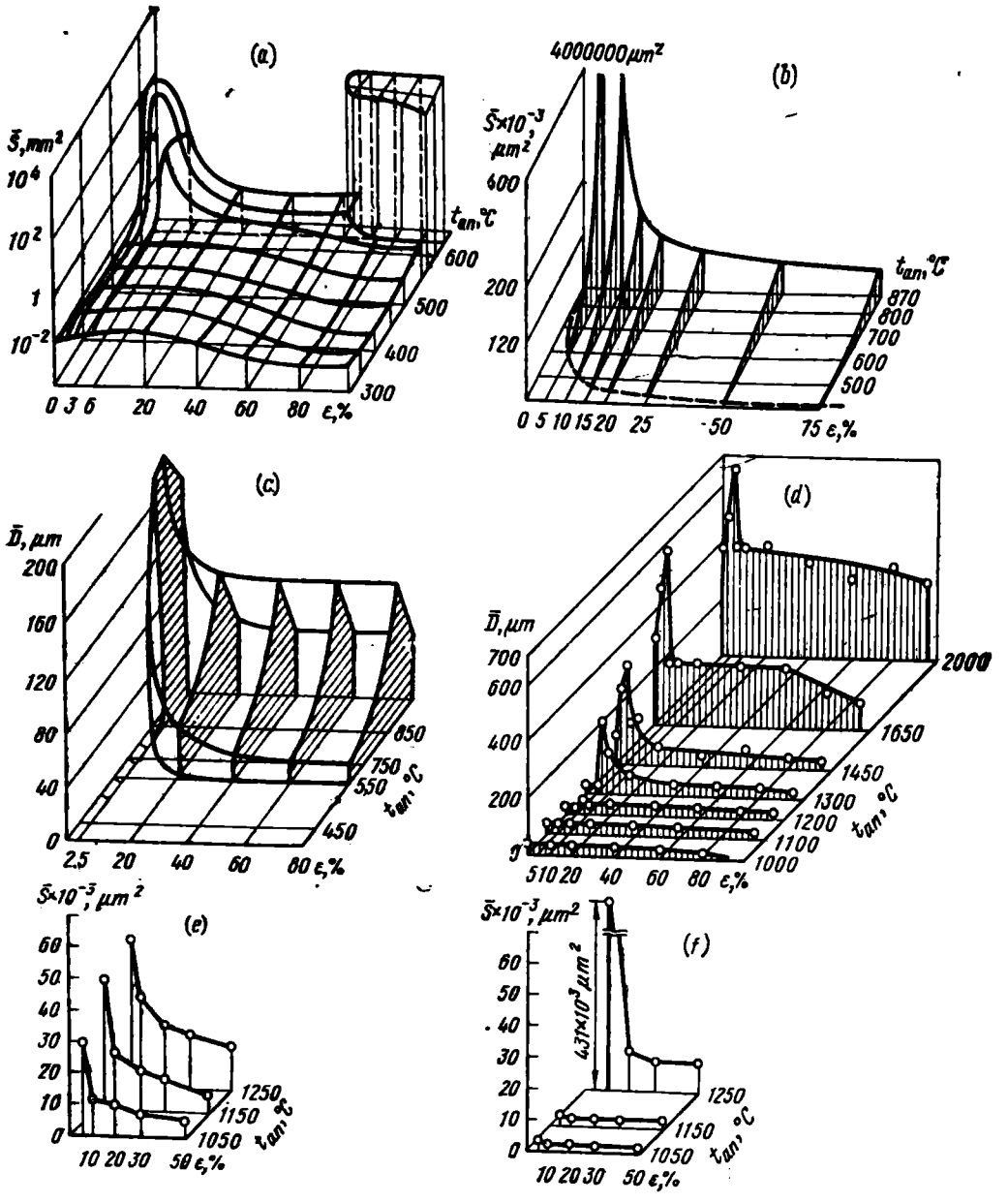

Fig. 193. First-order recrystallization diagrams
(*a*) aluminium (99.6%); (*b*) electrolytic iron; (*c*) commercial-purity titanium; (*d*) niobium; (*e*) austenitic steel X18H14M2; (*f*) austenitic steel X18H14M2Б1 containing NbC carbides and Fe_2Nb_2 intermetallics soluble above 1150°C

and relative reduction may differ substantially on heavy deformations, though they practically coincide on light (less than 10 per cent) deformations.

Owing, however, to the effect of friction forces between the specimen and deforming tool, the deformation is distributed non-uniformly along the height of specimen. It is at a minimum near end faces and at a maximum in the middle section. Non-uniformity of deformation is especially important on light deformations and at high rates of upsetting. Because of this non-uniformity, a deformation in the mid-section of a specimen may differ from the average deformation by 100 per cent and the temperatures of the beginning of recrys-

tallization in various sections may differ from one another by 100°C or more. I. M. Pavlov has suggested to construct what is called the 'actual' recrystallization diagram, with the actual deformation being determined by the screw method. A threaded bore is made along the axis of a cylindrical specimen to receive a screw made of the same material. Upon deformation, the specimen is cut along the direction of upsetting and the actual relative reduction is determined by variations of the screw pitch in various points along the height, using the formula:

$$\varepsilon_a = (s_0 - s_f)/s_0$$

where s_0 and s_f are the original and final screw pitch (i.e. before and after upsetting). It is better to determine the actual local deformation by using the formula $\varepsilon_{loc} = \ln s_0/s_f$. The average grain size is determined in the respective portions of the section upon annealing. These data are used to construct the actual recrystallization diagram.

In cases when slight variations in grain size are inessential and there are no conditions for the appearance of inequigranularity in the alloy, the common method of construction of recrystallization diagrams may be preferred as being less labour-consuming.

A rather efficient and quick method for constructing actual recrystallization diagrams is based on the use of tapered specimens deformed in tension. A number of marks are made on such a specimen before deformation. The actual deformation is determined by the changes in the distance between adjacent marks. After deformation, one obtains a set of deformation values: from near zero at the base of the specimen to the maximum value in the neck (or in the point of rupture). The gradient of deformations along the length of the specimen and the maximum deformation can be varied by varying the angle at the specimen base. For instance, this angle should be increased when it is essential to extend the range of low deformations.

By testing a single tapered specimen (deformed and annealed at a given temperature), an isothermal section of the recrystallization diagram can be determined and the whole diagram can be constructed by the results obtained on about 10-15 specimens. Furthermore, the method is quite illustrative, especially in cases when coarse-grained or inequigranular structure can appear in the respective intervals of strain and temperature. It can be readily revealed by macroetching, as illustrated in Fig. 187.

A drawback of the method of tapered specimens is that it is inapplicable to low-plastic materials where fracture occurs after a very small amount of plastic deformation. Besides, it should be kept in mind that the relations obtained on tensile-deformed specimens are not fully applicable to other types of deformation. A general draw-

back of common recrystallization diagrams is that they represent the grain size after various degrees of deformation and at various temperatures of annealing for the same time of annealing, i.e. essentially for different stages of recrystallization. With a given time of annealing, however, the metal may be in the stage of primary recrystallization in places where the deformation has been light and in a developed stage of grain growth or even secondary recrystallization in places deformed more heavily. In some important cases, it is essential to know grain size at the end of primary recrystallization or at various but definite stages of subsequent recrystallization and the conditions at which a desired state can be fixed.

Of large practical use could be diagrams showing the grain size by the end of primary recrystallization and, when desired, at various stages of the subsequent recrystallization processes. Such diagrams could be employed effectively for selecting the appropriate process conditions to form a desired structure. Unfortunately, the construction of such diagrams is quite a labour-consuming procedure, because of which they have found no practical application.

A large number of recrystallization diagrams for the most popular metals and alloys have been published in the specialist literature. For some alloys and steels of practical importance, in particular for structural steels, a number of diagrams have been constructed for various conditions of deformation and heating, various original structural states, etc. This has been done in view of the essential influence of these factors on the type of recrystallized structure. All the factors which can affect the size of grains (except for the amount of deformation and the temperature of annealing) must be kept constant in all the specimens tested for construction of a recrystallization diagram and the respective data should be indicated in the diagram. These data include the chemical composition and structural state of an alloy, the degree of purity and concentration of impurities for high-purity metals, the original grain size and texture, the method and rate of deformation, the rate of heating and cooling, the time of isothermal holding, etc.

The importance of these factors can be illustrated by the recrystallization diagrams (Fig. 194) for chrome bronze (Cu + 0.5% Cr) which have been constructed for two original states with different grain size and texture. The original state *I* was formed by hardening from 1020°C, followed by age-hardening (500°C, 20 h). The average grain diameter was $\bar{D} = 0.7$ mm, the size of chromium particles $\bar{d}_{Cr} = 50$ nm; the texture was of three-component type. State *II* was obtained by hardening from 700°C. The respective parameters were: $\bar{D} = 0.02$ mm, $\bar{d}_{Cr} = 2\text{-}4$ μm, the texture—single-component (cubic). The specimens were then cold-rolled to deformations of 20, 40, 60 and 80 per cent and annealed at 800, 900, 1000 and 1040°C to obtain data for constructing recrystallization diagrams. As may

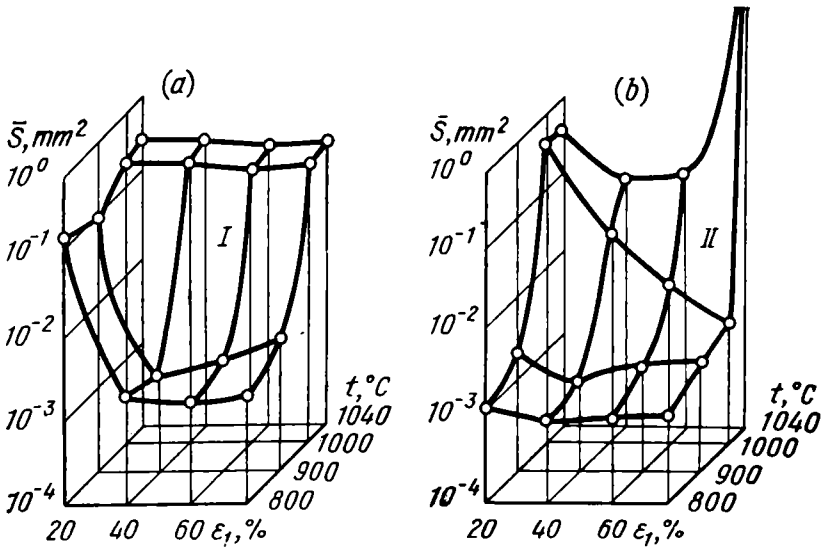

Fig. 194. First-order recrystallization diagrams for chrome bronze in various original states
(*a*) hardened from 1020°C and heated at 500°C for 20 h; (*b*) hardened from 700 °C

be seen from Fig. 194, the diagrams plotted for the two original states mentioned differ largely from each other.

Recrystallization at 800 and 900°C after moderate deformations refined the grain in state *I* and practically did not change it in state *II*. In heating at 1000°C, there was an inverse relationship. For the specimens in state *II* deformed 80 per cent, heating at 1040°C produced a sharply pronounced maximum of grain size due to secondary recrystallization in the cube texture matrix. Specimens in state *I* did not give such a maximum. This example shows that, for analysis of recrystallization diagrams of a particular metal (or alloy), it is essential to know the original (before the last deformation) state of the material.

An appreciable portion of the diagrams constructed up to 1950 have been collected by I. L. Rogelberg and E. S. Shpichenetsky in their book [2]. Among the later diagrams, it is worth to mention the recrystallization diagrams for high-melting and rare metals (E. M. Savitsky et al.) and those for nickel- and iron-base high-temperature alloys (N. I. Korneev et al.).

Despite their drawbacks mentioned above, these and similar recrystallization diagrams are used widely for selecting the process conditions of plastic working and of intermediate and final procedures of annealing. Using a recrystallization diagram, one can follow the variations in the size of recrystallized grains depending on (a) the amount of deformation ε for a given temperature of annealing t or (b) the temperature of annealing t for a given deformation ε.

As follows from the diagrams given here, the relationship between the amount of prior deformation and the size of recrystallized grain is not monotonous, but is described by curves with one, two or even

three maxima. The causes and mechanism of the appearance of the first two maxima of grain size have been discussed earlier. As to the third maximum, which appears in the region of heavy deformations, it has been detected in a few number of systems. An essential condition for its formation is a distinct deformation texture in the metal prior to annealing. This should evidently be a mono-texture, though the problem has not been studied properly. With such a texture, some of recrystallization nuclei having an orientation different from that of the matrix and favourable for their growth at the expense of the textured matrix (see Ch. 9) will grow much more intensively than nuclei of a different orientation, which will result in the formation of a coarse-grained structure.

The dependence of D on annealing temperature for a given amount of deformation is simpler. If a metal or alloy undergoes no polymorphous transformation in the temperature range considered, an increase of the temperature of annealing above t_r^s will result in a monotonous increase of grain size. A polymorphous transformation usually refines the grain, because of which heating to a temperature above or below the transformation point is associated with the formation of a coarser grain than on heating slightly above that point.

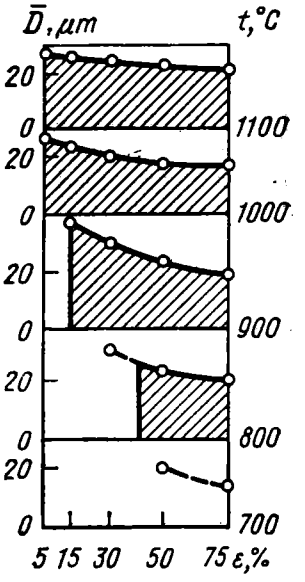

Fig. 195. Recrystallization diagram for induction-heated commercial iron ($v = 50$ °C/s)

In the presence of disperse phases, recrystallized grains remain fine up to the temperature of the beginning of dissolution of these phases. During heating to these temperatures, the size of grain usually increases jumpwise for any amount of deformation, but especially strongly for definite amounts of deformation corresponding to the first and second maxima. The jumpwise rise of grain size beginning with a definite temperature of annealing is a typical phenomenon which accompanies the dissolution of disperse phases and can serve as a reliable indication of this dissolution.

A special type is recrystallization diagrams for high-speed heating (induction or electric-contact heating) without isothermal holding at the heating temperature (Fig. 195). The construction of such diagrams is essential in view of the wide use of high-speed heating in industrial practice. A characteristic property of recrystallization diagrams for high-speed heating is that the size of a grain depends on the amount of deformation much less substantially than in heating at common speeds, so that secondary recrystallization processes, which are responsible for grain size maxima, have no time to develop fully.

Since the structure characteristics determined by the recrystallization process are quite numerous and can hardly be reflected in common recrystallization diagrams, special recrystallization diagrams have been developed to represent some particular characteristics of a material.

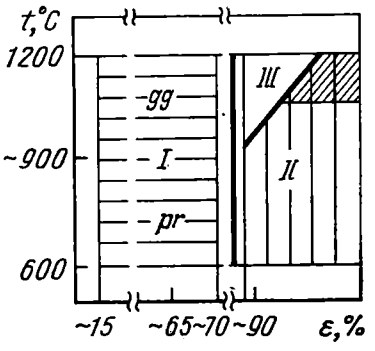

Fig. 196. Structural diagram of f.c.c. precision magnetic alloys after cold deformation and heating

I—the structure of primary recrystallization (*pr*) and grain growth (gg), without distinct texture; *II*—primary recrystallization structure with cube texture; *III*—secondary recrystallization structure with a weak texture

V. I. Ivèronova and G. S. Zhdanov have suggested a diagram which gives an idea of the time-temperature interval of occurrence of a process. These diagrams give the time of th · beginning (τ_r^s) and end (τ_r^f) of primary recrystallization depending on the temperature of annealing and the amount of prior deformation. They may be called kinetic recrystallization diagrams.

B. V. Molotilov et al. have proposed to construct special texture recrystallization diagrams for alloys whose properties depend substantially on texture. These diagrams are essentially a projection of a first-order recrystallization diagram on the deformation-annealing temperature plane on which regions with characteristic types of structure and texture are drawn. A diagram of this type for f.c.c. alloys is shown schematically in Fig. 196.

RECOMMENDED LITERATURE

1. Gorelik S. S., *Recrystallization in Metals and Alloys.* Moscow, Mir Publishers, 1981.
2. Rogelberg I. A., Shpichenetsky E. S., *Recrystallization Diagrams of Metals and Alloys.* A reference book. Moscow, Metallurgizdat, 1950 (in Russian).
3. Zasimchuk E. E., *Polygonization, Recrystallization and Thermal Stability of Properties of Materials.* Kiev, Naukova Dumka, 1976 (in Russian).

8 Recrystallization During Hot Deformation (Dynamic Recrystallization)

1. Effect of Conditions of Hot Deformation and Cooling on Recrystallization Mechanism

Hot plastic deformation includes processes occurring in a wide range of temperatures and deformation rates: from slow superplastic deformation (see Ch. 15) to modern high-speed processes of rolling, pressing, die-forging, extrusion, etc.

Hot deformation differs from cold deformation in that it occurs under the conditions which are favourable for dislocation movement, especially by cross slip and diffusion climb. As a result, two competing processes—strain hardening and softening—occur in parallel in the metal during hot deformation.

The strain-hardening effect is due to an increase in the dislocation density under the action of external forces and to the interaction of dislocations with one another. In hot deformation of supersaturated solid solutions, an additional strain-hardening effect is due to the dissociation of dislocations and their interaction with precipitates.

The processes of softening consist in a decrease of the dislocation density and in redistribution of dislocations into energetically more favourable configurations.

As distinct from cold deformation, hot deformation under proper conditions (temperature, amount and rate of deformation) may involve processes of redistribution of dislocations by diffusion climb and the formation and growth of recrystallization nuclei by migration of high-angle boundaries. By analogy with dynamic recovery, this process is often called dynamic recrystallization. Like the term 'dynamic recovery' which denotes partial softening in deformation due to cross slip of screw dislocations, the term 'dynamic recrystallization' implies that the process occurs directly during the deformation. The study of the mechanism and peculiarities of this process is associated with certain specifics and additional difficulties, as compared with recrystallization on cold deformation.

The processes of hardening and softening are time-dependent and their rates may depend substantially and differently on many factors: temperature, amount and rate of deformation, cooling rate, stacking

fault energy, the original structural state and phase composition, etc. Since strain-hardening and softening occur in parallel, their realization and the contributions to the final structure depend sharply and in a complicated manner on the factors mentioned above. The structure formed on dynamic recrystallization is much more sensitive to slight variations in these factors than the recrystallization structure obtained on cold deformation.

Further, it is sometimes difficult to distinguish between original and recrystallized grains in a hot-deformed material, since the processes of deformation and recrystallization occur in parallel and some recrystallized grains may be deformed again. In hot deformation, it is not always possible to distinguish between the structural changes taking place directly during deformation and those which occur in subsequent cooling. This circumstance should be always kept in mind. In hot deformation at practically common rates, if the deformed material is subjected to the action of high temperature for only a few fractions of a second, it is often sufficient to cause substantial structural changes in it (compared with its state just after the deformation). In many practically used steels and alloys, hot deformation and subsequent cooling may be associated with the processes of precipitation from the solid solution, which additionally complicate the course of recrystallization and the study of the process.

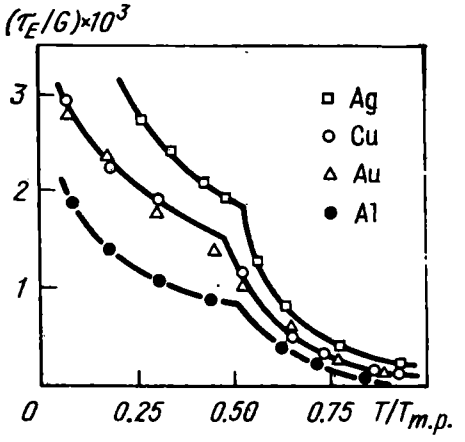

Fig. 197. Flow stress in single crystals of aluminium, gold, copper and silver as a function of homologous temperature (H. Mecking and F. Kirch)

An evidence of completion of dynamic recrystallization in the metal can be given by deformation traces within equi-axed grains (stretched sub-grains, distorted annealing twins, an elevated dislocation density). Such a substructure forms in recrystallized grains which have nucleated at earlier stages of deformation and have then been deformed.

Which of the mechanisms—either polygonization or recrystallization—is responsible for the softening effect, is determined by the conditions of deformation and the properties of the material, in particular, by its stacking fault energy E_{sf}. The results presented in Fig. 197 show that there is a correlation between E_{sf} and the behaviour of a metal in deformation in various temperature intervals. The figure shows the effect of temperature (related to the melting point) on the shear stress τ_E related to the G modulus for single crystals of selected f.c.c. metals with various values of E_{sf}. The curves are representative of the instant at which deformation is

substantial, more particularly, at the end of uniform elongation of the specimen, i.e. just before local contraction takes place.

As may be seen from the curves, there are two distinct temperature intervals: one up to $T = 0.5T_{m.p.}$, and the other above that temperature. The behaviour of the metals selected is clearly different, especially in the temperature range below $0.5T_{m.p.}$. The ratio τ_E/G turns out to be higher at a lower stacking fault energy E_{sf}, i.e. when dissociated dislocations are wider; in such cases the processes of cross slip that control dynamic recovery can occur less easily. This correlation suggests that the low-temperature interval should be associated with dynamic recovery. At temperatures above $0.5T_{m.p.}$, the contribution of diffusion climb of dislocations becomes noticeable and favours the onset of dynamic recrystallization.

A deeper insight into the processes occurring in deformation at elevated temperatures can be gained by analysing simultaneously the stress-strain curves (strain diagrams) and the structural changes at various stages of deformation and at various deformation rates and temperatures. An essential requirement for such studies is that the deformation rate be kept constant in the course of tests, instead of the constant speed of movement of the deforming tool as is the case in common tensile or upsetting tests. A constant rate of deformation can be obtained in special testing machines.

The pattern of curves obtained upon deformation at elevated temperatures differs from that of cold-deformation curves discussed in Ch. 4, Sec. 4. Let us analyse the typical σ-ε curves for two cases: (a) when deformation involves only dynamic recovery and (b) when dynamic recrystallization is realized (Figs. 198 and 199). In the former case, the curves have no Stage *I*. At the earliest stages of the

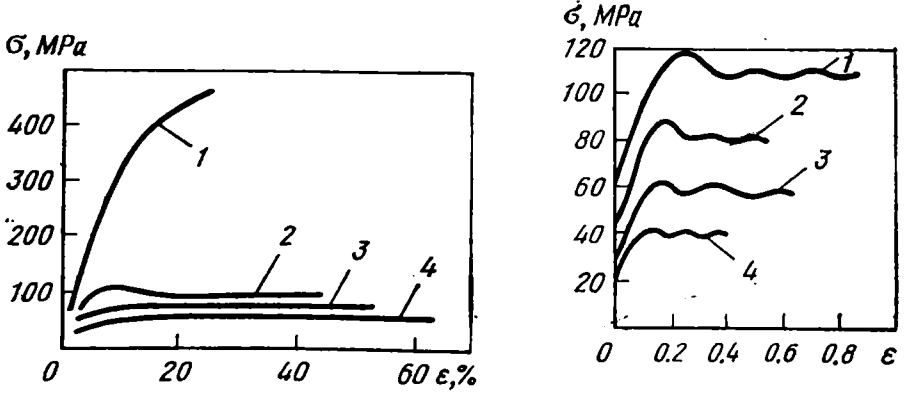

Fig. 198. (*left*) Stress-strain curves for cold and hot deformation of aluminium alloys (Yu. M. Weinblat, I. P. Rodina)
1—20°C; *2*—200°C; *3*—350°C; *4*—400°C

Fig. 199. Stress-strain curves for steel with 0.25% C at various deformation rates $\dot{\varepsilon}$ (s^{-1}) (C. Rossard and P. Blain)
1—0.29; *2*—0.032; *3*—0.0023; *4*—0.00038

process, the strain-hardening effect is typical of Stage *II*. As deformation proceeds, the initial hardening changes to slight softening, after which a stage of stable deformation begins (at a constant stress). This stable stage of deformation can be regarded as the principal characteristic feature of dynamic recovery in hot deformation, as compared to cold deformation. This difference is readily seen in Fig. 198 which gives σ-ε curves for aluminium alloy Grade Д16 taken at 20°C and at 300-400°C.

The flow stress at the stable stage is lower at a higher temperature of deformation and lower deformation rate. The initial ascending portion of the σ-ε curve is associated with an increase in dislocation density and the beginning of the formation of a cell structure. The drop of stress is caused by the process of annihilation of dislocations. At the stable stage of deformation, there is dynamic equilibrium between the dissociating dislocations and those which form anew; sub-grains are equi-axed and unvarying in size, with their misorientation angles remaining constant. A higher temperature of deformation increases the size of sub-grains and decreases the thickness of their walls and the dislocation density in them.

The effect of deformation rate, like that of temperature, is associated with the influence of these factors on the structure that forms in deformation due to thermally activated processes of dislocation movement. In view of the influence of many factors, the relationship can hardly be described quantitatively, but the following semi-quantitative expression seems to be satisfactory:

$$\dot{\varepsilon} = A' D E_{sf}^{3.5} (\sigma/E)^5$$

where A' is a constant, D is the coefficient of self-diffusion, and E is Young's modulus.

It follows from this expression that the hardening effect due to hot deformation is stronger in metals and alloys having a low coefficient of diffusion, high modulus of elasticity, and low stacking fault energy.

If hot deformation is accompanied with dynamic recrystallization (case *b*), the pattern of the σ-ε curves changes (see Fig. 200). The main difference is that, as soon as the stable stage sets in, further deformation is accompanied with periodically repeating cycles of hardening and softening and the pattern of the σ-ε curve becomes wavy.

As an example, Fig. 199 shows the curves obtained for carbon steel with 0.25 per cent C tension-deformed in austenitic state (at 1375 K) at four various deformation rates. As may be seen, the periodicity depends appreciably on deformation rate. At a high rate, there is actually only one peak immediately after the stable stage. At lower deformation rates, there are several peaks (hardening and softening cycles). A special test has shown that the softening (the descending

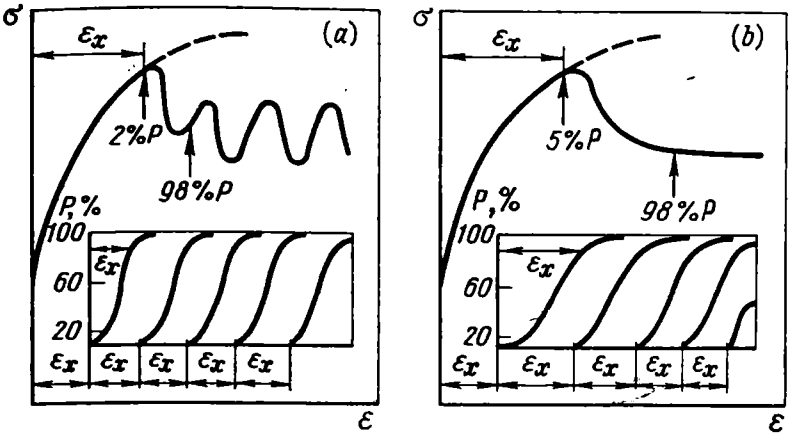

Fig. 200. Stress-strain curves for dynamic recrystallization in copper at $\varepsilon_{cr} > \varepsilon_x$ (*a*) and $\varepsilon_{cr} < \varepsilon_x$ (*b*); P is recrystallized volume, %

portion of the curve after a peak) is associated with dynamic recrystallization. To initiate dynamic recrystallization, a particular dislocation structure should be formed. This circumstance can probably explain why dynamic recrystallization in hot deformation ($T_{def} > 0.5T_{m.p.}$) is realized more easily in metals having a low E_{sf}. It is clear that in metals with a high E_{sf}, dynamic recovery can compete more successfully with recrystallization by preventing the formation of a dislocation structure favourable for the onset of recrystallization.

According to M. J. Luton and C. M. Sellars, the appearance of periodic hardening and softening cycles is associated with a particular relation between the critical deformation ε_{cr} required to initiate recrystallization (to form a favourable dislocation structure) and the deformation ε_x which takes place in dynamic recrystallization (Fig. 200). They assume in their reasoning that the two processes occur simultaneously at the recrystallization stage, but in different microvolumes: softening in those microvolumes where deformation has been most intensive and hardening, in adjacent microvolumes.

If $\varepsilon_{cr} > \varepsilon_x$ (Fig. 200*a*), recrystallization occurs not continuously but periodically, with softening and hardening cycles appearing on the σ-ε curve. If $\varepsilon_{cr} < \varepsilon_x$ (Fig. 200*b*), a given recrystallization cycle begins before completion of the previous cycle and, since the hardening and softening processes occur simultaneously but in different microvolumes, the macroscopic flow stress remains constant, i.e. there forms an apparent stable stage similar to that appearing in dynamic recovery. The difference is that the softening cycle before the stable stage is sharper in the case of dynamic recrystallization.

As may be concluded from the position of the first maxima of the σ-ε curves for a Fe + 0.25% C alloy (see Fig. 199) corresponding to four different deformation rates, the greater is the rate of deformation, the greater is the amount of deformation at which recrystalli-

zation begins (the first intensive softening). At a given deformation rate, ε_{cr} increases with an increase of deformation temperature. Using these important relationships, it is possible to control ε_{cr} and ε_x, and thus the formation of structure in hot deformation, by varying the temperature and rate of deformation.

Experimental studies of the principal characteristics of microstructure in hot-deformed metals and alloys at various stages of the process, in particular, at the stable stage and the stage of the beginning of recrystallization, have given the following results. At a stage close to the stable stage, a cell structure forms owing to intensive dynamic recovery. The amount of deformation at which a cell structure begins to form is lower at a lower deformation rate. A characteristic feature of the substructure formed on hot deformation is that the average misorientation angles between cells (sub-grains) do not exceed 1-3°, i.e. are only one-half to one-fourth of those in cold deformation. At high temperatures of deformation, most sub-grains are equi-axed even on very high amounts of deformation. The mechanism by which sub-grains remain equi-axed is very important, but yet not sufficiently clear. A large part is probably played by the processes of diffusion climb of edge dislocations and edge-oriented jogs on screw dislocations and by the processes of cross slip.

According to J. J. Jonas, 'repolygonization' is very likely to occur at the stable stage, which is understood by him as the process of continuous destruction of sub-boundaries, followed by their rearrangement and restoration. In that case, the structure at any moment in deformation should have a certain quantity of unstable sub-boundaries. This circumstance is very important and explains a whole number of specific phenomena which distinguish the substructure of hot-deformed and recrystallized metal from that of a metal recrystallized after cold deformation. Let us consider the main differences.

The sub-structure of hot-deformed metal is much less stable than that obtained on cold deformation and subsequent heating, in particular, its sub-boundaries are less stable. As a result, the formation of recrystallization nuclei in hot deformation relies quite appreciably on coalescence of sub-grains for which the existence of easily dissociating unstable sub-boundaries is essential. The poor stability of the sub-structure in hot-deformed metals and alloys is also confirmed by the fact of intensive softening at the stages of recovery and polygonization, which is much more intensive than at the same stages after cold deformation.

Recrystallized grains after hot deformation are usually characterized by an elevated dislocation density and often contain remnants of dislocation sub-boundaries. As a result, the hardness of recrystallized grains in a hot-deformed metal is higher than that of annealed metal, which is associated with the fact that the process of coalescence of sub-grains participates in the formation of recrystallization

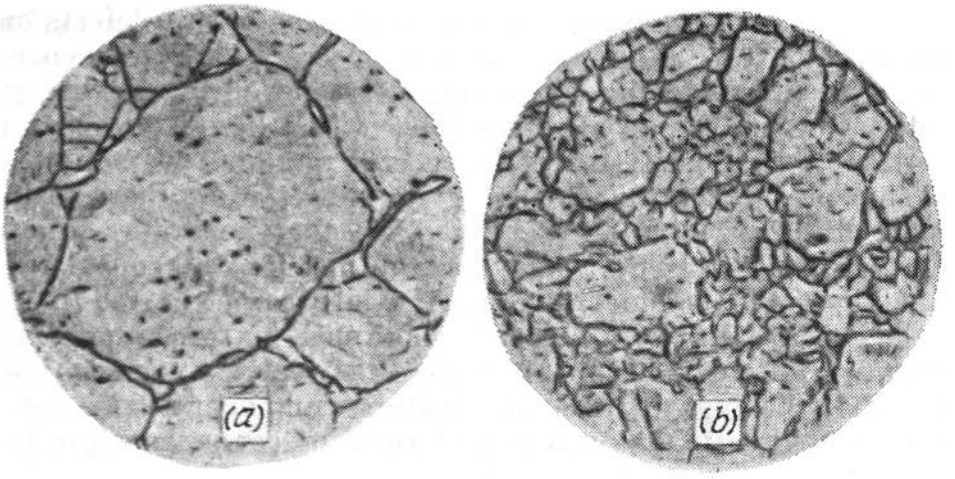

Fig. 201. Preferable formation of recrystallization nuclei at the boundaries of original grains in hot-deformed H36XTЮMB alloy, 300×
(*a*) $\varepsilon = 6\%$; (*b*) $\varepsilon = 30\%$

nuclei. Another factor of importance is that recrystallization nuclei which have appeared at an early stage may be strain-hardened in the course of further deformation. Since, as has been mentioned earlier, sub-grains are equi-axed and have low misorientation angles, it is rather improbable that recrystallization nuclei will form in the bulk of grains during hot deformation. The result is that recrystallization nuclei form during hot deformation preferably at boundaries of original grains (Fig. 201). Nucleation in the bulk of grains, which is quite common during heating after cold deformation, does not usually occur in hot deformation, except for the cases of very high deformation rates. Recrystallization nuclei formed at boundaries of original grains turn out to be initially separated by a high-angle boundary on one side only, i.e. relative to an adjacent original grain.

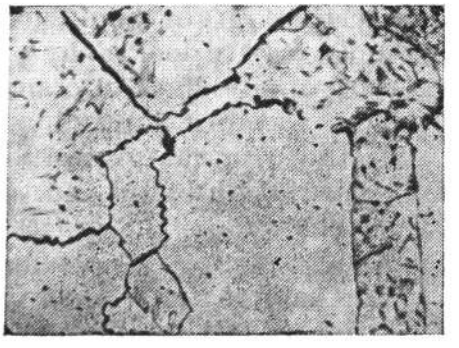

Fig. 202. Tooth-shaped boundaries of original grains formed due to local migration of portions of boundaries during hot deformation of steel ШХ15СГ in austenitic state, 270×

This mechanism of formation of recrystallization nuclei at original grain boundaries results in local migration of some portions of a high-angle boundary, i.e. in the formation of protrusions ('tongues'), so that the original grain boundary becomes tooth-shaped (Fig. 202). Tooth-shaped boundaries are a typical structural feature of dynamic recrystallization and are observed quite often.

The driving force for the formation of tongues (tooth-shaped boundaries) is the difference in the local densities of defects on two sides of a particular portion of a boundary. This difference may directly be caused by inhomogeneous deformation in adjacent grains. Another mechanism is also possible, which has been observed in aluminium. It consists in coalescence of one or more sub-grains on one side of a boundary, resulting in complete or, more probably, partial disappearance of the boundary that separates these sub-grains. The effect is that sub-grains formed on the considered side of the high-angle boundary are substantially larger in size than those on the other side. In a strongly deformed textured material, the mechanism discussed earlier is more often realized at grain boundaries which belong to different texture components. As has been found by calculations, a sub-grain formed by coalescence can become a recrystallization nucleus if only its size exceeds at least four or five times the average size of sub-grains in the adjacent grain.

In dynamic recrystallization, the role of oriented nucleation in the formation of recrystallization textures is more pronounced than in recrystallization after cold deformation (see Ch. 9). As a rule, the texture appearing due to dynamic recrystallization or to recrystallization during heating after hot deformation is recurrent of the original deformation texture.

The mechanism of recrystallization by migration of local portions of original grain boundaries cannot however be realized if these boundaries are locked by disperse phase particles. In that case, the growth of a nucleus into an adjacent grain is impossible. Recrystallization can proceed only by migration of the boundaries of the nucleus into the original grain. Since, however, the boundary has a low misorientation angle and therefore has a low mobility, it will migrate slowly and the process may reduce to in-situ recrystallization polygonization. The common case of boundary locking by disperse phases is associated with decomposition of the supersaturated solid solution occurring directly during hot deformation or in the course of subsequent isothermal holding and slow cooling.

The particular temperature intervals in which boundary locking and retardation of recrystallization by precipitating disperse phases is most effective depend on the composition of an alloy and the actual position of boundaries between phases. In steels, the disperse phases which precipitate on decomposition of the solid solution are carbides, carbonitrides, nitrides and intermetallics, whose solubility in steel varies with temperature. If the metal is heated prior to deformation to a temperature at which these phases can be dissolved (at least partially) and the subsequent deformation is completed at a temperature at which the solid solution turns out to be supersaturated, its decomposition will retard recrystallization. The intensity of this retarding effect depends on a number of factors. On the one hand, apart from supersaturation, it is essential that the diffu-

sion mobility be sufficient for decomposition to occur before the beginning of recrystallization. On the other hand, if the diffusion mobility is very high, the disperse phases will coagulate easily and their locking effect on boundaries will be weakened. In steels to be deformed at high temperatures, the retarding effect of carbides on recrystallization is utilized by adding carbide-forming elements, such as titanium, chromium or molybdenum. The retarding effect of titanium has been directly established by comparing two grades of steel: 06X18H11 and 06X18H11T, the latter alloyed with titanium. As compared with the former grade, recrystallization in the titanium-alloyed grade was retarded several times at 900°C, less appreciably at 1 000°C and was not practically retarded at 1 100°C.

In hot deformation, of special importance is the rate of deformation and the rate of cooling after high-rate deformation. By varying these two parameters, it is possible to control the structure, its homogeneity, thermal stability and, respectively, the properties of the metal. The role of the rate of hot deformation has been first noticed by E. N. Sokolkov in high-temperature alloys. Later, these problems have been more thoroughly analysed by Yu. M. Weinblat and coworkers on aluminium-base alloys.

Let us consider some examples. As has been mentioned, the critical amount of deformation to initiate dynamic recrystallization increases with a decrease of deformation rate. Using this relationship, it is possible to avoid dynamic recrystallization even at heavy hot deformations, merely by diminishing the deformation rate. Furthermore, deformation at a reduced rate gives a structure which turns out to be rather stable against recrystallization in subsequent holding at the temperature of deformation.

In a nickel alloy XH77TЮР deformed 30 per cent at 1 080°C, recrystallization begins only after a one-minute holding at that temperature. In 37X12H8Г8МФБ alloy deformed at a low rate at 1 100°C and held for a certain time at that temperature, no recrystallization occurred after a holding time of 30-40 minutes (or up to 20-25 minutes when held at 1 150°C). In a low-carbon iron-nickel alloy (0.02% C + 29.5% Ni) rolled at 980°C with a reduction less than 10 per cent and then annealed isothermally at the same temperature, recrystallization was not observed up to a holding time of 30 minutes.

As may be clear, the effect was due to dynamic recovery which took place during the slow deformation. In that case, a holding time allowed after the deformation results in further improvement of the structure of sub-grains and their boundaries due to a decrease in the concentration of thermally unstable dislocation pile-ups and individual dislocations in the bulk of grains. With a rather long holding time, growth of sub-grains and collective polygonization become possible.

Thus, recrystallization during heating after hot deformation at

a low rate is undesirable, whereas slow cooling after deformation or holding at the temperature of deformation are not only undangerous but, on the contrary, ensure the most stable sub-structure. In subsequent heating to a temperature higher than the deformation temperature, recrystallization begins earlier in specimens cooled quickly after the deformation than in those which have been cooled slowly. This circumstance should be considered in many practical cases, especially as regards large-size articles. In common cooling of such pieces after hot deformation, the rate of cooling will be different in various portions and accordingly the thermal stability of the portions will also be different. The highest stability will be found in portions cooled most slowly. In subsequent heating, the external portions, which have been cooled more quickly and therefore, are more liable to recrystallization, will be heated earlier to the hardening temperature. This can result in a sharp structural inhomogeneity.

Things are different when deformation is carried out at high rates. In that case, dynamic recovery is inhibited and the conditions are favourable for dynamic recrystallization and, what is especially important, recrystallization is accelerated not only in the course of deformation proper, but also in subsequent cooling or isothermal holding. Holding even for a few seconds after deformation can cause a noticeable development of recrystallization. Under proper conditions of cooling after hot deformation, even grain growth can occur partially.

As an example, let us consider the results of analysis of recrystallization in hot-deformed austenitic (18% Cr + 8% Ni) and ferritic (of the type of transformer) steels in which no phase transformations took place. Specimens of annealed steel were treated under the following conditions: heating at 1 200°C (holding for 10 minutes), air chilling to 1 100°C, deformation at this temperature by single-stroke upsetting (average deformation rate 10^2 s^{-1}) to the specified amount of deformation, chilling to various temperatures, and cooling in water. The amounts of deformation and conditions of chilling are indicated in Fig. 203. The grain size distribution (indices) was characterized by frequency curves.

The initial high-temperature annealing was done to eliminate traces of prior deformation and obtain coarse initial grain. In that case, the appearance of fine grains in the deformed structure, which were absent prior to deformation, was indicative of the occurrence of primary recrystallization, while subsequent coarsening of the structure was evidence of the occurrence of grain growth.

The analysis of the grain size distribution curves as a function of the amount of deformation and the conditions of chilling given in Fig. 203 has made it possible to conclude that during chilling of deformed metal recrystallization has enough time to occur in appreciable volumes of the material and that, as the amount of deformation increases, the process is intensified noticeably, more appre-

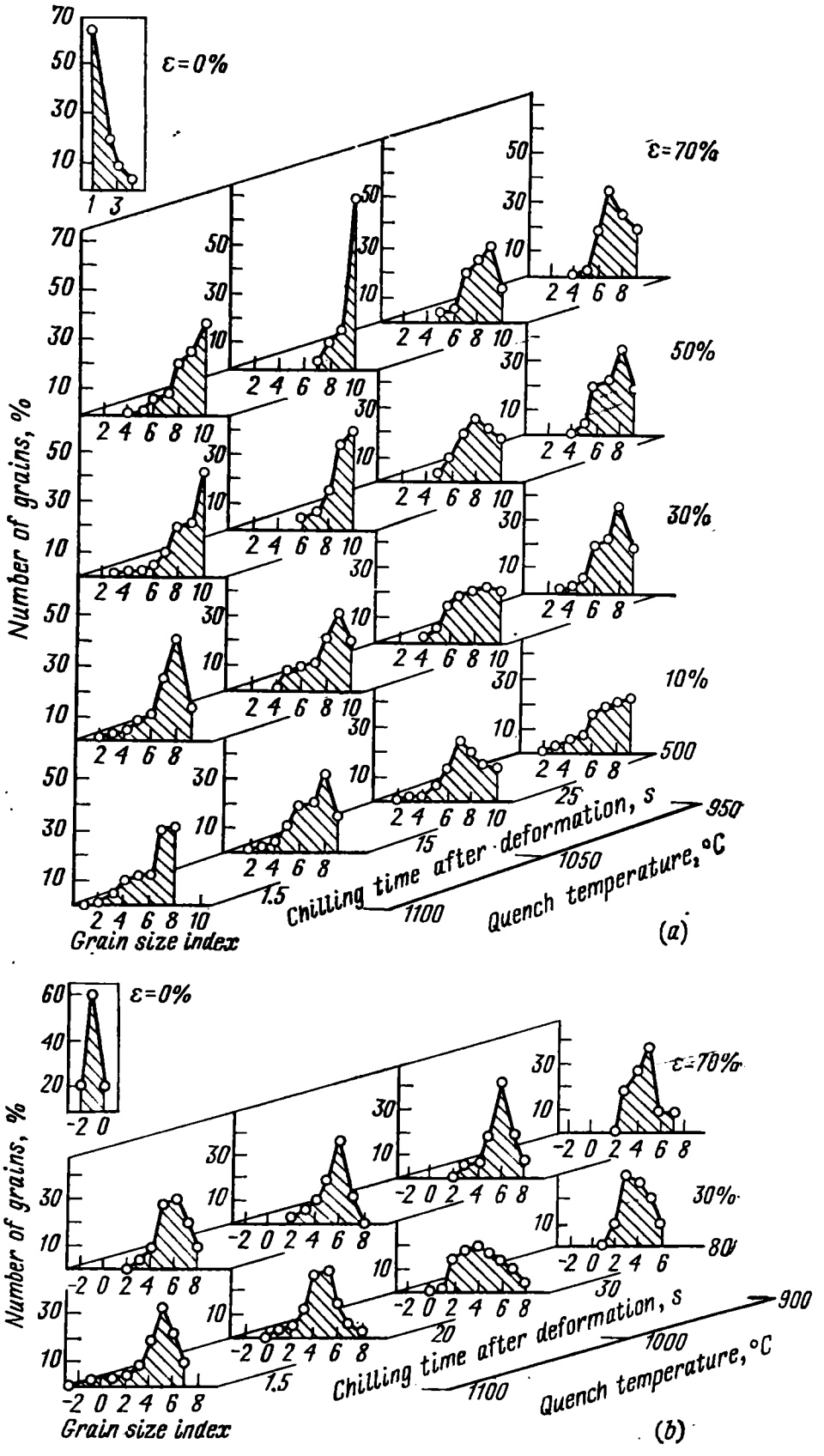

Fig. 203. Effect of post-deformation cooling of hot-deformed austenitic steel 01Х18Н10$^{V}_{2}$ (*a*) and ferritic steel 30ХГСА (*b*) on grain size distribution

ciably in austenitic steels and less so, in ferritic. For instance, after 50- or 70-per cent deformation, primary recrystallization in austenitic steel comes to its end already in 15 s. The time required for this in ferritic steel was several times longer. This agrees well with the fact that dynamic recovery in ferritic steel can occur easily. Accordingly, the driving force of recrystallization becomes lower. Thus, in order to avoid recrystallization in hot deformation at high rates, it is essential to employ high-speed chilling after the deformation. In practice, this is not always possible, especially in large-size articles. For that reason, it is more reasonable to use low deformation rates.

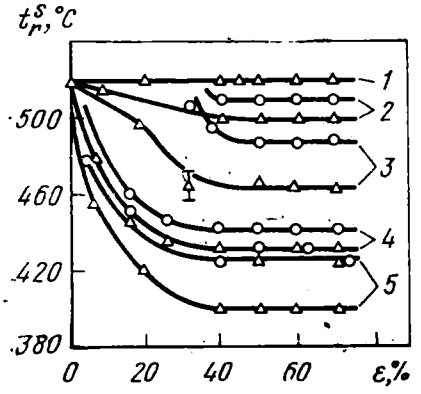

Fig. 204. Curves showing how t^s_r of an aluminium alloy increases with increasing temperature of deformation (°C)
1—480; *2*—450; *3*—400; *4*—350; *5*—300

An important and typical example of application of this technique is the method proposed by Yu. M. Weinblat and co-workers by which a homogeneous polygonized structure can be formed in articles made of aluminium alloys. A serious drawback of the common methods for making pressed aluminium-alloy parts is that the heating for hardening forms a very inhomogeneous microstructure in deformed articles. In some microregions where recrystallization can occur easily, a very coarse-grained structure forms. In pressed articles, such a structure usually appears at the periphery ('coarse-grained rim'). To avoid this, Yu. M. Weinblat and co-workers employed the method of deformation at a slow rate and elevated temperatures. The polygonized structure thus formed is rather stable and can recrystallize only at a temperature well above the temperature of hardening. In this method, both a low deformation rate and a high temperature of deformation are essential. As may be seen from the curves given in Fig. 204, the temperature of the beginning of recrystallization rises substantially with an increase in deformation temperature. Figure 205 shows the microstructures of two hardened pieces: one deformed by the common technology and the other by the method proposed.

The systematic study of the effect of various factors on the structural thermal stability of hot-deformed aluminium alloys has made it possible to conclude that it is not the type of stressed state, nor even so much the amount of deformation as the rate of deformation that plays the decisive role in this process. The rate of deformation in hot deformation has the same role as the amount of deformation in cold deformation.

Let us recall that the temperature of the beginning of recrystalli-

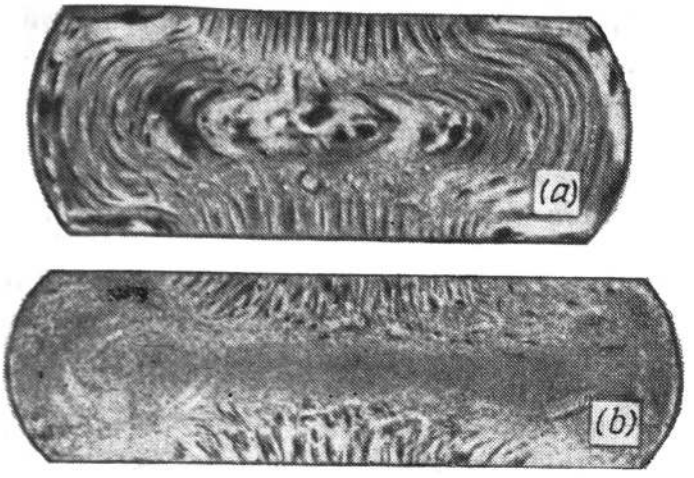

Fig. 205. Macrostructure of aluminium alloy parts after heat treatment and deformation at (*a*) common and (*b*) low rate

zation at a stable stage is independent of the amount of deformation, since at this stage a dynamically stable structure forms which practically is not changed with a further increase in the amount of deformation. This means that unvarying conditions set in for subsequent recrystallization. Hence, at relatively high amounts of deformation, this structure and these conditions can only be changed by varying the temperature and rate of deformation.

These variations can be illustrated by the results obtained for AK8 alloy (4.0% Cu, 0.6% Mg, 0.7% Mn, 0.70% Si, 0.25% Fe, balance aluminium). The thermal stability of the structure of this alloy was determined by the temperature of the beginning of recrystallization and by the lowest deformation during heating for hardening (500°C, 1 h) after which recrystallization began in the metal. This amount of deformation has been called by the authors the critical deformation ε_{cr}. Let it be denoted ε_{cr}^{hot}, in contradistinction to the critical amount of cold deformation.

Having obtained these results for a wide range of deformation rates and temperatures, the authors have constructed logarithmic curves of the effect of deformation rate on ε_{cr}^{hot} at various deformation temperatures. The curves for AK8 alloy are given in Fig. 206. For the lowest temperature of upsetting (300°C), the 'critical' deformation turned out to be practically independent of the rate of pressing (i.e. the case is similar to that observed in cold deformation).

For the specimens deformed at various rates at higher temperatures, the whole range of deformation rates can be divided into three intervals (see Fig. 206). In interval *I* (low deformation rates), ε_{cr}^{hot} is seen to depend heavily on the temperature of upsetting and only slightly, on the deformation rate. In interval *II* (high deformation rates), the structure is unstable and recrystallizes easily during

heating for hardening. Interval *III*, which lies between the former two, is most dangerous. In this interval, both the rate and the temperature of deformation have an appreciable effect on ε_{cr}^{hot}, and therefore, on structural stability. Under real conditions, especially with articles of large size and intricate shape, there always forms a gradient of deformation rates and often a gradient of temperatures. In such cases, the conditions of deformation which correspond to interval *III* will inevitably lead to zonal inequigranularity and inhomogeneous structure on subsequent heating. As applied to aluminium alloys, interval *III* of deformation rates is representative of the conditions of stamping.

The graphs of the type illustrated in Fig. 206 have been called by Yu. V. Weinblat the diagrams of structural state of alloys; they show the effect of the rate and temperature of deformation on the structure of alloys in a state immediately after hot deformation (P_{dyn}) and on the structure that forms in subsequent heating of deformed metal (P_{st}).

The phenomenon of metadynamic recrystallization, which has been discovered recently, can occur under appropriate conditions (rate and temperature) of hot deformation. It consists in the following. If hot deformation has been performed at an appreciable rate and in a definite temperature range, recrystallization during subsequent isothermal holding occurs not monotonously. Initially, grains are refined intensively, after which the average size of grains increases rapidly and the metal softens. At the next stage, grains are

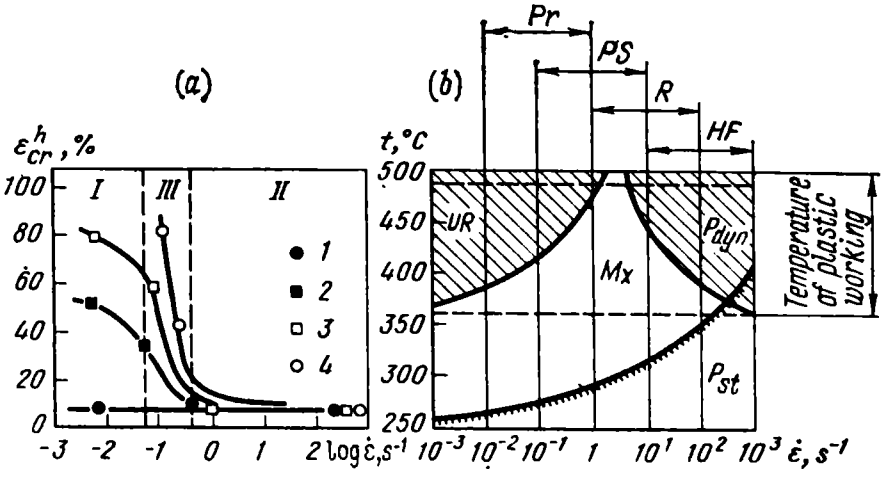

Fig. 206. Effect of hot deformation on the structure of aluminium alloys

(*a*) effect of deformation rate on ε_{cr}^{hot} of AK8 alloy (*1*—300°C, *2*—380°C, *3*—400°C, *4*—470°C);

(*b*) diagram of structural states of AMr6 alloy: *UR*—unrecrystallized structure; *Pst*—structure recrystallized during post-deformation heat treatment; *Pdyn*—structure recrystallized directly during deformation or subsequent cooling, i.e. without heating; *Mx*—mixed partially recrystallized structure; *Pr*—pressing; *PS*—press stamping; *R*—rolling; *HF*—hammer forging

refined again. At the finishing stage, slow coarsening of grains takes place.

This non-monotonous course of structural changes can be explained as follows. As hot deformation is stopped and dynamic recrystallization begins, the material turns out to have a definite number of formed nuclei for dynamic recrystallization. They play the same part as boundaries of original grains which have already started to migrate towards grains having an elevated dislocation density. In subsequent isothermal holding, these nuclei can continue to grow and the boundaries can migrate without any incubation period which is so essential in static recrystallization. The process of softening, which is the consequence of this growth and migration, has been called metadynamic (or post-dynamic) recrystallization. Since recrystallization of this type requires no incubation period, it begins at the earliest stages of annealing.

Simultaneously with this process, the processes of static recovery (without incubation period) and static recrystallization can take place during isothermal annealing in other, less deformed portions of crystallites. The process of static recrystallization begins after a certain incubation period, which may turn out to be rather long if disperse phase particles precipitate in the alloy under the given conditions. The beginning of delayed static recrystallization constitutes the essence of repeated refinement of the structure. An increase of the amount (or decrease of the rate) of deformation, on the one hand, shortens the incubation period required for static recrystallization and, on the other, increases the volume in which dynamic recrystallization has taken place and in which metadynamic recrystallization is realized in subsequent heating. Thus, the effect of grain refinement associated with delayed static recrystallization disappears.

The above considerations can be illustrated by the graphs in Fig. 207. As may be seen, a change in the amount of deformation changes the number of processes responsible for softening, the contribution of each of these processes to the softening effect, and the sequence in which these processes take place. On slight deformation, static recovery is predominant (region *1* in Fig. 207). With an increase in the amount of deformation, static recovery and static recrystallization are operative (regions *1*, *2*), then static recovery, metadynamic recrystallization and static recrystallization (regions *1*, *3*, *2*). Finally, on very heavy deformations, only static recovery and metadynamic recrystallization occur (regions *1*, *3*).

The kinetics of recrystallization during isothermal holding of hot-deformed metal offers large possibilities for controlling the grain size and therefore the properties of deformed metal. This can be illustrated by an example of successive deformation of steel in continuous rolling mills in which the number of passes and the length of pauses between deformation procedures are controlled. The length

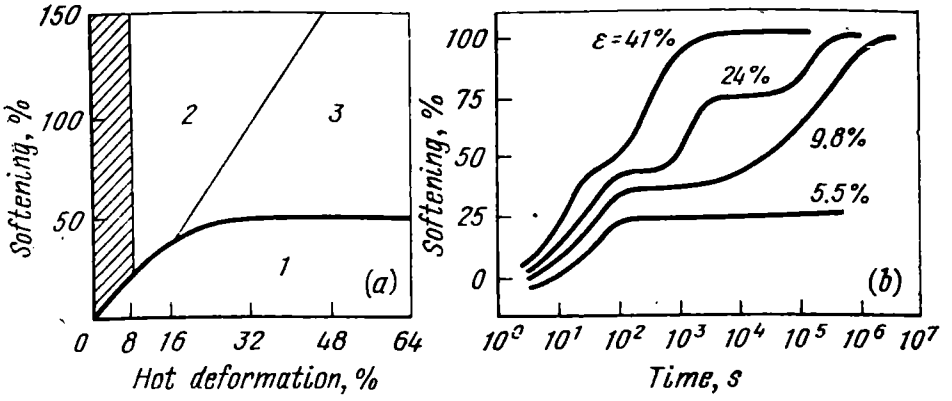

Fig. 207. Contributions of various processes to softening of hot-deformed austenite depending on

(*a*) amount of hot deformation (*1*—static recovery, *2*—static recrystallization; *3*—metadynamic recrystallization); (*b*) time of post-deformation isothermal annealing ($\varepsilon = 5.5\%$, static recovery; $\varepsilon = 9.8\%$, static recovery and static recrystallization; $\varepsilon = 24\%$, static recovery, metadynamic recrystallization and static recrystallization; $\varepsilon = 41\%$, static recovery, metadynamic recrystallization)

of a pause is chosen so that its end (i.e. the beginning of deformation in a next pass) corresponds to the completion of primary recrystallization after the previous pass. With such conditions of deformation, the grain size is refined successively from pass to pass and the mechanical properties of the metal are respectively improved.

For instance, steel Grade 45Г17Ю3 was hot-deformed at 1000°C in five passes, with the length of pauses between the passes being respectively 60, 10, 20, 10 and 10 s. The grain of original size 145 μm was refined respectively to 35, 18, 12, 9 and 7 μm. As may be seen from these data, the highest refinement of grain was obtained in primary recrystallization after the first pass. Later passes were less effective, though the absolute size of grains decreased continuously from pass to pass. In specimens with the original grain size of 35-25 μm, grains were refined after five passes to 3-4 μm. The yield limit of the metal increased from 230 MPa to 600 MPa.

2. Effect of Chemical and Phase Compositions

The effect of the chemical and phase compositions on recrystallization in hot deformation still has not been studied systematically.

The main relationships concerning the effect of additions on the temperature level of recrystallization in metals and alloys after cold deformation seem to be also true for hot deformation. The effect of additions on the stacking fault energy deserves special mentioning. With a decrease of the stacking fault energy, cross slip of dislocations is inhibited, so that dynamic recrystallization begins after a lower 'critical deformation' ε_{cr}.

The highest effect is produced by additions whose introduction results in supersaturation of the solid solution. In that case, recrystal-

lization can be influenced both by the decomposition occurring directly in the course of deformation and by that taking place during subsequent cooling. If the solution is supersaturated before deformation, its decomposition in the course of deformation will inhibit both recovery and recrystallization. Softening begins only in annealing and only at temperatures at which disperse phases can dissolve (at least partially) and coagulate. With deformation at temperatures corresponding to the single-phase state (when there is no supersaturation of the solid solution), the beginning of recrystallization is not delayed, but the development of recrystallization can be impeded by disperse particles which precipitate during cooling. In that case, it is essential how high the temperature of deformation is and especially how much does it exceed the temperature limit of solubility. With a higher difference, a greater degree of recrystallization will be achieved before decomposition begins. Besides, decomposition will be less complete, since the concentration of defects produced by deformation will be appreciably decreased to the moment of its initiation owing to recovery and recrystallization.

3. Recrystallization Diagrams in Hot Deformation

The recrystallized structure formed on hot deformation and the kinetics of the process are described by recrystallization diagrams which differ somewhat from the first-order diagrams (after cold deformation). Recrystallization diagrams of the second and third orders have become most popular. Second-order diagrams characterize the dependence of the average grain size $\bar{D}$ on the amount and temperature of hot deformation without subsequent annealing (Fig. 208).

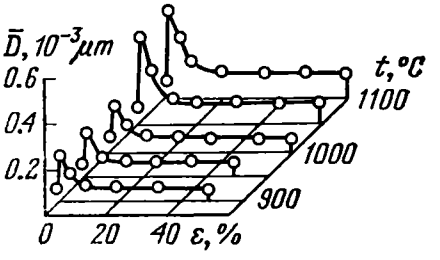

Fig. 208. Second-order recrystallization diagram for XH70BMTIO alloy press-forged and cooled in sand

Modern engineering widely employs various high alloys based on iron, nickel, molybdenum, titanium, aluminium, copper, etc. which are intended for use at high temperatures and stresses, in aggressive media, etc. The properties of such alloys depend substantially on their microstructure; the size of grains, the extent and type of inequigranularity, etc. Because of their low plasticity, these alloys are mostly deformed by hot plastic working. In order to form the desired structure, hot-deformed articles are subjected to the final heat treatment: heating for hardening, hardening and often age-hardening. The conditions of hot deformation can however influence substantially the type of the structure formed on heat treatment.

In such cases, third-order recrystallization diagrams, proposed by S.I. Gubkin, can be rather useful. Such a diagram gives the size

of grain not only after hot deformation, but also after the final heat-treatment procedure. The diagram presents two curves for each deformation temperature: one for the grain size immediately after the deformation (as in second-order diagrams) and the other for the grain size after the final heat treatment. An example of this diagram is shown in Fig. 209.

In order to obtain more information on the type of recrystallized structure from third-order recrystallization diagrams, some authors (D.I. Berezhkovsky et al.) have suggested special symbols which characterize the specific features of a structure (inequigranularity, texture, twins, etc.). It is recommended to inscribe these symbols not only at the upper curve, which characterizes the structure formed on heat treatment, but also at the lower curve which describes the structure immediately after hot deformation. Such a structure often consists partially of new recrystallized grains and partially of original grains (Fig. 201). Large original deformed grains are surrounded by fine new grains. The concentration of new grains is greater (and, accordingly, the concentration, or the area occupied by the rest of original grains, is smaller) after heavier deformations and at a slower rate of cooling. This is a kind of inequigranularity. In the case considered, however, grains differ from one another not only in size but also in the degree of perfection (dislocation density). Large original grains are deformed and disappear in subsequent heating. Fine, more perfect, new grains grow at the expense of larger ones; the picture is

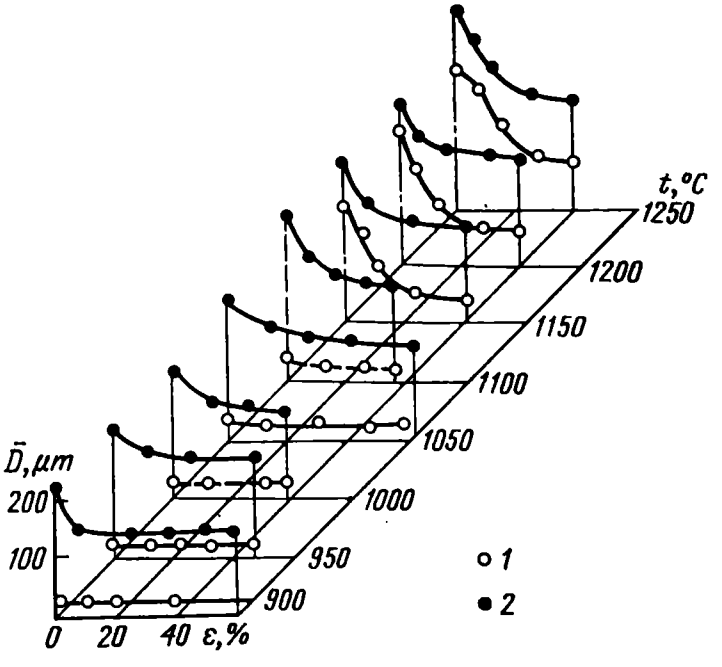

Fig. 209. Third-order recrystallization diagram of XH70BMTIO alloy
1—hot upsetting in press; *2*—hot upsetting in press and heating at 1200°C for 24 h and at 1050°C for 4 h

quite opposite to that observed during heating of a common inequigranular metal where large grains grow at the expense of finer ones. This can be illustrated by the data on variations in grain size distribution in austenitic and ferritic steels during continuous cooling with chilling before hardening (see Fig. 203).

Austenitic steel type X18H8 had a large number of grains of index 1 and 2 in the original state (prior to deformation). After plastic working at 1100°C and chilling for 1.5 s before hardening, all grains of index 1 disappeared, but a small number of grains of index 2-4 were detected on the background of fine grains. After the same amount of deformation and 15 s of chilling, the structure got refined, with index 6 grains being the largest. After chilling for 500 s, grains of index 5 and 4 appeared again. Therefore, large grains of index 3 and 4 in the metal chilled for 1.5 s were actually deformed grains which disappeared after a longer action of the high temperature.

It is then clear that the properties of these strain-hardened grains differ appreciably from those of recrystallized ones. For that reason, it is practically important that a third-order recrystallization diagram should indicate the nature of grains (deformed, recrystallized or both) which constitute the structure. Data on the presence or absence of textures, etc. would also be of much importance.

A probable system of symbols recommended for designation of various structures in recrystallization diagrams and a diagram constructed with the use of these symbols are given in Fig. 210.

Third-order recrystallization diagrams of some high-temperature nickel- and iron-base alloys are characterized by the appearance of two peaks of grain size. One of them is associated with recrystallization after the critical deformation and the other (on deformations of 20-40 per cent), with secondary recrystallization caused by the stabilization of most grains by disperse particles.

Apart from second- and third-order recrystallization diagrams, various kinetic diagrams of recrystallization can also be useful for characteristic of recrystallization in hot deformation. Such diagrams include the earlier discussed generalized diagrams of structural states which give the structural characteristics of a metal as a function of the rate and temperature of deformation and subsequent heat treatment.

An example of such a diagram for an aluminium alloy is illustrated in Fig. 206*b*. The conditions of deformation and heating corresponding to region *UR* are such that an unrecrystallized structure is retained in the metal. The softening effect in this region, which is characterized by a low deformation rate, is limited to polygonization. In many critical cases, these are the most favourable conditions. The region P_{dyn} corresponds to a structure recrystallized directly during the time of deformation and subsequent cooling (i.e. without subsequent heating) and region P_{st}, to a structure

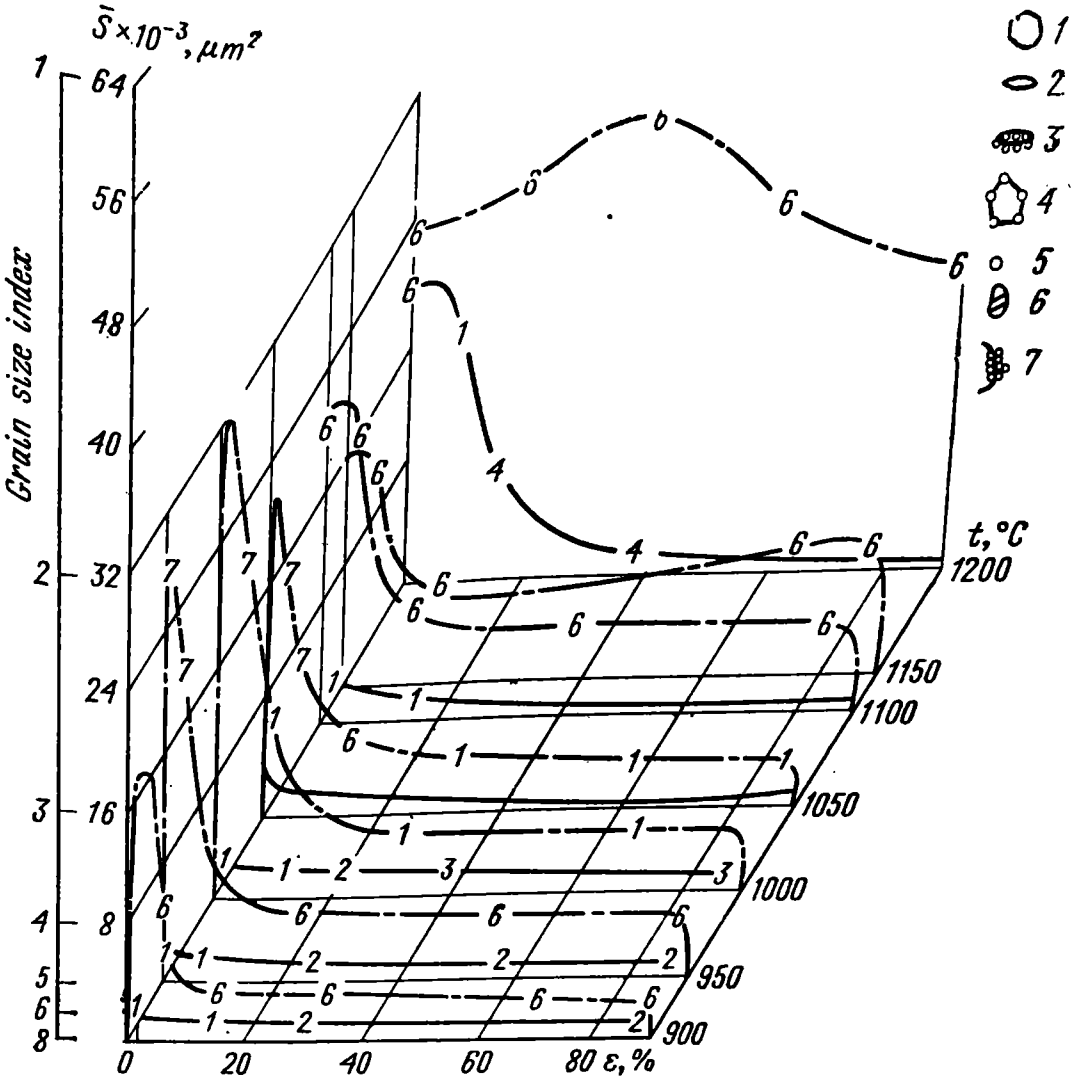

Fig. 210. Third-order recrystallization diagram characterizing the structure
1—equi-axed uniform grains; *2*—inequi-axed uniform grains; *3*—stretched old grains and new individual grains on their boundaries—beginning of primary recrystallization; *4*—equi-axed old grains and new fine individual grains on their boundaries, occupying 5% of the area (inequigranularity—beginning of primary recrystallization); *5*—new equi-axed grains occupy 100% of the area—beginning of grain growth; *6*—twins in most grains; *7*—inequi-granularity. Solid curves—after upsetting; dot-and-dash curves—after upsetting and heat treatment

recrystallized in the course of subsequent heat treatment. Region *Mx* is the region of partially recrystallized structure, i.e. the one having the most unfavourable properties.

The original state of the metal (prior to deformation) can have a noticeable effect on the stability of the structure formed on hot deformation and accordingly on the shape of the generalized diagram of structural states. If specimens whose structure has retained traces of earlier deformation are subjected to hot deformation, the region in which recrystallization can take place in subsequent annealing becomes appreciably wider and the temperature of recrystallization lowers.

A kind of kinetic recrystallization diagrams is a diagram giving fractions of recrystallized volume as a function of the temperature of deformation and the time of isothermal holding at that temperature.

RECOMMENDED LITERATURE

1. Bernstein M. L., *Structure of Deformed Metals.* Moscow, Metallurgiya, 1977 (in Russian).
2. Gorelik S. S., *Recrystallization in Metals and Alloys.* Moscow, Mir Publishers, 1981.

9 Recrystallization with Non-uniform Deformation and Inhomogeneous Phase Composition

1. Principal Types of Structural Inhomogeneity

The most common type of structural imperfection in deformed and heat-treated elements, especially in those of intricate shape and made of complex-composition alloys, is inhomogeneity of the granular structure over the volume of an element. This inhomogeneity may be very diverse in its topography (position in the element and size of portions of a different structure), nature and origin. The most common type of structural inhomogeneity is inequigranular structure, i.e. a large difference in the size of grains, which is far beyond the normal grain size distribution.

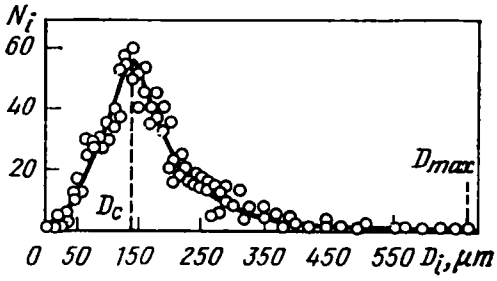

Fig. 211. Grain size distribution curve $N_i = f(D_i)$ for inequigranular structures

In practice of plastic working and heat treatment of many complex alloys (such as nickel- or iron-base high temperature alloys, aluminium alloys, etc.), cases are often when anomalously large grains form in the structure, exceeding tens or hundreds of times the size of original grains, i.e. much greater than recrystallized grains formed after critical deformation. This enlargement in grain size is sometimes called grain coarsening and the structure that results is termed coarse-grained.

Inequigranularity can be estimated quantitatively using certain characteristics which are determined by statistical metallography. Making a large number of measurements, it is possible to calculate the number of grains of a particular size, N_i, and construct a curve of grain size distribution $N_i = f(D_i)$ (Fig. 211). Using this curve, we can determine the size D_c of the most common grains (the maximum of the curve) and the largest size D_{max} which corresponds to the rightmost portion of the curve. The average grain size is found as $\bar{D} = (\Sigma D_i N_i)/N$, where N is the total number of measured grains of all sizes.

The curves of grain size distribution plotted from the results of measurements on plane microsections do not resemble in shape the curves of normal grain size distribution even if the structure is homogeneous. They are always asymmetric and stretched in the region of larger grain sizes and become symmetrical only when plotted in semilogarithmic coordinates. This is why the values of $\overline{D}$ and D_c never coincide. The percentage of grains whose size differs from the average is found by the formula

$$\frac{\Delta D}{\overline{D}} = \frac{\sum\limits_{R} (\overline{D} - D_i) N_i}{\overline{D}N} 100\%$$

where R is the total number of groups of grain sizes.

For homogeneous (equigranular) structures, $\Delta D/\overline{D} = 30\text{-}35$ per cent. A higher ratio is indicative of inequigranularity. This characteristic, however, gives no notion of the maximum deviation from the size D_c that is most probable statistically. For this purpose, use may be made of another characteristic, D_{max}/D_c, which determines the degree of asymmetricity of the grain size distribution curve. For structures composed of grains of equal size, the D_{max}/D_c ratio is equal to 2.5-3. For inequigranular structures it is greater than 3 and may reach 9-10 or more.

Thus, using these two characteristics, which complement each other, it is possible to estimate inequigranularity quantitatively.

Inequigranularity can be represented more clearly if, instead of grain size distribution curves $N_i = f(D_i)$, we construct curves of distribution of areas occupied in a microsection by grains of a particular size range as a function of grain size, i.e. $S_i = f(D_i)$ or $\sqrt{S_i} = f(D_i)$. For inequigranular structures it is typical that the $S_i = f(D_i)$ relationship is described by a curve with two maxima (or by two curves) separated by a wide interval (see Fig. 180*b*). This interval is wider at a higher degree of inequigranularity. The ratio of the areas under the two curves characterizes the relative area occupied by large grains and the ratio D_{max2}/D_{c1} characterizes the maximum difference between the size of the largest grains and that of the main quantity of fine grains.

When choosing an area in a microsection to calculate the number of grains and determine their sizes to plot $S_i = f(D_i)$, one should consider the topographic nature of inequigranularity in each particular case. If the region of anomalously large grains is located in certain macroportions of a metal part, say, at its periphery, as illustrated in Fig. 212, inequigranularity is of the zonal type. Typical examples of zonal inequigranularity are coarse-grained peripheral zones appearing during heating for hardening in pressed articles made from some popular aluminium alloys (Fig. 212*a*), in hot-

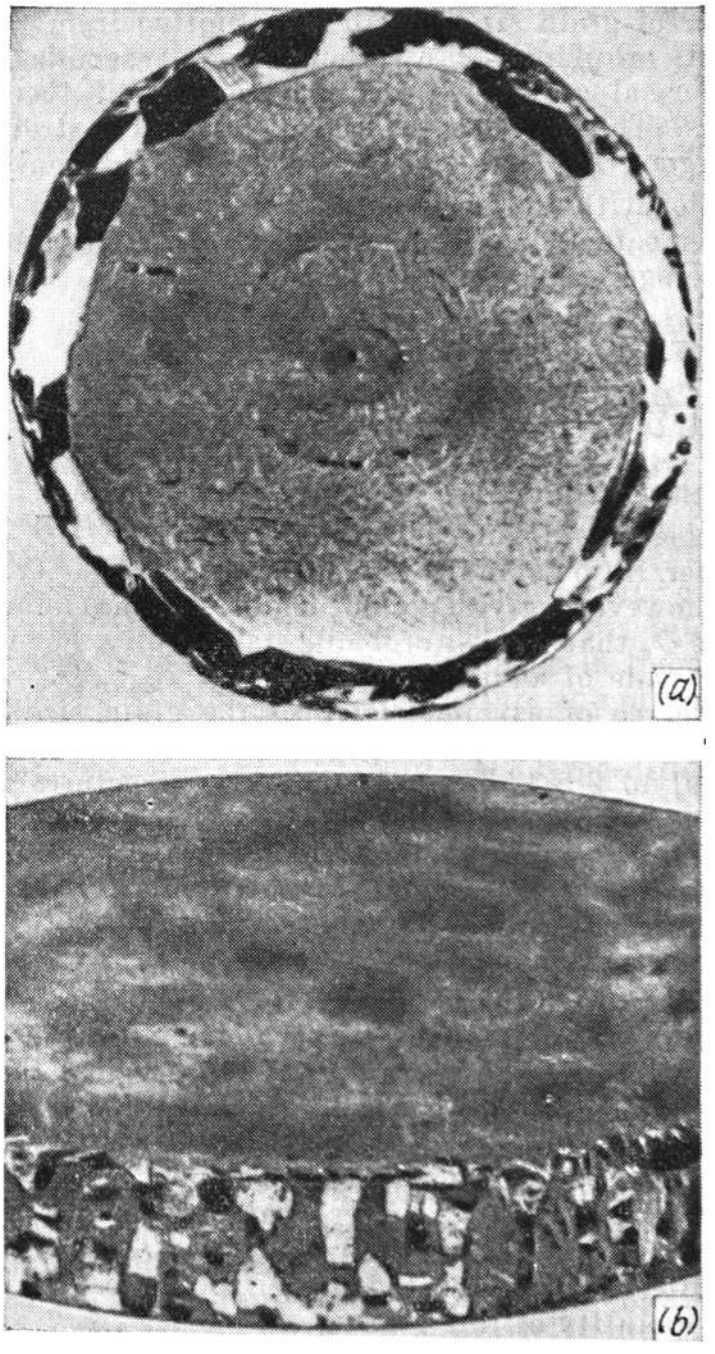

Fig. 212. Zonal inequigranularity formed in hot-deformed metal during heating for hardening
(*a*) pressed aluminium alloy (large-crystalline rim'); (*b*) carbon steel

deformed carbon steel pieces (Fig. 212*b*), etc. Zonal inequigranularity is also found in intricate-shape articles made of high-temperature alloys.

If anomalous grains are located in narrow bands alternating with fine-grain bands, this is the case of lineage inequigranularity. A typ-

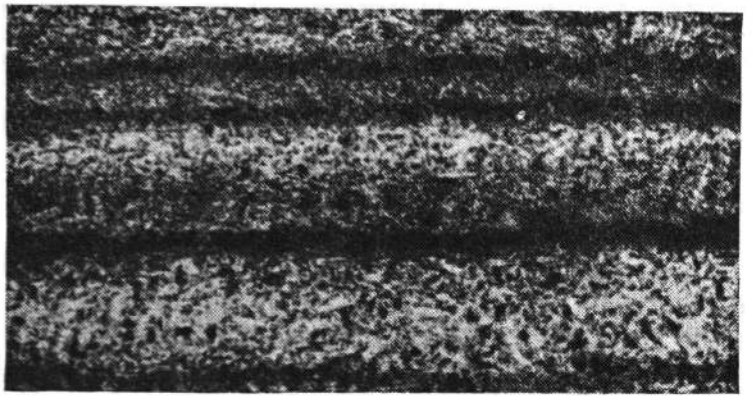

Fig. 213. Lineage (striated) microstructure in steel ШХ15 formed after rolling and heating

ical example is the lineage microstructure in steel ШХ15 after rolling and heat treatment (Fig. 213). If individual large grains or their small groups are distributed randomly over the whole volume of a piece, inequigranularity is of the islet type. A typical example is illustrated in Fig. 214.

Inequigranularity and coarsening of the structure have usually an adverse effect on the properties of the metal and often involve

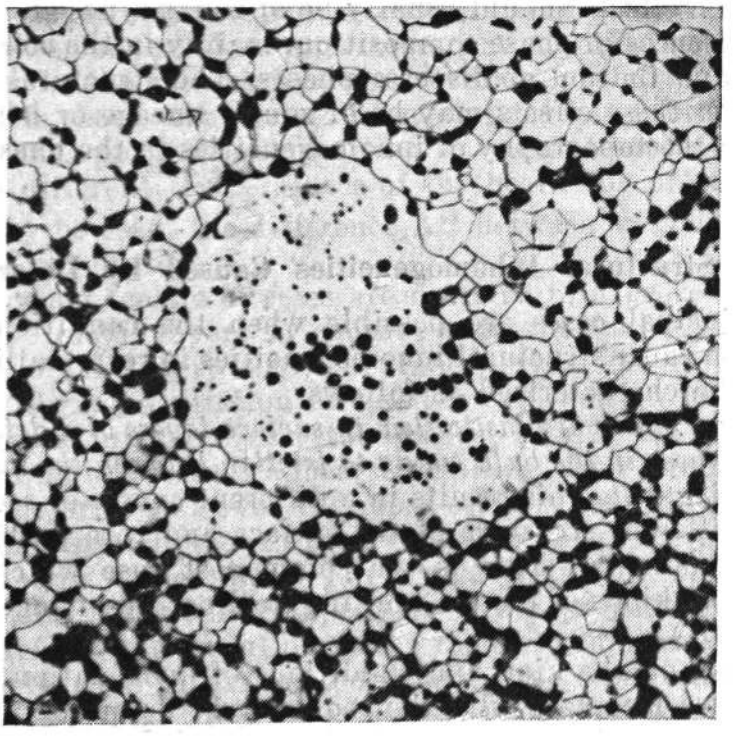

Fig. 214. Islet inequigranularity in Mn-Zn ferrite after pressing and recrystallization, 300×

large economic losses. Structure coarsening is especially dangerous in final articles made of alloys undergoing no phase transformations, since it cannot be amended. Coarse-grained portions, which usually have a negative effect on most properties, must often be removed by machining, which necessitates larger allowances in the dimensions of articles. Some articles can be spoiled entirely by lineage or islet inequigranularity.

Other kinds of structural inhomogeneity can also be encountered in practice. They may be associated with the formation of different textures in the volume of an article, with the appearance of recrystallized and unrecrystallized portions, etc. These kinds of inequigranularity can also be of zonal, lineage or islet type depending on their topography. The above-mentioned kinds of inhomogeneity can be caused by various reasons which can be divided into two large groups.

(1) Different conditions of deformation in various macrovolumes of an article and, as a consequence, different structure in as-deformed state. Under such conditions, recrystallization after deformation may occur in various macrovolumes by different mechanisms and, if the heat treatment conditions are the same for the whole article, will be stopped at various stages: from polygonization to well developed secondary recrystallization. The same group of causes can be responsible for textural inhomogeneity over the cross section and volume of articles. It is evident that the structural inhomogeneity due to these effects should usually be of zonal type.

(2) Differences in phase composition, mainly in the concentration, type and distribution of disperse phases. The structural inhomogeneity due to these effects may be of zonal, lineage or islet type depending on the topography of inhomogeneities in the phase composition.

2. Structural Inhomogeneities Caused by Deformation

Six principal cases are possible when the conditions of prior deformation cause structural inhomogeneities in recrystallized metal. They can be characterized as follows.

1. *The conditions of plastic flow in surface layers of a deformed piece differ from those in the bulk owing to friction between the metal surface and deforming tool.* This results in a different course of recrystallization and different structure of the surface and core portions of the recrystallized metal. This is the commonest case which can take place in most kinds of plastic working (rolling, upsetting, extrusion, drawing, etc.).

Depending on the kind and conditions of deformation, the metal layers in direct contact with the tool may be deformed more or less appreciably than the deeper layers. In cases when the external forces are normal to the direction of flow, i.e. when compressive forces are decisive in the process (such as in upsetting), the metal layers in

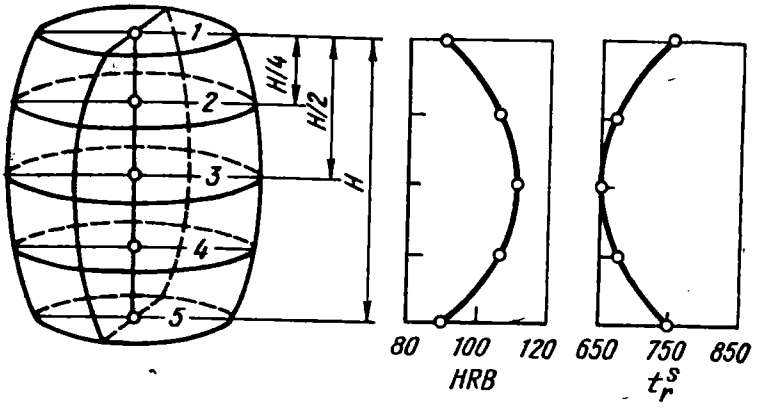

Fig. 215. Distribution of hardness (*HRB*) and t_r^s over the cross section of an upset cylindrical specimen of Ni + 13% Cr alloy, $\bar{\varepsilon} = 40\%$
1-5—sections, in which hardness was measured in the centre

contact with the tool are deformed less appreciably than the inner ones. Friction forces prevent metal flow in the layers at the end faces of the piece being deformed by upsetting. As a result, for a given average deformation $\bar{\varepsilon}$, the actual deformations vary along the height of the piece from $\varepsilon_{sur} < \varepsilon_{av}$ to $\varepsilon_{cor} > \varepsilon_{av}$. Since the degree of work hardening is different along the height of the piece, it is clear that its structure upon recrystallization annealing will be different in various sections and correspond to different amounts of deformation in the recrystallization diagram.

Figure 215 shows the distribution of hardness (work-hardening) in a Nichrome piece after upsetting at room temperature, which resulted in different temperatures of the beginning of recrystallization. As may be seen, the difference Δt_r^s between various sections is as high as 100 degrees C.

In cases when tensile stresses are decisive in a process of plastic working, the metal layers in contact with the tool turn out to be deformed more strongly than the inner layers (as in drawing or extrusion). Owing to friction forces, the deformation in the surface layers is more intensive and the plastic flow is more turbulent.

A more complex picture appears in rolling. The difference in the amount of deformation over the cross section depends on the ratio of the contact arc length l to the average height of the cross section h_{av} of the strip being rolled. For a relatively thin strip ($l/h_{av} \geqslant \geqslant 0.5\text{-}1.0$), i.e. when the compressive strain propagates fully over the whole height, the variation in the relative deformation ($\ln h_0/h_f$) of volume elements in various portions of the cross section is such as that shown in Fig. 216*b*. As may be seen, internal volumes of the strip are deformed (drawn) more intensively than those in contact with the rolls. For strips of an appreciable thickness ($l/h_{av} < 0.5\text{-}1.0$), deformation is more non-uniform over the cross section and can even

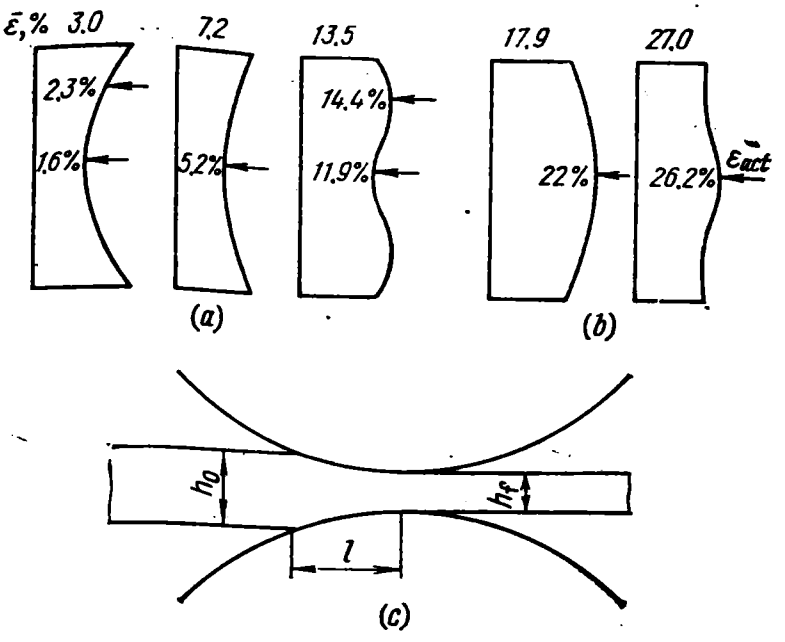

Fig. 216. Non-uniform deformation over the cross section of rolled strip (*a*) $(l/h_{av}) > (0.5\text{-}1.0)$; (*b*) $(l/h_{av}) \leqslant (0.5\text{-}1)$; (*c*) l is the length of contact arc; h_{av} —average thickness of strip $(h_0 - h_f)/h_0$. Numbers at (*a*) and (*b*) are actual amounts of deformation in a given section

change sign. For instance, in Grade Д16 aluminium slabs deformed slightly or moderately (reduction within 2.8-16.9 per cent), the l/h_{av} ratio was equal to 0.3-0.92 and inner layers were deformed less than outer ones (Fig. 216*a*). On heavy deformations (above 20 per cent), the l/h_{av} ratio changed to 1-1.25 and inner layers were deformed more strongly (Fig. 216*b*).

Figure 217 presents data on the distribution of various deformation textures over the cross section of a transformer steel blank. The main method for preventing or diminishing structural inhomogeneity due to friction forces acting between the metal being deformed and the deforming tool is naturally to reduce these forces; this can be achieved by using various lubricants.

2. *The conditions of plastic flow in surface layers of an article differ from those in the bulk owing to cooling of the surface by the tool.* Such conditions are realized in deformation of metal heated to a high temperature (hot deformation) by a tool that is cold or heated only to a lower temperature.

In that case, the temperature in the surface layers will be lower than that in the bulk, so that the processes of dynamic softening (recovery, polygonization, recrystallization) will be realized to a lesser extent or will not be realized at all. The deformation in the surface layers will be of an intermediate type between hot and cold deformation. These layers will have a higher degree of work hardening and a higher dislocation density. This can be illustrated by the data

on inhomogeneous recrystallization over the thickness of a specimen of steel X18H8 immediately after hot deformation by rolling at 1100°C without subsequent heating. The structure of the specimen was fully recrystallized in the core (at a depth of 7 mm from the surface) and fully unrecrystallized in the surface (to a depth of 2 mm). At a depth of 3 to 5 mm, the structure was partially recrystallized and extremely inhomogeneous. In this intermediate layer, the concentration of recrystallized grains increased respectively from 20 per cent to 100 per cent with increasing distance from the surface.

In hot deformation at low rates, the process of softening in middle layers may reduce to dynamic polygonization, while the work-hardening effect in the surface layers may play a double part. On the one hand, the work-hardening effect may turn out to be so high that early stages of dynamic recrystallization will occur in the layer. On the other, it may be retained after deformation and ensure conditions for static recrystallization in subsequent heating.

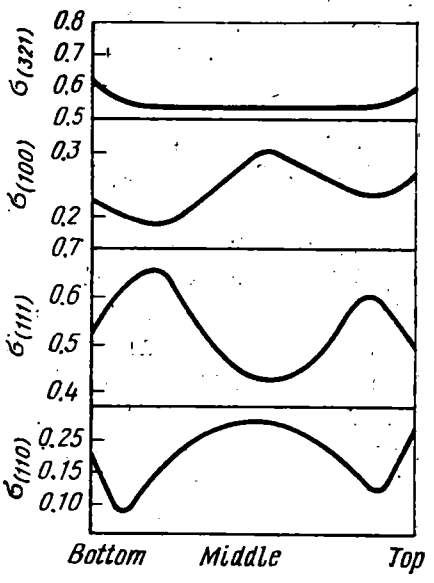

Fig. 217. Relative distribution of various components of deformation texture over the cross section of rolled transformer steel strip

The thickness of the near-surface layer X_{max} in which the cooling effect of the tool is sensible is called in the literature by a not very appropriate term the hardening zone. With certain assumptions, the thickness of the layer X_{max} can be found theoretically. V.I. Shilov and M.I. Sirotin have obtained the following relationship for the case of hot rolling:

$$X_{max} = 2.87 \frac{2c\sqrt{a_1\tau}}{\exp \delta_{max}}$$

where $c = \sqrt{(\exp \delta_{max} - 1)/\exp \delta_{max}}$; $\delta = \ln (h_0/h_1)$ is the maximum relative deformation (reduction) of the strip (h_0 and h_1 is its height before and after rolling in a pass, respectively); a_1 is the thermal diffusivity of the metal, which depends on its thermophysical properties and temperature; and τ is the time of contact between the metal and the roll (the time during which the roll moves through a path equal to the length of the deformation zone). Nomograms for determining X_{max} in hot rolling of steel 40 are illustrated in Fig. 218.

Heating after deformation can only in rare cases diminish such a high inhomogeneity of the structure across the thickness of the metal; in most cases inhomogeneity is enhanced. During heating, static primary recrystallization will take place in the surface layers

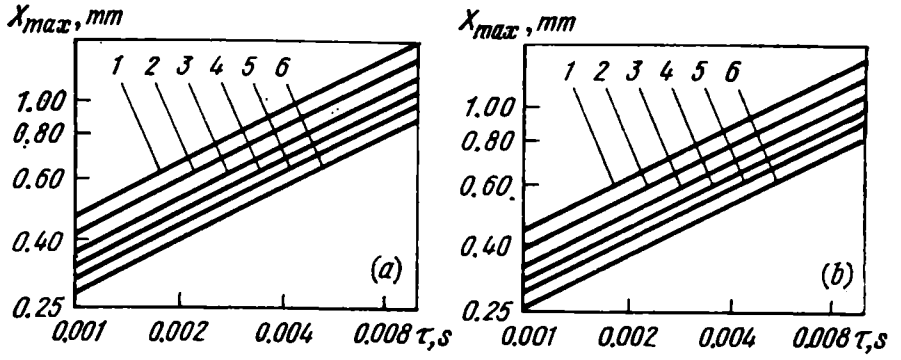

Fig. 218. Nomograms for determining the depth of cooled near-surface layer ('hardening zone' X_{max}) in hot rolled strip of steel 40
The initial temperature of the metal was 1200°C (*a*) and 900°C (*b*). The coefficient of reduction per pass, h_0/h_1, was: *1*—1.01; *2*—1.20; *3*—1.40; *4*—1.60; *5*—1.80; *6*—2.00

and growth of grains formed by dynamic recrystallization will occur in the inner layers.

The situation is much more complicated if the temperature of heating of the metal before deformation corresponds to the state of single-phase solid solution and the temperature of the cooled layer, to the two-phase state. In that case, deformation in the cooled surface layer will be accompanied with decomposition of the supersaturated solid solution and precipitation of particles of excess disperse phases. Under such conditions, recrystallization in as-deformed metal can produce a rather inhomogeneous microstructure, depending on the nature of precipitate particles and the rate of their reverse dissolution at the heating temperature and on how non-uniform is the decomposition over the volume of the article. If the decomposition has been intensive and the rate of dissolution is not high, the conditions of heating in the outer layers, which were cooled in deformation, may be favourable for growth of a small number of primary and secondary recrystallization nuclei, whereas the main quantity of grains will be stabilized for a while by disperse precipitate particles. An example of an inhomogeneous structure formed in this manner is a coarse-grained 'rim' which often appears in hot-pressed aluminium alloys and steels upon heating for hardening (see Fig. 212).

3. *The conditions of plastic flow in the bulk and in the surface layers are different due to friction heating in the surface.* This is essentially an opposite case to that discussed above. Such conditions most often appear in cold plastic working of hard-to-deform alloys. The temperature difference between the outer and inner layers may be as high as 100-200 degrees C and may cause various effects depending on the nature of an alloy. A higher temperature in the surface may favour the processes of dynamic recovery and even recrystallization in that zone or may form conditions which facilitate strain ageing.

These inhomogeneities in the state of the metal immediately after

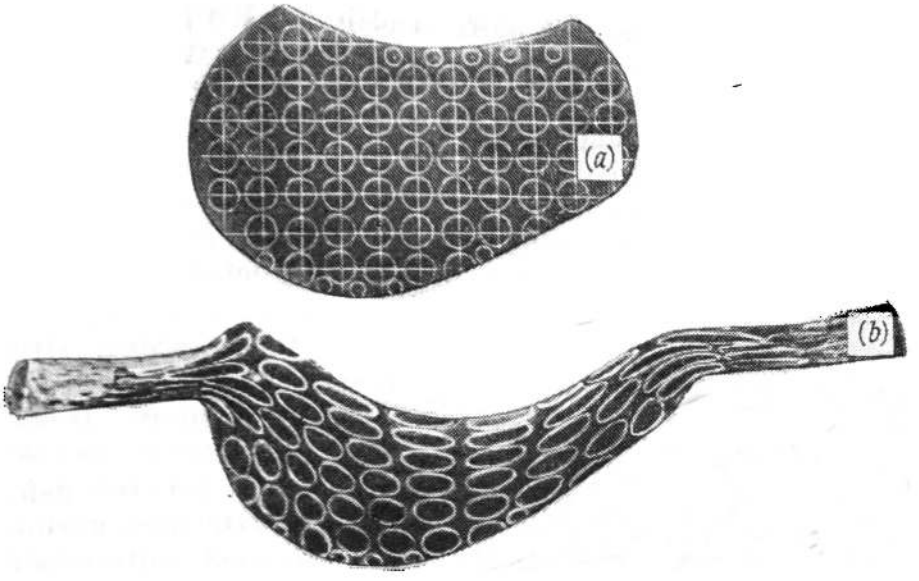

Fig. 219. Determination of actual deformations in a section of gas-turbine blade by means of coordinate grids
(*a*) original state; (*b*) $e_{av} = 38\%$

deformation can also influence the conditions of structure formation in subsequent annealing. At a higher temperature of heating before deformation, the additional heating of the surface layers becomes less noticeable and the temperature difference over the cross section diminishes.

4. *The conditions of plastic flow in various macrovolumes of the metal are sharply different owing to an intricate shape of the article.* In that case, the amount of deformation in the article is essentially non-uniform and may often vary from the critical or even lower deformation to the highest deformation possible in the given material.

For simulation of the process of plastic flow of metal in intricate-shape articles and determination of actual deformations in various macrovolumes, use is often made of the method of deformation of specimens made of lead (or any other plastic material) with coordinate grids applied on their end faces (Fig. 219). By examining shape variations of cells of the grid, it is then possible to determine the actual amount of deformation in a particular volume of the specimen.

Such conditions of deformation appear, for instance, in stamped blades of gas turbines, which have an intricate profile in cross section. The microstructure of such a blade, made of alloy Grade ХН65КМВЮБ, is illustrated in Fig. 220. A specific characteristic of this alloy is that cooling after hot deformation causes its decomposition with precipitation of a large amount of γ'-phase which is isomorphous with the matrix. Decomposition may occur in a different manner in unrecrystallized and recrystallized grains. In the former, it has a coherent nature and causes strong structural strain harden-

ing. These grains are etched more readily by Krupp's reagent and appear dark after etching. In recrystallized grains, the decomposition is incoherent, the phase is coagulated and the structural strain hardening is much weaker. Such grains are etched less strongly and appear bright. Such a peculiarity of the alloy makes it possible to reveal readily the structural inhomogeneity in various volumes of a blade which has been caused by non-uniform deformation. It is clear that the volumes which could recrystallize during deformation had been deformed more appreciably than those whose structure remained unrecrystallized.

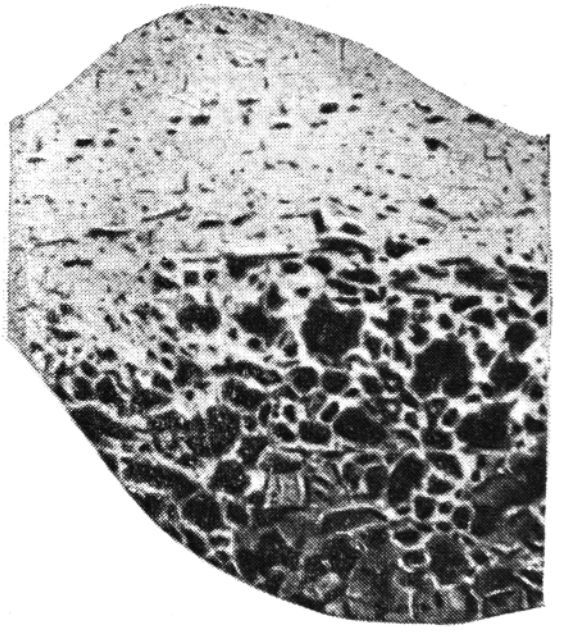

Fig. 220. Microstructure in a section of a stamped gas-turbine blade on hot deformation: etching has revealed recrystallized (bright) and unrecrystallized (dark) regions

The etching technique, which makes it possible to distinguish between deformed and recrystallized grains, can also be used quite effectively for studying the kinetics of recrystallization in hot deformation of other age-hardening alloys, if the conditions of etching and heat treatment are selected properly.

Figure 220 shows the microstructure in a section of a gas-turbine blade immediately after hot deformation. As may be seen, the structure has a high macro- and micro-inhomogeneity. There are macro-regions with fully recrystallized structure and others in which recrystallization even has not started. These extreme regions are separated by a region of partially recrystallized structure in which inhomogeneity is of the islet type. It should be clear that such a structure is rather unstable. In subsequent recrystallization annealing, recrystallization in various macro- and micro-regions will occur extremely non-uniformly and at a different rate. The existing inhomogeneity will be enhanced more due to the different state and distribution of second phase particles. The combination of these circumstances may lead to local growth of anomalously large grains in the range of light ('critical') and moderate (the second maximum) deformations.

Inhomogeneity of the structure in intricate-shape articles manufactured by hot plastic working can be diminished appreciably by lowering the rate of deformation. Another method for reducing this type of inhomogeneity is to change the shape of the work-piece

so as to minimize the gradient of deformation in various sections. An example is illustrated in Fig. 221.

5. *Deformation is strongly localized and its amount and rate can hardly be controlled.* This case includes the deformation in flash trimming, cutting-out, local bending, etc. Heating after such a deformation can result in the formation of local regions of either fine grain (if the local deformation was heavy) or coarse grain (if the deformation was nearly critical).

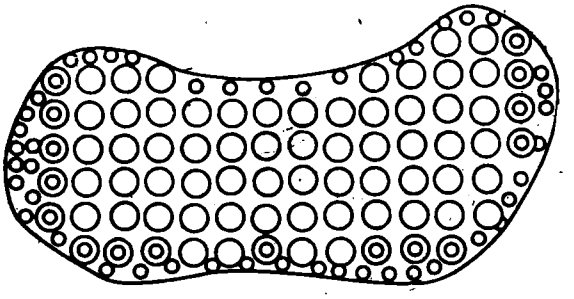

Fig. 221. A reasonable shape of a blank for stamping gas-turbine blades in which deformation gradient in various sections is minimized

6. *The rate of cooling of deformed metal is such that recrystallization can occur only partially and non-uniformly over the volume of the metal piece.*

In high-temperature deformation, recrystallization proceeds at a very high rate both in the course of deformation proper and in subsequent holding at the deformation temperature or even during cooling. In this process, noticeable structural changes can take place in a few seconds or sometimes in a few fractions of a second. This can be supported by Fig. 203 which gives the recrystallization diagrams for austenitic and ferritic steels after deformation and subsequent cooling without chilling or with chilling for a different time, beginning with rather short. By analysing recrystallization diagrams, one can predict the probable type of inhomogeneity in the structure depending on the actual conditions of deformation and cooling.

3. Structural Inhomogeneities Caused by Inhomogeneities in Phase Composition

Structural inhomogeneity can often appear due to an inhomogeneous phase composition, in the first place, due to the presence of disperse phase particles. It should be emphasized that phase composition, rather than chemical composition, is essential here. Inhomogeneous chemical composition cannot by itself cause a strong structural inhomogeneity if it does not result in phase inhomogeneity (due to decomposition of a supersaturated solid solution, etc.).

Let us consider the most important and frequent cases when phase inhomogeneity may be decisive.

A. Individual large particles of secondary phases or their colonies vary the conditions of plastic deformation and subsequent recrystallization in volumes of the matrix adjacent to these particles (or colonies).

The plastic flow in the matrix regions near disperse particles is of a more turbulent nature. In these regions, the deflection of the crystal lattice is more appreciable (due to an excess of like dislocations). The result is that recrystallization nuclei form in these regions at earlier stages of subsequent heating than in other volumes of the material (see Fig. 181*c*). This effect is stronger when inclusion particles and their boundaries have a less regular shape and a higher hardness. The subsequent behaviour of these nuclei, which have appeared earlier than others, depends on a number of factors, in the first place on how large is the difference between the thermal expansion of inclusions and matrix. If this difference is high, recrystallization nuclei will be work-hardened and their volume energy turns out to be larger than that of nuclei formed at a distance from inclusions; the latter will then 'consume' the former in the course of growth. If the difference is low, recrystallization nuclei formed at inclusions will survive and grow quicker than other nuclei. Preferable nucleation at inclusions results in dissipation and, under appropriate conditions, even in elimination of recrystallization textures.

B. Before cold plastic working, an alloy contains unevenly distributed disperse phase particles whose solubility can increase with temperature and the post-deformation annealing is carried out at a temperature corresponding to a relatively slow dissolution of these particles.

On heating to a temperature below the temperature of the beginning of dissolution of disperse phases, the microstructure of alloys containing disperse phases has a finer grain size. As the temperature is raised, however, and disperse phases begin to be dissolved, the rate of grain growth in less pure alloys becomes very high, much greater than in alloys containing no disperse phases. In this process, the growth of grains, especially at the initial stage, usually occurs very non-uniformly and leads to islet inequigranularity. This increase in inequigranularity always takes place before the total intensive growth of grains, except for the case when disperse phases are dissolved at a higher rate. This is why inequigranularity in alloys containing disperse phases tends to decrease as soon as the temperature of annealing becomes higher than that of the beginning of dissolutions of these phases. Qualitatively, the effect of temperature of heating on inequigranularity in alloys containing disperse phases can be illustrated by curves of the type shown in Fig. 222.

The most suitable conditions for the formation of an inequigranular or even coarsened structure are formed in cases when the above-discussed process of growth of grains with slow dissolution of disperse particles takes place after the critical amount of deformation.

Figure 193*e* and *f* gives recrystallization diagrams for two steels, X18H14M2 and X18H14M2Б1, the latter being characterized by an elevated concentration of disperse phase particles: NbC carbide

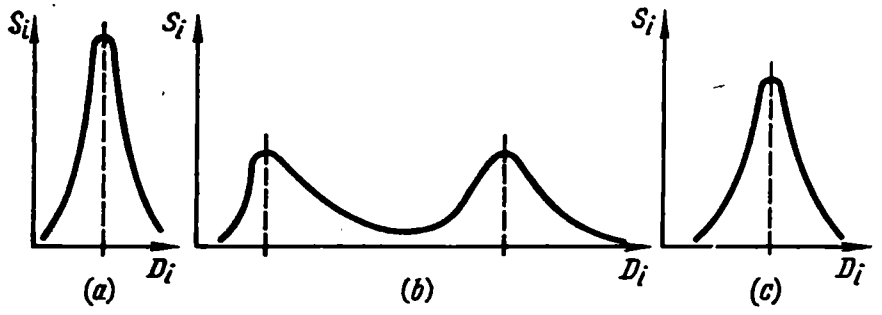

Fig. 222. Grain size distribution at various temperatures in an alloy containing disperse phase particles
(*a*) before dissolution of disperse phase particles; (*b*) partial dissolution; (*c*) much above the dissolution temperature; S_i – area occupied by grains of the *i*th size index; D_i – diameter of the *i*th size index grains

and Fe_3Nb_2 intermetallic compound. Both diagrams have a maximum of grain size in recrystallization after the critical amount of deformation, but the maximal grain size turns out to be many times greater in steel X18H14M2Б1 (containing disperse phases). The presence of disperse phases and their dissolution can also provoke structure coarsening on moderate deformations.

C. Before hot plastic working, an alloy was in a state of supersaturated solid solution and the deformation was accompanied with macro- and microscopically non-uniform precipitation of excess phases which were dissolved slowly and unevenly in subsequent recrystallization annealing.

This case differs from the previous one in that the metal contained no precipitates of a secondary phase (or phases) and these appeared in the course of deformation and/or subsequent cooling. The conditions and uniformity of deformation will here determine the uniformity of decomposition, the concentration and stability of disperse particles and thus the rate and uniformity of their dissolution.

As has been established, there is a certain correlation between the tendency to inequigranularity (selective growth of individual grains), on the one hand, and the average size of grains in the matrix at the end of primary recrystallization and the concentration of disperse phase particles, on the other. With a larger size of matrix grains at the end of primary recrystallization, the total surface of their boundaries is smaller and the density of disperse particles at grain boundaries is higher, and therefore, the retarding effect of these phases on grain boundary migration is stronger.

As dissolution of disperse phases begins, this effect is weakened, especially at higher temperatures of annealing. This forms favourable conditions for growth of grains. The driving force for grain coarsening, however, diminishes with an increase in their size, and therefore, with an increase in temperature. Thus, at a certain temperature for a given alloy, there should exist a critical size of matrix grains at which the driving force is counterbalanced by the retarding force.

With the beginning of dissolution of unevenly distributed disperse phases in local portions of boundaries, the retarding effect turns out to be smaller than the driving force, which will result in growth of individual grains, i.e. in the beginning of secondary recrystallization.

Under practical conditions, if we manage to avoid the formation of the critical grain size at the end of primary recrystallization (by referring to the recrystallization diagram), we can be sure that there will be no coarse inequigranularity in the metal. In particular, since the height of the second maximum reduces sharply with a decrease in the temperature and time of annealing, this method can be advised for diminishing inequigranularity in all cases when it is admissible by the process technology.

D. The phase composition and accordingly the nature of structural changes in plastic working and subsequent heating are substantially different in the surface layers and the core of articles, owing to the interaction of the surface of the metal with the atmosphere.

A typical and common example is the formation of a decarburized zone in surface layers of carbon steel articles upon heating in an oxidizing medium. Decarburization results in a sharp reduction of the concentration of carbide particles (cementite) which play the part of barriers to growth of grains in heating. Thus macro-inequigranularity appears in an article after deformation and heating: the decarburized surface zone has an appreciably coarser grain than the core metal. In other cases, a gaseous atmosphere may, on the contrary, enrich the outer layers with disperse phase particles and the surface layers will have finer grain than the core.

RECOMMENDED LITERATURE

1. Gorelik S. S., *Recrystallization in Metals and Alloys.* Moscow, Mir Publishers, 1981.
2. Shilov V. I., Sirotin M. I., *Proceedings of the Institute ol Metallurgy, Urals Division of the USSR Academy of Sciences*, No. 23, Sverdlovsk, 1971 (in Russian).
3. Tselikov A. I., *The Theory of Analysis of Forces in Rolling Mills.* Moscow, Metallurgizdat, 1962 (in Russian).
4. Zavyalov A. S., *Principal Factors Affecting the Temperature of Softening and Recrystallization in Iron Alloys.* Leningrad, LDNTP, 1974 (in Russian).

10 Recrystallization Textures

If a deformed material with a deformation texture is annealed, a recrystallization, or annealing, texture usually forms in it, which is either identical to or differs regularly from the original deformation texture. Recrystallization textures have a high practical significance since they cause anisotropy of the physical and mechanical properties. Examples of positive and negative effects of textures on the metal properties have been considered in Ch. 5.

The type of recrystallization texture is influenced by a larger number of factors than the type of deformation texture. The latter is formed in the course of shear deformation under the action of oriented external forces. The conditions and the type of deformation, the operative slip systems, and the behaviour of dislocations in the given material have a pronounced effect on deformation textures.

The formation of recrystallization textures takes place in heating and is associated with structural changes whose direction is determined by the tendency of the system to lower its energy and by certain internal driving forces of the process which may be rather inhomogeneous locally. It is realized through the thermally activated processes of the formation of primary recrystallization nuclei and their growth at the expense of the deformed matrix and other nuclei.

Dislocation slip is operative only at the earliest stage of nucleation. The further stages of the process are associated with dislocation climb, migration of high-angle boundaries, collective atomic displacements and diffusion of single atoms, the absolute and relative difference in the boundary and surface energy of grain boundaries of various texture components, and the retarding role of disperse phase particles.

For that reason, the crystallography of slip has only a slight effect on the type of recrystallization texture. More essential factors are the composition of the metal; the presence of impurities and especially of undissolved particles of secondary phases, their dispersity, distribution and their ability, in some cases, to interact selectively

with various boundaries; local variations in dislocation density; the original grain size; the original deformation texture, in particular in local volumes, i.e. the previous history of the specimen; the temperature and time of annealing; the atmosphere in which annealing has been done; the thickness of the specimen; etc.

The influence of the metal composition can be seen clearly by comparing the data for various isomorphous materials having identical slip systems, and therefore, identical deformation textures. A classical example is presented by the results obtained by R. Glocker et al. on copper and silver deformed 99.9 per cent by rolling. The rolling texture turned out to be the same in both cases, $\{011\}\langle 211\rangle$, but the recrystallization textures were different: $\{100\}\langle 001\rangle$ cube texture in copper and $\{113\}\langle 211\rangle$ texture in silver, which formed from the rolling texture by rotation through an angle of $\pm 31.5°$ about the $\langle 211\rangle$ axis. Besides, as the temperature of annealing was raised, the cube texture in copper remained distinct, whereas the $\{113\}\langle 211\rangle$ texture in silver became less pronounced. Minor additions (hundredths or tenths of an atomic per cent) have only a slight effect on deformation textures, but an extremely strong effect on the type of recrystallization texture.

The cube texture mentioned earlier is found very often in f.c.c. metals and alloys. It is formed during recrystallization after rolling in pure copper, nickel, gold, lead, silver [with the concentration of impurities less than $(5\text{-}10) \times 10^{-3}$ at. %], in Fe-Ni (30-100% Ni), Ni-Mn (1% Mn), and Cu-Zn (up to 1% Zn), and alloys in some ternary alloys based on iron, nickel and copper. On the other hand, cube texture has turned out to be very sensitive to minor additions. Additions of aluminium (0.2%) and cadmium (0.1%) to copper are favourable for the formation of cube texture, whereas an addition of 0.0025 at.% of phosphorus to pure copper (99.99% by mass) suppresses the formation of cube texture and ensures complete dissolution of the recrystallization texture upon annealing (rolling with 95-% reduction, annealing at 300°C for 1 h). It should be noted that phosphorus has no noticeable effect on the texture in cold-rolled copper.

Minor concentrations of iron dissolved in commercially pure aluminium (99.8%) eliminate the recrystallization texture, whereas a higher concentration of iron, at which it precipitates as an excess secondary phase, has no such an effect. Minor additions can eliminate recrystallization textures when they are surface-active, not isomorphous with the base metal and are dissolved in the latter. Some elements which are soluble in copper and increase intensively its hardness, produce in copper alloys a complicated type of recrystallization texture with less regular orientations.

The type of recrystallization texture can also be influenced to a high extent by the temperature and time of annealing. At present, however, it is still impossible to formulate the conditions which

would be necessary and sufficient to produce changes in the type of recrystallization texture.

An analysis of the mechanisms of recrystallization (see Chs. 6-8) suggests two conclusions which are important for understanding texture formation. Firstly, the course of recrystallization is determined by the structure formed in deformation and, in particular, by the specific features and differences of that structure in adjacent local volumes of the metal. Secondly, recrystallization cannot form orientations which were not present in the deformed metal or, more strictly, which would differ essentially from those existing in it.

As may be seen from the above examples, however, this by no means implies that the texture formed on deformation uniquely predetermines the recrystallization texture. Experience shows that, for the same original deformation texture, including its weaker components which cannot be detected by common techniques, it is possible to obtain various recrystallization textures on annealing. This can be achieved by varying the conditions of heating, the purity of metal, by making use of phase transformations, etc. Thus, the principal problem in the theory of texture formation is to know the stage at which the orientations causing the formation of a particular recrystallization texture are chosen, i.e. either the stage of nucleation or that of grain growth. The existing views on the problem will be briefly discussed below.

1. The Principal Theories of Formation of Recrystallization Textures

The theory of oriented nucleation. This theory reduces to the statement that primary recrystallization nuclei possess a particular orientation which is crystallographically associated with the deformation texture. A recrystallization texture results from the growth of these oriented nuclei at the expense of the deformed matrix.

By changing the conditions of heating (temperature and rate) and utilizing the effect of disperse phases, it is possible to vary the relation between the incubation periods for the formation of nuclei in differently oriented regions and thus to change recrystallization texture.

A drawback of the theory of oriented nucleation is that it fails to explain the phenomenon often observed in practice: that the type of texture often changes in the course of recrystallization. For that reason, the theory is not universally applicable.

The theory of oriented growth. This theory proceeds from the fact that the boundary mobility M and, therefore, the rate of grain boundary migration depend substantially on mutual orientation of adjacent crystals and on some other factors. By this theory, nuclei with diverse orientations exist at the early stage of primary recrys-

tallization, but are 'selected' in the course of growth: only the nuclei whose orientation relative to the deformed textured matrix corresponds to the highest mobility of their boundaries can survive and grow acceleratedly.

The theory of oriented growth is based on numerous experimental facts and explains well many analytical relationships. On the other hand, it fails to clarify some particular facts, for instance, why there is a correlation between recrystallization textures and deformation textures.

The combined theory of oriented nucleation and growth. Electron-microscopic analysis of the dislocation structure and crystallographic orientation of very small volumes (dislocation cells, sub-grains, recrystallization nuclei, boundary volumes, etc.) has shown that the orientation of recrystallization nuclei is indeed always associated in a definite manner with the orientation of the local volumes of the deformed matrix in which they have formed, or more strictly, recrystallization nuclei practically repeat this orientation (see Ch. 6). The rate of growth of various nuclei in the textured matrix may however be different.

This rate is the result of the competing effect of the driving and retarding forces, which is determined by the interaction of numerous factors. One or another of these factors may be decisive under particular conditions and at various stages of the process. Consequently, in each particular case it is essential to make a comparative analysis of the local orientations and averaged textures in as-deformed state and at various stages of recrystallization and collect data on the kinetics of enhancement of some orientations and attenuation of others and also on the presence and distribution of impurities in order to decide which of the two processes, either nucleation or grain growth, plays the leading part and why.

Thus, the modern theory of recrystallization textures is a combination of the two theories discussed earlier. As will be shown later, the generalized theory explains well many complicated cases, including the formation and consecutive changes of textures at various stages of recrystallization under the action of various factors.

It is reasonable to discuss the problem in relation to the following three types of texture variations which are likely to occur in annealing of deformed textured materials: (1) the deformation texture is not changed by recrystallization annealing; (2) the deformation texture is replaced in recrystallization, fully or partially by a different texture composed of one or more components; this replacement can occur at various stages of recrystallization: primary, grain growth or secondary recrystallization; in many cases, the texture formed at an early stage of recrystallization is replaced by another texture at a later stage; (3) the deformation texture is replaced in recrystallization fully or partially by randomly oriented new grains; this case is less common than the former two.

2. The Principal Types of Texture Changes in Recrystallization

Retention of deformation texture on annealing. The simplest explanation of the mechanism of retention of a deformation texture on annealing is that the decisive process here is the oriented nucleation of recrystallization centres having the same orientation as that of the deformed matrix. As will be shown later, this concept is true, but not exhaustive.

It is possible to indicate at least three methods for retaining the deformation texture; the first two of them are obviously universal and the third can be used only in some particular cases. Let us discuss these cases:

1. Short-time annealing of a material deformed heavily under the conditions of high-speed heating (say, induction or electric-contact heating) to a temperature exceeding the value of t_r^s for common heating rates.

Under these conditions, i.e. at a high temperature, recrystallization nuclei form quickly from sub-grains not only in portions having the highest distortion of the lattice, but also in places less favourable for nucleation. The orientation of nuclei corresponds to the orientation of the respective portions of deformed material in which they have originated, i.e. oriented nucleation in its pure form is realized. On the other hand, since the time of action of high temperature is short, neither grain growth nor secondary recrystallization can develop well enough. In this way, it is possible to preserve the deformation texture completely or at least its part with a small share of other orientations.

P. D. Izbranov, V. A. Pavlov and N. M. Rodigin analysed qualitatively variations in the recrystallization textures of transformer steel (3.54% Si by mass) with the time of annealing. Heating was performed at high rates (1 000-1 100 °C/s). At Stage I of recrystallization, the recrystallization texture was the same as the deformation texture, though more distinct. In the course of subsequent isothermal holding, this texture disappeared fully, after which a new, different, orientation appeared and became more and more distinct. A similar result was obtained for deformed steel Grade 10 heated at various rates.

2. Heating at a common rate to relatively low temperatures at which primary recrystallization has enough time for its completion by nucleation from a large number of centres, but grain growth does not practically develop at all. This case can be illustrated by the following examples.

In cold-drawn aluminium wire (99.95% Al), the original axial ⟨111⟩ texture was retained upon annealing at 500°C, but changed to the ⟨112⟩ texture upon annealing at 600°C. A Fe + 3% Si alloy was annealed at 650°C and 925°C. In the former case, the recrystalli-

zation texture was identical to the deformation texture; in the latter, a different texture was formed. With heavier deformations and more distinct deformation textures, these are repeated more clearly in the recrystallization texture formed on low-temperature annealing.

3. Recovery and the early stages of recrystallization occurring in parallel with the decomposition of supersaturated solid solutions. In that case, the growth of sub-grains and recrystallization nuclei and the associated 'consumption' of grains of one orientation by the faster growing grains of another orientation become impossible because of the barrier effect of particles.

This mechanism can be illustrated by the results obtained for sheets of low-carbon steel with additions of niobium (0.015% C, 0.126% Nb). Cold-rolled sheets deformed 40-90 per cent were annealed at 800°C for 10 h. The recrystallization texture turned out to be similar to the rolling texture, with the type {111} ⟨111⟩ component being the main one in both. The development of the {110} ⟨001⟩ component was retarded by niobium-containing precipitates of a size of about 15 nm. This effect was not observed in a steel with lower concentrations of niobium and carbon (0.039% Nb, 0.003% C).

Thus, the condition favourable for retention of a deformation texture in age-hardening alloys is a high concentration of highly disperse particles stable against coagulation. But disperse phase particles must not be coherent with the matrix, since otherwise they will precipitate on dislocations, retard the redistribution of dislocations and thus inhibit the formation of recrystallization nuclei as well as their growth.

In practice, some of the cases considered, for instance, short-term high-speed heating, low-temperature heating, decomposition of the solid solution occurring in parallel with recrystallization, etc., are technologically inevitable. As a consequence, the recrystallization textures formed will be identical with the deformation textures. In such cases, recrystallization textures can be controlled only by varying the deformation texture, i.e. by changing the conditions of plastic working (the amount and rate of deformation, temperature, etc.) or by alloying.

Texture variations at various stages of recrystallization. A variation of texture in the course of recrystallization, especially a multiple variation, is usually associated with the effect of oriented nucleation and oriented growth (with one of these two processes being predominant) or only with oriented growth.

Oriented growth is predominant where nuclei of various orientations form at the early stage of annealing, so that the desired texture can be obtained by forming favourable conditions for the preferable development of the respective component. Oriented nucleation plays a prevailing part in cases where the nucleation of an unwanted component is inhibited by special techniques.

Replacement of the main components by weaker components of

primary recrystallization texture in the course of secondary recrystallization. For a system composed of the main and a weaker component, the texture variations at the stage of secondary recrystallization can be generally characterized by partial transformation of grains of the weaker component into centres of secondary recrystallization, so that the weaker component becomes finally the main one.

Indeed, as soon as the grains of the main component surrounding a grain of the weaker component have grown at the expense of the latter, their further growth is stopped or retarded sharply, since they are now surrounded by grains of the same orientation. This retarding effect will be stronger with a lower scatter of the texture of the main component. As regards a small number of grains of the weaker component which will grow at the expense of the surroundings, the rate of migration of their boundaries will increase, but not decrease, in the process, since the driving force associated with the difference in surface energy (the difference in grain size) increases continuously. On the other hand, the boundary mobility, which is determined by misorientation of a growing grain relative to the surroundings, remains high. If, in addition, there is a favourable difference in the volume energy (grains of the weaker component are more perfect than those of the main one), the process considered will be even more probable.

Let this be illustrated by two particular examples.

Formation of a cube texture in recrystallization of f.c.c. metals and alloys. Many authors have shown that in some metals and alloys (copper and copper-base alloys, commercial aluminium and aluminium alloys, alloys of the system Fe-Ni, etc.), where the copper-type texture $\{110\}\langle 112\rangle + \{112\}\langle 111\rangle$ forms as the main texture on deformation, the $\{100\}\langle 001\rangle$ cube texture appears on recrystallization either as the main texture or more often in combination with a texture repeating the rolling texture.

Cube texture may cause sharp anisotropy of the mechanical ('earing') and physical (magnetic) properties of metals. In that connection, it is essential to study the mechanism of its formation and develop methods for preventing this effect.

As has been found, cube texture forms on annealing only when the deformation texture has contained the $\{112\}\langle 111\rangle$ component as one of the main components. The cube texture develops on annealing at the expense of that component. The recrystallized cube texture is more distinct and sharp on a heavier deformation and with finer size of grains before the last procedure of cold rolling. For instance, a distinct cube texture can form in recrystallized copper only when the amount of deformation has been not less than 80 per cent* and the size of original grains not more than 20 μm. With further

* Apart from the two components indicated, the components $\{100\}\langle 001\rangle$ and $\{011\}\langle 100\rangle$ also form as additional components of the deformation texture.

increase in the amount of deformation, the required minimal size of grains increases.

Cube texture can be observed in recrystallized metal also in cases when common methods fail to detect its trails in the deformation texture.

The most probable mechanism of the formation of cube texture has been proposed by C. S. Barrett and P. A. Beck and is based on the concept of oriented growth. By this mechanism, among the nuclei of various orientations formed in the metal, those oriented favourably relative to the matrix lattice have the highest rate of growth. For f.c.c. metals and alloys, this favourable orientation is obtained by rotation through 40° about the ⟨111⟩ axis. Any of the equivalent orientations in an ideal rolling texture has the ⟨111⟩ axis which may be common with a cube texture. These orientations coincide upon rotation through 45°.

Each pair from the four components of an ideal rolling texture has a favourable orientational relationship (the common ⟨111⟩ pole). The cube texture, however, has a favourable orientation relative to all the four components of the rolling texture. This is why the cube texture is usually accompanied by the rolling texture, but the former is predominant. With finer grain, it is more probable that growing grains of a cube orientation will be in contact with all the four components of the rolling texture. This is how the hypothesis mentioned explains the favourable role of fine original grains before the last rolling procedure.

The formation of cube texture can also be inhibited by the presence of highly disperse particles of a secondary phase in the alloy.

The formation of brass texture (30% Zn). The ideal texture in brass is {110} ⟨112⟩. In sheet brass, the {225} ⟨734⟩ texture usually forms on recrystallization, which is very close to the ideal orientation, as may be seen by comparing their crystallographic indices.

The {225} ⟨734⟩ texture has a favourable orientational relationship with the main deformation texture components {110} ⟨112⟩ and {110} ⟨001⟩ in brass. The former changes to the {225} ⟨734⟩ orientation by rotation through 30° and the latter, by rotation through 45° about the common ⟨111⟩ pole. In addition, the {225} ⟨734⟩ texture is oriented favourably relative to the region of scatter around the main texture components.

Texture changes caused by temperature-dependent selective growth. If a sharp main texture formed on primary recrystallization contains a small number of nuclei of a different orientation, these nuclei will grow at a particular temperature at the expense of the main component from which they are separated by mobile boundaries (secondary recrystallization). The activation energy of migration of differently oriented nuclei is however different. Nuclei with a lower activation energy Q will grow preferably at low temperatures and those with a high value of Q, at higher temperatures.

A similar effect can be obtained if the growth of nuclei is inhibited, up to a definite temperature, by disperse phase particles which are dissolved at a higher temperature and their barrier effect is thus eliminated.

It is also known from experience that successive changes of textures in annealing are sometimes caused by various stages of recrystallization following one another. Such effects have been examined most thoroughly in thin (0.3 mm) sheets of silicon iron (transformer steel). A multi-component texture of primary recrystallization changes here to the {110} ⟨001⟩ rib texture in the course of secondary recrystallization and the latter passes into a cube texture during annealing (at 1100°C) in deep vacuum.

Texture variation under the prevailing effect of oriented nucleation. Two practically important cases will be considered here as examples.

1. *Formation of texture in low-carbon steel for deep drawing.* The suitability of a material for deep drawing is estimated in terms of the coefficient of plastic anisotropy, R, which characterizes the change in the width of a flat tensile-deformed specimen relative to the change in its thickness. Any material with $R > 1$ is suitable for deep drawing. Common materials employed for the purpose have $R = 2$ or more.

The coefficient R is determined by the type of texture. The {111} ⟨*uvw*⟩ orientation is most favourable and the {001} ⟨110⟩ orientation is the worst. Any change in the relation between these components can change R appreciably. Thus, the problem reduces to changing a deformation texture (rolling texture) in annealing to a texture with the {111} ⟨*uvw*⟩ as the main component. In a rolling texture, the {111} + {001} components are the main ones. If no special measures are taken, both components will be retained in the primary recrystallization texture and the value of R will be unfavourable.

The principal steel grades used for deep drawing (making car bodies and the like) are killed steel Grade 08Ю (deoxidized by aluminium) and rimming steel Grade 08кп. During heating after cold rolling, recrystallization in both grades is accompanied with decomposition of the supersaturated solid solution. In this process, aluminium nitride AlN precipitates in steel 08Ю; the temperature of its intensive decomposition is above 600°C. In steel 08кп, iron carbide (cementite) precipitates, which is decomposed at temperatures near 500°C.

On the other hand, as has been demonstrated by careful X-ray structural and electron-microscopic examination, the {111} and {100} components of the deformation texture differ from each other in the degree of work-hardening. The {111} component is work-hardened more appreciably: it has a higher dislocation density, greater misorientation between adjacent cells, smaller size of cells, and greater scatter of sizes than the {100} component. Consequently, volumes

with the {111} component have, on the one hand, a higher rate of nucleation in recrystallization which begins in cold-rolled sheets roughly at 500°C and, on the other, a higher rate of decomposition of the supersaturated solid solution. Under such conditions, the formation of different texture components can be inhibited by varying the rate of heating.

In order to retard the development of the {100} component in steel 08Ю sheets, they should be heated slowly so as to allow recrystallization nuclei of the {111} component to form well before the beginning of intensive precipitation of aluminium nitrides. With a high heating rate, sheets will have a temperature of 600-700°C before the completion of the formation of {111} nuclei, so that the precipitation of nitrides, which is more intensive in more work-hardened {111} volumes, will retard the redistribution of dislocations and nucleation in these volumes. In {100} volumes, decomposition will be less intensive, accordingly with a weaker inhibiting effect on recrystallization. As a result, recrystallization nuclei formed in the metal will preferably have the {100} orientation.

On the contrary, in order to form the {111} recrystallization texture in steel 08кп sheets, they should be heated rapidly, so as to pass as quickly as possible through the temperature range of intensive precipitation of carbides (500°C) and thus avoid their retarding effect on the formation of {111} recrystallization nuclei. With slow heating, carbides precipitate preferably in {111} volumes and inhibit nucleation in them, whereas their inhibiting effect in {100} volumes is less pronounced.

2. *Formation of rib texture in transformer steel to reduce remagnetization losses.* In commercial transformer steel, the leading role of oriented nucleation shows up in the formation of the rib component {110} ⟨001⟩ in the texture after primary recrystallization, which is practically absent in the deformation texture.

As has been established, the condition essential for the formation of {110} ⟨001⟩ grains on primary recrystallization is the presence of the {111} ⟨112⟩ component in the deformation texture. Crystallites with the {111} ⟨112⟩ orientation contain at least five types of microzones which differ from one another in the dislocation structure, the nature of local misorientations and, as a consequence, in the conditions for occurrence of primary recrystallization. These are deformation bands with the {111} ⟨112⟩ orientation, microbands, deformation twins, boundary regions, and regions surrounding inclusions. Rib-oriented nuclei form preferably in microbands which connect coherently adjacent deformation bands. Microbands have a small width and are characterized by a regular misorientation of their sub-grains which ensure the structural link between adjacent deformation bands, for instance, (111) [11$\bar{2}$] and ($\bar{1}$11) [112]. The core volumes of such microbands have an orientation close to {110} ⟨001⟩ and are misoriented relative to the adjacent deformation bands

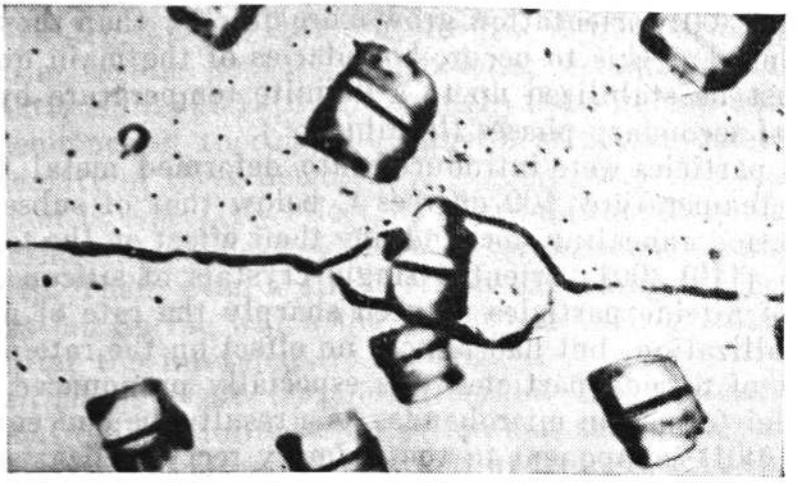

Fig. 223. Rib-oriented recrystallization nucleus in transformer steel. It has formed in a microband and grows into adjacent deformation bands of the type {111} ⟨112⟩

by approximately 30° about the common [110] axis, i.e. by an angle corresponding to the highest mobility of their boundaries. The conditions existing in these core volumes are most favourable for the quickest transformation of their sub-grains into recrystallization nuclei of the rib orientation. The angle of their misorientation relative to the matrix increases quicker in the course of growth than that of sub-grains in other microzones.

As has been shown by statistics, among all the possible orientations, ranging from {111} ⟨112⟩ to {110} ⟨001⟩, the last orientation has the highest contribution to nucleation in microbands. This can be explained by the fact that the misorientation angle of these nuclei increases more quickly than that of others. These nuclei are separated from the matrix, into which they will grow by boundaries of the highest mobility. Figure 223 shows a rib-oriented recrystallization nucleus which has formed in a microband and grows into adjacent deformation bands of the type {111} ⟨112⟩. With a slight magnification, a microband appears as a linear boundary.

The contribution of {110} ⟨001⟩ nuclei to a texture should be greater in a coarse-grained material where the volume concentration of microbands is higher.

On deformations above 70-80 per cent (depending on the size of original grains), the {112} ⟨110⟩ and {001} ⟨110⟩ orientations develop in a rolling texture at the expense of the {111} ⟨112⟩ orientation, which worsens the conditions for the formation of rib texture. The optimal amount of deformation is 40-70 per cent.

According to the foregoing, primary recrystallization results in that a distinct {110} ⟨001⟩ component appears in the texture, which however still is not the predominant one. It becomes predominant only at the stage of secondary recrystallization during which nuclei

of the {110} ⟨001⟩ orientation grow more quickly than those of other orientations. For this to occur, boundaries of the main quantity of grains must be stabilized up to a definite temperature by disperse particles of secondary phases ('inhibitors').

Nitride particles were introduced into deformed metal by nitriding at a temperature 100 degrees C below that of subsequent recrystallization annealing, for studying their effect on the texture formation in {110} ⟨001⟩ oriented single crystals of silicon iron. The presence of nitride particles reduced sharply the rate of nucleation in recrystallization, but had almost no effect on the rate of growth. The effect of nitride particles was especially pronounced on {110} ⟨001⟩ nuclei formed in microbands. As a result, the concentration of the {*hkl*} ⟨001⟩ component in the primary recrystallization texture in a single crystal with nitride particles was 80 per cent against 20 per cent in the absence of these particles. Thus, secondary phase particles produced a selective effect on oriented nucleation and changed the texture at the stage of primary recrystallization.

Weakening of texture in recrystallization. The possibilities for weakening deformation textures or preventing the formation of distinct recrystallization textures by recrystallization annealing are not yet studied sufficiently. They have been examined in more detail as regards the manufacture of low-textured electric (dynamo) steels. On the whole, the earlier discussion of the conditions favourable for producing various types of texture enables us to recommend some methods for texture weakening.

Addition of an appreciable concentration of coarse secondary phase particles (>0.1 μm in size) with simultaneous use of high rates of heating. In that case, plastic working forms a less distinct texture containing more components. The high rate of heating gives rise to the highest possible number of nuclei, including those near secondary phase particles, which will be oriented chaotically.

If secondary phase particles differ substantially from the matrix in the coefficient of thermal expansion, randomly oriented nuclei can additionally form as a result of structural strain hardening. In that case, thermocycling (alternating heating and cooling) can be quite effective.

It should be noted that the method discussed gives a desired effect only when the concentration of particles is high, and therefore, spacings between them are small. Recrystallization nuclei formed on secondary phase particles by structural strain hardening are less perfect than those formed in other portions of the lattice. Therefore, with a low concentration of particles, nuclei formed near them will be consumed during annealing by growing more perfect nuclei.

Control of texture and suppression of unwanted texture components having a short incubation period by an intermediate annealing procedure to cause partial recrystallization, followed by plastic working to a slight (near critical) deformation. This method is based on a number

of factors: firstly, on the different length of incubation period of nucleation in various texture components; secondly, on the orientational relationship of strain hardening in these nuclei; and thirdly, on the dependence of thermal stability of structure defects on the type and density of these defects.

The method is especially effective where unwanted nuclei formed during intermediate annealing have an orientation favourable for multiple slip. Then, even a slight strain hardening can cause their recrystallization during which the nuclei lose their orientation they have had after the intermediate heating.

Superposition of phase transformation on recrystallization. This technique has only a limited application and can be employed with alloys undergoing phase transformations at temperatures close to the recrystallization temperature. In some cases, a phase transformation can be initiated on addition of a very small quantity of an impurity. A typical example is dynamo steel. Addition of a small quantity of carbon (around 0.03 per cent) to a Fe + (2.5-3.0)% Si alloy causes the $\alpha \rightarrow \gamma$ transformation at a temperature near 800°C. The $\alpha \rightarrow \gamma$ transformation which takes place in quick heating and the reverse $\gamma \rightarrow \alpha$ transformation in subsequent cooling weaken the texture substantially.

The examples given above illustrate the laws of texture formation and the effect of various factors on it. They also demonstrate certain ways for controlling this important type of structural changes.

RECOMMENDED LITERATURE

1. Gorelik S. S., *Recrystallization in Metals and Alloys.* Moscow, Mir Pulbishers, 1981.
2. Kudryavtsev I. P., *Textures in Metals and Alloys.* Moscow, Metallurgiya, 1965 (in Russian).
3. Kudryavtsev I. P., *The Theory of Texture Formation in Metals and Alloys.* Moscow, Nauka, 1979 (in Russian).
4. Wassermann G., Grewen J., *Texturen metallischer Werkstoffe.* Berlin, Springer Verlag, 1962.

11 Fracture

Fracture of metals and alloys occurs by the formation and propagation of cracks in them*. Fractures are usually classified according to the amount of preceding plastic deformation and the nature of crack propagation in the metal.

Fracture is termed ductile if it has taken place after an appreciable plastic deformation; if the plastic deformation has been less than 1-2 per cent, fracture is called brittle.

Brittle fracture most often occurs along particular crystallographic planes within grains and is respectively called *transcrystalline* (*intragranular*) *fracture*. Under certain conditions (low temperatures, high concentration of disperse phases at grain boundaries or presence of impurities which weaken bonds between grains), however, metals and alloys can break along grain boundaries; this is what is called *intercrystalline* (*intergranular*) *fracture*.

Ductile fracture takes place after an appreciable plastic deformation (often up to 100 per cent or even more) and the microstructure of the fracture surface is quite complicated and may include portions of transcrystalline and intercrystalline fracture.

Transcrystalline fracture can be realized either by *shear* or by *cleavage*, which differ from each other in the type of the fracture surface. Shear fracture has no definite crystallographic orientation and the fracture surface is usually dull and fibrous. Cleavage fracture, on the contrary, gives a bright crystalline surface.

The concepts of ductile and brittle fracture should not be identified with shear fracture and respectively cleavage fracture. For instance, cast iron is considered brittle though, from the structural viewpoint, its fracture occurs by the mechanism of shear, rather than by cleavage. Intercrystalline fracture which is observed in creep and stress-induced corrosion occurs by an utterly different mechanism and the

---

* Except for ductile fracture of some single crystals which takes place by deformation without cracking.

metal may exhibit the features of both brittle and ductile fracture. The mechanism of this process is determined by the microstructural (crystallographic) classification of fracture phenomena.

1. The Phenomenological Theory of Brittle Fracture

Non-crystalline materials (such as glass) are absolutely brittle at room temperature. Their rupture stress (which is roughly equal to $E/500$) is substantially lower than the theoretical rupture stress (equal approximately to $E/5$). At low temperatures, many metals are liable to brittle fracture at stresses well below their theoretical strength. These phenomena are explained by the theory of brittle fracture whose object is to determine the critical state in which a crack is observed to propagate rapidly (catastrophically).

Fracture of solids is a structure-sensitive process, but its theoretical principles have been developed on the basis of mechanics of continua and without account of the structure. In particular, A. A. Griffith has proposed the following scheme for determining the stress to fracture.

If a plate of unit thickness without cracks is subjected to uniaxial tension, the elastic energy per unit volume is

$$e = \sigma^2/2E$$

If a crack of length $4l$, directed perpendicular to the tensile force, appears in a similar plate, the elastic energy of deformation in the crack zone, which has the form of an ellipse with semi-axes l and $2l$, will decrease by

$$(\sigma^2/2E)\, 2\pi l^2 = (\pi l^2 \sigma^2)/E$$

An additional work $4le_s$ must be spent to form the two new surfaces of length $4l$ (where e_s is the surface unit energy which is equal to the work performed for the formation of a unit surface in fracture). Thus, the portion of the internal energy U associated with the presence of a crack can be determined by the formula

$$U = 4le_s - \pi l^2 \sigma^2/E \tag{155}$$

The condition $dU/dl < 0$ corresponds to a catastrophic (instantaneous) propagation of a crack without any increase in energy. If $dU/dl > 0$, growth of a crack is impossible. The critical stress for propagation of a crack of length $4l$, σ_{cr}, is determined by the condition that $dU/dl = 0$:

$$\sigma_{cr} = \sqrt{2Ee_s/\pi l} \tag{156}$$

Since the stress is proportional to $l^{-0.5}$, the stress required for crack propagation decreases as a crack increases in length, i.e. crack propagation takes place acceleratedly. The stress σ_{cr} is often termed the *stress to fracture*. Substituting the typical values of σ, e_s and E

for brittle solids, we can find, for instance, for glass, that $l = 2 \times \times 10^{-4}$ mm, which is close to the size of cracks really observed in glass.

Equation (156) can also be derived by the theory of stress concentration in which the stress concentration coefficient is determined as the ratio of the maximum stress at the crack tip to the nominal stress σ:

$$(\sigma'_{max}/\sigma) = q = 2\,(l/r)^{0.5}$$

where l is the length of a crack and r is the radius of curvature at the crack tip. As $r \to 0$, the maximum stress σ'_{max} becomes infinitely large, and therefore, the tensile strength in the presence of initial cracks becomes negligible, since the theoretical strength is quickly attained as $r \to 0$. The expression $q = 2\,(l/r)^{0.5}$ has however been obtained under the assumption that the medium is linearly elastic and that deformations are small. According to the calculations made by I. Ya. Frenkel, the theoretical strength in crystalline materials is attained only after a substantial displacement $x = a/4$ (where a is the lattice parameter). In other words, deformations in the vicinity of the tip of a crack are large and the medium is non-linearly elastic, and therefore, there exists a region of diameter d at the crack tip to which the linear theory of elasticity is inapplicable; the stress in that region is roughly constant and equal to the stress at its boundary (Fig. 224). The magnitude of that stress can be estimated quite accurately by using the equations of the linear theory of elasticity. In that case, the radius of the crack tip can be taken to be $d/2 = a$, where a is the atomic spacing along which appreciable finite deformations and deviations from Hooke's linear law are noticeable. Assuming that a is the smallest radius of rounding off that is possible at the crack tip, the stress concentration coefficient is found as

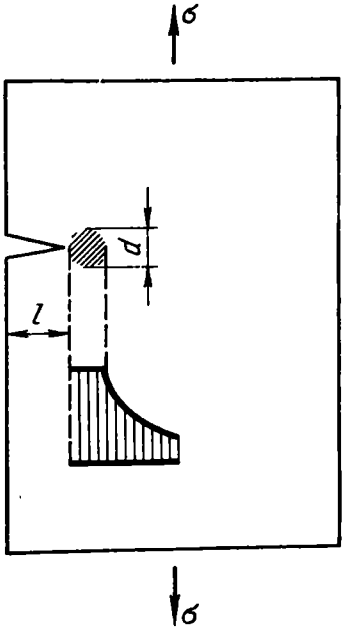

Fig. 224. Stress distribution at the tip of crack according to Neuber's approach of stress concentration

$$q = (\sigma'_{max}/\sigma) = 2\,(1/a)^{0.5}$$

Calculations of the theoretical strength of a crystal can give

$$\tau_{th} = G/2\pi = 2G\,(1 + \nu)/4\pi\,(1 + \nu)$$
$$= E/4\pi\,(1 + \nu)$$

and $\sigma_{th}/2 = \tau_{th}$ (in uniaxial tension). The normal stress at which the theoretical strength is attained in the crystal is

$$\sigma_{th} = E/2\pi\ (1 + \nu)$$

Assuming as earlier (see Ch. 1) that $\tau = \tau_{th} \sin (2\pi x)/a$, a displacement x will involve a corresponding work per unit surface area which is spent in fracture (i.e. at $x = a/4$, where the stresses τ and τ_{th} are equal to each other and to the theoretical strength of the metal) to form two new surfaces with the unit surface energy $2e_s$, i.e

$$A = \int_0^{a/4} \tau_{th} \sin (2\pi x/a)\, dx \quad \text{and} \quad (a/2\pi)\, \tau_{th} = 2e_s$$

Multiplying both sides of the last equation by G, we have:

$$\tau_{th} = \sqrt{2Ge_s/a} \text{ or } \sigma_{th} = 2\sqrt{Ee_s/(1+\nu)\, a} \tag{157}$$

Noting stress concentration at the crack tip (of radius a), we obtain the stress applied at which fracture can take place if $\sigma'_{max} = \sigma_{th}$

$$\sigma_{cr} = \sigma'_{max} \frac{1}{2} \left(\frac{a}{l}\right)^{0.5} = \frac{1}{2} \left(\frac{a}{l}\right)^{0.5} \left[\frac{Ee_s}{(1+\nu)\, a}\right]^{0.5} \times 2 = \left[\frac{Ee_s}{l\,(1+\nu)}\right]^{0.5} \tag{158}$$

Equation (158) is similar to Griffith's equation (156) derived earlier.

For brittle materials with the crack tip radius $r < a$, $(a/l)^{0.5}$ in formula (158) can be replaced by $(r/l)^{0.5}$ and we obtain an infinitesimal magnitude of σ_{cr} as $r \to 0$:

$$\sigma_{cr}^2 \approx \frac{Ee_s r}{(1+\nu)\, la} \tag{159}$$

When using Griffith's formulae (156) and (158) for metals, it is essential to consider the energy of plastic deformation in crack propagation. Otherwise, calculations by formulae (156) and (158) will give either too low values of the fracture stress at l = const or, at σ = const, too large dimensions of cracks (exceeding the dimensions of test pieces). This circumstance was induced by E. Orowan to replace the surface energy e_s in Griffith's formulae by $e = e_s + e_p$, the total energy required for increasing the unit surface area of a crack, which includes the surface energy and the work of plastic deformation e_p appearing due to stress concentration at the moving tip of a crack. Thus, for crystalline materials we have:

$$\sigma_{cr} = \left(\frac{2Ee}{\pi l}\right)^{0.5} \tag{160}$$

It is assumed here that the length l of a crack is equal to the grain diameter and that $e \approx 10^{-2}$-2×10^{-1} J/cm^2, i.e. 30 to 600 times the unit surface energy. Consequently, almost the entire energy should be spent for plastic deformation at the crack tip. This energy

is however only a very small fraction of the energy of plastic deformation. The energy $e \approx 10^{-2}$ J/cm^2 can be described as the work spent by a stress of 100 MPa to produce a deformation of 10 per cent in a layer of a thickness of 10^{-3} cm. The energy e is much greater than e_s but this does not imply that the unit surface energy has no effect on the process of fracture. On the contrary, it is decisive for determining the path of fracture (in particular, whether fracture will be intergranular or intragranular) and is essential for determining the stress to fracture. This follows from the fact that the tip of a crack can move further only if the tensile stress at the crack tip is equal to the strength of interatomic bonds immediately before the crack tip. The magnitude of stress is determined by the surface energy: with a lower energy, a smaller stress is sufficient for fracture, and therefore, the work of plastic deformation is lower. Replacing e in equation (160) by the sum $e = e_s + e_p = e_s + \alpha\sigma_{cr}^2$ (where α is a constant and $e_p = \alpha\sigma_{cr}^2$ is the work of plastic deformation), we obtain:

$$\sigma_{cr} = \left(\frac{2Ee_s}{\beta\pi l}\right)^{0.5} \tag{161}$$

where $\beta^{0.5} = 1 - (2E\alpha/\pi l)^{0.5}$.

Formulae (161) and (157) are similar in their structure, but fracture by formula (161) is controlled by the surface energy e_s. This energy also determines the work of plastic deformation which is much greater than the work e_s for the formation of new surfaces. J. J. Gilman has established the following relationship between e_s and e_p:

$$e_p = 9e_s \ln (G/\pi\sigma_y) \approx 9e_s \ln (\sigma_{th}/\sigma_y)$$

where σ_y is the yield limit.

Brittle metals can be divided into two classes by the magnitude of the e_p to e_s ratio: high-strength ($e_p \gg e_s$) and low-strength ones ($e_p \approx 10e_s$) of the type of glass for which equation (156) holds true.

2. Dislocation Mechanisms of Fracture

The phenomenological theory of brittle fracture does not consider the causes of cracking and assumes that cracks are present in the material. The physical mechanism of crack initiation can be explained by the theory of dislocations. An ample amount of experimental data has been accumulated in support of the proposed probable mechanisms of crack initiation, which show that brittle fracture in crystals is also preceded by plastic deformation*, but the path of dislocation movement and the corresponding deformation immediately before crack propagation are rather small.

* A. V. Stepanov has demonstrated, for the first time, that brittle fracture is preceded by plastic deformation.

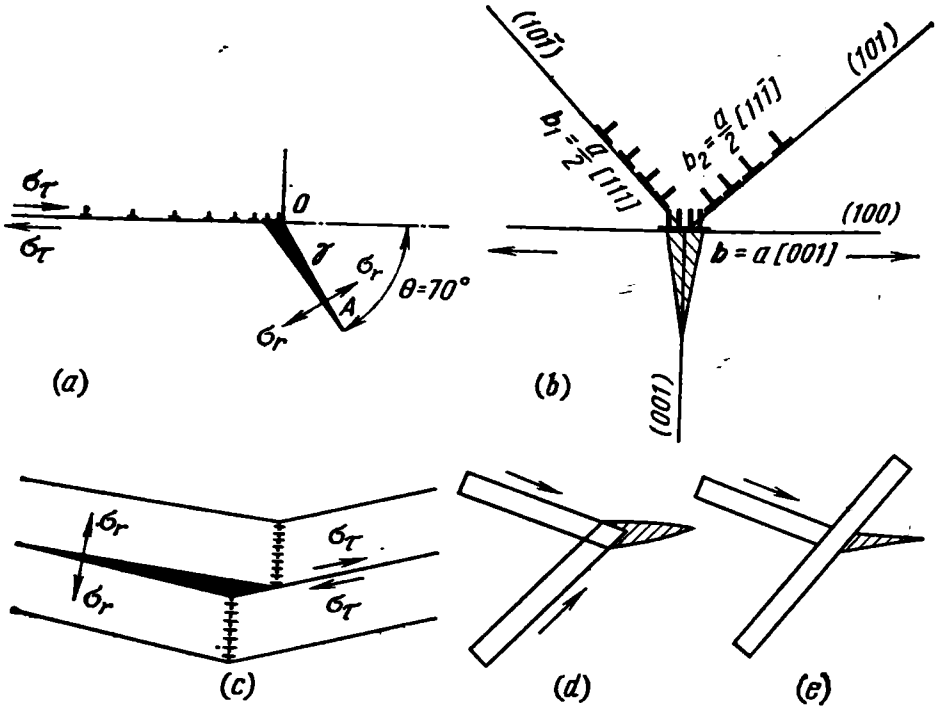

Fig. 225. Dislocation mechanisms for nucleation of submicrocracks
(*a*) Zener-Mott-Stroh model; (*b*) Cottrell model; (*c*) model of disruption of a dislocation array; (*d*) formation of a crack by two meeting twins; (*e*) locking of one twin by another

A number of dislocation schemes have been proposed to explain the formation of submicrocracks. By the simplest mechanism suggested by A. N. Stroh and N. F. Mott, flat pile-ups of gliding dislocations can form at various obstacles, resulting in strong stress concentration often sufficient for initiation of a crack. Dislocations moving in intersecting planes, dislocation arrays, twin, subgrain, grain and phase boundaries, foreign inclusions, etc. may serve as obstacles at which dislocation pile-ups form (Fig. 225*a*). The tensile stresses operative in the plane perpendicular to the slip plane may attain the theoretical rupture stress. A crack initiates, however, not perpendicular to the slip plane. As has been found by A. N. Stroh, the tensile stress σ_t at which fracture occurs attains a maximum at an angle $\theta = 70.5°$ to the slip plane and

$$\sigma = 2\,(L/3l)^{0.5}\sigma_\tau \qquad (162)$$

where $\sigma_\tau = Gbn/\pi L\,(1 - \nu)$ is the shear stress applied in the plane of dislocation pile-up; L is the length of the dislocation pile-up in the slip plane; and $2l$ is the length of the crack.

Calculations by formula (162) show that the number of dislocations in a pile-up may be as high as 10^2 to 10^3 when the local shear stresses at the tip of the pile-up are equal to $0.7G$. On passage onto the surface of a crystal, such a high number of dislocations can form a jog

of a size of a few thousand nanometres, which agrees well with the experimentally measured height of jogs. This demonstrates the principal possibility for the formation of a dislocation pile-up in a slip plane (slip pack), which will be sufficiently powerful to initiate a crack by the Stroh-Mott mechanism. A characteristic feature of this theory is that a crack is initiated only upon the accumulation of a substantial number of dislocations which produce an appreciably higher amount of plastic flow than that needed for the appearance of slip in adjacent grains.

By another mechanism, proposed by Cottrell, dislocations move in two intersecting slip bands, combine along the intersection line and form a splitting dislocation (Fig. 225*b*). In iron, this process occurs by the dislocation reaction $0.5a\,[11\bar{1}] + 0.5a\,[111] \rightarrow a\,[001]$, resulting in the formation of a crack in the plane (001) which is the cleavage plane. Multiple repetition of the reaction results in combination of $a\,[001]$ dislocations, thus forming an initial Griffith's crack. This mechanism requires no dislocation barriers. In contrast to the similar-type dislocation reaction which forms immobile Lomer-Cottrell dislocations, $a\,[001]$ dislocations are mobile and can be locked by barriers and form dislocation pile-ups.

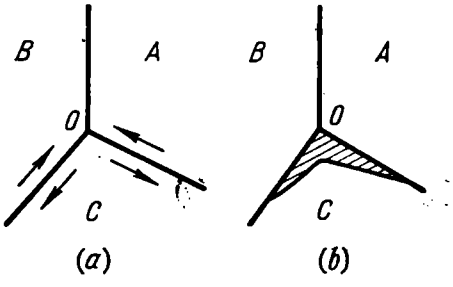

Fig. 226. Crack initiation by grain-boundary sliding in a triple point
(*a*) before displacement (arrows indicate directions of displacement); (*b*) upon formation of a crack

In c.p.h. metals, crack initiation is observed as a result of movement of dislocations in the basal plane, with the formation of a dislocation array (Fig. 225*c*). Shear stresses may turn out to be so high as to rupture the dislocation array: portions of a ruptured dislocation array move apart and, as the angle of misfit increases, the stresses σ_r normal to the slip plane increase and initiate a crack. The condition for the appearance of crack can be approximately written as follows:

$$\sigma_r = 1.3eG/\sigma_\tau L \qquad (163)$$

where σ_τ is the shear stress in the slip plane and L is the length of the dislocation array.

Other mechanisms of crack initiation have also been proposed. A detailed analysis of these mechanisms has been made by V. I. Trefilov, V. L. Indenbom, T. Yokobori and other researchers. For instance, a crack often initiates in a place where a twin meets a strong barrier, such as a grain boundary or another twin (Fig. 225*d*, *e*). Twins propagate at a high speed and, as they meet an obstacle, the appearing stresses have no time to relax. The conditions for crack initiation are especially favourable when a growing deformation twin

encounters an older twin characterized by a different twinning direction (see Fig. 225*e*). In that case, the stress concentration in the point of encounter may be very high. In polycrystals, especially with strongly developed intergranular deformation, cracks are more likely to appear at boundaries of crystallites which are in relative movement to one another (Fig. 226).

Intergranular displacements at a point where three grains meet (triple point) can result in the appearance of a microcrack which can then propagate as a Griffith's crack. This mechanism of crack initiation has been found in long-term tests at high temperatures.

3. The Ductile-brittle Transition

Brittle fracture is typical of some metals and is not found in others. One and the same metal may exhibit either brittle or ductile fracture, depending on the conditions. Cleavage fracture, as a variety of brittle fracture, occurs mainly at low temperatures. This type of fracture is impossible when the temperature of deformation is sufficiently high. Thus, a transition from brittle to ductile state of the metal takes place usually in a very narrow temperature interval. The ductile-brittle transition temperature is taken conditionally as a certain temperature within that interval. At the temperature of the transition, the energy required to fracture a test piece decreases abruptly (Fig. 227). The ductile-brittle transition temperature is not constant for a given metal, but is sensitive to a number of factors, the most essential among them being the purity of the metal and the size of grains; they depend on the conditions of melting and heat treatment.

The appearance of brittle fracture is observed in b.c.c. metals and alloys and becomes especially pronounced in the presence of

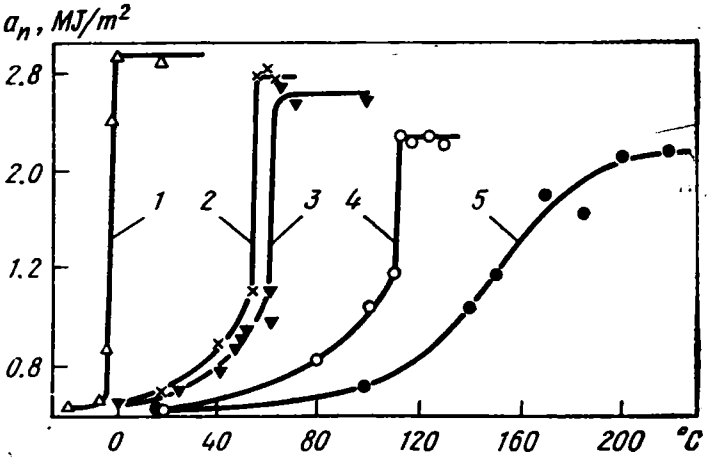

Fig. 227. Impact transition curves for a high purity steel with 0.12% C, showing effect of heat treatment

1—water quenching from 950°C; *2*—water quenching from 950°C + furnace cooling from 700°C; *3*—air cooling from 950°C; *4*—furnace cooling from 950°C; *5*—furnace cooling from 950°C + water quenching from 700°C

impurities forming interstitial solid solutions. In α-iron, a few carbon atoms per million of iron atoms can cause the ductile-brittle transition. Upon removal of carbon, say, by zone refining, the ductility of iron increases substantially (cross-sectional reduction up to 90 per cent), even at temperatures near 4.2 K.

B.c.c. metals of group VIA (tungsten, molybdenum and chromium) are more liable to brittle fracture than metals of group VA, and have a higher transition temperature, for instance, within 200-400°C for tungsten. At a high degree of purity (in zone-refined metal), fracture in the metals mentioned occurs within grains (transgranular fracture); in tungsten and molybdenum, it takes place in {001} planes and is determined, in the first place, by the surface energy, which according to the modified Griffith's equations (160) and (161) may constitute an appreciable portion of the total energy. At a higher concentration of impurities, cleavage planes coincide with grain boundaries, since the surface energy has been decreased due to impurity segregation, i.e. $e_s = 2e_{sf} - e_{gb}$. The surface energy required for fracture, $2e_{sf}$, decreases by the magnitude of the grain boundary energy e_{gb}. Besides, e_{sf} decreases owing to the presence of impurities, since $(e_{sf})_b < (e_{sf})_{\{001\}}$. This results in a change from transgranular fracture to fracture along grain boundaries (intergranular fracture). Embrittlement of iron at low concentrations of phosphorus and oxygen is a typical example of this change from transgranular to intergranular brittle fracture (owing to the appearance of impurity segregates at grain boundaries).

The principal role of intersticed impurity atoms consists in that they cause strong locking of dislocations, which is favourable for the formation of dislocation pile-ups and thus, of crack nuclei.

As the temperature decreases, the yield limit increases sharply, since the Peierls-Nabarro force in b.c.c. metals is strongly temperature-sensitive. When the critical flow stress becomes sufficiently high, the developing twinning process forms favourable conditions for crack initiation by some or other of the mechanisms based on the presence of twins (see Fig. 225*d*, *e*).

As has been mentioned earlier, as a crack propagates, the stress required for its propagation (as found by Griffith's formula) diminishes. If the stress remains constant, the rate of propagation of a crack increases as the crack grows in length. This ultimate speed of crack propagation constitutes 0.4-0.5 of the speed of sound, i.e. brittle fracture proceeds catastrophically.

In engineering practice, brittle fracture is a common phenomenon. For instance, of the total number of 5000 war-time 'Liberty' ships built in the USA in 1943-46, around 1500 broke due to brittle fracture. 19 ships crushed in half quite unexpectedly, one of them in the shipyard just after acceptance tests. All these failures occurred in winter time at temperatures below 0°C. This example shows clearly that the problem of brittle fracture is extremely important.

4. Ductile Fracture

Ductile fracture under the action of a tensile stress consists of three successive stages. A neck forms initially in a test piece; voids which appear at this stage in the necking region combine with one another (Fig. 228*a*). At the second stage, voids grow in size and coalesce into a larger void which can propagate rapidly in the direction perpendicular to the tension axis. At this stage, a crack propagates to the surface of the metal and at the third stage comes to the surface at an angle close to 45° relative to the axis of tension (Fig. 228*b*). At the third stage, the test piece breaks in two parts along a conical surface.

The first stage of fracture is the longest, since first voids and cracks are found only shortly before fracture. For instance, fracture of aluminium test pieces in tension is observed at a relative contraction $\psi_r = 80\text{-}81$ per cent, while first voids and cracks appear at $\psi_{cr} = 76\text{-}78$ per cent; the respective values for copper are $\psi_r = 53.7$ per cent and $\psi_{cr} = 51.7$ per cent and those for brass, $\psi_r = 47.4$ per cent and $\psi_{cr} = 41.9$ per cent. At the end of the first stage of fracture, say, in commercial copper (see Fig. 228*a*), a central crack begins to form, which is surrounded by fine voids formed in the case considered by rupture of metal from inclusion particles or by destruction of inclusion particles proper. In the case considered (copper, Fig. 228*a*), voids are seen unusually clearly, but in most cases it is difficult to detect voids even after fracture. As deformation increases, the

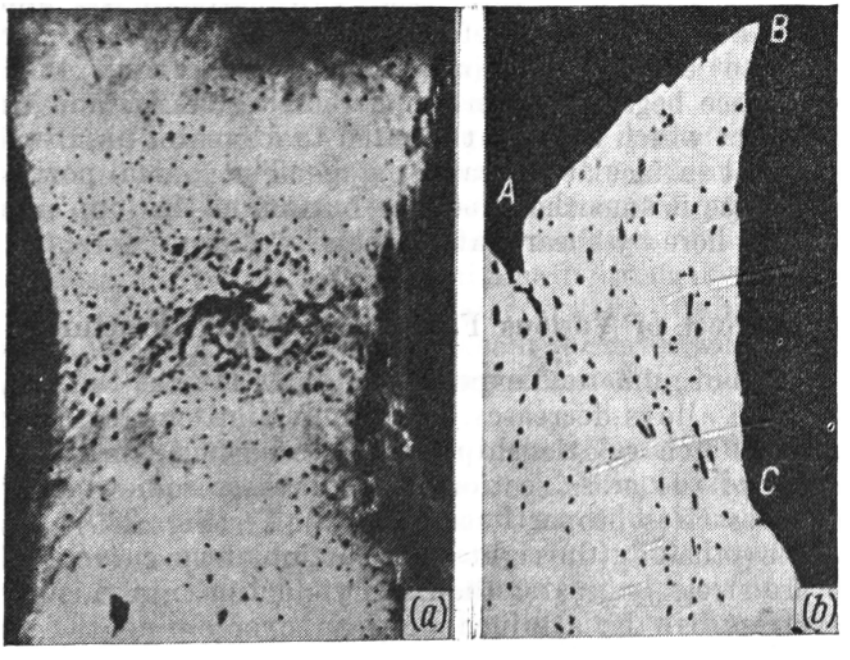

Fig. 228. Voids formed at the beginning of ductile fracture (*a*) and conical portion of a porous specimen (*b*)

appearing voids grow in size, coalesce near the axis of a test piece, and form a small central crack. The last two stages of ductile fracture develop after the ultimate stress has been attained in the plastic metal.

At the second stage of fracture, the main crack appears in the core of the tensioned test piece, which is due to the characteristic distribution of stresses in the necked portion (Fig. 229): the state of triaxial tension appears in the core. The shear stress at the test piece axis has the same magnitude as in other portions of the cross section, whereas the tensile stresses are at their maximum near the axis. Since the process of fracture is determined by the development of both shear and tensile stresses, it is natural to suppose that the development of a crack starts at the test piece axis where the metal is in uniform tension. No crack initiation is observed from the surface.

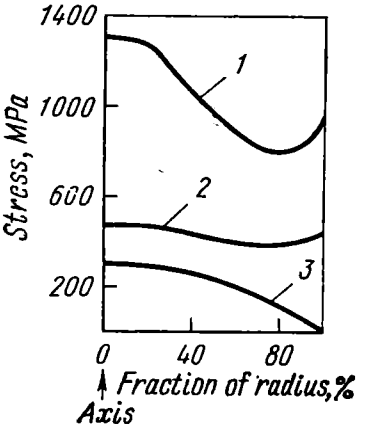

Fig. 229. Distribution of (*1*) longitudinal, (*2*) maximum shear, and (*3*) radial stresses in cross section of a tensioned necked specimen

The propagation of a growing crack is facilitated due to surfaces with intensive shear deformations at the crack tip. These surfaces are tilted roughly at 45° to the tensile axis; voids develop in them too (see Fig. 228*b*). At this third stage of fracture, the two surfaces AB and AC in which the highest shear deformations are operative are fully equivalent to each other; in the case considered, the conical fracture surface began to form along the surface AB and this is an occasional fact which can be attributed to a greater number of voids formed at that surface at the earlier stage. The conical portion of the fracture surface is smoother than the bottom of the 'cup', since new surfaces form here by shear, rather than by rupture.

5. Effect of Various Factors on Ductile Fracture

The results of numerous experiments show that as the grain size d of metals and alloys decreases, their yield limit increases according to the Hall-Petch relationship and at the same time the relative contraction of the cross section also increases somewhat. Also the rupture stress rises proportionally to $(d)^{-0.5}$ (Fig. 230)*. With the grain size less than d_1 (the right-hand portion of the curve in Fig. 230), the rupture stress is greater than the yield limit; in this region, the rupture stress can be attained only on overcoming the hardening effect. In the case considered, the elongation may be as high as 50 per

* This is true of b.c.c. metals.

cent. With the grain size above d_1 (the left-hand portion of the curve), the rupture stress is equal to or lower than the yield limit, which is indicative of brittle fracture. Thus, the effect of grain coarsening is similar to temperature reduction, i.e. results in the transition from ductile to brittle fracture. The experimental facts gathered to this time give a firm evidence that grain coarsening in metals results in a loss of ductility and in embrittlement.

Properties of cast and plastically worked metals usually exhibit anisotropy, especially the characteristics of ductility, such as relative elongation, relative reduction or impact toughness. A cast metal is usually less ductile than that worked plastically. The ductility of cast metals along the direction of columnar crystals is higher than crosswise. The anisotropy of the mechanical properties is retained partially even after plastic working, the specimens cut along the direction of the highest deformation being more ductile than those cut in other directions. Anisotropy may be due to the following reasons:

(1) retention of traces of laminated or striated inhomogeneity of the composition of cast metal (impurity segregates);

(2) oriented arrangement of inclusions in the metal, which is determined by the direction of the highest deformation;

(3) appearance of a preferable crystallographic orientation of crystals (texture).

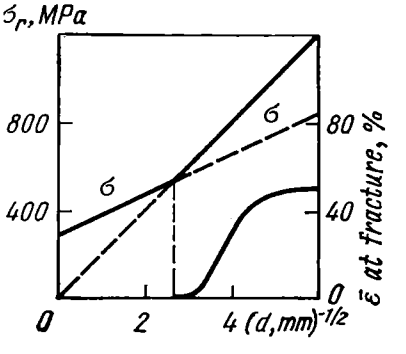

Fig. 230. Variations in rupture stress (solid line) and ductile-to-brittle transition in low-carbon steel depending on grain size

In b.c.c. metals, the anisotropy of properties is enhanced in the presence of interstitial impurities. In single-phase pure metals, anisotropy is mainly determined by texture. Upon annealing, which eliminates texture, the anisotropy of mechanical properties disappears. Alloying, which results in the formation of a solid solution or multiphase alloy, can raise the ultimate strength and sometimes the relative elongation, but practically always diminishes the relative reduction of the cross section, except for cases when the alloying element added reduces the embrittling effect of the impurity already present in the metal.

The relative reduction of the cross section in tensile tests increases at an increase of temperature. This can be explained by a greater number of operative slip systems and an additional development of diffusion processes at higher temperature, and also by the processes of dynamic softening which diminish the probability of fracture.

Changes of the deformation rate in tension within the range of 10^{-3} to 10^2 s^{-1} have, as a rule, no noticeable effect on the nature of ductile fracture. Beyond this range of deformation rates, for instance, at the rates of creep ($\dot{\varepsilon} < 10^{-4}$ s^{-1}) or in dynamic deformation ($\dot{\varepsilon} >$

$> 10^4\ s^{-1}$), certain specific effects can appear which vary the nature of ductile fracture and quite often induce brittle fracture.

At a long-term action of high temperature and stress (creep tests), the path of fracture passes along grain boundaries, rather than across bodies of crystallites. This type of fracture is caused by a process that is typical only of low deformation rates at high temperatures (see Ch. 15), i.e. slip along grain boundaries, rather than by the presence of impurities or of films of brittle substances on grain boundaries (because this type of fracture is found in pure metals as well as in commercial alloys). As has been noted earlier (see Ch. 4), grain boundary deformation cannot be very high, and therefore, the deformations observed before fracture are insignificant, which is typical of brittle fracture.

The effect of size factor in plastic flow and fracture. The effect of the size factor consists in that geometrically similar models and structures of different size exhibit different physical behaviour under comparable conditions. The geometrical similarity is rightfully considered here as macroscopic similarity which disregards the microscopic parameters, such as the size of grains, the distance between particles, and the size of particles. This makes the essence of scale simulation, since otherwise we would be obliged to rely only on full-scale tests. When using simulation, one should however remember that size effects appear in plastic flow and fracture as microprocesses at macroscopic level. For instance, the rounding radius of a sharp crack depends on a number of microstructural factors. In that connection, the ratio of the crack tip radius to the crack length and the ratio of the crack length to the size of test piece cease to be geometrically similar.

Owing to the size effect, larger test pieces or parts of the same metal have a higher brittleness and poorer mechanical characteristics. The statistical theory of defects explains this phenomenon in the following way. The probability of occurrence of a dangerous defect which can provoke initiation and development of cracks is lower in pieces of a smaller size. This conclusion of the statistical theory of defects has found direct experimental confirmation. It is well known, for instance, that thin glass fibres of a diameter of 5 μm have the strength 50 times that of massive specimens made of the same glass.

The size effect is closely associated with the state of the surface of a metal. In particular, etching of glass by hydrofluoric acid which removes the outer layer and forms a perfectly smooth surface, results in a sharply reduced probability of existence of dangerous defects on the surface and, according to the statistical theory of defects, should increase the strength of massive specimens to the value obtained in thin glass fibres. This supposition has been fully confirmed in experiments.

The effect of medium and state of surface on fracture processes. The state of the surface of metal is one of the most important factors which can influence the results of mechanical tests of specimens in laboratory conditions. Small ridges and recesses in a poorly finished metal surface may serve as stress concentrators. They may play the role of brittle cracks and thus reduce appreciably the strength characteristics of the metal as measured in the tests. For instance, rock salt crystals, which are brittle under common conditions, become plastic upon immersion into warm water which dissolves the defective surface layer (Ioffe's effect). Careful polishing of the surface of metallic test pieces can result in higher ductility and strength characteristics of the metal measured in tensile tests.

The stress to rupture for a test piece with a rough surface can be raised by forming compressive stresses in the surface layer so as to prevent opening of surface cracks. This phenomenon is made use of for raising substantially the service life of metal parts by special methods of surface treatment: shot-blasting, roll forming and some procedures of heat treatment and chemical heat treatment.

The effect of the surrounding medium on the mechanical characteristics of a material may be either irreversible or reversible. In the latter case, the mechanical characteristics of the material are restored fully upon removal of the substance that has produced the surface effect. Corrosion cracking under stress is associated with an irreversible action of a chemically active medium and can cause the ductile-brittle transition even in f.c.c. metals and alloys which cannot be made brittle by other methods.

Non-dissolving liquid media containing surface-active substances may have a strong effect on the mechanical properties of metals. In that case, the active substance adsorbed on the surface of cracks changes the surface energy of the metal. The effect of easier deformation and fracture of solids in the presence of such substances is known as the Rebinder effect. If the adsorbed substance decreases the effective surface energy, the liability of the metal to brittle fracture increases and its rupture stress and flow stress can diminish to a small fraction of the initial values.

6. Effect of Hydrostatic Pressure on Fracture

As follows from the earlier discussion, tensile stresses are an essential condition for brittle or ductile fracture. Uniform compressive stresses or a high hydrostatic pressure diminish the tensile stresses in a deformed body and thus can suppress the process of crack initiation.

Suppose, for instance, that a crack has formed by rupture of a dislocation array intersecting the slip lines in a hexagonal single crystal (see Fig. 225*c*). Then, according to equation (163) at constant e,

G and L, the stress σ_r will reach the critical (rupture) value at a definite magnitude of shear stress:

$$\sigma_\tau = 1.3eG/\sigma_r L \tag{164}$$

The normal stress acting on the crack will now be changed due to a stress σ_{av}, appearing under external (non-hydrostatic) forces and normal to the crack plane, and to the uniform compressive stress ($-\sigma$, hydrostatic pressure), so that expression (164) will take the form

$$\sigma_\tau = 1.3eG/(\sigma_r + \sigma_{av} - \sigma)\, L \tag{165}$$

At $\sigma \to \sigma_r + \sigma_{av}$, we have $\sigma_\tau \to \infty$, i.e. the stress that causes dislocation movement and plastic deformation can increase infinitely and the formation of a crack becomes impossible at the stress

$$\sigma \geqslant \sigma_r + \sigma_{av}.$$

Considering the Stroh-Mott model [see formula (162)] for a crack formed due to the action of tensile stresses produced by a group of dislocations piled up before a barrier in a slip line, we come to a conclusion similar to (165). Under the effect of average stresses $\sigma_{av} = (\sigma_1 + \sigma_2 + \sigma_3)/3$ caused by external forces, the stress σ σ_i in equation (162) can either decrease ($\sigma_{av} < 0$) or increase ($\sigma_{av} > 0$). Under the action of the hydrostatic pressure σ, the magnitude of σ_{cr} diminishes

$$\sigma_{cr} = 2\,(L/3l)^{0.5}\,\sigma_\tau + \sigma_{av} - \sigma \tag{166}$$

If σ is sufficiently high and greater than the two first terms in the right-hand portion of equation (166), $\sigma_{cr} < 0$ and crack formation is impossible.

Thus, a high hydrostatic pressure σ can impede or fully suppress the process of initiation of fracture cracks during deformation.

It should be emphasized that the tensile stresses to initiate microcracks are close in their magnitude to the theoretical ultimate strength. For hydrostatic pressure σ to inhibit or impede substantially the process of crack initiation, it should be of the same order of magnitude as σ_r in expression (164) or σ_{cr} in (162), i.e. a stress $\sigma = -(1\,000\text{-}2\,000)$ MPa can only insignificantly retard the initiation of fracture cracks. In practice, however, an appreciable increase of the ductility of metals is also observed at pressures $|\sigma| < 1\,000$ MPa.

This suggests the conclusion that the delayed appearance of fracture cracks under the influence of hydrostatic pressure cannot be the main cause of increased ductility of metals which is observed in the range of relatively low pressures.

When a microcrack becomes a macrocrack in the course of its growth and attains the critical size, its further propagation occurs at relatively low tensile stresses whose magnitude is the real strength

limit of metals. The pressure $\sigma = -1\,000$ MPa is roughly equal to the stress required for development of a Griffith crack. One can naturally suppose that hydrostatic pressure plays an essential part in increasing the metal ductility exactly at the stage of propagation of an initial crack which has attained the critical size. Thus, a high hydrostatic pressure can not only impede the formation of Griffith cracks [see formulae (165) and (166)], but also prevent their propagation.

The positive effect of a high hydrostatic pressure also consists in 'healing' of microdefects existing in the metal, during plastic deformation. An experimental evidence of 'healing' is the fact that the density of the metal increases noticeably upon plastic deformation. The phenomenon of 'healing' has been well demonstrated experimentally. After plastic tension of pure copper specimens, the metal in the neck zone was infected with micropores and microcracks. The ductility of the metal was essentially exhausted. The metal in the zone mentioned was then deformed plastically in uniform compression. Complete 'healing' of pores and cracks was observed and the ductility of the metal in uniaxial tension restored to the initial value. Uniform hydrostatic compression of specimens without prior plastic deformation gave however no noticeable improvement in the number and size of defects.

B. I. Beresnev et al. give the following explanation to the phenomenon of 'healing' of defects in plastic deformation under the action of hydrostatic pressure. Hydrostatic pressure suppresses the forces which tend to open cracks and does not allow the latter to grow. This provides the possibility for the formation of contact 'bridges' between the opposite sides of a defect. High stresses in the point of contact and 'jumps' of particles from one side of the defect to the other form favourable conditions for restoring the continuity of the deformed metal by the mechanism similar to cold welding. In this process, the metal in the points of contact may be heated locally which is favourable for activation of diffusion processes. Local heating in the contact points may be due to local plastic deformation or to the surface energy liberated in the metal as the protrusions of a defect move to each other by a distance of an order of the crystal lattice parameter.

Strength characteristics in tension with application of hydrostatic pressure. There is an experimental proof that a hydrostatic pressure $\sigma < 2\,500$ MPa has no essential effect on the yield limit, flow stress and ultimate strength.

For instance, with simultaneous application of uniaxial compression and hydrostatic pressure up to 200 MPa to annealed specimens of cast steel, the yield limit of the steel remained constant and equal to 284 ± 5 MPa. With low-carbon steel specimens, an increase of pressure up to 300 MPa gave only a slight decrease of the upper yield limit, from 190 MPa to 180 MPa. With copper, tungsten and

low-carbon steel, the yield limit and the pattern of stress-strain curves remained unchanged up to $\sigma = 1\,000$ MPa.

These facts prove the validity of the Tresca yield criterion and Von Mises-Hencky criterion, well known in the theory of plasticity, provided that the hydrostatic pressure is sufficiently high. The validity of these yield criteria is confirmed by the constant intensity of shear stresses at any fixed value of strain in the region of uniform tension (before formation of a neck at various values of σ).

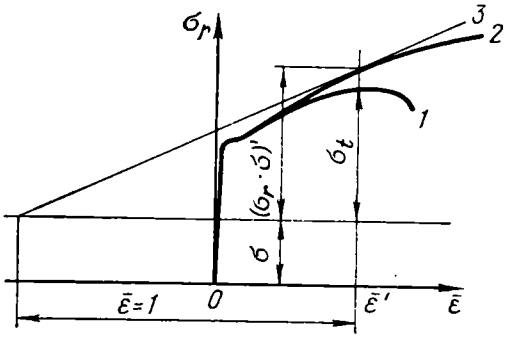

Fig. 231. Stress-strain diagram of low-carbon steel with application of hydrostatic pressure σ

1—conditional σ_{con}-$\bar{\varepsilon}$ diagram; *2*—actual $(\sigma_r$-$\sigma) = \sigma_{un} = f(\bar{\varepsilon})$ diagram; *3*—tangent to the actual curve at the point of the beginning of necking

A system of stresses consisting of transverse hydrostatic pressure σ and tensile stress σ_r is identical with two simultaneously applied stress systems of uniform hydrostatic pressure σ and uniaxial tension

$$\sigma_{un} = \sigma_r - \sigma$$

The load applied to the specimen

$$P = (\sigma_r - \sigma) F$$

where $F = F_0/e^{\bar{\varepsilon}}$ is the cross-sectional area of the specimen at deformation $\bar{\varepsilon} = \ln F_0/F$ and F_0 is the initial cross-sectional area, and the conditional stress

$$\sigma_{con} = P/F_0 = (\sigma_r - \sigma)/e^{\bar{\varepsilon}}$$

attain the maximum equal to the ultimate strength ($\sigma_{con.\,max} = \sigma_t$) at the point of necking at $\bar{\varepsilon} = \bar{\varepsilon}'$ (in the case considered, $P = P_{max}$), i.e.

$$\frac{d\sigma_{con}}{d\bar{\varepsilon}} = \frac{(\sigma_r - \sigma)' e^{\bar{\varepsilon}'} - e^{\bar{\varepsilon}'} \dfrac{d(\sigma_r - \sigma)'}{d\bar{\varepsilon}'}}{(e^{\bar{\varepsilon}})^2}\Bigg|_{\bar{\varepsilon}=\bar{\varepsilon}'} = 0 \qquad (167)$$

where $(\sigma_r - \sigma)' = \sigma_t \bar{\varepsilon}'$ is the actual stress at $\bar{\varepsilon} = \bar{\varepsilon}'$. The slope of the actual curve $(\sigma_r - \sigma)$-$\bar{\varepsilon}$ in the point $\bar{\varepsilon} = \bar{\varepsilon}'$, i.e. in the point of the highest conditional stress $\sigma_{con} = P/F_0$ (or the highest value of P) is (see Fig. 231):

$$\frac{d(\sigma_r - \sigma)'}{d\bar{\varepsilon}'} = \frac{(\sigma_r - \sigma)'}{1} \qquad (168)$$

With no hydrostatic pressure applied, expression (168) takes the form known in uniaxial tension $d\sigma_r'/d\bar{\varepsilon}' = \sigma_r' = \sigma_t \bar{\varepsilon}'$, i.e. when hydrostatic pressure is additionally applied, the whole stress-strain diagram is shifted by σ (see Fig. 231), while the yield limit, deform-

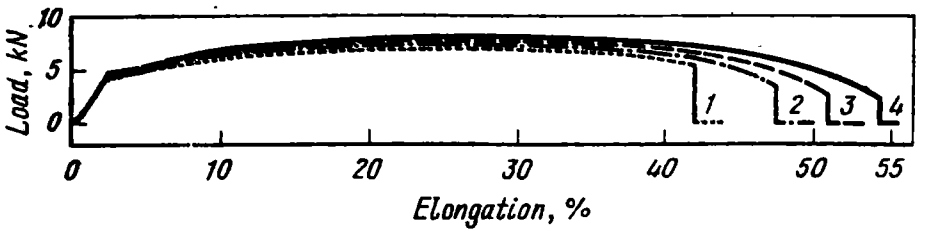

Fig. 232. Load-elongation curves for steel 20 at various pressures, MPa
1—0; *2*—400; *3*—600; *4*—700

ing stress, ultimate strength and the magnitude of uniform deformation at the beginning of necking, $\bar{\varepsilon}'$, remain unchanged. Thus, the shape of the conditional and actual stress-strain diagrams on application of hydrostatic pressure is the same as in uniaxial tension. Hydrostatic pressure does not increase the uniform deformation and does not retard the formation of a neck, but changes the length of the portion of non-uniform deformation in tension (Fig. 232) by increasing the highest deformation at fracture $\bar{\varepsilon}_r$, which is the measure of the metal ductility in uniaxial tension with additional application of hydrostatic pressure.

The actual diagrams in the coordinates actual stress—logarithmic strain are identical before necking (Fig. 233) and different at different pressures. The average actual stress in the neck first increases to the maximum (before fracture of the specimen) and then drops down to a very low value corresponding to the final fracture*. This drop of the stress upon attaining the maximum is associated with the formation of cracks which diminish the cross-sectional area of the specimen that withstands the load applied.

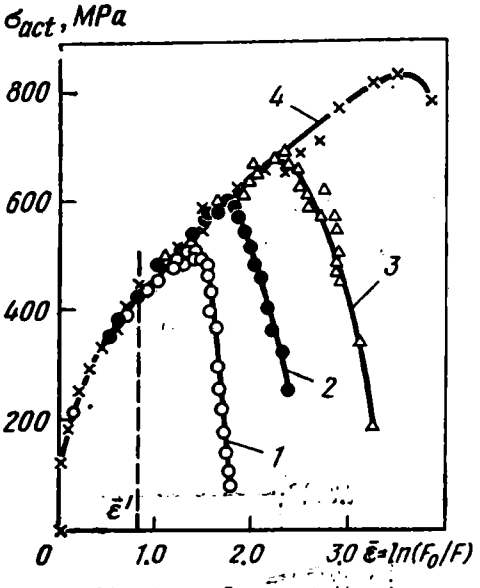

Fig. 233. Actual stress-strain curves for tensioned annealed oxygen-free copper at various pressures, MPa
1—0.1; *2*—78; *3*—157; *4*—113 ($\bar{\varepsilon}'$—deformation at the beginning of necking)

Numerous experiments with steel and tungsten have shown that hydrostatic pressure up to values of 1 000-2 500 MPa has no effect on the pattern of the actual stress-strain diagram, but, as in the case

* Diagrams of this type are obtained by measuring continuously the neck diameter (usually by high-speed photography) in 'stiff' testing machines, such as the Instron type.

of copper (see Fig. 233), only increases the deformation at fracture $\bar{\varepsilon}_r$.

Some published results of experiments on the effect of hydrostatic pressure on the pattern of actual stress-strain curves differ however from those just discussed. It has been established, for instance, that a hydrostatic pressure up to 220 MPa increases by 20-30 per cent the flow stress for bronze and a magnesium alloy with a slight rise in the degree of strain hardening, whereas in copper this increase of the flow stress is practically unnoticeable. Similar results have been obtained for brass and an aluminium alloy: their actual stress-strain curves shifted upwards with an increase of hydrostatic pressure at a constant value of the coefficient of strain hardening. According to some other results, the coefficient of strain hardening can either increase or decrease. The relationships obtained on the basis of experimental data are corrected mainly by using more advanced techniques of testing and measurements in tension with the application of hydrostatic pressure.

Most researchers agree with P. W. Bridgman that the actual tensile stress at rupture σ_r increases with increasing hydrostatic pressure (Fig. 234). It is an experimentally established fact that the actual average stress in the neck at rupture ($\sigma_r - \sigma$) is roughly constant and does not depend on pressure.

The effect of hydrostatic pressure on ductility of metals and alloys. Numerous experimental studies of the effect of hydrostatic pressure on the ultimate tensile strain at fracture, $\bar{\varepsilon}_r$, have shown that the ductility of metals increases on application of hydrostatic pressure and that four types of the $\bar{\varepsilon}_r$ (σ) relationship can be distinguished for various metals and alloys.

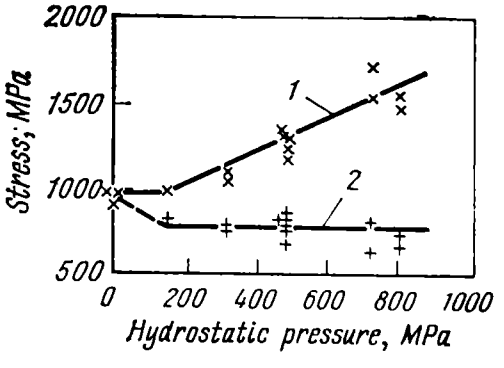

Fig. 234. (*left*) Effect of hydrostatic pressure on rupture stress in tension of low-carbon steel (0.085% C)
1—actual rupture stress σ_r; *2*—actual stress in the neck at rupture, $\sigma_r - \sigma$

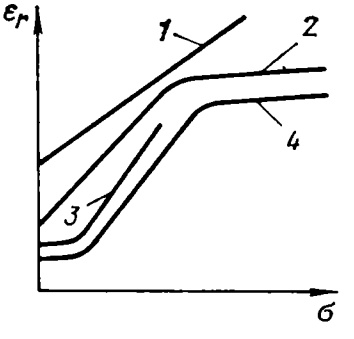

Fig. 235. Various shapes of $\bar{\varepsilon}_r$ (σ) relationship
1—linear; *2*—with saturation at $\sigma > \sigma_s$; *3*—with a threshold pressure σ_{th}; *4*—generalized relationship between pressure and ultimate ductility

The linear relationship $\bar{\varepsilon}_r$ (σ) (Fig. 235, curve *1*) has been found by Bridgman and then confirmed by other researchers. This type of the relationship has been established for carbon and stainless steels up to $\sigma = 1\,500$ MPa, duralumin Д16, and also for titanium up to $\sigma = 1\,200$ MPa.

The $\bar{\varepsilon}_r$ (σ) relationship of the type described by curve *2* in Fig. 235, with saturation upon increasing the pressure above a definite value, is observed in molybdenum, tungsten, and also in carbon steels at pressures above 1 500-2 500 MPa.

The appearance of a 'threshold' pressure σ_{th} (Fig. 235, curve *3*) was first detected in deformation of c.p.h. metals and explained by the development of other slip systems at $\sigma > \sigma_{th}$, in addition to slip in the basal plane. An increase in ε_r was attributed to the increased number of operative slip systems at $\sigma > \sigma_{th}$. Later experiments have shown however that the 'threshold' pressure σ_{th} also exists in deformation of chromium, molybdenum, tungsten and other very brittle metals and alloys.

B. I. Beresnev et al. take it for possible to describe the curves *1-3* in Fig. 235 by a generalized relationship including a 'threshold' pressure σ_{th} and 'saturation' pressure σ_s (Fig. 235, curve *4*). The threshold pressure can be determined approximately by the expression:

for *brittle metals*

$$\sigma_{th} = \frac{P}{F} - \left(\frac{2E\beta}{\pi l}\right)^{0.5} \tag{169}$$

and for *ductile metals*

$$\sigma_{th} = T\sqrt{3}\left(1 + \frac{r}{2R}\right) - \left(\frac{2E\beta}{\pi l}\right)^{0.5} \tag{170}$$

Ductile metals at atmospheric pressure break upon necking. In formulae (169) and (170), the second term on the right-hand side is the critical stress required for propagation of a fracture crack by the Griffith-Orowan theory; T is the average intensity of shear stresses in the neck of radius r of the test piece being tensioned; and R is the radius of curvature of the neck. For some ductile metals, the threshold pressure is not definitely pronounced, but for most metals and alloys formulae (169) and (170) agree well with the experimental data, with the magnitude of σ_{th} varying from 750 MPa for metalloceramic tungsten to 20 MPa for Grade Л68 brass. The $\bar{\varepsilon}_r$ (σ) relationships for selected metals and alloys are illustrated in Fig. 236. It can be stated upon analysis of these data that the type of the $\bar{\varepsilon}_r$ (σ) curve depends on the composition of a metal (alloy), its structure, presence of impurities, melting technology, and prior procedures of thermomechanical treatment. For instance, to attain the value $\bar{\varepsilon}_r = 2$, a pressure of 1 000 MPa is required for molybde-

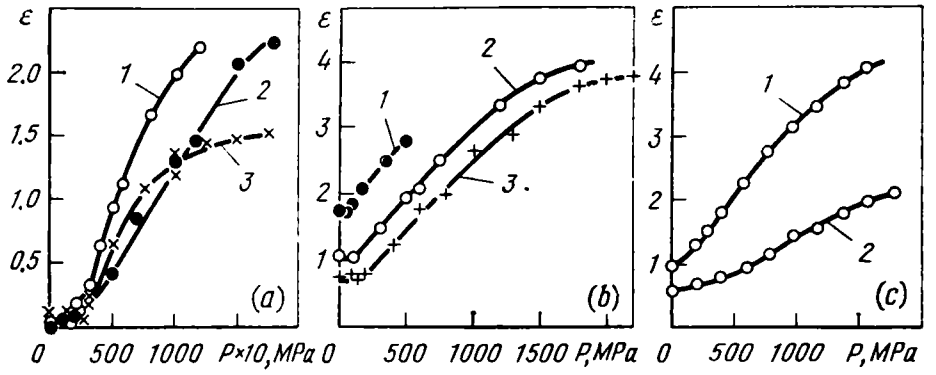

Fig. 236. Effect of hydrostatic pressure on maximum ductility $\bar{\varepsilon}_r$ of various materials

(*a*) molybdenum alloys (*1*—molybdenum МЧ; *2*—molybdenum MC; *3*—BM-1 alloy); (*b*) iron alloys (*1*—α-iron; *2*—steel with 0.46% C (modified); *3*—steel with 0.46% C (annealed)); (*c*) titanium alloys (*1*—BT1-1; *2*—BT5-1)

num Grade МЧ and 1 500 MPa for molybdenum Grade MC (see Fig. 236*a*).*

With BM1 alloy at $|\sigma| > 1\,000$ MPa, the ultimate ductility varies only slightly; with metalloceramic molybdenum MC, a slight decrease of the ultimate ductility and a decrease of $d\bar{\varepsilon}_r/d\sigma$ is observed only at 1 500 MPa. Since Grade MC molybdenum deforms uniformly to higher strains $\bar{\varepsilon}'$ than does BM1 alloy, it may be taken that the saturation pressure σ_s depends on the liability of a metal to localize strain in the neck: the stress σ_s is lower at a lower value of uniform deformation $\bar{\varepsilon}'$.

B. I. Beresnev and co-workers carried out interesting experiments with copper Grade M2 (99.96% Cu). Some specimens were tested under pressure after recrystallization annealing. Another portion of specimens was made of copper subjected to high-temperature creep which formed grain-boundary defects of the type of voids and cracks to simulate weak bond at grain boundaries of brittle metals. In deformation with hydrostatic pressure applied, the ductility of copper specimens with artificial defects rose to values close to those found in defectless metals. The authors have concluded from the results of these experiments that plastic deformation under pressure eliminates defects in brittle metals, which is one of the reasons why their ductility increases on application of hydrostatic pressure.

The reducing effect of hydrostatic pressure on the ductile-brittle transition temperature can be explained by reference to the diagram in Fig. 237. The transition temperature T_{tr} is determined by the point in which the temperature curve of rupture resistance (σ_r)

* Grade МЧ is commercially pure molybdenum (99.95% Mo) without special additives; molybdenum Grade MC contains Co (approx. 0.2 per cent); Grade BM1 is alloyed with titanium and zirconium (roughly 0.5 per cent each).

intersects the temperature curve of yield limit σ_y at atmospheric pressure. At atmospheric pressure and $T < T_{tr}$, a metal is brittle and $\sigma_r - \sigma = \sigma_0$, which is less than the value corresponding to the point O, Fig. 237; at $T > T_{tr}$, a metal is ductile and $\sigma_r - \sigma = \sigma_0$, which is greater than the value corresponding to the point O. The critical point O shifts to the position O' when hydrostatic pressure is applied and thus causes the transition temperature to be displaced into a lower temperature region. In a similar way, it can be concluded that the application of uniform tension $\sigma_0 = \sigma_r - \sigma_y$, which is greater than the value corresponding to the point O, causes the transition temperature to move into the region of higher temperatures (point O''). It has been proved experimentally that a hydrostatic pressure of 140 MPa shifts the ductile-brittle transition temperature of molybdenum from 50°C down to 2°C; at the same time, the stress to rupture increases by the magnitude of that pressure, i.e. by 140 MPa, which agrees well with the earlier considerations. The effect of hydrostatic pressure on transition temperature is described approximately by a linear equation (Fig. 238).

7. Criteria of Ductile Fracture

The liability of metals to ductile fracture cannot be characterized by a single criterion, say, by the stress criterion, for the following reasons.

In single crystals, fracture can occur at a constant shear stress component. It could be therefore supposed that a certain shear stress is a criterion of ductile fracture. It is known from practice, however, that uniform tension is realized in the core of the necked portion of a polycrystalline specimen in tension and it could be thus supposed that this uniform tension results in ductile fracture.

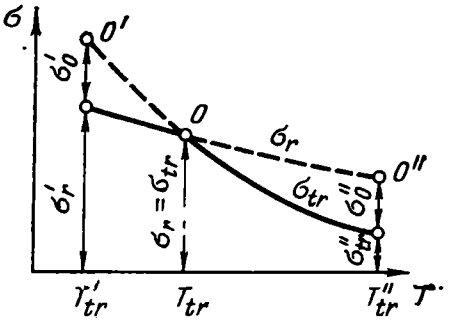

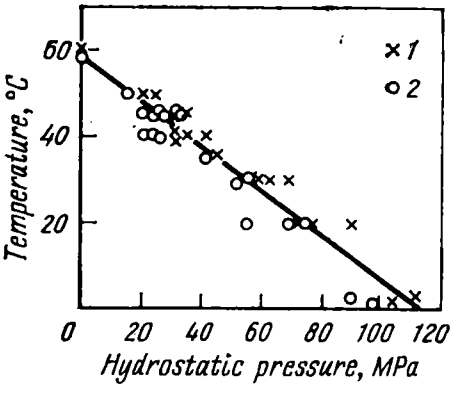

Fig. 237. (*left*) Effect of pressure on **ductile-to-brittle** transition temperature

Fig. 238. Effect of hydrostatic pressure **on ductile-to-brittle** transition temperature in zinc
1—ductile fracture; *2*—brittle fracture

On the other hand, if hydrostatic pressure is additionally applied in tension, the ultimate deformation to fracture increases quite appreciably, but the rupture stress increases only slightly, so that brittle metals exhibit ductile fracture with an appreciable deformation if hydrostatic pressure is applied. Considering the mechanisms of fracture from the standpoint of the theory of dislocations, I. A. Oding has noted that, since the interacting dislocation fields contain both shear and normal stresses, it is difficult to decide what stresses—tensile, compressive, or shear—are responsible for fracture. Shear stresses, which produce plastic deformation, increase the number of crystal lattice defects and the level of internal stresses which resist the external stresses applied and prepare the metal to fracture. Normal tensile stresses accelerate the fracture process, while normal compressive stresses, in particular the hydrostatic pressure applied, suppress the fracture process. Thus, a simple criterion of fracture associated with stresses is non-existent. Further, various experimental facts give evidence that a simple deformation criterion of ductile fracture would be erroneous for the following reasons.

On application of hydrostatic pressure, the contraction in the neck may sometimes be as large as 100 per cent, i.e. much greater than in common tensile tests; for that reason it is essential to specify the magnitude of hydrostatic pressure applied in addition to the magnitude of deformation.

The results of numerous experiments also show that the ultimate deformation at fracture depends on the concentration of defects of the type of micropores and micro- and macrocracks. These defects may either develop or be 'healed' depending on the conditions of deformation and the kind of stressed state. For instance, a twisted specimen subjected to tension fails at a lower rupture stress and exhibits a smaller reduction of the cross section, i.e. has a lower ductility. Thus, shears produced by prior twisting have caused the appearance of defects which open on application of tensile stresses. Similarly, a preliminarily tensioned specimen can be twisted in torsional tests to a smaller angle before fracture. The concentration of defects in a metal can be reduced if the specimen is subjected to sign-alternating torsion (twisted and untwisted) before the tensile test.

The experimental facts described show that for ductile fracture to be effected, it is essential to combine deformation with shear and tensile stresses and to consider the prior history of deformation and probable application of hydrostatic pressure.

Thus, it can be stated, not without reason, that the plastic deformation accumulated at all stages of the process up to fracture and depending on the hydrostatic pressure applied and the prior history of deformation, should be taken as the fracture criterion (see Ch. 13).

RECOMMENDED LITERATURE

1. Beresnev B. I., Martynov E.D., Rodinov K.P., et al. *Ductility and Strength of Solids at High Pressures.* Moscow, Nauka, 1970 (in Russian).
2. Bridgman P. W., *Studies in Large Plastic Flow and Fracture.* New York, McGraw-Hill, 1952.
3. Bulychev D.K., Beresnev B.I., Gaidunov M.G. et al. *Fizika Metallov i Metallovedenie* 18, No. 3 (1964) (in Russian).
4. McLean D., *Mechanical Properties of Metals and Alloys.* New York, John Wiley, 1962.
5. *Mechanical Behaviour of Materials under Pressure.* Ed. by H.L.D. Pugh. Amsterdam-London-New York, 1970.
6. Oding I. A., *Proceeding of the USSR Academy of Sciences. Engineering Sciences* 3: 4-16 (1960) (in Russian).
7. Ratner S.I., *ZhTF* 19, No. 3 (1949) (in Russian).

12 Resistance of Metals to Plastic Deformation

The strain resistance in uniaxial tension (or compression) σ_s is the flow stress, i.e. the actual stress that causes stable plastic flow under the given deforming conditions.

The flow stress σ_s is independent of the hydrostatic pressure applied, at least at $\sigma < 1000$ MPa (see Ch. 11) and, if the metal obeys Von Mises yield criterion, the strain resistance in a complex stressed state is the intensity of shear stresses T_s causing stable plastic flow under the given deforming conditions. Since

$$T = \frac{1}{\sqrt{6}} \times \sqrt{(\sigma_{11}-\sigma_{22})^2+(\sigma_{22}-\sigma_{33})^2+(\sigma_{33}-\sigma_{11})^2+6(\sigma_{12}^2+\sigma_{23}^2+\sigma_{31}^2)}$$

we have for uniaxial tension:

$$T_s = \sigma_s/\sqrt{3} = 0.577\sigma_s$$

For torsion of thin-walled tubular specimens, $T_s = \tau_s$, where τ_s is the flow stress in torsion.

Since σ_s, T_s and τ_s are actual stresses causing stable plastic flow, it is essential to establish their functional relationship with plastic deformations $\bar{\varepsilon}_{pl}$, $\bar{\Gamma}_{pl}$ and γ_{pl}, respectively. The actual stress-strain diagrams of the type σ-$\bar{\varepsilon}$, T-$\bar{\Gamma}$ and τ-γ are constructed for the total deformations $\bar{\varepsilon}$, $\bar{\Gamma}$, and γ which have an elastic and a plastic (residual) component.

The strain resistance (flow stress) is an important mechanical characteristic of deformed metal, since it determines to an appreciable extent the energy and kinematic parameters of the process. The energy parameters of the process depend practically linearly on strain resistance.

The strain resistance T_s (or σ_s) depends on the type of crystal lattice, chemical and phase composition of the metal, the amount of deformation ($\bar{\varepsilon}$); the temperature and rate of deformation (t, °C;

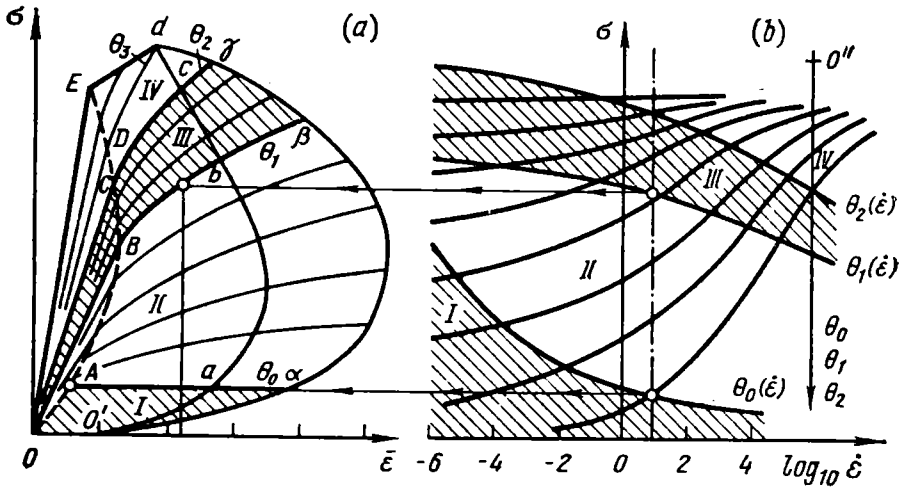

Fig. 239. The σ-$\bar{\varepsilon}$ diagrams for various homologous temperatures θ at $\dot{\bar{\varepsilon}}$=const (*a*) and the σ-$\dot{\bar{\varepsilon}}$ diagrams for various temperatures θ at $\bar{\varepsilon}$=const (*b*)
OABCDE—limiting state line corresponding to the yield limit; *abcd*—limiting state line corresponding to uniform elongation; *O'αβγd*—curve of fracture; *O''*—origin of critical temperatures $\theta_0(\dot{\varepsilon})$, $\theta_1(\dot{\varepsilon})$, $\theta_2(\dot{\varepsilon})$ which determine the development of regions *I-IV* ($\theta_0 > \theta_1 > \theta_2$)

$\dot{\varepsilon}$); the time history of deformation, $\varepsilon(\tau)$; the geometrical factor; and the surrounding medium.

The determination of T_s is, as a rule, associated with substantial difficulties in realization of mechanical tests in a complex stressed state. For that reason, simpler mechanical tests are employed in which it is possible to establish the relationship between the actual stress and logarithmic deformation in a monotonous process of plastic working. Torsion of thin-walled tubular specimens is a simple test, but the deformation process in it is not monotonous, so that this type of test is only seldom used for constructing T_s-$\bar{\Gamma}_{pl}$ diagrams, especially with heavy deformations. The most suitable tests are uniaxial tension and uniaxial compression in which the effect of friction forces is not substantial.

To construct a σ-$\bar{\varepsilon}$ diagram, tests are carried out at various deformation rates $\dot{\bar{\varepsilon}}$ and various homologous temperatures $\theta = T/T_{m.p.}$, where T, K, is the test temperature and $T_{m.p.}$, K, is the melting point of the metal. Using a σ-$\bar{\varepsilon}$ or a σ_s—$\bar{\varepsilon}_{pl}$ diagram, it is possible to construct a T_s-$\bar{\Gamma}_{pl}$ diagram for a complex stressed state. For uniaxial tension with $\bar{\varepsilon} \geqslant 6$ per cent (and Poisson's ratio $\mu \approx 0.5$), the following relationship holds true:

$$\bar{\Gamma}_{pl} = (2/\sqrt{6})\sqrt{(\bar{\varepsilon}_1 - \bar{\varepsilon}_2)^2 + (\bar{\varepsilon}_2 - \bar{\varepsilon}_3)^2 + (\bar{\varepsilon}_3 - \bar{\varepsilon}_1)^2} = \sqrt{3}\,\bar{\varepsilon}_{1pl}$$

The pattern of σ-$\bar{\varepsilon}$ diagrams varies substantially if they are plotted for various temperatures at $\bar{\varepsilon}$ = const or for various deformation rates at θ = const (Figs. 239, 240). Diagrams of this type have been

constructed by P. Ludwik and N. N. Davidenkov for explaining the ductile-to-brittle transition and used for analysis of the σ-ε diagrams and the corresponding limiting states at various temperatures and deformation rates.

The limiting states have been considered to be as follows: (1) the beginning of flow and the corresponding σ_y and ε_y; (2) the beginning of necking in tension (parameters σ' and $\bar{\varepsilon}'$), which characterizes the ability of metals and alloys to uniform physical strengthening along the length of tensioned specimens (see Fig. 231); (3) macrofracture of a specimen described by the parameters σ_{fr} and ε_{fr}; (4) temperature θ_2 and the corresponding deformation rate $\dot{\varepsilon}_2$ at the beginning of intensive and dynamic polygonization; (5) temperature θ_1 and the interrelated deformation rate $\dot{\varepsilon}_1$ of the beginning of dynamic recrystallization; (6) temperature θ_0 and deformation rate $\dot{\varepsilon}_0$ at which dynamic recrystallization has time to proceed completely.

Since it is possible, by the type of microstructure, to separate the parameters θ_i, ε_i, $\dot{\varepsilon}_i$ ($i = 0, 1, 2$) and $\theta_0 > \theta_1 > \theta_2$ at which either only polygonization takes place or dynamic recrystallization has time to proceed partially or completely, we can establish the interrelation (or combinations) of the parameters θ_0-$\dot{\varepsilon}_0$, θ_1-$\dot{\varepsilon}_1$ and θ_2-$\dot{\varepsilon}_2$ which will correspond to complete hot, incomplete hot or warm plastic working.

The indicated limiting state parameters naturally depend on the same factors as the strain resistance σ_s. Their relationships with

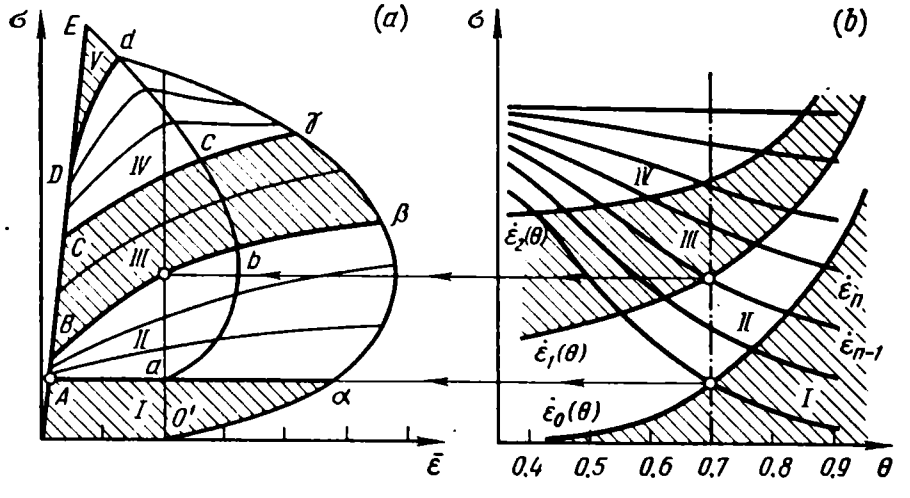

Fig. 240. The σ-$\bar{\varepsilon}$ diagrams at θ = const (*a*) and the σ-θ diagrams at $\bar{\varepsilon}$ = const (*b*) at various deformation rates $\dot{\varepsilon} = 10^{-5}$ to 10^{5} s^{-1}

A, *B*, *C*, *D*—points corresponding to the yield limit in each region; *abcd*—curve of uniform elongation; $O'\alpha\beta\gamma d$—curve of limiting state at fracture; $\dot{\varepsilon}_0(\theta)$, $\dot{\varepsilon}_1(\theta)$, $\dot{\varepsilon}_2(\theta)$ — curves of critical deformation rates determining the development of regions *I-V*

deformation conditions and the form of the σ_s-θ-$\bar{\varepsilon}$-$\dot{\varepsilon}$ diagram are often very intricate and have a number of anomalies (see p. 383). For some pure metals and alloys exhibiting no anomalies, however, the diagrams σ_s-θ, σ_s-$\dot{\varepsilon}$, σ_s-$\bar{\varepsilon}$ have the forms shown schematically in Figs. 239 and 240.

1. General Characteristic of σ_s-θ-$\bar{\varepsilon}$-$\dot{\varepsilon}$ Diagrams

For analysis of the strain resistance as a function of the temperature and the rate of deformation, $\sigma_s = \sigma_s(\bar{\varepsilon}, \dot{\varepsilon}, \theta)$, the original experimental data are represented in the form of σ-$\bar{\varepsilon}$ curves taken at various homologous temperatures with $\dot{\varepsilon} = \text{const}$ (see Fig. 239*a*) or at various deformation rates with $\theta = \text{const}$ (see Fig. 240*a*).

Region I in the diagrams of Figs. 239*a* and 240*a* is the region of completed dynamic recrystallization at deformation temperatures $\theta \geqslant \theta_0$ and deformation rates $\dot{\varepsilon} \leqslant \dot{\varepsilon}_0$. In that case, the absorbed (latent) energy is not increased with increasing deformation, so that $\sigma_s = \text{const}$ ($\partial\sigma_s/\partial\bar{\varepsilon} = 0$) at constant values of θ and $\dot{\varepsilon}$ and does not depend on the amount of deformation, too. The metal behaves as an ideally plastic medium for which σ_s decreases at higher temperatures and lower deformation rates. The deformation rate $\dot{\varepsilon}_0$ below which dynamic recrystallization can proceed completely is a function of homologous temperature: $\dot{\varepsilon}_0 = \dot{\varepsilon}_0(\theta)$ (Fig. 240*b*) and is higher at higher θ. At low homologous temperatures, dynamic recrystallization becomes impossible even at very low deformation rates comparable with creep rate.

The deformation rate $\dot{\varepsilon}_0$ at various homologous temperatures (see Fig. 240*b*) can be established by the type of fracture: with $\dot{\varepsilon} < \dot{\varepsilon}_0$, fracture is intercrystalline; with $\dot{\varepsilon} > \dot{\varepsilon}_0$, the proportion of transcrystalline fracture increases progressively.

Except for region *I*, all other regions in the σ-$\bar{\varepsilon}$ diagram can be characterized by that the ratio $\partial\sigma/\partial\varepsilon \neq 0$ and the absorbed energy increases with increasing deformation.

Region II (partial dynamic recrystallization*) is within the temperature range $\theta_1 < \theta(\dot{\varepsilon}) < \theta_2$ and the deformation rate range $\dot{\varepsilon}_2 < \dot{\varepsilon}(\theta) < \dot{\varepsilon}_1$. In this region, deformation rate has the most marked effect on strain resistance, plasticity, and generally on the pattern of the σ-$\bar{\varepsilon}$ curve. In this region, intensive softening, due to dynamic polygonization and recrystallization, can occur in

* The process of plastic working with partial dynamic recrystallization was formerly called 'incomplete hot plastic working'.

parallel with strengthening. With an increase of deformation temperature (see Fig. 239*a*), the value of $\partial\sigma/\partial\varepsilon$ (intensity of strengthening) diminishes. With a higher rate of deformation, there is less time for occurrence of dynamic softening processes, and for that reason the temperatures of the beginning and end of recrystallization rise and region *II* becomes narrower. The boundary between regions *II* and *III* at a given temperature and amount of deformation is also determined by the deformation rate $\dot{\varepsilon}_1$ (see Fig. 240*b*) at which recrystallization cannot follow the processes of deformation and hardening. At low homologous temperatures, $\dot{\varepsilon}_1$ is quite low, since appreciable interval of time is needed for dynamic recrystallization to occur. At higher homologous temperatures, $\dot{\varepsilon}_1(\theta)$ increases (see Fig. 240*b*).

Region III lies within the temperature range $\theta_2 < \theta(\dot{\varepsilon}) < \theta_1$ and deformation rate range $\dot{\varepsilon}_1 < \dot{\varepsilon}(\theta) < \dot{\varepsilon}_2$. In this case, the effect of deformation rate on strain resistance (i.e. the value of $\partial\sigma/\partial\dot{\varepsilon}$) is smaller than in region *II* (see Fig. 239*b*). At $\theta = \text{const}$ (see Fig. 240*a*), stress-strain curves are roughly parallel to one another. In this range, dynamic polygonization can take place. Under the temperature and rate conditions of this region, incomplete cold, or 'warm', plastic working can be realized. Naturally, the temperatures θ_1 and θ_2 rise with increasing deformation rate, when there is not enough time for dynamic polygonization (see Fig. 239*b*). A lower deformation rate gives a wider temperature interval $(\theta_2 - \theta_1)$ in which polygonization processes can occur (see Fig. 239*b*). With an increase of deformation temperature θ, the critical deformation rate $\dot{\varepsilon}_2$ increases (see Fig. 240*b*). At a given temperature $\theta = \text{const}$, $\dot{\varepsilon}_2 > \dot{\varepsilon}_1 > \dot{\varepsilon}_0$, since the process of prerecrystallizational dynamic polygonization has enough time to proceed at high deformation rates, while dynamic recrystallization, which is characterized by the critical deformation rate $\dot{\varepsilon}_1$, has no time for its realization.

Region IV is the region of cold plastic working. With an increase of deformation rate and further reduction of temperature in this region (see Figs. 239*a* and 240*a*), softening processes are not realized and strain resistance can increase only due to inertia effects at high deformation rates. The plasticity of the metal decreases compared with that it had in regions *I* and *II*, since deformation is localized (a neck forms). An additional stress field superposed on the main field leads to non-uniform distribution of stress and strain along the length of a tensioned specimen: they concentrate near the moving grip of the testing machine. This is why specimens in impact tension are fractured closer to the point of load application. In this region, high-speed cold deformation is observed. A region

of complete cold deformation is also observed in a temperature interval near the ductile-to-brittle transition. Below these temperatures (see Fig. 239*a*), brittle fracture takes place and the plasticity of a metal is at its minimum.

Region V (see Fig. 240*a*) relates to very high deformation rates $\dot{\varepsilon} \approx (10^7\text{-}10^8)\ s^{-1}$ and is characterized by brittle fracture.

The σ_{ss} (θ) relationship. An exponential temperature relationship for strain resistance (see Fig. 240*b*) has been first proposed by N. S. Kurnakov and confirmed experimentally by S. I. Gubkin. Using the principles of thermodynamics of irreversible processes, M. A. Zaikov [8] has obtained a theoretical exponential relationship between temperature and strain resistance:

$$\sigma_s = \sigma_0 \exp(-bT) \quad (171)$$

$$\sigma_s = \sigma_{m.p.} \exp[bT_{m.p.}(1 - \theta)] \quad (172)$$

where σ_0 and $\sigma_{m.p.}$ is the strain resistance extrapolated to 0°C and to the melting point, respectively, and b is the temperature coefficient depending on the amount, rate and temperature of deformation, chemical composition and microstructure of the metal, and the type of crystal lattice.

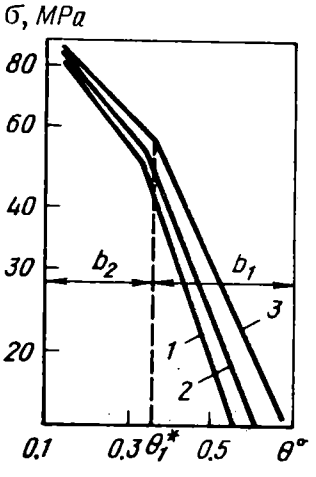

Fig. 241. Effect of temperature on flow stress (strain resistance) of thallium at $\varepsilon = 0.4$ and various deformation rates $\dot{\varepsilon}$, s^{-1}: *1*—2×10^{-3}; *2*—2×10^{-2}; *3*—2×10^{-1}

A similar relationship has been found for the flow stress controlled by the movement of thermally activated double kinks. The temperature relationship for the flow stress controlled by intersection of dislocation forest (see Fig. 123) has also confirmed the fact that the strain resistance-temperature relationship can well be described by an exponential function. The dislocation theory, however, suggests a more intricate shape of σ_s (θ) relationship. As has been established in later studies, relationships (171) and (172) are valid for pure metals only in rather narrow ranges of temperatures ($\theta \approx \approx 0.4\text{-}0.8$) and deformation rates. An evidence in support of this is the appearance of inflections on linear ln σ_s-θ and log σ_s-θ curves. These inflections are associated with the temperature of the beginning of dynamic recrystallization θ_1 (Fig. 241) which shifts towards higher temperatures as the rate of deformation decreases [see $\dot{\varepsilon}_1$ (θ) curve in Fig. 240*b*]. In that case, the exponent b takes on a value b_2 for the temperature range $\theta < \theta_1$ and b_1 for $\theta > \theta_1$. The values of b_1 and b_2 are higher at a lower deformation rate (the slope of σ_s-θ curves in Fig. 240*b* increases with decreasing deformation rate). With an increase of homologous temperature, b_1 and b_2 diminish,

as also does the slope of σ_s-θ curves (see Fig. 240*b*), especially at lower deformation rates (see Fig. 241). The effect of the amount of deformation turns out to be complicated: at heavier deformations, b_1 increases and b_2 decreases.

The σ_s-$\dot{\varepsilon}$ relationship. This relationship is determined to an appreciable extent by the relation between the competing processes of hardening and softening. At a higher deformation rate, there is less time for the occurrence of softening processes, which results in a higher yield limit (see Fig. 240*a*) and higher flow stress (strain resistance).

The principal experimentally established fact that agrees well with the dislocation theory is that strain resistance increases with increasing deformation rate (see Fig. 240). Exceptions from this rule are the anomalies analysed in Sec. 2 of this chapter.

As the rate of deformation (in the range of high deformation rates $\dot{\varepsilon} > (10^3\text{-}10^5)\ s^{-1}$) increases, strain resistance will either increase or remain unchanged. This is an evidence that softening processes have no time to occur in high-speed cold plastic working, so that strain resistance is practically independent of deformation rate. Exceptionally high deformation rates can cause anomalous changes in the σ_s-$\dot{\varepsilon}$ diagram due to the effect of inertia phenomena which increase the strain resistance in region *V* (see Fig. 240*a*). In some cases where inertial effects are still insignificant, an anomalous change of the σ_s-$\dot{\varepsilon}$ diagram may be associated with what may be called the adiabatic effect. In that case, the deformed metal is heated strongly and, as a consequence, its strain resistance decreases with increasing deformation rate. In other cases (except for the anomalies discussed in Sec. 2 of this chapter), the σ_s-$\dot{\varepsilon}$ curve is essentially of the form illustrated in Fig. 239*b*.

The dependence of strain resistance on deformation rate, σ_s-$\dot{\varepsilon}$, which varies strongly with the temperature of deformation, can be described by the equations:

$$\sigma_s = a\dot{\varepsilon}^n \tag{173}$$

$$\sigma_s : \sigma_0 = (\dot{\varepsilon} : \dot{\varepsilon}')^n \tag{174}$$

$$\sigma_s = \sigma_0 + c \ln (\dot{\varepsilon} : \dot{\varepsilon}') \tag{175}$$

where σ_s and σ_0 is the flow stress (strain resistance) at deformation rates $\dot{\varepsilon}$ and $\dot{\varepsilon}'$, respectively; n is a speed exponent; c is a speed coefficient which depends on temperature, amount and rate of deformation, but remains constant within a given range of deformation conditions.

The exponent n $(0 < n \leqslant 1)$ characterizes qualitatively the extent of softening and is greater at a higher contribution of softening processes. It increases at higher temperature and lower deformation rate. Taking $n = 1$ in formulae (173) and (174), we obtain the law of viscous flow with full completion of dynamic recrystallization (complete hot plastic working). Linear viscous flow is true of region *I* in Figs. 239 and 240. In that case, the intensity (rate) of softening is time-independent and proportional to the stress applied; the rate of deformation is quite low and is less than the rate of softening. This results in viscous flow occurring preferably on grain boundaries, say, by the Herring-Nabarro mechanism. Formulae (173) and (174) are also valid at higher deformation rates. In that case, $n < 1$ and softening is controlled by dynamic processes of recrystallization and polygonization. At still higher deformation rates, the σ_s-$\dot{\varepsilon}$ relationship is described by equation (175) and the process is controlled by the mechanism of dynamic polygonization only which gives a relatively low softening effect.

As has been noted, the linear σ_s-log $\dot{\varepsilon}$ relationship (175) agrees satisfactorily with the results of experiments in the region of low homologous temperatures (for instance, aluminium at room temperature). At higher temperatures, experimental curves in these coordinates bend upwards from the straight line. They can be rectified if plotted in the logarithmic coordinates log σ_s-log $\dot{\varepsilon}$, i.e. the law of variation of strain resistance will be described by (173) and (174). Relationships of this type (see Fig. 242*b*) have been obtained by many researchers, in particular by N. P. Ageev, M. A. Zaikov, L. D. Sokolov et al.

The coefficient n increases with increasing temperature (see Figs. 242*b* and 239*b*, where $\left.\frac{\partial \sigma_s}{\partial \dot{\varepsilon}}\right|_{\theta_a} > \left.\frac{\partial \sigma_s}{\partial \dot{\varepsilon}}\right|_{\theta_b}$ at $\dot{\varepsilon} = \text{const}$ and $\theta_a > \theta_b$). At high homologous temperatures $\theta > \theta_1$, n is higher on heavier deformations and, on the contrary, when $\theta < \theta_1$, n decreases with increasing deformation. At low homologous temperatures, $\theta < \theta_2$, an increase of deformation has practically no effect on the σ_s-$\dot{\varepsilon}$ relationship.

Analysis of numerous experimental results obtained by various researchers has shown that the linear relationship log σ_s-n log $\dot{\varepsilon}$ holds true satisfactorily for a particular value of n at relatively low values of $\theta = 0.3$-0.55 and for a different value of n at higher homologous temperatures $\theta = 0.55$-0.8 and any amount of deformation. Thus, two regions can be distinguished in the log σ_s-log $\dot{\varepsilon}$ diagram: (1) region with a high n_1 in which recrystallization and hardening processes occur simultaneously and (2) region with a low n_2, in which hardening occurs simultaneously with dynamic polygoniza-

tion. For every metal, there is a particular combination of θ and deformation ε at which a linear portion with a higher $n = n_1$ of the log σ_s-log $\dot{\varepsilon}$ diagram changes to another linear portion with a lower $n = n_2$ (Figs. 242-244). The point in the log σ_s-log $\dot{\varepsilon}$ diagram

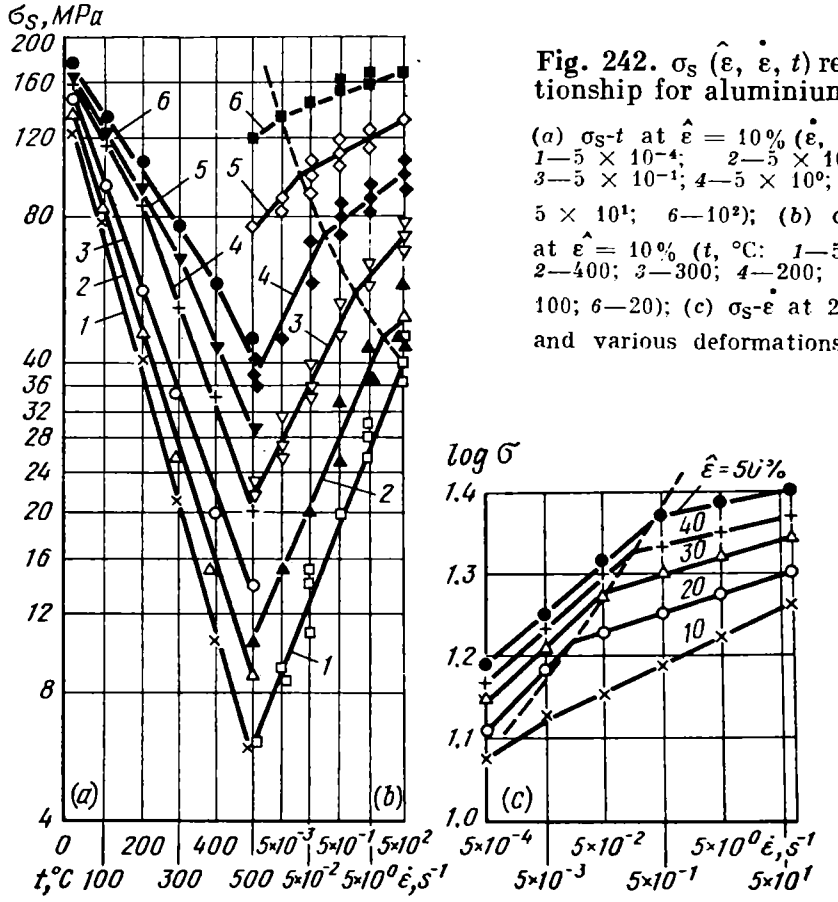

Fig. 242. σ_s ($\hat{\varepsilon}$, $\dot{\varepsilon}$, t) relationship for aluminium

(a) σ_s-t at $\hat{\varepsilon} = 10\%$ ($\dot{\varepsilon}$, s^{-1}: *1*—5×10^{-4}; *2*—5×10^{-3}; *3*—5×10^{-1}; *4*—5×10^{0}; *5*—5×10^{1}; *6*—10^{2}); (b) σ_s-$\dot{\varepsilon}$ at $\hat{\varepsilon} = 10\%$ (t, °C: *1*—500; *2*—400; *3*—300; *4*—200; *5*—100; *6*—20); (c) σ_s-$\dot{\varepsilon}$ at 20°C and various deformations $\hat{\varepsilon}$

where $n' = n_1 = n_2$ (Fig. 242*b*) corresponds to the critical deformation rate $\dot{\varepsilon}_1$ ($\bar{\varepsilon}$, θ) which separates region *II* from region *III* (see Fig. 243*b*). Naturally, if the temperature of deformation is raised, the critical rate point $\dot{\varepsilon}_1$ is shifted towards higher deformation rates (see Figs. 240*b* and 242*b*). The dependence of $\dot{\varepsilon}_1$ (θ) for the critical deformation rate can be approximated by a linear equation (Figs. 243, 244): $\log \dot{\varepsilon}_1 = a_1 + b_1\theta$, where a_1 ($\bar{\varepsilon}$) and b_1 ($\bar{\varepsilon}$) are coefficients depending on the amount of deformation; as may be seen from Fig. 243, they are practically constant for a number of metals.

With a heavier deformation (see Fig. 242*c*), recrystallization processes are intensified and the critical deformation rate $\dot{\varepsilon}_1$, as in the case of increasing deformation temperature, is shifted rightwards, i.e. towards higher deformation rates.

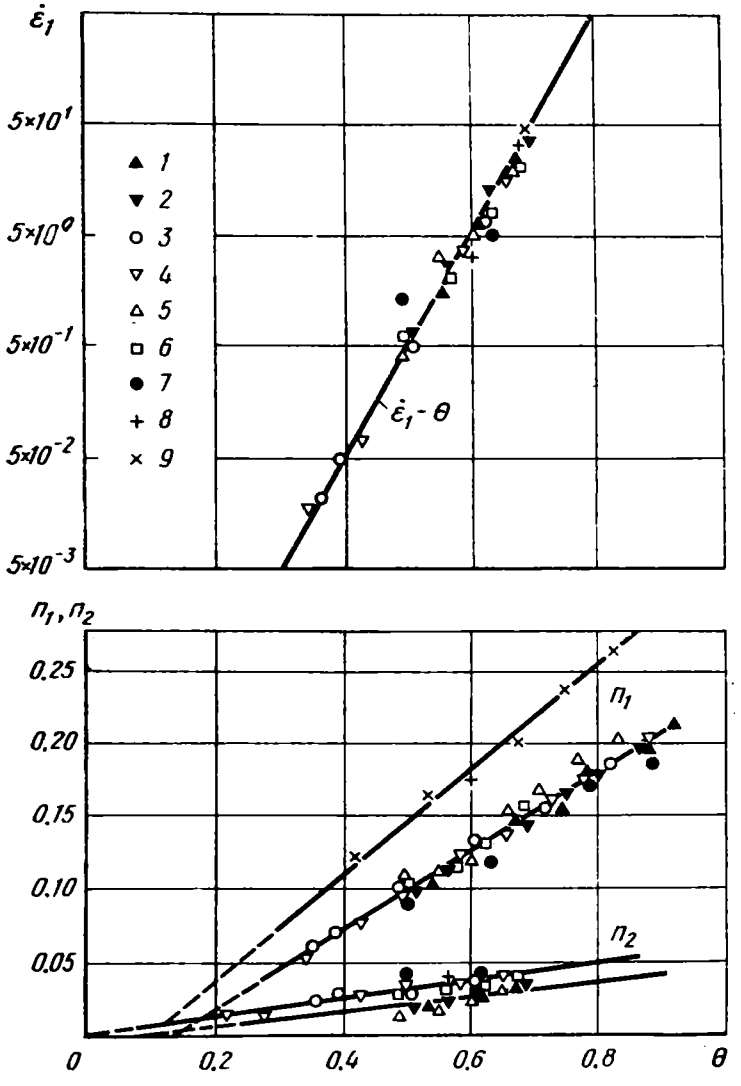

Fig. 243. Effect of homologous temperature on critical rate $\dot{\bar{\varepsilon}}_1$ and speed coefficients n_1 and n_2 of metals and carbon steels at deformation 20% (M. A. Zaikov)
1—steel У10; *2*—steel 5; *3*—aluminium; *4*—copper; *5*—steel 3; *6*—nickel; *7*—lead; *8*—tin; *9*—zinc

The value of n_1 for the steeper branches of $\log \sigma_s = n_1 \log \dot{\bar{\varepsilon}}$ curves increases with increasing temperature; the same is true of the coefficient n_2 (see Fig. 242), while the relationship $n(\theta)$ can be represented by two straight lines (see Fig. 244): (1) $n_2 = m_2\theta$ in the temperature range $\theta_1 \geqslant \theta > 0$ and (2) $n_1 = n' + m_1(\theta - \theta_1) = m_1\theta - k_1$ in the range $\theta_1 \leqslant \theta < 1$. The coefficients m_1, m_2 and k_1 depend on the amount of deformation and the nature of metal (Table 13).

Thus, the combination of the critical values $\dot{\bar{\varepsilon}}_1$ and θ_1 at a given amount of deformation corresponds to the transition from region *II*

(incomplete hot plastic working) to region *III* [incomplete cold ('warm') plastic working], as may be seen in Figs. 239 and 240.

It should be emphasized that the linear n (θ) relationships given above are valid only in a relatively narrow range of homologous temperatures: $\theta = 0.4$-0.8 and deviate from linearity in a wider temperature range. Since, however, the range $\theta = 0.4$-0.8 is typical of most plastic working processes, the principal conclusions and methods of calculation of strain resistance proposed by L. D. Sokolov and M. A. Zaikov on the basis of linearization are quite applicable in engineering practice.

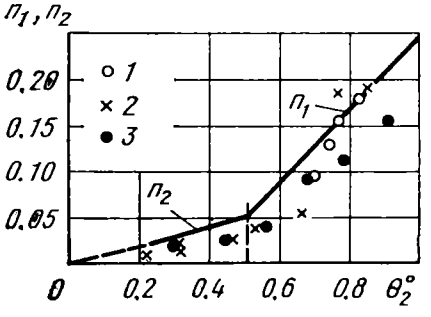

Fig. 244. Effect of homologous temperature on speed coefficients n_1 and n_2 at deformation 40%
1—aluminium; *2*—copper; *3*—steel

The value of σ_s can be influenced substantially by the anomalies of the temperature and speed relationships. In such cases, σ_s will deviate substantially from the ideal relationships valid for most metals and alloys and analysed in this section. Analysis of these anomalies, with regard to the type of crystal lattice and chemical composition of metal will be done in the next section.

Table 13. Coefficients m_1, m_2, and k_1

Metal	Sn	Zn	Pb, Al, Cu	Steels: Ст. 3, Ст. 5, У10*
		$\hat{\varepsilon} = 10\%$		
m_1	0.33	0.33	0.228	0.228
m_2	0.815	0.815	0.815	0.064
k_1	0.03	0.275	0.03	0.03
		$\hat{\varepsilon} = 20\%$		
m_1	0.365	0.365	0.278	0.278
m_2	0.061	0.061	0.061	0.044
k_1	0.036	0.324	0.039	0.039
		$\hat{\varepsilon} = 30$-50%		
m_1	0.382	0.382	0.302	0.302
m_2	0.0456	0.0456	0.0456	0.0282
k_1	0.0382	0.0376	0.0422	0.0422

* Homologous temperature of steels has been determined by the solidus line on the Fe-Fe_3C constitutional diagram; the melting point, °C, of these steels is taken respectively to be 1500, 1450 and 1330.

2. Effect of Type of Crystal Lattice, Chemical Composition and Structure of Metal on Strain Resistance

The difficulties associated with determination of the strain resistance are quite evident. For that reason, the strain resistance will be characterized in this section in terms of the yield strength, ultimate strength and also the hardness (*HB*), since, as has been established, there is a definite correlation between the ultimate strength and hardness of a metal. This seemingly will not change qualitatively the general conclusions on the effects of the group of factors mentioned on flow stress.

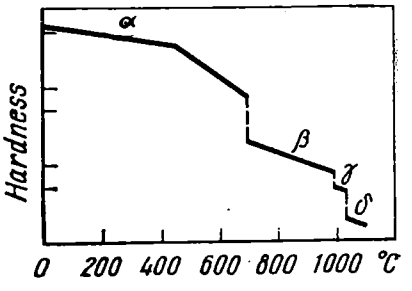

Fig. 245. Effect of temperature on hardness of manganese

Non-monotonous σ_s-θ relationship. This relationship is observed to be non-monotonous mainly at temperatures of polymorphous transformations (Fig. 245) when the hardness and strength of a metal change abruptly. For metals undergoing no allotropic transformations, the σ_s-θ curves will have inflection points (see Sec. 1), which can be explained by polygonization and recrystallization phenomena. Similar phenomena are observed in polymorphous metals whose σ_s-θ curves show up discontinuities at the temperatures of polymorphous transformations and inflections at some other temperatures. In some cases, the temperature of recrystallization may be close to the point of polymorphous transformation, and therefore, an inflection point on the σ_s-θ curve will coincide with a discontinuity.

Polygonization and recrystallization are factors which determine changes in the slope of lines on the diagram (Fig. 246). The temperature of recrystallization can however change substantially in the presence of alloying additions (see Ch. 7). This is an evidence that the σ_s-θ diagrams are sensitive to the composition of a metal and the temperature of recrystallization.

Some metals of commercial purity exhibit a strain-ageing 'hump' on the σ_s-θ diagram in the temperature range $\theta_{sa} = 0.2\text{-}0.5$ (Figs. 246, 247); for b.c.c. metals, θ_{sa} is lower ($\theta_{sa} = 0.2\text{-}0.28$) than that for c.p.h. metals ($\theta_{sa} = 0.35\text{-}0.4$).

Electron-microscopic analysis has shown that, for the same amount of deformation, the dislocation density in the temperature range of strain-ageing (i.e. in the process of what is called 'dynamic strain ageing') is higher than in cold deformation with subsequent heating to θ_{sa} (i.e. in 'static strain ageing'). Dynamic strain ageing is the result of the formation of atmospheres from interstitial atoms (carbon and nitrogen in iron and additionally oxygen in tungsten,

molybdenum and chromium) around moving and multiplying dislocations. Due to diffusion, which is facilitated as the deformation temperature rises up to θ_{sa}, interstitial atoms form atmospheres around the dislocations created in plastic deformation. Atmospheres lock the movement of newly formed dislocations, i.e. the concentration (density) of locked dislocations increases compared with their concentration in cold deformation, resulting in a higher strain-ageing effect than that obtained in cold deformation and subsequent heating to θ_{sa}.

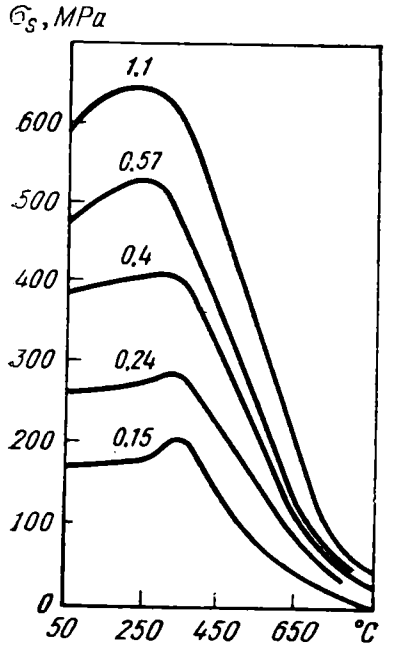

Fig. 246. Effect of temperature on ultimate strength of carbon steels. Numbers at curves—carbon content, %

Since the probability of appearance of impurity atmospheres around new (multiplied in deformation) dislocations is determined by the relation between speeds of dislocation movement and diffusion of interstitial atoms, an increase in dislocation density will depend on the temperature and rate of deformation. At $\theta > \theta_{sa}$, dislocations become more mobile due to a high diffusion mobility of interstitial atoms. For that reason, the strain resistance is observed to drop down sharply at $\theta > \theta_{sa}$ (see Fig. 247). At a higher deformation rate, the diffusion mobility of interstitial atoms turns out to be insufficient for locking

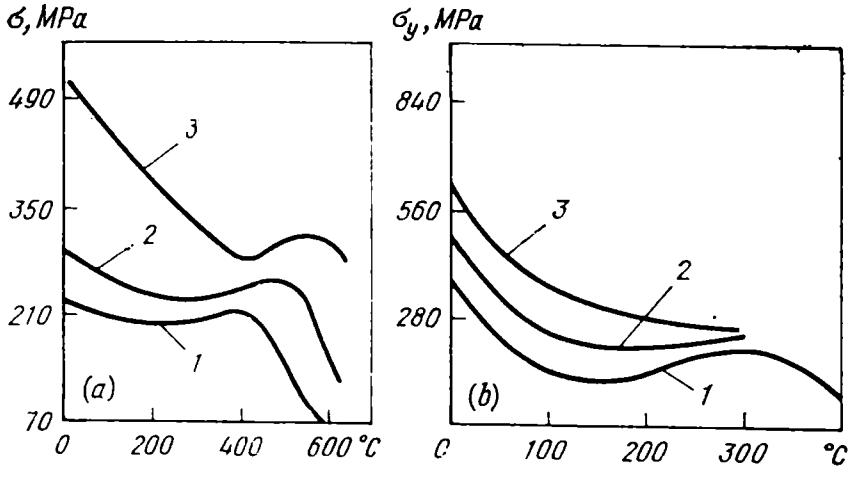

Fig. 247. Effect of temperature on σ_y of various materials

(*a*) low-carbon steel ($\dot{\varepsilon}$, s^{-1}; *1*—8.5×10^{-4}; *2*—0.5; *3*—3×10^{2}); (*b*) molybdenum ($\dot{\varepsilon}$, s^{-1}: *1*—2.8×10^{-4}; *2*—4×10^{-3}; *3*—0.17)

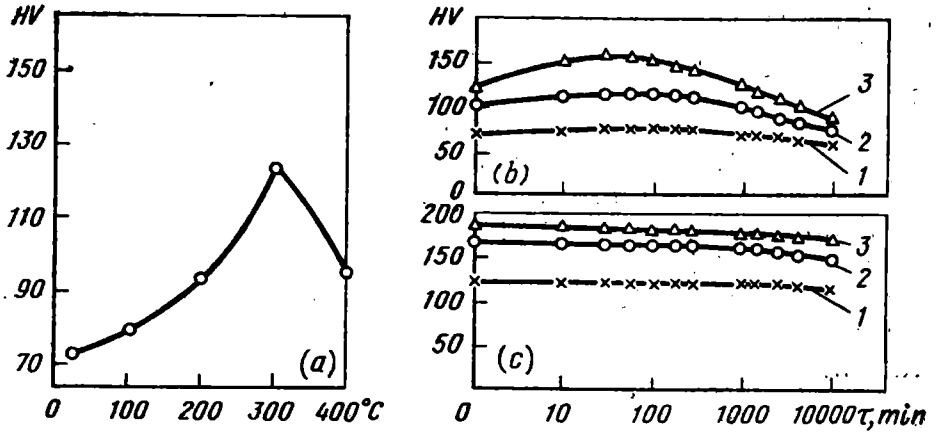

Fig. 248. *HV* **hardness** of commercial pure iron (0.02% C) as a function of: temperature of rolling with 4-% reduction (*a*); time when heated to 300°C from cold deformed state (*b*); and time when rolled at the optimal temperature 300°C (*c*). (ε_r, %: *1*—4; *2*—13; *3*—20).

new dislocations which now move at a higher speed. Thus, as the rate of deformation increases, the strain-ageing peak may be displaced towards higher temperatures or disappear (see Fig. 247).

The improving effect of dynamic strain ageing on mechanical properties is utilized in 'warm' plastic working (see region *III* in Figs. 239 and 240). The temperature and rate of deformation should however be selected properly and controlled quite accurately. For instance, the values of hardness, and therefore, of strength can be increased two times or even more by using controlled warm plastic working (Fig. 248). In the example considered, the original hardness is 72 *HV* and that after plastic working, 180 *HV*.

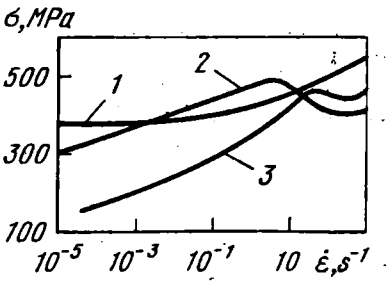

Fig. 249. Effect of deformation rate at various temperatures on strain resistance of low-carbon steel. The curves have distinct maxima due to dynamic strain ageing
1—20°C; *2*—400°C; *3*—500°C

The maximum of flow stress on strain ageing in b.c.c. metals is observed (Fig. 249) at lower homologous temperatures than in f.c.c. and c.p.h. metals, which can be explained by differences in the interaction of dislocations with solute atoms and the speed of diffusion of impurities in lattices of various types.

The tetragonality produced in a b.c.c. lattice by intersticed atoms results in that the stress field of an intersticed atom begins to interact with the normal and shear stress fields of dislocations, which ensures interaction of interstitial impurities with screw and edge dislocations. In an f.c.c. lattice, interstitial atoms produce preferably a spherically symmetrical distortion, and the stress field

of an interstitial atom cannot interact with the stress fields of screw dislocations. The thermal energy required to tear off dislocations from an impurity atmosphere is higher in b.c.c. metals than in f.c.c. metals. This circumstance is partially responsible for the fact that the yield limit of f.c.c. alloys is relatively less temperature-sensitive than that of b.c.c. alloys.

The solubility of interstitial impurity atoms in a b.c.c. lattice is lower than that in an f.c.c. lattice, since the volume of interstices in the former is smaller. For that reason, for instance, disperse particles precipitate from a γ-iron solution more slowly than from α-solution.

Non-monotonous σ_s-$\dot{\varepsilon}$ relationship. This relationship can be non-monotonous due to polymorphous transformations, strain ageing, dynamic phenomena and adiabatic processes observed in high-speed plastic working and associated with heat evolution and subsequent drop in the flow stress. Inflections at the critical temperatures θ_0, θ_1, θ_2, as in the cases discussed earlier, can also appear (see Fig. 239*b*). In a wide range of deformation rates, varying by a factor of 10^{10}, various metals may exhibit up to five typical portions on the σ_s-$\dot{\varepsilon}$ curve, with inflections and anomalies caused mainly by dynamic strain ageing.

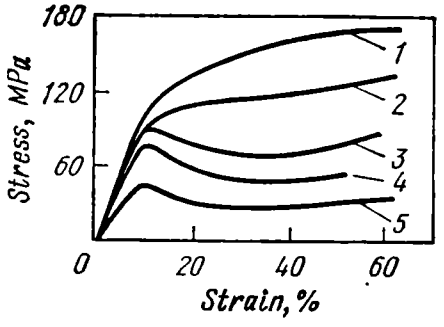

Fig. 250. Stress-strain curves for copper compressed at a rate of 100 mm/min at various temperatures (S. I. Gubkin)
1—500°C; *2*—550°C; *3*—650°C; *4*—700°C; *5*—850°C

In impact loading ($\dot{\varepsilon} > 10^5\ s^{-1}$, portion *V* in Fig. 240*a*), a change in the flow stress may be due to certain structural changes occurring in the metal, such as twinning, a change from one slip system to another, phase transformations, etc.

In region *V*, the adiabatic effect of reducing flow stress can be observed, which is the stronger the higher is the strength of the metal and the lower its thermal conductivity and the deformation temperature. The flow stress peak then displaces to the region of lower deformation rates.

Dynamic strain ageing may show up in a lower strain resistance at a higher deformation rate, as for instance is shown in Fig. 249, where curve *2* obtained at 400°C has an inflection point at $\dot{\varepsilon} = 5\ s^{-1}$ and curve *3* (500°C) at $\dot{\varepsilon} = 50\ s^{-1}$. The reduction of σ_s at particular (high) deformation rates can be explained by insufficient time for decomposition of the solid solution. If a σ_s-$\dot{\varepsilon}$ diagram is replotted in σ_s-θ coordinates, σ_s will increase with temperature at definite deformation rates and a maximum of strain hardening will appear.

This is one and the same phenomenon, but considered from various standpoints, i.e. in σ_s-θ and σ_s-$\dot{\varepsilon}$ coordinates.

Polymorphous transformations can cause anomalous changes in σ_s-$\dot{\varepsilon}$ curves, similar to those found in σ_s-θ curves. For instance, the speed coefficient of brass (38% Zn) has been observed to drop down sharply in the temperature range 500-700°C against its values at lower temperatures. The phenomenon has also been found in brass with 52 per cent Zn. In these brasses, the phase transformations $\alpha \rightleftarrows \alpha + \beta$ and $\beta \rightleftarrows \beta + \gamma$ take place in the range 600-700°C. They result in the appearance of a fine-grained structure which weakens the speed effect.

A slower rise or even a decrease in the speed coefficient with increasing temperature has also been observed in steels at the temperatures of their phase transformations.

Non-monotonous σ_s-$\bar{\varepsilon}$ relationship. With low deformation rates and high homologous temperatures, the σ-$\bar{\varepsilon}$ diagrams may exhibit maxima in the deformation range $\bar{\varepsilon} = 0.1$-0.4 (Figs. 250 and 251). In that case, the rate of diffusion of impurity atoms is so high that they move freely and do not interact with dislocations. With increasing rate of deformation, a maximum shifts towards higher temperatures (see Fig. 250) and heavier deformations. At high deformation rates, there is not enough time for diffusion of impurity atoms and a maximum will disappear, i.e. the curve becomes monotonously rising. A maximum on the σ-$\bar{\varepsilon}$ diagram will also disappear at an appreciable concentration of alloying additions.

The appearance of a maximum can be explained by the fact that dynamic polygonization in plastic deformation may be due to different mechanisms: cross slip of screw dislocations, dislocation climb, etc. The two mechanisms are associated with recombination of extended dislocations whose activation energy depends on the stacking fault energy E_{sf}. With a higher temperature, lower deformation rate, and higher E_{sf}, a maximum will appear closer to the origin of coordinates. In metals with low E_{sf} (such as austenitic steels, see Fig. 251), a maximum appears in the region of heavier deformations.

Another factor probably responsible for a drop of the flow stress on a definite amount of deformation $\bar{\varepsilon}'$ corresponding to the maximum of strain resistance, is the retardation of softening processes at low deformations $\varepsilon < \varepsilon'$ and their intensification at heavy deformations $\varepsilon > \varepsilon'$, when dynamic recrystallization begins, which is enhanced at a given homologous temperature as deformation increases above ε'. Grain refinement occurring at $\varepsilon > \varepsilon'$ can probably cause a further increase in strain resistance with deformation.

Effect of grain size on σ_s. The linear σ-$d^{-0.5}$ relationship for b.c.c. metals (Hall-Petch relation) is indicative of an essential effect of

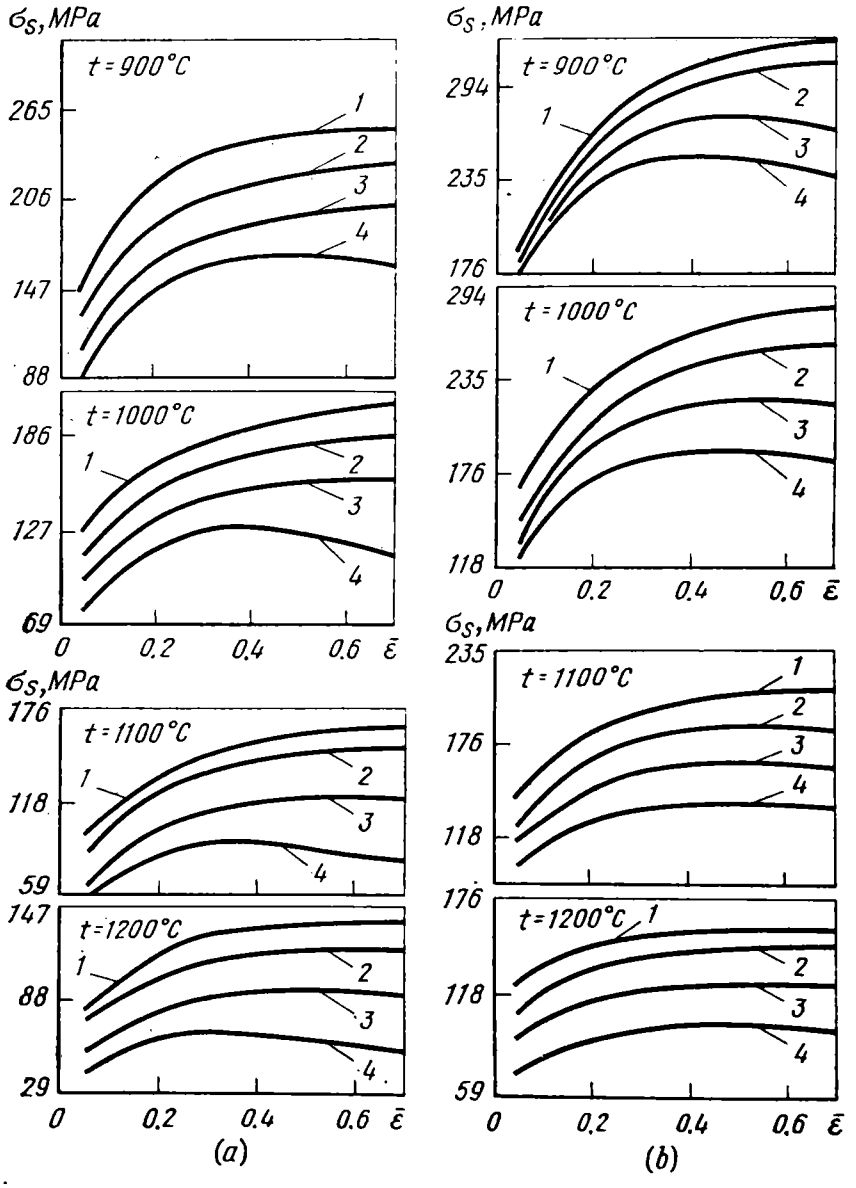

Fig. 251. Strain resistance of steels in compression at various temperatures and various deformation rates (P. M. Kuk)

(*a*) low-carbon steel (0.15%C, 0.68% Mn); (*b*) stainless steel (0.07%C, 18.6%Cr, 7.7%Ni). ($\dot{\varepsilon}$, s^{-1}: *1*—100; *2*—40; *3*—8; *4*—1.5)

grain size on strain resistance at common deformation rates (above 0.1 s^{-1}) (Fig. 252).

At low homologous temperatures, recrystallization proceeds so slowly that the originally disperse submicrostructure is retained in the metal upon plastic deformation, i.e. no grain coarsening takes place. At temperatures $\theta > \theta_1$, the temperature for dynamic recrystallization, the size and number of grains in a polycrystal change and become dependent on the rate of deformation and the

conditions of subsequent heating and cooling. For that reason, grain size affects the speed relationship for strain resistance: the speed coefficient increases with the size of grains (Fig. 253), the effect of deformation rate being more pronounced with larger original grains. Thus, with development of deformation and refinement of grains, the effect of deformation rate on σ_s becomes weaker.

In a coarse-grained polycrystal, there are more possibilities for realization of shear processes than in a fine-grained one. The barrier effect is enhanced with grain refinement. The complicating effect, which is expressed stronger with a larger number of operative slip systems, is also enhanced with grain refinement. For that reason, in the initial portion of the σ_s-$\bar{\varepsilon}$ diagram, the flow stress is higher with finer grains and the difference in strain resistance is higher with a higher difference in the size of grains in a given specimen. On heavy deformations, this difference is levelled off, since the influence of the barrier effect and complicating effect on strain resistance comes to saturation. Thus, the size of grains can have an essential effect on the σ_s-$\bar{\varepsilon}$ diagram and strain resistance only in the initial portion of the diagram, at $\varepsilon < 0.3$.

Effect of type of crystal lattice and chemical composition of metal on strain resistance. The differences in the σ_s-θ, σ_s-ε and σ_s-$\bar{\varepsilon}$ curves of various metals are due to the type of crystal lattice and the associated stacking fault energy E_{sf}.

High hardening coefficients in many f.c.c. metals, except for aluminium, which have been observed experimentally, can be explained by their low stacking fault energy. As is well known [see formula (55)], a lower stacking fault energy E_{sf} involves a correspondingly higher equilibrium width d_0 of extended dislocations, which impedes cross slip and climb of dislocations and increases

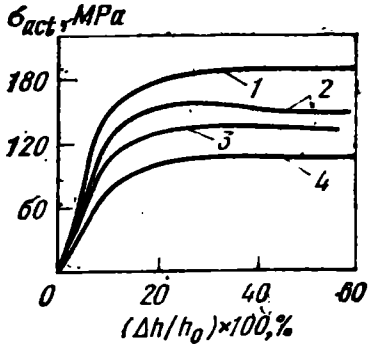

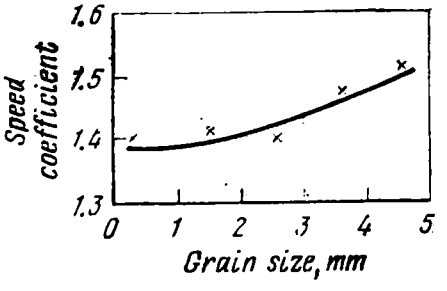

Fig. 252. (*left*) The σ-$\hat{e}$ curves for aluminium with grain size 0.5 mm (*1*, *3*) and 4.6 mm (*2*, *4*) at different rates of compression, mm/s: *1*, *2*—1; *3*, *4*—0.01

Fig. 253. Effect of grain size on the speed coefficient $n = \sigma^{\cdot}_{\varepsilon_1}/\sigma^{\cdot}_{\varepsilon_2}$ ($\dot{e}_1 = 6 \times 10^2$ s^{-1}, $\dot{e}_2 = 6 \times 10^{-4}$ s^{-1}) upon compressive deformation $\hat{\varepsilon} = \Delta h/h_0 = 20\%$

the stress required for a dislocation to intersect a dislocation forest. Notwithstanding substantial differences in the dislocation structure of metals with various lattices, low hardening coefficients in b.c.c. metals can be explained satisfactorily by their high number of probable slip systems and high stacking fault energy, and therefore, by a greater freedom for the operation of softening mechanisms, since cross slip of screw dislocations occurs in b.c.c. metals more easily than in f.c.c. metals and thus facilitates dynamic softening.

In c.p.h. metals where the number of probable slip systems is small, softening is most likely to occur by the mechanism of climb of edge dislocations. The probability of operation of some or other softening mechanism (cross slip of screw dislocations or climb of edge dislocations) is also determined to an appreciable extent by the stacking fault energy.

Stacking fault energy is the controlling factor of thermally activated processes of cross slip. At a higher E_{sf}, these processes occur more easily. It should be expected in that connection that the σ_s-θ relationships of b.c.c. metals and aluminium are more temperature-sensitive than those of f.c.c. metals, i.e. they are steeper, and that the temperature coefficients $b_1(\theta)$ and $b_2(\theta)$ in formulae (171) and (172) should be higher for b.c.c. metals than for f.c.c. For metals with the same type of crystal lattice, the greater is the stacking fault energy E_{sf}, the higher must be the temperature coefficients $b_1 T_{m.p.} = b_1'$ and $b_2 T_{m.p.} = b_2'$.

Stacking fault energy can influence thermal activation and thus control the rate of relaxation and softening processes. The latter is higher at a higher E_{sf}. For that reason, the strain resistance of metals with higher values of E_{sf} is more temperature-sensitive, i.e. their σ_s-θ curves at $\bar{\varepsilon} = \text{const}$, and $\dot{\varepsilon} = \text{const}$, are steeper and the hardening coefficients $n_1(\theta)$ and $n_2(\theta)$ are greater.

The effect of metal composition on $n_1(\theta)$, $n_2(\theta)$, b_1, b_2 and the critical deformation rate $\dot{\varepsilon}_1$ can also be associated with variations in the stacking fault energy. This relates, first of all, to the 'non-anomalous' regions in the σ_s-θ and σ_s-$\dot{\varepsilon}$ diagrams, where an increase in the concentration of impurities leads to a decrease of $n(\theta)$ and $\dot{\varepsilon}_1$ and to an increase of the temperature of the beginning of recrystallization θ_1.

Cases are known however when an increased concentration of carbon and chromium in steels produced an inverse effect at high temperatures, i.e. increased b_1 and $n_1(\theta)$, which was due to lowering of the melting point. The result is that the strain resistance of high-carbon steels at a low deformation rate is higher than that of low-carbon grades. The phenomenon is well known in engineering practice.

It would be improper to explain the effect of the type of crystal lattice on the σ_s-$\dot{\varepsilon}$-$\bar{\varepsilon}$-θ diagrams solely by variations in the stacking

fault energy. The pattern of these diagrams depends undoubtedly on the number of slip systems and on the dislocation structure formed by deformation. Some other causes will be discussed later.

It has been observed, in particular, that the σ_s-θ diagrams for metals with various crystal lattices differ substantially in the region of low temperatures. For instance (see Fig. 254), the yield limit has the general tendency to decrease with increasing temperature, but the tendency is much more pronounced in tantalum, iron, tungsten and molybdenum than in nickel. The low-temperature plateau observed in tungsten and molybdenum may be attributed to twinning. It is supposed that the strong temperature dependence of flow stress in b.c.c. metals and their low temperatures of ductile-to-brittle transition are due to the effect of interstitial impurities (C, N) and to the contribution of Peierls-Nabarro forces to σ_s. The contribution from intersection of dislocation forest is insignificant for b.c.c. metals and turns out to be more effective for f.c.c. metals (see Ch. 3).

In most alloy steels, no peak of strain ageing is practically found.

The strain resistance of alloys is generally more temperature-sensitive than that of pure metals, especially at low temperatures.

At high temperatures, alloying can produce an especially high strengthening effect if it retards recrystallization. In particular, the high strain resistance of austenitic and martensitic steels is attributed to their low rate of recrystallization at high temperatures.

The *effect of temperature on strain resistance* σ_s of solid substitutional alloys is stronger than that for pure metals, which is associated with the formation of clouds of impurity atoms around extended dislocations (Suzuki atmospheres). The hardening effect in f.c.c. metals arises due to variations in the concentration of solute atoms in stacking faults. The chemical interaction by the Suzuki mechanism

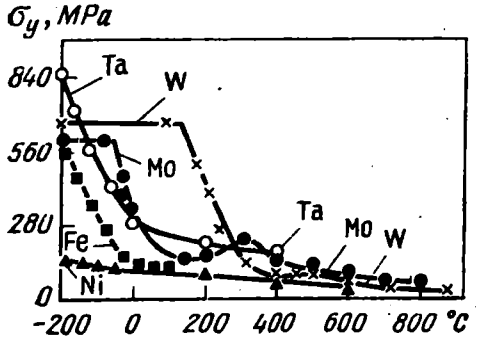

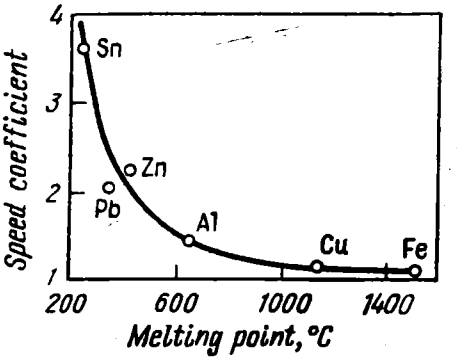

Fig. 254. (*left*) Effect of temperature on the yield limit of polycrystalline metals with various types of crystal lattice

Fig. 255. Correlation between the speed coefficient and melting point of metals (L. D. Sokolov)

is substantially weaker than that observed in b.c.c. metals due to lattice distortion. For that reason, the temperature relationship for σ_s of f.c.c. metals is weaker than that of b.c.c. ones; this is true both for pure metals and substitutional solid solutions.

The stronger σ_s-θ relationship of alloys is also due to the circumstance that impurities strengthen grain boundaries more substantially than grains proper, which increases the interaction between grains and impedes grain-boundary sliding. The role of barrier effect is enhanced and thus favours more substantial strengthening.

The effect of the composition and structure of the metal on the σ_s-θ-$\dot{\varepsilon}$ relationship becomes weaker at higher temperatures of deformation. Exceptions are high-chromium ferritic steels in which recrystallization can develop at high temperatures much more strongly than in other types of steel. This can explain the higher speed effect in ferritic class steels (containing at least 23% Cr) compared with other types. The high speed effect and low strain resistance of high-chromium steels at high temperatures are due more to their structure than to composition, and also to the fact that diffusion processes can occur rather quickly in the b.c.c. lattice. The strain resistance of ferritic steels decreases with increasing temperature more appreciably than that of austenitic steels. Addition of chromium to steel increases noticeably the strength at room temperature, but on the other hand, high-chromium steels are known to have a reduced strain resistance at temperatures of 1100-1200°C.

The *effect of deformation rate on strain resistance* is more pronounced in low-melting metals and less so, in high-melting ones. In the latter, a change of deformation rate by 5-6 orders of magnitude results in an increase of the strain resistance by only 10-30 per cent, whereas in tin, zinc and lead this increase may be some hundred per cent (Fig. 255).

In high-melting metals, the effect of deformation rate on strain resistance appears at low deformations; in low-melting metals, on the contrary, the effect is stronger with heavier deformations.

The dependence of σ_s on $\dot{\varepsilon}$ in alloys is less stronger than in pure metals and the effect of deformation rate on flow stress decreases with increasing concentration of alloying elements. For instance, this effect is greater in iron than in steel.

The differences in the temperature-rate relationship for strain resistance of various steels should mainly be attributed to variations in the critical deformation rate $\dot{\varepsilon}_1$, for which the following regularities have been established.

It has been noticed that impurities may have a double effect on the speed coefficient. On the one hand, they inhibit dynamic polygonization and thus weaken the effect of deformation rate. A further increase in the concentration of an impurity may however lower the melting point of the metal. This in turn will enhance

the effect of deformation rate on strain resistance. These two factors influence the σ_s-$\dot{\varepsilon}$ relationship in opposite directions: the former prevails at low temperatures and the latter, at high temperatures. This circumstance can explain why the speed coefficient of steels at high temperatures increases with increasing concentration of carbon.

Numerous experiments on determining the strain resistance of steels of various classes have made it possible to establish the following regularities of variations of $\dot{\varepsilon}_1(\theta)$, $n_1(\theta)$, and $n_2(\theta)$ in the σ_s-$\dot{\varepsilon}$-θ relationship:

(1) in all steels and alloys, $\dot{\varepsilon}_1$ increases with rising temperature;

(2) at the same absolute temperature, $\dot{\varepsilon}_1(\theta)$ increases in carbon steels with increasing concentration of carbon;

(3) for the same concentration of carbon in steels, small additions of other impurities (up to 2-3 per cent) have practically no effect on $\dot{\varepsilon}_1$; exceptions are Mn, Ni, W, and Ni + Cr, which diminish $\dot{\varepsilon}_1$;

(4) the critical rate $\dot{\varepsilon}_1$ in carbide steels is substantially (by an order of magnitude) lower than in pearlitic class steels; it depends on carbon content and only weakly depends on the concentration of other alloying elements; a high concentration of W or Ni lowers $\dot{\varepsilon}_1$;

(5) the recrystallization inflection in the σ_s-$\dot{\varepsilon}$ diagram of ferritic steels is shifted, compared with other classes of steels, towards higher deformation rates (due to a relatively low temperature of recrystallization);

(6) the presence in ferritic steels of some elements favourable for grain coarsening (such as aluminium) may have an appreciable effect on strain resistance and speed coefficient.

The *speed coefficients* $n_1(\theta)$ and $n_2(\theta)$ increase with rising temperature in all metals, steels and alloys (see Figs. 243 and 245).

The magnitude of $n_1(\theta)$ in pearlitic class steels only weakly depends on the concentration of alloying elements, but increases with increasing content of carbon. In high-chromium steels of ferritic class, n_1 is markedly higher than in pearlitic class steels. The lowest values of $n_1(\theta)$, as could be expected, are found in steels of austenitic and carbide class.

Variations in $\dot{\varepsilon}_1(\theta)$ and $n_1(\theta)$ depending on steel composition are of the same nature, but the differences in the σ_s-$\dot{\varepsilon}$ relationship of various steels are mainly due to the critical rate $\dot{\varepsilon}_1$, rather than to n_1.

The coefficient $n_2(\theta)$ is small and only slightly sensitive to variations in chemical composition; it decreases somewhat with an increase in carbon content.

Table 14. Thermally Activated Mechanisms of Plastic Deformation Which Control Strain Resistance at Various $\dot{\varepsilon}$ and θ

Lattice	Metals	The most probable mechanism	Alternative mechanism
		$T < 0.25\ T_{m.p.}$, $\dot{\varepsilon} > \dot{\varepsilon}_1$	
c.p.h.	Zn, Cd, Mg	Intersection of dislocation forest	Non-conservative movement of jogs
f.c.c.	Al, Cu, Ag, Au, Ni	Ditto	Conservative
b.c.c.	V, Nb, Ta, Cr, Mo, W, Fe	Overcoming Peierls-Nabarro locks	Non-conservative*
		$T = (0.25\text{-}0.5)\ T_{m.p.}$, $\dot{\varepsilon} \approx \dot{\varepsilon}_1$	
c.p.h.	Zn, Cd, Mg	Climb of edge dislocations	Non-conservative movement of jogs
f.c.c.	Al, etc.	Cross slip of screw dislocations	Destruction of Lomer-Cottrell locks
b.c.c.	V, Nb, Ta, Cr, Mo, W, Fe	Elastic interaction between dislocations and interstitial solute atoms	Intersection of dislocation forest
		$T > 0.5\ T_{m.p.}$, $\dot{\varepsilon} < \dot{\varepsilon}_1$	
c.p.h.	Be, Ti, Zn, Mg	Dislocation climb ($0.5\ T_{m.p.} < T < 0.8\ T_{m.p.}$)	Non-conservative movement of jogs
f.c.c.	Al, Cu, Au, Pb	Dislocation climb	Non-conservative
b.c.c.	Nb, Mo, Ta, Fe	Ditto	Non-conservative, intersection of dislocations

* Overcoming interstitial atoms and disperse precipitates, intersection of dislocations, cross slip.

3. Mechanisms of Plastic Deformation in Various Ranges of ε, $\dot{\varepsilon}$ and θ Parameters

It seems practically impossible to generalize the discussed peculiarities in the pattern of σ_s-ε-$\dot{\varepsilon}$-θ diagrams from the standpoint of the mechanisms which control the processes of plastic deformation, since in each particular case it would be necessary to analyse the phenomena in correlation with the chemical composition, structure, type of lattice, etc. For that reason, our discussion will be limited to the principal mechanisms controlling strain resistance and plasticity of metals. The respective data are summarized in Table 14.

4. Effect of Surrounding Medium and Size Factor on Strain Resistance

The surrounding medium may cause: (1) dissolution of surface layers of the deformed body; (2) corrosion of these layers; (3) variations in the chemical composition of surface layers; (4) easier deformation due to adsorption. All these factors can have an essential effect on plasticity and strain resistance of metals.

In 1928, P. A. Rebinder discovered the adsorption effect in metals, i.e. the effect of reduced flow stress in the presence of surface-active substances. It has been later called the Rebinder effect. If, for instance, a tin single crystal is deformed in an active medium containing oleic acid and petrolatum oil, the resistance to slip and the thickness of slip packets will diminish more than by one order of magnitude and the number of slip packets will increase (Fig. 256). Therefore, strain localization in slip packets will be diminished

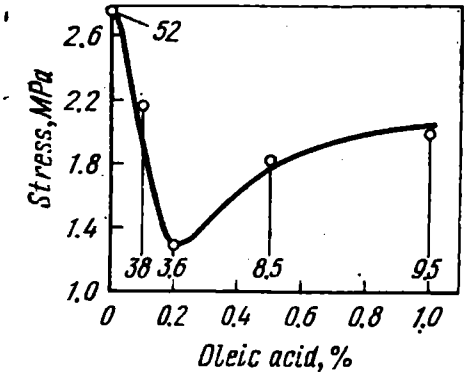

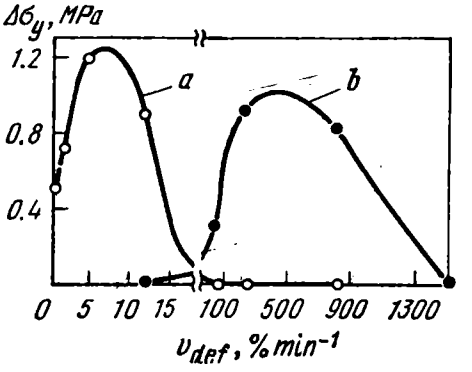

Fig. 256. (*left*) The flow stress on elongation 30% as a function of the content of oleic acid in petrolatum. Numbers indicate the thickness of slip packs, μm (S. I. Gubkin)

Fig. 257. Influence of deformation rate at 20°C (*a*) and 100°C (*b*) on the adsorption effect $\Delta\sigma_y$ in tension of tin single crystals. $\Delta\sigma_y = \sigma_y - \sigma_{y.a.}$, where σ_y is the yield limit for tension in air and $\sigma_{y.a.}$ is that in a surface-active substance

sharply. Since the thickness of slip packets can increase with progressive deformation to values typical of deformation without surface-active substances, the plasticity of the metal will be substantially higher.

The adsorption effect depends appreciably on the temperature and rate of deformation, the highest effect being obtained at a particular combination of temperature and deformation rate (Fig. 257).

The loss of strain resistance in the presence of surface-active substances is attributed to decreasing level of the surface energy, which makes it easier for dislocations to emerge onto the surface.

The splitting effect produced by surface-active substances on microdefects in surface layers of a deformed body results in reduction of the flow stress. The phenomenon can be explained by interaction of dislocations with the free surface. A dislocation is attracted to a free surface with the force* $F = Gb^2/4\pi l$, where l is the distance from the dislocation to the surface. If a film is present on the surface with the value of G' different from G of the base metal, the dislocation will be attracted to the surface (to its image) if, as has been shown by calculations, $G' < G$ and will be repulsed if $G' > G$. For oxidized surfaces of many metals, $G' > G$, and therefore, an oxide film usually prevents dislocations from emerging onto the surface. Removal of oxides during deformation (see Ch. 3) can lower the strain resistance.

To emerge onto the surface, a dislocation must form a jog of width b on that surface, and therefore, requires an additional energy $E_s = \gamma b$ per unit length of dislocation (γ = surface energy). This energy must be substantially higher if an oxide film is present on the surface. The energy E_s can be lowered by dissolution of the film or by action of a surface-active substance, which will facilitate plastic flow.

A change of the metal composition in the surface of deformed body can lead to a substantial change in strain resistance. This effect is especially pronounced in zirconium, niobium, vanadium, tantalum whose structures and properties can be affected by interstitial impurities: carbon, nitrogen, etc. For instance, the ultimate strength and hardness of niobium increase by 25 per cent upon rolling at 1200°C with 50-% reduction in air, compared with the values obtained on the same rolling deformation in vacuum ($6.67 \times \times 10^{-3}$ MPa), and its ductility decreases roughly to one-sixth of the original value.

The surrounding medium can influence more substantially the ductility of a metal and less so, the strain resistance (for more detail see Ch. 13). The ductility and strain resistance of a deformed body may depend substantially on its dimensions. S. I. Gubkin recom-

* It is called the image force and represents the attraction force from a dislocation of opposite sign at the same distance from the boundary.

mends that two components of this effect should be considered: the structural factor and the surface factor.

The structural factor may be caused by inhomogeneous and non-uniformly distributed grains and phases and by the presence of stress concentrators and defects in volumes of the metal. This in turn may produce non-uniform stress and strain fields, their non-uniformity being more pronounced in bodies of larger size.

The surface factor can be characterized by the ratio F/V, i.e. the surface area of a body related to its volume. If cylindrical specimens of similar shape but different size, made of one and the same metal, are tested in compression, the strain resistance will be greater in smaller specimens. S. I. Gubkin explains this effect by supposing that the conditions formed in smaller specimens are more favourable for uniform volume compression, due to a more developed contact surface and the appearance of relatively higher compressive stresses from contact friction. The effect of increasing stress is however insignificant, so that a more essential influence of the F/V factor should evidently be attributed to a more developed surface in smaller specimens, and therefore, to a more essential effect of the surrounding medium on their ductility and strain resistance. In this respect, variations in the ductility and strain resistance can arise from the effect of: (1) surrounding medium; (2) the state of surface layers where the structure and properties of the metal may have been changed by machining; and (3) contact friction and surface tension.

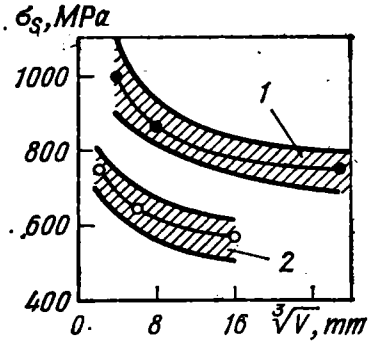

Fig. 258. Variations of the rupture stress of phosphorus steel in bending (*1*) and tension (*2*) depending on the size of test pieces

Experiments have shown that the effect of the F/V factor on the mechanical properties disappears beginning from a certain critical volume (Fig. 258). This is associated with the fact that surface tension can influence only surface layers of an exceptionally small thickness, so that in bodies with less developed surface it can produce no noticeable effect on the mechanical properties of the metal.

The size factor can also influence substantially the ductility of metals (see Ch. 13).

5. Effect of Loading History on Strain Resistance

The structure that forms in hot plastic working is thermodynamically unstable, and therefore, the relationship between stresses, strains and deformation rates is not unique. The magnitude of stress depends substantially on how the deformation has been deve-

loped in time. In other words, the prehistory of the process has an essential effect on the strain resistance and stressed-strained state of metals in plastic working.

This can be explained by the fact that the stress level is also determined by the effects of hardening, recrystallization and polygonization which accompany hot plastic deformation. The relative contributions from these processes depend on the history of loading, because of which the correlation between stress and strain at given values of instantaneous deformation rate and temperature cannot be unique. Let, for instance, a number of specimens be tensioned so that the final strain ε_2 and the final deformation rate $\dot{\varepsilon}_2$ are the same in all cases (Fig. 259). In one case, a specimen may be deformed at a low rate $\dot{\varepsilon}_1$, so that, if the temperature is high enough, complete softening will occur in parallel with hardening, i.e. the process is practically equilibrium and the strain resistance remains constant and equal to σ_{s1}. On attaining the strain ε_1, let the deformation rate be changed to $\dot{\varepsilon}_2$ (see curve *1* in Fig. 259). In another case, a specimen is tensioned to the strain ε_2 at a constant deformation rate $\dot{\varepsilon}_2$ (curve *2* in Fig. 259). This will produce a noticeable hardening effect and a higher strain resistance ($\sigma_{s2} > \sigma_{s1}$) for the same values of $\dot{\varepsilon}_2$ and ε_2.

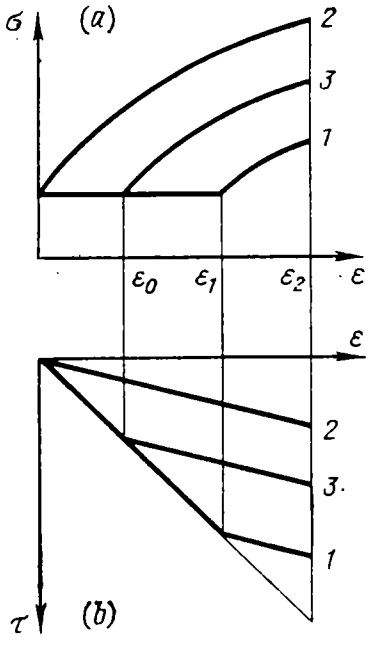

Fig. 259. Dependence of strain resistance on the amount of deformation (*a*) under various conditions of deformation (*b*)

The same values of strain ε_2 and deformation rate $\dot{\varepsilon}_2$ can however be obtained by carrying out the deformation process first at a deformation rate $\dot{\varepsilon}_1$ up to the strain ε_0 and then at a rate $\dot{\varepsilon}_2$ (curve *3* in Fig. 259). Thus, the deformation processes may be varied infinitely and will accordingly give an infinite number of different values of σ_s for the same ε_2 and $\dot{\varepsilon}_2$. Therefore, the stress cannot be determined uniquely by the strain and deformation rate, but depends additionally on the loading history.

Thus, stress and strain calculations in plastic working of metals must consider the prior state of the metal and should be carried out so as to use the stress-strain curves obtained at constant temperature and constant deformation rate (see Figs. 239 and 240) for determining $\sigma_s = \sigma_s(\varepsilon, \dot{\varepsilon}, \tau)$ which account for the time history of deformation.

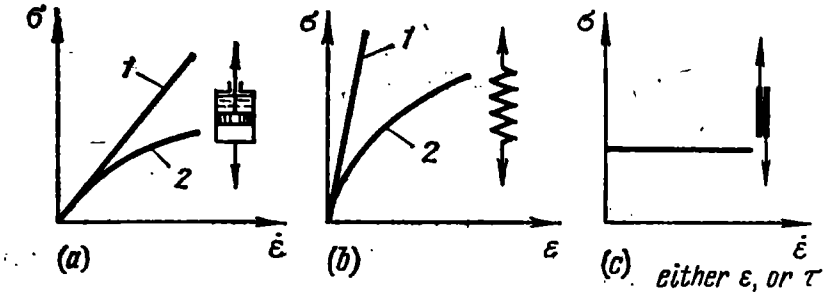

Fig. 260. Rheologic relationships for simplest media
(*a*) viscous (*1*—linear; *2*—non-linear); (*b*) elastic (*1*—linear, *2*—non-linear); (c) ideally plastic

In that case, the increment of flow stress σ is determined by the formula:

$$d\sigma = \frac{\partial \sigma}{\partial \varepsilon} d\varepsilon + \frac{\partial \sigma}{\partial \dot{\varepsilon}} d\dot{\varepsilon} + \frac{\partial \sigma}{\partial \tau} d\tau \tag{176}$$

where $\partial\sigma/\partial\varepsilon$ and $\partial\sigma/\partial\dot{\varepsilon}$ characterize the hardening effect due to strain and deformation rate respectively and $\partial\sigma/\partial\tau$ characterizes the variations of strain in time.

Equating to zero one of the terms in (176) which determine the various types of hardening and softening of the metal, we obtain rheologic relationships* constituting the following groups of equations:

by the theory of flow

$$\partial\sigma/\partial\varepsilon = 0; \quad F_f(\sigma, \dot{\varepsilon}, \tau) = 0 \tag{177}$$

by the theory of ageing

$$\partial\sigma/\partial\dot{\varepsilon} = 0; \quad F_a(\sigma, \varepsilon, \tau) = 0 \tag{178}$$

and by the theory of hardening

$$\partial\sigma/\partial\tau = 0; \quad F_h(\sigma, \varepsilon, \dot{\varepsilon}) = 0 \tag{179}$$

In particular, using the flow equation (177) for the case of $\partial\sigma/\partial\tau = 0$ or the hardening equation (179) for $\partial\sigma/\partial\varepsilon = 0$, we obtain: $F(\sigma, \dot{\varepsilon}) = 0$, whose solution gives:

$$\sigma - a\dot{\varepsilon} = 0 \quad \text{or} \quad \sigma = a\dot{\varepsilon} \tag{180}$$

i.e. an equation for a linearly viscous medium if $a = \mu = \text{const}$ and equation for a non-linearly viscous medium if $a = \mu(\dot{\varepsilon})$, where μ is the viscosity coefficient (a model of a medium in the form of a cylinder with liquid, Fig. 260*a*).

* Rheology is the science of flow of materials, or the science studying correlations between stresses, strains and their higher time derivatives.

Using the ageing equation for a particular case $\partial\sigma/\partial\tau = 0$ or the hardening equation with $\partial\sigma/\partial\varepsilon = 0$, we obtain: $F_H(\sigma, \varepsilon) = 0$ whose general solution is $\sigma - b\varepsilon = 0$, or

$$\sigma = b\varepsilon = E\varepsilon \tag{181}$$

The last equation relates to a linearly elastic (Hookean) medium if $b = E = \text{const}$ or to a non-linearly elastic medium if $b = E(\varepsilon)$, where E is the modulus of elasticity (a model of a medium in the form of a spring, Fig. 260*b*).

Considering one of the probable variants of real behaviour of metals, i.e. taking in expression (176) that $\partial\sigma/\partial\varepsilon = \partial\varepsilon/\partial\tau = \partial\sigma/\partial\dot{\varepsilon} = 0$, we get:

$$\sigma = c = \text{const} \tag{182}$$

which is the rheologic equation of an ideally plastic medium (simulated by a friction pair in Fig. 260*c*).

In equations (180)-(182), $a = \mu$, $b = E$, and $c = \sigma_0$ are rheologic constants. The behaviour of such media can be simulated by simple mechanical models (see Fig. 260); series and parallel connections of these simplest models give models of a more complicated rheology. Without discussing complex rheologic models and their equations, let us note the following concepts obtained for plastic deformation processes in plastic working of metals.

The *theory of flow* reflects correctly the relationship between the increasing deformation and the processes of hardening, dynamic polygonization and recrystallization which determine strain resistance. For construction of a generalized mechanical model of a medium, use is made of the concepts formulated by A. R. Rzhanitsin. For developed processes of plastic working, the medium is considered to be absolutely stiff and the hardening due to deformation rate, non-linear. The adopted mechanical model and the corresponding rheologic equations describe the hardening due to strain and deformation rate and also the phenomenon of reverse creep. It is assumed in the derivation of rheologic equations that $\dot{\varepsilon}$ is a known time function. Such processes are most typical of plastic working of metals.

From the rheological equations derived by the flow theory, it follows, in agreement with experiment, that there exists a limit of hardening at a given deformation rate and that the strain resistance at low deformation rates is independent of deformation (ideal plasticity).

The rheologic model is however unsuitable for calculation of stress for a given law of stress variation (in that case, unloading is described not by a linear portion parallel to the loading curve, but follows the line of the initial stage of deformation); it also fails to explain stress relaxation.

The *theory of ageing** assumes that the metal properties vary in time. It is supposed therefore that the flow stress level is determined by the relation between the rates of the competing hardening and softening processes, the intensity of the latter being substantially time-dependent.

Rheological equations based on the ageing theory describe the hardening due to deformation rate and strain, stress relaxation, and creep. A disadvantage of these equations is that they cannot account for the nature of time development of strain. They describe well the behaviour of metals at constant or slightly varying stresses.

The *theory of hardening* makes it possible to determine the flow stress (strain resistance) as a function of strain, deformation rate, and time history of deformation. With heavy deformations typical of plastic working of metals, however, it is difficult to account for time development of stresses and strains, which makes this theory inapplicable to calculations of the processes of plastic working of metals.

The *theory of heredity* uses the equations of Boltzmann's theory of elastic aftereffect. The equations of the Boltzmann-Volterra theory of heredity are the most generalized equations for describing time variations of stress and strain. Rheological equations of this theory describe satisfactorily the aftereffect, stress relaxation, hardening due to strain and deformation rate, and stress variations with a given law of time variation of strain $\varepsilon(\tau)$.

Using the theory of hereditary media, it is possible to obtain the σ-ε curves at a given temperature and $\dot{\varepsilon} = \text{const}$ in tests in stationary testing machines (plastometers) with a given time history of deformation, $\varepsilon(\tau)$, or at $v = \text{const}$ (tests at a constant deformation rate). Numerous experiments have demonstrated that stress-strain curves at constant temperature and constant deformation rate, when taken in a plastometer ($\dot{\varepsilon} = \text{const}$), have a maximum. When taken in a hydraulic press ($v = \text{const}$), the stress-strain curves approach asymptotically a limit.

An explanation to this is that the metal is hardened intensively at the initial stage of deformation and stores internal energy. The intensity of hardening decreases with developing deformation, since the hardening effect produced and the stored internal energy favour the softening processes. If there is enough time for their occurrence, the softening processes can fully compensate for the current hardening and even be prevalent. The strain resistance then begins to drop down, producing a maximum on the stress-strain curve.

The phenomenon is not observed in stress-strain curves taken in a hydraulic press (at a constant reduction rate), since, as the specimen is upset, its height diminishes and the deformation rate increas-

* The term has nothing in common with the phenomenon of ageing considered in physical metallurgy.

es accordingly. This leads to more intensive hardening of the metal, which is compensated for by softening only on attaining a definite limit. For that reason, stress-strain curves taken in a hydraulic press exhibit no maximum.

The equation of the theory of hereditary media makes it possible to determine strain resistance for a known law of time variation of strain, which can be established more or less reliably for various processes of plastic working of metals. It has been found, in particular, that the deforming force may vary as much as by a factor of two if the real history of loading has not been accounted for (Fig. 261). Thus, it is not only possible to determine σ_s directly in the deformation zone per one stroke of the press or one pass of rolling, but also to establish the law of variation of σ_s and pressure in view of the deformation history, calculate stress variation in rolling with interstand tension, and account for its effect on the pressure and strain resistance in each pass.

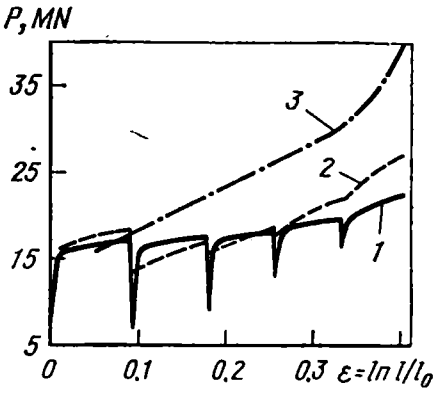

Fig. 261. Curves of upsetting force in steel 45 specimens obtained experimentally (*1*) and by calculation (*2* and *3*) with (*2*) or without (*3*) account of the history of loading at 1 200°C (A. A. Pozdeev et al.)

The effect of time history of deformation on strain resistance has been discussed in this section in phenomenological aspects. The relationships obtained could be explained by using only the principal physical concepts. This approach can be used, however, for a more substantiated experimental study of factors affecting strain resistance, for correct planning of experiment, and for formulating the principal requirements to be met by testing equipment. This approach seems to be useful in plastic working of metals.

RECOMMENDED LITERATURE

1. Ageev N. P., Karatushin S. I., *Mechanical Tests of Metals at High Temperatures and Short-term Loading.* Moscow, Metallurgiya, 1968 (in Russian).
2. Bernstein M. L., *The Structure of Deformed Metals.* Moscow, Metallurgiya, 1977 (in Russian).
3. Pozdeev A. A., Tarnovsky V.I., Eremeev V.I. and Baakashvili V.S., *Applications of the Theory of Creep in Plastic Working of Metals.* Moscow, Metallurgiya, 1973 (in Russian).
4. Rzhanitsin A. R., *Selected Problems of Mechanics of Systems Deformed in Time.* Moscow, Gostekhizdat, 1949 (in Russian).
5. Sokolov L.D., *Dislocations and Properties of Metals.* A course of lectures. Parts 1, 2. Gorky, Polytechnical Institute, 1973 (in Russian).
6. Sokolov L.D., *Izvestiya Vuzov. Ferrous Metallurgy*, 4: 91-95 (1965) (in Russian).
7. Sokolov L. D., *Reststance of Metals to Plastic Deformation.* Moscow, Metallurgizdat, 1963 (in Russian).
8. Zaikov M.A., *Deformation Conditions and Forces in Hot Rolling.* Sverdlovsk, Metallurgizadt, 1960 (in Russian).

13 Ductility and Deformability of Metals and Alloys

The ability of a metal to deform residually (irreversibly) without macrofracture is called *ductility*.

The measure of ductility is the amount of deformation at the moment of fracture, Λ_r. For cold deformation

$$\Lambda_r = \int_0^{t_r} H(\tau)\, d\tau \tag{183}$$

where $H(\tau)$ is the intensity of shear strain rates $\dot{\varepsilon}_{ij} = 0.5\,(\partial V_i/\partial x_j + \partial V_j/\partial x_i)$; $i, j = 1, 2, 3$; and V_i are components of the velocity vector. H is determined along the path of movement of a material point, which in a steady-state process coincides with a flow line:

$$H = \frac{2}{\sqrt{6}} \times \sqrt{(\dot{\varepsilon}_{11}-\dot{\varepsilon}_{22})^2+(\dot{\varepsilon}_{22}-\dot{\varepsilon}_{33})^2+(\dot{\varepsilon}_{33}-\dot{\varepsilon}_{11})^2 + 6\,(\dot{\varepsilon}_{12}^2+\dot{\varepsilon}_{23}^2+\dot{\varepsilon}_{31}^2)} \tag{184}$$

The strain at fracture is essentially the total strain stored during the prior history of deformation. According to A. A. Ilyushin, the *amount of deformation*, or the Odqvist parameter, is the measure of total accumulation of crystal lattice defects to the moment of fracture, so that Λ_r differs from any arbitrary Λ in being the *highest*, or *ultimate*, *deformation*.

By analogy with other mechanical characteristics of metals, the ultimate deformation at fracture, Λ_r, will be called the *plastic limit*.

For a monotonous deforming process, Λ_r coincides with $\overline{\Gamma}_r$, the intensity of logarithmic deformations:

$$\overline{\Gamma}_r = \frac{2}{\sqrt{6}} \sqrt{(\bar{\varepsilon}_1-\bar{\varepsilon}_2)^2+(\bar{\varepsilon}_2-\bar{\varepsilon}_3)^2+(\bar{\varepsilon}_3-\bar{\varepsilon}_1)^2} \tag{185}$$

where $\bar{\varepsilon}_k$ ($k = 1, 2, 3$) are the principal logarithmic deformations at fracture.

Uniaxial tension is a monotonous process until necking takes place and is close to monotonous in the portion of non-uniform deformation, so that

$$\Lambda_r \approx \bar{\Gamma}_r = \sqrt{3}\,\bar{\varepsilon}_1 = \sqrt{3}\ln(F_0/F_n)$$

where F_0 is the original cross-sectional area and F_n is the area of the neck at fracture.

The plastic limit Λ_r is a complex function of many variables and depends on the chemical composition and structure of the metal, the temperature and rate of deformation, the type of stressed state, the prior time history of stress and strain, the size factor, and the surrounding medium.

Other definitions and quantitative formulae of ductility may be found in the literature. For instance, many scientists hold that ductility is not a property of a metal, but its ability (tendency) to deform residually without macrofracture, which is supposed to be associated with the circumstance that a given metal may or may not be capable of plastic deformation depending on deforming conditions, in particular, on the type of stressed state.

As an example, in support of this view, it is usually referred to the ability of marble to elongate twice at high stresses in uniform compression, though it undergoes brittle fracture in common uniaxial tension. In this example, marble possesses plastic properties which depend substantially on the type of stressed state and its plastic limit, as determined by formula (185), at a high hydrostatic pressure for $\bar{\varepsilon}_2 = \bar{\varepsilon}_3 = -0.5\bar{\varepsilon}_1$ ($\bar{\varepsilon}_1 = \ln 2$ in double elongation), is $\Lambda_r = \bar{\Gamma}_r = \sqrt{3}\,\bar{\varepsilon}_1 = \sqrt{3}\ln 2$, whereas its Λ_r in uniaxial tension is practically zero. It is not a rare fact that a quantitative measure of a metal property equals zero. For instance, the strain resistance of metals at the melting point and the electric resistance of superconducting alloys at definite temperatures are also practically equal to zero. Thus, it should not be concluded from Λ_r being approximately zero under particular conditions that the ductility of a metal is merely its ability to undergo residual deformation without macrofracture. Noting that plastic deformations are observed even in brittle fracture of metals, i.e. the metal exhibits plastic properties, we shall further regard ductility as a property of a metal, like its strain resistance, electric resistivity, heat conductivity, etc., but not as a property of specimens or articles made of that metal (forgings, blanks, rolled stock, etc.).

Attempts have been made to find a quantitative measure of ductility as a general characteristic independent of the stressed-strained state. For instance, the averaged deformation obtained in tensile or compressive tests was taken as the measure of ductility. Each type of mechanical tests can however be characterized by a particular

type of stressed state, so that the plastic limit determined in various tests be different.

Some characteristics measured in mechanical tests, such as the relative elongation $\delta = (l_f - l_0)/l_0$ (l_0 and l_f being the original and the final length of a specimen); the relative reduction $\psi = (F_0 - F_n)/F_0$ (F_0 = original cross-sectional area and F_n = cross-sectional area of the neck); or the number of turns n to fracture in torsional tests, are not proper measures of ductility, but can characterize it quantitatively under the given conditions; they are called the *characteristics of ductility*, or *ductility indices.*

Some (especially dimensionless) characteristics of ductility can be used for determining the plastic limit, for instance, the following ones: in tension $\Lambda_r = \sqrt{3} \ln [1/(1 - \psi)]$; in torsion $\Lambda_{r.av} = \pi\, dn/l_0$ or $\Lambda_{r.l} = \tan \varphi$, where $\Lambda_{r.av}$ is the deformation obtained after n turns in torsion, averaged along the length l_0 of a specimen of diameter d; $\Lambda_{r.l}$ is the local torsional deformation, i.e. obtained in the point of torsional fracture [usually $\Lambda_{r.l} \approx (2\text{-}4)\, \Lambda_{r.av}$]; or the angle φ of inclination of a mark which has been originally applied parallel to the axis of a cylindrical specimen.

Other characteristics of ductility, such as the relative elongation, impact toughness*, the depth of indentation of a sphere in drawability tests of sheet materials (Erichsen's cupping test**), or the bending angle and the number of bends in bending-unbending tests of sheet materials, cannot be used for determining the plastic limit without recalculating them to Λ_r by appropriate methods.

The diversity of ductility characteristics is associated, on the one hand, with difficulties involved in determination of Λ_r and, on the other, with the fact that $\Lambda_r = \Lambda_r(k)$, i.e. depends on the type of stressed state [k is the coefficient of stiffness of the stressed state, determined as the ratio of the average stress (the first invariant of the stress tensor) to the shear stress intensity]. The coefficient $k = \sigma/T$ characterizes the ratio of the stresses which tend to rupture the metal in the presence of tensile stresses, i.e. at $k > 0$ (or, on the contrary, favourable for healing of defects and increasing of the ductility with increasing uniform compression, i.e. at $k < 0$) to the stress intensity T which ensures plastic flow.

For instance, $k = 1{:}\sqrt{3}$ in uniaxial tension, $k = 0$ in torsion, and $k = -1{:}\sqrt{3}$ in uniaxial compression, so that the ductility indices and the plastic limit may be different in magnitude, i.e. the strain level attained at fracture is different for different values of k. For that reason, it is considered, for instance, that the torsional test can better reflect the technological peculiarities of the behaviour of

* *Impact toughness* (J/cm^2) is the unit potential energy spent to fracture a notched specimen in a lateral impact test carried out in a pendulum impact testing machine.

** The ductility characteristic is measured in millimetres.

a metal under real conditions of plastic working, since the deformation obtained in torsion is greater than that in tension and approaches the value typical of the processes of plastic working of metals. It is natural that many researchers tend to make the mechanical tests as close as possible to the stressed state type existing in real processes of plastic working. Since these processes are numerous, a large number of ductility indices and methods of tests for ductility have been proposed.

Another characteristic of ductility is the deformability of the metal, i.e. its ability to vary its shape without macrofracture in a particular process of plastic working. By introducing this ductility characteristic, researchers attempted, even more appreciably than in standard tests (impact toughness, tension, torsion, Erichsen's test, etc.), to correlate the stressed state in the test with that existing in a real process of plastic working.

Again, the diversity of plastic working processes makes it impossible to suggest a unified method for measuring deformability and, for that reason, there exist a large number of deformability indices.

In forging, rolling, piercing, stamping, etc., the deformability, like ductility, will be different, because k and the functions $k(\tau)$, $\varepsilon_{ij}(\tau)$ and $\dot{\varepsilon}_{ij}$ are different. But, when making various tests for a particular, unknown exactly, scheme of stressed state and the history of development of stresses and strains in time, these parameters, which influence ductility, are replaced by the type of process, after which the deformability is determined in terms of forgeability, rollability, pierceability, etc.

Deformability depends on the chemical composition and structure of a metal or alloy; the temperature and rate of deformation; the type of plastic working process with its typical (and not necessarily known) stressed-strained state and its time variation, which additionally depends on the form of blank and tool; the size factor; and the surrounding medium.

The quantitative characteristics of deformability are as follows:

(1) the highest relative reduction in rolling upon which a crack forms in the side surface of a wedge-shaped specimen rolled in smooth rolls or an equal-thickness specimen rolled in rolls with a varying gap; this characteristic is called rollability;

(2) the highest relative reduction in upsetting of cylindrical specimens at the moment of appearance of a crack in the unloaded barrel-shaped surface; this is called forgeability;

(3) the resulting highest deformation in screw rolling of conical specimens determined in the cavity appearing in a longitudinal template; this is pierceability.

In the following analysis of the factors affecting ductility, we shall use the following concepts which can characterize quantitative-

ly the possibilities of realization of a particular process of plastic working: the plastic limit; a characteristic (index) of ductility; and a characteristic (index) of deformability.

1. Effect of Chemical and Phase Composition on Ductility of Metals and Alloys

The ductility of a metal or alloy depends on the type of crystal lattice and the tendency of that metal to form solid solutions. It is assumed that f.c.c. metals (Al, Cu, Ni, Pb, Au, Ag, etc.) are most ductile; then follow b.c.c. metals (Fe, Cr, W, Mo, β-brass, etc.) and finally, c.p.h. polycrystals (Zr, Hf, Ti, etc.) which are least ductile. This regularity is however not general and is largely determined by temperature, deformation rate, texture, presence of impurities, chemical composition and other factors.

Ductility and strain resistance are interrelated properties: as the latter increases, the former decreases, and vice versa. This simple rule is however sometimes disobeyed and the respective deviations will be considered specially.

The principal laws which determine the properties of alloys at room temperatute depending on their chemical and phase composition have been formulated by N. S. Kurnakov. For instance, variations in the hardness (*HB*) value and strain resistance of a continuous series of solid solutions are represented in a composition-property diagram by a continuous curve with a maximum (Fig. 262*a*); the hardness of binary alloys containing various concentrations of

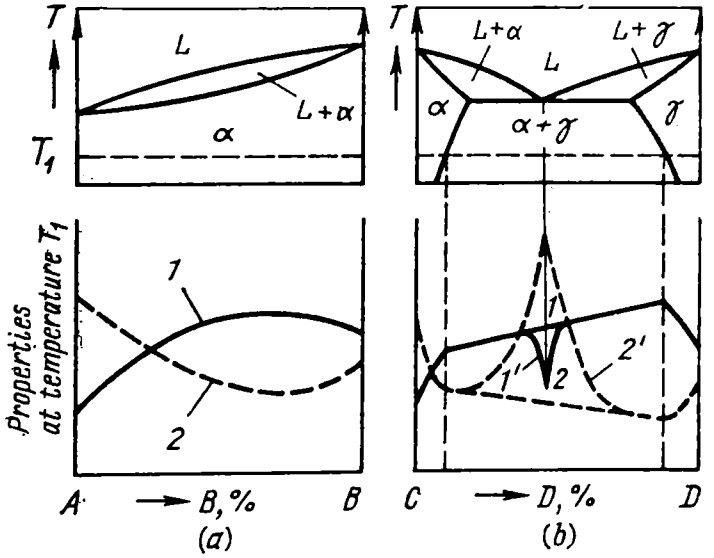

Fig. 262. Constitutional diagrams (at the top) and composition-property diagrams (below) for continuous solid solutions (*a*) and eutectic-type solutions of limited solubility (*b*) at temperature *T*

1—strain resistance; *2*—plasticity index; *1'*, *2'*—respectively strain resistance and plasticity index in cases of superplasticity at high temperatures

eutectic changes by an additive law (curves *1* and *2* in Fig. 262*b*) and that of systems of limited solubility, by a mixed law (see Fig. 262*b*). Kurnakov's composition-property diagrams have been obtained for strain resistance, ductility, physico-chemical, working and other properties of alloys.

The ductility of alloys of the type of continuous or limited solid solutions can be affected by the following factors:

(1) lattice distortions due to the presence of foreign solute atoms; (2) elastic interaction between solute atoms and dislocations (Cottrell's atmospheres); (3) chemical interaction (the Suzuki mechanism); (4) short-range order effects (the Snoek mechanism).

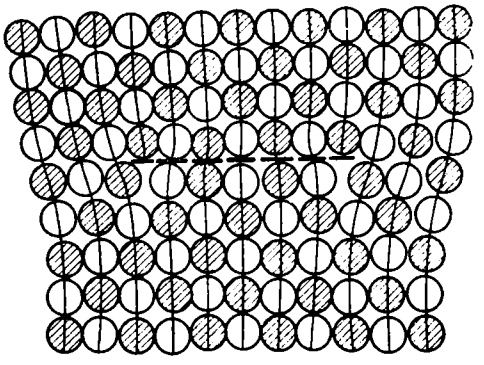

Fig. 263. A double dislocation (super-dislocation) in an ordered solid solution

Numerous alloys of the systems Cu-Ni, Fe-Ni, Fe-Cr, Ni-Cr, Ni-Mo, Fe-Co, Al-Si, Fe-Cr-Al, Fe-Si, and Fe-C have been tested and the following general relationships have been established.

The effect of hardening and reducing ductility in continuous and limited solid solutions is more pronounced at greater difference in atomic diameters of the solute element and solvent metal. Under identical conditions, alloying additions of lower solubility in a solid solution reduce the deformability of the alloy more appreciably (both at high temperatures and in cold plastic working).

The ratio of the melting points of the components in an alloy can serve not only as a criterion for estimating the solubility of the elements, but also as a characteristic for predicting the loss of deformability in a solid solution. A greater difference gives a larger loss of ductility.

A typical feature of plastic deformation in partially ordered solutions, i.e. those containing ordered and disordered regions, is the presence between ordered and disordered regions of so-called super-lattice dislocations (super-dislocations). A super-dislocation is essentially a pair of common dislocations separated by an anti-phase boundary (Fig. 263). The occurrence of super-dislocations has been established experimentally. The width of an anti-phase boundary is determined by the elastic repulsion of the two dislocations of the same sign at the two sides of an anti-phase boundary.

When alloys are ordered, they are strengthened and lose ductility due to the formation of anti-phase boundaries which lock dislocations in their positions. Ordering leads to distortions of the crystal structure of the matrix. For instance, when ordering takes place in the Au-Cu system, ordered volumes possess a tetragonal f.c.c. lat-

tice, compared with the disordered f.c.c. lattice of the matrix. The appearing stresses lock additionally the dislocation movement. In cases when the matrix lattice and the super-lattice are isomorphous, stresses may appear solely due to variations in the lattice periods of disordered and ordered volumes ($FeNi_3$, in the Fe-Ni system).

Intensive cold deformation of formerly ordered alloys can lead to partial disordering. Preliminary cold deformation of disordered alloys, which are liable to ordering, facilitates subsequent diffusion and leads to ordering in subsequent heat treatment. An interesting fact is that the strain resistance σ_t and the yield limit σ_y ($\sigma_{0.2}$) increase (after heat treatment conducive to ordering in the Fe-Ni system, see Fig. 264) simultaneously with an increase in the ductility indices δ and ψ near the region of $FeNi_3$ (curves *2* in Fig. 265). This effect can be explained by a slight deviation of the alloy composition from the precise stoichiometric formula $FeNi_3$.

In some cases, ordering in a system may result in a noticeable reduction of deformability indices of the alloys and in their embrittlement in low-temperature plastic deformation. Examples are alloys of the Fe-Co system (Fig. 266*a*) in which alloying of iron with cobalt is associated with widening of the region of γ-solid solutions up to pure cobalt at temperatures above 1 000°C. At lower temperatures,

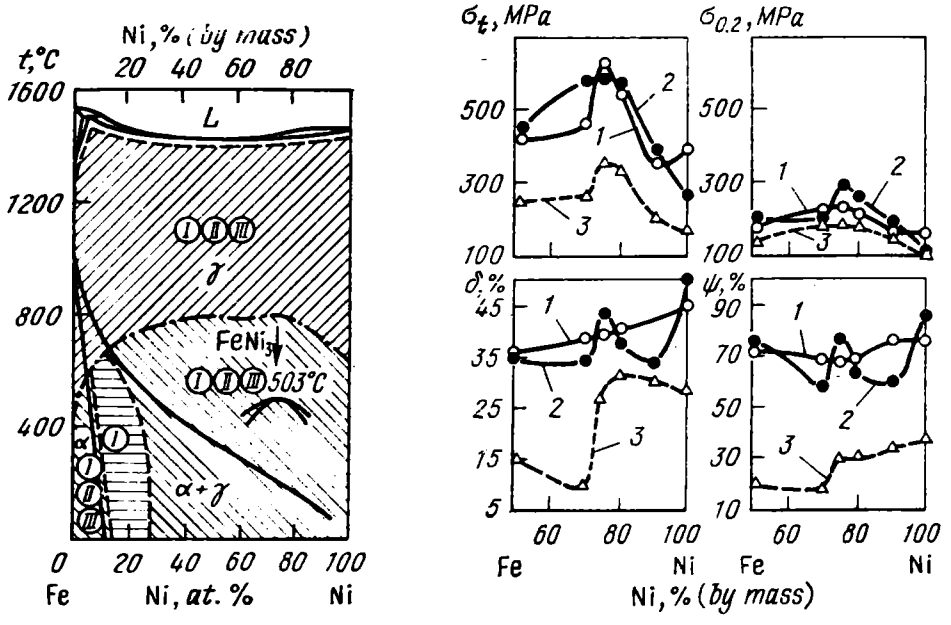

Fig. 264. (*left*) Fe-Ni constitutional diagram indicating recommended methods of plastic working in deformed state

I—pressing, hydroextrusion; *II*—rolling, forging, stamping; *III*—drawing. For as-cast metal, methods *I* and *II* are recommended in the γ-region only

Fig. 265. Effect of various prior procedures on σ_t, $\sigma_{0.2}$, δ and ψ in a portion of the Fe-Ni system

1—homogenizing annealing at 900°C for 24 h, t_{test} = 400°C; *2*—vacuum annealing at 450°C for 360 h, t_{test} = 400°C; *3*—ditto, t_{test} = 600°C

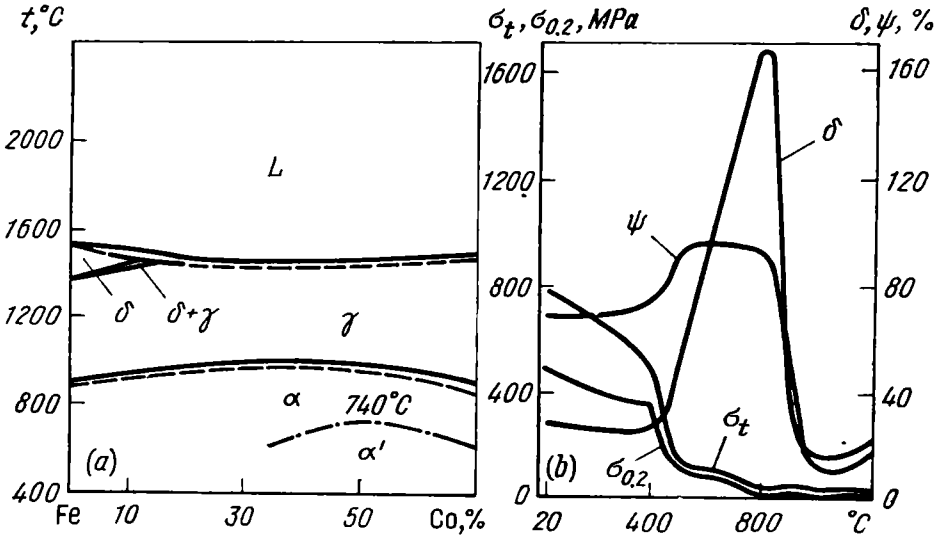

Fig. 266. Constitutional diagram of Fe-Co alloys (*a*) and effect of temperature on plasticity characteristics (ψ, δ) and strain resistance ($\sigma_{0.2}$, σ_t) of a Fe-Co alloy with 68.4% Co (*b*). Homogenizing annealing at 1 050°C for 24 h was carried out before the tests

a series of α-solid solutions exist in the temperature interval from 0 to 75 per cent Co.

With the cobalt content from 30 per cent to 70 per cent (by mass), alloys of this system are capable of ordering with the formation of a super-lattice phase FeCo. Ordering in Fe-Co alloys of the indicated composition occurs at temperatures below 740°C during slow cooling (say, in a furnace) from a high temperature. When being heated continuously, these alloys undergo two phase transformations. One of them is the α'-α (order-disorder) transformation and the other is the transformation of ferrite into austenite ($\alpha \rightarrow \gamma$). The first transformation (α'-α) results in a noticeable decrease of strain resistance and sharp rise of ductility indices (Fig. 266*b*). The ductility of the Fe-Co alloys considered is especially high at a temperature slightly above the point of the beginning of the second phase transformation and some of them tend to exhibit superplasticity (see Ch. 15). For instance, a Fe + 68.4% Co alloy has the following deformability indices at 800°C: ψ = 96 per cent and δ = 170 per cent (σ_t = 35 MPa, σ_y = 25 MPa, see Fig. 266*b*, i.e. strain resistance decreases noticeably under the conditions of superplasticity).

The $\alpha \rightarrow \gamma$ transformation of these alloys (roughly at 1 000°C) leads to a slight increase of strain resistance and a decrease of the relative elongation and reduction; at a higher temperature, ductility is observed to increase and σ_t and σ_y diminish.

Similar regularities have been observed in ductility tests of Fe-Co alloys in the temperature range of hot and warm rolling. At subcritical temperatures (t_{cr} = 740°C), ordered alloys with 40-60 per cent Co cannot be practically subjected to warm plastic working.

The highest ductility is observed in rolling within the temperature range t_{cr}- $t_{\alpha\to\gamma}$; on the transition into the γ-region, the rollability of the alloys again decreases, but will rise slightly if the temperature is raised from 1 000°C to 1 100°C.

Ductility and strain resistance of two-phase alloys belonging to systems of eutectic (eutectoid) or peritectic (peritectoid) type depend on their phase state (see Sec. 2 in this chapter), as well as on chemical composition.

The structure of two-phase alloys is a mixture of two phases, such as $\alpha + \gamma$ in steels or $Ti_\alpha + Ti_\beta$ in titanium (Fig. 267*a*) or a matrix with uniformly distributed precipitate particles of a second phase having a particular degree of dispersity (Fig. 267*b*).

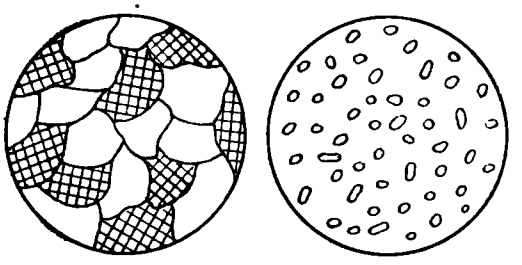

(*a*) (*b*)

Fig. 267. Various types of structure in two-phase alloys

It has been established experimentally that the ductility of two-phase alloys at common deformation rates is lower than that of single-phase ones (an inverse relationship, under conditions of superplasticity), which is largely determined by the characteristics of the phases, i.e. the volume concentration, pattern and nature of distribution, and properties. The ductility of alloys decreases with an increase in the concentration of secondary phases or of the size of their particles, on a change from oval to lamellar shape, and at a higher non-uniformity of their distribution. For instance, inclusions of austenite in a ferritic base (or of ferrite in austenitic base) can cause inhomogeneous deformation in the volume of a polycrystalline aggregate, which is associated with different deformability of austenite and ferrite.

It has been found that the highest ductility at high temperatures (above T_{rec}) is shown by single-phase alloys with the structure of α-ferrite. It has been established in deforming of a steel (1X21H5T) that the deformation of the α-phase (a low value of $\sigma_{s,\alpha}$) at temperatures above 1 000°C is substantially higher than that of the γ-phase (high $\sigma_{s,\gamma}$); at 1 200°C, the difference may be six-fold. The high difference in the strain resistance of the two phases leads to local deformations and stress concentration. Stresses may reach the critical value and cause microcracking in hot plastic working. The lower strain resistance and higher ductility at high temperatures can be explained by a higher stacking fault energy and greater rate of diffusion processes in the α-solid solution, and therefore, by more intensive processes of dynamic polygonization and recrystallization, with diffusion climb of dislocations being the principal mechanism of plastic deformation at elevated temperatures.

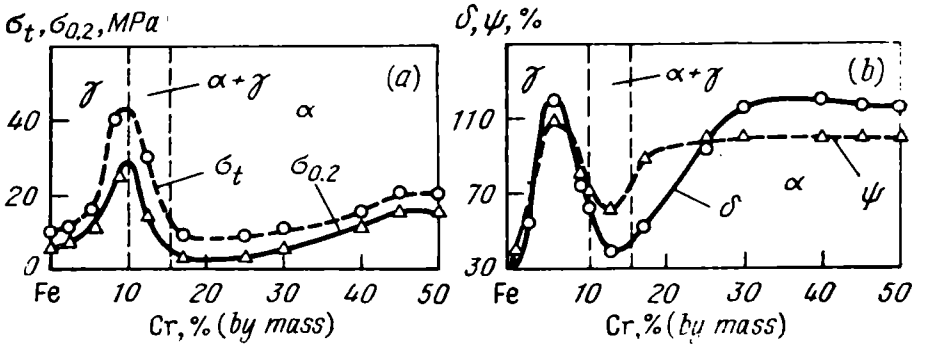

Fig. 268. Effect of chemical and phase composition of Fe-Cr alloys on their strength (*a*) and plastic (*b*) properties at 900°C

Austenite formed in the ferritic matrix can be regarded as a harder inclusion which is an effective barrier for dislocation movement. Dislocation pile-ups formed on such barriers cause an appreciable stress concentration and may even be the source of fracture under proper conditions. Ferrite in the austenitic base can also weaken the latter and produce substantial stress concentrations and, as a consequence, premature fracture of the metal.

Thus, it is essential to consider the combined effect of the chemical and phase composition on ductility and strain resistance. For instance, the strength curves of alloys of the Fe-Cr system at 900°C depending on the chemical and phase composition exhibit two maxima: one of them corresponds to the highest alloying of austenite with chromium (roughly 10% Cr, see Fig. 268) and the other, to the stoichiometric concentration of σ-phase (45% Cr) in Fe-Cr alloys. A two-phase austenite-ferritic alloy (12.5% Cr) occupies an intermediate position, as regards its strength, between the purely austenitic (10% Cr) and the purely ferritic (17% Cr) alloy. Besides, the transition into the two-phase ($\alpha + \gamma$) region involves a sharp drop in ductility indices (Fig. 268). The same picture has been observed at 1 000-1 100°C.

In alloys of the second type of structure, especially in precipitation-hardening alloys, the factors which determine the state of the phases in an aggregate (volume concentration, size, and shape of particles and spacing between them) become even more important. The dislocation theory of precipitation hardening in alloys of this type has been developed in the works of N. F. Mott and F. R. N. Nabarro, E. Orowan, and others (see Ch. 3).

Intermetallics and intermetallic alloys can be characterized by an extremely high brittleness and elevated values of strength at low temperatures. For instance, the hardness (H_μ) of the σ-phase (FeCr) formed in the Fe-Cr system is 10 000-12 000 MPa at room temperature.

Plastic deformation of alloys of this type becomes only possible at temperatures very close to the point of dissociation or melting of the intermetallic compound. As has been proved experimentally for certain intermetallic compounds, dislocation glide begins at $\theta = 0.44$ and cracks cease to appear at $\theta > 0.65$, which is obviously the result of thermal fluctuations which favour dislocation movement in the slip planes. In the crystal structure of intermetallics, covalent and/or ionic bonds play usually an essential part, in addition to metallic bonds, which fact is responsible for their brittleness at low temperatures. As temperature rises and approaches the solidus line, these rigid bonds are weakened due to thermal fluctuations, so that plastic deformation of intermetallic compounds becomes possible in certain cases. Ductility of these compounds increases noticeably on application of hydrostatic pressure.

2. Effect of Structure and Structural and Chemical Inhomogeneity on Ductility of Metals and Alloys

An important factor which can influence ductility is the extent of structural and chemical inhomogeneity. The most substantial effect on deformability is produced by zonal inhomogeneity.

In the further discussion we shall pay special attention to the structural characteristics associated with grain size, length of grain and interphase boundaries, and the extent of chemical inhomogeneity in crystals, which can influence the ductility and strain resistance of metals and alloys.

The structure of cast metals and alloys; anisotropy of plastic properties. A cast metal differs from as-deformed in a greater extent of structural and chemical inhomogeneity:

(1) the density of a cast metal or alloy is lower due to the presence of macro- and micro-voids usually concentrated at the top and along the axis of ingots. Rimming-steel ingots have a developed zone of subcutaneous blowholes. Subcutaneous blowholes, often opening to the surface, may also be found in other kinds of steel;

(2) ingots of steels and alloys obtained by common casting techniques often exhibit an appreciable segregation of harmful impurities (sulphur, phosphorus, etc.), especially at the top and along the axis;

(3) in larger ingots, dendritic segregation may develop progressively;

(4) in two- and polyphase steels and alloys, a secondary phase can form inclusions which often surround individual grains.

With such an inhomogeneous structure, the mechanical properties of the cast metal become anisotropic and its ductility and strain resistance reduce compared with as-deformed or recrystallized metal. The size of grains in an ingot is determined by the rate of solidification. An increase of this rate by two orders of magnitude (from

0.2 cm/min to 20 cm/min) diminishes the distances between dendritic axes roughly to 1/50: from 2 mm to 0.04 mm. The rate of solidification is inversely proportional to the size of ingot, and therefore, a coarser structure should form in a larger ingot. The typical macrostructure of ingots has three zones, which is determined by the different rate of solidification over the cross section.

A zone of fine equi-axed grains appears near the surface where solidification proceeds fastly. Then follows a zone of columnar crystals and then the central zone of large equi-axed grains. A similar structure is formed in continuously cast ingots. In continuously cast ingots, which are usually of smaller cross-sectional area and cooled intensively during solidification, a finer structure forms and the components and impurities segregate less appreciably. This has a favourable effect on their deformability. The structural inhomogeneity of an ingot is closely associated with its chemical inhomogeneity. The extent of dendritic segregation depends on the particular type of constitutional diagram of a steel or alloy.

Dendritic segregation develops in alloys more intensively when the distribution coefficient $K = c_s/c_l$ (where c_s is the concentration of a solid phase and c_l is that of a liquid) differs more from unity, the solidus and liquidus lines are less steep, and when there is a larger temperature interval between the beginning and end of solidification, and also when elements of an alloy can interact strongly in the liquid state. The last effect is typical of alloys with the constitutional diagram having a singular melting point of an intermetallic compound.

The coefficient of segregation K' (the ratio of the concentration of an element in a zone between dendrites to its concentration at a dendritic axis) is 2.3-4 for alloying elements in alloys Ni + 3% Ti, Ni + 2.1% Si, Ni + 4% Sn, and Ni + 5% Sb. Binary alloys Fe + (13-45)% Cr, Fe + 45% Ni, Mo + 0.5% Al, Mo + 0.12% Zr, and Ni + 3% Al, in which chemical interaction of the elements in the liquid state is typically weak, exhibit only a slight tendency to segregate. For these alloys, $K' = 1\text{-}1.2$. The same is also true of ternary alloys of the Fe-Ni-Cr system and Ni + 20% Cr alloys with additions of aluminium, titanium, niobium, and molybdenum.

Carbon segregation can develop only in the presence of carbide-forming elements (Ti, Cr, V, etc.). A stronger dendritic segregation increases the difference in the plastic properties and strain resistance between dendritic axes and spaces between them. This leads to inhomogeneous deformation, enhanced stress concentration, and lower ductility. An analysis of the constitutional diagram of a new alloy can therefore estimate qualitatively the expected deformability of its ingots.

Progressive processes (electroslag remelting, vacuum-arc, induction, and electron-beam zone melting) produce alloys of higher purity and with less segregated components. They reduce the concen-

trations of gases, impurities and non-metallic inclusions in non-ferrous metals, which decreases the anisotropy of their properties, especially in the temperature range of hot deformation. For instance, the coefficient of anisotropy of mechanical properties of an XH55BMTKIO alloy at 1 150°C can be reduced from 1.2 to 1.15 by double vacuum-arc remelting.

Another popular method for obtaining better chemical homogeneity in ingots is high-temperature (homogenizing) annealing. In alloy systems with unlimited or partial solubility of components, annealing for a reasonably long time can equalize the chemical composition and reduce the anisotropy of properties and thus improve substantially the ductility of alloys which are brittle as-cast. For instance, niobium alloy with 0.25-0.3% C, 0.01-0.02% O_2 and 0.02-0.03% N_2, when made by double vacuum-arc or electron-beam remelting, has almost zero ductility at room temperature. Annealing (of ingots 150 mm in diameter) at 1 300-1 500°C can raise the relative elongation at room temperature up to 15-20 per cent and the relative reduction, up to 25-45 per cent. The improved plastic properties of annealed niobium alloys can be explained by the formation of a more stable structure (which is retained during heating before deformation), rounded-off shape of precipitated secondary-phase carbides, and relaxation of temperature stresses existed in the as-cast alloy. The time of homogenizing annealing can be shortened substantially by subjecting the alloy to plastic deformation. In that case, the initial stage of annealing will be accompanied with primary recrystallization and the formation of vacancy groups which accelerate diffusion.

The structure of ingots can also be improved by acting chemically (modifying additions) or physically (ultra-sound) on the process of solidification. Silumin with 10.8% Si, a typically 'casting' alloy, can be deformed by hot or cold rolling when modified by 20% LiF + + 80% LiCl.

Ultrasonic treatment of a liquid metal which solidifies in a mould can increase substantially the number of crystallization nuclei, and therefore, refine grain and diminish the extent of dendritic segregation in the solidified ingot, and in some cases increase the metal deformability. In particular, ultrasonic treatment of steel У9 and У10 refined the grain size down to index 5-7, which resulted in an increase of the ultimate strength by 75 per cent and of the ductility characteristics, by 30-60 per cent. Ultrasonic treatment is very effective with iron alloys containing chromium, silicon and aluminium which are especially liable to grain coarsening. Ultrasonic treatment eliminates the columnar structure in ingots, which leads to an increase of the ultimate strength by a factor more than 1.5 and of the relative reduction and elongation, 4-13 times, with the critical temperature interval of embrittlement being simultaneously narrowed. The difficulty of application of ultrasound in the metal-making

industry is however in that it is a power-intensive process (up to 1.5-2.5 kW/kg).

In cast steel or alloy, the plastic properties are largely anisotropic. For instance, the impact toughness, relative elongation and relative reduction measured at 20°C in specimens of XH78T alloy cut from ingots along columnar dendrites were two-four times higher than the values obtained on specimens cut across dendrites.

In most cases, specimens are cut from an ingot along the main axis, i.e. across columnar dendrites, so as to determine the lowest ductility of as-cast metal. This is correct from the standpoint of estimating the technological properties of the metal, since the most dangerous tensile stresses which appear during rolling act in the same direction. The highest ductility characteristics, measured along dendritic axes, can show the reserve of ductility possessed by the material.

Anisotropy of properties appears in hot deformation more appreciably in ingots containing more metallurgical impurities. Ingots of transformer steel with 3% Si produced by electroslag remelting contain only one-third or one-fourth of the non-metallic inclusions present in open-hearth ingots. Accordingly, the number of turns to fracture in torsion at 800-1 000°C was for electroslag remelted steel 20-30 per cent higher than for the open-hearth. With temperature raised to 1 100-1 200°C, this difference diminished to 3-5 per cent.

In rolling of wedge-shaped specimens, electroslag remelted steel had a better isotropy, notwithstanding its transcrystalline structure. The difference in the highest reductions to fracture in axial and transverse directions of an ingot was 2.5-5 per cent at 800°C and disappeared at 1 000°C and higher temperatures. For open-hearth steel, the relative reduction to fracture in longitudinal direction was 30-70 per cent higher than that in transverse direction, though the structure of the ingot was predominantly equi-axed.

The results of analysis of the anisotropy of properties in large ingots are indicative of large reserves of deformability of as-cast metal because its ductility along dendritic axes is higher than otherwise. This suggests an important conclusion that the energy consumption in rolling deformation can be lowered appreciably if ingot metal is rolled with dendritic axes oriented along the rolling direction, since this is the direction of the highest ductility.

Columnar crystals can be oriented parallel to the ingot axis by controlled cooling of the solidifying metal. In particular, in electroslag remelting it is possible to obtain ingots in which crystal axes will only slightly deviate from the longitudinal axis of the ingot.

Plastic deformation changes the structure of cast steel, leading to a noticeable improvement of its mechanical properties at 20°C. On attaining a definite amount of deformation, the values of ultimate strength, yield strength, impact toughness, and relative elongation and reduction increase markedly. This is associated with destruction

of the cast structure, compaction of the metal, refinement of structural units (grains, secondary phase inclusions), and reduction of chemical inhomogeneity. For instance, upon rolling of ingots of two-phase steel X21H5T of a mass of 14.7 t into slabs with the total reduction around 85 per cent, the mechanical properties of the steel become homogeneous irrespective of direction at 20°C. The ultimate strength of the rolled metal is by 200 MPa higher than that in cast steel, the relative elongation increases from 10-16 per cent to 20-25 per cent, and impact toughness, from 150-210 kJ/m^2 to 800-1 100 kJ/m^2. The microstructure of slabs is more disperse than that of ingots.

With steel P18, the impact toughness, relative elongation and relative reduction at 20°C and in the range 800-1 200°C increased after forging several times. For instance, impact toughness at 1 000°C increased from 120 kJ/m^2 to 720 kJ/m^2, relative elongation from 15 per cent to 38 per cent, and relative reduction, from 12 per cent to 70 per cent.

High-speed steels containing a high concentration of the eutectic component in as-cast state, which forms a continuous brittle network, show a tendency to increase their ductility on plastic deformation due to disintegration of this network and decrease of carbide inhomogeneity. In some cases, the ductility of as-deformed metals was higher than that of as-cast ones in any range of testing temperatures.

Some general relationships for deformation of ingots are as follows:

1. Of essential importance is the method by which the metal is made: for instance, electroslag remelted steel differs only slightly in its ductility from as-deformed steel.

2. The difference in the ductility of as-cast and as-deformed metal increases with increasing concentration of alloying elements.

3. An elevated hydrostatic pressure (for instance, in extrusion) decreases the lowest deformation of an ingot necessary for obtaining the optimal deformability. This deformation roughly corresponds to 3-10-fold drawing. For some steels and alloys with a developed network of a secondary phase, 20-fold or greater drawing is required.

4. The effect of prior deformation on ductility increases with increasing size (mass) of ingots.

5. The difference between the ductility indices of as-cast and as-deformed metal depends on the method of testing. It is the lowest in wedge rolling of cast and deformed steels and higher in more sensitive tensile tests and even more so, in torsional tests. An especially high difference is obtained in dynamic tests (for instance, impact toughness tests).

Ductility of two-phase and polyphase alloys is lower than that of single-phase alloys. There are however exceptions from this general rule. In particular, different results can be obtained by properly selecting such factors as the dispersity of structure or the rate and

temperature of deformation. In that case two-phase alloys may exhibit superplastic properties (see Ch. 15).

6. Under real working conditions with a coarse structure and high deformation rates, the presence of a two-phase structure always lowers the ductility of the metal.

Carbon steels with the structure of granular pearlite have a reduced ductility in the temperature region of existence of two phases. Their ductility increases to a maximum in the point Ac_1, which is attributed to the development of recrystallization. In the two-phase $\alpha + \gamma$ region, ductility drops down again to a minimum and then increases sharply on transition in the region of austenite in hypoeutectoid steel. The ductility of relatively coarse-grained eutectoid steel begins to rise upon completion of the transformation in the range of Ac_1. With a very fine-grained structure in two-phase state, ductility can increase.

Hot deformation of carbon steels in the range of low temperatures (700-900°C) can provoke the appearance of structural inhomogeneity affecting the metal properties.

The presence of a secondary phase can lower the deformability of materials which are high-plastic in hot state, such as electric steels with the silicon content up to 4.5 per cent. For instance, transformer steel with 3 per cent Si is single-phase only at the carbon concentration less than 0.02 per cent. With the carbon content around 0.05 per cent, the structure of transformer steel in the temperature range 1 000-1 250°C contains at least 20-30 per cent austenite. This disturbs the continuity of the steel structure in rolling. A similar effect is produced by other austenite-forming elements, such as manganese. Sulphur and oxygen are harmful impurities in Fe-Si alloys. Silicon steels are more sensitive than pure iron to the presence of sulphur, since silicon reduces the solubility of sulphur in iron. Even with a low concentration of sulphur, around 0.02 per cent, iron sulphides can precipitate on grain boundaries during cooling. Sulphide eutectics become liquid at temperatures above 988°C. With a higher concentration of oxygen in steel, ferrous oxide lowers additionally the melting point of the sulphide eutectic and thus lowers the red-shortness temperature.

Manganese is an austenite-forming element, but, on the other hand, it increases the melting point of sulphide eutectics and thus prevents the development of red-shortness. The solubility of sulphur in iron decreases to a few per cent of the original value if the metal contains only a fraction of a per cent of manganese. Some other elements (chromium, titanium, zinc, beryllium) act like manganese, though less efficiently. Nickel, cobalt and molybdenum lower the melting point of sulphide eutectic and in this respect are harmful impurities in silicon steel.

Typical examples of two-phase alloys are chrome-nickel stainless steels with 0.08-0.12 per cent C, whose ductility may vary depending on the chemical and phase composition.

In austenitic alloys of the Fe-Cr-Ni system, variations in the absolute content of chromium (within 13-22 per cent) and of nickel (5-18 per cent) have no essential effect on strain resistance and ductility, provided that the Cr : Ni ratio remains constant.

An increase in the Cr : Ni ratio involves an increase in the concentration of ferrite and a loss of strain resistance which in purely ferritic steels at 800-1 200°C is only one-third to one-fifth of that in austenitic steels.

The ductility of stainless steels depending on phase composition is described by a curve with a minimum which is most likely to appear at 30-50 per cent ferrite. Purely ferritic steels have the highest ductility. In torsional tests, they show up three-five times higher characteristics than ferrite-austenitic steels (Fig. 269).

Additions of other alloying elements (apart from nickel and chromium) increase the strain resistance and vary the ductility in accordance with the phase composition.

The ductility curves obtained by various workers in tests of various types of steel are however very similar in shape (see Fig. 269). The curves are plotted in relative units, i.e. the highest ductility obtained for steels of each group is taken as unity.

The phase ratio of steels depends largely on their chemical composition and the ratio of the concentrations of ferrite-forming and austenite-forming elements. In a particular grade of steel of a standard chemical composition, it is possible to form different phase ratio. For that reason, one of the measures for improving ductility is to diminish the concentration of austenite in ferrite-austenitic steels by melting a particular steel grade within a narrower range of chemical compositions than that specified by the standard. The phase compo-

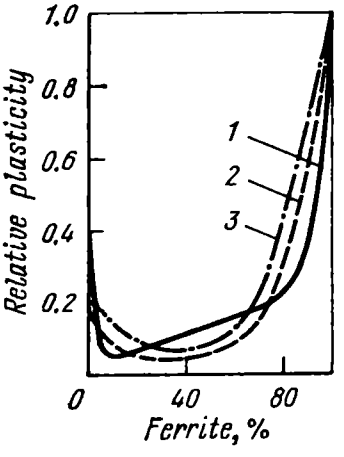

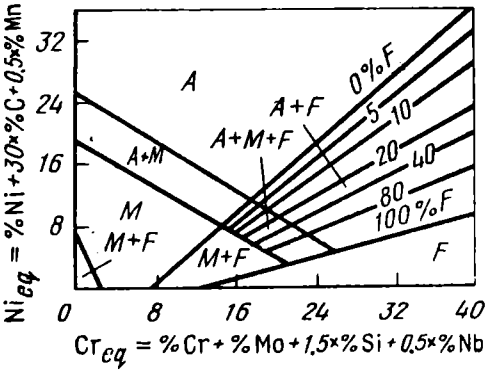

Fig. 269. (*left*) Effect of phase composition of stainless steels on the results of torsional tests at 1 000°C according to M. I. Sinelnikov (*1*); V. M. Yufarov and I. G. Reiko (*2*); Židek (*3*)

Fig. 270. Scheffler's diagram for determining phase composition

sition of a steel (or alloy) for a given chemical composition can be determined by using Scheffler's diagram (Fig. 270). Chromium equivalents (for ferrite-forming elements) and nickel equivalents (for austenite-forming elements) can be calculated by Scheffler's formulae: $Cr_{eq} = Cr + Mo + 1.5\ Si + 0.5\ Nb$; $Ni_{eq} = Ni + 30\ C + 0.5\ Mn$ or by more accurate formulae: $Cr_{eq} = Cr + Mo + 1.5\ Si + 0.5\ Nb + 3.5\ Ti + V + W$; $Ni_{eq} = Ni + 30\ C + 0.5\ Mn + 0.5\ Co$. In these formulae, Cr, Mn, W, etc., are the respective concentrations, per cent.

As follows from the foregoing, there is a close correlation between the chemical composition and structure of alloys, so that their combined effect must be considered properly.

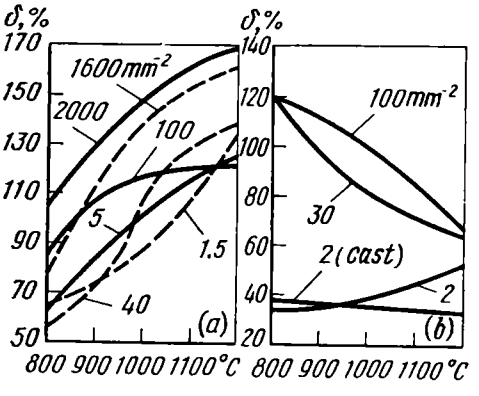

Fig. 271. Effect of deformation temperature and grain size on elongation of steel 000X28 (dashed lines) and steel X28 (solid lines) (*a*), and of steel with 3% Si (*b*)

Numbers at the curves give average number of grains per mm^2

Grain size has a strong influence on the mechanical properties of metals and alloys. A decrease of grain size leads to an increase in ductility characteristics and in strength characteristics at 20°C (see Ch. 4).

The effect of grain size on ductility and strain resistance at high temperatures still has not been studied properly. It has been established, however, that the general tendency indicated earlier is retained at high temperatures too, i.e. strain resistance and ductility diminish with grain coarsening.

In some cases, the ductility of a fine-grained steel decreases with rising temperature, which can be explained by coarsening of grain during heating. This, in particular, has been observed in single-phase silicon steel in a temperature range 800-1 000°C. In two-phase steels, grain coarsening at increasing temperature is impeded, so that they are observed to increase the ductility with temperature due to the development of diffusion and increasing number of slip systems and plastic deformation mechanisms. In chromium steels, however, grain refinement was observed to increase the ductility and diminish the strain resistance, which might be associated with the effect of superplasticity, since these steels (000X28 and X28) are essentially two-phase at elevated temperatures and contain a stable σ-phase. It is not occasionally, therefore, that the effect of grain size on ductility is more pronounced in stainless steels with roughly equal concentrations of two phases (see Fig. 271).

Thus, when analysing the effect of grain size on ductility and strain resistance, it is essential to consider the effect of phase com-

position. For that reason, the effect of grain refinement in single-phase steels at 800-1 000°C is similar to the effect at room temperature, i.e. the ductility and strain resistance increase, whereas two- and polyphase systems can be characterized by decreasing strain resistance and increasing ductility.

Inequigranularity leads to a greater non-uniformity of deformation and the appearance of additional stress fields, which lower the ductility at room and higher temperatures.

3. Effect of Temperature and Rate of Deformation on Ductility

The effects of temperature and rate of deformation on ductility of metals and alloys should be analysed in common, in view of the occurrence of completing hardening and softening processes.

In that connection, it should not be expected that the relationships between ductility and temperature and rate of deformation will be simple. Experimental results show, on the contrary, that they are rather complex: as the temperature and rate of deformation increase, the ductility may increase in some cases and decrease or remain unchanged in others, depending on a number of factors. Pure metals, however, have a general tendency to increase their ductility at higher temperatures due to the development of softening processes and increasing number of operative slip systems and generally of the number of mechanisms by which plastic deformation occurs. With increasing deformation rate, the hardening processes begin to prevail over the competing softening processes.

In commercial-purity metals and alloys, ductility usually depends in a more complicated manner on temperature and deformation rate. Since ductility is closely interrelated with strain resistance (see Ch. 12), the material in this section is presented in a concise form so as to avoid unnecessary repetitions.

Low-temperature ('cold') plastic deformation. At room temperature and up to the point of beginning of recrystallization ($\theta \approx \approx 0.3$-$0.4$ in pure metals and $\theta \geqslant 0.5$ in alloys) and at deformation rates 10^{-4}-10^{-3} s^{-1}, slip is the prevailing mechanism of plastic deformation.

For many b.c.c. metals and alloys, there exists a narrow temperature interval in this region where ductility drops down abruptly, often to zero (the ductile-to-brittle transition temperature). In Fe, W, Mo, Cr and their alloys, a higher contamination of the metal with impurities and greater grain size shift the ductile-brittle transition into a region of higher temperatures. With a decrease of temperature or increase of deformation rate, the number of operative slip systems diminishes and the role of twinning deformation increases at the expense of slip, which leads to a sharp loss of ductility. With

an increase of temperature (to the range of 'warm' deformation), the twinning mechanism changes to slip and ductility increases. Hexagonal metals behave in a similar manner. F.c.c. metals undergo no embrittlement even at low (sub-zero) temperatures.

In the ductile-to-brittle transition range, it becomes practically reasonable to reduce the rate of cold plastic working if the brittle transition temperature of the metal (alloy) is close to room temperature. With low deformation rates, the ductile-to-brittle transition moves into a region of lower temperatures. If the transition point is above room temperature, a higher deformability can be obtained by increasing the deformation rate. Intensified unit reductions will then be favourable for increasing the ductility by increasing the temperature due to the heat of deformation. This technique is used practically in cold rolling of transformer steel: due to heavy reductions in high-speed rolling mills, the temperature of rolled strip increases to 100-300°C. In that way, one can manage to 'jump' through the ductile-to-brittle transition range of the steel, which lies at temperatures below 100°C.

Moderate-temperature ('warm') plastic deformation. In the temperature range of 'warm' plastic deformation, strain ageing often takes place and leads to an increase of strain resistance and loss of ductility. Strain ageing can be observed in steels at temperatures around 400°C (blue brittleness) and in high-melting metals, especially at higher concentrations of oxygen, nitrogen and carbon. The hardening and loss of ductility are due to the precipitation of high-disperse particles—compounds of these elements, and appear at deformation rates $\dot{\varepsilon} = 10^{-3}\ s^{-1}$. At higher deformation rates, precipitation hardening has no time for development and therefore, there is no loss of ductility.

In modern high-speed rolling mills, the plastic deformation of steels and iron- and nickel-base alloys is finished at temperatures below 800-950°C, i.e. 'warm' plastic deformation actually takes place, which is characterized by multiple intragranular slip and suppression of recrystallization processes. In this case, an elevated ductility is observed, since the temperature relationship for ductility is characterized by an increase of ductility long before the temperature of the beginning of recrystallization is reached. This is especially noticeable in c.p.h. metals (beryllium, magnesium) and can be explained by easier slip on non-basal planes. In that case, twinning is suppressed by easy slip.

With f.c.c. metals (copper, nickel, aluminium, etc.), an increase of temperature in the range of warm plastic deformation has practically no effect on ductility. This is associated with the fact that the number of operative slip systems varies only slightly and that intragranular deformation develops intensively already at low temperatures. For that reason, the effect of temperature on ductility in that case is insignificant and an increase of the deformation rate

in this temperature range decreases ductility inessentially.

The effect of increasing ductility at $\theta = 0.2\text{-}0.5$ due to adiabatic heating of the deformed metal is lower than in the low-temperature range, because of the lower evolution of heat.

The upper boundary of the range of 'warm' plastic deformation is the temperature of the beginning of recrystallization. The typical features of high-temperature mechanisms of deformation (diffusion mechanisms, grain-boundary sliding, etc.) usually appear at temperatures 100-200°C above the temperature of the beginning of recrystallization (for steels). An increase in the deformation rate shifts the boundary of high-temperature mechanisms to higher temperatures. For instance, distinct features of high-temperature mechanisms appear in steels at 500-600°C and $\dot{\varepsilon} = 10^{-6}\text{-}10^{-5}$ s^{-1} or at 1 000°C with $\dot{\varepsilon} = 10^{-3}\text{-}10^{-2}$ s^{-1}. High-temperature deformation of molybdenum begins at 1 000°C with $\dot{\varepsilon} = 10^{-6}\text{-}10^{-5}$ s^{-1} and at 1 200°C, with $\dot{\varepsilon} = 10^{-3}$ s^{-1}. An especially noticeable increase of ductility in the temperature range of 'warm' deformation occurs in b.c.c. metals; it reduces however with increasing deformation rate. C.p.h. and b.c.c. metals may have deviations from this general rule, associated with the occurrence of phase transformations.

High-temperature ('hot') plastic deformation. As temperature is raised further, ductility increases. For each metal, however, there is a narrower temperature range within the interval up to $\theta = 0.5\text{-}0.8$ where ductility is observed to drop down abruptly and fracture is typically intercrystalline. The sharp loss of ductility at temperatures above the recrystallization temperature is referred to as red-shortness and is typical of iron, nickel, tungsten, molybdenum, niobium, copper, magnesium, beryllium and their alloys and of stainless and other types of steel. As regards high-melting metals (molybdenum, tungsten, etc.), a correlation has been established between this loss of ductility and the completion of primary recrystallization, because of which the phenomenon is often called recrystallization brittleness (see Ch. 8). Red-shortness appears in metals and alloys containing relatively high concentrations of impurities: oxygen, nitrogen, hydrogen, carbon. The critical concentration of impurities that causes red-shortness is different for various metals. For instance, in steel with 0.3 per cent C, the content of oxygen must be below 0.04 per cent, that of sulphur, below 0.01 per cent; in oxygen-free copper, the total concentration of impurities must not exceed 0.02 per cent; in molybdenum and tungsten, only a few thousandth fractions of a per cent are allowable.

Red-shortness is caused by segregation of various fusible or brittle phases on grain boundaries. These may be fusible compounds

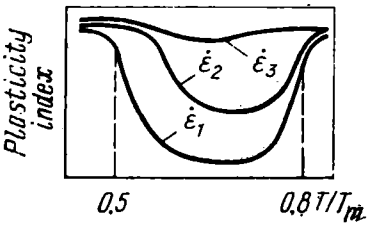

Fig. 272. Effect of deformation rate on ductility of metals liable to red-shortness; $\dot{\varepsilon}_3 > \dot{\varepsilon}_2 > \dot{\varepsilon}_1$

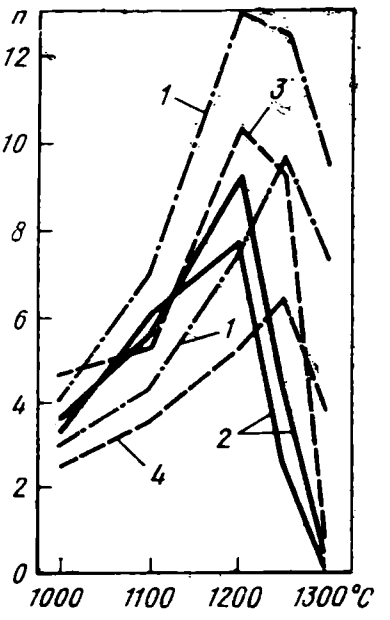

Fig. 273. Ductility (number n of twist turns to fracture) of steel Grade X23H18
1—deoxidized by silico-calcium; *2*—with addition of boron; *3*—with addition of ferro-titanium; and *4*—made by the common technology

(oxides, sulphides), fusible metals (lead, tin, antimony), brittle compounds (carbides, nitrides), etc.

The type of fracture is the same in either case, but the effects may be due to different mechanisms. Segregation of impurities is a diffusion process, because of which the factors which facilitate diffusion are conducive to red-shortness. In view of this, vacancies formed at the stage of primary recrystallization may probably be one of the causes of recrystallization brittleness (see Ch. 6).

Owing to segregation of fusible compounds on grain boundaries, these are melted and lose strength compared with the bulk of grain. Fracture takes place by the formation of a lustrous melted surface. Such phenomena are, for instance, observed in steels.

Brittle compounds cause red-shortness in high-melting metals and alloys. Hard brittle compounds inhibit grain-boundary sliding, so that the continuity of deformation along grain boundaries is disturbed (due to lower accommodation by transgranular deformation), leading to intergranular fracture.

The effect of red-shortness is suppressed on increasing the deformation rate from $\dot{\varepsilon} = 10^{-5}\ s^{-1}$ to 10^{-1}-$10^{0}\ s^{-1}$ (Fig. 272), which is associated with suppression of thermally activated diffusion processes controlling intergranular fracture and with lower contribution of grain-boundary deformation to the total deformation of the metal. With low deformation rates and at temperatures corresponding to the minimum of ductility in the red-shortness interval (see Fig. 272), impurity atoms migrate intensively under the action of stresses. Impurities segregate to grain boundaries and provoke intergranular fracture.

In some metals, red-shortness is not observed, which can be associated with increasing solubility of interstitial impurities. A more essential factor is the migration of grain boundaries which prevents growth of grain-boundary cracks. In some cases (iron, nickel and their alloys), an increase of the rate of deformation from 10^{-4} to 10^{-2} s^{-1} does not prevent 'red-shortness', but only shifts the interval of reduced ductility into a region of higher temperatures (by 200-250°C).

One of the methods for preventing red-shortness is to lower the concentration of the harmful impurities which can cause the phenomenon or to eliminate their effect by chemically active modifying additions (zirconium, cerium, boron, etc.). For instance, boron in a concentration of 0.002 per cent increases the ductility of stainless steel in the interval 800-1 100°C (Fig. 273). Boron combines interstitial impurities and forms highly disperse particles on grain boundaries.

Ductility curves have a maximum in the temperature range $\theta = 0.6\text{-}0.85$ (i.e., 800-1 200°C for steels), see Fig. 273. Upon attaining this maximum, ductility drops down due to superheating (excessive growth of grains) and, with a further increase of temperature, due to burning (oxidation on grain boundaries). Curves relating ductility to deformation rate also have a maximum in the same temperature range at $\dot{\varepsilon} = 10^{-3}\text{-}10^{-4}$ s^{-1} (for chrome-nickel alloys $\dot{\varepsilon} = 10^{-2}\text{-}10^{-1}$ s^{-1}, for steel 01X18H10T $\dot{\varepsilon} = 10^{0}$ s^{-1}). A further increase of deformation rate results in a loss of ductility, which is associated with suppression of diffusion processes.

Though the relationship between ductility and the temperature and rate of deformation is rather complicated, it is possible to establish the following general rules for the range of deformation rates typical of real processes of plastic working of metals, $\dot{\varepsilon} = 10^{-3}\text{-}10^{2}$ s^{-1} (Fig. 274).

An increase of temperature in the region $\theta > 0.9$ decreases sharply the deformability of a metal (superheating and burning). An increased rate of deformation of steels and alloys having a high strain

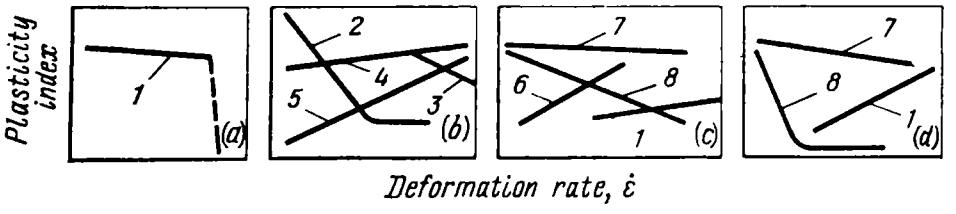

Fig. 274. Effect of deformation rate on ductility of metals and alloys at various homologous temperatures (schematically)

(*a*) $T/T_{m.p} = 0.9$; (*b*) 0.5-0.9; (*c*) 0.2-0.5; (*d*) 0-0.5; *1*—adiabatic heating; *2*—superplastic materials; *3*, *4*—high-plastic steels and fine-grained high-purity alloys not liable to red-shortness; *5*—metals and alloys liable to red-shortness; *6*—precipitation hardening in the region of warm deformation; *7*, *8*—metals and alloys respectively with f.c.c. and b.c.c lattice

resistance can produce a negative effect, since even a slight rise of temperature due to the heat of deformation can lead to melting of fusible components on grain boundaries, and therefore, to fracture (Fig. 274*a*). Microsections corresponding to this region reveal traces of fusible eutectics and internal oxidation on grain boundaries (burning).

The region of high ductility of metals lies within the range (0.7-0.9) $T_{m.p.}$; some types of alloys, in particular precipitation-hardening nickel-base alloys, may have a narrower range. Most steels in this range have high ductility characteristics at various deformation rates. Two- and polyphase steels and alloys exhibit 'isothermal' superplasticity in this temperature range. These fine-grained materials are characterized by reducing ductility as the deformation rate in tensile tests increases from 10^{-3} to 10^{1} s^{-1}. The process stops, however, at a relatively high level and causes no substantial loss of deformability (see curve *2* in Fig. 274*b*).

The ductility of cast and coarse-grained steels and alloys may increase slightly or remain unchanged with increasing deformation rate. The curve of deformability depending on deformation rate for this temperature range should have a typical maximum, such as curve *3* in Fig. 274*b*. With finer grain size, the position of the maximum moves towards higher deformation rates.

In the region of red-shortness (0.5-0.8$T_{m.p.}$), the ductility of pure, fine-grained and modified steels and alloys is high and varies only slightly with increasing deformation rate (curve *4* in Fig. 274*b*).

Coarse-grained steels and alloys of commercial purity are characterized by red-shortness which is associated with the development of grain-boundary cracks in triple joints. A higher rate of deformation improves somewhat the ductility of these steels (see curve *5* in Fig. 274*b*) and prevents grain-boundary fracture.

The region of 'warm' deformation (θ = 0.2-0.5), where transgranular slip is predominant, is characterized by an increase of the ductility of steels and alloys as the deformation temperature approaches the upper boundary. Ductility can rise with increasing deformation rate at very high deformation rates when adiabatic heating of the material takes place (see curve *1* in Fig. 274*c*) or, at lower rates, in precipitation-hardening metals and alloys (curve *6* in Fig. 274*c*).

In the region of cold deformation (θ=0-0.2), the phenomena observed are similar to those typical of the region of 'warm' deformation. The only difference is that high deformation rates can produce greater heating of the cold metal (see curve *1* in Fig. 274*d*). The ductility of b.c.c. metals and alloys decreases with increasing deformation rate, as in the region of 'warm' deformation, due to the change from the slip mechanism to twinning, but the effect is more pronounced (see curve *8* in Fig. 274*d*).

As regards f.c.c. metals, their ductility decreases less appreciably with increasing deformation rate (curve *7* in Fig. 274*d*).

4. Effect of the Type of Stressed State on Ductility

The positive effect of hydrostatic pressure on ductility of metals and alloys and the dislocation mechanisms of crack initiation under pressure have been discussed in Ch. 11. As has been noted, the positive effect of pressure consists in decreasing the tensile stresses, which might produce cracks, and in increasing the critical stress for crack propagation.

In deformation of commercial metals and alloys, the positive role of hydrostatic pressure (uniform compression) is more substantial and consists in the following:

(1) hydrostatic pressure inhibits intergranular deformation which might cause brittleness;

(2) the metal is compacted additionally due to 'healing' of micro- and macro-defects and macro-voids appeared during plastic deformation; defects formed in casting or prior plastic deformation (cracks, cavities, macro-pores) are also 'healed';

(3) the effect of various inclusions and particles of other phases, which serve as stress concentrators in plastic deformation, is eliminated or suppressed;

(4) the ductility of the most brittle components, in particular of intermetallics, increases; and

(5) the harmful effect of fusible eutectics is reduced or eliminated.

Under hydrostatic pressure, the points of phase transformations may be shifted from their positions. The general rule is that hydrostatic pressure facilitates the phase transformations which result in a decrease of the specific volume and impedes those after which the specific volume increases. For instance, the formation of the σ-phase in alloys of the Fe-Cr system occurs at 815°C; with an increase of pressure, the temperature of the α-σ-transformation increases. Hydrostatic pressure can also change the solubility of phases and even transform the constitutional diagram. In particular, the constitutional diagram of a system of continuous solid solutions can change on an increase of pressure to a diagram of the eutectic type, and vice versa.

It follows from the foregoing that the dependence of the ductility on the type of stressed state will be different for various metals and alloys and depends on the type of crystal lattice, the presence of impurities, phase composition, temperature and rate of deformation, structure, and some other factors which can influence ductility. Irrespective of the effect of hydrostatic pressure on the ductility of a metal or alloy, the latter increases as the spherical stress tensor diminishes algebraically, i.e. as the coefficient of stiffness of the stressed state $k = \sigma/T$ becomes lower. It should be noted in this connection that tests in high-pressure chambers are not necessarily needed for establishing the relationship between ductility and k

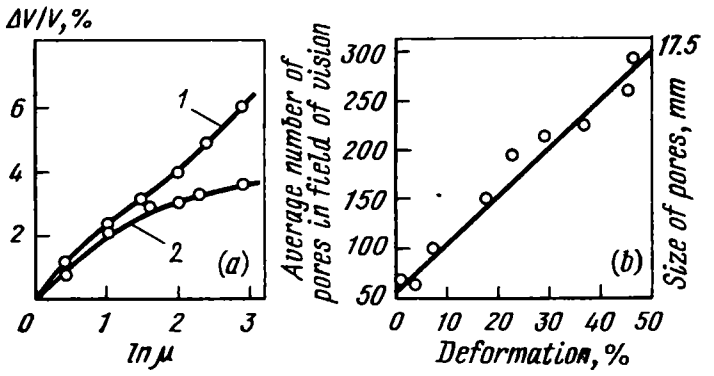

Fig. 275. Variations of unit volume of steel У8 during wire drawing (*a*) and effect of deformation on the number of pores (*b*)
Wire diameter, mm: *1*—2.5; *2*—5

(or for constructing the Λ_r-k diagram). It is sufficient to know the values of Λ_r in tension ($k = 1:\sqrt{3}$), torsion ($k = 0$), and compression ($k = -1:\sqrt{3}$).

The *phenomenological theory of fracture* does not presume a single criterion of stress or strain (see Ch. 11), but is based on the necessity to develop a criterion which would account for the history of deformation, $\varepsilon(\tau)$, the stressed state, and its variations in time, $k(\tau)$.

As applied to plastic working processes, which are characterized by complex functional relationships $\varepsilon(\tau)$, $\dot{\varepsilon}(\tau)$ and $k(\tau)$, the most consistent is the phenomenological theory of fracture suggested by G. A. Smirnov-Alyaev and V. L. Kolmogorov. The theory is based on some well-known facts which will be discussed below:

1. The process of plastic deformation involves plastic 'loosening' of the metal due to increasing dislocation density at the initial stages of plastic working, with subsequent formation of micro-voids and micro-cracks. The volume of the metal is observed to increase monotonously with increasing plastic deformation (Fig. 275).

2. At the same time with plastic 'loosening', 'healing' of defects takes place, which is stimulated by an increase in temperature, by application of hydrostatic pressure, and by the development of diffusion processes, including grain boundary migration, dynamic recovery, and recrystallization.

3. Even a high hydrostatic pressure cannot eliminate defects in a metal if it involves no plastic deformation. The effect of plastic deformation can be explained by closure of sides of cracks and enhancement of diffusion processes (the diffusion coefficient increases by a few orders of magnitude), due to strong distortions at sides of cracks, which increases the intensity of healing.

4. The period of accumulation of defects and plastic loosening with the formation of micro-voids and micro-cracks, up to the appearance of Griffith's cracks of the critical size, is the longest period

of plastic deformation. The strain corresponding to this period is ε_I. The second period, associated with crack propagation, occupies less time. It is characterized by the strain $\varepsilon_{II} = \varepsilon_r - \varepsilon_I$, where ε_r is the strain at rupture. A Griffith's crack propagates at a high speed, so that ε_{II} has no time to increase substantially. For that reason, $\varepsilon_I \gg \varepsilon_{II}$ and it can be assumed approximately that $\varepsilon_r = \varepsilon_I$, i.e. the strain to rupture is determined by the first period.

In accordance with the foregoing, it is assumed that the strain suffered by an elementary volume in the vicinity of a material point to the moment of maximum 'loosening' and the beginning of formation of a Griffith's crack is equal to Λ_r. The increment of concentration of defects in the metal, $d\psi_1$, will be the higher, the greater is the strain increment $d\Lambda = Hd\tau$ and the lower Λ_r. Thus,

$$d\psi = c_1 (Hd\tau/\Lambda_r)$$

where c_1 is the coefficient characterizing the intensity of plastic loosening or the intensity of accumulation of defects. In particular, for the data represented in Fig. 275*a*, c_1 is roughly constant [for curve *1* $c_1 = c_1(\mu)$ and $c_1 = c_1(\Lambda)$ for curve *2*].

In cold deformation, defects (voids, looseness, micro-cracks) can be healed more effectively at a heavier deformation and, naturally, they will be healed less quickly at a higher plastic limit of the metal, i.e. at higher Λ_r. The concentration of defects decreases, which can be expressed in the following form:

$$d\psi_2 = -c_2 \, d\Lambda/\Lambda_r = -c_2 (Hd\tau/\Lambda_r)$$

and the final result will be

$$d\psi = d\psi_1 + d\psi_2 = (c_1 - c_2) Hd\tau/\Lambda_r \tag{186}$$

But $c_2 = c_2(k)$, since healing is more effective at a higher hydrostatic pressure.

Noting that $H = H(\tau)$, i.e. is time-variable, and that $\Lambda_r = \Lambda_r(k)$ and $k = k(\tau)$, formula (186) takes the form:

$$d\psi = [c_1(\Lambda) - c_2(k)] \frac{H(\tau)\, d\tau}{\Lambda_r [k(\tau)]} = B(\tau) \frac{H(\tau)\, d\tau}{\Lambda_r [k(\tau)]} \tag{187}$$

In hot plastic deformation, defects are healed due to diffusion processes and recrystallization, so that $d\psi$ in formula (187) decreases and does it more intensively with a larger interval between t and τ. With H and θ being constant, this reduction can be accounted for by a hereditary function $E(t - \tau)$ which varies from 1 in complete 'cold' deformation to zero in complete 'hot' deformation. Expression (187) will then be:

$$d\psi = E(t-\tau) B(\tau) \frac{H(\tau)\, d\tau}{\Lambda_r [k(\tau)]} \tag{188}$$

The convenience of this notation consists in that it gives the plastic limit in hot deformation in the following form:

$$\Lambda_r = \int_0^{t_r} [H(\tau)/E'(t-\tau)]\,d\tau \tag{189}$$

where at $E(t-\tau) = 0$, $\Lambda_r = \infty$, which corresponds to an infinitely large plastic deformation with full completion of softening processes* or, with infinitesimal E, to the effect of superplasticity.

Integration of formulae (186) and (187) gives ψ, the coefficient of utilization of ductility, and the condition for deformation without fracture at $\psi < 1$ in cold deformation:

$$\psi = \int_0^t B(\tau)\{H(\tau)/\Lambda_r[k(\tau)]\}\,d\tau < 1 \tag{190}$$

and in hot deformation

$$\psi = \int_0^t E(t-\tau)\,B(\tau)\{H(\tau)/\Lambda_r[k(\tau)]\}\,d\tau < 1 \tag{191}$$

In cold plastic deformation with $k = \text{const}$, i.e. with a monotonous process of plastic working, and with $B = \text{const}$, we have from formulae (187) and (190) [noting that $\Lambda_r(k) = \text{const}$]:

$$\psi = B\int (H/\Lambda_r)\,d\tau = B\Lambda/\Lambda_r \tag{191a}$$

At the moment of fracture, $\psi = 1$ and a rule can be derived from formula (191a) for determining the amount of deformation to fracture in simplest tests at $k = \text{const}$. Usually, k is not constant, but varies from 0.577 to +2.0 or more in tension or from —0.577 to —0.2 or +0.5 in compression of a cylinder, so that it is recommended to take average values of k for the whole period of a test. The results of tests in tension, tension with stress concentrators (this test makes it possible to obtain a high value of k: $k = 2$-3), tension with torsion ($0.6 > k > 0$), torsion ($k = 0$), compression ($k = -0.577$), compression with application of hydrostatic pressure ($k < -0.577$), are used for constructing Λ_r-k diagrams in cold and hot deformation (Figs. 276 and 277).

Analysis of Λ_r-k diagrams suggests the following conclusions.

1. The plastic limit Λ_r increases with decreasing k (i.e. with increasing hydrostatic pressure and decreasing spherical stress tensor).

---

* In 'hot' plastic deformation, an extension $\mu \approx 510$ (in a wire drawbench) and a deformation $\Lambda = \sqrt{3}\ln\mu \approx 11 > \Lambda_r$ (i.e. much above the value of Λ determined in high-temperature tests) can be obtained after single heating

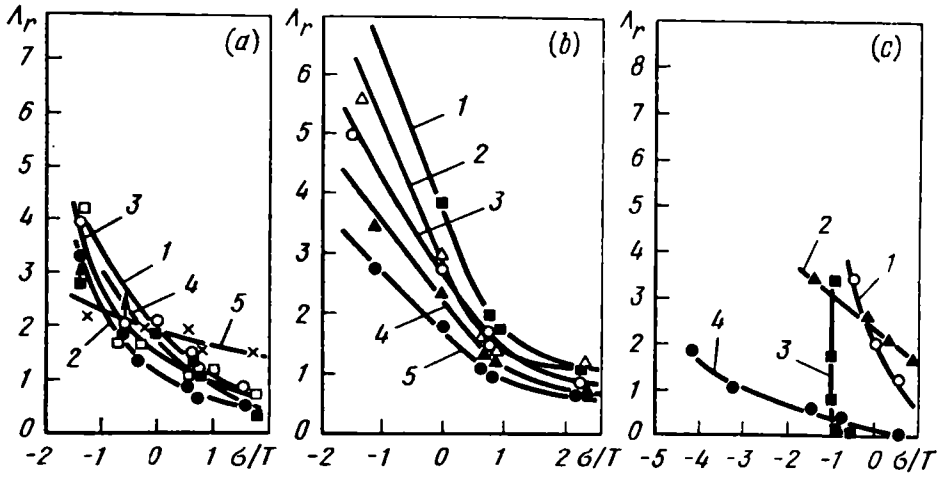

Fig. 276. The Λ_r-k diagrams for various materials
(*a*) steels (*1*—steel 20, *2*—steel 45, *3*—ШХ15, *4*—30ХГСА, *5*—Х18Н10Т); (*b*) aluminium alloys (*1*—Grade AB, *2*—АМг2, *3*—Д1, *4*—Д16, *5*—АМг5В); (*c*) pure metals (*1*—Mo, *2*—Cu, *3*—Zn, *4*—Be)

2. The intensity of growth of Λ_r with variation of k (the sensitivity of the type of stressed state) and the ratio $\partial\Lambda_r/\partial k$ are different for various metals and alloys.

3. In the practical range of $k = -1.5$-2.5 attainable in plastic working without application of hydrostatic pressure, Λ_r may vary by a factor of 2 to 8 or even more (Fig. 277), which is comparable with the variations of the plastic limit depending on temperature in the allowable temperature range of hot plastic working (see Fig. 278).

5. Effect of Surrounding Medium and Size Factor on Ductility of Metals and Alloys

The *surrounding medium* may cause: (1) dissolution of surface layers of the deformed body; (2) corrosion and oxidation of these layers; (3) variation in the chemical and phase composition and structure of surface layers; and (4) easier deformation due to adsorption.

The effect of the last factor has been discussed in Ch. 12 and all the conclusions derived there are fully applicable to ductility, with the only difference that ductility will increase where strain resistance decreases, and vice versa.

S. I. Gubkin has given the following examples to emphasize the importance of the factors mentioned above.

When nickel and its alloys are heated in an atmosphere containing sulphur, the latter can diffuse into the metal and form Ni_3S_2 sulphide which causes embrittlement. Even a very low concentration of sulphur (0.005 per cent) is sufficient to make the metal brit-

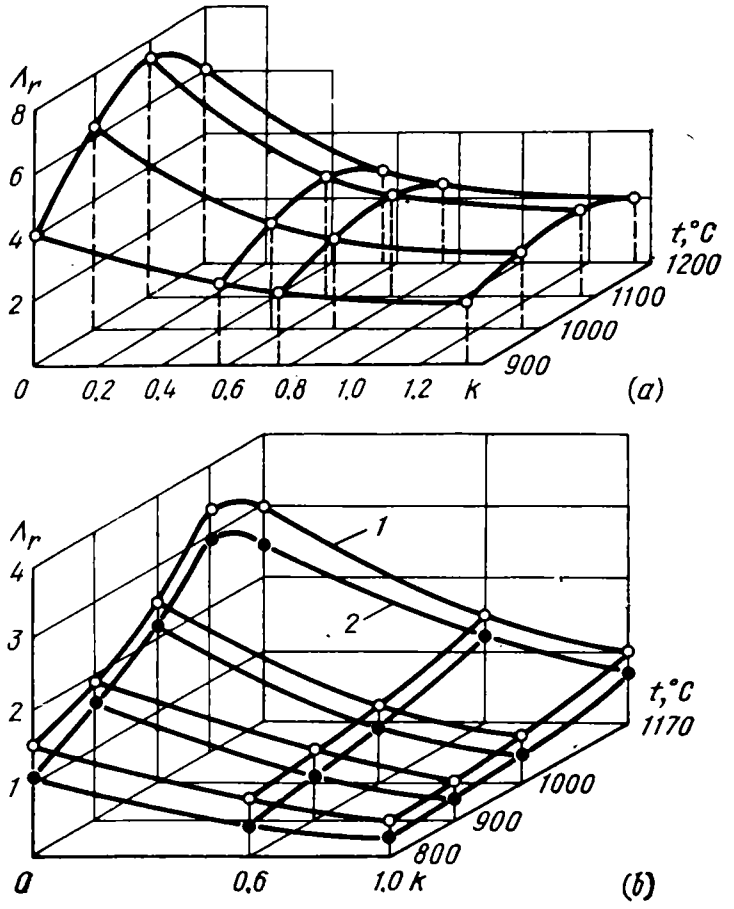

Fig. 277. The Λ_r-k-t°C diagrams for deformed steels 07X19H105CB (*a*) and P6M5 (*b*)

1—core zone of ingot; *2*—middle portion

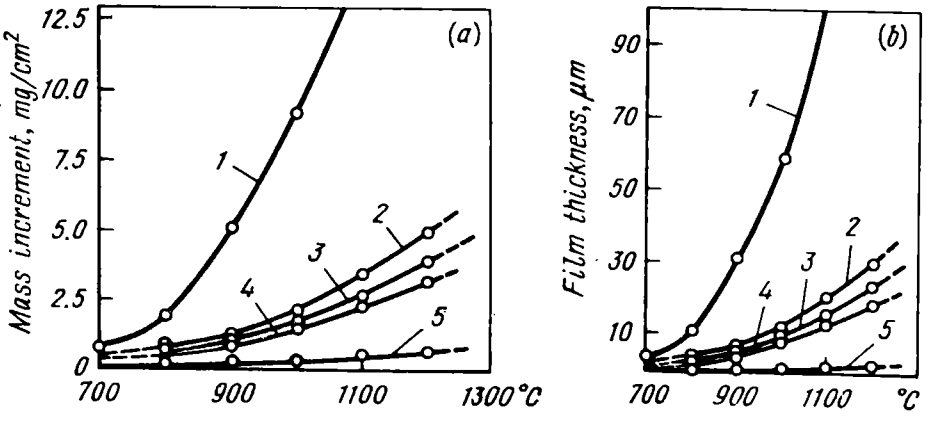

Fig. 278. Effect of temperature on absorption of gases (*a*) and thickness of oxide film (*b*) of zirconium on heating for 15 minutes in various media

1—air; *2*—vacuum 26.6 MPa; *3*—helium; *4*—vacuum 1.3 MPa; *5*—vacuum 0.066 MPa

tle. For that reason, the atmosphere in nickel-smelting reverberatory furnaces must be absolutely pure from sulphur.

Hydrogen can cause copper embrittlement, so that it is intolerable in reducing atmosphere for heating copper.

Nitrogen and oxygen of the air can react intensively with high-melting metals, which makes hot deformation of these metals difficult or even impossible because of the risk of oxidation of surface layers and saturation of the metal with gases which can thus change its chemical composition.

High-melting metals can interact readily with oxygen, nitrogen, hydrogen and carbon which form either interstitial solid solutions (if the state of limited solubility does not appear) or compounds of the type of carbides, oxides, nitrides and hydrides; in either case, the plastic properties of the metal are impaired.

If the concentration of interstitial impurities does not reach the solubility limit, high-melting metals remain ductile at low temperature, but lose ductility if the concentration of impurities is above that limit. As a rule, the limits of solubility of C, H_2, N_2 and O_2 in high-melting metals are quite low (see Table 15).

Table 15. Solubility Limits of Interstitial Impurities for Selected High-melting Metals after Slow Cooling to 20°C

Metal	Impurities, % (by mass)			
	H_2	C	N_2	O_2
Tungsten	Not found*	0.00001	0.00001	0.0001
Molybdenum	0.00001	0.0001	0.0001	0.0001
Niobium	0.9	0.1	0.03	0.1
Tantalum	0.4	0.07	0.1	0.02
Vanadium	1.0	0.1	0.5	0.3
Chromium	0.0001	0.0001	0.00001	0.00001

* Hydrides and nitrides are not formed.

Hydrogen has no embrittling effect on tungsten and molybdenum, but lowers the ductility of niobium and tantalum. With a concentration of 0.014 per cent H_2, niobium exhibits brittle fracture in cold plastic working. At 200°C or higher temperatures, hydrogen produces no embrittlement of niobium in concentrations up to 0.2 per cent (by mass).

Chromium and niobium can react strongly with nitrogen. The embrittling effect of nitrogen on niobium is lower than that of hydrogen, but the ductility of niobium reduces if it contains nitrogen: the deformability indices in cold rolling decrease with increasing conc-

entration of nitrogen from 75% [for Nb + (0.003 — 0.22)% N_2 (by mass)] to 10 per cent [for Nb + 0.73% N_2 (by mass)].

Oxygen, even in low concentrations (see Table 15), can impair the ductility of tungsten, molybdenum and chromium, due to the formation of oxides on grain boundaries.

In tungsten and molybdenum, oxygen has a substantial effect on the ductile-to-brittle transition temperature. For instance, the ductile-to-brittle transition temperature of molybdenum increases from —60°C to +200°C in the presence of 0.0001-0.0006 per cent O_2. Molybdenum ingots with more than 0.008 per cent O_2 (by mass) cannot be forged in view of their brittle fracture. The ductility of niobium is impaired when the content of oxygen in it is raised from 0.03 per cent to 0.23 per cent; in particular, ψ diminishes from 65 per cent to 36 per cent and δ, from 23 per cent to 15 per cent. The deformability of niobium in cold rolling remains quite high (ε = = 75 per cent) at oxygen concentrations up to 0.135 per cent.

When high-melting metals are heated or deformed in air, their surface layers may become brittle due to saturation with H_2, O_2 and N_2 from the atmosphere. Specimens either break in deformation or have cracks and fissures in the surface. For that reason, high-melting metals are deformed in vacuum, protective gas atmospheres or protective shells.

In order to prevent oxidation of the metal during heating and deformation, the partial pressure of the gas must not exceed the dissociation pressure of the oxide at a given temperature. For metals having a high dissociation pressure of oxides, non-oxidizing conditions of deformation can be formed in a relatively low vacuum (13.3-1.33 MPa) or in an inert-gas atmosphere of appropriate purity. Metals of this (first) group include tungsten, molybdenum, rhenium, copper, and nickel. Thermodynamic calculations show, for instance, that non-oxidizing conditions for deformation of molybdenum can be realized at 1 700 K in a vacuum of 1.3 MPa.

Non-oxidizing conditions of hot and warm deformation of niobium, tantalum, titanium, zirconium, vanadium, and chromium (the second group), which have a low dissociation pressure of oxides, cannot be ensured in a technically feasible vacuum. Analysis of the oxidation kinetics shows however that the rate of oxidation reactions drops down sharply on a change to a lower vacuum. For that reason, a change of vacuum can change the thickness and properties of the oxide film on a metal (see Fig. 278).

Variation in the partial pressure of active gases may not only influence the kinetics of metal oxidation, but also determine saturation of metals with gases or, on the contrary, their degassing. A change in the properties of gases can lead to variation in the physicochemical properties of the deformed metal, in particular, of its ductility, strength, corrosion resistance, etc.

If the concentration of a gas in the surrounding medium (in par-

ticular, in a vacuum) is lower than that in the metal, the latter will be degassed. The ductility of a metal can be increased if it has been protected against gas saturation and oxidation during hot deformation. For instance, rhenium is brittle (red-shortness) when hot-deformed in air and exhibits no residual deformation. In a vacuum, it can however be rolled with the total reduction 50 per cent. For some metals, their deformability in rolling increases in a vacuum by as much as 60-80 per cent, i.e. metals which are absolutely brittle in air become quite plastic when deformed in a vacuum.

For metals of the second group, gas saturation is not excluded in any technically feasible vacuum ($\sim 1.33 \times 10^{-3}$ MPa), but vacuum helps in lowering the rate of the oxidation reaction, decreases the thickness of oxide film (see Fig. 278), the degree of gas saturation and the depth of gas-saturated layer (Fig. 279). This, in turn, leads to increased ductility in deformation and after hot plastic working (Fig. 280), thus improving substantially the properties of the metal: strength, ductility, corrosion resistance, etc.

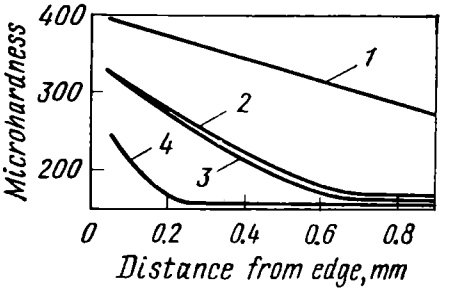

Fig. 279. Variations of gas saturation of zirconium during heating at 1 200°C in various media, as measured by variations in microhardness *HV*
1—air; *2*—helium; *3*—vacuum 1.33 MPa; *4*—vacuum 0.013 MPa

The metals which are chemically active with gases of the air can also influence the ductility of other metals when they are present in the latter as alloying additions. For instance, the ductility of steel 12X21H5T at 1 300°C, when deformed in a protective gas atmosphere (argon) is 12-15 times that for deformation in air (Fig. 281). In other steels and alloys (for instance, steel 45Г17Ю3), the effect of gases of the air is not so substantial.

Since the surrounding medium can have a strong effect in deformation of alloyed steels and alloys, a differentiated approach is essential for studying the ductility of surface (oxidized) and internal (unoxidized) layers of the metal.

The effect of size factor. Like strain resistance, ductility depends on the size factor whose role may appear in two aspects: the ratio of surface area to volume (or the surface factor according to S. I. Gubkin) and variations in the structure (the structural factor).

The size factor has a more substantial effect on ductility than on strain resistance, which can be explained as follows. With an increase of the F/V ratio (F = surface area and V = volume of a specimen), i.e. with a decrease of the absolute dimensions of specimens, the role of friction forces acting on the contact surfaces increases, which contributes more to the relative magnitude of the compressive component of the spherical stress tensor, and therefore, smaller speci-

mens will show up a greater deformation at fracture (greater ductility). S. I. Gubkin gives the following examples illustrating this effect.

In impact upsetting of zinc specimens 20 mm in diameter and 20 mm high (t = 20°C), first crack appears on a relative reduction 35-40 per cent. With smaller specimens of the same metal (10 mm), cracks appear on a reduction of 75-80 per cent. Experiments with brass specimens of the same size gave the following results: 50 per cent reduction for larger specimens and 70-75 per cent for smaller ones. Similar results were obtained for bronze Б2.

This effect of increasing ductility in smaller specimens can be observed not only in compression. Ya. B. Fridman has obtained the following results in tension of steel 30ХГСА: the relative contraction in specimens 20 mm in diameter was 25 per cent lower than that in specimens 10 mm in diameter.

With a more developed unit surface area (greater F/V ratio), the effects of the surrounding medium, machining, surface cold work, contact friction, and surface tension become more noticeable. Surface tension is effective only in extremely thin surface layers, but in fine (micrometre-size) articles produced by rolling or drawing, its effect on ductility may be substantial. Surface tension naturally has no effect on ductility of a metal in large specimens. As has been found, beginning from a definite critical volume, the characteristics of ductility and strain resistance remain unchanged as the volume

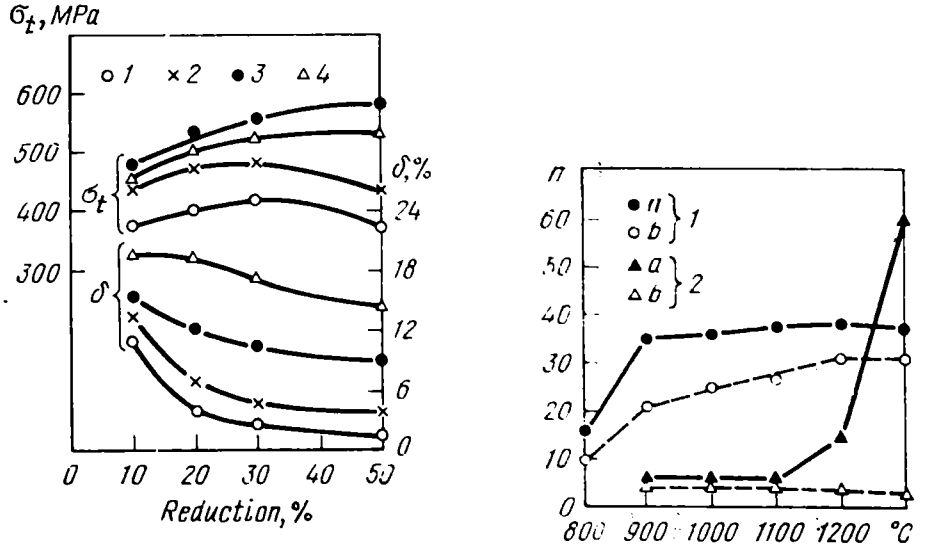

Fig. 280. (*left*) Variations of mechanical properties of niobium after rolling at 1 000°C with different reductions in various media
1—air; *2*—helium; *3*—vacuum 1.33 MPa; *4*—vacuum 0.07 MPa

Fig. 281. Effect of temperature on ductility index of steels 45Г17Ю3 (*1*) and 12Х21Н5Т (*2*) in heating and twisting deformation in argon (*a*) and in the air (*b*) (V. I. Seleznev)

is increased further. This regularity may however be disobeyed in specimens (forgings, blanks, ingots) of large mass where structural inhomogeneity begins to have a noticeable effect.

With a larger volume of deformed metal, its structure is less uniform over the cross section, so that, for the same density of stress concentrators, they may be distributed less uniformly. This leads to a non-uniform distribution of stress and strain during deformation. Local strains and stress concentrators reduce the metal ductility. This in turn determines the conditions of deformation of large ingots in presses, hammers, blooming and slabbing mills: the initial passes in hammers, presses and rolling mills are carried out at slight reductions and low deformation rates.

RECOMMENDED LITERATURE

1. Bulat S.I., Tikhonov A.S., Dubrovin A.K., *Deformability of Structurally Inhomogeneous Steels and Alloys.* Moscow, Metallurgiya, 1975 (in Russian).
2. Dzugutov M.Ya., *Plastic Deformation of High-alloyed Steels and Alloys.* Moscow, Metallurgiya, 1971 (in Russian).
3. Gubkin S. I., *Plastic Deformation of Metals.* Vol. II. Moscow, Metallurgizdat, 1960 (in Russian).
4. Kolmogorov V. L., *Stresses, Strains, Fracture.* Moscow, Metallurgiya, 1970 (in Russian).
5. Kolmogorov V.L., Bogatov A.A., Migachev B.A., Zudov E.G., Freidenson Yu.E., Freidenson M.E., *Ductility and Fracture.* Moscow, Metallurgiya, 1977 (in Russian).
6. Krupin A. V., Pavlov I. M., Solovyev V.Ya., et al. *Vacuum Rolling of High-melting Metals and Bimetals.* Moscow, Metallurgiya, 1971 (in Russian).
7. Krupin A.V., Solovyev V.Ya., *Plastic Deformation of High-melting Metals.* Moscow, Metallurgiya, 1971 (in Russian).
8. Tikhonov A. S., *Elements of the Physico-chemical Theory of Deformability of Alloys.* Moscow, Nauka, 1972 (in Russian).
9. *Vacuum Rolling of Metals and Bimetals.* Proceedings of Moscow Institute of Steels and Alloys, 46, Moscow, Metallurgiya, 1972 (in Russian).

14 Thermomechanical Treatment

1. The Essence and Types of Thermomechanical Treatment

A very important problem in the field of metallic structural materials is to obtain alloys with elevated strength properties and a reliable reproducibility and stability of these properties*. This is dictated by the following: (a) the conditions of operation of structures have become much more complicated (high stresses and high rates of their application, more complicated stressed states, and more frequent schemes with simultaneous action of a whole complex of factors) and (b) an essential need to decrease the mass of structures where possible (i.e. to raise the unit strength of the materials) and increase their durability.

Analysis shows, on the other hand, that high-strength materials often break by brittle fracture under real conditions of operation at stresses well below their ultimate strength. In other words, high-strength materials exhibit an elevated tendency to brittle fracture which does not allow us to utilize their potential strength to the full extent. It then follows naturally that an indispensable condition for realization of the high strength of a material is that it must at the same time possess an ample ductility or toughness.

The strength of a material (i.e. its resistance to plastic deformation) and its ductility (the resistance to the formation and development of cracks which might result in fracture) are structure-sensitive properties but depend differently on a particular structure. Therefore, a high structural strength can be ensured by forming a structural state in which the strength and ductility are in an optimal combination.

In strain-hardened polycrystalline materials, a high strength is ensured by a high density of dislocations whose movement under the effect of external stresses must be locked by internal barriers. The nature of these barriers and their distribution are however essential for ductility. Under particular conditions ('stiff' barriers),

* The aim is to raise the strength of mass grades of structural and other types of steel by 15-30 per cent and attain a level of 3 000 MPa or probably higher in high-strength steels.

dislocation pile-ups may turn out to be highly concentrated locally, resulting in the appearance of high local stresses which might exceed the ultimate strength of the material in local volumes. As a result, these local stresses will be relaxed by the formation and development of a crack and finally cause fracture of the material.

According to M. L. Bernstein, relaxation of peak stresses by crack formation and development can be prevented by the formation of so-called 'semipermeable' barriers. The essence of this term consists in that these barriers must allow relaxation of local 'peak' stresses to occur by breakthrough of piled-up dislocations into adjacent volumes of the material well before these stresses attain the ultimate strength.

In this respect, both the number of barriers per unit volume and the nature of their distribution are of importance. With more frequent and more uniformly distributed 'barriers', the distribution of dislocations is more uniform over the volume of material and the formation of large local dislocation tangles will be less probable.

'Impermeable' barriers include randomly oriented high-angle boundaries, low-plastic particles of other phases which are incoherent with the matrix, and Lomer-Cottrell locks; among 'semi-permeable' barriers are low- and medium-angle boundaries and plastic particles of other phases coherent with the matrix.

In a search for optimizing the structure and distribution of such barriers, it has been shown that in steels and many alloys undergoing phase transformations it is possible to form such barriers by subjecting the material simultaneously to plastic deformation and heat treatment in a single process. This method has been called thermomechanical treatment (TMT) and can be defined as follows: *thermomechanical treatment* is a combination of operations of plastic working, heating and cooling of alloys capable of undergoing phase transformations, performed in a single technological cycle in a particular sequence. The structure, phase composition, and therefore, the properties of an alloy are formed in thermomechanical treatment under the effect of the structural imperfections produced by the plastic deformation on the mechanism of phase transformation and structure of the new phases, or vice versa.

Thermomechanical treatment differs essentially from the conventional methods of deformation and heating. For instance, in common strengthening treatment by cold deformation, the metal can be strengthened, but at the same time its ductility is impaired sharply. In common hot plastic working, heating before the deformation is carried out in order to make the metal sufficiently ductile and avoid its strengthening in deformation. The aim of heating after cold deformation is to soften the work-hardened metal.

A characteristic feature of thermomechanical treatment is that the simultaneous effect of deformation and heat treatment produces a particular structural state, and often a phase state, of the metal,

which is distinguished by a high strength and elevated ductility. By varying the sequence of operations of plastic working and heat treatment and their particular conditions (amount, rate and temperature of deformation, rate of heating and cooling, length of isothermal holding, etc.), it is possible to control the structure and properties of a metal in a wide range.

In this country, the studies into the specifics and possibilities of thermomechanical treatment and development of various versions of the process are associated with the names of M. L. Bernstein, A. P. Gulyaev, V. D. Sadovsky, E. N. Sokolkov, R. I. Entin and others.

A large number of versions of thermomechanical treatment have been developed to account for the nature of phase transformations in an alloy, the temperature of deformation, and the sequence of the procedures of plastic working and heat treatment. These versions have some common principal features for two groups of alloys which differ from each other in the type of phase transformation, namely: (a) alloys undergoing polymorphous (including martensitic) transformations and (b) those in which decomposition of the solid solution takes place (precipitation-hardening alloys).

The conditions of thermomechanical treatment are also often classified by the position of the deformation temperature relative to the temperature limit of recrystallization t_r^a (see Ch. 6). In this respect, it is distinguished between low-temperature and high-temperature thermomechanical treatment (the respective abbreviations are LTHT and HTHT).

By the generally recognized definition, LTHT is a process in which the deformation is done below t_r^s, while HTHT is the process in which the metal is deformed at a temperature above t_r^s. This definition is, however, not perfectly correct, since one may imagine that HTHT is associated with recrystallization, whereas actually recrystallization in HTHT must usually be avoided.

The following definitions seem to be more correct.

LTHT is understood as a process including the deformation of an alloy at such a temperature that the subsequent holding at that temperature for any reasonable time will not result in the onset of recrystallization;

HTHT is a process of thermomechanical treatment with deformation being done at a temperature at which recrystallization cannot proceed directly during the deformation or during a short post-deformation holding.

Briefly, the principal versions of thermomechanical treatment reduce to the following.

In HTHT (Fig. 282), the metal is deformed in a single-phase high-temperature state and, without allowing it to recrystallize, is cooled to realize the phase transformation which thus occurs in the material

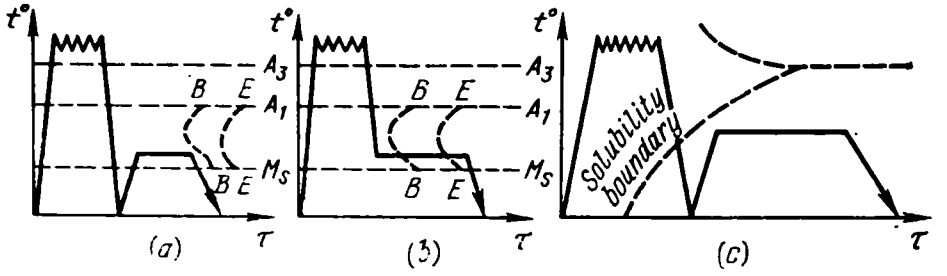

Fig. 282. Diagrams of HTHT of steel (*a*, *b*) and ageing alloys (*c*)
A_3—temperature of the end of $\alpha \rightarrow \gamma$ transformation; A_1—temperature of the beginning of $\alpha \rightarrow \gamma$ transformation; M_s—temperature of the beginning of austenite-to-martensite transformation; lines *B-B* and *E-E* define the beginning and end of isothermal transformation of austenite; wavy line shows deformation

that retains a particular fraction of the structural imperfections produced by the deformation.

In HTHT of steel, the deformation is done in the austenitic region above the temperature of pearlitic transformation Ac_1. This allows two versions of the process, depending on the temperature to which the steel is cooled. If cooling is effected to a temperature below the martensitic point M_s, the martensitic transformation will take place in the deformed austenite (Fig. 282*a*). If the metal is cooled to the region of elevated stability of undercooled austenite (Fig. 282*b*), the transformation will have an intermediate nature between the pearlitic and martensitic transformation (bainitic transformation). In this version of the process, the transformation is allowed to take place under isothermal conditions where possible and accordingly the process is often called the *high-temperature thermomechanical isothermal treatment.* In both cases discussed, the new phase (or a mixture of phases) inherits the defects of the deformed high-temperature phase.

In HTHT of age-hardening alloys, these, too, are deformed in the single-phase region (Fig. 282*c*) and then cooled to the temperature of the two-phase region so as to induce the decomposition of the supersaturated solid solution in the work-hardened matrix, in the first place, near deformation defects.

In LTHT, an alloy (or steel) is heated to the single-phase state in order to dissolve the disperse phases and then cooled sharply to the temperature of deformation and deformed, so that the phase transformation processes take place in parallel with deformation.

In LTHT of steel, the metal is more often deformed in the low-temperature region of stable austenite (Fig. 283), with the deformation being either completed before the beginning of the austenitic transformation (Fig. 283*a*) or effected in parallel with the transformation (Fig. 283*b*).

In LTHT of age-hardening alloys (Fig. 283*c*), the deformation is carried out at room temperature or an elevated temperature within the two-phase region. Deformation under conditions of LTHT ensu-

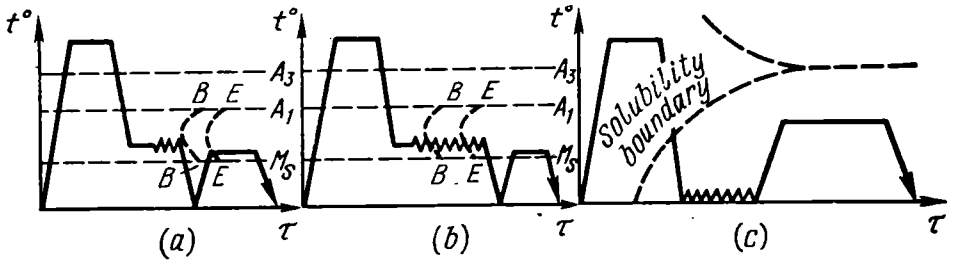

Fig. 283. Diagrams of LTHT for steel (*a*, *b*) and ageing alloys (*c*). Other designations as in Fig. 282.

res an elevated dispersity of precipitated phases and a high strength of the metal.

In some cases, thermomechanical treatment may include double deformation (high-temperature and low-temperature) performed in various sequences (Fig. 284). Double cold deformation is performed in the process of patenting carbon-steel wire (0.45-0.85% C) (Fig. 285); it may be regarded as a variety of LTHT.

The process of wire patenting includes cold deformation, heating at 870-920°C to form coarse-grain austenite, isothermal breakdown of the undercooled austenite with the formation of fine-lamellar sorbite, and the final deformation ($\varepsilon = 75\%$ or more), in the course of which a very disperse fine cellular structure forms in the ferrite, the spacings between cementite platelets diminish, and a high dislocation density is produced at interphase boundaries. Patenting allows the strength of steel wire and rods to be raised quite appreciably, up to about 4 000 MPa.

Practical realization of thermomechanical treatment is linked with certain difficulties. The rate of structural and phase changes is rather high, especially in HTHT, and depends on a large number of factors. To form reliably and reproducibly the desirable structure and properties of the metal, one has to understand perfectly the nature of structural and phase transformations which are to take place in THT and the various factors affecting them, and to observe carefully the conditions (temperature and time) of deformation, heating and

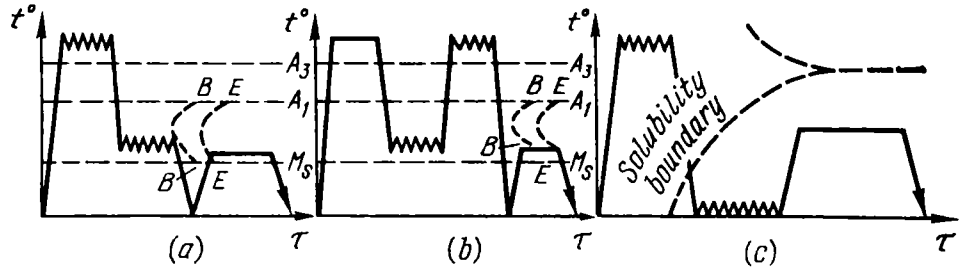

Fig. 284. Diagrams of TMT with double deformation for steel (*a*, *b*) and ageing alloys (*c*)

(*a*, *c*) high-low-temperature treatment (HLTHT); (*b*) low-high-temperature treatment (LHTHT)

cooling with an accuracy well above that required in conventional processes of plastic working of metals, which naturally requires special instruments.

In view of its effect on steel properties and for some technological considerations, HTHT seems to be the most promising version of thermomechanical treatment for industrial application to improve the quality of structural and constructional steels and of steels and alloys for operation under heavy and complicated loads.

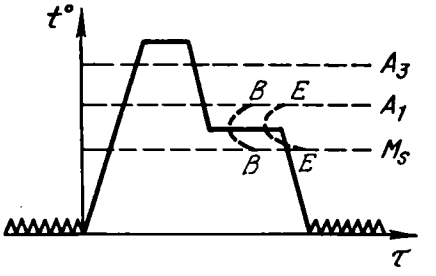

Fig. 285. Diagram of patenting of carbon-steel wire

HTHT gives a somewhat lower strength than LTHT, but makes it possible to obtain a higher ductility (see Table 16), and increases impact toughness, lowers the liability to brittle fracture and the temperature limit of cold

Table 16. Properties of Structural Steel (30ХГСА) after THT

Procedure	σ_t, MPa	$\sigma_{0.2}$, MPa	δ, %	ψ, %	a_n, kJ/m²
I	2200-2600	1900-2100	7-10	20-40	400-500
II	2400-2800	2000-2300	5-7	15-30	300-400

Note. I — HTHT + low annealing (flat specimen); II — LTHT + low annealing (round polished specimen).

brittleness, suppresses crack propagation, and improves contact and impact endurance and notch sensitivity.

In that connection let us discuss the variations of the structure and properties of the metal in the principal version of HTHT.

2. Structural Changes in HTHT. The Role of Process Factors

The laws of structural changes occurring in HTHT can be understood on the basis of the specifics of hot deformation which have been analysed in Ch. 8. The following facts seem to be most important for HTHT.

In addition to the nature of an alloy (phase composition, type of lattice, stacking fault energy) and the amount of deformation, other factors, such as the temperature and rate of deformation and the conditions of cooling, can also have a strong and sometimes decisive effect on the nature of structural changes taking place in the metal upon hot deformation.

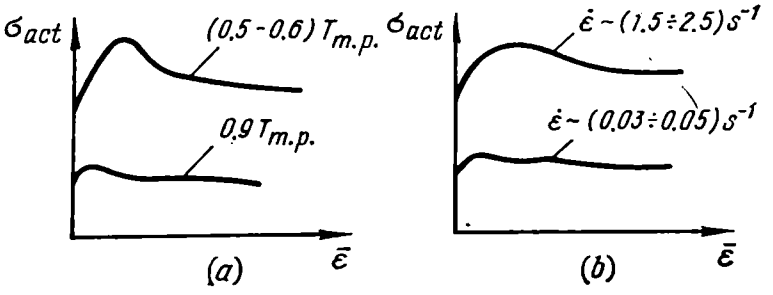

Fig. 286. Effect of deformation temperature (*a*) and deformation rate (*b*) on the shape of the σ-ε curves in hot plastic working

The type of lattice and the stacking fault energy E_{sf} may influence the intensity of strengthening in deformation and the tendency to cross slip. Other things being equal, f.c.c. metals can be strengthened more appreciably than b.c.c. ones, since there are less slip systems in the f.c.c. lattice. On the other hand, a high value of the stacking fault energy in most b.c.c. metals decreases sharply the width of extended dislocations and thus facilitates cross slip, resulting in a weaker strengthening effect (dynamic recovery).

For that reason, the liability to strengthening cannot be attributed to the type of lattice only. Among metals and alloys which are weakly hardenable on deformation, there are aluminium and ferrite-structure alloys, while the group of strongly hardenable alloys includes nickel, copper and austenitic alloys. These materials behave differently also as regards their liability to dynamic polygonization and recrystallization.

Of special significance are here the conditions of cooling after deformation. Since the deformation in HTHT is carried out at a high temperature (above 0.6 $T_{m.p.}$), the processes of static polygonization and recrystallization may take place during the post-deformation cooling (especially in large-size articles), which will change substantially the structure of the metal against that existed at the moment of the end of deformation. The rate of these processes increases sharply with an increase in the rate, amount and temperature of deformation. Accordingly, the rate of cooling gains in importance.

For that reason, thermal stability is an important factor among the parameters by which the structure formed in the course of deformation in HTHT is evaluated. The structure (and accordingly the properties) of the phase which forms on hardening (martensite) inherits in many respects the structure of the original phase (subgranular structure, dislocation pile-ups, etc.). It is therefore essential to retain the optimal structure formed on deformation during heating for hardening.

Amount of deformation. The sequence of structural changes with an increase of the amount of hot deformation can in the general case be described schematically as follows (see σ-ε curves in Fig. 286).

1. An increase in the density of dislocations statistically distributed in the bulk of grains and the more so, at grain boundaries (the first stage in Fig. 286). This results in an increase of strength (more sharply in readily hardenable materials) and brittleness.

2. The beginning of the formation of subgranular structure due to interaction of dislocations by cross slip and climb (the descending portion of the curve in Fig. 286). Subgrains are strengthened somewhat along the direction of deformation; subgrain boundaries are thickened and have an elevated dislocation density (i.e. subgrains still retain traces of the cellular structure). At this stage, the strength reduces somewhat, but the ductility characteristics increase slightly.

3. Intensive dynamic polygonization with the formation of a stable substructure—for weakly hardening materials, or intensive dynamic recrystallization with the formation of new grains (mainly by the mechanism of subgrain coalescence) in places of the highest work-hardening—for those which can be hardened appreciably; this corresponds to the stable stage on the σ-ε curves (see Fig. 286).

Subgrains formed at this stage have an equi-axed shape, a small thickness of sub-boundaries, and a lower dislocation density compared with the second stage. These new grains (dynamic recrystallization nuclei) are less perfect than those formed in static recrystallization, i.e. have a higher density of dislocations (remained from coalesced subgrains or introduced by the continuing deformation).

The structure which forms on dynamic polygonization possesses the best combination of mechanical properties. Since subgrains are small, the strength is still quite high. On the other hand, a reduced dislocation density in some sub-boundaries makes them 'semi-permeable' barriers which ensure relaxation of the peak stresses created by piled-up dislocations and by 'breakthrough' of these dislocations into adjacent subgrains. Thus, the risk of brittle fracture decreases (i.e. ductility increases). Therefore, the nature of subgranular structure—the size of subgrains and the dislocation density in them—may have a very important role.

An important advantage of the substructure formed at the stage of dynamic polygonization is that it also has a high thermal stability.

The structure formed by the mechanism of dynamic recrystallization is less favourable, since it is less homogeneous and less stable thermally. The average level of mechanical properties is however still quite high in that case, so that the structure of dynamic recrystallization is quite admissible in many cases (in constructional steels, etc.).

Grain growth. Under particular conditions (a high temperature at the end of deformation, slow cooling, which often takes place in large-size articles), the process of grain growth can be realized in

the course of static recrystallization after deformation. It is accompanied with 'sweeping-out' of defects by migrating high-angle boundaries, coarsening of grains and subgrains and, as a result, a sharp drop in strength properties. In view of this, the conditions of HTHT must be such as to avoid grain growth. Therefore, the most favourable conditions of deformation in HTHT are such which ensure the formation of a stable and more or less homogeneous structure of dynamic polygonization.

These considerations should be the basis for analysing the effects of the principal process parameters and characteristics of the material on the formation of the optimal structure and properties of alloys in HTHT.

Deformation temperature. An increase of temperature, like an increase of deformation rate, shifts the beginning of all the four stages towards lower amounts of deformation. The effect of these factors is however more intricate.

An increase of the deformation temperature at the second stage results in an increased size of subgrains, more perfect structure of their sub-boundaries, and a lower dislocation density in sub-boundaries. As a result, the structure has an elevated thermal stability. The dependence of the structure formed in HTHT and of the structure-sensitive mechanical properties of the metal on the temperature of heating before deformation has however an extremum which is associated with the fact that the temperature of heating can influence a number of important characteristics.

As has been demonstrated by many workers, coarse original grain (prior to deformation) is undesirable, since it impedes deformation and makes it less homogeneous. This facilitates dynamic recrystallization and its inhomogeneous course.

For that reason, the highest temperature of heating for deformation must be at least slightly below the temperature at which intensive enlargement of grains can take place (grain growth and secondary recrystallization). An excessively high temperature is especially dangerous for unalloyed carbon steels in which the barrier mechanism of retardation of boundary migration is not pronounced.

A high temperature of deformation is also dangerous for the reason that the time of cooling after deformation from the high temperature may be sufficient for the realization of static recrystallization—not only primary recrystallization, but even grain growth (see recrystallization diagrams in Fig. 203), which will impair the metal properties. For instance, an increase of the temperature of HTHT for steel 30ХГСА from 900°C to 1250°C resulted in a drop of strength (determined by tensile test at —196°C) from 1500 MPa to 1300 MPa and of elongation, from 18 per cent to 10 per cent.

On the other hand, with a low temperature of heating for deformation, the latter may become inhomogeneous in microvolumes, which inhibits dynamic polygonization. For the reasons mentioned, it is

essential to find the optimal temperature of heating for deformation and that of deformation proper.

Deformation rate. As has been indicated, the structure in hot deformation is formed due to the competing effects of the processes of strengthening and softening. All softening processes are thermally activated, i.e. probabilistic, and require a certain time interval for their realization.

A higher rate of hot deformation, which decreases the probability of softening processes, should therefore act in the same sense as increasing amount of cold deformation or else decreasing stacking fault energy which impedes cross slip.

As has been demonstrated experimentally by E.N. Sokolkov and co-workers on heat-resisting iron and nickel alloys and by Yu. M. Weinblat et al. on aluminium alloys, a higher rate of hot deformation makes more probable the processes of dynamic recrystallization instead of those of dynamic polygonization, decreases sharply the thermal stability of the structure and properties, and, in the whole, has an adverse effect on the properties of the metal.

HTHT with a low rate of deformation is more preferable. In this case too, however, the relationship is not monotonous. At very low rates of deformation, the processes of softening become predominant, so that the strengthening effect, which is the main aim of TMT, cannot be achieved.

It is impossible to recommend absolute values of deformation without consideration of the rate and temperature of deformation and the composition of the metal. In the most general case, in order to obtain optimal structure and properties, it is advisable to use moderate deformations, within 20-40 per cent. Low deformations cannot produce the optimal strengthening effect, while heavy deformations are dangerous, since they can cause strong strain hardening (cold work) and provoke impairment of the thermal stability of the structure and development of dynamic recrystallization. The risk is especially high in operation with carbon and low-alloyed steels in which dynamic recrystallization can proceed more intensively.

In cases when heavy deformations are essential for shaping of the metal, it may be advised to resort to fractional deformations. In such cases, it is extremely important to select proper pauses between deformation cycles. This selection should be done on the same considerations as the selection of the optimal holding time and cooling conditions after the last deformation. This holding time (pause) should be sufficiently long for the processes of dynamic recovery and polygonization to have time to occur and, on the other hand, should be shorter than the incubation period of post-deformation static recrystallization.

After the final deformation, cooling of carbon steels must be done under different conditions from those required for alloyed steels. In HTHT of carbon steels, the metal after hot deformation must be

cooled quickly, whereas alloyed steels require a short holding time after the last deformation to allow polygonization processes to take place. For instance, the best mechanical properties in carbon steel Ст. 3 are obtained on sharp quenching. For alloyed steel 40X1HBA, a pause of 20-30 s is needed between the end of hot deformation and quenching in order to obtain the optimal properties.

Mechanical scheme of deformation *. Systematic studies of the effect of the mechanical scheme of deformation on substructure are still scarce. Schemes of principal stresses close to uniform compression (such as extrusion) increase noticeably the resistance to crack initiation and propagation. Deformation by rolling gives the highest gain in strength.

The effect of deformation scheme should also be seen in another phenomenon which has not yet been studied properly. In practically any mechanical scheme of deformation employed in the industry, the plastic flow of the metal is more or less inhomogeneous macroscopically. As a consequence, macrostresses appear in the deformed piece, which may be tensile in some local volumes and compressive in others. At high temperatures, this may cause ascending diffusion in micro- and macrovolumes.

Depending on the degree of alloying, the state of the solid solution, the density and distribution of dislocations, and the time-temperature conditions of deformation, this may result either in the formation of impurity atmospheres around dislocations or in some phenomena preceding decomposition, or even in initial decomposition of the solid solution.

In view of these phenomena, the extent and effectiveness of locking of dislocations, sub-boundaries and grain boundaries in various local volumes may be different. It is important to note that, if these effects are realized, they will show up differently in compressed and tensioned volumes of the metal, in particular, atoms of elements of smaller size will flow into compressed regions and those of larger size, into tensioned.

An additional but rather important factor that can accelerate diffusion and precipitation from the solution in HTHT, irrespective of the presence of macrostresses, is the presence of vacancies, which can appear both directly during hot deformation due to intersection and annihilation of dislocations and in the course of dynamic and static recrystallization.

The effect of these vacancies in hot deformation (in HTHT) should evidently be much stronger than in cold deformation, which can be explained as follows.

The structure formed on cold deformation contains a large number of closely located dislocation sinks. During heating after the deforma-

* Mechanical scheme of deformation is understood as a combination of the schemes of principal stresses and principal strains (or principal deformation rates).

tion (or even during storage at room temperature) vacancies can move into these sinks well before the temperature reaches the level sufficient for diffusion decomposition.

In hot deformation, the density of dislocations (sinks) is two or three orders of magnitude lower than in the former case and the distances between them are correspondingly larger. Besides, the stage of post-deformation heating is absent in HTHT, since vacancies appear in the metal that has already been heated to a high temperature. If, under such conditions, an alloy (phase) or some of its volumes are in the state of solid solution supersaturated in a particular component, it will decompose more readily in the presence of vacancies.

As a supporting illustration, let us note that, for instance, the time of holding to the beginning of precipitation of disperse phases in hot-deformed austenitic steel 01X18H10T turns out to be much shorter (by a factor of 30-40) than in undeformed steel.

Depending on whether the decomposition of the solid solution takes place with precipitation of incoherent or coherent particles (relative to the matrix) or is limited to pre-decomposition formations within the solid solution, the decomposition products will precipitate on high-angle boundaries, sub-boundaries or individual dislocations and will respectively impede their redistribution and migration. This will result in structure stabilization, and therefore, will facilitate HTHT. The stabilizing effect will be retained up to the beginning of reverse dissolution or coagulation of precipitates.

There is much evidence in the published literature data that carbide- and nitride-forming alloying elements in steels (Nb, V, Ti, Al, etc.) retard dynamic recrystallization and especially effectively when the corresponding carbo-nitride phases are less liable to coagulation.

For instance, the beginning of recrystallization in steel 01X18H10T during post-deformation holding at 900°C is delayed by a factor of 30 or more compared with a similar steel 01X18H10 which contains no titanium.

In addition to the factors discussed, the structure and properties of alloys undergoing polymorphous transformations and subjected to HTHT can be affected substantially due to the fact that the defects formed on hot deformation of the high-temperature phase (say, austenite) can be 'inherited' by the low-temperature phase (martensite).

The shear nature of $\gamma \rightarrow \alpha$ and $\alpha \rightarrow \gamma$ transformations results in that the new phase 'inherits' not only the size and shape of grains of the original phase, but also the structural imperfections existed in the original grains, i.e. their substructure. For instance, there is a distinct correlation between the grain size and substructure of austenite and the product of its transformation—martensite. If the substructure formed on dynamic polygonization is sufficiently stable, it may be inherited not only after heat treatment (quenching)

which follows immediately the hot deformation, but also after repeated quenching procedures. Accordingly, the mechanical properties will also be inherited.

3. Examples of Application of HTHT

The introduction of HTHT in mass industrial production (say, in rolling) involves certain difficulties associated with the need to alter certain process parameters adopted in the conventional technology, with more rigid requirements for the speed and time-temperature parameters of the process, and the need for special equipment.

Under conditions of HTHT, it is necessary to lower the temperature of heating for hot deformation (without lowering noticeably the temperature of the end of deformation), reduce the rate of deformation (which will adversely affect the productivity of the process equipment), diminish the highest admissible deformation per pass, employ fractional deformations, etc. Nonetheless, the introduction of HTHT is stimulated by the evident advantages which it can provide.

Among the first objects on which the effectiveness of HTHT was tested was spring steel. Springs made from strips of steel Grade 55ХГР were subjected to HTHT at 950°C in a continuous section-rolling mill ($\varepsilon = 70\%$) with the use of the inheritance effect and exhibited an essentially higher durability. According to Ford Motor Co., HTHT of springs made of steel type 50ХГ (SAE 5150) increased their durability several (5-7) times. The durability of steels for drilling tools (33ХС, 30ХГСА) can be raised by HTHT two or three times.

For articles operating under complicated loading conditions, positive results have been obtained by hot deformation with subsequent decomposition of the deformed austenite during isothermal or nearly isothermal holding (high-temperature thermomechanical treatment with isothermal holding). This method increases the durability of springs 1.5 times. A similar treatment of pipes for petroleum industry makes it possible to diminish the mass of drill pipe strings by 20-30 per cent.

A variety of HTHT which is promising for low-alloyed steels (in particular, constructional steels) in order to increase their structural strength, ductility and toughness is what is called *controlled rolling*. It makes it possible to raise the yield strength of steel by 10-30 per cent and the impact toughness by 30 per cent and to lower the ductile-to-brittle transition temperature by 30-50°C.

Since such steels are used widely (in civil engineering, construction of large-diameter pipelines, ship-building, etc.), the introduction of controlled rolling becomes an important task, as it may help substantially in decreasing the mass of structures. In contrast to the conventional HTHT which reduces to the formation of a structure of dynamic polygonization, controlled rolling is aimed at forming

fine homogeneous grain by dynamic and static recrystallization.

The temperature of heating for hot rolling, the temperature, rate and amount of deformation in individual passes (fractional deformations), the length of pauses between passes and the time of post-deformation holding, the rate of final cooling of the steel, and the required additions—all these factors must be selected so as to avoid grain growth during or after the hot deformation and to produce homogeneous fine grain (5-10 μm or even finer) by primary recrystallization.

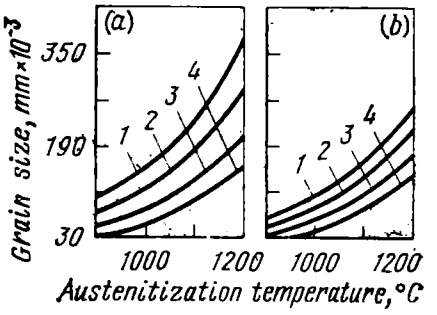

Fig. 287. Effect of additions of vanadium and niobium on grain size of austenite (*a*) and ferrite (*b*) in steel (0.08% C, 1.4% Mn) heated before controlled rolling

1—without additions; *2*—0.06% V; *3*—0.04% Nb; *4*—0.04% Nb+0.06% V

Grain growth can be prevented most effectively by forming disperse phase particles (usually carbonitrides) in the steel, which can be done by alloying with the elements indicated earlier. The retarding effect of these phases is stronger if they precipitate from the solid solution (austenite) in the course of deformation or in subsequent cooling. In order to ensure the required supersaturation of the solid solution before the deformation, the temperature of heating for deformation must be sufficiently high to dissolve carbonitride phases. On the other hand, it must not be excessively high so as not to provoke intensive growth of austenitic grains.

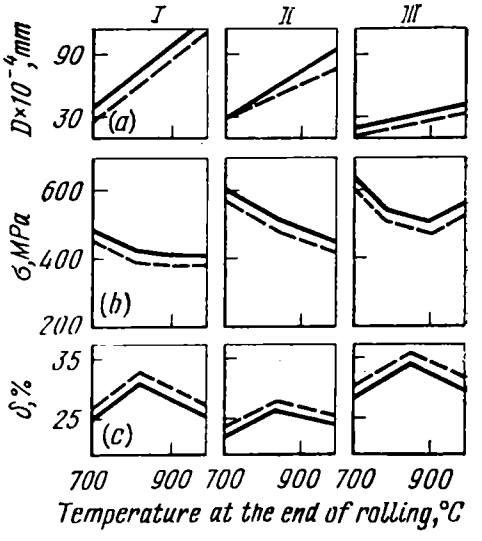

Fig. 288. Effect of temperature at the end of rolling on (*a*) grain size, (*b*) ultimate strength and (*c*) elongation of structural steel (0.08% C, 1.4% Mn) with additions of vanadium and niobium. The temperature of heating before rolling was 1 200 °C (solid lines) or 1 050°C (dashed lines)

I—without additions; *II*—0.06% V; *III*—0.04% Nb

The curves in Fig. 287 illustrate the effect of vanadium and niobium additions on grain size of austenite (Fig. 287*a*) and ferrite (Fig. 287*b*) in steel with 0.08% C and 1.4% Mn during heating for controlled rolling.

The temperatures of the beginning and end of rolling should be chosen so as to ensure precipitation of carbonitride phases in a fine disperse state. On the other hand, they must be not too low so as not to produce strong strain hard-

ening and embrittlement. As an example, Fig. 288 shows the effect of temperature of the end of rolling on the strength, ductility and grain size of constructional steels.

RECOMMENDED LITERATURE

1. Bernstein M. L., *The Structure of Deformed Metals.* Moscow, Metallurgiya, 1977 (in Russian).
2. Bernstein M. L., *Thermomechanical Treatment of Metals and Alloys.* **Vols. 1,** 2. Moscow, Metallurgiya, 1968 (in Russian).

15 Superplasticity and Its Applications in Plastic Working of Metals

Under common conditions of deformation, polycrystalline metals and alloys possess a plasticity which allows the dimensions of articles made of them to be varied uniformly (for instance, the length or a specimen in tension without necking) by not more than a few pef cent, at best 20-30 per cent. In single crystals of metals with a low number of slip systems and with a favourable orientation of external shear stresses to these systems, it is sometimes possible to obtain two- to four-fold elongation in specimens. This is typical, for instance, of c.p.h. metals (cadmium, zinc).

As has been found, however, it is possible to obtain a very high plasticity in certain polycrystalline metals and alloys in a particular structural state and under special conditions of deformation, so that the length of specimens can be increased, even by a low force, 10-30 or more times without necking or with the formation of what is called running neck.

In 1945, Academician A. A. Bochvar called this phenomenon *superplasticity* and the term is now generally recognized. A. A. Bochvar and Z. A. Sviderskaya first discovered the phenomenon of superplasticity on a Zn + 22% Al eutectoid alloy in which an ultrafine-grain structure had been formed. Later, this alloy has become the classical object for studying superplasticity.

Since the 1960's, the phenomenon has been studied extensively in view of its promising practical applications. As has been established, the principal conditions for the appearance of superplasticity are as follows: small size of crystallites (1-10 μm), low deformation rate (especially with a larger size of crystallites), in the range of 10^{-4}-10^{-1} s^{-1}, a relatively high temperature (not less than 0.5 $T_{m.p.}$), and respectively a low stress.

The phenomenon of superplasticity has much in common with creep but differs from the latter in that the process is much more sensitive to the size and shape of grains and there is a sharper dependence of stress on deformation rate.

On this basis, superplasticity can be defined as the ability of polycrystalline (ultrafine-grain) materials to undergo a very high uniform plastic deformation at relatively high temperatures and low stresses and, respectively, low deformation rates, with the flow stress being extremely sensitive to deformation rate.

The most important feature of superplasticity is that plastic flow occurs very uniformly. In common plastic deformation, an occasional local thinning of the specimen (necking) stimulates quicker deformation, and therefore, further thinning in that section. In contrast to this, plastic deformation under superplastic conditions is devoid of this defect, which explains why the flow of the material is steady and uniform.

The kinetics of the process can be analysed, without going into its atomic mechanism, by resorting to the mathematical body of analytical mechanics (mechanics of continua), which makes it possible to find the formal parameters responsible for the stable uniformity of metal flow.

1. Principal Characteristics of Plastic Deformation under Conditions of Superplasticity

In isothermal deformation, the actual stress of plastic flow, σ, is a function of the amount ε and rate $\dot{\varepsilon}$ of deformation

$$\sigma = f(\varepsilon, \dot{\varepsilon})$$

In differential form, this relationship is

$$d\sigma/d\varepsilon = \partial\sigma/\partial\varepsilon + (\partial\sigma/\partial\dot{\varepsilon})(d\dot{\varepsilon}/d\varepsilon)$$

where $\partial\sigma/\partial\dot{\varepsilon}$ in the second term characterizes the sensitivity of flow stress to deformation rate.

Assuming that small variations of σ depend linearly on small variations of ε and $\dot{\varepsilon}$, the relationship between σ, ε and $\dot{\varepsilon}$ can be expressed as follows:

$$d\sigma = \sigma_{\varepsilon} d\varepsilon + \sigma_{\dot{\varepsilon}} d\dot{\varepsilon} \tag{192}$$

or, dividing by dt,

$$\dot{\sigma} = \sigma_{\varepsilon}\dot{\varepsilon} + \sigma_{\dot{\varepsilon}}\ddot{\varepsilon} \tag{193}$$

The rate of deformation may be written as

$$\dot{\varepsilon} = \frac{1}{l}\frac{dl}{dt} = \frac{\dot{l}}{l} = -\frac{\dot{A}}{A} \tag{194}$$

where A is the cross-sectional area. The 'minus' sign implies that the sign of variation of A is opposite to that of variation of the specimen length:

$$\ddot{\varepsilon} = \frac{\ddot{l}}{l} - \left(\frac{\dot{l}}{l}\right)^2 = -\frac{\ddot{A}}{A} + \left(\frac{\dot{A}}{A}\right)^2 \tag{195}$$

On the other hand, the force that causes deformation

$$F = \sigma A \tag{196}$$

and its time variation is

$$\dot{F} = \dot{\sigma}A + \sigma\dot{A}$$

Dividing the latter equation by the former, we get:

$$\dot{F}/F = \dot{\sigma}/\sigma + \dot{A}/A$$

Let us substitute the corresponding values from expressions (193)-(195) into the right-hand portion and introduce the following notation:

$$\gamma = (1/\sigma)\sigma_\varepsilon \tag{197}$$

and

$$m = (\dot{\varepsilon}/\sigma)\dot{\sigma}_\varepsilon \tag{198}$$

We get

$$\frac{\dot{F}}{F} = -\frac{\dot{l}}{l}(1-\gamma+m) + m\left(\frac{\dot{l}}{l}\right)^2 \tag{199}$$

Analysis of expression (199) under various boundary conditions can provide us with important information on the physical essence of the coefficients γ and m.

For instance, substituting σ_ε from (192) into (197), we get:

$$\gamma = (1/\sigma d\varepsilon)\,(d\sigma - \dot{\sigma}_\varepsilon d\dot{\varepsilon})$$

For the case when the material is insensitive to deformation rate, the second term turns to zero and

$$\gamma = (d\sigma/d\varepsilon)/\sigma = n/\varepsilon$$

where n has the sense of the strengthening factor

$$n = d\,(\log\delta)/d\,(\log\varepsilon)$$

Therefore, γ is a parameter which describes the sensitivity of the factor n to deformation, i.e. the liability of the material to strengthening in deformation.

In a similar manner, substituting $\dot{\sigma}_\varepsilon$ from (192) into (198), we have:

$$m = [1/\sigma d\,(\log\dot{\varepsilon})]\,(d\sigma - \dot{\sigma}_\varepsilon d\varepsilon) \tag{200}$$

If the material is not strengthened in deformation (which corresponds to the conditions of viscous flow and superplasticity), the second term is equal to zero and we have:

$$m = d\,(\log\sigma)/d\,(\log\dot{\varepsilon}) \tag{201}$$

Therefore, m is a parameter of the material which describes the sensitivity of the plastic flow stress to deformation rate, i.e. the liability of the material to strengthening at an increase of deformation rate.

For a case of uniform deformation, the resulting dependence of the strengthening in a material on the amount and rate of deformation can be described in terms of the parameters n and m in the following way:

$$\sigma = \text{const}\, \varepsilon^n \dot{\varepsilon}^m \tag{202}$$

This relationship, called the equation of state of a viscoplastic solid has two typical extreme cases.

(a) The dependence of σ on the amount of deformation is negligible ($n \to 0$). Then

$$\sigma = \text{const}\, \dot{\varepsilon}^m \tag{203}$$

and the material behaves as a viscous solid, i.e. the one having the highest plasticity; with $m = 1$, there is a direct proportionality between σ and $\dot{\varepsilon}$ (called Newtonian behaviour).

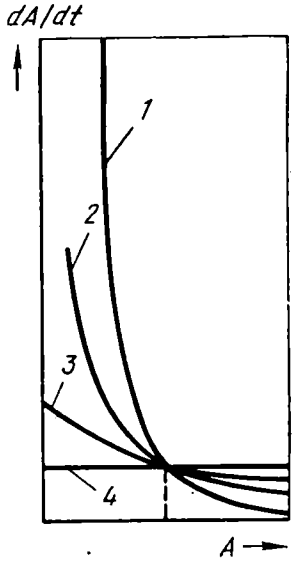

Fig. 289. The rate of variation of cross-sectional area as a function of cross sectional area at various values of m: *1*—0.25, *2*—0.5, *3*—0.75, *4*—1

(b) The dependence of σ on the deformation rate is negligible ($m \to 0$). Then $\sigma = \text{const}\, \varepsilon^n$ and the material behaves as a perfectly plastic solid whose strengthening is determined by the amount of deformation.

Substituting corresponding quantities from (194) and (196) into (203), we obtain a relationship describing the rate of variation of the cross-sectional area dA/dt depending on A and m:

$$-dA/dt = (F/k)^{1/m} [1/A^{(1-m)/m}]$$

In Fig. 289, this relationship is represented graphically in the coordinates dA/dt-A for various values of m. As may be seen, the pattern of the curves is different for various values of m.

With low values of m (0.2-0.4) and $n=0$, the rate of variation of cross-sectional area depends strongly on the size of that area, the dependence being stronger as m decreases. This means that, with a low m, the appearing non-uniformity of the cross section (local thinning) will increase sharply as deformation proceeds.

With an increase in m, the dependence becomes weaker and, at $m = 1$, the rate of variation of the cross-sectional area ceases to depend on non-uniformity in the magnitude of A.

Thus, m characterizes the liability of a material to necking, and therefore, its tendency to superplasticity.

Figure 290 shows an experimentally found correlation between m and the maximum relative elongation δ, per cent, which characterizes the highest plasticity. Superplasticity can appear in alloys for which $m > 0.3$, while materials with $m < 0.2$ exhibit common plasticity. As has been demonstrated in many works, however, one and the same material, with constant m, may show up different elongation δ, per cent, depending on grain size and the nature of structural changes in the course of deformation*.

Thus, a high value of m, i.e. a high sensitivity of the flow stress σ to the deformation rate $\dot{\varepsilon}$ is a necessary, but not sufficient condition for appearance of superplasticity.

At present, there is no unique criterion that might characterize the tendency of a material to exhibit superplasticity.

For that reason, other characteristics must be determined, in addition to m, in order to judge on the plasticity of a material and on its tendency to superplasticity. The most valuable information may be given by the maximum relative elongation δ, per cent, and by data on the extent of the stage of stable deformation on actual stress-strain diagrams.

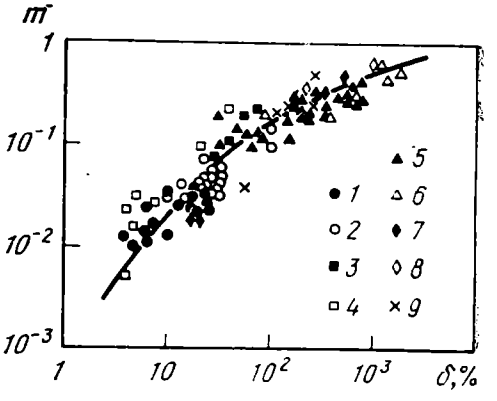

Fig. 290. Relationship between m parameter and the maximum elongation determined experimentally: *1-9*—data of various authors

As regards external effects of superplasticity, they, apart from a high value of m, also include uniform elongation of the specimen without necking and a very slight strengthening in the course of deformation, which passes through its maximum at the early stages of deformation.

The value of m can be obtained from the results of mechanical tensile tests. With the use of a stiff testing machine, the test is most often carried out by Backofen's method or its modifications, in which the rate of tension is varied jumpwise. In Backofen's test, the rate of deformation is changed by varying the load F. A steady flow of the metal is obtained, however, only in a certain time interval after a change of the load, because of which m cannot be found directly

* It should be noted that the theoretically attainable plasticity at $m < 1$ is quite low, for instance $\hat{\varepsilon} \approx 150$ per cent at $m = 0.7$. Hence, superplasticity should not be considered as the problem of stability against necking, since, on the formation of a neck, a specimen may deform further by as much as 500–1 000 per cent.

on the stress-strain diagram. Usually, the relationship $\sigma = f(\varepsilon)$ is extrapolated in order to obtain the same deformations at different rates of tension.

Figure 291 shows schematically the load-time curve obtained on a stiff testing machine in the case when the rate of tension was increased at a certain time (point D) instantaneously from v_1 to v_2. The steady state established upon this increase of the load is described by the point A.

To determine m, the line of steady flow is extrapolated from the point C at a lower rate v_1 up to the point B which corresponds to the same amount of deformation as that obtained in the point A at a higher rate of tension. After that, one can find on the graph the forces corresponding to the points A and B and, neglecting slight variations of m in the extrapolated region, determine its magnitude from the relationship:

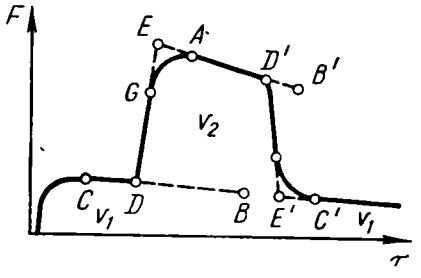

Fig. 291. Time-load curve of tension with jumpwise variation of tension rate v_1 and $v_2 > v_1$ (to determine m parameter)

$$m = \log (F_A/F_B)/\log (v_2/v_1) \quad (204)$$

where F_A and F_B are the loads respectively at the rates v_2 and v_1.

In modified versions of the calculation, it is possible to eliminate the effect on m of some structural changes which may be caused in the material by an increase in the force F, and therefore, in the rate of deformation. This change in the conditions of deformation must result in an increased density of structural defects, which in turn must alter the magnitude of m and the value of n in equation (202).

In order to eliminate the effect of structural changes, it is reasonable to determine m in terms of the forces corresponding to the points G and D, rather than those for the points A and B (see Fig. 291), that is:

$$m = \log (F_G/F_D)/\log (v_2/v_1) \quad (205)$$

The physical sense of this replacement may be explained as follows. As the rate of deformation varies, the instantaneous variation of the stress from the point D to the point G characterizes the strain resistance for two given deformation rates with the lowest difference in the amount of deformation, i.e. the lowest difference in the structure.

As has been shown by comparison of the data obtained by various researchers, relationship (204) gives too high and often unreproducible values of m, while relationship (205) gives lower and less scattered values.

2. Effect of the Conditions of Deformation, Microstructure and Composition of Metal on Superplasticity and Principal Parameters of the Process

Deformation rate. The most characteristic feature of superplasticity of an alloy (more strictly, of its state of superplasticity) is a typical pattern of the curve relating m to deformation rate $\dot{\varepsilon}$.

This may be readily seen from Fig. 292 which gives such curves for an alloy in a state of superplasticity (curve *1*) and a state when it is not liable to exhibit this effect (curve *2*). The former has a maximum, while the latter is almost linear.

In view of this typical pattern of the m-$\dot{\varepsilon}$ curve, it can be divided into three sections according to the deformation rate. Superplasticity appears in the range of deformation rates near the maximum of the curve (region *II*). As a rule, this corresponds to values of m within the range of 0.3 to 0.8 and to deformation rates between 10^{-4} and 10^{-1} s^{-1}. Both at lower (region *I*) and higher deformation rates (region *III*), m is smaller and the tendency to superplasticity is accordingly lower; at $m < 0.3$, the material ceases to be superplastic. The position of region *II* on the scale of deformation rates depends on a number of factors, the most important among them being the size of grains (see below). The temperature of deformation is essential too.

The relationship between σ and $\dot{\varepsilon}$ (between flow stress and deformation rate) is less unique and more unusual. It has been reliably established that in the state of superplasticity σ is low, a few MPa or even fractions of a MPa. Most authors note that no strengthening of the material takes place upon deformation in region *II*. Under conditions of superplasticity, the yield limit $\sigma_{0.2}$ of the material

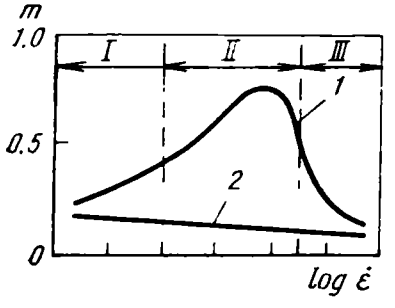

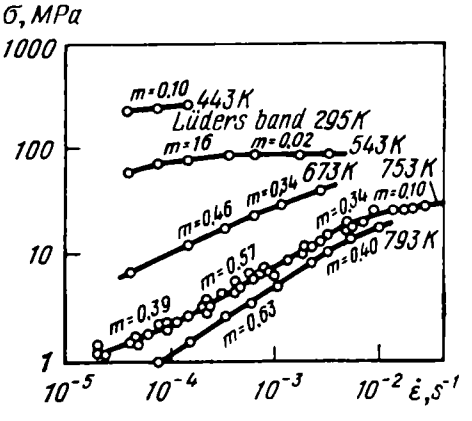

Fig. 292. (*left*) Effect of deformation rate on m parameter
1—ultrafine-grain alloy in a state liable to superplasticity; *2*—coarse-grain alloy in a state not liable to superplasticity

Fig. 293. Effect of deformation temperature on the shape and position of the σ-$\dot{\varepsilon}$ curves of superplastic Al + 33% Cu alloy (grain size 7 μm)

remains practically unchanged after the deformation, i.e. equals the original value.

In contrast to this, deformation of the material in the region *III* of deformation rates gives a noticeable strengthening effect.

The relation between deformation rate and elongation δ, per cent, is seen in the correlation between m and δ. It follows from the data given in Fig. 291 that superplasticity is not accompanied with a jumpwise variation of δ, but there is a correlation between m and δ, which, in the first approximation, is of the form:

$$\delta\% = (100^m - 1) \times 100$$

Many exceptions are however known which disobey this relationship and still have not been explained properly.

Deformation temperature T_d. A change of deformation temperature has a strong effect on the pattern and position of the $\sigma = f(\dot{\varepsilon})$ curve. With increasing temperature, the curve shifts towards higher deformation rates and lower stresses. In Fig. 293, this is illustrated for a superplastic Al + 33% Cu alloy. Various values of the m parameter are also indicated at the $\sigma = f(\dot{\varepsilon})$ curves for different temperatures. As may be seen, the value of m for superplastic states increases sharply with increasing temperature. For instance, $m = 0.10$ at 443 K ($0.35\ T_{m.p.}$) and $m = 0.63$ at 793 K ($0.7\ T_{m.p.}$). In contrast to this, in hot deformation of common metals and alloys (which are not in the state of superplasticity), m increases from roughly 0.02 at $T_d = 0.4\ T_{m.p.}$ to roughly 0.20 at $T_d \approx T_{m.p.}$.

On the other hand, m does not exceed 0.3 up to temperatures close to $0.4\ T_{m.p.}$. This means that superplasticity appears at temperatures always above $0.4\text{-}0.5\ T_{m.p.}$, i.e. this is a typical high-temperature process.

As in the case of creep, the correlation between T_d, $\dot{\varepsilon}$ and σ can be described by the Arrhenius equation. Noting that the parameter m is temperature-sensitive, the relationship is of the form:

$$\dot{\varepsilon} \approx \sigma^{1/m} \exp(-Q/RT) \tag{206}$$

and

$$\sigma \approx \dot{\varepsilon}^m \exp(Qm/RT) \tag{207}$$

where Q is the effective activation energy of the process. Analysis of these relationships can provide a useful information on the mechanism of superplastic flow.

For instance, according to many workers, the activation energies for region *II* of deformation rates are close to the values of activation energy of boundary diffusion, and for region *III*, to those of volume diffusion.

Great care should be given to the explanation of the physical sense of Q values found experimentally. Superplasticity is a compli-

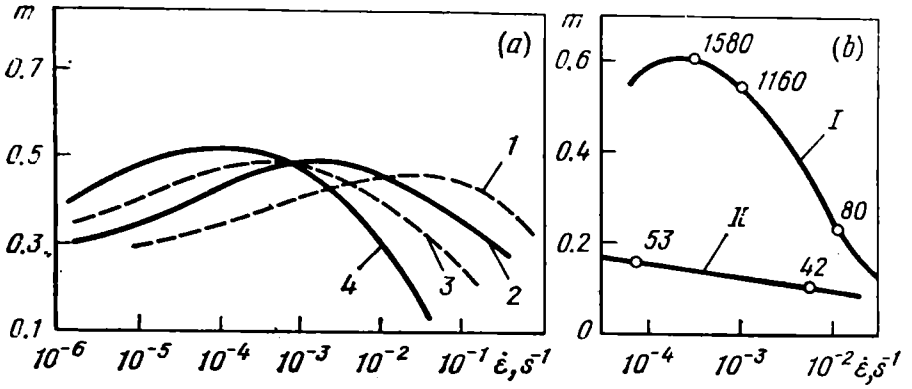

Fig. 294. Effect of size and shape of grains on superplasticity (m parameter) of alloys

(a) eutectoid Zn-Al alloy (grain size, μm: *1*—0.5, *2*—0.8, *3*—11, *4*—1.8); (b) eutectic Pb-Sn alloy (*I*—equi-axed grains, *II*—lamellar grains). Numbers at curves are elongations, %

cated phenomenon associated with simultaneous occurrence of a number of elementary processes: whose relative contributions depend on many factors. For that reason, Q represents the effective activation energy of the process and characterizes the temperature dependence of the rate of that process.

Values of Q can be found by the slope of a straight line plotted in the coordinates $(1/m)\log\sigma$-T^{-1} at constant $\dot{\varepsilon}$ when using relationship (206) or by the slope of a line in the coordinates $m\log\dot{\varepsilon}$-T^{-1} at constant stress σ if relationship (207) is used.

Deformation scheme. An important fact in practice is that superplasticity is insensitive to the type of deformation. Experiments with alloys of the same composition deformed in tension, compression and twisting have given identical results. This is true however only of perfectly texture-free materials.

It should be noted that the conditions of high hydrostatic pressure which inhibit crack initiation should be favourable for superplasticity and should probably lower the temperature at which the effect can appear.

Grain size, texture, phase and chemical composition. As has been established in the earliest studies, ultrafine-grain structure is indispensable for the appearance of superplasticity. The size of crystallites must be less than 10 μm and smaller sizes are preferable. It is precisely ultrafine grain that is responsible for the unusually strong sensitivity of the flow stress σ of superplastic materials to deformation rate $\dot{\varepsilon}$. The shape of grains is of no less importance. With lamellar grains, even of a sufficiently small size, the effect of superplasticity disappears. The strong effect of these two factors is illustrated by the curves in Fig. 294. With an increase of grain size from 0.5 μm to 1.8 μm, the region of high values of m (region *II*) is shifted towards higher deformation rates (by three orders of magnitude). A superplastic alloy with equi-axed grains 2.5 μm in size may exhibit an elonga-

tion up to 1500 per cent, but becomes a common alloy with the maximum elongation around 70 per cent if the shape of its grains, for the same size, is changed from equi-axed to lamellar. This strong adverse effect of lamellar shape of grains is evidently associated with that it facilitates crack initiation at the early stages of the process, which results in the loss of superplasticity.

It should be noted that the effect of grain size d on the stress of superplastic flow σ_{sp} is opposing to the effect on the yield stress in common deformation and has the form:

$$\sigma_{sp} \approx d^{a}$$

where a is a coefficient close to unity; compare it with the Hall-Petch relationship $\sigma_s \approx d^{-0.5}$ (see Ch. 4).

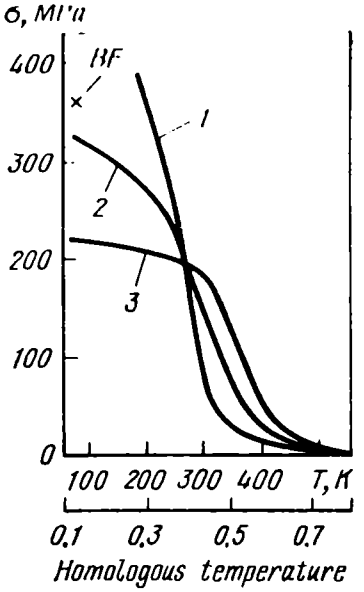

Fig. 295. Effect of deformation temperature on superplastic flow stress in specimens of Zn + 22% Al alloy with grain size 1.1 μm (*1*), 2.5 μm (*2*) and 4.5 μm (*3*). *BF*—brittle fracture

The difference is clearly seen from the data on the effect of deformation temperature on σ_{sp} of specimens of the classical Zn + 22% Al alloy with various grain size—from 1.1 μm to 4.5 μm (Fig. 295). Below $0.4\,T_{m.p.}$, σ_{sp} is higher with lower grain size; at temperatures above $0.4\,T_{m.p.}$, it increases with increasing grain size. The temperature at which the shape of the σ-d curve changes is the point of transition to superplastic state.

The first results relating to superplasticity were obtained on eutectoid and eutectic two-phase alloys. For that reason, it was believed for a long time that the presence of two phases is one of the essential conditions for the appearance of superplasticity. Later, however, superplasticity was discovered not only in two-phase alloys, but also in single-phase alloys and even in pure metals, though in the latter case δ was noticeably lower than in eutectic alloys, though appreciably higher than in common deformation.

A typical feature of two-phase alloys is that, in addition to low- and high-angle grain boundaries within a particular phase, they contain boundaries between different phases (called interphase boundaries), which are barriers for the growth of grains within the given phase at the expense of one another, i.e. they inhibit recrystallization. Hence it follows that the principal role of secondary phase particles reduces to that they prevent growth of grains during superplastic flow, i.e. ensure stability of ultrafine-grain structure of the main phase. It should be clear that this role can only be taken by those particles of secondary phases which are highly stable thermally themselves and are not liable to coagulation at the temperature of

deformation. This implies that the melting point of the second phase cannot be lower than that of the matrix.

In two-phase alloys, the shape of grains of both phases and their distribution are also of importance. Grains of each of the two phases must be close to equi-axed shape and distributed evenly. As has been first demonstrated by A. A. Bochvar, both phases must occupy approximately equal volumes in order to ensure the maximum elongation. In that case the number of adjacent grains of the same phase will be at a minimum, and therefore, the conditions will be least favourable for growth of grains by recrystallization (see Ch. 6).

This approach explains well why pure metals and single-phase alloys cannot exhibit such a high superplasticity as two-phase alloys. This is obviously associated with the fact that, when there are no stabilizers, grains are coarsened in operations of superplastic deformation, which require a long time and high temperature, by the mechanism of recrystallization. This conclusion was confirmed experimentally. On the other hand, it seems improper to reduce the role of secondary phase particles only to stabilization of microstructure. As has been established on two-phase iron alloys, Al-Si alloys, etc., even when specimens had an ultrafine structure and a high value of m, they fractured on elongation of only 200-300 per cent due to cracks formed at interphase boundaries. It is characteristic that particles of secondary phases in these alloys had different plasticity. Thus, in addition to their own stability against coagulation, which is essential for playing the role of stabilizers, secondary phase particles must also possess a high plasticity, close to that of the main phase.

In the atomic mechanism of superplasticity, slip on interphase boundaries seems to have an important role. Therefore, with a high concentration of a secondary phase, of essential importance should be the structure of interphase boundaries and the rate of diffusion through these boundaries as compared to interphase boundaries between grains.

The role of alloying impurities present in the solid solution still has not been studied properly. In most cases, binary alloys exhibiting superplasticity contain elements with the melting point and diffusion characteristics close to the respective characteristics of the matrix. There are however many exceptions from this general rule. As follows from the same data, the purity of the original materials has no noticeable influence on superplasticity.

Anisotropy of superplasticity, its correlation with the texture of the matrix, and variations of this texture in superplastic deformation have not yet been studied thoroughly, though they are important for understanding the mechanism of the process. As has been found in experiments with rolled alloys Zn + 0.4% Al, Sn + 38% Pb and aluminium bronze, specimens cut at different angles to the rolling direction differ in the magnitude of m and the maximum elongation, the difference depending on the rate of deformation and being the

highest in the range where the m parameter is at its maximum.

O. A. Kaibyshev established for specimens of Zn + 22% Al alloy rolled under different conditions that anisotropy of σ and δ was not found in rolled specimens which had no texture (texture was eliminated by dynamic recrystallization). In textured specimens, σ was independent of direction, but was smaller in magnitude than that in untextured specimens. The plasticity index δ, per cent, was found to be highly anisotropic. It increased from 950 per cent to 1 200 per cent in the rolling direction, was equal to 1 000 per cent at an angle of 45°, and dropped to only 730 per cent at an angle of 90° to the direction of rolling.

The following fact, which has been marked by a number of authors, seems to be most essential and evidently most reliable: in superplastic deformation at the optimal rates corresponding to the maxima of m and δ (i.e. in the rate range *II*, see Fig. 292), the original texture was observed to be weakened (in Al + 33% Cu, $CuAl_2$). In contrast to this, deformation at high rates (region *III*) in some cases resulted in stronger texture of specimens.

The following facts are also of practical importance. The effect of superplasticity in rolled (textured) alloy is observed in a wider range of deformation rates. Even at $\dot{\varepsilon} = 3.6 \times 10^0\ s^{-1}$, i.e. at the level of common deformation rates, the relative elongation may be as high as 150 per cent.

Besides, the flow stress σ reduces in a textured material quite noticeably, so that this effect can overbalance the effect of grain size. For instance, the magnitude of σ in a rolled alloy with the grain size $d = 1$ μm turns out to be lower than in hardened (untextured) alloy with $d = 0.5$ μm.

3. The Atomic Mechanism of Superplasticity

The knowledge of the atomic mechanism of superplasticity is indispensable for substantiated selection of the optimal conditions of superplastic deformation, the composition of alloys and their structural and phase states. Besides, analysis of this mechanism is also of principal importance for the physics of plasticity.

For some time, researchers attempting to elucidate the mechanism of superplasticity were misled by the circumstance that the effect was first discovered in and for a long time studied on two-phase alloys only. At a later time, as has been given earlier, superplasticity was also discovered in single-phase alloys and even in pure metals.

In accordance with the concepts discussed in Chs. 2 and 8, the plastic flow at elevated temperatures and low deformation rates may in the general case include the following mechanisms: dislocation mechanisms—slip and climb; directed mass transfer by diffusion (diffusion creep); and slip of adjacent grains relative to one another

(grain-boundary sliding). The following peculiarities should be considered in the analysis of the probable contribution of each of these mechanisms.

(1) Superplasticity appears most often in ultrafine-grain metals, but can appear in pure metals, as well as in two-phase alloys, though the effect in the latter is usually higher.

(2) The process occurs at a low rate.

(3) The flow stress under the conditions of superplasticity (region *II*) is usually strongly sensitive to deformation rate, the relationships $\sigma = f(\dot{\varepsilon})$ and $m = f(\dot{\varepsilon})$ have an extremum; further, the flow stress decreases with decreasing grain size.

(4) Though the amount of deformation in superplastic flow is very large, grains of the metal remain equi-axed or are only stretched slightly in the direction of deformation, the dislocation density in them remains almost unchanged, no dislocation pile-ups are formed, even at grain boundaries, and therefore, the strengthening effect in the metal is very low. In contrast to this, deformation in range *III* of deformation rates is accompanied with an increase in the dislocation density and with strengthening of the metal.

(5) The presence of texture in the original state can influence σ, but affects more appreciably the relative elongation δ, per cent, which becomes anisotropic. Besides, the nature of texture may vary in the course of plastic flow.

The dependence of m on deformation rate cannot be explained by the mechanism of diffusion creep. The role of the latter should increase with decreasing deformation rate. This suggests that the plasticity and the m parameter should be expected to increase monotonoulsy as the deformation rate diminishes, though actually these characteristics pass through a maximum and then begin to decrease.

The deformation rate $\dot{\varepsilon}_{dc}$ based on the Nabarro-Herring classical model of diffusion creep is expressed as follows:

$$\dot{\varepsilon}_{dc} = 14 \frac{V_a}{kT\, d^2} \sigma D_v \left(1 + \frac{n\delta}{d} \frac{D_b}{D_v}\right)$$

where V_a is the atomic volume; D_v and D_b are the coefficients of volume and boundary diffusion; δ is the width of grain boundary; d is the size of grain; and n is an empirical constant.

In many cases, however, the deformation rate calculated by the theory of diffusion creep turns out to be one or two orders of magnitude lower than that observed experimentally. Finally, the theory of diffusion creep fails to explain texture variations.

Most of the available results provide a convincing evidence that the most important part under optimal conditions of superplasticity (region *II*) is played by grain-boundary sliding.

A. A. Bochvar has supposed already in his earliest publications on the subject (1945-46) that superplastic flow must include two processes: (a) intergranular displacement (which has been later termed grain-

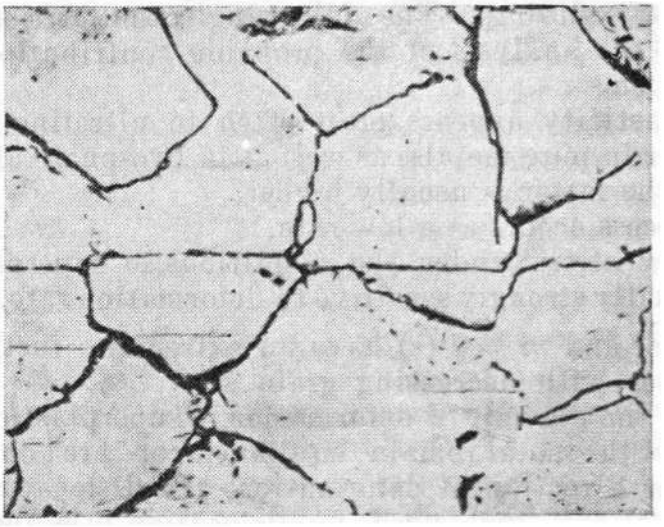

Fig. 296. Displacement of scratches made on a polished specimen, due to superplastic flow

boundary sliding) and (b) healing of microdiscontinuities (submicropores) which appear on grain boundaries in the course of grain-boundary sliding. Later, this process, which ensures the integrity of the material and accommodation of the surfaces of adjacent crystallites and effected by diffusion mass transfer in a stress field (diffusion creep) has been called the accommodation process.

According to A. A. Bochvar, diffusion mass transfer in two-phase alloys is realized by the 'dissolution-precipitation' mechanism (the dissolution of boundary volumes of grains of one phase in the boundary volumes of adjacent grains of another phase, by diffusion through the volumes of these second-phase grains, and by precipitation on other grains of the first phase); in single-phase alloys (pure metals), it is realized by recrystallization growth, owing to oriented movement of vacancies.

These suppositions have later been confirmed experimentally and the concepts on the atomic mechanism of grain-boundary sliding have been further developed by a number of authors, among them M. F. Ashby and R. A. Verall*.

The role of the processes occurring in grain boundaries is enhanced due to the fact that ultrafine-grain structure is the most important condition for the appearance of superplasticity. This role must become more essential as the temperature increases.

The effect of grain-boundary sliding has been confirmed experimentally by the results of metallographic observations obtained by many workers. For instance, scratches made on polished surface of specimens, which pass prior to deformation as straight lines through a number of grains, turn out after the superplastic deformation to consist

* Ashby M. F., Verall R. A., *Acta Met.* **21**: 149-160 (1973).

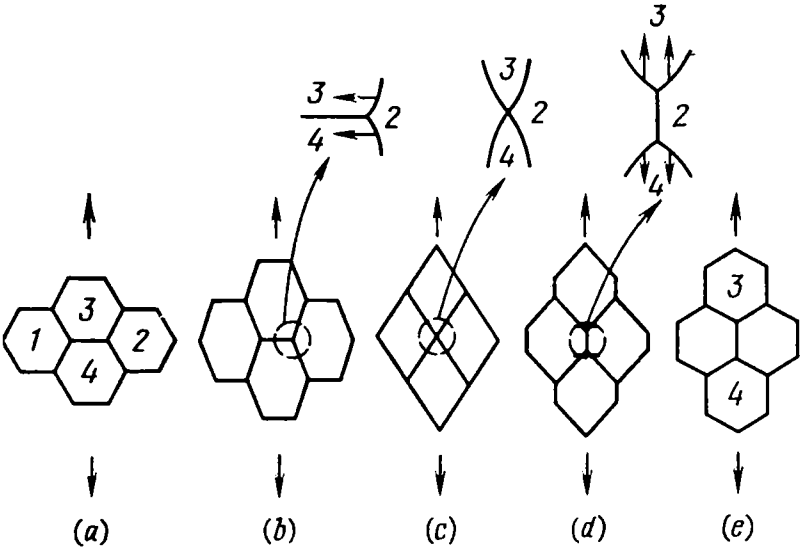

Fig. 297. The Ashby-Verall model of superplastic deformation

of individual sections which are straight within a grain but displaced obliquely relative to one another on passage from one to the next grain (Fig. 296). Transmission electron microscopy of thick foils has revealed displacements and rotations of adjacent grains relative to one another and, in some cases, full replacement of some grains by their neighbours.

Semiquantitative estimations have shown that the maximum of deformation caused by grain-boundary sliding is observed in the same range of deformation rates as the maximum of m parameter and constitutes up to 60-70 per cent of the total deformation of a specimen. Ashby and Verall proposed a model of superplastic deformation in which the decisive role belongs to grain-boundary sliding which is matched with diffusion accommodation occurring simultaneously. Their model is illustrated schematically in Fig. 297 which shows the positions of four grains in the original (*a*), intermediate (*b-d*) and final (*e*) states.

During deformation, some grains may move farther from one another (grains *3* and *4* in the figure)*. Neighbouring grains move not in parallel, but in perpendicular paths (grains *1* and *2* move perpendicular to the paths of grains *3* and *4*) and rotate in this movement. An important feature is that the flow of the material occurs non-uniformly.

The passage of grains from the original to final state includes the following processes:

(a) grain-boundary sliding—grains move by shear relative to

* This has been confirmed experimentally by observations on Zn + 22% Al alloy.

one another in the plane of their boundary; this shear is greater than in the model of diffusion creep;

(b) diffusion transfer along the normal to the boundary by the mechanism of volume and boundary diffusion; as may be seen from

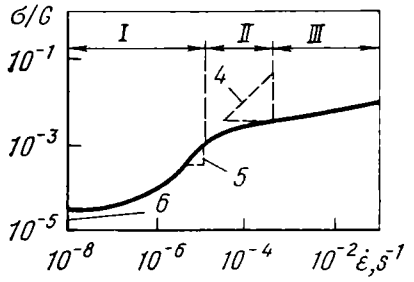

Fig. 298. Analytical relationship for normalized stress σ/G and m parameter depending on deformation rate at $\theta = 0.5$ and grain size $d = 1$ μm (after Ashby and Verall)

1—diffusion creep is predominant; *2*—contribution from both mechanisms; *3*—dislocation creep is predominant; *4*—contribution of dislocation creep; *5*—$m_{max} = 0.9$; *6*—limiting stress

Fig. 297*d*, diffusion paths are not long (roughly $0.3d$) and the displaced volume constitutes not more than 25 per cent of the volume of a grain;

(c) variations in the surface area of grains—the area of grain boundaries increases on the passage into an intermediate state.

This ensures an increase of the flow rate roughly by an order of magnitude compared with uniform flow of the metal by the mechanism of diffusion creep.

In Ashby-Verall's model, the expression for the flow rate $\dot{\varepsilon}_{AV}$ is of the form:

$$\dot{\varepsilon}_{AV} = 98 \frac{V_a}{kT\,d^2} \left(\sigma - \frac{0.27E_{gb}}{d}\right) \times D_v \left(1 + \frac{\pi\delta D_b}{dD_v}\right) \qquad (208)$$

where E_{gb} is the grain-boundary energy.

According to Ashby and Verall, another mechanism of superplasticity may be dislocation creep which comprises conservative slip and climb of dislocations. The flow rate by dislocation creep $\dot{\varepsilon}_d$ may be expressed as follows:

$$\dot{\varepsilon}_d = A\,(Gb/kT)\,(\sigma/G)^n \exp(-Q_d/kT) \qquad (209)$$

where Q_d is the activation energy of dislocation creep.

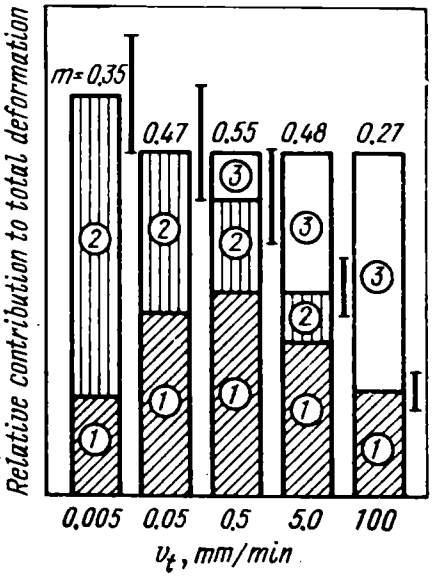

Fig. 299. Contribution of various deformation mechanisms to tension of Zn + 22% Al alloy ($\delta = 20\%$) at various deformation rates

1—grain-boundary sliding; *2*—diffusion creep; *3*—intragranular dislocation creep

The total flow rate can be written as the sum

$$\dot{\varepsilon} = \dot{\varepsilon}_{AV} + \dot{\varepsilon}_d$$

The results of calculation of the normalized stress σ/G and the indices of speed-induced hardening m depending on the rate of deformation for lead by the relationships (208) and (209) are shown in Fig. 298. The figure also gives the contributions of particular flow mechanisms depending on deformation rate.

The estimated contributions of various deformation mechanisms in Zn + 22% Al alloy at different rates of tension are shown in Fig. 299 (according to I. I. Novikov and V. K. Portnoi). These data suggest that, under the optimal conditions of superplastic flow (region *II*, Fig. 298), the main contribution to the total deformation is due to grain-boundary sliding matched with diffusion accommodation. At lower deformation rates (region *I*), the role of diffusion creep increases, and at higher rates (region *III*), dislocation creep gains in importance. The contribution of dislocation creep increases with an increase in grain size (within 0.5-10 μm) and deformation rate and a decrease of temperature.

4. Practical Application of Superplasticity in Plastic Working of Metals

Superplastic deformation belongs to the most promising processes of plastic working of metals. In many cases it is much more efficient than the conventional processes. Besides, it offers new possibilities for improving the properties and deformability of metals.

On the other hand, the method is by no means universally applicable. For the best utilization of the method, one has to know its possibilities, advantages and drawbacks.

Advantages and drawbacks of superplastic deformation. The principal advantages of superplastic deformation are as follows.

1. The high deformability of alloys in superplastic state widens appreciably the possibilities of shaping by plastic deformation, especially as regards articles of intricate shape. Articles of an intricate configuration can be shaped in a single operation. Besides, it is possible to reduce the use of metal and the expenditures on machining and welding operations.

2. Superplastic deformation is done under a very slight force (stress), which makes it possible to increase substantially the size of blanks (articles) to be deformed or to use less powerful equipment.

In addition, since the deforming stresses are low, it is possible to use the method effectively for shaping metals and alloys by new deformation processes, such as vacuum shaping which is used widely in the manufacture of plastics. This method seems to be especially efficient for drawing of sheet metal. Besides, it is possible to reduce the wear of tools and the cost of dies.

3. In some cases, superplastic deformation makes it possible, even at heavy deformation, to avoid uneven gauge of deformed articles, a defect often encountered, for instance, in deep drawing.

4. Since superplastic flow causes practically no residual elastic macro- and micro-stresses, shaped articles have a high stability of dimensions and high corrosion resistance.

5. An equi-axed ultrafine-grain structure with weak or no texture, which is formed on superplastic deformation, ensures a favourable complex of the mechanical properties of the metal for operation at moderate temperatures: high and isotropic values of yield strength, impact toughness and fatigue strength, and a good surface finish.

It is essential that in cases when fine grain is unwanted in the final product, for instance, when it is needed to prevent or diminish creep in articles for long operation at elevated temperatures, the structure can be coarsened by final heating (heat treatment).

On the other hand, one should be aware of certain drawbacks of the method and seek rational ways for overcoming them. The main drawbacks which do not allow superplastic deformation to be used in mass production are as follows.

1. Low rate of deformation at which metals and alloys can exhibit superplastic properties (when $m > 0.3$). As has been indicated earlier, this rate varies within 10^{-4} to 10^{-1} s^{-1}.

Let us estimate the time of deformation corresponding to these rates. It can be found by the formula

$$\tau_{def} = \bar{\varepsilon}/\dot{\varepsilon}$$

Let the required amount of deformation be 200 per cent. The time of deformation for the deformation rate of 10^{-4} s^{-1}, 10^{-3} s^{-1} and 10^{-1} s^{-1} will then respectively be 5 h, 30 min, and 20 s. As may be seen, as the rate of deformation is increased by an order of magnitude, the time of deformation is shortened by an order of magnitude.

The main ways for increasing the allowable deformation rate, as follows from the material of Sec. 3 of this chapter, is to diminish grain size.

2. Blanks for superplastic deformation must have ultrafine grain (1-10 μm) and the structure must retain this property during the whole process of superplastic deformation. This condition is especially difficult or sometimes impossible to observe for single-phase alloys and pure metals. Some methods for decreasing grain size have been discussed in Ch. 8; other methods will be considered later in this section.

3. Tools for superplastic working must be hot and retain the specified temperature during the whole time of the process. Cooling of a deformed blank on contact with a cold tool may result in a sharp drop of m and loss of superplasticity.

Special difficulties arise in superplastic deformation of high-

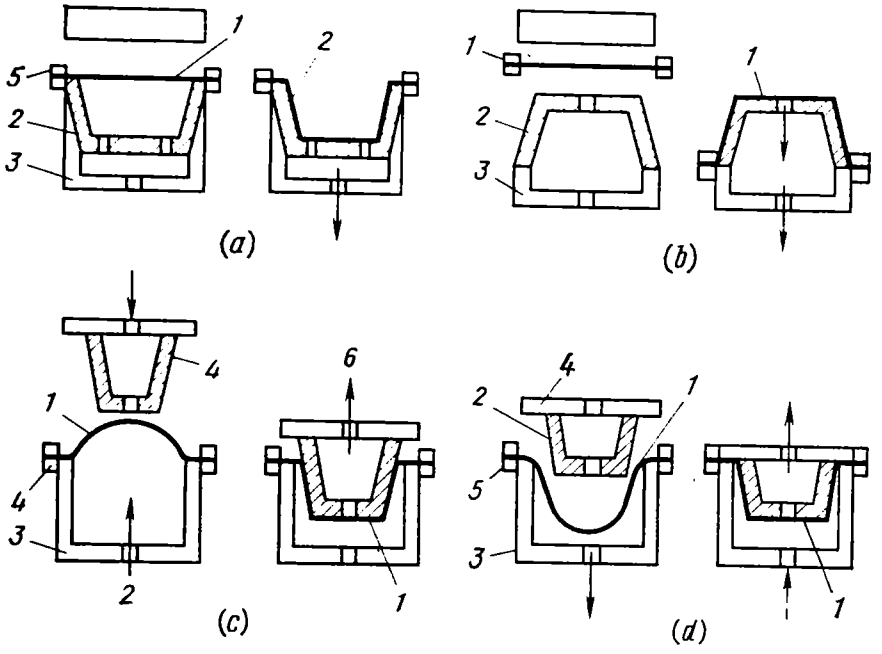

Fig. 300. Diagram of vacuum-gas superplastic shaping
1—blank to be deformed; *2*—die; *3*—vacuum chamber; *4*—cover; *5*—clamp. Direction of evacuation is indicated by arrows

temperature materials (heat-resisting nickel alloys, alloys of high-melting metals, etc.).

4. Articles must be held in the die until their temperature drops down below the limit of superplasticity; otherwise, i.e. when removed hot, they change their shape or dimensions under an occasional slight stress.

Methods of shaping in superplastic deformation. These methods depend on a number of factors, in particular, on the shape of original blanks. In modern practice of superplastic deformation, the most popular methods are shaping and deep drawing of sheet metal.

Along with sheep drawing in conventional presses, methods of vacuum and vacuum-gas pressing (pneumoshaping) are used increasingly. In cases when oxidation of a metal or alloy is not critical, air can be used instead of inert gases. The gas pressure may range from a few to a few tens atmospheres, depending on the desired stress σ.

Some methods of vacuum-gas thermoplastic shaping are illustrated in Fig. 300. These methods ensure a high uniformity of elongation and can be used for deformation of intricate-shape articles in a single operation without intermediate annealing and, in many cases, without finishing (prepressing) operations.

An original method using superplastic flow has been developed for dieless drawing of tube blanks. A tube blank (Fig. 301) is clamped at one end in a holder (*1*) and drawn at the other end at a controlled rate v_2. An inductor (*2*) heats up the tube locally to the temperature

of superplastic state and is moved at a rate v_1 in the direction opposite to drawing. The resulting reduction is determined from the relationship

$$(D_1/D_2)^2 = (v_2/v_1) - 1$$

The reduction per pass is up to 50 per cent, but heavier reductions can be obtained in two or more passes. This method can also be applied for shaping tube blanks into conical parts. In that case, one of the two speeds must be constant and the other, variable.

Modern superplastic metals and alloys. The list of metals and alloys possessing superplastic properties increases gradually as more metals and alloys become known to exhibit superplasticity. It is now clear that very many alloys are potentially superplastic. The available literature data on the metals and alloys in which the phenomenon of superplasticity has been found and used in practice are summarized in Table 17.

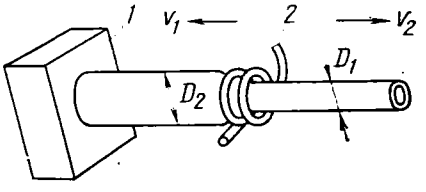

Fig. 301. Dieless drawing of tube blank in superplastic state

As may be seen from the table, among superplastic materials there are pure metals, single-phase alloys and poly-phase alloys containing from two to eight or even more components. Analysis shows that the highest superplasticity is found in two-phase alloys with roughly equal concentration and uniform distribution of the two phases. A few examples to be mentioned are the classical eutectoid Zn + + 22% Al alloy; beryllium-base alloy (Be + 38% Al) with nearly eutectoid structure; (α + β)-titanium alloys in which the maximum of superplasticity has been found at temperatures corresponding to the (α + β) region; complex-alloyed nickel alloys containing roughly equal concentrations of γ + γ' phases with respectively f.c.c. and c.p.h. lattice; and chrome-nickel stainless steel (Fe + 26% Cr + + 6.5% Ni) which contains fine austenitic inclusions in the ferritic matrix.

High-purity metals and single-phase alloys with a low temperature of recrystallization are less promising as regards superplasticity. In such materials, it is difficult to prevent grain coarsening at the temperatures of superplasticity and low rates of deformation. The sole possible way is to introduce small concentrations of low-soluble additions to form fine-disperse secondary phase particles which can stabilize grain boundaries.

In Table 17, superplastic metals and alloys are divided into groups depending on the temperature range of deformation in which their superplasticity may appear.

The medium-temperature group is of the highest interest in modern practice and the high-temperature one will be of large interest in the

Table 17. Superplastic Metals and Alloys

Composition		Optimal temperature of superplasticity, °C	Grain size, μm	$\dot{\varepsilon}_{opt}$, s^{-1}	m	δ, %
chemical	phase					
Medium-temperature materials						
β-plutonium	β	180		10^{-3}	0.33	680
Al + 33% Cu		500	1-2	10^{-4}-10^{-2}	0.4-0.9	500
Al + 5% Mg	—	350-475				1000
Mg + 32% Al	—	375	2.2	2×10^{-1}	0.8	approx. 1500
Zn + 22% Al	α + β	250-270	0.7	10^{-2}-10^{-1}	0.4	1500
Al + 6% Cu + 0.5% Zr	α + β	450	6	10^{-3}	0.45	800
High-temperature materials						
W + (15-30)% Re	—	2000			0.5	200
Cu + 10% Al + 4% Fe + 0.8% Zn	—	800	10-12	10^{-3}	0.6	700
Fe + 26% Cr + 6.5% Ni + 0.6% Ti + 0.1% Al + 0.2% C	α + β	—	—	—	—	—
Ni + 10% Cr + 18% Co + 4.5% Ti + 3.5% Al + 3% Mo + 0.75% V + 0.17% C + 0.015% B + 0.05% Zr	γ + γ′	1050-1150	5	10^{-4}-10^{-3}	0.5	1000
Ti + 6% Al + 4% V	α + β	900-950	2	10^{-4}	0.85	1000

nearest future. This group includes heat-resisting nickel-base alloys, titanium-base structural alloys, etc.

The difficulty in practical application of the latter group of alloys consists in the need for developing special techniques for forming ultrafine grain in the original state (prior to superplastic deformation). Some of these techniques will be discussed later. The metals and alloys given in Table 17 can also be classified by the method for forming ultrafine-grain structure in them. This in turn is associated with the phase composition and ductility of these alloys under common conditions of deformation. In view of this, all the materials mentioned in the table can be divided into three groups.

A. Eutectic and eutectoid alloys which possess a fine-grain two-phase structure. A typical example is the classical Zn + 22% Al alloy. Since, however, the eutectic is usually lamellar, the solidified alloy must be subjected to hot deformation and heating to acquire superplastic properties.

B. Alloys subjected to thermomechanical treatment. These include two-phase alloys in which two phases form due to decomposition of the supersaturated solid solution or phase transformation. Fine-grain structure is formed by hot deformation at the temperatures of the two-phase state. The particular conditions (temperature, rate, scheme) of deformation are determined by the nature of an alloy, its ductility, the kinetics and mechanism of phase transformation, and thermal stability of its phases. For instance, according to I. I. Novikov and V. K. Portnoi, good results for two-phase brasses can be obtained by thermomechanical treatment consisting of hardening and rolling at the temperatures of bainitic transformation and for two-phase titanium alloys and stainless Cr-Ni steel by heavy hot deformation in the $\alpha + \beta$ and $\alpha + \gamma$ region, respectively.

C. Alloys produced by powder metallurgy methods. This group includes brittle alloys and those having a pronounced tendency to segregation. In that case, the metal before superplastic deformation is cast, crushed into powder, pressed, sintered and subjected to thermomechanical treatment or its powder is prepared by spraying or else the metal is deformed in the two-phase region by extrusion (or generally by any other scheme close to uniform compression). It should be kept in mind that the surface of metal particles can be oxidized readily during pressing and sintering, so that these operations are usually made in a vacuum.

Examples of utilization of superplasticity and methods for formation of ultrafine-grain original structure. The experience gained up to the present time in practical applications of superplasticity makes it possible to indicate the fields where the method is most effective.

In the first place, one has to mention deep drawing where superplasticity makes it possible to reduce the number of operations (i.e. to reduce labour consumption and cost of tools), improve the accuracy of the size and shape of products, especially of those of intricate

shape with abrupt junctions, and diminish the loss of metal caused by unfavourable texture ('earing'). Articles of this kind include various sleeves, cylinders, aircraft wing panels, tool boxes, etc. Examples of articles made by deep drawing of steel 12X18H10T are shown in Fig. 302.

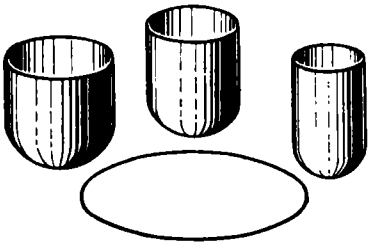

Fig. 302. A sleeve formed by drawing of steel 12X18H10T in superplastic state

In conventional deep-drawing process, a sleeve of steel 12X18H10T is made by deep drawing in three passes with intermediate annealing, etching, etc. In the superplastic state of the metal, the same sleeve can be drawn in one pass in a 100-t hydraulic press (instead of a 630-t press needed in the former case); the drawn article has a higher uniformity of wall thickness, and the loss of metal reduces by 10-12 per cent. Since the metal has a uniform fine-grain structure, its mechanical properties are improved. The conditions of superplastic deformation are as follows: $t^\circ \approx$ 780-850°C and $\dot{\varepsilon} = 10^{-2}$-$10^{-1}$ s^{-1} (i.e. 4 min per article). Ultrafine grain was formed by high-speed recrystallization after cold rolling. For this purpose, rolled blanks were heated in a salt bath up to 780°C at a rate of 30-50 °C/s and quenched in water.

The use of superplastic deformation in shaping of aircraft wing panels makes it possible to increase the rigidity of panels, since there is no thinning of the metal in the edges (see point *A* in Fig. 303). In bulkhead panels, spring-back of sheets is avoided, since there are no macrostresses.

Superplasticity offers large advantages in cases when good fil-

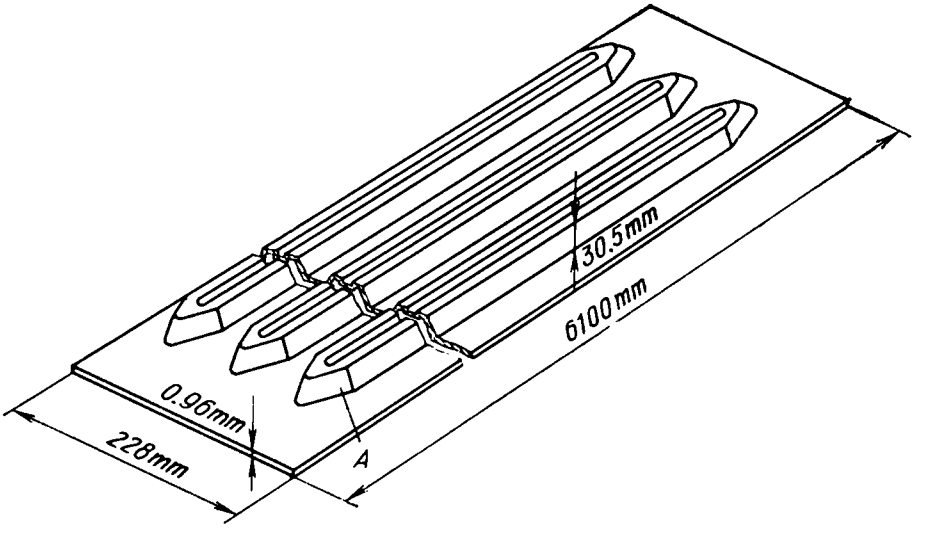

Fig. 303. A wing panel formed from sheet of Ti + 6% Al + 4% V alloy using the superplasticity effect

ling of the die and accurate reproduction of the die impression are essential.

In recent time, there is an increasing trend to use superplasticity in the manufacture of articles from brittle heat-resisting alloys, which are usually made by casting (turbine blade disks, etc.). By this method, the properties of the metal in articles are improved substantially due to its more homogeneous microstructure.

A wider utilization of the effect of superplasticity in such alloys is mainly retarded by the difficulty in forming ultrafine grain. Promising methods for forming ultrafine grain are utilization of heterophase alloys, deformation under conditions close to uniform compression followed with recrystallization and also the methods of powder metallurgy.

RECOMMENDED LITERATURE

1. Davydov V. A., *Metallovedenie i Termicheskaya Obrabotka* **10**: 5-35 (1976) (in Russian).
2. Grabsky M.V., *Structural Superplasticity of Metals.* Moscow, Metallurgiya, 1975 (in Russian).
3. Kaibyshev O.A., *Plasticity and Superplasticity of Metals.* Moscow, Metallurgiya, 1975 (in Russian).
4. Novikov I.I., Portnoi V.K., *Superplasticity of Ultrafine-grain Alloys.* Moscow, Metallurgiya, 1981 (in Russian).

INDEX

Accommodation bands 138
Accommodation kinking 138
Activation energy 32
Actual recrystallization diagram 294
Adiabatic effect 378
Adsorption effect in metals 395
Ageev N. P. 249, 379, 402
Airy's function 42
Alloy texture 239
Amelinckx S. 102
Anelastic deformation 142
Anelasticity 200
Anisotropy, elastic 28
  in textured materials 243
Annealing twins 123
Aristov V. V. 179
Ashby M. F. 187, 466, 468
Asterism 136
Atomic mechanism of superplasticity 464
Axial ratio 17
Axial texture 220, 233

Baakashvili V. S. 402
Backofen's test 457
Bands of secondary slip 139
Barrett C. S. 138, 342
Barrier work hardening 192
Basal planes 17
Bauschinger effect 150, 199
Beck P. A. 264, 342
Beresnev B. I. 363, 367, 368, 371
Berezhkovsky D. I. 316
Berner R. 166, 179
Bernstein M. L. 29, 216, 218, 319, 402, 439, 440, 452
Bishop J. F. W. 202
Blain P. 301
Blue brittleness 144
Boas W. 135, 179, 234
Bochvar A. A. 284, 453, 463, 465, 466
Body-centred cubic lattice 19
Bond energy 11, 16
Bond forces in crystals 11
Borodkina M. M. 249
Brass texture 239, 342
Bridgman P. W. 366, 367, 371
Brittle fracture 348
Bulat S. I. 437
Bulychev D. K. 371
Bunge H. J. 249
Burduksky V. V. 102
Burgers W. 85
Burgers circuit 34
Burgers vector 34

Cahn R. W. 29, 179, 274
Carbon segregation 414
Cell structure 212
Chalmers B. 16, 29, 204, 218
Chemical properties of grain boundaries 89
Cleavage 348
Cleavage fracture 355
Climb of edge dislocations 118
Close-packed hexagonal lattice 17
Coble's model of diffusion creep 189
Coherent boundaries 123
Coincidence site lattice 86
Cold work 76, 110
Collapse of vacancy discs 101
Complete texture 221, 238
Compressive texture 238
Concentration coefficient 204
Conical texture 221
Conservative movement of dislocations 36, 55
Controlled rolling 450
Coordination numbers of crystals 12
Copper texture 239
Cottrell A. H. 10, 21, 29, 81, 102, 136, 156, 179, 192, 215, 354
Cottrell atmospheres 78, 145
Cottrell-Bilby pole mechanism 130
Covalent bond 13
Criteria of ductile fracture 369
Critical shear stress 145
Cross slip of dislocations 37
Crystallographic textures 219
Crystal structure of pure metals 16
Cube texture 221, 336
Curie P. 231

Davidenkov N. N. 374
Davydov V. A. 476
Debye rings 224
Decarburization 334
Decoration of dislocations 97
Deformability 406
Deformation bands 136
Deformation, by slip 103
  by twinning 122
Dendritic segregation 414
Diffusion creep 189
Diffusion-dislocation mechanisms of plastic deformation 143
Diffusion of point defects 250
Dislocations 33
Dislocation density 39
Dislocation forests 163, 214

Dislocation jogs 77
Dislocation kinks 73
Dislocation mechanisms of fracture 352
Dislocation mechanism of twinning 129
Dislocation movement by double kinks 120
Dislocation pile-up 353
Dislocation tangles 214
Dislocation width 56
Double cross slip 155
Double kinks 120
Drawing textures 235
Dubrovin A. K. 437
Ductile-brittle transition 355
Ductile fracture 348, 357
Ductility 403
Durnev V. D. 249
Dynamic recrystallization 260, 299
Dynamic strain ageing 215
Dzugutov M. Ya. 437

Earing 245
Easy glide planes 56
Edge dislocations 33
Elastic accommodation 186
Elastic anisotropy 28
Elastic deformation of crystals 24
Elastic properties of dislocations 40
Energy of dislocations 43
Entin R. I. 440
Equi-axed grains 414
Eremeev V. I. 402
Erichsen's cupping test 405
Etch-pit method 98
Extended dislocations 62
Extra-plane 34

Face-centred cubic lattice 16
Field-ion microscopy of dislocations 91
First-order recrystallization diagrams 291
Firstov S. A. 179, 218
Flow stress 372
Fracture 348
Frank criterion 60
Frank dislocations 63
Frank-Read dislocation source 59
Free-path length of dislocation 57
Frenkel I. Ya. 350
Frenkel Ya. I. 10, 23, 55, 143
Frenkel defect 31
Fridman E. M. 179
Fridman Ya. B. 436
Friedel J.. 10, 102

Gaidunov M. G. 371
Geminov V. N. 102
Geometrical softening 116
Gilman J. J. 169, 352
Glocker R. 336
Gorelik S. S. 102, 179, 251, 274, 298, 319, 334, 347
Goss texture 222
Grabsky M. V. 476
Grain-boundary diffusion 89
Grain-boundary sliding 180
Grain coarsening 320
Grain growth 260, 445
Grain size, effect on plasticity 202
Grewen J. 249, 347
Griffith A. A. 349
Grigoryev A. K. 10
Gubkin S. I. 315, 377, 395, 397, 431, 436, 437
Gulyaev A. P. 440

Hall-Petch relation 203
Hardening coefficients 145
Hardening stages 145
Herring C. 143
Heterodiffusion 32
Heteropolar bond 12
High-angle boundaries 80
High-temperature annealing 415
High-temperature thermomechanical treatment 440
Hill R. 202
Hirsch P. B. 170
Hirth J. P. 102, 125, 135, 179
Homogenizing annealing 415
Homopolar bond 13
Honeycombe R. W. K. 125, 136, 139, 179, 196, 218, 249
Hydrostatic pressure, effect on fracture 361

Ilyushin A. A. 403
Impact toughness 405
Imperfections in crystals 30
Impermeable barriers 439
Incoherent boundaries 123
Indenbom V. L. 354
Inequigranular structure 320
Initiation of dislocations 100
Interaction of dislocations 72
Interatomic forces 11
Intercrystalline fracture 348
Intermetallic alloys 413
Intersection of extended dislocations 76
Interstice, octahedral 17
tetrahedral 17
Interstitial atoms 30
Intragranular diffusion plasticity 143
Intragranular plastic deformation 103
Ioffe's effect 361
Ionic bond 12
Islet inequigranularity 323
Ivanova V. S. 102
Iveronova V. I. 298
Izbranov P. D. 339

Jogs 77
Jonas J. J. 304

Kaibyshev O. A. 179, 464, 476
Karatushin S. I. 402
Kinks 73
Kink band 136
Kinking 136
Kirch F. 300
Kolmogorov V. L. 428, 437
Konobeevsky S. T. 254
Kopetsky Ch. V. 10
Korneev N. I. 296
Kronmüller H. 179
Krupin A. V. 437
Kudryavtsev I. P. 249, 347
Kuhlmann-Wilsdorf D. 169
Kuk P. M. 388
Kurdyumov G. V. 10
Kurnakov N. S. 377, 407

Lacombe P. 85
Lamellar cell structure 215
Larikov L. N. 274
Laue patterns 136
Lineage inequigranularity 322
Linear defects 33

Locality of deformation in polycrystals 193
Lomer-Cottrell dislocations 67
Long-range bond 13
Lothe J. 102, 179
Low-angle boundaries 80
Low-temperature thermomechanical treatment 440
Lüders-Chernov bands 198
Ludwik P. 374
Luton M. J. 303

Macroscopic continuity 193
Marynov E. D. 371
McLean D. 29, 179, 183, 185, 186, 192, 195, 371
Mechanical hysteresis 198
Mechanical textures 219
Mechanisms of diffusion plasticity 140
Mechanisms of grain-boundary plastic deformation 180
Mecking H. 300
Menter J. 96
Metadynamic recrystallization 312
Metallic bond 15
Microscopic continuity 191
Mil'man Yu. V. 179, 218
Mirer I. I. 254
Mirkin L. I. 102
Misfit factor 86
Mixed bond 15
Moiré effect 96
Moiseev V. O. 207, 218
Molecular bond 14
Molotilov B. V. 234, 298
Mott N. F. 138, 167, 170, 353
Mott's islet model of high-angle boundaries 89
Mott's theory of work hardening 167
Movement of dislocations 54
Multi-component texture 222
Multiple dislocations 35
Multiplication of dislocations 58

Nabarro F. R. N. 143, 145, 191
Necking 156
Non-conservative movement of dislocations 36
Novikov I. I. 102, 469, 474, 476
Nye J. F. 29

Octahedral void 17
Oding I. A. 10, 102, 370, 371
Oriented growth 337
Oriented nucleation 337
Orowan E. 24, 254, 351

Partial dislocations 60
Pavlov I. M. 294, 437
Pavlov V. A. 149, 179, 339
Peierls-Nabarro locks 45
Peierls-Nabarro stress 55
Pencil slip 38
Petch-Stroh equation 208
Pfeil L. 138
Planar texture 221
Plastic accommodation 187
Point defects 30
Point group 231
Polanyi M. 24
Pole figures 224
Polygonization 254
Portevin-Le Chatelier effect 198
Portnoi V. K. 469, 474, 476
Pozdeev A. A. 402
Prerecrystallizational polygonization 257
Primary recrystallization 259, 261
Primary slip system 113
Prismatic planes 17
Pugh H. L. D. 371
Pyramidal planes 17

Ratner S. I. 371
Read W. T. 10, 83, 102, 179, 182
Rebinder P. A. 395
Rebinder effect 395
Recovery 251
Recrystallization 259
Recrystallization diagrams 292
Recrystallization textures 335
Red-shortness 424
Reiko I. G. 419
Repolygonization 304
Resolved shear strain 110
Resolved shear stress 106
Rib texture 222, 344
Ring texture 221
Rodigin N. M. 339
Rodina I. P. 301
Rodinov K. P. 371
Rogelberg I. L. 296, 298
Rolling texture 221, 234, 238
Rossard C. 301
Rotational slip 136, 139
Rzhanitsin A. R. 400, 402

Sachs' grid 226
Sadovsky V. D. 440
Savitsky E. M. 296
Scheffler's diagram 420
Schmid E. 108, 135, 179, 234
Schmid factor 108
Schottky defects 30
Schwindlerman L. S. 85, 179
Screw dislocations 36
Secondary recrystallization 260
Second-order recrystallization diagrams 315
Seeger A. 10, 155, 163, 168, 176
Seleznev V. I. 436
Self-diffusion 32, 141
Sellars C. M. 303
Semipermeable barriers 439
Sessile dislocations 68
Shewmon P. 143, 179
Shilov V. I. 327, 334
Shockley W. 83
Shpichenetsky E. S. 296, 298
Simple shear 36
Sinelnikov M. I. 419
Single-component texture 222
Sirotin M. I. 327, 334
Size effect 360
Slip of dislocations 36, 55
Slip systems of metals and alloys 104
Slip zones 153
Smirnov V. S. 249
Smirnov-Alyaev G. A. 428
Snoek atmosphere 79, 179
Sokolkov E. N. 307, 440, 447
Sokolov L. D. 379, 382, 391, 402
Solovyev V. Ya. 437
Spektor E. N. 249
Sperry P. R. 264
Stabilizing polygonization 257
Stacking faults 60

Stair-rod dislocations 66
Standard cubic projection 112
Static recrystallization 260
Stepanov A. V. 352
Stereographic projection 112
Stiffness 24, 28
Stokes R. J. 156
Stored strain energy 209
Strain ageing 144
Strain hardening 76, 110
Strain-induced migration 264
Strain-induced vacancies 33
Strain resistance 372
Strain softening 156
Sress field on a dislocation 40
Stress relaxation 142
Stress-strain curves 109
Stress to fracture 349
Stroh A. N. 353
Structural inhomogeneity 320
Sub-grain boundaries 80
Superdislocations 35, 408
Superlattice 86
Superplasticity 453
Surface defects 80
Suzuki atmosphere 79, 179, 391
Sviderskaya Z. A. 453
Symmetry group 231

Tarnovsky V. I. 402
Taylor G. I. 24, 201, 202
Taylor's theory of work hardening 166
Temperature level of recrystallization 284
Tensile textures 238
Tetrahedral void 17
Texture axis 220
Texture scatter 223
Texture strengthening 247
Texture transition 239
Theories of work hardening 166
Thermomechanical treatment 438
Thin-foil transmission microscopy 92
Third-order recrystallization diagrams 316
Thompson's reference tetrahedron 64
Tikhonov A. S. 437
Tooth-shaped boundaries 305
Transcrystalline fracture 348
Transmission electron microscopy of dislocations 92
Trefilov V. I. 10, 175, 179, 207, 208, 214, 218, 354
Tresca yield criterion 364
Tselikov A. I. 334
Tube texture 241
Twins 123
Twinning planes 123
Twinning 122

Unit dislocations 35, 59
Upsetting texture 221, 238

Vacancies 30
Vacancy discs 101
Van Bueren H. G. 252
Van der Waals forces 15
Verall R. A. 466, 468
Vladimirov V. I. 16, 29
Volterra's model of dislocations 40
Volume defects 90
Von Mises-Hencky criterion 364

Wassermann G. 249, 347
Weinblat Yu. M. 301, 307, 310, 312, 447
Wilman H. 140

X-ray diffraction analysis of textures 224
X-ray diffraction topography of dislocations 96

Yieldability 24
Yield elongation zone 78
Yield stress peak 78
Yokobori T. 354
Yufarov V. M. 419

Zaikov M. A. 377, 379, 381, 382, 402
Zaimovsky V. A. 29
Zasimchuk E. E. 298
Zavyalov A. S. 334
Zener C. 290
Zhdanov G. S. 298
Zonal inequigranularity 322

Printed in the Union of Soviet Socialist Republics

Prof. Petr I. POLUKHIN, D.Sc. (Eng.), Academician of the Academy of Sciences of the Kazakh SSR, Honoured scientist of the USSR, USSR State Prize winner, is a prominent authority in the theory and technology of plastic working of metals. His published works include many articles and a number of monographs, textbooks and study aids on plastic working of metals, in particular, on lengthwise and screw rolling. He heads the chair and laboratory of plastic deformation and hardening of metals and alloys at the Moscow Institute of Steels and Alloys.

Prof. Semen S. GORELIK, D.Sc. (Eng.), is a prominent specialist in physical metallurgy, materials science of semiconductors and X-ray structural analysis. He has published many articles and a number of monographs and textbooks on recrystallization of metals and alloys, materials science of semiconductors and ferrites, methods of structural analysis, and various effects on the structure and properties of inorganic materials. Prof. Gorelik heads the chair of materials science of semiconductors at the Moscow Institute of Steels and Alloys.

Prof. Vyacheslav K. VORONTSOV, D.Sc. (Eng.), USSR State Prize winner, is the author of numerous articles and four monographs on plastic deformation of metals and alloys and experimental methods of analysis of plastic deformation. He has been among the initiators of the advanced course of lectures on the physical principles of plastic deformation which is being delivered at the Moscow Institute of Steels and Alloys to specialists in plastic working of metals.

ABOUT THE PUBLISHERS

Mir Publishers of Moscow publish Soviet scientific and technical literature in sixteen languages—English, German, French, Italian, Spanish, Portuguese, Czech, Slovak, Finnish, Hungarian, Mongolian, Arabic, Persian, Hindi, Vietnamese and Tamil. Titles include textbooks for higher technical schools and vocational schools, literature on the natural sciences and medicine, including textbooks for medical schools, popular science and science fiction. The contributors to Mir Publishers' list are leading Soviet scientists and engineers in all fields of science and technology and include more than 40 Members and Corresponding Members of the USSR Academy of Sciences.

Skilled translators provide a high standard of translation from the original Russian. Many of the titles already issued by Mir Publishers have been adopted as textbooks and manuals at educational establishments in France, Switzerland, Cuba, Egypt, India, and many other countries.

Mir Publishers' books in foreign languages are exported by V/O "Mezhdunarodnaya Kniga" and can be purchased or ordered through booksellers in your country dealing with V/O "Mezhdunarodnaya Kniga"